LNCIS
Lecture Notes in Control and Information Sciences
362

Tzyh-Jong Tarn
Shan-Ben Chen
Changjiu Zhou (Eds.)

Robotic Welding, Intelligence and Automation

Springer

Lecture Notes
in Control and Information Sciences 362

Editors: M. Thoma, M. Morari

Tzyh-Jong Tarn, Shan-Ben Chen,
Changjiu Zhou (Eds.)

Robotic Welding, Intelligence and Automation

Springer

Editors

Tzyh-Jong Tarn

Cupples 2, Room 103
Campus Box 1040
Washington University
St. Louis, MS 63130
USA
Email: Tarn@wuauto.wustl.edu

Shan-Ben Chen

Institute of Welding Engineering
Shanghai Jiao Tong University
Shanghai, 200030
P.R. China
Email: sbchen@sjtu.edu.cn

Changjiu Zhou

Advanced Robotics and Intelligent
Control Centre (ARICC)
School of Electrical and
Electronic Engineering
Singapore Polytechnic
500 Dover Road
Singapore 139651
Singapore
Email: ZhouCJ@sp.edu.sg

Library of Congress Control Number: 2007927163

ISSN print edition: 0170-8643
ISSN electronic edition: 1610-7411
ISBN-10 3-540-73373-6 Springer Berlin Heidelberg New York
ISBN-13 978-3-540-73373-7 Springer Berlin Heidelberg New York

Typesetting: by the authors and SPS using a Springer LaTeX macro package

Printed on acid-free paper SPIN: 11898481 89/SPS 5 4 3 2 1 0

Preface

Robotic welding systems have been used in different types of manufacturing. They can provide several benefits in welding applications. The most prominent advantages of robotic welding are precision and productivity. Another benefit is that labor costs can be reduced. Robotic welding also reduces risk by moving the human welder/operator away from hazardous fumes and molten metal close to the welding arc. The robotic welding system usually involves measuring and identifying the component to be welded, welding it in position, controlling the welding parameters and documenting the produced welds. However, traditional robotic welding systems rely heavily upon human intervention. It does not seem that the traditional robotic welding techniques by themselves can cope well with uncertainties in the welding surroundings and conditions, e.g. variation of weld pool dynamics, fluxion, solid, weld torch, and etc. On the other hand, the advent of intelligent techniques provides us with a powerful tool for solving demanding real-world problems with uncertain and unpredictable environments. Therefore, it is interesting to gather current trends and to provide a high quality forum for engineers and researchers working in the filed of intelligent techniques for robotic welding systems. This volume brings together a broad range of invited and contributed papers that describe recent progress in this field.

This volume is mainly based on the papers selected from the 2006 International Conference on Robotic Welding, Intelligence and Automation (RWIA'2006), December 8-11, 2006, Shanghai, China, which was supported by the National Natural Science Foundation of China (NSFC) and the special fund for international conference of Shanghai Jiao Tong University. We have also invited some known authors as well as announced a formal Call for Papers to several research groups related to welding robotics and intelligent systems to contribute the latest progress and recent trends and research results in this field. The primary aim of this volume is to provide researchers and engineers from both academic and industry with up-to-date coverage of new results in the field of robotic welding, intelligent systems and automation.

The volume is divided into five logical parts containing sixty-four papers. In Part 1 (11 papers), the authors introduce the recent development of intelligent robotics. In Part 2 (18 papers), the authors deal with some intelligent techniques for robotic welding. In Part 3 (11 papers), the authors describe their work on vision sensing and intelligent control of arc welding processing. Various applications such as vision sensing and control of welding process are discussed. In Part 4 (8 papers), the authors present different applications of welding automation. Finally, in Part 5 (16 papers), the

authors introduce some emerging intelligent control techniques and their applications, which may contribute significantly to the further development of intelligent robotic welding systems.

We would like to thank Professors R. C. Luo, T. Fukuda, X.P. Yun, J.L. Pan, C.B. Feng, S.Z. Yang, B.S. Xu, S.Y. Lin, T.R. Wang, S.W. Xie, T.H. Song, L. Wu, Y.X. Wu for their kind advice and support to the organization of the RWIA'2006 and the publication of this book; to Drs Hongbo Ma, Fanhuai Shi, Xixia Huang, Jing Wu, Fenglin Lv for their precious time to devote all RWIA'2006 correspondences and to reformat and edit the most final submissions into the required format of the book; to Dr Lingyun Hu, Advanced Robotics and Intelligent Control Centre (ARICC) of Singapore Polytechnic, for her editorial assistance, last but not least to Dr. Thomas Ditzinger for his advice and help during the production phases of this book.

December 2006

Tzyh-Jong Tarn, Washington University at St. Louis, USA
Shan-Ben Chen, Shanghai Jiao Tong University, China
Changjiu Zhou, Singapore Polytechnic, Singapore

Contents

Behavior-Based Intelligent Robotic Technologies in Industrial Applications

Z.X. Gan[1], H. Zhang[2], and J.J. Wang[2]

[1] Robotics Department, ABB Corporate Research Center, Shanghai, P.R. China, 200131
[2] ABB Corporate Research, Windsor, CT, USA, 06095
Zhongxue.gan@cn.abb.com

Abstract. This paper gives a brief review on intelligent robotic technologies in industrial applications. The goal is not to conduct a thorough analysis of the state-of-art technologies, but rather to point out the directions for future technology development. Based on the market success of force control and machine vision in industry automation, this paper contends the arrival of the golden period of intelligent robotic technologies. The potential growth markets at present and in the near future are primarily assembly, and machining, where vision and force sensing continue to be the enabling technologies. As robot manufacturers start to embrace this technology wave, there are many technical challenges to be solved. The major problem for industrial R&D is how to safely and cost-effectively integrate sensor-driven functionalities with existing pure planning based position control system. For academic research, robust, efficient and effective sensor fusion and data mining methods should be the focus.

1 Introduction

It has been forty years since the first industrial robot called UNIMATE was online in a General Motors automobile factory in 1961. Automotive is still the primary industry for industrial robots, although its share has constantly decreased over the years as robots expand to general industries like plastics, food, consumer, and pharmaceutics. Worldwide, spot welding, arc welding, and material handling are still the dominant applications, where robots are mainly used to move materials, parts, tools, or specialized devices through various programmed motions. Contrary to the highly intelligent creatures described in science fiction, current industrial robots are deaf and dumb devices, working in a perfectly created and controlled environment. Expensive and often inflexible peripheral devices, such as conveyors, pallets, grippers and positioners, are the building elements of this well structured environment to provide accurate fixturing, tooling and positioning for the robot.

The unambiguousness of a structured environment provides unparallel repeatability, shorter cycle time and deterministic behavior of a robotized cell or line, at expense of cost and flexibility. Only large volume production can afford this kind of setup. This explains why the majority of current robot users are big revenue companies such as automotive manufacturers.

It is amazing that this approach dominates robotics industry since the birth of first industrial robot, while at the same period computer and sensor technologies have

T.-J. Tarn et al. (Eds.): Robot. Weld., Intellige. & Automation, LNCIS 362, pp. 1–12, 2007.
springerlink.com

advanced dramatically. It is until the beginning of 21st century automotive industries officially accepted sensor-assisted intelligent robots running on their production floors. The reception of Henry Ford Technology award by BrainTech's TrueView technology marks a historic turning point, the beginning of a golden period for intelligent robotic technologies.

2 Success of Machine Vision in Robotics Automation Marks the Start of the Golden Period for Intelligent Robotic Technologies

Unlike a LVDT sensor that can be immediately plugged and readily used, machine vision is one of the most complicated sensor technologies. Firstly it demands very stringent setup to ensure proper lighting, correct field of view and clean lens protection. Classic stories of early machine vision spoke of applications that were successfully installed at plants but failed when the season changed or sunlight came in a nearby window. Secondly, to get useful information from images, high computation power is needed. This explains why machine vision systems in 1980s and 1990s were often quite bulky and expensive. Thirdly, robust image processing algorithms are very difficult to design to suit different kinds of applications. A machine vision system often requires careful customization before the deployment.

With such complexity, it is not surprising that it took twenty years for vision technology to enter automotive production floor, although most of the theoretical advances that form the basis of modern industrial machine vision existed since 1980s. The recent history of machine vision is essentially the history of the adaptation of evolving computer technology to the commercialization of image processing for industrial automation. Vision system has become much faster, cheaper and smaller, but at the same time much simpler to use.

The success of machine vision in robotics automation is significant. It not only demonstrates that intelligent technologies are mature and ready to be used in industrial environment, but more importantly it refreshes the image of sensor based intelligent technologies, once perceived unreliable and costly by automation industry. The doors leading to huge amount of opportunities are now opened. As a result, one could declare that the success of machine vision in robotics automation marks the golden period of intelligent technologies.

Now days, once viewed largely as a way to save on labor costs, robots have taken on more significant roles in manufacturing with the growing intelligent capabilities. They have become part of global competitiveness plans, when manufacturing industry faces unprecedented cost pressure for outsourcing. North American manufacturing industry has realized, for tomorrow's manufacturing winners, the competitive determinant will be how robots fit into a total manufacturing/automation strategy -- not just labor cost. In this competition, sensor based intelligent technologies will play a vital role.

3 Current Successful Intelligent Robotic Technologies

Sensor based intelligent technologies, especially machine vision, have already achieved market successes in several applications, among which are seam tracking in welding application and vision-aided part locating in packaging applications.

3.1 Seam Tracking in Welding System

One of the earliest implementations of machine vision in robotics was in welding (Fig.1). Today welding vision has become important part of robotic welding system.

Fig. 1. Laser vision Seam Tracker™ from Meta vision systems (www.meta-mvs.com)

Seam Tracker™ is a laser seam tracking system designed for high performance applications such as spiral pipe manufacture and tailor welded blanks. Using data acquired from the sensor the control system will display joint geometry, the gap and mismatch as well as calculate the optimum lateral and vertical position of the weld torch.

Welding vision systems are generally based on structured light or range data collection. In the case of structured light-based systems, laser diodes are used to project a pattern of light at a preset angle in the shape of a single line, multiple lines or a cone of light yielding a projected circle. Triangulation mathematics determines the Z-axis data. In the case of the range data arrangement, a laser light sweeps across the joint of the part(s) being welded and the time it takes the laser to reflect to the 3-D camera head determines the location of the joint. In both cases, the systems eliminate all wavelengths of light associated with the welding process by using filters that only pass the wavelength of light associated with the lasers used.

The use of welding vision in robot welders helps compensate the positional inaccuracy in the robot manipulator, part fixture and tooling and the workpiece itself. Programming the robot to follow complex weld joint paths is also simplified as the vision system can adjust the path automatically. In addition to that, some vision systems can also measure the width and depth of welds for real time process monitoring and control.

Welding vision systems are a proven technology in spite of the harsh environment. The payback from using welding vision is better weld quality, higher productivity, lower production costs and less environmental impact.

3.2 Vision Guided Part Locating in Packaging Applications

Not other robotized application is as much dependent on machine vision as packaging. The products to be packed, cookies, fruits, pills or mails, are simply placed randomly on the conveyor. A robot, synchronized with continuously moving conveyor, locates the position and the orientation of each part through its vision

system, and then quickly picks it up and places into a carton. The use of machine vision system totally eliminates expensive and inflexible sorting machine and other positioning packages.

ABB's FlexPicker robot together with PickMaster software provides the perfect solution to any packing needs, as shown in Fig.2. The FlexPicker is an extremely versatile parallel-arm robot with a potential speed of more than 150 picks per minute (a cycle time of just 0.4 seconds). To pinpoint random objects, the PC-based software PickMaster uses a high performance robust vision system from Cognex (A company focus on machine vision). It identifies and transfers 360 degree random objects in 50 to 200 ms to the robot.

Fig. 2. Packing application using FlexPicker and vision system

4 Assembly, Guidance and Machining Are the Growth Markets

The industrial opportunities for intelligent robotic technologies are huge. The projected growth markets in the near future are primarily vision-based guidance, robotic assembly and machining.

4.1 Vision-Based Guidance Continues to Grow

BrainTech is the pioneer for vision-guided robot. Currently their products are mainly sold to automotive industry for the purpose of part locating. One such installation is in a transmission production plant, where BrainTech TrueView system guided an ABB robot to locate heavy transmission castings on pallets, moved the castings to a work area, and then picked up the empty dunnage and placed it on a conveyor. This vision guided robotic solution enables the end users to do away with expensive precision dunnage used in the past, and switch to inexpensive part trays instead.

According to the Automated Image Association, the market for vision-guided robots in material handling and assembly exceeds $2 billion per year on a global basis. Moreover, in 2000 the world machine vision market was $6.2 billion --- addressing just 10% of potential robotic applications --- with forecasted growth expected to exceed 20% per year through 2006.

4.2 Robotic Assembly Is Entering Powertrain Automation

Industrial robots have established their superiority over humans in most areas of manufacturing requiring endurance or repeatability. One important application domain, however, has so far lagged behind the industry's expectations: mechanical assembly. In automotive industry, assembling automotive powertrains is traditionally manual work, performed by skilled, experienced operators. Such operations, however, take their toll on human labor. Tedious and fatiguing, they can lead to repetitive-motion stress injury as well as lower product quality and efficiency. A robot, which is able to perform at the same level as a human operator, would obviously make the prospect of automation in this application area attractive.

As fast, precise and dependable as they are traditional industrial robots just not seems able to perform certain assembly operations as well as a skilled human worker. A task as simple as screwing a light bulb into a lamp socket shows why. Applying the right amount of force and turning the bulb at just the right time, at exactly the right angle, is something a human does intuitively. How can a robot be programmed to do this? For robots to successfully emulate humans on an assembly line, they need to have force-sensing capability and exhibit compliance. They must be able to direct forces and moments in a controlled way, and react to contact information.

Using admittance-based force control concept as a foundation together with advanced programming concepts such as search pattern and attraction force, ABB's engineers [1] developed intelligent assembly functions that integrate seamlessly with existing advanced motion system.

ABB's system has been successfully running on the automotive product floor, and convincingly demonstrated its ability to improve cycle time and agility in different assembly applications. In one application, F/N torque converters were assembled in an average time of 6.98 seconds with the contact force limited to 200 N (Fig.3).

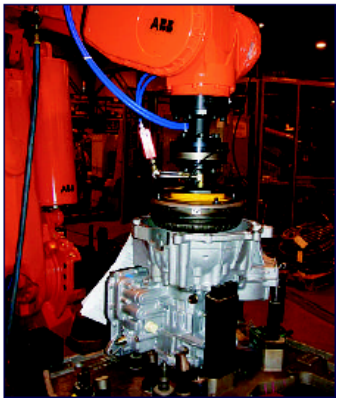

Fig. 3. F/N torque converter assembly with force controlled IRB6400. The part itself weighs about 25Kg. The allowed positional tolerance was +/- 2mm.

The initial market for intelligent assembly robot is powertrain applications, where hard automation machines and human workers are still the dominant labor forces. Major automakers start to introduce this new technology into their production lines.

With less than 30 such units currently on the production floor, the market potential is enormous. In powertrain applications alone, there are lots of opportunities as shown in Fig.4.

4.3 Robotic Machining Will Be the Next High-Valued Added Application

The automotive industry represents the fastest-growing market segment of the aluminum industry, due to the increasing usage of aluminum in cars. The drive behind this is not only to reduce the vehicle weight in order to achieve lower fuel consumption and improved vehicle performance, but also the desire for more sustainable transport and the support from new legislation. Cars produced in 1998, for example, contained on average about 85 Kg of aluminum. By 2005, the automotive industry will be using more than 125 Kg of aluminum per vehicle. It is estimated that aluminum for automotive industry alone will be a 50B$/year market.

Most of the automotive aluminum parts start from a casting in a foundry plant. The downstream processes usually include cleaning and pre-machining of the gating system and riser, etc., machining for high tolerance surfaces, painting and assembly. Today, most of the cleaning operations are done manually in an extremely noisy, dusty and unhealthy environment (Fig.5). Therefore, automation for these operations is highly desirable. However, due to the variations and highly irregular shape of the automotive casting parts, solutions based on CNC machining center usually presented a high cost, difficult-to-change capital investment.

To this end, robotics based flexible automation is considered as an ideal solution for its programmability, adaptability, flexibility and relatively low cost, especially for the fact that industrial robot is already applied to tend foundry machines and transport parts in the process. Nevertheless, the foundry industry has not seen many success stories for such applications and installations. Currently, more than 80% of the application of industrial robots is still limited to the fields of material handling and welding.

Machining processes, such as grinding, deburring, polishing, and milling are essential force tasks whose nature requires the end effectors to establish physical contact with the environment and exert a process-specific force. The inherent lower stiffness of the robot has presented many challenges to execute material removal applications successfully. The first one is the structure deformation and loss of accuracy due to the required machining force. As a result, a perfect robot program without considering contact and deformation will immediately become flawed as the robot starts to execute the machining task. Secondly, the lower stiffness presents a unique disadvantage for machining of casting parts with non-uniform cutting depth and width. In conventional robot programming and process planning practice, the cutting feed rate is constant even with significant variation of cutting force from part to part, which dictates a conservative cutting feed rate without violating the operational limits.

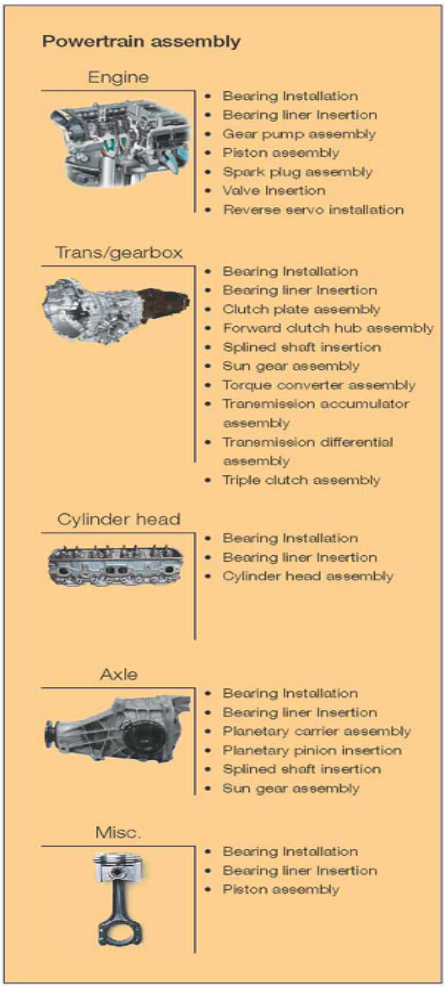

Fig. 4. Application map for assembly robot in the automotive industry

Fig. 5. Manual cleaning operations in a foundry plant

ABB engineers [2, 3] developed innovative yet practical methods to attack these challenges. Specifically, (1) to address deformation problem, stiffness modeling and real time deformation compensation are applied. Fig.6 compared the surface error before and after the deformation compensation, which clearly showed the improved surface accuracy of 0.5mm. (2) To address the inefficiency in machining parts with uneven cut depth and width, an intelligent control strategy was utilized to adjust the cutting feed rate based on the measured cutting force or spindle current. By optimizing the feed rate in real time, process variations can be compensated to help maximize material removal rate (MRR) and minimize cycle time (Fig.7).

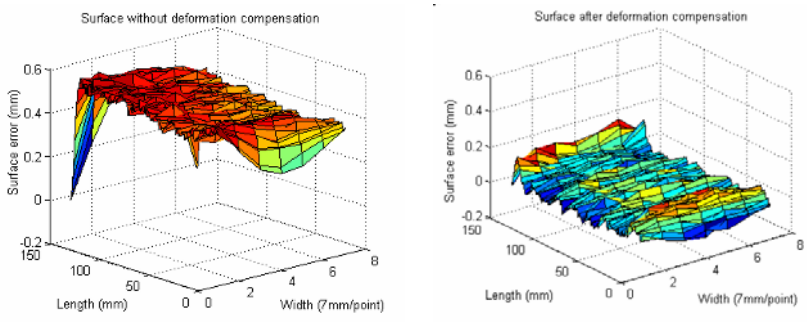

Fig. 6. Deformation compensation results

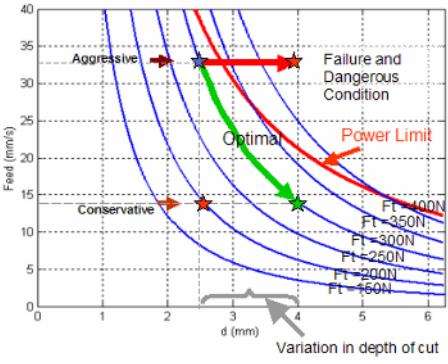

Fig. 7. Controlled material removal rate

A comprehensive utilization of intelligent sensor technologies across the entire machining process is found in ABB's another innovative project [5, 6, 7, 8] ---- turbine blade grinding and polishing system (Fig. 8).

This system was designed for high productivity, ease of use, flexibility on part variation, and excellent product quality in terms of dimensional accuracy and surface smoothness. Fig.9 shows the various components in the system. The work flow started with robot path generation from the CAD model using offline programming and simulation tool RobotStudio, followed by accurate calibration of work piece and grinding tool location with respect to the robot. The final quality check was then

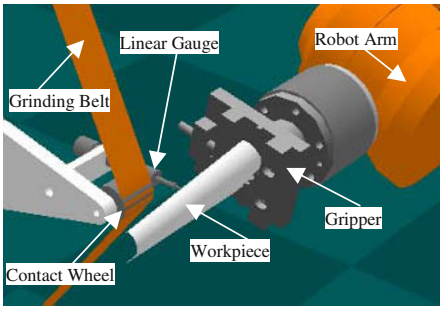

Fig. 8. Turbine blade griing system

performed on the selected locations of the blade to ensure dimensional accuracy. A high accuracy (±1mm) and high resolution (0.5mm) DB-G linear gauge with 25mm traveling range was used during the calibration and quality check phases. The so-called relative calibration, a patented technique from ABB [9] which only measures the difference of a blade relative to the golden piece, ensured the calibration was done quickly, economically and accurately. During the actual grinding and polishing phases, a force sensor mounted on the robot wrist provided force feedback to the robot controller for regulating the contact pressure acting on the blade.

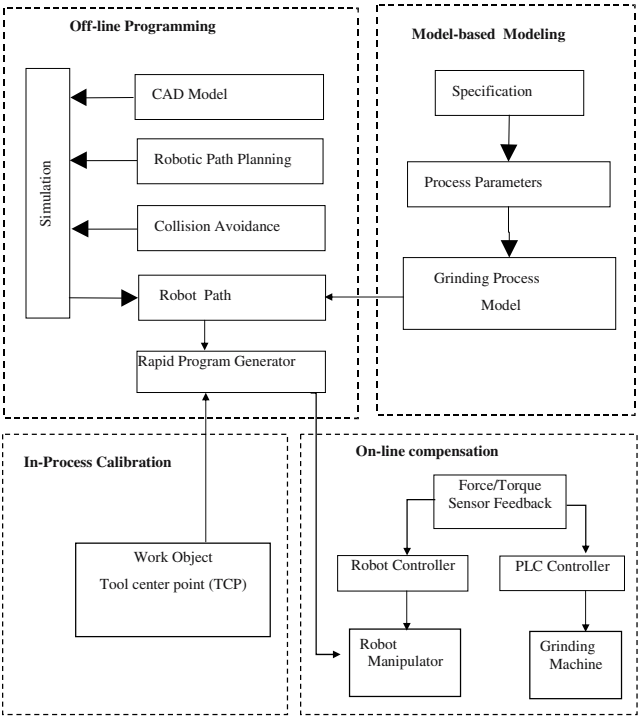

Fig. 9. Components of blade grinding and polishing system

5 Extensive R&D Efforts Needed to Ensure Market Success

The future growth markets for intelligent robotic technologies clearly show that vision and force, the two fundamental sensors for both human and intelligent machines, remain the focus of technology development. Intelligently applying these two sensing technologies for killer applications are the key to the market success.

Intelligent robotic technologies can roughly be divided into three sub domains: sensor technology, control & interface technology, and application specific process knowledge. Fig.10 shows an evaluation of these three sub domains.

5.1 Sensor Technology

The trend for machine vision system is to integrate everything on a networked, palm-sized embedded device known as vision sensor. Such miniature will greatly lower the cost and simplify the usage. While for force sensor, currently available products on the market are too expensive. This might be solved through massive production, but an innovative approach should also be pursued.

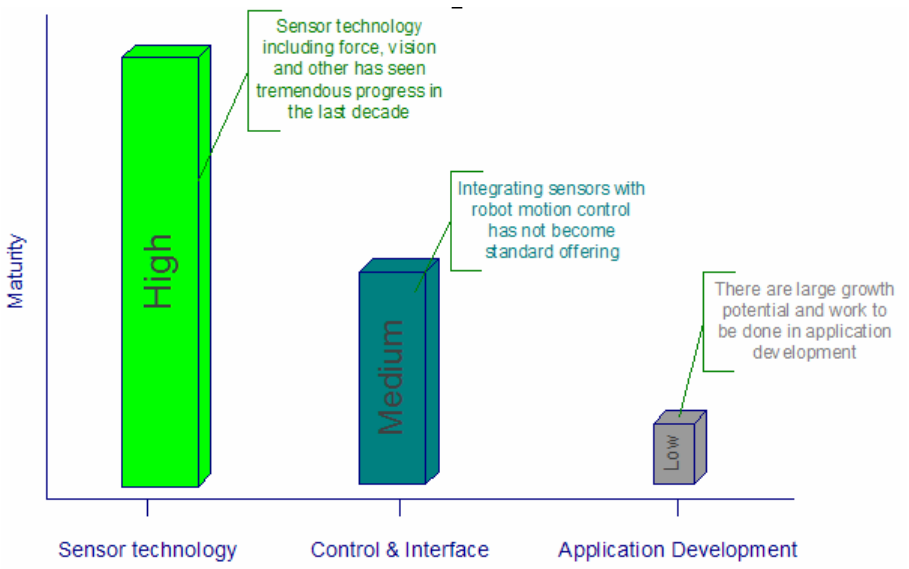

Fig. 10. Assessment of intelligent robotic technologies

5.2 Control and Interface

The majority of sense based intelligent systems on the current market, no matter it is machine vision system or assembly system, and is not tightly integrated with robot controller. The problem for this approach is that the performance is severely limited as most industrial robots only offer around 20Hz feedback loop through the programming interface. As a result, the robot cannot respond to the sensor

information quickly, resulting sluggish and sometimes unstable performance. Harmonically integrating sensor based control into existing complicated position system without compromising the safety and performance proves to be a difficult task.

Researchers from both academic world and robot manufacturers are looking for solutions that ultimately lead to the so-called open robot controller. Among others, the "open platform for skilled motions in productive robotics" [4], developed by Lund University in collaboration with ABB Robotics, provides the industrial robot with 250 Hz feedback loop in addition to meeting the industrial requirements regarding safety.

5.3 Application Specific Data Mining Techniques

Even a robot is equipped with machine vision and force sensor; there is huge gap between what a robot can do and what a human can do. This is major due to the lack of fundamental breakthrough of artificial intelligence. While this expects to be a long journey for human to pursue, application specific techniques, especially intelligent sensor fusion and data mining methods should be developed to make the industrial robots more adaptable to the industrial environment. Exemplar areas include interpretation of force signals to improve assembly performance, automatic program generation from human demonstration and intelligent fusion of force and vision information.

6 Conclusions

This paper gave a brief review of intelligent robotic technologies used in industry applications: the current successful applications and the future growth markets. To ensure future market success, extensive R&D efforts are needed in the areas of sensor technology, control technology and killer application development.

References

1. H. Zhang, Z. Gan, et al. Robotics technology in automotive powertrain assembly. ABB Review, vol.1, 2004.
2. Z. Pan, et al. Chatter analysis of robotic machining process. Journal of Materials Processing Technology, No. 173, 2006, pp301-309.
3. H. Zhang, et al. Machining with flexible manipulator: toward improving robotic machining performance. Proceedings of the IEEE/ASME International Conference on Advanced Intelligent Mechantronics (AIM), 2005.
4. A. Blomdel, et al. Extending an Industrial Robot Controller. IEEE Robotics & Automation Magazine, September, 2005.
5. A. Lindqvist, Z. Gan and Y. Sun. Interactive Program Generation for Air Foil Finishing with Blue Intelligence. Proceedings of the 32nd ISR (International Symposium on Robotics), 19-21 April 2001.

6. Y. Zhang, Z. Gan and Y. Sun. Force Sensor Based Calibration of Robot Grinding. ASME 2002 Design Engineering Technical Conferences and Computers and Information in Engineering Conference. September 29-October 2, 2002, Montreal, Canada.
7. J. Wang, Y.Sun, Z. Gan, et al. Process Modeling of Flexible Robotic Grinding. International Conference on Control, Automation, and Systems. 2003, Gyeongju, Korea.
8. J. Wang, Y.Sun, Z. Gan, et al. In-Process Relative Robot WorkCell Calibration. International Conference on Control, Automation, and Systems. 2003, Gyeongju, Korea
9. Z. Gan, Y.Sun and Q. Tang. In-process relative robot workcell calibration. United States Patent, Patent No. 6812665.

Detecting System Modeling and Hand-Eye Calibration for a Robot to Detect the Ablation of Hydro-turbine Blades

Wang Shenghua, Du Dong, Zhang Wenzeng, Chang Baohua, and Chen Qiang

Key Lab for Advanced Materials Processing Ministry of Education P.R. China
Dept. of Mechanical Engineering, Tsinghua Unicersity, Beijing 100084, China

Abstract. In order to detect the ablation on the hydro-turbine blade in the turbine room, a scheme of the ablation detecting by a robot under the operator's assistance was proposed. And the relevant system was designed. The system included two on-vehicle sensors and the computer and control center were located on the floor. The on-vehicle sensors included the laser range finder and the industry camera which were both fixed at a robot's end-link. The blade was observed through the camera. When an ablation was found, its dimensions could be measured by the system. A mathematic model of the robot and the laser range finder was constructed. Besides, to calibrate the homogeneous transformation matrix between the coordinates of robot's end-link and those of laser range finder, a calibration method by measuring a fixed point with different poses was proposed. Experimental results showed that the detecting scheme was appropriate for the turbine blade ablation detection, the model of the ablation detecting system was correct, and the proposed calibration method was effective.

1 Introduction

During the hydro-turbine rapid running, the overflowing part of the runner was damaged by the abrasion of silt and cavitation, therefore it should periodically be repaired[1]. As the running time of hydro-tubine in Three Gorges increases, the blades should periodically be detected and repaired if cavitation or abrasion (also called ablation together) was found. Before repairing the dimensions of the ablation should be measured, as shown in Fig.1. In order to reduce the labor intensity and to protect the repairers, it is necessary to replace the repairers with a detecting robot.

The shape of turbine blade is a complex spatial curved face, and the space between two blades is cabined, so it is hard to detect and measure the ablation in the turbine room. Though there are many methods for measuring the blade, for example, template method, theodolite method[2], three-coordinate measuring machine method, mechanical arm method[3], underwater photography method, robot spatial vision, telemeter method, and so on, most of them are not suitable for the robot to detect the blade ablation in the turbine room. A template should previously be prepared during the template method. The theodolite method and three-coordinates measuring machine method are suitable for measuring the shape of blade only when the turbine is lift out to the floor. Because it is a method of contact measure and it would cause a lager error, the mechanical arm method is not suitable either. And a matching point should be found in the images of the two cameras[4], but it is impossible to find them in the images of ablation blade.

T.-J. Tarn et al. (Eds.): Robot. Weld., Intellige. & Automation, LNCIS 362, pp. 13–20, 2007.
springerlink.com

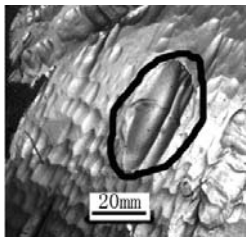

Fig. 1. The ablation of the blade of axial-flow hydro-turbine

So a scheme of detecting the ablation by a robot under the operator's assistance was proposed, base on analysis on the requirements for ablation detection and researches on robot detecting technology. The relevant system was then designed. And in this paper the modeling of the system was conducted, and a calibration method was proposed to calibrate the robot hand-eye.

2 Inner Detecting System for the Ablation of Hydro-turbine Blades

2.1 The Composition of the System

It is a detecting system which detects the ablations under the control of an operator. It is constructed with a mobile robot platform and a multiple-degree-freedom arm fixed on the platform. And it includes two parts, as shown in Fig.2. One is the on-vehicle sensors which are fixed at the robot's end-link. The other is the computer and control center which is located on the floor. The on-vehicle sensors include an industry camera to observe the blade surface, and a laser range finder to measure the pattern of the blade with the robot. The computer and control center would communicate with the on-vehicle sensors, the mobile robot platform and the arm, control the movements of the platform and the arm, process the data of the sensors and the robot, and show the graphic results on the display.

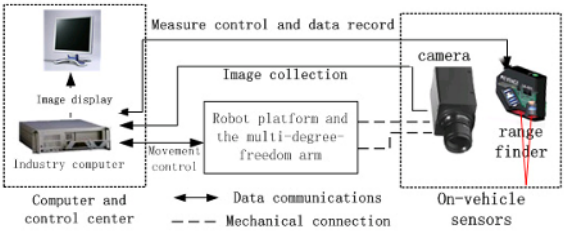

Fig. 2. The composition of the detecting system

2.2 The Working Process and the Function of the Detecting System

During the detecting process, the operator gives orders to move the robot to one position of the blade, to change the pose of the arm so that the blade surface can be suitably observed and the ablation could be measured. By reason of the multiple-degree-freedom arm, a large part of blade surface can be observed and detected. When detection at this position has finished, the operator can move the robot to another position and repeat the detecting process. With this detecting system, the type, position, area, and depth of the ablation can be measured. It offers the basic parameters for the blade repair. And the measurement of the ablation depth and the area is the most important process.

When the measurement is operated with the arm at some pose, the laser range finder is pointed to the blade surface. Then the system records the data of the range finder and the arm pose, and transmits them to the computer and control center. There, the data are processed by the mathematical model based the robot kinematics, and the coordinate of the measured point under a fixed coordinate system. After multiple points are measured under a given rule, the depth and area of the ablation, even the local pattern of the blade can be gained. Further more, utilizing the robot position technology and the surface reconstruction technology[5], the total pattern of the blade can be reconstructed.

3 The Mathematical Model of the Detecting System

3.1 The Model of the On-Vehicle Sensors and the Multiple-Degree-Freedom Arm and Their Coordinate System

The on-vehicle sensor — the laser range finder and the industry camera are fixed at the end of the multiple-degree-freedom arm, as shown in Fig.3. The mobile platform stops on the blade, with the arm at different poses. The data of the range finder and the arm pose are recorded. In order to get the relationship of the different points, the mathematical model should be constructed, and the range finder's pose relative to the robot's end-link should also be calibrated in advance. And first of all, the coordinate systems should be constructed.

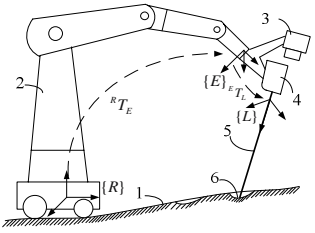

1-blade; 2-mobile platform and multiply-degree-freedom arm;

3-camera; 4- laser range finder; 5-laser; 6-ablation pit

Fig. 3. The on-vehicle sensors and the robot

The coordinate systems of the robot base, the end-link, and the laser range finder are constructed, as shown in Fig.3:

$\{R\}$——the coordinate system fixed at the robot mobile platform,
$\{E\}$——the coordinate system fixed at the arm's end-link,
$\{L\}$——the coordinate system of the range finder, the initial point locate on the laser beam, the Z-axis is set along the laser beam and pointing to the measured point, and the X-axis and Y-axis whose directions are optional, are located in the plane vertical to the Z-axis.

Suppose there is a point M on the blade surface, and ${}^{L}\mathbf{p}_{M}$ is the coordinate under the coordinate system $\{L\}$, ${}^{R}\mathbf{p}_{M}$ is the one under $\{R\}$. According the robot kinematics, the follow equation can be established:

$$ {}^{R}\mathbf{p}_{M} = {}^{R}\mathbf{T}_{E}\,{}^{E}\mathbf{T}_{L}\,{}^{L}\mathbf{p}_{M} \tag{1} $$

while the ${}^{R}\mathbf{T}_{E}$ is the homogeneous transformation matrix between coordinate systems $\{E\}$ and $\{R\}$, which can be calculated out with the pulsed coordinate of the arm's pose, and the ${}^{E}\mathbf{T}_{L}$ is the relation between the range finder's pose and the robot's end-link, which is needed to be calibrated. It is usually called hand-eye calibration[6].

Then, if we find an ablation pit, we can measure some point of the pit. Though the equations (1), we can get some reference pionts of the pit, and then know the depth, the area and even the dimesion of the pit by some mathematic methods.

3.2 Calibration Method for the Robot's End-Link and the Laser Range Finder

In order to calibrate the relation between the robot's end-link and the laser range finder, a calibration method by measuring a fixed point with different poses (FPDP method), is proposed as follows: (1) operate the robot to measure a point, let the reticle of the point at the center of the laser spot, then record the data of the range finder—the distance, and the pulsed coordinate of the arm pose; (2) change the pose of the arm, measure the same point and record the data; (3) repeat step (2); (4) construct a system of equations with the element of the ${}^{E}\mathbf{T}_{L}$ as the unknown number using the parameters get above, calculate it by utilizing the least-squares principle, and then the ${}^{E}\mathbf{T}_{L}$ can been calibrated.

When the same point M is measured at the different poses, a series of data are recorded, the coordinate of the point under the $\{L\}$ and the robot pulsed coordinate c_{ij}, while $(i=1,2,\cdots,n;\ j=1,2,\cdots,m)$. The ${}^{R}\mathbf{T}_{E}$ —the homogeneous transformation matrix between coordinate systems $\{E\}$ and $\{R\}$, can be calculated out with the c_{ij} by utilizing robot kinematics [7]. Because the range finder is fixed at the end-link, the matrix ${}^{E}\mathbf{T}_{L}$ needed to be calibrated keeps constant, no matter how the arm pose changes. The matrix ${}^{E}\mathbf{T}_{L}$ is supposed as follows:

$$ {}^{E}\mathbf{T}_{L} = \begin{bmatrix} r_{11} & r_{12} & r_{13} & t_1 \\ r_{21} & r_{22} & r_{23} & t_2 \\ r_{31} & r_{32} & r_{33} & t_3 \\ 0 & 0 & 0 & 1 \end{bmatrix} = \begin{bmatrix} \mathbf{r}_1 & \mathbf{r}_2 & \mathbf{r}_3 & \mathbf{t} \\ 0 & 0 & 0 & 1 \end{bmatrix}. $$

As a result, a series of equations (2) are gained.

$$ {}^{R}\mathbf{p}_{M} = {}^{R}\mathbf{T}_{Ei}\,{}^{Ei}\mathbf{T}_{Li}\,{}^{Li}\mathbf{p}_{Mi} = {}^{R}\mathbf{T}_{Ei}\,{}^{E}\mathbf{T}_{L}\,{}^{Li}\mathbf{p}_{M}, \qquad (i=1,2,\cdots,n). \tag{2} $$

The left part of the equations (2) is the coordinate of the same point M under the coordinate systems $\{R\}$, so the right part of the equations (2) are equal to each other.

$$ {}^{R}\mathbf{T}_{Eb1}\,{}^{E}\mathbf{T}_{L}\,{}^{Lb1}\mathbf{p}_{M} = {}^{R}\mathbf{T}_{Eb2}\,{}^{E}\mathbf{T}_{L}\,{}^{Lb2}\mathbf{p}_{M}, \quad (b1,b2=1,2,\cdots,n; b2\neq b1). \tag{3} $$

Replace the matrix ${}^{E}\mathbf{T}_{L}$ in (3), the Equ.3 can be deduced as:

$$ \left(d_{b2}\mathbf{R}_{b2}-d_{b1}\mathbf{R}_{b1}\right)\mathbf{r}_3+\left(\mathbf{R}_{b2}-\mathbf{R}_{b1}\right)\mathbf{t}=\mathbf{t}_{b1}-\mathbf{t}_{b2}, \quad (b1,b2=1,2,\cdots,n; b2\neq b1). \tag{4} $$

The Equs.4 can be rewritten as matrix:

$$ \mathbf{A}\mathbf{x}=\mathbf{c}, \tag{5} $$

while, $\mathbf{A}=\begin{bmatrix} d_2\mathbf{R}_2-d_1\mathbf{R}_1 & \mathbf{R}_2-\mathbf{R}_1 \\ \vdots & \vdots \\ d_{m1}\mathbf{R}_{m1}-d_{m2}\mathbf{R}_{m2} & \mathbf{R}_{m1}-\mathbf{R}_{m2} \\ \vdots & \vdots \\ d_n\mathbf{R}_n-d_{n-1}\mathbf{R}_{n-1} & \mathbf{R}_n-\mathbf{R}_{n-1} \end{bmatrix}$, $\mathbf{c}=\begin{bmatrix} \mathbf{t}_2-\mathbf{t}_1 \\ \vdots \\ \mathbf{t}_{m1}-\mathbf{t}_{m2} \\ \vdots \\ \mathbf{t}_n-\mathbf{t}_{n-1} \end{bmatrix}$, $\mathbf{x}=\begin{bmatrix}\mathbf{r}_3\\ \mathbf{t}\end{bmatrix}$,

$(m1,m2=1,2,\cdots,n; m2>m1)$.

Then the vector $\mathbf{r}_3$ and $\mathbf{t}$ of the matrix ${}^{E}\mathbf{T}_{L}$ can be solved out from Equs.5 by utilizing the least-squares principle. So the matrix ${}^{E}\mathbf{T}_{L}$ can be rewritten as:

$$ {}^{E}\mathbf{T}_{L}=\begin{bmatrix} * & * & \mathbf{r}_3 & \mathbf{t} \\ 0 & 0 & 0 & 1 \end{bmatrix}. \tag{6} $$

The vector $\mathbf{r}_1$ and $\mathbf{r}_2$ are unnecessary to solve, because the coordinate of the point M under the $\{L\}$ is ${}^{L}\mathbf{p}_{M}=[0 \;\; 0 \;\; d \;\; 1]^{T}$, the first two elements of which are zero. It also proves that it is unnecessary to set the direction of X-axis and Y-axis of the coordinate system $\{L\}$.

3.3 The Depth Measurement of the Ablation Pit

The depth measurement of the ablation pit is a major problem of the ablation detecting of hydro-turbine blade. In order to increase the detecting efficiency, a simplified method is proposed. Because the area of the ablation pit is usually small, the blade surface around the pit could be considered as a plane. So the depth measurement of the ablation pit can be operated as follows.

Firstly, measure a point M at the bottom of the ablation pit and more than three points Q_i $(i=1,2,\cdots,n)$ which are around the pit and not collinear, shown as Fig.4, then record the data of the pulsed coordinate of the arm pose and the range finder, and finally, calculate out the coordinate of the points under the $\{R\}$ system:

$$ {}^{R}\mathbf{p}_j = {}^{R}\mathbf{T}_{Ej}\,{}^{E}\mathbf{T}_L\,{}^{Lj}\mathbf{p}_j = {}^{R}\mathbf{T}_{Ej}\left(d_j \begin{bmatrix} \mathbf{r}_3 \\ 0 \end{bmatrix} + \begin{bmatrix} \mathbf{t} \\ 1 \end{bmatrix} \right), \tag{7} $$

while j is M, Q_1, Q_2, …, Q_n,

${}^{R}\mathbf{T}_{Ej}$ is the homogeneous transformation matrix of the robot,
${}^{E}\mathbf{T}_L$ is hand-eye calibration result of the robot,
${}^{Lj}\mathbf{p}_j = [0 \quad 0 \quad d_j \quad 1]^T$ is the result of the laser range finder.

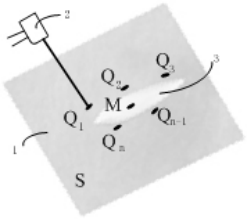

1-blade surface; 2-range finder; 3-ablation pit

Fig. 4. The depth measurement of the ablation pit

It is obviously that a plane can exclusively be defined through three points that are not collinear. Then a plane S can be defined though the points Q_1, Q_2, …, Q_n by utilizing least-squares principle. Therefore, the depth of the ablation pit can defined with the distance between point M and plane S.

4 Experiments and Results

4.1 The Hand-Eye Calibration Experiment

The hand-eye calibration experiment was carried out by utilizing the FPDP calibration method. The Motoman-SK6 which is a six-axes industrial robot, and the FT50RLA220 which is a laser range finder with an operation range of 80~300 mm and the resolution of 0.2 mm are used. The parameters recorded during the process are shown as Tab.1. The pulsed coordinate of the arm is the parameters of the homogeneous transformation matrix of the robot ${}^{R}\mathbf{T}_{Ej}$, and the distance is d in the equation(5). Then the result is as follows:

$$ \mathbf{r}_3 = [-0.0373,\ 0.2162,\ 0.9771]^T, $$

$$ \mathbf{t} = [60.79,\ -107.90,\ 158.60]^T. $$

Table 1. The parameters of the hand-eye calibration

No.	Pulsed coordinate of the arm	distance/mm
1	3537, 86280, -86712, 12419, 31818, 2146	127.6
2	2953, 90224, -88144, 13089, 31786, 2272	104.5
…	…	…
24	2785, 85616, -87112, 10869, 32266, 2125	128.3

4.2 The Experiment of Pit Depth Measurement

The experiment of pit depth measurement was carried out based on the result of the above calibration experiment and the pit depth measure method proposed in Section.3.3. In the experiment a pit 26.00 mm deep was used, which was measured by vernier caliper as a true value. The result of the experiment shows that the maximum error is 0.3 mm, as shown in Fig.5.

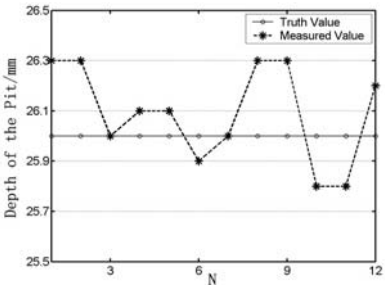

Fig. 5. The result of the pit depth measurement experiment

The experimental results show that the model of the ablation detecting system is appropriate, that the FPDP method of hand-eye calibration is effective, and the ablation pit measurement is of high accuracy. It also proves that the scheme is suitable to the ablation detecting on the hydro- turbine blade in the turbine room.

5 Conclusion

In this paper, a scheme of the ablation detecting by a robot under the operator's assistance was proposed, so that the ablation on the hydro-turbine blade could be detected by robot in the turbine room. And the relevant system was designed. The system included a laser range finder and an industry camera which were fixed at the robot's end-link, and the computer and control center which is located on the floor. The mathematic model of the robot and the laser range finder was constructed. Besides, the homogeneous transformation matrix between the coordinates of the

robot's end-link and the laser range finder was calibrated. Experimental results showed that the detect scheme was effective for the turbine blade ablation detection and the FPDP calibration method was effective.

References

1. Liang Wuke, Liao Weili, Luo Xingqi. Cavitation abrasion of Hydraulic Turbine in Silt laden Flow. JOURNAL OF HYDROELECTRIC ENGINEERING, 1998, 62(3): 78~83
2. LAI Xi-de. CNC Machining Technology with 5-Axis Simultaneous Operation for X-Shape Blade of Francis Hydraulic Turbine. O. I. Automation, 2001, 20(3): P40~43
3. HUANG Zhi xiong, HE Qing hua, WU Wan rong, et al. Kinematics analysis of field measuring manipulator of large turbine blades. Journal of Central South University of Technology(Natural Science), 2003, 34(2): P170~174
4. ZHANG Ai wu, LI Ming zhe, HU Shao xing. New stereo precise matching method for 3D surface measurement with computer vision. Optical Technology. 2001,27(2):P115~117
5. YANG Guijun, LIU Qinhuo, WU Wenbo. Research on 3D Laser Scan Surface Reconstruction Algorithms. Chinese Journal of Scientific Instrument. 2005, 26(11): P1181~1183
6. LU Jianfeng, TANG Zhenmin, YANG Jingyu, et al. The associated calibration method of multiple sensors[J]. Robot, 1997, 19(5): 365－371.
7. WANG Tingshu. Robot Kinematics and Dynamics [M]. 1990.

Dynamic Model and Control for an Omnidirectional Mobile Manipulator

Dong Xu, Dongbin Zhao, and Jianqiang Yi

Key Lab of Complex Systems and Intelligence Science,
Institute of Automation, Chinese Academy of Sciences P.O. Box 2728,
Beijing 100080, P.R. China
dong.xu@ia.ac.cn

Abstract. Mobile manipulation is a key capability to many robotic applications in construction, space, underwater, nuclear plant and home services. Dynamic modeling and trajectory control for a holonomic omnidirectional mobile manipulator are principle problems for mobile manipulation, and are presented in this paper. Considered the redundantly-actuated property of omnidirectional mobile platform, the kinematic model of the whole mobile manipulator is presented. Then, an integrated dynamic model for the system is developed by the kinematic model and Lagrangian formalism. According to the dynamic model, a modified inverse dynamic control is addressed to track the trajectories of the mobile platform and end-effector simultaneously. Then, the simulations results show the effectiveness of the proposed modeling and control approach.

1 Introduction

Mobile manipulator is generally regarded as a manipulator mounted on a moving platform. Due to the mobility of the platform, this system can perform manipulations in a much larger workspace than a fixed manipulator. The mobile manipulator's advantage is significantly decided by the properties of the moving platform which is a mobile robot in essence. Since the omnidirectional mobile robot can fully use the null space motions to improve the workspace and overall dynamic endpoint properties, lots of literatures were devoted to the problems of modeling and control of an omnidirecitonal mobile robot. The problem of modeling, control of omnidirectional mobile robot in general case are analyzed an d addressed in [1,2,4]. The kinematic model and dynamic model of an omnidirectional mobile robot with three castor wheels are presented in [3,10]. Holmberg and Khatib [7] developed a holonomic mobile robot and presented a dynamic control method for a parallel redundant system.

In recent years, the studies on mobile manipulator with both mobile ability and manipulating function are very attractive because they can contribute to the flexible automation in factory and the assistance of life. Among them, some studies [5,6,14] proceeded on a manipulator with a mobile platform. However, most of the mobile manipulators studied adopt a nonholonomic mechanism system; the movable scope of the platform must be taken into account for setting of desired trajectory. For this reason, Khatib studied a holonomic mobile manipulator and proposed several control strategies for a coordinative task using multiple mobile manipulators [8]. Watanabe [9] analyzed the dynamic modeling, control and tracking problem of an

T.-J. Tarn et al. (Eds.): Robot. Weld., Intellige. & Automation, LNCIS 362, pp. 21–30, 2007.
springerlink.com

omnidirectional mobile manipulator whose platform consist of three lateral orthogonal wheels. Egerstedt and Hu [12] addressed coordinated trajectory planning and following problem by the inverse kinamatic model. On account of the holonomic mechanisms design, the control researches were mainly conducted from kinematic perspective. But without dynamic control, it is difficult to perform coordinated motion of the mobile platform and the dynamically controlled manipulator. Because of the complex coupling effect between the platform and manipulator, Tan and Xi [11] regarded the integrated system as a redundant robot arm and proposed a unified model approach for planning and control of the mobile manipulator. However, the redundantly-actuated property of the platform was not emphasized and integrated dynamic model of the omnidirecitonal mobile manipulator derived from the driving wheels was not explicitly addressed.

This paper addresses the explicit dynamic modeling and trajectory tracking control of a mobile manipulator with a redundantly-actuated platform. Based on the kinematic model of the omnidirectional mobile platform, the kinematic model of the mobile manipulator is obtained by the geometric characteristic in section2. Simultaneously taking account of the features of the mobile platform and the manipulator, dynamic model of the integrated system is derived in section 3 by the kinematic model and Lagrangian formalism. In section 4 a modified inverse dynamic controller is designed to track the trajectories of the platform and manipulator in phase. The effectiveness of the dynamic model and the tracking control is verified in section 5 by the simulation results. Finally, we reach the conclusions.

2 Kinematic Model

The mobile manipulator addressed here moves on a fixed plane which is OXY in the global frame. It is cylinder-shaped; three identical castor wheels are axed symmetrically on the bottom of the platform and manipulator arm which has one degree of freedom locates on the gravity center of the platform, as shown in Fig. 1. Each wheel module has two motors and the platform is redundantly driven by six motors to accomplish omnidirectional motion.

The angle between two neighboring wheels is $2\pi/3$. *Wheel* 1, 2, 3 are assigned clockwise to indicate the three wheels. *C* is the gravity center of the platform. In the global frame OXY, the platform position (*x*, *y*) can be represented by the position of *C*. The orientation of the platform can be denoted by θ, which is the angle between the axis OX and the line crossing *C* and the center of the vertical axis of *Wheel* 1. Thus the pose of the platform can be represented by $\xi = (x, y, \theta)^T$ .In addition, (x_A, y_A) is the coordinate of the link center in OXY and l is the length of the link. θ_1 is the angle displacement of the link.

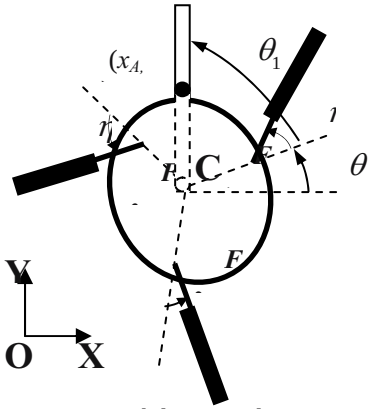

Fig. 1. Mobile manipulator

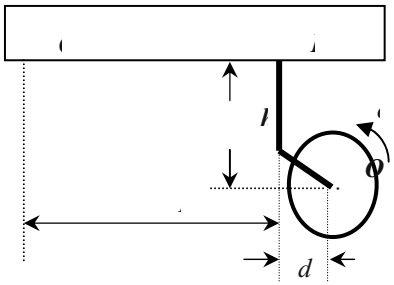

Fig. 2. Side view of *Wheel* i

The side-view of the wheel module is shown in Fig.2. The radius of each wheel is *r* and the horizontal distance between *C* and the center of the vertical axis of each wheel that is indicated by F_i is *D*. The offset *d* is the horizontal distance between the center of each wheel O_i and F_i. The angle displacements for wheel rolling and steering are φ_i and η_i, respectively. Then with the assumption of no-slip, the kinematic model of *Wheel i* can be derived as

$$\begin{bmatrix} \dot{x} \\ \dot{y} \\ \dot{\theta} \end{bmatrix} = J_i(\beta_i, \theta) \begin{bmatrix} \dot{\varphi}_i \\ \dot{\eta}_i \\ \dot{\theta} \end{bmatrix} \tag{1}$$

$$J_i(\beta_i, \theta) = \begin{bmatrix} -r\cos\beta_i & d\sin\beta_i & D\sin(\alpha_i + \theta) + d\sin\beta_i \\ -r\sin\beta_i & -d\cos\beta_i & -D\cos(\alpha_i + \theta) - d\cos\beta_i \\ 0 & 0 & 1 \end{bmatrix} \tag{2}$$

where $\beta_i = \alpha_i + \eta_i + \theta$ is the orientation of *Wheel i* in the global frame OXY, $\alpha_1 = 0, \alpha_2 = -2\pi/3, \alpha_3 = 2\pi/3$.

For the sake of achieving the mobile manipulator's kinematic model, the six drive motors' speeds of the mobile platform are computed by the inverse matrix of $J_i(\beta_i, \theta)$. Then, considering the motion of the manipulator, the kinematic relation of the whole system can be described as

$$J_i^{-1}(\beta_i, \eta_i) = \begin{bmatrix} -\frac{1}{r}\cos\beta_i & -\frac{1}{r}\sin\beta_i & -\frac{d}{r}\sin\eta_i \\ \frac{1}{d}\sin\beta_i & -\frac{1}{d}\cos\beta_i & -\frac{D}{d}\cos\eta_i - 1 \\ 0 & 0 & 1 \end{bmatrix} \tag{3}$$

$$\dot{\varepsilon} = J_\gamma(\beta,\eta)\dot{\gamma} \tag{4}$$

$$J_\gamma(\beta,\eta) = \begin{bmatrix} -\frac{1}{r}\cos\beta_1 & -\frac{1}{r}\sin\beta_1 & -\frac{D}{r}\sin\eta_1 & 0 \\ \frac{1}{d}\sin\beta_1 & -\frac{1}{d}\cos\beta_1 & -\frac{D}{d}\cos\eta_1 - 1 & 0 \\ -\frac{1}{r}\cos\beta_2 & -\frac{1}{r}\sin\beta_2 & -\frac{D}{r}\sin\eta_2 & 0 \\ \frac{1}{d}\sin\beta_2 & -\frac{1}{d}\cos\beta_2 & -\frac{D}{d}\cos\eta_2 - 1 & 0 \\ -\frac{1}{r}\cos\beta_3 & -\frac{1}{r}\sin\beta_3 & -\frac{D}{r}\sin\eta_3 & 0 \\ \frac{1}{d}\sin\beta_3 & -\frac{1}{d}\cos\beta_3 & -\frac{D}{d}\cos\eta_3 - 1 & 0 \\ 0 & 0 & 0 & 1 \end{bmatrix} \tag{5}$$

where $\varepsilon = [\varphi_1 \quad \eta_1 \quad \varphi_2 \quad \eta_2 \quad \varphi_3 \quad \eta_3 \quad \theta_1]^T$, $\gamma = [x \quad y \quad \theta \quad \theta_1]^T$, $\beta = [\beta_1 \quad \beta_2 \quad \beta_3]^T$, $\eta = [\eta_1 \quad \eta_2 \quad \eta_3]^T$.

3 Dynamic Model

In order to obtain the dynamic model of the omnidirectional mobile manipulator, the Lagrange formalism is applied. Define $\zeta_i = [\varphi_i, \eta_i]$, $i = 1,2,3$, $P_i(\beta)$ is the Jacobian matrix from $\dot{\zeta}_i$ to the speed of the bracket support point F_i, $\vec{V}_{F_i}$, and Q_i be the Jacobian matrix from the speed of the platform $\dot{\xi}_i$ to $\vec{V}_{F_i}$. Thus the dynamic model can be deduced by

$$\begin{aligned} &\frac{d}{dt}\frac{\partial K_{\zeta_i}}{\partial \dot{\zeta}_i} - \frac{\partial K_{\zeta_i}}{\partial \zeta_i} = \tau_i - \tau_{d_i} - P_i^T(\beta_i) f_i \\ &\frac{d}{dt}\frac{\partial K_C}{\partial \dot{\gamma}} - \frac{\partial K_C}{\partial \gamma} = B^T \tau_\gamma \\ &Q_i \ddot{\xi} + \dot{Q}_i \dot{\xi} = P_i \ddot{\zeta}_i + P_i \ddot{\zeta}_i \end{aligned} \tag{6}$$

where $\tau_i = [\tau_{ir}, \tau_{is}]^T$ represents the torques produced by the rolling and steering motors of *Wheel* i. τ_{d_i} is the torque caused by disturbances or generated by frictions. $\tau_\gamma = [f \quad \tau_{link}]^T$ represents the interaction forces and torque of the mobile manipulator respectively.

The Jacobian matrix from $\vec{V}_{F_i}$ to $\dot{\zeta}_i$ is

$$P_i^+ = \begin{bmatrix} -\frac{1}{r}\cos\beta_i & -\frac{1}{r}\sin\beta_i & 0 \\ \frac{1}{d}\sin\beta_i & -\frac{1}{d}\cos\beta_i & -1 \end{bmatrix} \tag{7}$$

Define P_i is a general inverse of P_i^+. Due to $\dot{\theta}$ being coupled with $\dot{\eta}_i$, P_i is a variable structure Jacobian matrix from $\dot{\zeta}_i$ to $\vec{V}_{F_i}$. As we analyzed before, omnidirecitonal platform has universal mobility in the plane. Therefore, even the platform orientation θ keeps constant; we can drive the platform to anywhere. If $\theta \equiv \theta_0$ and then $\dot{\theta}$=0, the problem of variable structure Jacobian matrix will be eliminated.

Assume $\dot{\theta}$=0, the kinematic of the mobile manipulator will be simplified and the (5) can be expressed as

$$J_\gamma(\beta) = \begin{bmatrix} -\frac{1}{r}\cos\beta_1 & -\frac{1}{r}\sin\beta_1 & 0 \\ \frac{1}{d}\sin\beta_1 & -\frac{1}{d}\cos\beta_1 & 0 \\ -\frac{1}{r}\cos\beta_2 & -\frac{1}{r}\sin\beta_2 & 0 \\ \frac{1}{d}\sin\beta_2 & -\frac{1}{d}\cos\beta_2 & 0 \\ -\frac{1}{r}\cos\beta_3 & -\frac{1}{r}\sin\beta_3 & 0 \\ \frac{1}{d}\sin\beta_3 & -\frac{1}{d}\cos\beta_3 & 0 \\ 0 & 0 & 1 \end{bmatrix} \tag{8}$$

It is easy to deduce that rank $J_\gamma(\beta)$=3. This special property implies that the left Moore-Penrose inverse matrix of $J_\gamma(\beta)$ can be described as

$$J_\gamma^{++}(\beta) = J_\gamma(\beta)[J_\gamma^T(\beta)J_\gamma(\beta)]^{-1} \tag{9}$$

The dynamic equations can be simplified and rewritten in compact matrix form as

$$\begin{aligned} &M_\zeta \ddot{\zeta} = \tau - \tau_d - P^T(\beta) f \\ &M_C(\gamma)\ddot{\gamma} + V_C(\gamma,\dot{\gamma})\dot{\gamma} = B^T\tau_\gamma \\ &Q\ddot{\xi} = \dot{P}\dot{\zeta} + P\ddot{\zeta} \end{aligned} \tag{10}$$

where $\gamma = [x \quad y \quad \theta_1]^T$, $\xi = [x \quad y]^T$, $\zeta = [\varphi_1 \quad \beta_1 \quad \varphi_2 \quad \beta_2 \quad \varphi_3 \quad \beta_3]^T$. The Jacobian matrixes, inertial matrixes and centrifugal and coriolis matrix are as follows.

$$P^T = \begin{bmatrix} P_1^T & & \\ & P_2^T & \\ & & P_3^T \end{bmatrix}, P_i = \begin{bmatrix} -r\cos\beta_i & d\sin\beta_i \\ -r\sin\beta_i & -d\cos\beta_i \end{bmatrix}$$

$$B^T = \begin{bmatrix} I_2 & I_2 & I_2 & 0_{2\times1} \\ 0_{1\times2} & 0_{1\times2} & 0_{1\times2} & I_1 \end{bmatrix}, Q^T = [I_2 \quad I_2 \quad I_2]$$

$$M_C = \begin{bmatrix} M_{C_{11}} & M_{C_{12}} \\ M_{C_{21}} & M_{C_{22}} \end{bmatrix}, M_{C_{11}} = \begin{bmatrix} m_0 + m_1 & \\ & m_0 + m_1 \end{bmatrix}$$

$$M_{C_{12}} = \begin{bmatrix} -\frac{1}{2} m_1 l \sin\theta_1 \\ \frac{1}{2} m_1 l \cos\theta_1 \end{bmatrix}, M_{C_{22}} = \left[I_1 + \frac{1}{4} m_1 l^2 \right], M_{C_{21}} = \begin{bmatrix} -\frac{1}{2} m_1 l \sin\theta_1 & \frac{1}{2} m_1 l \cos\theta_1 \end{bmatrix}$$

$$M_\zeta = diag\begin{bmatrix} I_{wb} & I_{bw} & I_{wb} & I_{bw} & I_{wb} & I_{bw} \end{bmatrix}$$

$$V_C = \begin{bmatrix} V_{C_{11}} & V_{C_{12}} \\ V_{C_{21}} & V_{C_{22}} \end{bmatrix}, V_{C_{11}} = \begin{bmatrix} 0 & 0 \\ 0 & 0 \end{bmatrix}, V_{C_{12}} = \begin{bmatrix} -\frac{1}{2} m_1 l \cos\theta_1 \dot{\theta}_1 \\ -\frac{1}{2} m_1 l \sin\theta_1 \dot{\theta}_1 \end{bmatrix}, V_{C_{21}} = \begin{bmatrix} 0 & 0 \end{bmatrix}, V_{C_{22}} = [0]$$

where I_n is an $n \times n$ identity matrix and $0_{m \times n}$ is an $m \times n$ zero matrix.

For controller design, the following properties are assumed to be hold always:

Property 1: ζ and θ_1 is twice differentiable, and $\dot{\zeta}, \ddot{\zeta}, \dot{\theta}_1, \ddot{\theta}_1$ are all bounded.

Property 2: Assume the disturbance torque τ_d of the platform is bounded.

From above equations one can solve f as [13] explicitly from (11) as

$$\begin{aligned} f = & [Q(M_{C_{11}} - M_{C_{12}} M_{C_{22}}^{-1} M_{C_{21}})^{-1} Q^T + P M_\zeta^{-1} P^T]^{-1} \{ \dot{P} \dot{\zeta} \\ & + P M_\zeta^{-1} (\tau - \tau_d) - Q(M_{C_{11}} - M_{C_{12}} M_{C_{22}}^{-1} M_{C_{21}})^{-1} [-M_{C_{12}} M_{C_{22}}^{-1} \tau_{link} \\ & + M_{C_{12}} M_{C_{22}}^{-1} V_{C_{21}} \dot{\xi} + M_{C_{12}} M_{C_{22}}^{-1} V_{C_{22}} \dot{\theta}_1 - V_{C_{11}} \dot{\xi} - V_{C_{12}} \dot{\theta}_1]\} \end{aligned} \tag{11}$$

4 Trajectory Tracking Control

According to the dynamic model of the mobile manipulator, a modified inverse dynamic controller is designed to track the trajectories of the platform and manipulator simultaneously. Define $q = [\gamma \quad \zeta]^T$. Abstract the first six rows and first two columns of $J_\gamma(\beta)$ to construct the matrix A and it is described as

$$A = \begin{bmatrix} J_\gamma(\beta)_{([1,2,3,4,5,6],[1,2])} & 0_{6\times1} & -I_6 \\ 0_{1\times2} & 0_{1\times1} & 0_{1\times6} \end{bmatrix} \tag{12}$$

where A is a 7×9 matrix, I_m denotes an $m \times m$ identity matrix， and $0_{m \times n}$ denotes an $m \times n$ zero matrix. Then the constraint equation is depicted by

$$A\dot{q} = 0 \tag{13}$$

If the friction between the wheels and the ground are ignored, the whole system dynamic model can be expressed as

$$M\ddot{q} + V\dot{q} = u + A^T \lambda \tag{14}$$

where λ is a $7-D$ vector. $u=\begin{bmatrix}0_{2\times1}\\ \tau_m\end{bmatrix}$, $\tau_m=\begin{bmatrix}\tau_{link} & \tau^T\end{bmatrix}^T$ is a $7-D$ vector. Then the inertial matrix is $M=diag[M_C \quad M_\zeta]$ and the coriolis matrix is $V=diag[V_C \quad 0_{6\times6}]$.

By applying the relation $B^TA^T=0_{3\times7}$ $\left(B=\begin{bmatrix} I_2 & 0_{2\times1}\\ 0_{1\times2} & I_{1\times1}\\ J_\gamma(\beta)_{([1,2,3,4,5,6],[1,2])} & 0_{6\times1}\end{bmatrix}\right)$, the Lagrange multiplier λ can be eliminated. In order to simple computation, abstract the last seven rows and three columns of B to construct a new matrix $\hat{J}$ and it has the same property of $J_\gamma(\beta)$, so one can easily obtain

$$\hat{J}^T\tau=B^TM\ddot{q}+B^TV\dot{q} \tag{15}$$

Consequently the tracking controller τ_m for the mobile manipulator (14) can be solved and expressed as

$$\begin{aligned}&\tau_m=\hat{J}^{++}B^TM\ddot{q}_0\\ &\ddot{q}_0=B(\ddot{\gamma}_r-K_d\dot{\gamma}_e-K_p\gamma_e-K_i\int_0^t\gamma_e(s)ds)+\dot{B}\dot{\gamma}+M^{-1}VB\dot{\gamma}\end{aligned} \tag{16}$$

Substitute (16) into (15) and suppose that $u_d=0$, one can achieve the identical equation

$$B^TMB(\ddot{\gamma}_e+K_d\dot{\gamma}_e+K_p\gamma_e+K_i\int_0^t\gamma_e(s)ds)=0 \tag{17}$$

It is easy to check B^TMB is nonsingular matrix. Therefore, let the K_p, K_d, K_i are diagonal matrixes whose elements are positive constants, we can deduce from (17) that, when $t\to\infty, \gamma_e\to0$.

5 Simulation

This section discusses the simulation study of a mobile manipulator mounted on an omnidirectional mobile platform to verify the proposed dynamic model and tracking controller. The physical parameters for the omnidirectional mobile manipulator are shown in Table 1.

Table 1. Parameter set for the mobile manipulator

r(m)	d(m)	m_0(kg)	I_{wb}(kgm^2)	I_{bw}(kgm^2)	m_1(kg)	I_1(kgm^2)	(m)
0.10	0.015	60	0.15	0.05	4	0.030	0.30

We now apply the inverse dynamic control algorithm proposed in (16) to the problem of tracking control of the mobile manipulator. Since we assume the $\theta\equiv\theta_0=0$ and let the desired output trajectory γ_d be

$$
\begin{aligned}
x(t) &= 4.0 + 4.0\sin(\frac{t}{20}) \\
y(t) &= 3.0 + 3.0\sin(\frac{t}{20}) \\
\theta_1(t) &= \sin(t)
\end{aligned} \tag{18}
$$

For the controller, we select K_p, K_d, K_i as

$$
\begin{aligned}
K_p &= diag\begin{bmatrix} 2.5 & 2.5 & 1.0 \end{bmatrix} \\
K_d &= diag\begin{bmatrix} 2.5 & 2.5 & 1.5 \end{bmatrix} \\
K_i &= diag\begin{bmatrix} 0.25 & 0.25 & 0.25 \end{bmatrix}
\end{aligned} \tag{19}
$$

The mobile manipulator's initial position is $\gamma_0 = (2.0 \quad 2.0 \quad 0)$.

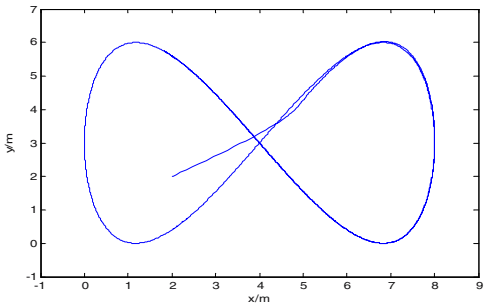

Fig. 3. The trajectory of platform

Fig.3 shows the actual trajectory of the mobile platform. From Fig.4 and Fig.5, it is clear that the system quickly converges to the desired value, so the proposed controller is able to achieve trajectory tracking successfully.

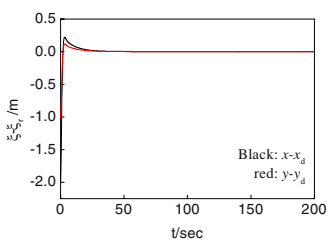

Fig. 4. Response of the ξ

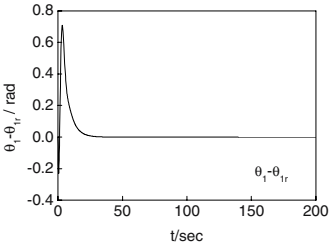

Fig. 5. Response of the θ_1

6 Conclusion

In this paper, dynamic modeling and tracking problem is addressed for a manipulator mounted on a redundantly-actuated omnidirectional mobile platform. Based on the geometric characteristic, the kinematic model is presented to describe the whole system. The proposed dynamic model adequately considers the redundantly-actuated property of the platform. Then a modified inverse dynamic trajectory tracking controller is designed at the dynamic level. The simulation results show the proposed control method can guarantee the asymptotical tracking of the desired trajectory.

This paper's research tests the validity of the integrated dynamic model of the omnidirectional mobile manipulator. Its satisfying results provide a framework for further research about the motion condition that $\dot{\theta} \neq 0$ and complex manipulator mechanism, such as two of more links for manipulator.

Acknowledgment

This work was supported partly by NSFC Project (No.60475030), Joint Laboratory of Intelligent Sciences & Technology and MOST Project (No. 2004DFB02100), China.

References

1. Campion, G., Bastin, G.: Structural Properties and Classification of Kinematic and Dynamic Models of Wheeled Mobile Robots. IEEE Transactions on Robotics and Automation. Vol.12.No.1 (1996) 47-62
2. B´etourn´e, A., Campion, G.: Dynamic Model and Control Design of a Class of Omnidirectional Mobile Robots. Proceedings of the 1996 IEEE International Conference on Robotics and Automation. (1996) 2810-2815
3. Chung, J.H., Yi, B.J., Kim, W.K., Lee, H.: The Dynamic Modeling and Analysis for an Omnidirectional Mobile Robot with Three Castor Wheels. Proceedings of the 2003 IEEE International Conference on Robotics and Automation. (2003) 521-527
4. SicilianO, B., Wit, C.C., Bastin, G.: Theory of Robot Control. Springer-Verlag. (1996)
5. Yamamoto, Y., Yun, X.P.: Coordinating Locomotion and Manipulation of Manipulator. IEEE Transaction on Automation Control. Vol.39.No.6 (1994) 1326–1332
6. Huang, Q., Sugano, S., Kato, I.: Stability Control for a Vehicle-mounted Manipulator – stability Evaluation Criteria and Manipulator Compensatory Motion. Transactions of the Society of Instrument and Control Engineers Vol.31.No.7 (1995) 861–870
7. Holmberg, R., Khatib, O.: Development and Control of a Holonomic Mobile Robot for Mobile Manipulation Tasks. International Journal of Robotics Research. Vol.19.No.11. (2000) 1066-1074
8. Khatib, O., Yokoi, K., Chang, K., Ruspini, D., Holmberg, R., Casal, A.: Coordination and Decentralized Cooperation of Multiple Mobile Manipulators. International Journal of Robotic Systems. Vol.13.No.11 (1996) 755–764
9. Watanabe, K., Sato, K.: Analysis and Control for an Ominidirectional Mobile Manipulator. International Journal of Intelligent and Robotic System. No. 3 (2000) 3-20
10. Yi, B.J., Kim, W.K.: The Kinematics for Redundantly Actuated Omnidirectional Mobile Robots. IEEE International Conference on Robotics and Automation. (2000) 2485-2492

11. Tan, J.D., Xi, N.: Unified Model Approach for Planning and Control of Mobile Manipulators. IEEE International Conference on Robotics and Automation. (2001) 3145-3152
12. Egerstedt, M., Hu, X.M.: Coordinated Trajectory Following for Mobile Manipulation. IEEE International Conference on Robotics and Automation. (2000) 3479-3484
13. Montemayor, G., Wen, J.T.: Decentralized Collaborative Load Transport by Multiple Robots. IEEE International Conference on Robotics and Automation. (2005) 374-379
14. Tcho′ n, K., Jakubiak, J., Muszy′ nski, R.: Kinematics of Mobile Manipulators: a Control Theoretic Perspective. Archives of Control Sciences. Vol.11.No.3–4.11 (2001) 195–221

Soft Touch Control Strategy of Remote Teaching Based on Force Sensing

L.J. Liu[1,2], H.M. Gao[1], G.J. Zhang[1], and L. Wu[1]

[1] State Key Laboratory of Advanced Welding Production Technology, Harbin Institute of Technology, Harbin 150001, P.R. China
[2] School of Material Science & Engineering, Harbin University of Science and Technology, Harbin 150080, P.R. China
lijunliumail@yahoo.com.cn

Abstract. To avoid producing strong collision between the slave robot and workpiece, the soft-force touch control strategy is brought forward by analyzing the dynamics model of the touch force during remote teaching process (RTP). It includes the subsection control strategy of the touch force, and the task self-adapting human-simulation intelligent control (HSIC) touch force. By comparing with the performance of PID controller, the experiment results show that the soft-force touch control strategy can obviously reduce the oscillating scope of touch force, shorten the stabilizing time of touch force, and improve the operated capability of touch force between the remote teaching slave robot and the workpiece.

1 Introduction

The information of the mutual force between the slave robot and the workpiece is truly fed back to the teaching operator by the force telepresence. The teaching operator effectively perceives remote teaching location and controls the slave robot to fulfill the teaching task by the force telepresence together with the other telepresence systems[1]-[4]. Because the remote teaching robot generally works in the unknown environment, it is difficult for vision feedback to make operator obtain environmental dynamic characteristic, surface characteristic and accurate position of the goal real-time. The remote slave robot easily happen the inappropriate mutual force with the workpiece. The strong collision causes the slave robot and welding workpiece to be damaged. Because the remote teaching was limited by such technologies as the machine, sensing, etc, it is difficult to has perfect force telepresence and for the teaching operator to handle the collision moment between the slave robot and workpiece welded well[5]-[9]. Some researchers have put forward the methods which can reduce the colliding intensity effectively, including the limiting speed to the workpiece in the definite distance, and adding the flexible link to the slave robot end. But the former consumes time too longer and causes easily operator to be tired, the latter causes the errors of the force and position of master-slave robot, reduces the force telepresence, and makes easily operator produce the fault of perceiving[10]-[12].

Human-simulation intelligent control is that human's control behavior is further studied and imitated based on the macroscopical simulation of the human's control structure. Namely, human's control experience and skill are imitated. The size of controlled parameter is adjusted in time to suppress the change of deviation according to

T.-J. Tarn et al. (Eds.): Robot. Weld., Intellige. & Automation, LNCIS 362, pp. 31–39, 2007.
springerlink.com

the direction and the trend of the deviation of the parameter. The pre-adjustment is made out according to the adjusting experience before and the present change of the deviation. The size and the direction of adjustment come from the experience before. As the model of the target is not needed, the HSIC is suitable for the teaching process control instead of the PID control. The HSIC touch force strategy can reduce the force oscillating scope during the force touch, shorten the stabilizing time of touch force from the beginning to end, and improve the operated capability of touch force between the slave robot and the workpiece, reduce the colliding intensity between them, and achieve the purpose to soft-force touch[13]-[15].

2 The Analysis of the Touch Force in Remote Teaching

The touch force belongs to the second order system in the remote teaching. The change process of the teaching touch force is showed in Fig.2.1 by the step-up response curve of the second order system. ε_0 is the threshold of stabile touch force. δ_p is the overshoot of touch force .

The e_n is the nth force deviation , $e_n = f_{s,n} - f_{e,n}$. The $f_{s,n}$ is the nth output force of slave robot. The $f_{e,n}$ is the nth force collected by the force sensor. The e_{n-1} and e_{n-2} separately is the (n-1)th and (n-2)th force deviation.

$$\begin{aligned} \Delta e_n &= e_n - e_{n-1} \\ \Delta e_{n-1} &= e_{n-1} - e_{n-2} \end{aligned} \tag{1}$$

When $e_n \cdot \Delta e_n < 0$, the dynamic process of the touch force is changing toward the decreasing direction of the touch force deviation in the BC and DE segment. Namely, the absolute value of the touch force deviation is gradually decreased. When $e_n \cdot \Delta e_n > 0$, the dynamic process of the touch force is changing toward the increasing direction of the touch force deviation in the AB and CD segment. Namely, the absolute value of the touch force deviation is gradually increased. When $\Delta e_n \cdot \Delta e_{n-1} < 0$, the touch force appears the limit value. When $\Delta e_n \cdot \Delta e_{n-1} > 0$, the touch force does not appear the limit value. When the $\Delta e_n \cdot \Delta e_{n-1}$ and $e_n \cdot \Delta e_n$ are used together, the change trend of the touch force deviation can be judged after it has appeared the limit value. The $\left|\Delta e_n / e_n\right|$ describes the change posture of the touch force deviation. When the $\left|\Delta e_n / e_n\right|$ and $e_n \cdot \Delta e_n$ are used together, the different change posture of the dynamic process of the touch force deviation can be taken, the middle segments in BC and DE sects can also be described. The $\left|\Delta e_n / \Delta e_{n-1}\right|$ reflects the local change trend of the touch force deviation, and indirectly denotes the prophase control effect. If $\left|\Delta e_n / \Delta e_{n-1}\right|$ is big, the prophase control effect is not

remarkable. The $\Delta(\Delta e_n)$ is the change ratio of the touch force deviation, namely second differential. It is a characteristic quantity describing the dynamic process of the touch force deviation. When $\Delta(\Delta e_n) > 0$, the ABC in Fig.2.1 is the overshoot segment. When $\Delta(\Delta e_n) < 0$, the CDE in Fig.1 is the call-back segment. The human-simulation intelligent is used to control the touch force by the forgoing characteristic variable in RTP.

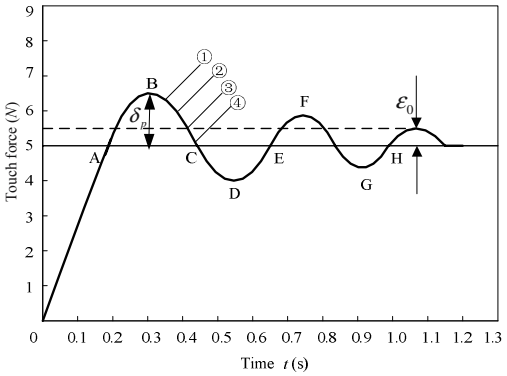

Fig. 1. The typical step response curve of the second order system of the touch force in remote teaching

3 Subsection Control Strategy of the Touch Force in RTP

A different control algorithm is used to improve the flexibility of the touch force in remote teaching. With the increasing of the force deviation, when $e_n \cdot \Delta e_n \geq 0$ in the AB segment in Fig.2.1, the control mode of the proportion, integral and differential are used to avoid the force deviation to increase, and to make the force deviation turn round as soon as possible.

$$f_{s,n} = K_p \cdot e_n + K_d \cdot \dot{e}_n + K_i \int e_n dt \tag{2}$$

With the decreasing of the force deviation corresponding to the curve segment ① in the BC section of Fig.2.1, if the change speed of the force deviation lower and $e_n \cdot \Delta e_n \leq 0$, the proportional control mode is adopted.

$$f_{s,n} = K_p \cdot e_n \tag{3}$$

If the change rate of the force deviation is big, corresponding to the curve segment ② and ③in the BC section in Fig.2.1, the control mode of proportion and differential is adopted.

$$f_{s,n} = K_p \cdot e_n + K_d \cdot \dot{e}_n \tag{4}$$

If the touch force deviation and its change rate are small, namely, corresponding to the curve segment ④in the BC section in Fig.2.1, the maintenance control mode is adopted to meet the adjusting need of the touch force.

$$f_{s,n} = f_{s,(n-1)} \tag{5}$$

The above analysis is suitable for section CD and DE too. In equation (2) ~(5), $f_{s,n}$ is the nth output of the slave robot controller. $f_{s,n-1}$ is the (n-1)th output of the slave robot controller. $\dot{e}_n$ is the change rate of the nth force deviation. K_d is differential coefficient. K_i is integral coefficient, K_p is proportional coefficient.

4 The Task Self-adapting HSIC Algorithm of Touch Force

In Fig.2, t_r is ascending time. δ_p is overshoot. t_p is peak value time. and e_{ss} is stability deviation, $e_{ss} = e(\infty) \times 3\%$. Point A is the characteristic point of ascending time t_r. L_{1u} is the first upper bound characteristic straight line. L_{1l} is the first lower bound characteristic straight line. The point B is the peak value characteristic point. L_{2u} is the second upper bound characteristic straight line. L_{2l} is the second lower bound characteristic straight line .

The L_{1u} is fix by the starting point （0, e0）and the characteristic point A $(t_r, 0.03e_0)$. Its slope is

$$k_{1u} = \frac{0.03e_0 - e_0}{t_r} = -\frac{0.97}{t_r}e_0 \tag{6}$$

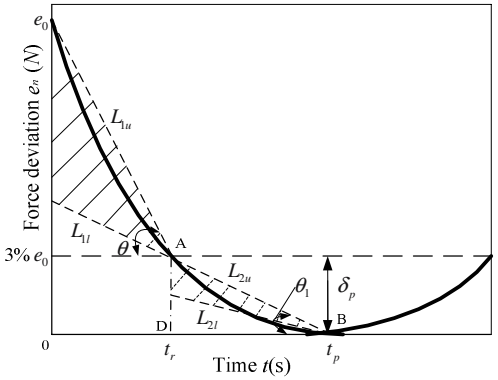

Fig. 2. The analysis of the ideal deviation curve with overshoot

The straight line L_{1u} is defined as the threshold track of the characteristic variable. So long as the actual deviation $e(t)$ is under straight line L_{1u} in time segment $(0,\ t_r)$, the performance of the ascending time t_r can be meet.

The L_{1l} is the bisector of an acute angle between L_{1u} and the time axes. According to the half-angle formula, the L_{1l} slope is

$$k_{1l} = -tg\frac{\theta}{2} = \frac{0.97}{t_r + \sqrt{(0.97e_0)^2 + t_r^2}} e_0 \tag{7}$$

The ideal deviation curve $e(t)$ lies between straight line L_{1u} and L_{1l} in the ascending time t_r .

$$\begin{aligned} e(t) < e_{1u}(t) &= k_{1u}(t - t_r) + 0.03e_0 \\ e(t) > e_{1l}(t) &= k_{1l}(t - t_r) + 0.03e_0 \end{aligned} \tag{8}$$

The L_{2u} is fix by the characteristic point A $(t_r, 0.03e_0)$ and the characteristic point B $(t_p, -\delta_p)$. Its slope is

$$k_{2u} = \frac{-\delta_p - 0.03e_0}{t_p - t_r} = -\frac{\delta_p + 0.03e_0}{t_p - t_r} \tag{9}$$

The L_{2l} is the bisector of an acute angle between L_{2u} and the time axes. According to the half-angle formula, the L_{2l} slope is

$$k_{2l} = -tg\frac{\theta_1}{2} = \frac{\delta_p + 0.03}{(t_p - t_r) + \sqrt{(\delta_p + 0.03e_0)^2 + (t_p - t_r)^2}} e_0 \tag{10}$$

The ideal deviation curve $e(t)$ lies between the straight line L_{2u} and L_{2l} from the time t_r to t_p .

$$\begin{aligned} e(t) < e_{2u}(t) &= k_{2u}(t - t_p) - \delta_p \\ e(t) > e_{2l}(t) &= k_{2l}(t - t_p) - \delta_p \end{aligned} \tag{11}$$

Based on the analysis above-mentioned, the force message space is divided, the corresponding characteristic model is set up.

$$\Phi_{04} = \{\Phi_{041}, \Phi_{042}, \Phi_{043}, \Phi_{044}, \Phi_{045}, \Phi_{046}, \Phi_{047}\} \tag{12}$$

Among them:

$$\Phi_{041} \Rightarrow \left\{t < t_r \bigcap \left|e_n\right| \geq \left|e_{1u,n}\right|\right\}$$

$$\Phi_{042} \Rightarrow \left\{t < t_r \bigcap \left|e_{1l,n}\right| \leq \left|e_n\right| \leq \left|e_{1u,n}\right|\right\}$$

$$\Phi_{043} \Rightarrow \left\{t < t_r \bigcap \left|e_n\right| \leq \left|e_{1l,n}\right|\right\}$$

$$\Phi_{044} \Rightarrow \left\{t_r \leq t < t_p \bigcap \left|e_n\right| \geq \left|e_{2u,n}\right|\right\}$$

$$\Phi_{045} \Rightarrow \left\{t_r \leq t < t_p \bigcap \left|e_{2l,n}\right| \leq \left|e_n\right| \leq \left|e_{2u,n}\right|\right\}$$

$$\Phi_{046} \Rightarrow \left\{t_r \leq t < t_p \bigcap \left|e_n\right| \leq \left|e_{2l,n}\right|\right\}$$

$$\Phi_{047} \Rightarrow \left\{t \geq t_p\right\}$$

Control model set ψ_{04} :

$$\psi_{04} = \left\{\psi_{041}, \psi_{042}, \psi_{043,} \psi_{044}, \psi_{045}\right\} \tag{13}$$

Among them:

$$\psi_{041} \Rightarrow \left\{K_p = K_p + p_1 \cdot K_p\right\}$$

$$\psi_{042} \Rightarrow \left\{f_{s,n} = f_{s,(n-1)}\right\}$$

$$\psi_{043} \Rightarrow \left\{K_p = K_p - p_1 \cdot K_p\right\}$$

$$\psi_{044} \Rightarrow \left\{K_p = K_p + p_2 \cdot K_p\right\}$$

$$\psi_{045} \Rightarrow \left\{K_p = K_p - p_2 \cdot K_p\right\}$$

The reasoning regulation set Ω_{04} :

$$\Omega_{04} = \left\{\Omega_{041}, \Omega_{042}, \Omega_{043}, \Omega_{044}, \Omega_{045}\right\} \tag{14}$$

Among them:

$$\Omega_{041} : \Phi_{041} \Rightarrow \psi_{041}$$

$$\Omega_{042} : \Phi_{042} \bigcap \Phi_{045} \bigcap \Phi_{047} \Rightarrow \psi_{042}$$

$$\Omega_{043} : \Phi_{043} \Rightarrow \psi_{043}$$

$$\Omega_{044} : \Phi_{044} \Rightarrow \psi_{044}$$

$$\Omega_{045} : \Phi_{046} \Rightarrow \psi_{045}$$

Corresponding to characteristic model Φ_{042}, Φ_{045} and Φ_{047}, the maintenance control mode is used. Because the proportional adjusting coefficient of $e(t)$ in the overshoot section (t_r, t_p) is smaller than in the ascending time section （0, tr）, namely $p_2 < p_1$, the adjusting oscillation is avoided.

Under the unusual change of the touch force in remote teaching, The task self-adapting HSIC algorithm can detect the unusual control process and fulfill the fore-casting control by the reasoning regular algorithm of above-mentioned Ω_{04}, also revise control regulation or newly install the other parameters. The measures make the force in remote teaching touch softly the workpiece welded.

Fig. 3. The experimental set

5 The Experiment Results Analysis of the Touch Force in RTP

The experimental set shown in Fig.5.1 is mainly composed of the slave robot, the 6-axis force sensor, the operator, master robot controller, communication link and welding workpiece.

The touch force in RTP is given 5 N by the master computer. The force track curve is obtained by the 6D Force sensor that records the touch force between the slave robot and the workpiepce.

Fig.5.2 (a) is the force track curve of the slave robot controlled by PID. The dashed in Fig.5.2 (a) represents the force track curve given by the master computer. The solid line in Fig.5.2 (a) shows the touch force track curve. In the beginning of the contact course, there are many times collisions between the slave robot and the workpiece. The vibration phenomenon of the slave robot is produced. The time is longer from the touch beginning to the stability.

Fig.5.2 (b) is the force track curve of the slave robot controlled by HSIC. Firstly, the force signal of the slave robot can rapidly follow the output force signal of the master computer. In the beginning of the contact course, the vibration amplitude of the touch force is obviously decreased. The time is shortened from the touch beginning to the stability. The limit amplitude of the touch force becomes soft.

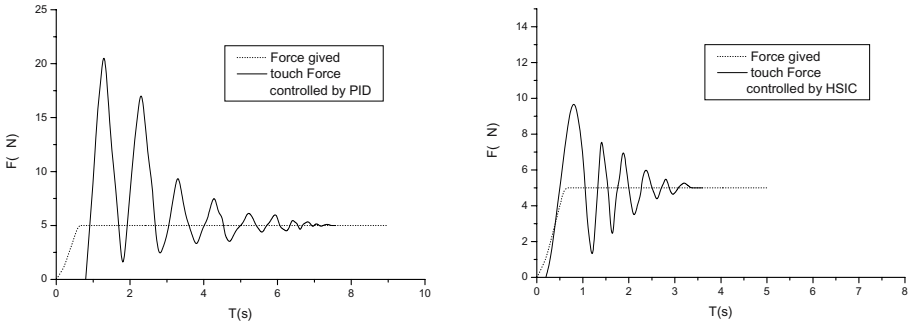

(a) (b)

Fig. 4. The force track curve of the slave robot: (a) PID control touch force; (b) HSIC touch force

6 Conclusion

The strategy of human simulation intelligent control is a change structural controller. It can adjust parameter automatically in the controlling process by analyzing the value and the direction of the force deviation. As the HSIC deviation is employed for the reasoning factor, compared with the traditional PID control, the control process has the characteristics, such as relatively simple algorithm, fast computation, and high accuracy. It is more suitable for the on-line detecting and compensating in the remote teaching process (RTP).

The experimental results show that the force deviatio is reduced, the stability time of RTP shortened, the efficiency of the RTP improved by comparing the intelligent soft-force touch control strategy with PID control. The perception and control of the collision is realized by soft-force touch control strategy of the remote teaching.

Acknowledgments

The authors would like to thank Foundation of State Key Laboratory of Advanced Welding Production Technology and Hei-Long-Jiang educating science and technology Foundation (10051053) for their help during the study.

References

1. Zhao DB, Xiong YL, Huang LL(1995)Automatic Tracking and Modeling of Unknown Environment by A Robot With for Force Control. Robot 17（1）：7-12.
2. Yin YH,Zhu JY(1999)Force Sensing & Control for Intelligent Machine: An Overview. ACTA Aeronautica 20(1):1-7.
3. Han LL, Ning Y, Bai L(1998)Study on Force Sensing Telepresence System of Stanford Master Manipulator. Journal of Zheng Zhou Institute of Light Industry 13(2):17-20.

4. Penin LF, Matsumoto K and Wakabayashi S(2000)Force reflection for time-delayed teleoperation of Space robots, Proceedings Of the IEEE International Conference onRobotics and Automation,pp3120–3125.
5. Rovetta A, Cosmi F and Tosatti L M(1995)Teleoperator response in a touch task with different display conditions, IEEE Tran. on systems, man and cybernetics 25(5):878-881.
6. Murakami,Tsudoi(1990)Application of off-line teaching system for arc welding robots. Technology Review, pp58-61.
7. Choi,Myoung Hwan(2000)Force/moment direction sensor and its use for human-robot interface in robot teaching. 2000 IEEE International Conference on Systems, Man and Cybernetics,pp2222-2227.
8. Makoto J, Michihiro U(1999)Teaching-less Robot System for Finishing Workpieces of Various Shapes Using Force Control and Computer Vision. Proceedings of the 1999 IEEERSJ international Conference on Intelligent Robots and Systems,pp573-578.
9. Urbano N, Almeida AT(1994)Robot 3D Force-Based Surface-Tacking. Proceedings of the 20th International Conference on Industrial Electronics, Control and Instrumentation,pp788-793.
10. Hannaford B, Anderson R(1998)Experimental and Simulation Studies of Hard Contact in Force Reflection Teleoperation IEEE Int Conf on Rob and Auto,pp584- 589.
11. Shoji Y, Inaba M,Fukuda T(1990) Stable Contact Force of a Link Manipulator with Collision Phenomena. IEEE Workshop on Intel Rob and Svs,pp501-507.
12. Xun YQ,Li ZS(1994)Design Method for a Novel Human Simulating Intelligent Controller. ACTA Automatica Sinica 20（5）：616-621.
13. Cheng Z,Yan Wi, Li ZS(2003)NPID controller based on HSIC. Control and Decision 18(6):694-697.
14. Matsuhira N, Asakura M, Bamba H(1994)Manoeuvra-bility of a master-slave manipulator with different configurations and its evaluation tests.Advanced Robotics 8(2):185～203.
15. Kammermeier P,Buss M(1999)Multi-model sensory feedback based on a mathematical model of human perception. In: Proc of IEEE/RSJ Int Conf on intelligent Robots and systems,pp1537-1542.

A Novel Pose Estimation System for Indoor Mobile Robots Based on Two Optical Sensors

Xiang-min Tan, Dongbin Zhao, and Jianqiang Yi

Key Lab of Complex Systems and Intelligence Science,
Institute of Automation, Chinese Academy of Sciences P.O. Box 2728,
Beijing 100080, P.R. China
xiangmin.tan@ia.ac.cn

Abstract. This paper proposes a novel pose system for mobile robots, which can provide cheap and robust solution for pose estimation. Its pose estimation approach is based on at least two optical sensors. The pose system also presents a method for system calibration to improve accuracy. There are several advantages with respect to this system: (1) the measurement from the optical sensors is insensitive to slipping and crawling; (2) this pose estimation system is independent from the kinematics of the robot; (3) compared to incremental encoders, our system is a low-cost and flexible solution for indoor mobile robots. Some simulations have been done to validate our system.

1 Introduction

Pose (position and orientation) estimation is one of fundamental problems in robotics, especially for mobile robots. This problem can be simply described as follows: How to estimate a robot's pose with respect to a global reference frame? A number of solutions for this problem have been developed in the last decades. On the whole, existing methods can be approximately divided into three groups: absolute pose estimation, relative pose estimation and the appropriate combination of them [1-4].

Absolute pose estimation methods usually rely on (1) satellite-based navigation signals, (2) navigation beacons, (3) active and passive landmarks, or (4) map matching. Each of these absolute pose estimation approaches can be implemented by a variety of methods and sensors. Yet, none of the currently existing systems is particularly elegant. Satellite-based navigation (GPS) can be used only outdoors and has poor accuracy [5]. Navigation beacons and landmarks usually require costly installations and maintenance, while map matching methods are either very slow or inaccurate [6].

As for these methods, relative pose estimation is mostly based on dead reckoning, which updates the robot pose incrementally by measuring distance from a known point, i.e., the initial position and orientation of a robot. Although dead reckoning is a simple, cheap, and easy method for pose estimation. Its disadvantage is its unbounded accumulation of errors. In most cases, this method provides a good short-term accuracy with highly precise odometric sensors. Many researchers have adopted this method in their navigation systems [7,8]. Typically, odometry depends on measures of the space covered by the wheels gathered by incremental encoders that equipped on the wheels or on the engine axis. However, there are several disadvantages by using

T.-J. Tarn et al. (Eds.): Robot. Weld., Intellige. & Automation, LNCIS 362, pp. 41–49, 2007.
springerlink.com

the sensor. First, slippages between wheels and the ground will cause large errors. Second, the resolution of these systems relies on the diameter of the wheel and the resolution of the encoder itself, but the wheel's diameter varies with load, and the precise encoder is very expensive. Moreover, it is difficult to install these encoders in some occasions.

In order to overcome these difficulties, this paper presents a novel pose estimation system, which based on the measures taken by at least two optical sensors fixed on the bottom of a robot. Its optical sensor, which has been used extensively, is robust and low-cost.

In the following section, we briefly introduce the pose estimation system and present the geometrical derivation in details. In section 3, we describe a procedure to calibrate systematic errors of this pose estimation system. Section 4 shows some simulations to verify our approach. Some conclusions of this paper are reached and some briefly comparison to related works is introduced in the last section.

2 Method for Pose Estimation

In this section we propose a novel pose estimation system based on at least two optical sensors that is independent from the kinematics of the robot. The method used for pose estimation becomes very simple because of an appropriate placement of those two optical sensors. In order to give a clear description of the pose estimation system, we would like to show our pose estimation system in the form of answering three questions as follows: (1) What is the basic structure of the pose estimation system? (2) Why at least two sensors are needed? (3) How to estimate the robot pose?

2.1 Basic Structure of the Pose Estimation System

Fig.1 (a) shows the basic structure of our pose estimation system. The system is very simple and low-cost. In fact, it only consists of two optical sensors and an 8-bit microcontroller.

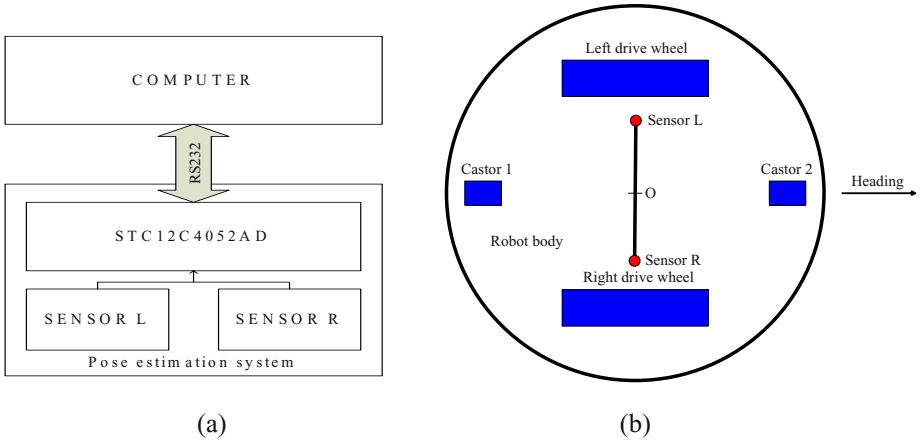

Fig. 1. Basic structure of the pose estimation system and placement of two sensors

In **Fig.1** (b) sensor L and sensor R are two optical sensors. They measure the robot's movement along their x-axis and y-axis, and transfer the movement information to the microcontroller. Once the microcontroller captures the movement information, it will estimate the robot pose and communicate with the computer by RS232. On the other hand, it is very important to place these two optical sensors properly at the bottom of the robot. For sake of ease, we place sensor L at the left side and the sensor R at the right side. They are symmetrical to the robot centerpoint ***O*** and have a certain distance ***D*** (see **Fig.1** (b)). Therefore, these two optical sensor's y-axes parallel the robot heading direction.

2.2 Why at Least Two Sensors Are Needed

In literature [9], M.Santos has presented a pose estimation system based on an optical sensor and a magnetic compass. In their approach, the robot is equipped with an analogue magnetic compass and an optical odometer made out from a commercially mouse. It implies that, with a single optical sensor, we are unable to estimate the pose. We can easily illuminate this problem with **Fig.2**. As in **Fig.2**, (a) stand for the robot rotates with respect to the robot's centerpoint. In this procedure, the angle α between the x-axis of the optical sensor and the tangent to its trajectory is constant, especially, α = 90 degree. It is obvious that the readings of the optical sensor are as follow: $\Delta x = 0, \Delta y = l$. However, the robot translates directly along the direction of y-axis and the length of this translation equals l in (b). For this case, the readings of the optical sensor are just the same as (a) but the robot's pose is obviously different. In literature [10], Bonarini.A presents a pose estimation system based on two mice in details. It adequately illuminates that at least two sensors are needed for pose estimation. More than two sensors provide more redundant information and improve the robustness of the pose estimation system.

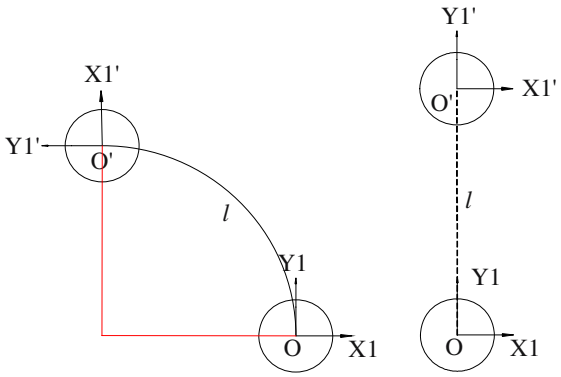

Fig. 2. Same reading but different movement with a single optical sensor

2.3 Method for Pose Estimation

To estimate the robot pose, we present the geometrical derivation that estimates the robot pose by the readings of the two optical sensors. For sake of ease, in this section

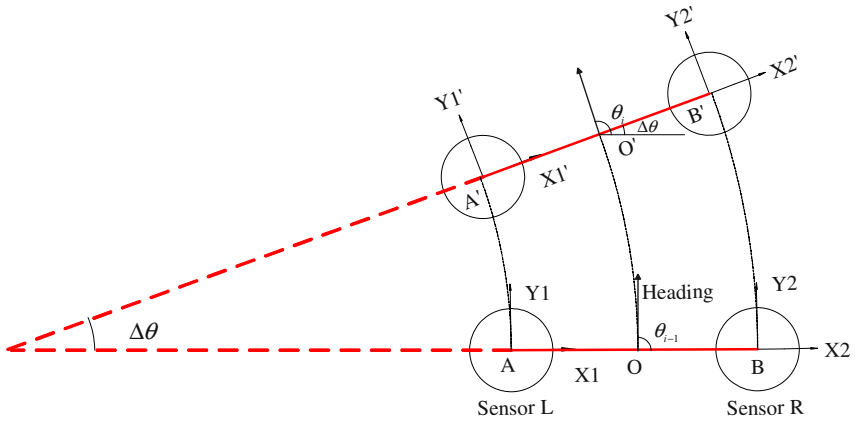

Fig. 3. The movement occurs at instant ***i***

we only consider the geometrical derivation in ideal situation, i.e., no errors in sensor assembling and distance measuring.

Each sensor measures its movement along its x-axis and y-axis. If the robot makes an arc of circumference, it can be shown that each sensor makes an arc of circumference, which is characterized by the same center and the same angle (see **Fig.3**). Suppose that during the sample interval ***T***, a sensor moves along an arc of length l, and the angle α between the y-axis of sensor and the tangent to its trajectory is constant. We can write the following relations:

$$\Delta x = l \cdot \cos\alpha \tag{1}$$

$$\Delta y = l \cdot \sin\alpha \tag{2}$$

From equation (1) (2), we can compute l as follow:

$$l = \sqrt{(\Delta x)^2 + (\Delta y)^2} \tag{3}$$

We assume that, the reading of sensor L is N_l, M_l and the reading of sensor R is N_r, M_r at the sample interval ***T***. According to equation (1) (2), we can obtain:

$$\Delta x_l = R_l \cdot N_l \tag{4}$$

$$\Delta y_l = R_l \cdot M_l \tag{5}$$

$$\Delta x_r = R_r \cdot N_r \tag{6}$$

$$\Delta x_r = R_r \cdot N_r \tag{7}$$

where R_l is the resolution of sensor L and R_r is the resolution of sensor R.

According to equation (3), we can compute the incremental travel distance Δl_l of the sensor L and Δl_r of the sensor R as follows:

$$\Delta l_l = \sqrt{(\Delta x_l)^2 + (\Delta y_l)^2} \tag{8}$$

$$\Delta l_r = \sqrt{(\Delta x_r)^2 + (\Delta y_r)^2} \tag{9}$$

And the incremental linear displacement of the robot's centerpoint $\boldsymbol{O}$, denoted by Δl, according to

$$\Delta l = \frac{\Delta l_l + \Delta l_r}{2} \tag{10}$$

Next, we compute the robot's incremental change of orientation, denoted $\Delta\theta_i$,

$$\Delta\theta_i = \frac{\Delta l_r - \Delta l_l}{D} \tag{11}$$

where D is the distance between sensor L and sensor R.

The robot's new pose can be computed as follow:

$$\begin{cases} x_i = x_{i-1} + \Delta l \cdot \cos\theta_i \\ y_i = y_{i-1} + \Delta l \cdot \sin\theta_i \\ \theta_i = \theta_{i-1} + \Delta\theta_i \end{cases} \tag{12}$$

where x_i, y_i denotes the relative position of the robot's centerpoint at instant $\boldsymbol{i}$.

3 System Calibration

In this section, we analyze the systematic errors that can affect our pose system and propose a calibration procedure in order to correct them. In our approach, two aspects can cause systematic errors: (1) the sensor's resolution, which depends on the moving surface and the sensor itself; (2) errors in the installation of two sensors.

We design a procedure, which consists of two practical rotational measurements: the translational and the rotational measurement. Then we are able to obtain the systematic parameters through these two practical measurements. These systematic parameters include: the distance $\boldsymbol{D}$ between sensor L and sensor R, the resolution R_l of the sensor L and the resolution R_r of the sensor R. The translational measurement consists of making the robot travel (manually) $\boldsymbol{C}$ (mm) for several times. For each time, the readings of these two sensors are stored. At the end of the measurement we can compute the averages of the four readings $\widehat{N}_l, \widehat{M}_l, \widehat{N}_r, \widehat{M}_r$, which allow us to estimate the sensors actual resolution R_l and R_r:

$$R_l = \frac{25.4 \cdot \sqrt{\widehat{N}_l^{\,2} + \widehat{M}_l^{\,2}}}{C} \tag{13}$$

$$R_r = \frac{25.4 \cdot \sqrt{\widehat{N}_r^{\,2} + \widehat{M}_r^{\,2}}}{C} \tag{14}$$

Note that: 1 inch equals 25.4mm in equations (13) and (14).

In the rotational measurement, we make the robot turn 360 degrees around its centerpoint in counter-clockwise for several times, and then store these readings. The averages of these readings allow us to estimate the distances between the centerpoint ***O*** and the two sensors r_l , r_r .

$$r_l = \frac{25.4 \cdot \sqrt{\widehat{N}_l^{\,2} + \widehat{M}_l^{\,2}}}{2\pi \cdot R_l} \tag{15}$$

$$r_r = \frac{25.4 \cdot \sqrt{\widehat{N}_r^{\,2} + \widehat{M}_r^{\,2}}}{2\pi \cdot R_r} \tag{16}$$

Then we can estimate the actual distance between sensor L and sensor R as follow:

$$D = r_l + r_r \tag{17}$$

As we all know, the robot's incremental change of orientation is constant at instant ***i***. Then we can obtain following relation:

$$\frac{\Delta l - \Delta l_l}{r_l} = \frac{\Delta l_r - \Delta l}{r_r} \tag{18}$$

When the robot's centerpoint ***O*** is not at the middle point of the link line of sensor L and sensor R (see **Fig. 4**), we compute Δl with equation (19) instead of equation (10) according to equation (18):

$$\Delta l = \frac{r_r \cdot \Delta l_l + r_l \cdot \Delta l_r}{r_r + r_l} \tag{19}$$

Therefore, we can estimate the robot pose more accurately with equation (12).

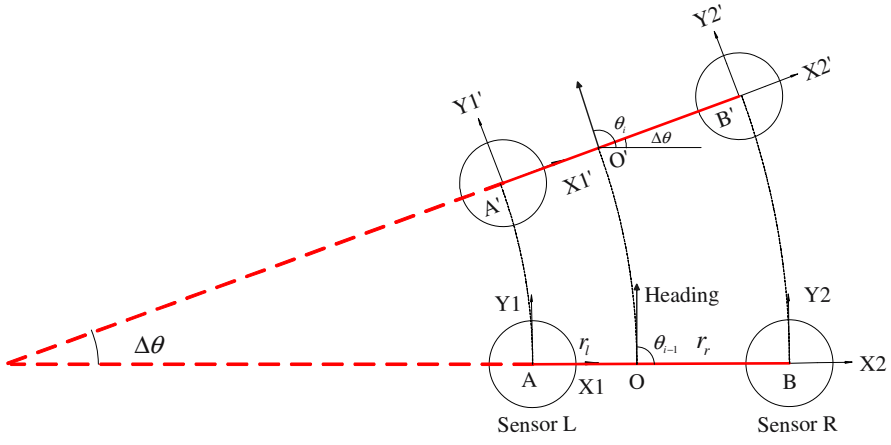

Fig. 4. When the robot's centerpoint is not at the middle point of the link line of two sensors

4 Simulations

In this section, we show some simulations to verify our pose estimation system. In order to test our pose estimation system, a preliminary UMBmark simulation is adopted, which is presented by [1,10]. The UMBmark procedure consists of measuring the absolute reference position of the robot in order to initialize the on-board dead-reckoning starting position. Then, we make the robot travel along a 4×4m square in the following way : the robot stops after each 4m straight leg and then it makes a 90° turn on the spot. When the robot reaches the start point, we are able to obtain a series of readings. Then we calculate the pose by these readings with our approach. Compared to actual pose, errors are introduced by systematic and nonsystematic factors. We repeated this procedure five times in clockwise and five times in counter-clockwise. In addition, we have done some experiments for calculating the resolution of an optical sensor, and we obtain the resolution of an optical sensor, which is about 362cpi.

We assume actual parameters as follows: r_l = 46.5mm, r_r = 51.5mm, the robot's translational velocity is 0.2m/s on each straight leg and the robot's rotational velocity is $\pi/6$ rad/s on each spot. **Fig.5** shows one of the trajectories of the test. Before calibration we assume that r_l = r_r = 50mm. Green dot line denotes the trajectory before calibration and red dash line denotes the trajectory after calibration, i.e., r_l = 46.5mm, r_r = 51.5mm. It is obvious that our system is more accurate after calibration. However, due to the characteristics of moving surface, our system still suffer from nonsystematic errors. To simulate the effects caused by nonsystematic errors, we also select a noise signal satisfied standard normal distribution and multiplied by factor $6.35*10^{-5}$.

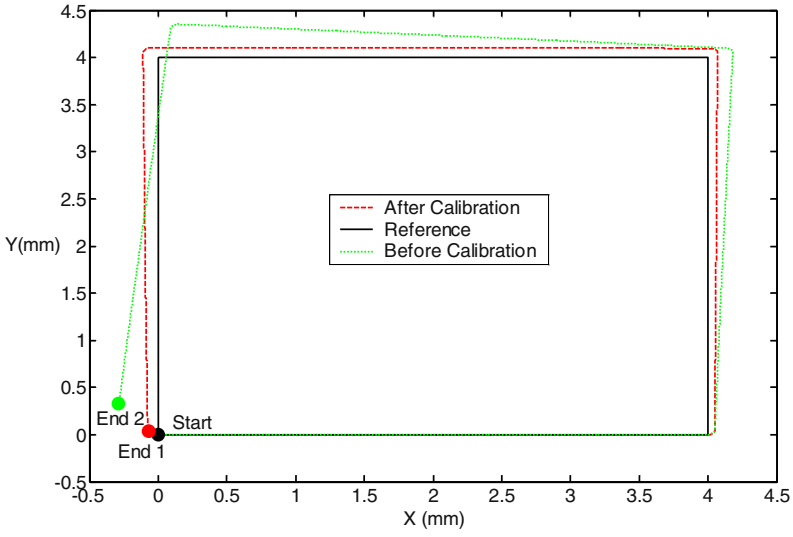

Fig. 5. Trajectories of UMBmark test before calibration and after calibration

Fig.6 demonstrates the errors of this experiment in details. Before calibration the maximum distance between the estimated pose and actual pose is 629mm and after calibration it is only 74mm. As we can see, the last result is comparable with those achieved by other dead-reckoning systems tested with UMBmark.

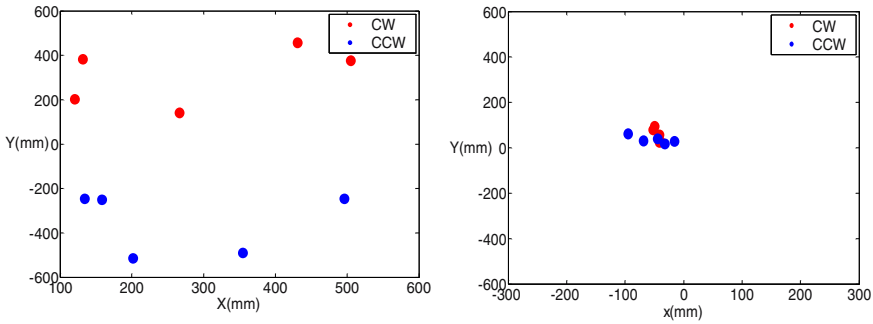

Fig. 6. Errors of UMBmark test before calibration (a) and after calibration (b)

5 Conclusion

In this paper, we propose a pose estimation system based on two optical sensors. Compared to traditional method and other work, such as the system proposed by Bonarini.A.[10], our system is more flexible and easy. Furthermore, it provides a relative reliable positioning with relative cheap cost. This system is especially suitable for RobCup robot; because the moving surface is relative unique and the slipping and crawling were reduced in our system. However, there are some problems in this system: The resolution of the optical sensor is sensitive to the speed and the robot's speed is limited for accurate measurement. Thus we have still a lot of work to do in the future.

Acknowledgment

This work was supported partly by NSFC Project (No.60475030), MOST Project (No. 2004DFB02100), and the Joint Laboratory of Intelligent Sciences & Technology, China.

References

1. Borenstein, J., and Feng, L.: UMBmark – A Method for Measuring Comparing, and Correcting Dead-reckoning Errors in Mobile Robots. In Proceedings of SPIE Conference on Mobile Robots, Philadelphia, October (1994).
2. Borenstein, J., Koren,Y.: Motion Control Analysis of a Mobile Robot. Transactions of ASME, Journal of Dynamics, Measurement and Control, Vol.109, No.2 (1986) 73-79.

3. Tardos, J., Neira, J., Newman, P., Leonard, J.: Robust Mapping and Localization in Indoor Environments Using Sonar Data. The International Journal of Robotics Research , Vol.21,No.4, Sage Publication(2002) 311-330.
4. Guivant, J., Nebot, E., Baiker, S.: Localization and Map Building Using Laser Range Sensors in Outdoor Applications. Journal of Robotics Systems, Vol.17,No.4, John Wliey&Sons(2000) 565-583.
5. Kazunori Ohno, Takashi Tsubouchi, Bunji Shigematsu, Shoichi Maeyama: Outdoor Navigation of a Mobile Robot Between Buildings based on DGPS and Odometry Data Fusion. In Proceedings of the IEEE International Conference on Robotics and Automation (2003) 1978-1984.
6. I. J. Cox: Blanche - An Experiment in Guidance and Navigation of An Autonomous Mobile Robot. IEEE Trans. on Robotics and Automation, Vol.7,No.2 (1991)193-204.
7. Yamauchi, B.: Mobile Robot Localization in Dynamic Environments Using Dead Reckoning and Evidence Grids. In Proceedings of the IEEE International Conference on Robotics and Automation. Minneapolis, Minnesota (1996) 1401-1406.
8. Chong, K., Kleeman, L.: Accurate Odometry and Error Modeling for A Mobile Robot. In Proceedings of the IEEE International Conference on Robotics and Automation (1997) 2783-2788.
9. Santos, F.M., Silva, V.F., Almeida, L.M.: A Robust Self-localization System for a Small Mobile Autonomous Robot. In proceedings of International Symposium on Robotics and Automation (2002).
10. Bonarini, A., Matteucci, M., Restelli, M.: A Kinematic-independent Dead-reckoning Sensor for Indoor Mobile Robotics. In Proceedings of the International Conference on Intelligent Robots and Systems (2004) 3750-3755.
11. Agilent Technologies Semiconductor Products Group. Agilent ADNS-3060 High Performance Optical Mouse Sensor Datasheet, Technical Report 5989-1401EN, Agilent Technologies Inc., June 2004.

Haptic Teleoperation of Robotic Manipulator

Wusheng Chou[1] and Jing Xiao[2]

[1] Robotics Institute Beijing University of Aeronautics & Astronautics
[2] Dept. of Computer Science University of North Carolina at Charlotte

Abstract. In teleoperated robotic systems, a user controls a robotic manipulator via an input device. Generally the position and velocity commands generated by the user in free space can be arbitrary in the workspace of the input device. However, due to the mechanical limitation and workspace constraints of a manipulator, the manipulator cannot always exactly follow the input command and often runs into a stop. This paper proposes a haptic teleoperation method to enable a user to control a manipulator conveniently and without violating constraints of the manipulator. The configuration constraints and mechanical limits, such as singularities and joint limits, are converted into a constraining force. It is then fed back to the user via a haptic device to restrict the motion of the user's hand so that the manipulator can be operated smoothly without being interrupted by constraint violation. Experimental results demonstrate the feasibility of the proposed method.

1 Introduction

A teleoperated robotic system consists of a device (master) that a user holds and a robotic tool (slave) on the other site, and the bilateral control method is often used in such a system [1]. Most of the literature in the field of teleoperation assumes that an input position/velocity command from a user is always reasonable and the slave manipulator has the ability of replicating the input command. In fact, because the slave manipulator has a finite workspace due to its mechanical limitations, not all input commands can be followed by the slave manipulator.

In addition, even during the motion of an actuated manipulator within its workspace, the manipulator may run into singularity configurations. For instance, in the course of teleopreation, the exact path is not known a priori and hence singularity-free paths cannot be preprogrammed, and as a result the robot manipulator can easily run into a small neighborhood of a singularity configuration. In this case, the manipulability of the robot is compromised, and the user usually has no instructive information on how to back away from such a configuration.

While much work focuses on designing control architectures and algorithms to guarantee the stability and transparency of teleoperation with/without time delay in virtual or real world applications [2], or focuses on the physically accurate force feedback of the interaction between the robot and environment [3], little literature has addressed the issue of restricting the input command of a user during teleoperation. Some assistive virtual force generated by "virtual pipe" or "virtual fixtures" [4,5] are fed back to guide a user's hand motion to improve the efficiency of teleoperation in

T.-J. Tarn et al. (Eds.): Robot. Weld., Intellige. & Automation, LNCIS 362, pp. 51–59, 2007.
springerlink.com

free space. However, they are not concerned with the configuration constraints and mechanical limits and do not restrict the motion of the user hand from violating such constraints. Recently, there is work [6] to reflect the topological constraints of an unactuated virtual serial linkage through haptic forces on a user when the user manipulates any link of the virtual linkage, and a haptic device controller is designed to penalize a user's departure from the configuration manifold of the virtual linkage. The directions of topological constraints are not very accurate for the sake of real time computation, and the impedance controller alone cannot restrict the user's motion according to the virtual topology.

This paper considers teleoperating a real robot manipulator by a user holding and moving a virtual replica via a haptic device. We present how to produce a (virtual) constraining force to provide the user the perception of a singular configuration or a joint limit and prevent the user's hand motion from violating these constraints. Obstacle avoidance and compliant motion constraints can also be easily incorporated into such a constraining force. The combined effect provides the user information for selecting appropriate motion directions for the manipulator to follow.

The rest of this paper is organized as follows. Constraints on the motion of an articulated manipulator are analysed in Section 2. Haptic rendering of these constraints via a constraining force is described in Section 3. In Section 4, we present the implementation of the proposed method, and in Section 5, the preliminary results are given. Section 6 concludes the paper.

2 Constraints of an Articulated Manipulator

A manipulator's motion is limited by its workspace determined by the mechanical structure of the manipulator and the travel limits of its joints. If a joint moves to its limit, then it will reach a stop.

Besides joint limits, a manipulator is constrained by singular configurations. If the end-effector of the manipulator cannot be rotated about a certain axis or translated along a certain direction, even though none of the joints of the manipulator has reached its limit, then the manipulator is in a singularity or singular configuration.

In addition to joint limits and singular configurations, a manipulator's motion is also constrained by obstacles in its workspace. A manipulator needs to either avoid an obstacle or move compliantly along an obstacle surface.

3 Haptic Rendering of Configuration Constraints

Our idea is to feedback a constraining force to the user's hand via the haptic device as it leads the motion of a manipulator when the measure of singularity or joint limit is below a threshold or when the manipulator is near an obstacle in order to prevent violations of their constraints on the manipulator.

The total constraining force can be represented as

$$\mathbf{F}_c = \mathbf{F}_s + \mathbf{F}_j + \mathbf{F}_o \tag{1}$$

Where $\mathbf{F}_s$ is the constraining force caused by a singularity, $\mathbf{F}_j$ is the constraining force caused by joint limits, and $\mathbf{F}_o$ is the constraining force caused by interaction with an obstacle.

Each of these forces is calculated by a spring model as detailed below.

3.1 Constraining Force Caused by Singularities

A manipulator *M* with *n* joints is shown in Fig. 1.

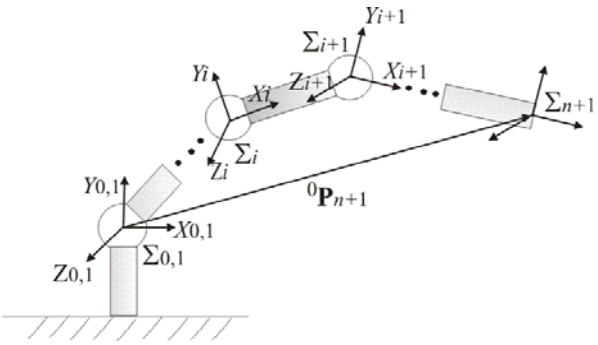

Fig. 1. Link Frames

The Jacobian matrix of *M* can be expressed as

$$\mathbf{J} = \begin{bmatrix} \mathbf{J}_{l1} \mathbf{J}_{l2} & \cdots & \mathbf{J}_{ln} \\ \mathbf{J}_{\omega 1} \mathbf{J}_{\omega 2} & \cdots & \mathbf{J}_{\omega n} \end{bmatrix} \tag{2}$$

Where $\mathbf{J}_{li}$ and $\mathbf{J}_{\omega i}$ (i=1,2,…,n) denote the linear and angular velocities of the end-effector of *M* contributed by the ith joint, respectively.

When the manipulator *M* is at a singular configuration, either the non-zero components of the first row or the non-zero components of the second row of equation (3) are coplanar or two of them are collinear[7]. The singular direction $\mathbf{d}s$ along which the manipulator cannot be moved satisfies the following equations:

$$\mathbf{d}s \cdot \mathbf{J}_{li}(\boldsymbol{\theta}_s) = 0\,,\ (i=1,2,\ldots,n) \tag{3}$$

or

$$\mathbf{d}s \cdot \mathbf{J}_{\omega i}(\boldsymbol{\theta}_s) = 0\,,(i=1,2,\ldots,n) \tag{4}$$

where $\boldsymbol{\theta}_s = (\theta_{1s}, \theta_{2s}, ..., \theta_{ns})$ denotes a singularity of *M*.

Thus the singular direction of *M* when it is at a singular configuration can be obtained:

$$\mathbf{d}_{sl} = \frac{\mathbf{J}_{li} \times \mathbf{J}_{lj}}{\left\| \mathbf{J}_{li} \times \mathbf{J}_{lj} \right\|} \tag{5}$$

Or

$$\mathbf{d}_{s\omega} = \frac{\mathbf{J}_{\omega i} \times \mathbf{J}_{\omega j}}{\left\| \mathbf{J}_{\omega i} \times \mathbf{J}_{\omega j} \right\|} \tag{6}$$

Where $\mathbf{J}_{li}$ and $\mathbf{J}_{lj}$ are non-zero components of $\mathbf{J}$ and are not collinear. $\mathbf{J}_{\omega i}$ and $\mathbf{J}_{\omega i}$ are also non-zero components of $\mathbf{J}$ and are not collinear.

Let ${}^{n+1}\mathbf{P}_e$ denotes the error between the position of the hand proxy in the virtual environment and the position of the end-effector when it is virtually held by the user through the haptic device. Let ${}^{n+1}\Omega_e$ (which can be expressed as the product of a nominal vector and a certain angle) denotes the orientation increment commands of $\sum n+1$ with respect to the last time step. Using a spring model, we can compute the constraining force $\mathbf{f}_{sl}$ and moment $\mathbf{m}_{s\omega}$ at a singular configuration acting on the origin of $\sum n+1$ respectively. We have

$$\mathbf{F}_s = [\mathbf{f}_{sl} \quad \mathbf{m}_{s\omega}]^T \tag{7}$$

$$\mathbf{f}_{sl} = k_{sl}({}^{n+1}\mathbf{P}_e \cdot \mathbf{d}_{sl}) \tag{8}$$

$$\mathbf{m}_{s\omega} = k_{s\omega}({}^{n+1}\Omega_e \cdot \mathbf{d}_{s\omega}) \tag{9}$$

Where k_{sl} and $k_{s\omega}$ are the stiffness coefficients.

3.2 Constraining Force Caused by Joint Limits

If the *i*th joint is close to its limit, then the constraining force $\mathbf{f}_{jl}$ and moment $\mathbf{m}_{j\omega}$ caused by the limit of this joint can be calculated as:

$$\mathbf{F}_j = [\mathbf{f}_{jl} \quad \mathbf{m}_{j\omega}]^T \tag{10}$$

$$\mathbf{f}_{jl} = \sum_{i=1}^{n} k_i k_{jl} \left| \theta_i - \theta_{i\lim} \right| \mathbf{d}_{jl} \tag{11}$$

$$\mathbf{m}_{j\omega} = \sum_{i=1}^{n} k_i k_{j\omega} \left| \theta_i - \theta_{i\lim} \right| \mathbf{d}_{j\omega} \tag{12}$$

Where k_{jl} and $k_{j\omega}$ are the stiffness coefficients, $k_i = 1$ if the *i*th joints reaches its limit, otherwise $k_i = 0$. $\mathbf{d}_{jl}$ and $\mathbf{d}_{j\omega}$ denote the directions of the constraining force and moment acting on the origin of $\sum n+1$ respectively as derived below.

Let ${}^{j}\mathbf{p}_i$ denote the position vector from the origin of $\sum j$, O_j, to the origin of $\sum i$, O_i, expressed in $\sum j$. For a revolute joint i, suppose that link i is driven by the ith joint. If ${}^{i}\mathbf{p}_{n+1}$ is zero, then $\mathbf{f}_{jl}$=0, and $\mathbf{d}_{j\omega}$ aligns with the joint i axis. If ${}^{i}\mathbf{p}_{n+1}$ is not zero, then $\mathbf{m}_{j\omega}$=0, and $\mathbf{d}_{jl}$ is the cross product of ${}^{i}\mathbf{p}_{n+1}$ and the Z axis Z_i of $\sum i$.

$$\mathbf{d}_{jl} = \frac{Z_i \times {}^{i}\mathbf{P}_{n+1}}{\left\| Z_i \times {}^{i}\mathbf{P}_{n+1} \right\|} \tag{13}$$

For a prismatic joint i, $\mathbf{m}_{j\omega}$ is equal to zero, and $\mathbf{d}_{jl}$ aligns with the joint i axis.

3.3 Constraining Force Caused by Obstacles

When a manipulator is close to an obstacle so that the minimum distance $\mathbf{d}_0$ between the robot and the obstacle is less than a pre-defined threshold ε, the constraining force $\mathbf{F}_o$ can be calculated as:

$$\mathbf{F}_o = k_f(\varepsilon - d_o)\mathbf{d}_f \tag{14}$$

Where k_f is the stiffness coefficient, and $\mathbf{d}_f$ is a unit vector along the direction of $\mathbf{d}_0$.

4 Implementation

We have implemented the proposed method in C++ and OpenGL in a virtual environment connected to a PHANToM desktop device. The virtual environment includes a virtual planar manipulator with 3 revolute joints. The length of each link is 7 units. A user can virtually hold and move the end-effector of the manipulator via the haptic device. As the user moves the manipulator, the constraining force is calculated in real-time and fed back to the user by haptic rendering to constrain the user's motion.

Since the real-time requirement on graphic display and haptic rendering are different (20~30Hz for the former and 300~1000Hz for the latter), graphic rendering and the haptic rendering loops are decoupled and communicated via the virtual environment. By doing so, the haptic rendering loop can achieve 1000 Hz update rate to guarantee the stability and fidelity of the force feedback.

A user input command is given in the Cartesian space, and the manipulator should reproduce the input command in its joint space. If the manipulator is not close to a singularity, the pseudo-inverse technique [8] is adopted to calculate the joint velocity.

5 Experimental Results

In the following experiments, the ranges of the three joints of the planar manipulator are (-11π/12, 11π/12), (-π/6, π/6) and (-11π/12, 11π/12), respectively.

When some joint reaches one of its limits (as shown in Fig. 2, joint 1 reaches 11π/12 after time step 10), the constraining force is shown as Fig. 3. The trajectories of the user's hand and the manipulator's are shown in Fig. 4. The arrow in Fig. 4 indicates the motion directions, and the shadow area represents the unreachable region when joint 1 reaches its limit under certain joint configuration A (2.848, -0.9718, -2.229) (in radian), as the user's hand is mechanically restricted by the feedback force. Note that the input motion command is a velocity. Thus, there is an offset between the positions of the user hand and the manipulator end-effector.

In Fig.5, the initial configuration is (1.491, -1.018, -1.247). Joint 2 and joint 3 are zero, and the manipulator is singular between time step 16 and time step 38, as well as the interval of time step 58 and time step 99. Under these situations, the constraining force is shown as in Fig. 5. When the manipulator is not singular, there is no constraining force. Fig. 6 gives the trajectories of the user hand and the manipulator end-effector. The motion of the user is restricted by the manipulator's singular configurations.

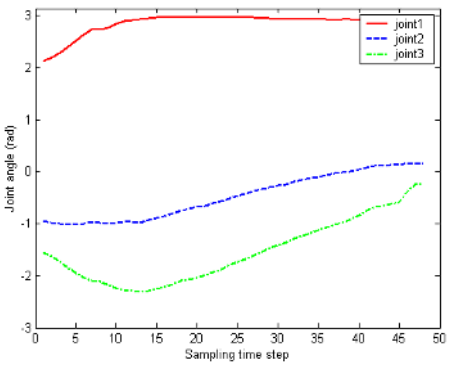

Fig. 2. Joint trajectories When Joint 1 Reaches a Limit

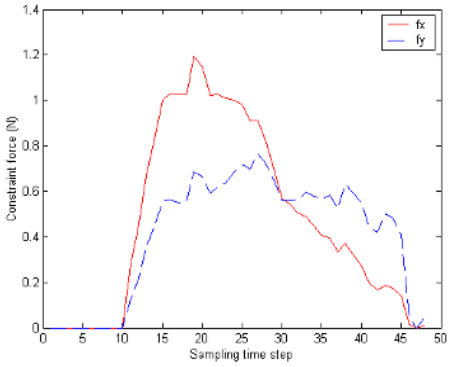

Fig. 3. Constraining Force From Joint 1's Limit

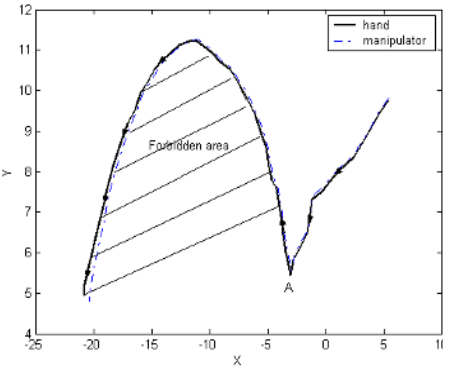

Fig. 4. Trajectories of the Hand and the End-effector When Joint 1 Reaches Limit

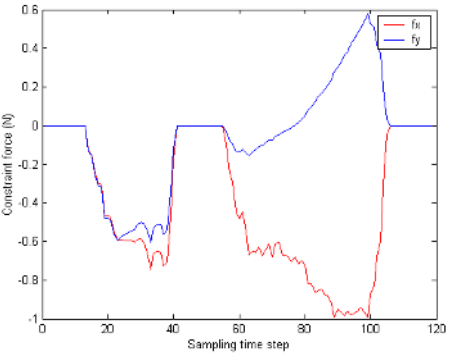

Fig. 5. Constraining Force at a Singularity

Fig. 7 and Fig. 8 present interaction force and the hand trajectory respectively, when the third link of the manipulator interacts with an obstacle located at (10,10). The initial configuration of the manipulator is (2.973151, -0.693032, -2.003396). From time step 42, the third link interacts with the obstacle. The constraining force restricts the user hand motion, and the third link slides along the obstacle surface.

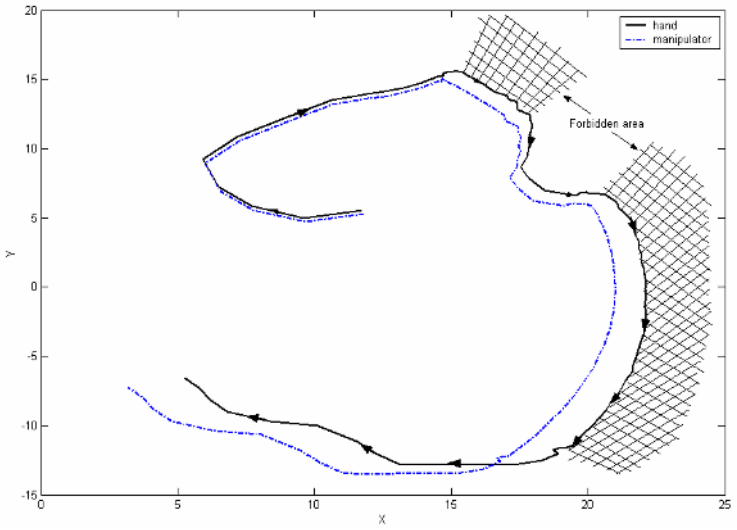

Fig. 6. Trajectories of Hand and the End-effector at a Singularity

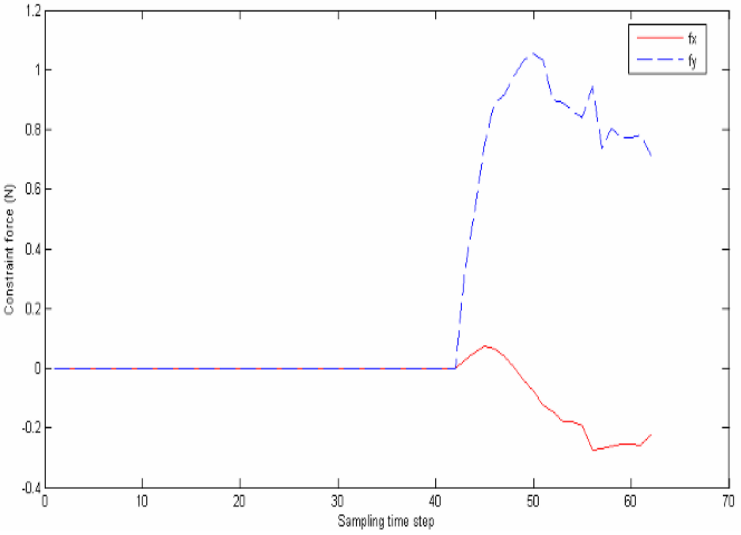

Fig. 7. Constraining Force Caused by Contact

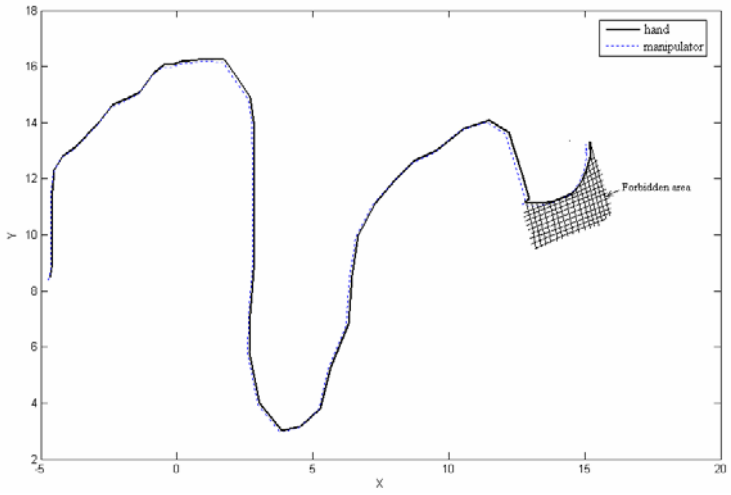

Fig. 8. Trajectories of the Hand and the End-effector with an Obstacle

6 Conclusions

This paper proposes a method to convert configuration constraints on an articulated manipulator into haptic force feedback to a user's hand moving the manipulator via a haptic device. The haptic force can restrict the motion of the user's hand and give the user perception of the configuration status and mechanical characteristics of a manipulator during the course of teleoperation. It can also be helpful to the user in devising an optimal path for the manipulator to perform certain tasks without violating the constraints on the manipulator. The proposed method could also be used for computer aided design of an articulated manipulator to appreciate its workspace and its mobility and dexterity under different configurations, as well as the teaching of articulated manipulator in industrial application.

Acknowledgement

The authors are grateful to the support of National Science Foundation of U.S. under grants IIS-0328782 and EIA-0203146.

References

1. D. Lawrence, "Stability and transparency in bilateral teleoperation," IEEE Transactions on Robotics and Automation, vol. 9, no. 5, pp. 624–637, 1993.
2. J. T. Dennerlein, D. B. Martin, and C. Hasser, "Force-feedback improves performance for steering and combined steering-targeting tasks," Proceedings of the Conference on Human Factors in Computing Systems, pp. 423-429, 2000

3. D. Constantinescu, S. Salcudean, and E. Croft, “Haptic Feedback using Local Models of Interaction,” in 11th International Symposium on Haptic Interfaces for Virtual Environment and Teleoperator Systems, Los Angeles, Ca, 2003, pp. 416–421.
4. J. J. Abbott, G. D. Hager and A. M. Okamura, “Steady-hand teleoperation with virtual fixtures,” 12th IEEE International Workshop on Robot and Human Interactive Communication, pp.145-151,2003
5. W. Yu, R.Dubey, N.Pemalete, “Telemanipulation enhancement through user's motion intention recognition and fixture assistance”, IEEE/RSJ International Conference on Intelligent Robots and Systems, pp2235-2240,2004
6. D. Constantinescu, S. Salcudean, and E. Croft, “Haptic rendering of topological constraints to users manipulating serial virtual linkages”, IEEE International Conference on Robotics and Automation, 2005.
7. W.Chou, T.Wang, Z.Wu at el., “Singularity analysis of robotic manipulator”, Chinese Journal of Mechanical Engineering, Vol.36, No.9, 2000
8. Y. Nakamura and H. Hanafusa. “Inverse kinematics solution with singularity robustness for robot manipulator control”, ASME Journal of Dynamics Systems, Measurements, and Control, pp.108-163, 1986.

Practical Stabilization of Nonholonomic Mobile Robots Moving on Uneven Surface

Xiaocai Zhu, Guohua Dong, and Dewen Hu

College of Mechatronics and Automation, National University of Defense Technology, Changsha 410073, P.R. China
xczhu@nudt.edu.cn

Abstract. The stabilization problem of nonholonomic mobile robots that move on uneven surface is investigated. Smooth control laws ensuring practical stabilization are proposed based on the transverse function approach and the integrator backstepping technique. Firstly, a transverse function which defines a smooth embedded submanifold is constructed, and an augmentation procedure is applied to the kinematic model of the robots. Then, the left-invariance property of the kinematic model is explored, and after the defining of the error variables via group operation, smooth exponential stabilizing control laws are derived for the error dynamic system, thus the kinematic model is rendered practically stable. Finally, the obtained control laws are utilized in the integrator backstepping process to stabilize the dynamic model. Simulations are provided to demonstrate the effectiveness of the algorithm.

1 Introduction

There have been numerous studies on the control problem of wheeled mobile robots (WMRs) over the past twenty years [1]. One reason is that WMRs are more and more widely used in different settings ranging from shopping centers, hospitals, manufactories for applications such as security, transportation, inspection, planetary exploration, etc. The other reason comes from theoretic challenge. As pointed out by the celebrated work of Brockett [2], nonholonomic systems, which include WMRs as special cases, cannot be asymptotically stabilized by any smooth time-invariant state feedback law. This makes the feedback stabilization problem of nonholonomic systems nontrivial. To deal with the technical obstacle, researchers have proposed three types of controllers that utilize smooth time-varying control laws, discontinuous time-invariant control laws, or a hybrid form of them to solve the stabilization problem. Another basic control problem is trajectory tracking, on which rapidly expanding researches have been carried out in the recent years. For an in-depth overview of the control of nonholonomic systems we refer to the early survey paper [1] and the recent one [3], as well as the references cited therein.

It seems that the problem of controlling certain classes of nonholonomic systems is virtually solved. Nevertheless, there are still many issues that deserve further attention for the WMRs control designer. An interesting issue which has often been overlooked is the control of WMRs moving on an uneven surface. It is assumed in most of the existing literatures that WMRs move on a plane. This is not the case when WMRs are utilized to perform tasks in some outdoor environment, e.g., planetary exploration.

T.-J. Tarn et al. (Eds.): Robot. Weld., Intellige. & Automation, LNCIS 362, pp. 61–70, 2007.
springerlink.com

From an engineering perspective, one should take into account the practical ground information to improve the performance of the control laws. An early result in this direction is [4], in which a discontinuous stabilizer is obtained under the high-order generalized chained systems framework.

From the above discussion, the objective of this paper is to present a method for solving the control problem of WMRs moving on an uneven surface. Smooth control laws are proposed based on the combination of transverse function method which is a new and still maturing control approach for nonlinear system [5-9], and the popular backstepping technique.

2 Modeling and Problem Formulation

Consider a differentially driven WMR moving on an uneven surface described by the equation $z = W(x, y)$. Assume that the wheels are rolling on the surface without slipping. It is the case if the friction in the contact point is sufficient large, and the grads of the surface are bounded. For the sake of simplicity, assume further that $W(x, y)$ is a quadratic polynomial described as follows:

$$W(x, y) = W_0 + \tfrac{1}{2}W_1 x^2 + W_2 x + W_3 xy + W_4 y + \tfrac{1}{2}W_5 y^2 , \tag{1}$$

where $W_i, i = 1,\ldots,5$ are some known constants. This simplified assumption meets with most real-world situations, at least locally, because any curved surface can be locally approximated by a quadratic surface.

The motion of the mobile robot will be certainly affected by the gravity. A simplified dynamic model of the mobile robot is described by the following equations

$$\begin{aligned} \dot{x} &= v\cos\theta \\ \dot{y} &= v\sin\theta \\ \dot{\theta} &= \omega \\ m\dot{v} &= \frac{\tau_1 + \tau_2}{r} - mg\left(\frac{\partial W}{\partial x}\cos\theta + \frac{\partial W}{\partial y}\sin\theta\right) \\ J\dot{\omega} &= \frac{(\tau_1 - \tau_2)}{r} l \end{aligned} \tag{2}$$

with θ the heading angle with respect to the x-axis of the inertial reference frame, v the translational velocity of the center of mass, and ω the angular velocity around the vertical axis of the body frame. The radii of the wheels is denoted as r, and the distance between the two rare wheels is $2l$. τ_1 and τ_2 are the applied torques of two motors driving the two rear wheels respectively. In what follows, the mass m, the moment of inertia J, the radii r, the distance l, and the gravitational constant g are all set to 1 for simplicity. The configuration of the mobile robot is described by the vector $(x, y, z, \theta)^T$, with $(x, y, z)^T$ the coordinates of the center of mass in the inertial

reference frame. The effect of the gravity to the motion is presented by the two partial derivative terms.

As we all know that the asymptotic stabilization problem of the wheeled mobile robot is not trivial. Actually, as pointed out in [7], the classical asymptotic stabilization is too restrictive and too constraining in some extent. Therefore, settling for practical stabilization other than asymptotic stabilization can be a more realistic control project to pursue.

3 Controller Design

3.1 Lie Group and Group Operation

First, let us consider the kinematic model of the wheeled mobile robot given by the first three equations of Eq. (2):

$$\begin{aligned} \dot{x} &= v\cos\theta \\ \dot{y} &= v\sin\theta \\ \dot{\theta} &= \omega \end{aligned} . \tag{3}$$

The configuration of the above subsystem is denoted as $q = (x, y, \theta)^T$. The subsystem is a system on the Lie group $SE(2)$, i.e., $R^2 \times S^1$, and the corresponding group operation $\phi : SE(2) \times SE(2) \to SE(2)$ is defined by

$$q_1 \circ q_2 = \phi(q_1, q_2) = \begin{pmatrix} \begin{pmatrix} x_1 \\ y_1 \end{pmatrix} + R(\theta_1) \begin{pmatrix} x_2 \\ y_2 \end{pmatrix} \\ \theta_1 + \theta_2 \end{pmatrix}, \tag{4}$$

where the matrix $R(\theta)$ presents the rotation in R^2 of angle θ.

Obviously, under the group operation, the unit element of the Lie group is $e = (0,0,0)^T$, and the right-inverse of $q \in SE(2)$ is defined as the unique element $q^{-1} \in SE(2)$ satisfying $\phi(q, q^{-1}) = e$.

One of the reasons we introduce the concept of Lie group is that the subsystem (3) possesses a particular invariance property with respect to the group operation of $SE(2)$.

Proposition 1: The subsystem (3) is left-invariant with respect to the group product (4).

Proof: The proof is trivial, thus we leave it out here.

3.2 Transverse Function and Dynamic Augmentation

The following theorem declares the relation between the existence of bounded transverse functions and the controllability of the system.

Theorem 1 [7]**:** Let G denotes a Lie group of dimension n, whose Lie algebra is Δ. Let $X_1,\ldots, X_m \in \Delta$ denote some independent vector fields. Then, the following properties are equivalent:

1. Lie Algebra Rank Condition (**LARC**): $Lie(X_1,\ldots, X_m) = \Delta$;
2. Transversality Condition (**TC**): For any neighborhood U of the unit element e in G, there exist a function $f \in C^\infty(T^{n-m};U)$ such that

$$G_{f(\theta)} = span\{X_1(f(\theta)),\ldots, X_m(f(\theta))\} \oplus df(\theta)(T_\theta^{n-m}),\ \forall \theta \in T^{n-m}. \tag{5}$$

Define the "transversality matrix" $H(\theta)$ as

$$H(\theta) = \left(X_1(f(\theta)),\ldots, X_m(f(\theta))\ \frac{\partial f}{\partial \theta_{m+1}}(\theta)\cdots\frac{\partial f}{\partial \theta_n}(\theta) \right), \tag{6}$$

then the coordinate-dependent version of the transversality condition (5) is

$$\det(H(\theta)) \neq 0,\ \forall \theta \in T^{n-m}. \tag{7}$$

There are many ways to compute the transverse function. A simple one is introduced in the proposition below.

Proposition 2 [9]***:*** For $\forall \varepsilon \in (0, \frac{\pi}{2})$, the mapping $f: T \to SE(2)$ defined by

$$f(\alpha) = \begin{pmatrix} \varepsilon \sin\alpha \\ \frac{1}{4}\varepsilon^2 \sin 2\alpha \\ \varepsilon \cos\alpha \end{pmatrix} \tag{8}$$

is a transverse function.

The submanifold M is a smooth embedding defined by the transverse function $f: T \to SE(2)$ of 1-torus (or the circle) $T = R/2\pi Z$ into the Lie group $SE(2)$, and its size is determined by the parameter ε. A sufficient small ε will make the submanifold M close enough to the origin. Now a dynamic augmentation procedure is applied to the kinematic subsystem as

$$\begin{aligned} \dot{q} &= B(q)u = \begin{pmatrix} X_1(q) & X_2(q) \end{pmatrix} \begin{pmatrix} v \\ \omega \end{pmatrix}, \\ \dot{\alpha} &= \zeta \end{aligned} \tag{9}$$

where the additional state $\alpha \in T$ is directly controlled by the augmented input ζ.

3.3 Error Dynamic System

The definition of the error variable is important because that a good definition may bring convenience to the control design. Instead of define the error variable in a

"natural" way as $z = q - f(\alpha)$, we take benefit of the invariance property of the subsystem on Lie group and define the error variable as follows:

$$z = f(\alpha) \circ q^{-1} = \phi(f(\alpha), q^{-1}) . \tag{10}$$

Differentiating the above equation leads to

$$\dot{z} = dr_{q^{-1}}(f(\alpha)) \frac{\partial f}{\partial \alpha}(\alpha)\dot{\alpha} + dl_{f(\alpha)}(q^{-1}) \frac{d}{dt}(q^{-1}) .$$

From $\phi(q, q^{-1}) = 0$ we get

$$\frac{d}{dt}(q^{-1}) = -\left(dl_q(q^{-1})\right)^{-1} dr_{q^{-1}}(q) B(q) u ,$$

then

$$\dot{z} = dr_{q^{-1}}(f(\alpha)) \frac{\partial f}{\partial \alpha}(\alpha)\dot{\alpha} - dl_{f(\alpha)}(q^{-1})\left(dl_q(q^{-1})\right)^{-1} dr_{q^{-1}}(q) B(q) u .$$

Notice that the subsystem is left-invariant, then

$$\begin{aligned} \dot{z} &= dr_{q^{-1}}(f(\alpha)) \frac{\partial f}{\partial \alpha}(\alpha)\dot{\alpha} \\ &\quad -dl_{f(\alpha)}(q^{-1})\left(dl_q(q^{-1})\right)^{-1} dr_{q^{-1}}(q) dl_{q \circ f(\alpha)^{-1}}(f(\alpha)) B(f(\alpha)) u \end{aligned} . \tag{11}$$

Further calculation shows that:

$$\begin{aligned} \dot{z} &= dr_{q^{-1}}(f(\alpha)) \frac{\partial f}{\partial \alpha}(\alpha)\dot{\alpha} \\ &\quad -dl_{f(\alpha)}(q^{-1}) dl_{q^{-1}}(e) dr_{q^{-1}}(q) dl_{q \circ f(\alpha)^{-1}}(f(\alpha)) B(f(\alpha)) u \\ &= dr_{q^{-1}}(f(\alpha))[\frac{\partial f}{\partial \alpha}(\alpha)\dot{\alpha} - B(f(\alpha)) u] \\ &= -dr_{q^{-1}}(f(\alpha)) H(\alpha) \begin{pmatrix} u \\ -\zeta \end{pmatrix} \end{aligned} , \tag{12}$$

where the matrix H is the nonsingular "transverse matrix" given in Eq. (6). The inverse of the matrix $dr_{q^{-1}}(f(\alpha))$ multiplying on the left of H is given by

$$\left(dr_{q^{-1}}(f(\alpha))\right)^{-1} = dr_q(z) ,$$

hence the selection of the following control law is straightforward for us so as to exponentially stabilize the origin $z = 0$ of the error dynamic system:

$$\begin{pmatrix} v \\ \omega \\ \zeta \end{pmatrix} = \begin{pmatrix} -1 & & \\ & -1 & \\ & & 1 \end{pmatrix} \left[H(\alpha)\right]^{-1} dr_q(z) K z , \tag{13}$$

with K any Hurwitz-stable matrix, Thus the resulting closed-loop system is expressed as

$$\dot{z} = Kz\,. \tag{14}$$

Eq. (13) is the "virtual" control law for the backstepping process in the next subsection. A Lyapunov function for the practical linearized subsystem (14) is $V_1 = z^T z/2$, and under the control law (13) the derivative of V_1 is negative-definite.

Remark: From Eq. (14) we see that the system is linearized by the control law (13), and will be decoupled by diagonal matrix K. Such kind of linearization is called "practical linearization". The common points which it shares with the dynamic feedback linearization are that the linearization results are both exact, and they all experience a dynamic augmentation procedure. The difference is that for wheeled mobile robots, there is a potential singularity in dynamic feedback linearization algorithm, and it is an intrinsic property of the nonholonomic system, whereas there is no singularity in the practical linearization algorithm.

3.4 Backstepping

Owing to its smoothness, the control law (14) can be utilized in integrator backstepping process to handle the dynamic system. Define $\overline{\tau}_1 = (\tau_1 + \tau_2) - \dfrac{\partial W}{\partial x}\cos\theta - \dfrac{\partial W}{\partial y}\sin\theta$, $\overline{\tau}_2 = (\tau_1 - \tau_2)$, then the dynamic model (2) can be rewritten as

$$\begin{aligned} \dot{q} &= X_1(q)v + X_2(q)\omega \\ \dot{v} &= \overline{\tau}_1 \\ \dot{\omega} &= \overline{\tau}_2 \end{aligned}\,. \tag{15}$$

The virtual control inputs of the kinematic subsystem (3) are denote by v_d and ω_d, respectively. Define the control errors as $\tilde{u} = u - u_d = (\tilde{v}, \tilde{\omega})^T$ with $\tilde{v} = v - v_d$ and $\tilde{\omega} = \omega - \omega_d$, and a candidate Lyapunov function for the system (15) as

$$V_2 = \frac{1}{2} z^T z + \frac{1}{2}(\tilde{v}^2 + \tilde{\omega}^2)\,.$$

Differentiate the above equation and it leads to

$$\begin{aligned} \dot{V}_2 &= z^T \left(-dr_{q^{-1}}(f(\alpha))H(\alpha)\begin{pmatrix} u_d \\ -\zeta \end{pmatrix} \right) + z^T \left(-dr_{q^{-1}}(f(\alpha))H(\alpha)\begin{pmatrix} \tilde{u} \\ 0 \end{pmatrix} \right) \\ &\quad + \tilde{v}(\dot{v} - \dot{v}_d) + \tilde{\omega}(\dot{\omega} - \dot{\omega}_d) \\ &= -z^T K z + z^T \left(-dr_{q^{-1}}(f(\alpha))H(\alpha)\begin{pmatrix} \tilde{u} \\ 0 \end{pmatrix} \right) + \tilde{v}(\dot{v} - \dot{v}_d) + \tilde{\omega}(\dot{\omega} - \dot{\omega}_d) \end{aligned}\,. \tag{16}$$

Define the matrix $Q = dr_{q^{-1}}(f(\alpha))H(\alpha) = [c_1, c_2, c_3]$ for convenience. Thus we have

$$\begin{aligned}\dot{V}_2 &= z^T Kz + z^T(-\tilde{v}c_1 - \tilde{\omega}c_2) + \tilde{v}(\dot{v} - \dot{v}_d) + \tilde{\omega}(\dot{\omega} - \dot{\omega}_d) \\ &= z^T Kz + \tilde{v}(\overline{\tau}_1 - z^T c_1 - \dot{v}_d) + \tilde{\omega}(\overline{\tau}_2 - z^T c_2 - \dot{\omega}_d)\end{aligned}.$$

If the control inputs $\overline{\tau}_1$ and $\overline{\tau}_2$ are selected as

$$\overline{\tau}_1 = -k_v \tilde{v} + z^T c_1 + \dot{v}_d , \tag{17}$$

$$\overline{\tau}_2 = -k_\omega \tilde{\omega} + z^T c_2 + \dot{\omega}_d . \tag{18}$$

with k_v and k_ω both positive, then the derivative of candidate Lyapunov function V_2 is

$$\dot{V}_2 = z^T Kz - k_v \tilde{v}^2 - k_\omega \tilde{\omega}^2 ,$$

and obviously, it is negative-definite. It is easy to derive the practical control inputs τ_1 and τ_2. The calculation of the derivatives $\dot{v}_d$ and $\dot{\omega}_d$ of the virtual control laws (17) and (18) is cumbersome but not very hard, and due to the space limit we leave it out here.

4 Simulations and Discussions

The uneven surface is given by the equation $z = W(x, y) = 0.4 + 0.4x^2 + 0.1xy - 0.1y^2$ in the simulations as in [4]. The matrix K is set to $diag(-1, -1, -2)$, and ε is set to 0.2. The control gains are set to $k_v = k_\omega = 1$. The initial states are $(5, 4, 3)^T$.

Fig.1 shows the time evolution of the states of the robot system. We can see that the states of the kinematic subsystem are stable after about four seconds. The oscillation frequency is decrease, and finally there is no oscillation. This is because that in the transverse function method, the additional state plays the role of time-varying term, and its frequency is also a freedom for the control design. The virtual control law is depicted in Fig.2 Notice that at the beginning, great control efforts are need. Nevertheless, the "virtual" control law remains bounded, and the envelopes of them are exponentially degenerate. It is obviously from Fig.3 that the error variables exponentially converge to zero, as a result, the state of the kinematic subsystem is stabilized to the embedding *M* defined by the transverse function. The actual control inputs remain bounded, and they are enclosed by exponentially degenerating envelopes too, as shown in Fig.4. The 3-dimensional trajectory on the uneven surface from the initial state to the origin is illustrated in Fig.5. It is not strange that there are so many cusps in the Cartesian trajectory due to the oscillation. The mobile robot is finally stabilized to the vicinity of the origin, thus coincides with the theoretic analysis.

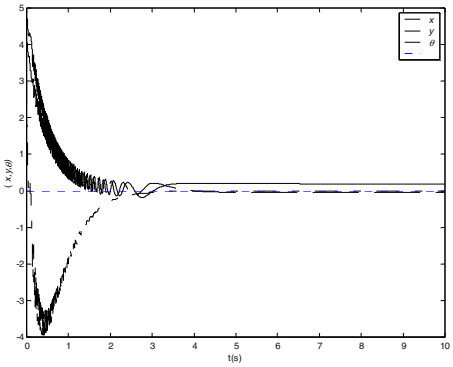

Fig. 1. The time evolution of the states $(x, y, \theta)^T$ of the kinematic subsystem

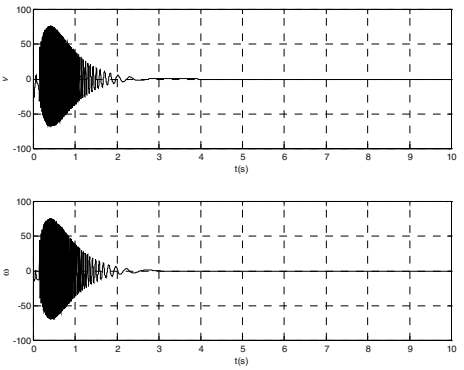

Fig. 2. The time evolution of the kinematic control inputs $(v, \omega)^T$

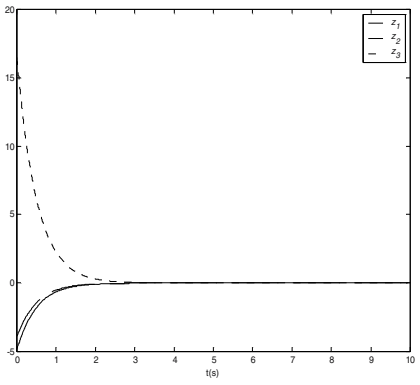

Fig. 3. The evolution of the error variables z

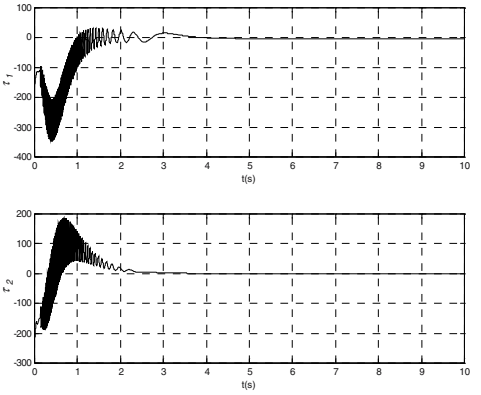

Fig. 4. The control inputs τ_1 and τ_2

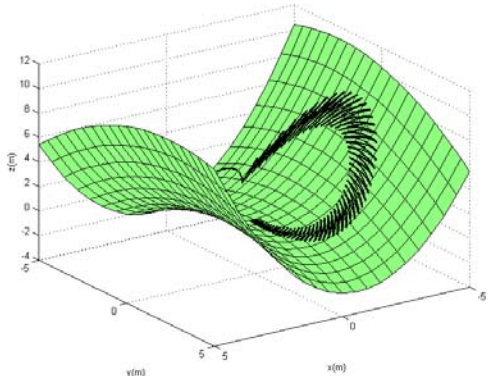

Fig. 5. The 3-dimensional Cartesian trajectory from the starting point to the origin

5 Conclusions

Smooth control laws are developed in this paper for the practical stabilization of WMRs moving on an uneven surface. The design procedure is based on the combining use of a newly developed method called "transverse function approach" and the widely used backstepping technique. The ideal is readily extended to the trajectory tracking problem, thus allow the simultaneously tracking and stabilization control problem be solved in an elegant way. Some future work will be carried out in different directions. One of them is to design adaptive control laws for the case the parameters of the uneven surface are unknown. It is of more practical meanings if the control laws can adapt to the grads of the surface. Another one concerns on an intrinsic property of the transverse function method. Because the mechanism of the transverse function method is to render the submanifold M asymptotically stable, so as to make the origin system practically stable. The submanifold M is a smooth embedding of the torus T^k, therefore the system states are attracted to the torus. Such a mechanism displays a drawback, i.e., although the system states are closer to the origin than to the torus initially, they are still attracted to the torus eventually, thus leads to larger errors. In order to improve the performance of the proposed control laws, we need some "switching" schemes which can take different actions to the states within or outside the torus.

Acknowledgement

This work was partially supported by the key project of NSFC under Grant 60234030, Distinguished Young Scholars Fund of China under Grant 60225015, and Ministry of Education of China (TRAPOYT Project).

References

1. Kolmanovsky I, McClamroch NH (1995) Developments in nonholonomic control systems. IEEE Control System Magazine 15(6): 20-36.
2. Brockett RW (1983) Asymptotic stability and feedback stabilization. In: Brockett RW, Millman RS, Sussmann HJ (eds) Differential Geometric Control Theory. Birkhauser, Boston, pp 181-191.

3. Luca AD, Oriolo G, Vendittelli M (2001) Control of wheeled mobile robots: An experimental overview. In: Nicosia S, Siciliano B, Bicchi A, et al. (eds) RAMSETE - Articulated and Mobile Robotics for Services and Technologies. Springer, pp 181-226.
4. Laiou MC, Astolfi A (1999) Discontinuous control of high-order generalized chained systems. System & Control Letters 37: 309-322.
5. Morin P, Samson C (2000) Practical stabilization of a class of nonlinear systems: Application to chain systems and mobile robots. 39th IEEE Conf. Decision Control, Sydney, Australia, pp2989-2994.
6. Morin P, Pomet JB, Samson C (2000) Design of homogeneous time-varying stabilizing control laws for driftless controllable systems via oscillatory approximation of Lie brackets in closed loop. SIAM Journal on Control and Optimization 38(1): 22-49.
7. Morin P, Samson C (2003) Practical Stabilization of Driftless Systems on Lie Groups: The Transverse Function Approach. IEEE Transactions on Automatic control 48(9): 1496-1508.
8. Morin P, Samson C (2002) A characterization of the Lie algebra rank condition by transverse periodic functions. SIAM J. Control Optim. 40(4): 1227-1249.
9. Morin P, Samson C (2004) Practical and Asymptotic Stabilization of Chained Systems by the Transverse Function Control Approach. SIAM Journal on Control and Optimization 43(1): 32-57.

An Efficient Method for Collision Detection and Distance Queries in a Robotic Bridge Maintenance System

J. Xu[1], D.K. Liu[1], and G. Fang[2]

[1] ARC Centre of Excellence for Autonomous Systems (CAS), Faculty of Engineering, University of Technology, Sydney, P.O. Box 123, Broadway, NSW 2007, Australia
{jiex, dkliu}@eng.uts.edu.au
[2] School of Engineering, University of Western Sydney, Locked Bag 1797, Penrith South DC 1797, Australia
g.fang@uws.edu.au

Abstract. When applying autonomous industrial robotic systems in an unknown/partially known or cluttered environment, mapping and representation of the environment as well as collision detection becomes crucial. Existing techniques in these areas are generally complex and computationally expensive to implement. In this paper an efficient sphere representation method is introduced for environment representation, collision detection and distance queries. In particular, this method is designed for the application in an autonomous bridge maintenance system. Simulation results show that this method is effective in environment representation and collision detection. Furthermore, the proposed method is also computationally efficient for real-time implementation.

1 Introduction

Industrial robots have been widely used in manufacturing, painting, welding and material handling. Most applications require industrial robots to perform repetitive jobs. Once they are programmed, they will repeat the same movements by following pre-planned paths. When there are uncertainties in either the robot work environment or the robot locations, the robot needs to "know" or "resolve" these uncertainties before it can take any actions.

Therefore, when industrial robots are to be used in the maintenance of large and complex infrastructures, such as steel bridges, the traditional systems need to be extended to deal with the major challenges that include:

1) Time critical: the robot has to be able to detect potential collisions and take actions in real-time.
2) Varying environment and non repetitive tasks: since the robot will be facing different structures or different aspects of the same structure, the robot is required to move in different paths. Furthermore, due to the non repetitive nature of the tasks, the planning and collision detection for the robot have to be performed in real-time.

T.-J. Tarn et al. (Eds.): Robot. Weld., Intellige. & Automation, LNCIS 362, pp. 71–82, 2007.
springerlink.com

3) Complex and tight environment: the structure, or the environment may be complicated or cluttered, and the work environment is small and crowded compared to the robotic work place in a workshop. Thus, efficient collision detection and avoidance become critical and difficult problems that must be solved in real-time.
4) Partially known environment: even though the CAD drawings of a structure or bridge always exist, it is difficult to guarantee that all refurbishments and upgrades are recorded in the drawings. Thus, the environment is most likely to be partially known.

These challenges have led to the need of developing effective and efficient methods to accurately map the environment, detect potential collisions and plan collision-free paths.

In general, the path planning in such applications as infrastructure maintenance uses the geometry information of the structure to generate an effective and efficient trajectory to cover the structure surface that needs to be treated. Any potential collision must be detected to verify if the entire trajectory is "valid", i.e., collision-free.

When using the robot for infrastructure maintenance, such as steel bridge cleaning, the accuracy of the robotic system is not as critical as in traditional applications such as welding and material handling. This gives some flexibility in developing the control algorithm.

In this research, an efficient sphere based approach is introduced for environment representation, virtual surface generation, collision detection, and robot arm pose calculation for applications in an autonomous robotic bridge maintenance system, based on the environmental map obtained from mapping. In this approach, the environment and the robotic arm are represented with a number of spheres, which give a simple and quick way for collision detection and distance queries. This approach will be presented in Section 3 after the review of related work in Section 2. Section 4 presents the simulation results, which is followed by discussions and conclusions in Section 5.

2 Related Works

Collision detection and distance measurement is a time-consuming but important task when an industrial robot is applied in a crowded environment. The computational time of intersection test and distance measurement highly depends on the types of primitives, the number of primitives (or the number of objects) and the algorithms used [1].

The general approach to solve this problem is to use hierarchy of bounding volume which is suitable for performing 3D proximity queries between general polyhedra [2]. The volumes can be discrete orientation polytope (k-DOPs) [3], oriented bounding boxes (OBB) [4], spheres [5]-[10], axis aligned bounding boxes (AABB) [4][11], swept sphere volumes (SSV) [12][13], convex hull [4][14], ellipsoids [15] or spherical shells [16], depending upon the requirements of computational time and accuracy.

Although OBBs, k-DOPs and ellipsoids can describe an object more precisely than spheres and AABBs in most cases, they are more time consuming [4]. Hubbard [5][6] used Octree and medial-axis surface to generate spheres and Bradshaw [7] improved it by using adaptive medial-axis approximation. Pobil et al. [8]-[10] used spherical approximation to represent a robot arm and heuristic methods to build the hierarchy and refine sub-region when it is necessary.

Distance query is more computationally expensive than collision detection because of additional geometric analysis and distance calculation [18]. Johnson et al. [19] used OBB and AABB to measure the distance under a lower-upper bound tree framework. One benefit of OBB is that the tree does not need to be recomputed when the orientation of an object changes [17]. However, the algorithm for building an OBB Tree is more expensive than AABB in terms of computational time.

Okada et al. [11] and Caselli et al. [20] evaluated most of the proximity query packages (I-COLLIDE, RAPID, V-COLLIDE, SOLID, V-Clip, PQP, and SWIFT) using the C/C++ platform, and found the performance was highly dependent on the problem to be solved.

Reichenbach et al. [21] used OBB to perform on-line trajectory re-planning. Redon et al. [22][23] introduced a general method, continuous collision detection (CCD), to detect possible collisions between two collision-free way-points.

In general, the sphere based approach is computationally more efficient than the rectangle based methods. As a result, in the applications where accuracy is less critical than efficiency, a sphere representation should be used.

3 The Efficient Spherical Approach

As discussed in Section 2, the spherical approximation approach has been investigated by many researchers for object and robotic arm representation. In this section, a simplified spherical approach is presented for environment representation, distance queries and robot joint pose calculation in an application to steel bridge maintenance.

3.1 The Efficient Spherical Representation

Conventionally, spheres have been used to approximate an object by minimising the difference between the real object and the virtual object represented by the spheres. In this research, however, the difference between the virtual and the real objects is used as a buffer to prevent the collision between the environment and the robotic system. A set of spheres can create a safety strip between the robot and the environment. Thus, instead of trying to minimise the difference, we determine the difference value based on the robot speed and required safety distance between the robot arm and the environment.

Fig. 1 shows the spherical representation of a robot arm and a environment consisting of I-beams and bridge deck in a bridge structure. Five spheres with different radius are used to represent the robotic arm. A number of spheres with the same radius are used to represent I-beams and the bridge deck.

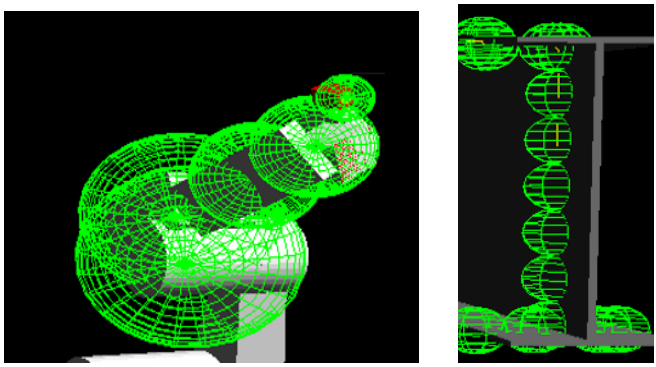

Fig. 1. Spherical representation of a robot arm (left) and I-beams and bridge deck (right)

With this spherical representation of the environment, the buffer (the shaded area in Fig. 2a) is used for collision avoidance. The minimum difference in distance, D_s, is defined as the safety distance (Fig. 2a) which is greater than or equal to the preset requirement D_{smin}, i.e. $D_s \geq D_{smin}$. With this safety distance requirement, the distance between the two adjacent spheres, d, can be calculated as:

$$d = 2 \times \sqrt{(R_1 + R_2)^2 - (R_2 + D_s)^2} \tag{1}$$

Where R_1 *is* the radius of the sphere representing the environment and R_2 is the smallest radius among the 5 spheres representing the robot arm (Fig. 2b). The centres of the environment spheres, e.g., O_1 and O_2, are located on the real surface.

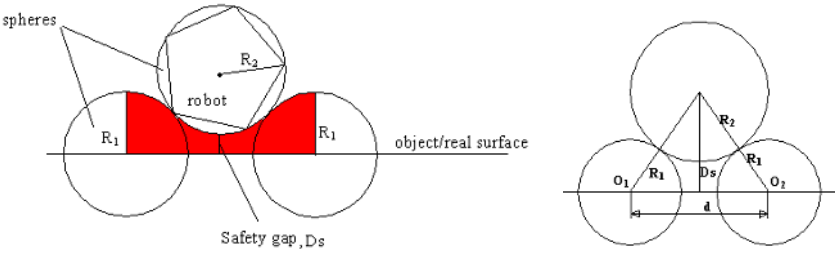

Fig. 2. (a) The buffer area used as the safety area (left) and (b) distance calculation (right)

In real-time collision detection and distance queries between the robot arm and the environment presented by the spheres, the distance can be simply calculated according to the centres of the robot spheres and the environmental spheres:

$$D = \min\left\{\sqrt{(X_{ri} - X_{ej})^2 + (Y_{ri} - Y_{ej})^2 + (Z_{ri} - Z_{ej})^2}\right\} \tag{2}$$
$$\forall\, i = 1,2,\ldots,N_r\,;\, j = 1,2,\ldots,N_e$$

where (X_{ri}, Y_{ri}, Z_{ri}) is the centre of the robot arm spheres, N_r is the number of spheres used to represent the robot arm. (X_{ej}, Y_{ej}, Z_{ej}) is the centre of a sphere representing the environment and close to the robot arm. N_e is the number of spheres in the environment and close to the robot arm. Although this is an approximation, safety distance D_{smin} is guaranteed.

The number of spheres used to represent the environment has a significant effect on the computational efficiency of collision detection and distance queries. The number and the radius are determined based on the complexity of the environment, safety distance requirement, maximum moving speed of the robot arm, etc. On a flat surface and with slow robot moving speed, the number of spheres, N_s, for the surface representation can be approximately calculated as:

$$N_s = \left(\frac{L_1}{d} + 1 \right) \times \left(\frac{L_2}{d} + 1 \right) \tag{3}$$

Where, L_1 and L_2 are the length and width of the surface, respectively.

3.2 Virtual Surface

With the spherical representation of an environment, surface of the buffer area forms what can be called a *virtual surface* (Fig. 3a) which prevents the robot arm from penetrating into the buffer area. Fig. 3b shows a part of a virtual surface in 3D. The virtual surface is a hard constraint to the robot arm movement in a 3D environment and is helpful for analysing any possible collisions and the motion of the robot arm.

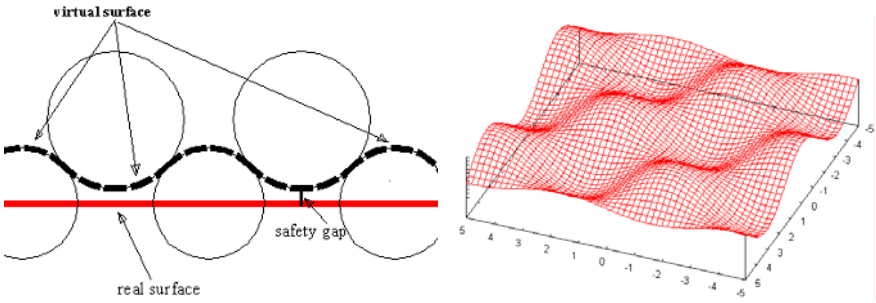

Fig. 3. (a) Virtual surface generation (left) and (b) a virtual surface in 3D (right)

3.3 Optimal Pose Calculation Based on the Spherical Representation

The distance between the robot arm and the environment, D, is used to determine the joint movement. Instead of using the traditional inverse kinematics method, an optimisation based pose calculation approach is applied. This optimisation method can effectively avoid singularity which occurs commonly in the inverse kinematic solutions. It can also obtain the optimal pose for joint movements by satisfying various constraints. The objective function of the pose selection is:

$$\min_{\theta_j} \quad \left(f_0 + f_1 + f_2 + f_3 + f_4 + f_5 \right) \tag{4}$$

Where, θ_j are the joint angles of the robot (j = 1, 2, …, 6) and subjected to the constraints of the robot joint movements. $f_0, f_1, \ldots, f_5$ are the measurement vectors (or residual vectors).

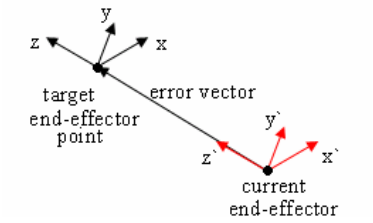

Fig. 4. x, y and z represent target orientation; x`, y` and z` represent current orientation

The difference between the end-effector/nozzle's current position and the target position is defined as *error vector* (Fig.4). End-effector/nozzle's position and orientation are expressed in a 4×4 matrix:

$$T = \begin{bmatrix} n_x & s_x & a_x & p_x \\ n_y & s_y & a_y & p_y \\ n_z & s_z & a_z & p_z \\ 0 & 0 & 0 & 1 \end{bmatrix} \tag{5}$$

where the top left 3×3 elements define the orientation in x, y and z directions, p_x, p_y and p_z represent the position.

$$f_0 = \text{(error vector)} \bullet \text{(x` direction)} \tag{6}$$

$$f_1 = \text{(error vector)} \bullet \text{(y` direction)} \tag{7}$$

f_0 and f_1 are used to make sure that the nozzle is pointing at the target. In addition, the angle between z' direction and z direction is constrained in the range of [-45°, +45°]. This constraint is expressed in the following equation:

$$f_2 = e^{-k(\alpha+45^o)} + e^{k(\alpha-45^o)} \tag{8}$$

where α is the angle between z` and z, k is a non-negative slope coefficient. f_3 represents the distance between the nozzle and its target position:

$$f_3 = \|\text{distance vector}\| \tag{9}$$

f_4 represents the constraints of robot joint angles and is expressed in the following equation:

$$f_4 = \sum_{j=1}^{6} (e^{-k_j(\theta_j - \min_j)} + e^{k_j(\theta_j - \max_j)}) \tag{10}$$

where θ_j is the jth joint angle while min_j and max_j represent the minimum and the maximum allowed joint angles of the jth joint of the robot. f_5 is a function of the distance between the robot arm and the environment represented by the spheres:

$$f_5 = \sum_{i=1}^{n} e^{-k \times D_i} \tag{11}$$

where, n is the number of distance queries; and D_i is the distance between the robot arm and the environment and is calculated in Equation (2).

By minimising the objective functions, the angular displacement of each joint, θ_j, of the robot arm at any instance can be obtained. A least square algorithm [24] is employed to solve the optimal pose selection problem.

4 Simulation Results

Simulations are conducted based on a Denso robot (model VM-6083D-W). It is assumed that the robot is used to clean a steel bridge that consists of I-beams and a deck (Fig.5a). The Denso robot has 6 joints and is placed between the two I-beams under the deck. The robot joint ranges of θ_1 to θ_6 are listed in Table 1.

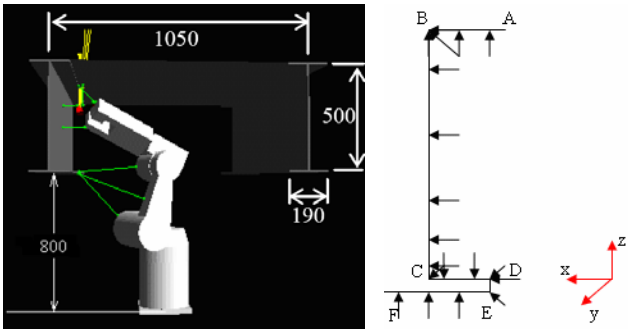

Fig. 5. (a) The robot and the bridge structure (left); (b) a path from A, B, C, D, E to F along the I-beam, arrows point to the surface represent the orientation of the nozzle (right)

At a position, the robot will clean one section of the bridge. The paths of the robot arm for cleaning the section are designed by a path planner. Fig.5b shows an example path along the surface of an I-beam from point A, B, C, D, E, to F. The arrows in the figure represent the orientation (perpendicular to the surface) of the cleaning nozzle.

Table 1. Denso VM-6083D-W joint angle range (degree)

	Minimum	Maximum
θ_1	-170	170
θ_2	-90	135
θ_3	-10	165
θ_4	-185	185
θ_5	-120	120
θ_6	-360	360

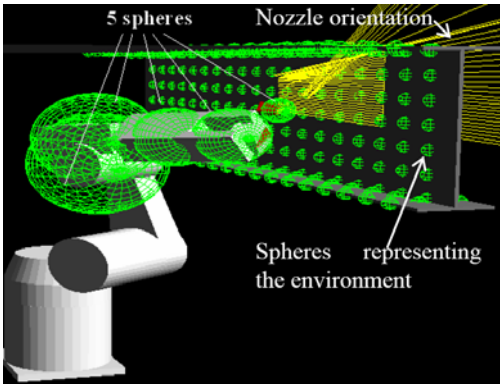

Fig. 6. A path and nozzle orientation in a strictly constrained structural environment

88 pre-defined waypoints are set along the path from A to F. The robot moves the cleaning nozzle installed on the robot end-effector along the path. In this movement, the nozzle orientation can vary between 45° to 90° in order to maintain the cleaning quality and productivity. The challenge of this operation is that the robot arm needs to move from the top side to the bottom side of the I-beam with a 180°orientation change in a tightly constrained environment. Fig.6 shows the robot arm represented by 5 spheres and the spherical approximation of the environment. A path from the top is also shown with nozzle orientation displayed.

The radii of the 5 spheres of the robot arm are 0.2m, 0.18m, 0.10m, 0.044m, and 0.11m, respectively, based on the size of the robot arm. The spheres presenting the I-beams and the deck have the radius of 0.02m. When the minimum safety distance is D_{smin}=0.006m and R_2 is 0.044m (the 5th radius), d is 0.08m according to Equation (1). Thus, d should be less than or equal to 0.08m.

When the robot moves along the path, the distances between the robot arm and the environment are calculated for collision detection at the waypoints. In addition, if any one of the 6 joint angles changes significantly (e.g., more than 10°) between the consecutive waypoints, collision should also be checked during the robot movement between these two waypoints although there is no collision at the two waypoints. This collision detection is simply done by adding more points between the two and then checking those added points.

Fig.7 shows how the robot tracks a path and satisfies the nozzle orientation requirement without any collision. The four figures in Fig.7 show different robot arm positions and nozzle orientations. The robot joint movements at each time step are calculated by the optimal pose calculation method discussed in Section 3.3.

The simulation results show that the movements of the 6 joints from waypoint to waypoint are continuous and smooth. The spherical approach based optimal pose selection method can find appropriate poses for joints to make the robot motion smooth and collision free. Even when the robot is dealing with the bottom surface of the I-beam

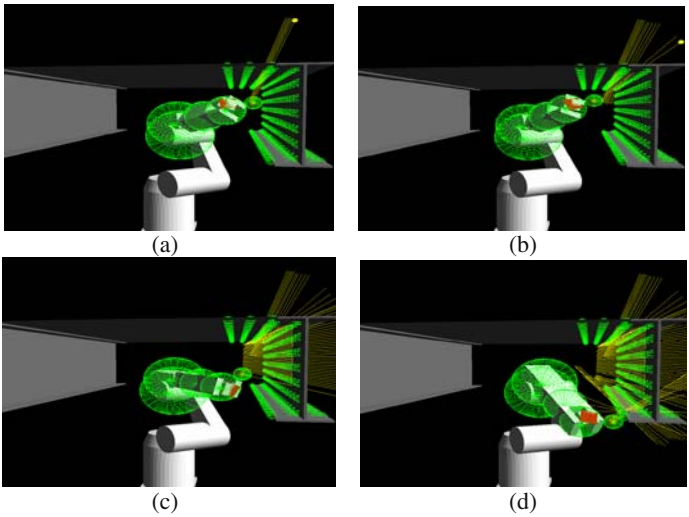

Fig. 7. The robot moves from the top to the bottom of the I-beam

where the nozzle orientation changes sharply, the selected robot movement still does not cause any collisions. Fig. 8a shows how the joint angle changes along the path from waypoints 1 to 88. It can be seen that the 6^{th} joint has significant angular changes in its movement from waypoints 14 to 20 and from waypoints 75 to 77. Collision detection in these two parts of the path confirms that it is collision free.

The distance between the robot arm and the environment during the movement of the robot along the path is shown in Fig.8b. Seven distance queries are recorded during the process. They are d_1 to d_5 representing the distance between the five spheres of the robot arm and the environment, d_6, the distance from the end-effector of the robot arm to the environment and d_7 the distance from the nozzle (installed on the end-effector) to the environment. It can be seen that d_6 and d_7 increase sharply from waypoints 74 to 88 while others decrease. This is because the nozzle and the end-effector of the robot arm move away from the deck when they approach the bottom surface of the I-beam. It can also be seen that all the distances are greater than 0 at any time along the path, which demonstrates that there is no collision.

In order to investigate the efficiency of the spherical approach introduced in this research, PQP approach is also applied. Both approaches were used for distance queries and collision detections on different paths. Due to the space limitation of the paper, only the results of six (6) randomly selected paths are shown. The computational time required by the two approaches is presented in Table 2. It can be seen that, for the application discussed in this research, the represented spherical approach is more efficient than the PQP. It is clear from the table that the average reduction of computational time is about 80%.

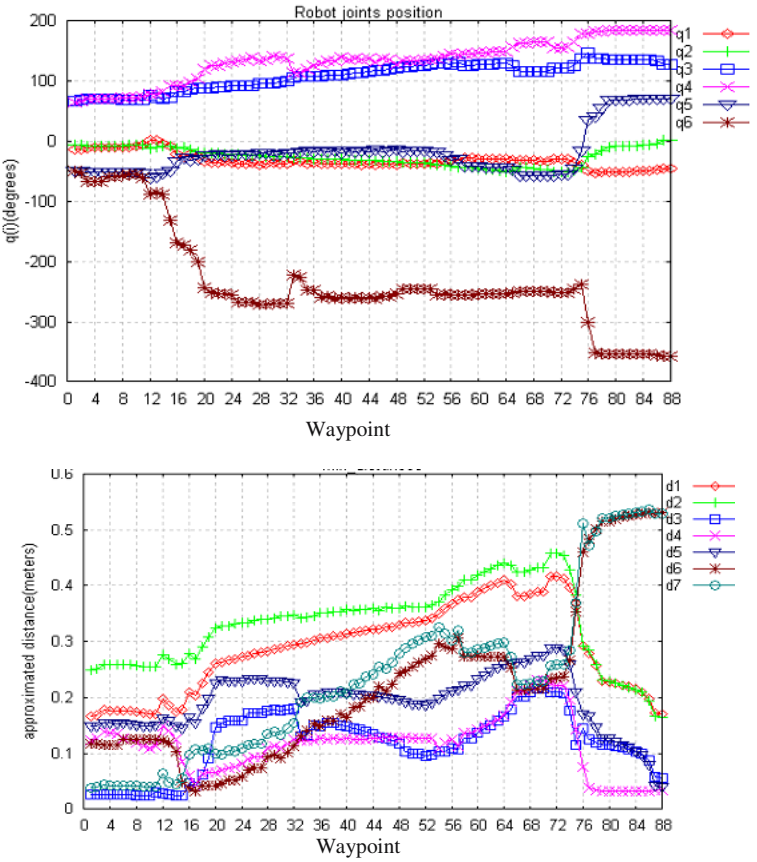

Fig. 8. (a) The changes of angles (unit: degree) of joints q1 to q6 (upper), (b) distances between the spheres of the robot arm and the environment (bottom)

Table 2. Efficiency comparison

Computational time (sec) / Path / Methods	1	2	3	4	5	6
PQP	89.2	83.8	82.4	81.0	83.3	75.4
The approach in this paper	18.9	16.6	14.5	13.5	9.6	13.8
Reduction (%)	78.7	80.2	82.5	83.3	88.4	81.7

5 Conclusions

In this paper, a simplified spherical approach is studied for application in a robotic bridge maintenance system. This approach is shown to be computationally efficient for distance queries and collision detection in complex and constrained environments. Although this efficiency gain is at the cost of a reduced accuracy in representing the

robot and the environment, it is acceptable for applications where the computational time is more critical than accuracy. This simplified spherical approach can be used to represent the robot and the environment with much less number of spheres. It can also generate a virtual surface that can be used to evaluate the safety distance requirement in collision avoidance. When combined with an optimization method, this sperical representation approach can be successfully used to calculate the joint movements of a robot arm without collision with the environment.

We are working now to improve the method to: (1) achieve an automatic sphere generation strategy to minimize human intervention; (2) test in more complex environments; and (3) develop collision avoidance strategies using the distance information obtained from this approach.

References

1. Schwarzer, F., Saha, M., and Latombe, J. C., Adaptive Dynamic Collision Checking for Single and Multiple Articulated Robots in Complex Environments, *IEEE Transactions on Robotics*, Vol. 21, No. 3, June 2005.
2. Weghorst, H., Hopper, G., and Greenberg, D. P., Improved Computational Methods for Ray Tracing, *ACM Transaction on Graphics*, Vol. 3, No. 1, January 1984.
3. Klosowski, J.T., Held, M., Mitchell, J.S.B., Sowizral, H., and Zikan K., Efficient Collison Detection Using Bounding Volume Hierarchies of k-DOPs, *IEEE Transactions on Visualization and Computer Graphics*, Vol. 4, No. 1, 1998.
4. Gottschalk, S., Lin, M.C., and Manocha, D., OBBTree: A Hierarchical Structure for Rapid Interference Detection, *Proc. of 23rd Annual Conference on Computer Graphics and Interactive Techniques*, ACM press, 1996.
5. Hubbard, P.M., Interactive Collision Detection, *Proc. of IEEE Symposium on Research Frontier in VR*, 1993.
6. Hubbard, P.M., Approximating Polyhedra with Spheres for Time-Critical Collision Detection, *ACM Transaction on Graphics*, Vol. 15, No. 3, 1996.
7. Bradshaw, G., O'Sullivan, C., Adaptive medial-axis approximation for sphere-tree construction, *ACM Transactions on Graphics,* Vol. 23, 2004.
8. Del Pobil, A.P., Serna, M. A., Llovert, J., A new representation for Collision Avoidance and Detection, *Proceeding of the IEEE International Conference on Robotics and Automation,* 1992.
9. Del Pobil, A.P., Pkrez, M., Martinez, B., A Practical Approach to Collision Detection between General Objects, *Proceeding of the IEEE International Conference on Robotics and Automation,* 1996.
10. Martinez-Salvador, B., Perez-Francisco, M., Del Pobil, A.P., Collision Detection between Robot Arms and People, *Journal of Intelligent and Robotic Systems,* Kluwer, Vol. 38, 2003
11. Okada, K., Inaba, M., Inoue, H., Real-Time and Precise Self Collision Detection System for Humanoid Robots, *Proceeding of the IEEE International Conference on Robotics and Automation*, 2005.
12. Larsen, E., Gottschalk, S., Lin, M.C., Manocha, D., Fast Distance Queries with Rectangular Swept Sphere Volumes, *Proceeding of the IEEE International Conference on Robotics and Automation*, 2000.
13. Larsen, E., Gottschalk, S., Lin, M.C., Manocha, D., *Fast Distance Queries with Swept Sphere Volumes*, Department of Computer Science, UNC, Rep. TR99-081, 1999.

14. Ehmann, S., Lin, M.C., Accelerated Distance Computation between Convex Polyhedra by Multi-Level Marching, Technical Report, Department of Computer Science, UNC at Chapel Hill, 1999.
15. Kimoto, T., Yasuda, Y., Shape Description and Representation by Ellipsoids, *Signal Processing: Image Communication*, Vol. 9, No. 3, Elsevier Science, March 1997.
16. Füfzig, C., Ullrich, T., Fellner, D.W., Hierar chical Spherical Distance Fields for Collision Detection, *Computer Graphics and Applications*, IEEE, 26(1), 2006.
17. Sanchez-Ante, G., *Single-Query Bi-Directional Motion Planning with Lazy Collision Checking*, PhD thesis, Department of Computer Science, Instituto Tecnologico Y De Estudios, Mexico.
18. Latombe, J.-C., *Robot Motion Planning*, Kluwer Academic, 1991.
19. Johnson, D.E., Cohen, E., A Framework for Efficient Minimum Distance Computations, *Proceeding of the IEEE International Conference on Robotics and Automation*, 1998.
20. Caselli, S., Reggiani, M., Mazzoli, M., Exploiting Advanced Collision Detection Libraries in a Probabilistic Motion Planner, *Journal of WSCG*, 10(1-3), 2002.
21. Reichenbach, T., Kovacic, Z., Collision-Free Path Planning in Robot Cells Using Virtual 3D Collision Sensor, *Cutting Edge Robotics*, ISBN 3-86611-038-3, pp. 683~704, ARS/plV, 2005.
22. Redon, S., Kim, Y.J., Lin, M.C., Manocha, D., Fast Continuous Collison Detection for Articulation Models, *ACM Symposium on Solid Modeling and Application*, 2004.
23. Redon, S., Fast Continuous Collision Detection and Handling for Desktop Virtual Prototyping, *Virtual Reality*, Springer, Vol. 8, No. 1, 2004.
24. Nocedal, J. and Wright, S. J., Numerical Optimization, Springer-Verlag, New York, 1999

Laser Vision System Based on Synchronized Scanning Method

Victor S. Cheng[1,*], L.J. Hao[1,*], X.Z. Chen[2], S. Zhang[1], and Y.Z. Chen[1]

[1] Institute of Biomedical Instrument, Shanghai Jiao Tong University, 1954 Huashan Rd., Shanghai 200030, P.R. China
chengsheng@ieee.org
[2] Institute of Welding Engineering, Shanghai Jiao Tong University, 1954 Huashan Rd., Shanghai 200030, P.R. China

Abstract. In this paper, a laser vision system based on synchronous scanning technology is developed. The proposed system is composed of a fixed CCD camera, a fixed line laser projector and a scanning mirror. While the scanning mirror rotates under the control of a stepping motor, the optical paths of projection and receiver are changed synchronously. The geometrical relation is discussed for designing an experimental prototype. The experiment results obtained from the scanning system are also shown. The measurement accuracy is equivalent to the conventional vision sensors. The system utilizing the less complex mechanism can realize a wide angle-of-view 3D surface acquisition.

1 Introduction

Machine vision plays an important role in research and commercial activities. Main stream of application fields involve industrial automation [1-3], virtual reality [4] and medicine [5]. Meanwhile, there are three popular 3D imaging techniques which are stereo, structured light and time of flight [6]. Among these different techniques reported in the literatures [6-9], the structured light based on triangulation method has been recognized to evolve toward a low-cost 3D camera. In the general structured light 3D sensor, the system projects a laser stripe onto the inspected object and uses a CCD camera to capture the deformed stripes, and then extracts the trace of laser stripe. After calculating the relative 3D coordinate of the illuminated pixels on the series of CCD images, the spatial profile of inspected object can be got. However, the most existing 3D imaging methods can be merely realized in the relatively small spatial scope because of the constrained common field-of-view. Movements of the vision system can gain the distance information of a large object, but these methods are expensive as a result of their complex mechanical systems.

A novel imaging technology based on a synchronized scanner is presented in this study. By changing the reflected optical path of the laser projection and CCD camera simultaneously, the system can measure the size of the inspected object in a large view range. This technology is suited for design the kind of compact vision system applied in acquiring 3D surface of the large object in the relatively short distance.

* Corresponding authors.

T.-J. Tarn et al. (Eds.): Robot. Weld., Intellige. & Automation, LNCIS 362, pp. 83–89, 2007.
springerlink.com

The rest of this paper is arranged as follows: in Section 2, the geometric models of the vision system are addressed in detail. Section 3 describes the operation of the experimental prototype. Afterwards, the experiments on this system are performed. Finally, conclusions are drawn in the last section.

2 Geometrical Analyses

Fig.1 shows the principal geometrical layout of the proposed vision system. At the origin of the system coordinates *OXYZ*, there is the middle point of the distance between the camera lens and the line laser projector. The focus length of lens from position *O'* (*-a, 0*) is *f*. And the angle between the lens axis and *X*-Axis is δ. Then, the projector generates a laser stripe with the angle ϕ from position (*a, 0*) in *OXZ*. Meanwhile, the mirror rotates synchronously the optical path of the laser projector and the CCD camera with the angle θ at the point *A* (*0, b*).

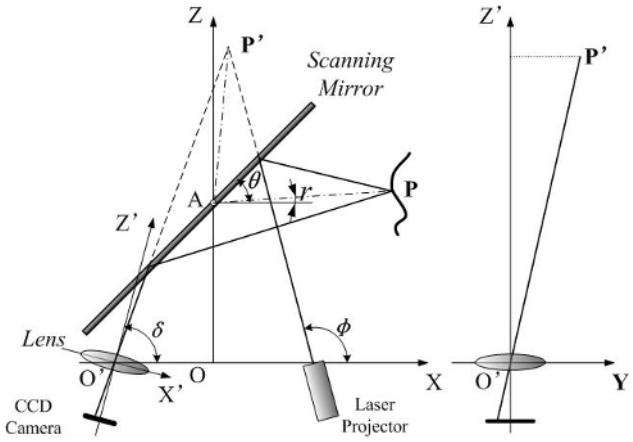

Fig. 1. Schematic layout and spatial geometry analysis of the proposed vision system

Any point on the laser stripe illuminates a spatial point *P* (*x, y, z*) in *OXYZ*, which forms an image (*m*, *n*) on the CCD image plane. The angle of *AP* from *X*-Axis is defined as *r*, and the image of Point *P* in the mirror be *P'* which is viewed as reference point in the vision system. According to the relationship between an object and its image, the length of |*AP*| is always equal to the distance between the rotation center *A* and the point *P'*, and independent on the variation of θ. And *x* and *z* value of the point *P'* can be expressed as follows:

$$\begin{pmatrix} x_{P'} \\ z_{P'} \end{pmatrix} = \frac{1}{\tan\phi - \tan(\delta + \Delta\delta)} \begin{pmatrix} a & 0 \\ 0 & a \end{pmatrix} \begin{pmatrix} \tan\phi + \tan(\delta + \Delta\delta) \\ 2\tan\phi\tan(\delta + \Delta\delta) \end{pmatrix} \tag{1}$$

Where $\Delta\delta$ is defined as $\tan^{-1}(m/f)$. Then,

$$|AP|^2 = |AP'|^2 = x_{P'}{}^2 + (z_{P'} - b)^2 \tag{2}$$

Moreover, it is noticed that the trajectory of the point P in OXZ plane is a circle with radius $|AP'|$ centered on the rotation axis A (0, b) of the mirror. Also, the rotation angle r is obtained as two times of the scanning angle θ, which is

$$r = 2\theta - \tan^{-1}\left(\frac{z_{P'} - b}{x_{P'}}\right) \tag{3}$$

By trigonometry the relationship between the coordinates (x, z) and the geometry parameters can be derived as

$$\begin{pmatrix} x \\ z \end{pmatrix} = |AP'| \begin{pmatrix} \cos r \\ \sin r \end{pmatrix} + \begin{pmatrix} 0 \\ b \end{pmatrix} \tag{4}$$

Where $|AP'|$ can be obtained from Equation (2). Also, Y-axis and Y'-axis are in the same direction. Similarly, the image point P' is fixed in OXZ plane although the coordinate (x, z) of point P can be changed by the rotation of the scanning mirror. So the y value of the point P can be gained by calculating the y value of the point P'. The Z' coordinate is the prolongation of the Lens axis through the mirror. The Z' value of the point P' can be denoted by

$$z'_{P'} = |O'P'| \cos \Delta\delta \tag{5}$$

where $|O'P'|$ is defined as $\sqrt{(x_{P'} + a)^2 + z_{P'}^2}$. Thus, the y value of P is obtained by

$$y = y_{P'} = \frac{n|O'P'| \cos \Delta\delta}{f} \tag{6}$$

Then, the computer simulation is programmed to study the 3D space trajectory of the vision system reported here. The point P' is assumed to the intersection point of the axes and angle δ is equal to angle ϕ. Let the value of θ be varied from 30^o to 60^o. For assumed that the value of the angle-of-view of the 3D profilometer and the CCD camera are 16^o in OYZ. If $a = 100mm$, then $b = 200mm$ and $|AP'| = 1000mm$. In Fig.2, the mesh diagram shows the results from the derived equations, which is a part of a cylinder with the radium defined as the spatial referred trajectory of the scanning system.

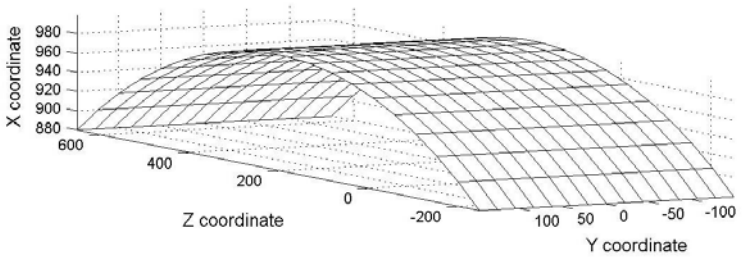

Fig. 2. Mesh diagram for the scanning trajectory of $a = 100mm$, $b = 200mm$ and $|AP'| = 1000mm$

3 Operation Descriptions

The apparatus designed in this study is shown in Fig.3. The 3D imaging sensor includes one self-developed line-laser light source and one high resolution CCD camera (1/3 inches, 0.01lux, Sony Co.). And a 16-mm, F 1.6 TV lens (AVENIR Co. SE1616) is equipped.

Fig. 3. Picture of the experimental apparatus: the proposed wide angle-of-view integrated vision system and the inspected model

In order to simplify the operation and calibration of the vision system, the lens axis is designed to be vertical to the experimental table. During the manufacture of the proposed vision system, the camera has been fixed in the bracket of device which guarantees the vertical condition. And the *X*-Axis of the device is tilted at angle δ with the horizontal direction in this study. The stepping motor (2-phase, Oriental Motor Co.) is applied in these experiments with high precision in operation. The rotation of the scanning mirror keeps pace with the 3D surface and CCD images acquisition to store ongoing valid information in time. And the rotation axis of scanning mirror is adjusted carefully to be parallel with the *Y*-axis of CCD and CCD image plane. An external trigger signal synchronizes the startup of the vision system.

4 Experiments

The performance of the proposed vision system is evaluated by some experiments. The aim at the first stage is to determine the repetitive precision of the range value *x*, *y* and *z* of 3D profilometer by using the proposed system. In Fig.4 the results of a plane surface in *OXZ*, which is located at a distance of about 1000 mm from the lens axis, are scanned in this experiment. The solid line shows the expected theoretical results while the values measured in the experiments are indicated by the other different symbols. The variation of the range value in this test is about 10 mm as shown in Fig.4. The

reproducibility of the experimental results is shown for this case as well. Over this range the three sets of data points shown by O, + and * symbols are matching well and the range distance *X* is shown as a linear function of the *Z* coordinate.

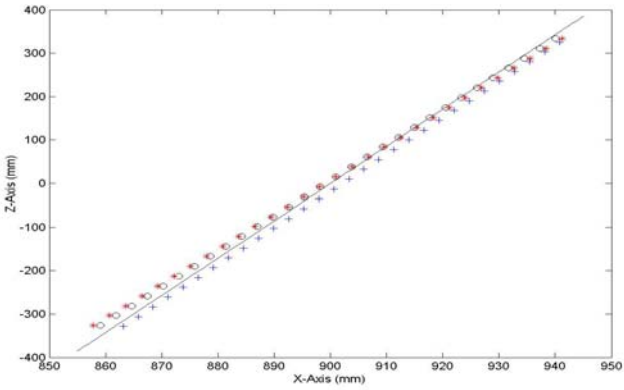

Fig. 4. Results for the case of scanning a plane surface: The solid line shows the theoretical results while data points indicated by O, + and * show the experimental ones

In the next experiment, a plane object and a cylinder object have been recorded respectively with the above-described prototype. For this stage, the sample is scanned from a distance of about 1100 mm from the lens axis. In the digital processing of 3D data, the mesh result is rotated with *Z*-Axis in order to improve the view effectiveness. Both Fig.5 and Fig.6 are the grid images of range data that show an average measurement accuracy of 2 mm can be obtained for about the 450×400 mm^2 range image. The experimental prototype associated with a synchronized scanner owns over 60 degree scanning angle.

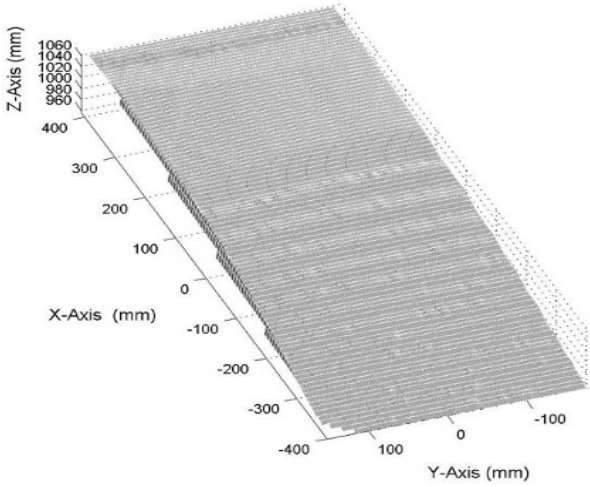

Fig. 5. The measured plane profile obtained from the prototype

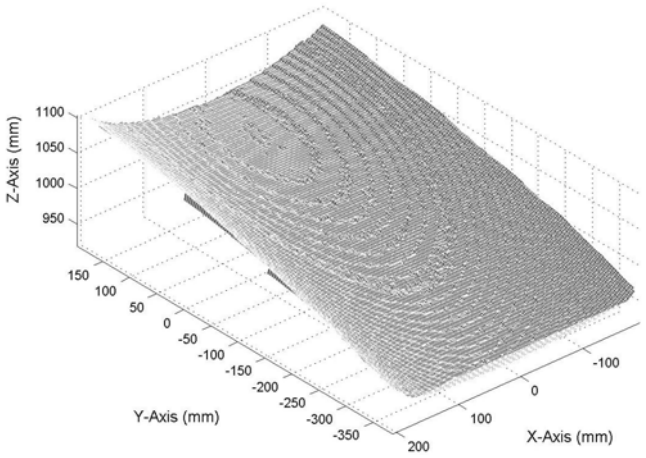

Fig. 6. The measured cylinder profile obtained from the prototype

5 Conclusions

A wide angle-of-view 3D vision system has been described in this paper. As an application of synchronized technology, the vision system is less complex and expensive. The spatial geometric has been addressed in detail. Furthermore, an experimental prototype has been developed. Experimental results from two models show that the vision system owns inherently the advantages of the wide-angle 3D measurement. This technique proves to be a valuable tool of 3D surface acqusition in different environments

Acknowledgement

The authors gratefully acknowledge the support of the National Natural Science Foundation of China, under project No. 30470488.

References

1. Chen S.B., Qiu T., Lin T. et al. Intelligent Technologies for Robotic Welding. Robotic Welding, Intelligence and Automation, LNCIS 299, pp. 123-143, 2004.
2. Lee, M.F., Solva, C.W., Croft, E.A., and Wu Q.M.: Machine vision system for curved surface inspection. Machine Vision and Application, 2000(12), 177-188.
3. Shen, J., Shen, W., Sun, H. J. and Yang, J. Y. Orthogonal moments and their application to motion detection in image sequences. International Journal of Information Acquisition 2004(1): 77–87.
4. Zetu, D., and Akgunduz, A. Tracking-based depth recovery for virtual reality applications. Machine Vision and Applications 2005.(16): 122–127.

5. Hoole, A. C., Twyman, N, Langmack, K. A., et al. Laser scanning of patient outline for three-dimensional radiotherapy treatment planning. Physiological Measurement 2001(22): 605-610.
6. Moss J.P., Linnery A.D., Grindrod S.R. and Mosse C.A. A laser scanning system for the measurement of facial surface morphology. Optics and laser in Eng. 1989(10): 179-190.
7. Zhang G.j., Wei Z.Z. A novel calibration approach to structured light 3D vision inspection. Optics and Laser Technology 2002, 34(5): 373-380.
8. Hyun Kwangik, Gerhardt A. Lester. The use of laser structured light for 3D surface measurement and inspection. IEEE Proc. Of the fourth int. Conf. on computer integrated manufacturing and automation technology, 1991: 215-221.
9. Cheng S., TU D.W., Li G.Z., Yin H.R., Yang J. Data Fusion in Machine Vision Integrated Sensor. in Advanced Materials and Devices for Sensing and Imaging, Proceedings of SPIE, 2002: 135-143.

An Object Oriented Robot Programming Approach in Robot Served Plastic Injection Molding Application

J.G. Ge and X.G. Yin

Robotics Department, ABB Corporate Research Center, Shanghai,
P.R. China, 200131
Jingguo.ge@cn.abb.com

Abstract. An object oriented model of robotic work cell is proposed in this paper based on domain analysis of robotic work cell. An easy robot programming application is implemented which hide the complexity of RAPID (ABB robot programming language) by an intuitive graphical programming approach. Customer test has demonstrated that it can simplify and speed up the process of programming ABB robot in plastic injection molding application.

1 Introduction

Since the industrial robot was first introduced in the USA in 1961 and the first applications were tested within the car industry in North America, many researchers and engineers have made great effort to apply industrial robot in different kinds of industrial process in the past decades. And the effort is still continuing with new emerging application. The main goal of these efforts is either to improve production quality or improve the programming efficiency. Thomas pettersen proposed an AR (augmented reality) system which using virtual graphics presented on a head-up display to visualize the programmed path in relation to the object. Benchmarking results between conventional robot programming using a teach pendant and this AR method indicate time-saving of more than 50% [1]. In robotic grinding process area, J.J.Wang proposed a new 3D process model among force, material removal rate and contact area after researching the difference between conventional grinding process and robot grinding process, experimental result has shown that this model can produce high quality and consistent work piece [2].

In this paper, an approach to decrease the difficulty of robot programming in plastic industry is proposed, which aims at injection molding automation.

Plastic industry is a new emerging industry and becoming important more and more to the world. In some developing country, more than half robots installed in 2004 are used in plastic molding [3].

Programming of industrial robot is different from conventional computer programming in many ways. This means that the following factors have to be considered:

- Programming of movements where a manipulator moves in 6 DOF (Degree of Freedom) and an optimization regarding different motion parameter is required.

T.-J. Tarn et al. (Eds.): Robot. Weld., Intellige. & Automation, LNCIS 362, pp. 91–97, 2007.
springerlink.com

- Interaction and integration with other machines and physical objects in the robot's work envelope.
- Communication and interaction with operators with a limited knowledge often in combination with high demands on productivity.
- Handling of errors resulting from internal events or other factors

The RAPID language (ABB robot programming language), the FlexPendant (Flexible Teach Pendant Unit, ABB new generation teach pendant) and the IRC5 controller (5^{th} generation industrial robot controller of ABB) offer good possibility to develop different solutions for all of these areas.

RAPID program consists of a number of modules, routines and instructions which describe the work of robot in a Pascal-like syntax. There are specific instructions for the various commands, such as to move the robot or to set an output etc. There are three types of routines: procedures, functions and trap routines. There are three types of data classify by life cycle: constants, variables and persistent and two types data classify by definitions: atomic and record. There are three types of expression: arithmetic expression, logical expression and string expression. Other features in the languages are: routine parameters, error handler and backward hander, multi moving and multi tasking [4]. So RAPID is a powerful language with complex syntax which provides a stiff learning curve for those process experts in factory to learn it.

In another side, RAPID is a process oriented, interpretive language. For interpretive language, parts of programs and any modifications can be tested immediately without having to be compiled. It's very easy-to-use to see result immediately. The main draw back of this kind of language, however, is that program complexity will increase exponentially when program become large. Object oriented programming language has shown more advantages in making big program than process oriented language.

With its window-based display, customer designed menus, graphical touch screen and standard 3-way joystick, FlexPendant provides a much more user-friendly interface to customer than before. Furthermore, FlexPendant have a controller-independent computer in itself, which make it unaffected by controller load.

The purpose of this paper is to take full advantage of graphical FlexPendant to avoid writing any RAPID code.

2 Domain Analysis and Object Oriented Modeling of Plastic Injection Molding

The work cell model is obtained through domain analysis. Domain analysis is the process of organizing knowledge about a class of problems (i.e., a problem domain) for the purposes of developing software abstraction.

Typically, a plastic injection molding work cell is built up of several stations (equipment which can hold or process material), such as 1-2 robots, 1-2 injection molding machine, scrap, conveyor, insert, vision, sprout cutting, etc.

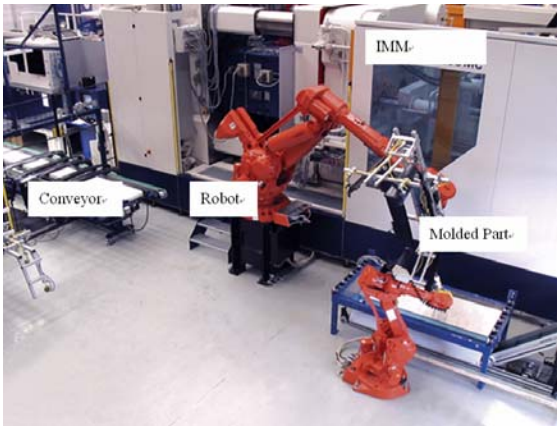

Fig. 1. A typical work cell of plastic injection molding

The interaction between the IMM (Injection Molding Machine) and the robot is the most critical part of the robot cycle both for cycle time and for safety reasons. The IMM is the main station in the cell i.e. it's more important than the robot. The IMM can be run in automatic mode when it is served by a robot from the back door, in manual mode when it is served by an operator from the front door. It is of major concern to always keep the IMM running even if the surrounding equipment goes down. The mould process cycle includes of the following phases: feed granular, mechanical and thermo plastic melting phase; injection; post pressure phase; cooling; part extraction. A typical part flow may be described as following. The IMM opens its mould after finishing molding; robot goes into mould; robot takes out the molded part; robot takes the part to a vision station for quality inspection; if quality is OK, then robot takes it to a deburring machine for post-processing otherwise throws it into scrap and goes to IMM door waits for mould open; robot takes the good part to a tray and palletize it into the cave; at last, goes to the IMM door and waits for mould open. Robot and IMM must work in parallel to save cycle time and they have to use signals to synchronize each other to make the process safely. These signals are defined as regional standard such as Euromap 67, SPI. Fig.2 shows the parallel work and communication between robot and IMM. The average cycle time ranges from seconds to minutes.

Based on the analysis of plastic injection molding process, the following entities in plastic plant are abstracted.

- Cell entity abstracts the work space a robot works in. A cell consists of a set of stations, robots, tools, part flows (the sequence of molded part being moved from one machine to another in the work space)
- Station entity abstracts the manufacturing equipment which can hold or process the part. Thus, a station is a building block for devices such as conveyor, cutting machine or gluing machine. Hence, a station has a work object coordinate system, a list of operations (Initialization, signal triggering, movement, etc.) and a processing state (i.e., its current activity status, which may, for example, be "OK", "Busy" or "Not OK").

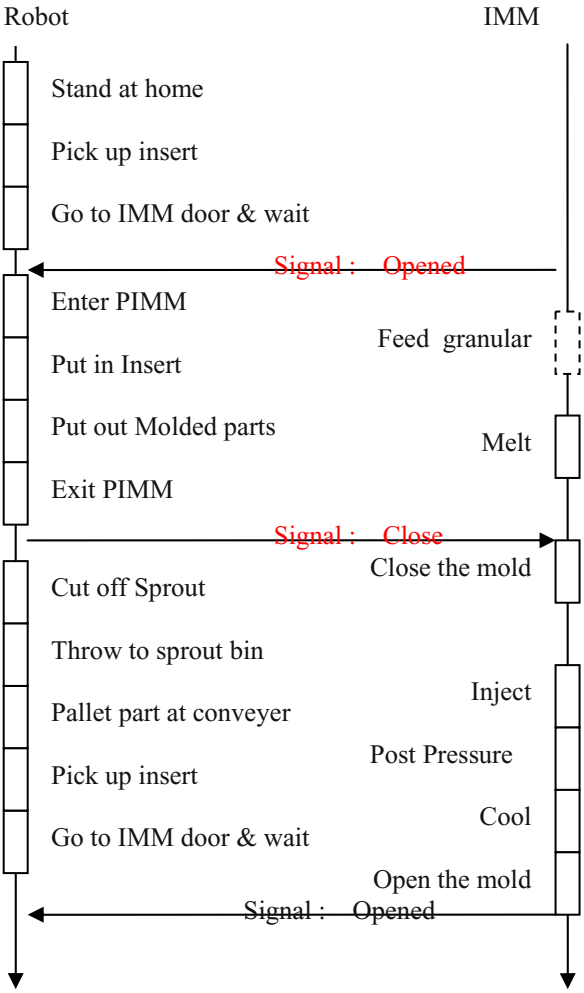

Fig. 2. Parallel work and communication between robot and IMM

- Tool entity abstracts the gripper hold by robot to operate the part. A tool consists a set of actions (e.g. Open, Close, Rotate 90 degree, half open etc.) and a state ("OK", "Busy" or "Not OK").
- Path entity abstracts the robot track which consists of a list of robot targets and some operations (e.g. Initialize, Error handle, Get Next Target, Get Previous Target).

Taken together, these entities form the object oriented model of robot served plastic injection molding work cell. These are implemented as a set of C# classes and a set of RAPID module templates.

3 Implementation

The software architecture has been defined as a typical 3-tier application. As show in Fig.3, it has RAPID code layer, communication layer and GUI (Graphical User Interface) layer. Each layer only has communication to its adjacent layer. Its implementation consists of more than 50 KLOC (Lines of Code) of C# language divided into approximately 140 classes and more than 5 KLOC of RAPID language.

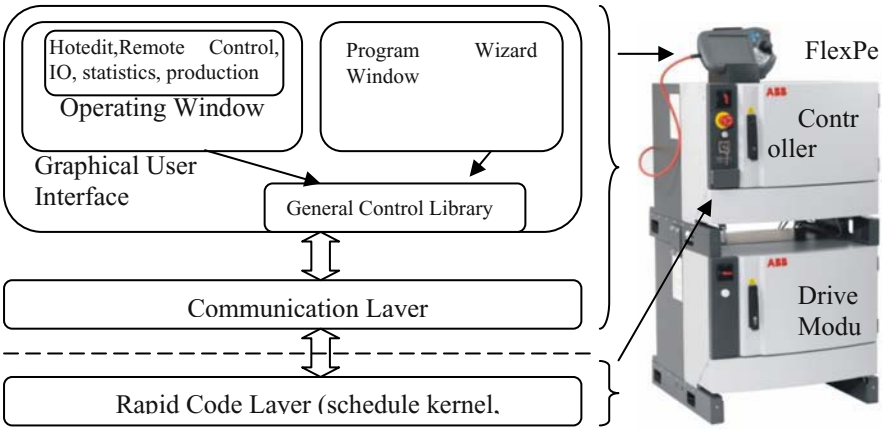

Fig. 3. 3-tier software architecture

GUI layer is the graphical representation of the work cell in real world. It uses an intuitive and dynamic way to show the cell layout, running status and those invisible robot tracks in 3D real world space when programming or producing, shown in Fig.4. This makes it possible for programmer to create a robot program just by select and drag icons on the touch screen of the FlexPendant instead of write RAPID code line by line. The communication layer is the bridge between GUI and RAPID code layer, which send user's selection down and read data value up through Ethernet interface between controller and FlexPendant. These two layers run in the CPU of FlexPendant.

The RAPID layer is the layer which direct control robot movement. It has some predefined template and routines. Some predefined RAPID code need to be configured by GUI. Some can be generate dynamically when needed. Based on the object oriented methodology, a fixed scheduling kernel and an expandable template library for entities are abstracted according to above analysis. These make it possible for RAPID layer to adapt to different industrial process, e.g., Die-casting, Foaming, Cutting, by adding customer's entity template with domain-specific logic into the library. This layer runs in the CPU of ABB IRC5 controller.

For the purpose of easy-to-use, the software also implemented some utility functions, such as the hotedit and remote control. The hotedit function makes it possible to modify robot movement parameters (e.g., tuning positions, speed, etc.) when robot is running. The remote control function makes it possible to control robot from the other machine's control panel.

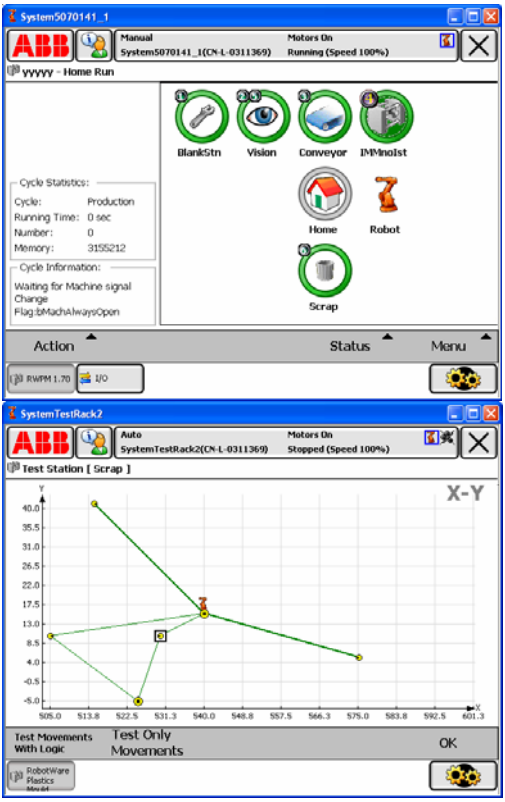

Fig. 4. GUI design (a) Intuitive representation of work cell layout (b) 2D map of robot tracks

4 Results

A 1.5 days' training course of the developed PlasticWare based on the above model has been designed for customers. Students after training can create robot program in a couple of hours for a true work cell instead of days. The PlasticWare is now entering custom service in Europe. Customer test has verified the efficiency of the proposed approach for injection molding process. Especially when reprogramming frequently and workers is process expert with limited knowledge of robotic system, this software shows more advantage in easy-to-setup, easy-to-use and easy-error-diagnostic.

5 Conclusions and Future Work

This paper proposes an object oriented model of industrial robot programming and gives a product implementation based on domain analysis of plastic injection molding process. Compared to conventional RAPID robot programming, the proposed model can create program in a more intuitive and faster way which makes it possible for

process expert to focus on process logic in work cell instead of detailed RAPID coding. This can shorten the programming time from days to hours.

Future work includes:

- Combine experiences from multiple research areas, e.g. artificial intelligence, into the model to create domain specific solutions.
- Path fine-tuning algorithm to save cycle time.
- A more ease-use interface between user and robot.
- And the product should be more reliable, safe and maintainable.

References

1. Thomas Pettersen, Charlotte Skourup, Torbjorn Engedal. Users regain control of industrial robot programming. Mechatronics & Robotics 2004.
2. Jianjun Wang, Yunquan Sun, Zhongxue Gan, Process Modeling of Flexible Robotic Gringding. ICCAS 2003.
3. World Robotics 2005, UNECE and IFR.
4. ABB RAPID Reference Manual 4.0.40, ABB Flexible Automation.

A Wide Angle-of-View Thermal Imaging System Utilizing the Rotation of Optical Path

Victor S. Cheng[1], Su Zhang[1], Xue-Song Lu[1], Xi-Zhang Chen[2], and Ya-Zhu Chen[1,*]

[1] Institute of Biomedical Instrument, Shanghai Jiao Tong University, 1954 Huashan Rd., Shanghai 200030, P.R. China
chengsheng@ieee.org, yzchen@sjtu.edu.cn
[2] Institute of Welding Engineering, Shanghai Jiao Tong University, 1954 Huashan Rd., Shanghai 200030, P.R. China

Abstract. A wide angle-of-view far infrared (FIR) system based on the method of optical path rotation is presented. The system integrated one FIR camera and one rotating Gold-sprayed mirror controlled by one stepping motor. The FIR camera takes image sequence from the rotating mirror in the real-time monitor. Meanwhile, the speed of pixel movement on the FIR imaging plane is analyzed to obtain the rapidest data acquisition without motion blur. Besides, the view range of the proposed system is considered. Then, the prototype has been designed according to the results of simulation. The experiment data has verified the theory of motion blur. This thermal imaging technique is complexless, noninvasive and feasible for many fields involving the automatic temperature acquisition module.

1 Introduction

In recent years the FIR thermal imaging has been developed to one kind of huge application technology in temperature measurement [1-4]. A highly sensitive focal plane arrays FIR camera can easily detect a temperature difference of 0.1°C generating between the inspected object and the environment [5]. In the conventional thermal imaging method, however, the FIR camera is focused on the interesting area by the operator moving the device itself [6-8]. Due to the effective field-of-view range limitation, the image resolution is conflicted with the inspected distance. And the relatively farther inspected distance would degrade the sensibility of FIR image.

In this study, the thermographic system composed of a mono FIR camera and a rotating mirror is proposed. This device aims at large wide-of-angle depth acquisition using the method based on the charge of reflective optical path. Under rotation of the scanning mirror, the FIR camera acquires the serial images of the changing scene in the real-time monitor. By rotating the reflected optical path of the FIR camera with the long-focus lens, the system is designed without compromising between the resolution and the field-of-view. As the feature of heat or cold source is easily recognized in the thermal image during the warming or re-freezing phase of the inspected object,

* Corresponding author.

T.-J. Tarn et al. (Eds.): Robot. Weld., Intellige. & Automation, LNCIS 362, pp. 99–104, 2007.
springerlink.com

the system has the advantage of distinguishing the object from the a large scope background.

In Section II, the configuration of the infrared imaging system is discussed. In Section III, the experiment prototype has been developed and the data has been analyzed for verifying the theory. Finally, conclusions are drawn in the last section.

2 System Configurations

The principle framework of proposed far-infrared imaging system is shown in Fig.1. The system coordinates *OXYZ* is set up on the rotation center *O* of the rotating mirror. The focus length of *lens* from position *A* is *f*. And the angle between the scanning mirror and *X*-Axis is θ . Also, the optical axis is *Z*-Axis and the distance between point *O* and *lens* center *A* is *d*. Then, the distance from *O* to the object point *P* is *R*. Also, the angle between *OP* and *X*-Axis is Ψ and the angle between *OP'* and *X*-Axis is $2\theta+\Psi$.

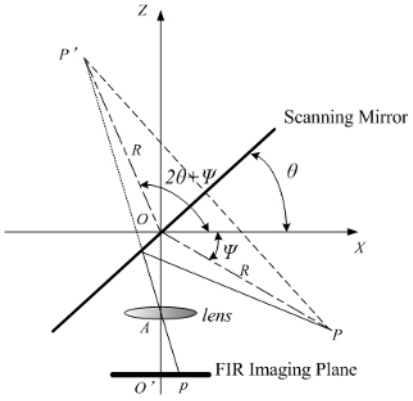

Fig. 1. Schematic layout of the proposed far-infrared imaging system

2.1 Motion Blurring Caused by Imaging Pixel Movement

The projection point on the *X*-Axis and *Z*-Axis of the object point *P'* is

$$\begin{pmatrix} x' \\ z' \end{pmatrix} = R\begin{pmatrix} \cos(2\theta+\psi) \\ \sin(2\theta+\psi) \end{pmatrix} \tag{1}$$

Then, if the image point of *P'* on the FIR imaging plane is *p*, it can be obtained that

$$\frac{p}{f} = \frac{R\cos(2\theta+\psi)}{d+R\sin(2\theta+\psi)} \tag{2}$$

After the differentiation of equation (2) and some arrangement, the pixel movement speed can be obtained as

$$\dot{p} = -2\dot{\theta}\left(f+\frac{fd}{R}\sin(2\theta+\psi)\right)\Big/\left(\frac{d}{R}+\sin(2\theta+\psi)\right)^2 \tag{3}$$

As the serial images are acquired with the rotation of the scanning mirror, the problem of the imaging blur easily occurs as results of the scene movement and the thermal imaging response delay of detector. From equation (3), the pixel speed $\dot{p}$ is dependent on the parameters f, d, R, $\dot{\theta}$, θ, and Ψ. Then, if the parameters f, d, R, θ, and Ψ are constant, the pixel speed is the function of the rotation speed. In other words, if the parameters f, d, R, θ, and Ψ are known, the pixel speed is another function of the distance R. To investigate two relationships, the programs were arranged in which the pixel movement speed is commonly given as the output.

The four sets of the different parameters are respectively indicated by O, X, * and + symbols shown in the Table I. For the real-time monitoring of the application field, the serial images are taken from a scanning mirror in 50 Frames/Sec. The delay time value of the thermal time constant in the simulation programs is 7 ms according to the performance of uncooled infrared detector UL 03 08 1 produced by SOFRADIR.

Table 1. Parameter conditions

Symbol	Parameters
O	f=50 mm d=70 mm and R=800mm
X	f=67 mm d=150 mm and R=800mm
*	f=67 mm d=150 mm and R=1200mm
+	f=67 mm d=70 mm and R=1200mm

In Fig.2 the pixel movement speed is shown as a nearly linear function of the rotation speed $\dot{\theta}$ with the distance R. With the increase of f value, the imaging blur occurs easily. Meanwhile, the imaging blur would occur when the pixel movement distance in 7ms is over half of one pixel size on the detector, which 320 x 240 pixel array with a pixel pitch of 35 μm has been simulated.

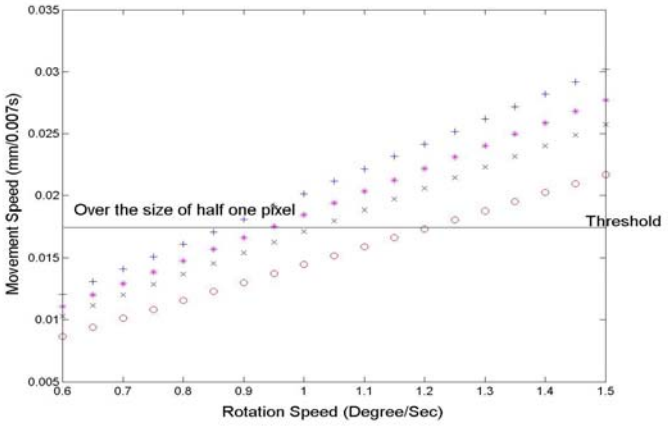

Fig. 2. The relationship between the rotation speed and pixel movement speed in the condition of 7*ms* with θ=15° and Ψ=30°

2.2 Effective Field of View

For the achievement of the wide angle-of-view temperature obtain, the covering range of effective field of view is also considered. In Fig.3 the point *A'* and *A"* is the respectively corresponding point of *lens* center *A* in the mirror at angles θ_1 and θ_2. Then, the coordinates value of the point *A'* is $\left(\frac{2d\tan\theta_1}{1+\tan^2\theta_1}, \frac{d(\tan^2\theta_1-1)}{1+\tan^2\theta_1}\right)$ and of the point *A"* is $\left(\frac{2d\tan\theta_2}{\tan^2\theta_2+1}, \frac{d(\tan^2\theta_2-1)}{\tan^2\theta_2+1}\right)$.

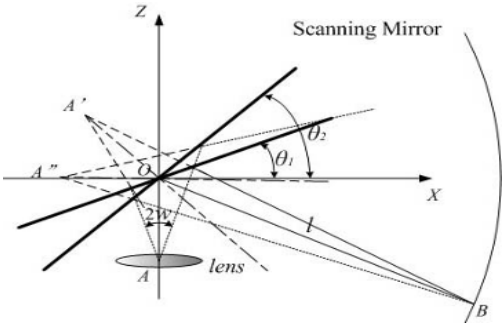

Fig. 3. Sketch of the effective viewing range in the proposed imaging system

The point *B* is the intersection of two margins of view field from scanning angle θ_1 to θ_2 so that the region covered by the rotation of distance *l* represents the scope of effective viewing.

3 Experiment Descriptions

An uncooled FIR camera (IR112, Guide Ltd., Wuhan, China) with a 67mm/F1.0 lens has been applied in the experiment. The focal plane array detector is equipped with ULIS's long wave, two-dimensional uncooled microbolometer infrared detector (UL 03 08 1). The detector with the spectral range of 8~14 μm, pixel numbers: 320X240 format, pixel size 35 μm, and thermal 0.1 ℃ is installed in this camera. In Fig.4 the thermal imaging system has the capability of detecting about 0.2 mm dimensional nickel wire in the distance *R* of 800 mm. The scanning Gold-sprayed mirror which is coated with an alloy of Gold and Ti over the 1500A depth, in front of the camera about 70 mm, rotates at the selectable speed under the control of a stepping motor (2-phase, 0.9DEG/STEP, Oriental Motor Co.) with a 1:60 gear reducer. The scanning angle is from 30° to 60°. The motor driver is interfaced with a MS2051 microcomputer. An external trigger signal synchronizes the startup of the system.

(A) (B)

Fig. 4. Pictures of experiment prototype: (A) the proposed system and its observe object —Φ 0.2mm nickel wire ; (B) an intimate view of the platform

The performance of the proposed thermal imaging system is evaluated by the following experiment shown in Fig.4 (A). The aim is to determine the motion blur theory mentioned above. The resistance of theϕ0.2mm nickel wire is about 10Ω.The distance d between *lens* center and rotation axis point *O* is 70 mm. The temperate of the nickel wire can raise 2℃ with 2V DC. In Fig.5 the images of a live nickel wire that has been measured under the different conditions. Fig.5 (A) shows the picture taken under the static condition of scanning mirror and the width of nickel wire clarify occupies 5 pixels in the thermal image. Afterwards, in Fig.5 (B) the motion blur occurs with the scanning mirror at the rotation speed of 2 Deg/Sec. Then, the rotation speed of the scanning mirror is lowered to 0.92 Deg/Sec and the motion blur can be disappeared in Fig.5(C). So the 0.92 Deg/Sec is the rapidest rotation speed without motion blur under the distance R about 800 mm.

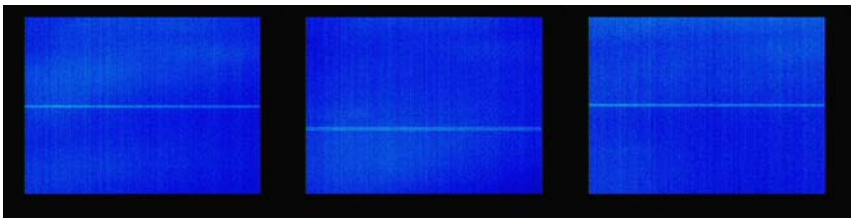

(A) (B) (C)

Fig. 5. Experiment images of a heated nickel wire observation: (A) the static condition of scanning mirror; (B) taken at the rotation speed of 2 Deg/Sec; (C) taken at the rotation speed of 0.92 Deg/Sec.

4 Conclusions

A novel thermal imaging system applied in the real-time temperature monitoring has been developed in this study. The system can acquire the image sequence by rotating the optical path of one fixed FIR camera for realizing the wide angle-of-view FIR

imaging in an appropriate distance. With this method, the system is designed without compromising between the resolution and the field-of-view in *OXZ* coordinates. Meanwhile, the structure parameters are simulated for evaluating the imaging system performance. The described theory about motion blur is verified to provide a reliable design of the thermal imaging device. The experimental data is in accord with the simulation. The thermal imaging technique can be applied in many automation fields involving the heating control.

Acknowledgement

The authors gratefully acknowledge the support of the National Natural Science Foundation of China, under project No. 30470488. And the authors are also thankful to Ms. Zhen-Zhen Fan for her kindly revision of this paper.

References

1. Bendada A., Cole K., Lamontagne M., Simard Y. A hollow waveguide infrared thermometer for polymer temperature measurement during injection moulding. *Journal of Optics A: Pure and Applied Optics*, Vol.5 (5), 2003, 464-470.
2. Menaka M., Vasudevan M., Venkatraman B., Raj Baldev. Estimating bead width and depth of penetration during welding by infrared thermal imaging. *Insight: Non-Destructive Testing and Condition Monitoring* , Vol. 47(9), 2005: 564-568.
3. Doumanidis C.C. Thermal identification for control of the scan welding process. *Proceedings of the ASME-JSME Thermal Engineering Joint Conference*, Vol. 4, 1995: 151-158.
4. Boctor E.M., Fichtinger G., Yeung A., Awad M., Taylor R.H., Choti M.A. Robotic strain imaging for monitoring thermal ablation of liver. *LNCS*, Vol.3217, n 1 PART 2, *Medical Image Computing and Computer-Assisted Intervention*, *MICCAI 2004 - 7th International Conference*, 2004: 81-88.
5. Cheng S. Victor, Zhang S., Chen Y.Z., Hao L.J. A Stereo Thermographic System for Intraoperative Surgery. *27th Annual International Conference of the IEEE Engineering in Medicine and Biology Society* (EMBC05) Shanghai.
6. Kaczmarek M., Nowakowski A., Siebert J., and Rogowski J. Infrared Thermography applications in heart surgery. *Proceedings of SPIE*, Vol. 3730:184-188.
7. Pinson L.J. Robot vision: an evaluation of imaging sensors. *Proceedings of SPIE*, Vol.442, 1983: 15-26.
8. Caillas C. Autonomous robot using infrared thermal camera to discriminate objects in outdoor scene. *Proceedings of SPIE*, Vol.1293 pt 2, 1990:801-812.

On the Key Technologies of Intelligentized Welding Robot

S.B. Chen

Welding Engineering Institute, Shanghai Jiao Tong University,
Shanghai 200030, P.R. China
sbchen@sjtu.edu.cn

Abstract. This paper addresses on key intelligentized technologies for robotic welding, which contains computer vision technology for recognizing weld seam and starting, locally autonomous guiding and tracking seam, real-time intelligent control of weld penetration, seam forming and welding pool dynamics. A locally autonomous intelligentized welding robot (LAIWR) systems was developed, which could realize detecting and recognizing weld surroundings by visual sensing technology, identifying the initial position of weld seam, autonomously guiding weld torch to the weld starting and tracking the seam, real-time control of pulsed GTAW pool dynamics by vision computing and intelligent strategies.

1 Introduction

At present, the most welding robots serving in practical production still are the teaching and playback type, and can't well meet quality and diversification requirements of welding production because this type of robots don't have adaptive ability to circumstance changes and uncertain disturbances during welding process[1-5]. In practical production, welding conditions are often changing, such as the errors of pre-machining and fitting work-piece would result in differences of gap size and position, the change of work-piece heat conduction and dispersion during welding process would bring on weld distortion and penetration odds. In order to overcome or restrain various uncertain influences on welding quality, it will be an effective approach to develop and improve intelligent technologies for welding robots, such as vision sensing, recognizing welding surroundings, autonomously guiding and tracking seam, and real-time intelligent control of robotic welding process[5-12].

In former researches, although some significant results were obtained in vision sensing, modeling and intelligent control of weld quality and pool dynamics[13-18], these intelligent technologies are still not realized effectively in welding robot systems due to complexity of welding process, real-time and opening limits of robot systems[5].

Therefore, developing intelligentized technology for improving current teaching and playback welding robot is necessary and exigent to satisfy high quality and flexible requirements for welding products and advanced manufacturing uptrend[1-5,12].

T.-J. Tarn et al. (Eds.): Robot. Weld., Intellige. & Automation, LNCIS 362, pp. 105–115, 2007.
springerlink.com

2 The Structure of an Intelligentized Welding Robot Systems

The principle scheme of an intelligentized welding robot systems is shown as Fig.1, Which is consisting of a 6-freedom manipulator and a freedom visual servo unit (VSU) installed on the sixth axis of the robot for turning a dual camera sensor; a welding seam guiding unit (SGU), a seam tracking unit (STU), a welding penetration control unit (PCU), a knowledge data unit (KDU) and a system simulation unit (SSU), all units are dominated by a central control computer (CCC). This combined welding robot system could realize autonomously recognizing weld starting and seam by vision sensing in the local circumstance, guiding robot to the starting, tracking seam, and real-time control of welding pool dynamics and seam forming during pulse GTAW by appropriate intelligentized strategies. It is called the locally autonomous intelligentized welding robot (LAIWR) systems in this paper[20].

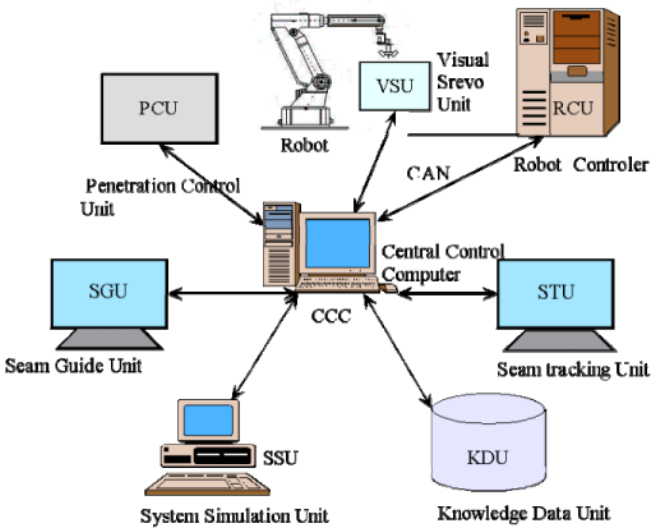

Fig. 1. The hardware structure of the LAIWR systems

3 Key Technologies of Intelligentized Welding Robot Systems

3.1 Recognizing and Guiding of Weld Starting Position for Welding Robot

Realizing welding robot to recognize the weld start position by visual information and autonomously guide the robot to the starting would make the current teaching and playback robot improve its adaptability to the practical varying welding circumstance, it is one of the key technologies for the intelligentized welding robot. In the LAIWR systems, the recognizing and guiding technologies include to acquire the images of work-piece at welding space by visual sensing, to extract the characteristic of weld starting by proper image processing algorithms, to calculate the three dimension

coordinate values of the starting point by stereo matching methods, and to guide welding robot moving to the starting point. The recognizing and guiding technology subsystem is shown as Fig.2.

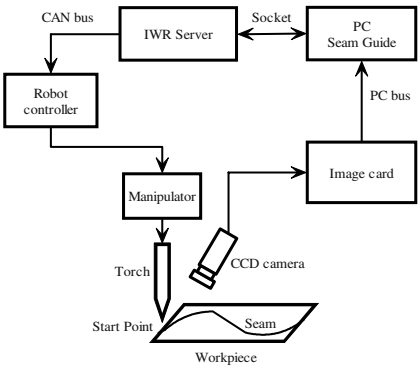

Fig. 2. The recognizing and guiding subsystem based on visual information

The main recognizing and guiding steps of the LAIWR system as following[21]:

1) Image segmentation and region picking-up of weld joint
2) Image processing and recognizing of the weld starting
3) Stereo matching algorithms for weld starting point
4) Autonomously guiding strategy for robot moving to the weld starting

A recognizing and guiding program flow chart is shown as Fig. 3, the detail algorithms and the guiding experiment results on the LAIWR systems are omitted here [21].

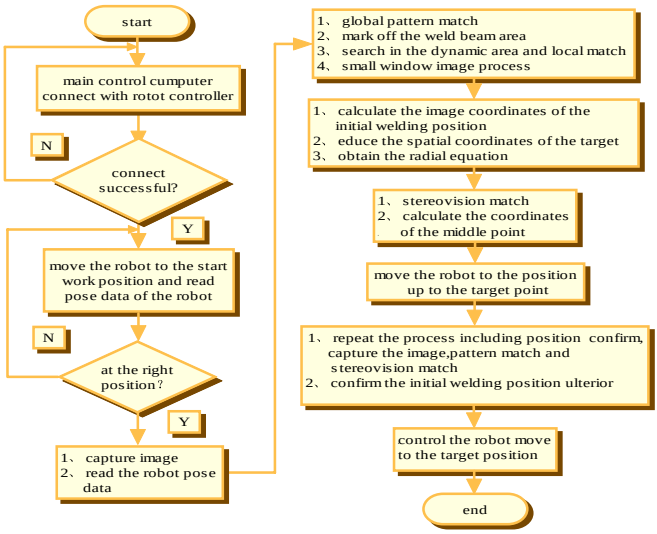

Fig. 3. Recognizing and guiding program flow chart for the LAIWR systems

3.2 Autonomously Programming and Tracking of Robotic Welding Path Based on Servo Vision

Realizing welding robot to recognize weld seam, autonomously programming and real-time tracking of welding path by visual information would make the current teaching and playback robot improve its adaptability to the practical varying welding conditions, such as the error of assemble gap and processing work-piece, distortion and variation of the joint position and size during welding, it is another key technology for the intelligentized welding robot. In the LAIWR systems, it includes recognizing seam curve, autonomously program and track weld path by a servo vision. The principle of welding robotic programming and tracking subsystem with servo vision is shown as Fig.4.

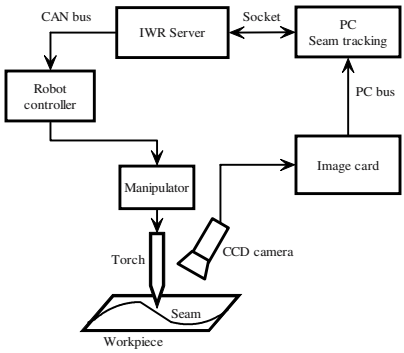

Fig. 4. The welding robotic programming and tracking subsystem with servo vision

Main steps of programming and tracking seam in LAIWR system as following[22]

Using the frontal CCD camera of servo vision sensor, the LAIWR could take the joint image in the front of weld torch. Obtain the deflecting error to the joint and built a correct robotic coordinate value and path for robot tracking weld seam. The main steps is following as:

1) Processing of the joint image to obtain the seam curve
2) Extracting angle and distance deflections of weld seam

The seam and angle deflection are defined as Fig.5, in the image coordinate U-V, the seam deflection is d, and the seam angle deflection is α.

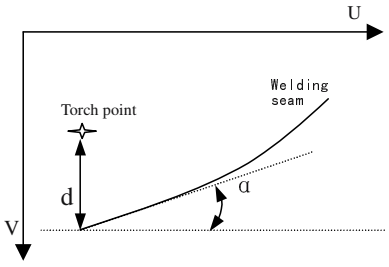

Fig. 5. Definitions of The seam deflection and angle

3) Detecting the end of weld joint

In order to obtain the curve coordinates of a whole complete seam, it is necessary to detect the end of weld joint by the seam image. An image of the seam end is shown as Fig 6, which is the junction of three lines in the processing image of the weld joint.

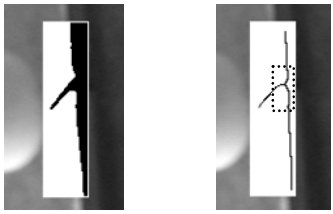

Fig. 6. Processing images of the weld joint

4) Control strategy for robot to track seam curve coordinates

The detail algorithms of programming and tracking seam for LAIWR systems are omitted.

An experiment result of autonomously programming welding robotic path by servo vision is shown as Fig.7.

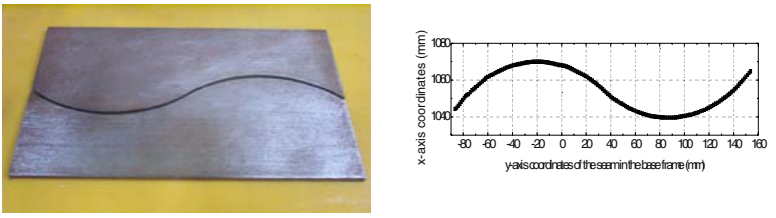

(a) S shape seam workpiece (b) Robotic programming and tracking curve

Fig. 7. Experiment of robotic programming and tracking path by servo vision

3.3 Real-Time Control of Weld Pool and Seam Forming During Robotic Welding

Realizing real-time control of dynamics of welding pool and seam forming is one of most crucial technologies for robotic welding quality. At present, almost teaching playback welding robot is non real-time control of dynamics of welding pool. In the LAIWR system, a real-time control subsystem as Fig.8 was developed for dynamical process of robotic welding.

(1) Adaptive neural PID controller for real-time control of robotic welding

In the LAIWR systems, an adaptive neural PID controller is developed for real-time control of dynamical pool and fore seam during robotic welding. Control, the controller

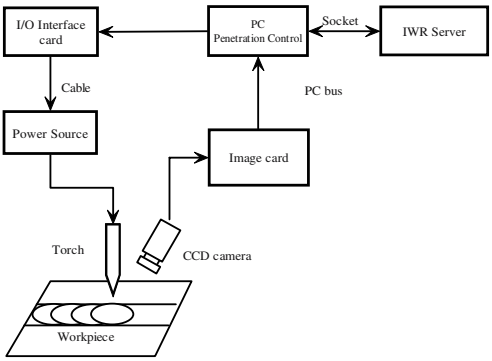

Fig. 8. Real-time control subsystem for dynamical process of robotic welding

framework is showing as Fig.9, which includes common PID regulator, learning algorithms, neural networks NN1 and NN2 for modeling welding dynamics and modifying PID parameters. The controller algorithms are omitted here[20].

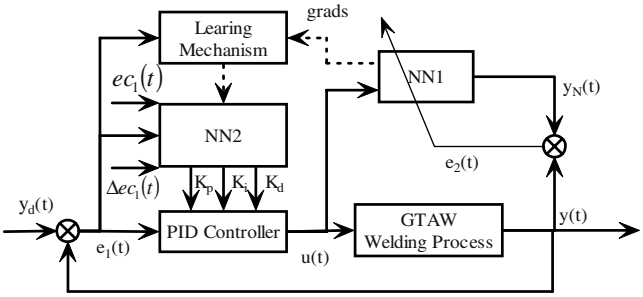

Fig. 9. The framework of adaptive neural PID controller for robotic welding process

(2) Image processing and feature acquiring of weld pool during robotic welding

The controlled welding processing and results on the LAIWR systems are shown as Fig.10, it is showing the image processing results of the pool during robotic welding. The details are omitted here[19].

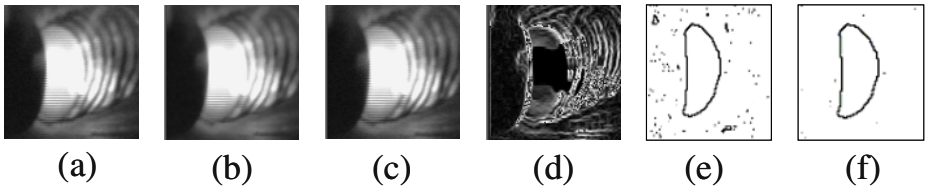

(a) Original (b) Median filter (c) Image reinforcing (d) Edge detecting (e) Profile extracting (f) Filtering

Fig. 10. The results of Al alloy pool image processing during robotic welding

In the robotic welding, the image shape would be changed with seam curve and robot motion direction. The Fig.11 is shown Al alloy pool images in three direction of the S shape seam during robotic welding. The corresponding image processing algorithms were developed in LAIWR systems[20], and here it is omitted.

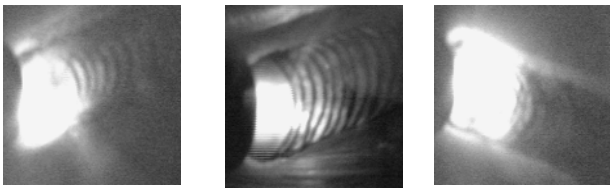

a) The left rear direction b) The positive rear direction c) The right rear direction

Fig. 11. Al alloy pool images in three direction of the S shape seam during robotic welding

(3) Real-time control experiment during robotic welding[20]

Using the characteristic information of the welding pool, the closed loop feedback control in LAIWR systems was structured and real-time control of dynamic welding process was realized. The experiments of the constant technical parameters, i.e. without the loop feedback control, and simple PID control scheme were conducted for comparing with the designed adaptive neural PID controller in this paper, the compared results is showing that the adaptive neural PID controller in the LAIWR systems is effective for real-time control of weld pool dynamics and fine seam formation during Al alloy pulse GTAW, the details are omitted here. The Fig.12 and Fig.13 are showing the controlled welding results on the LAIWR systems. The trapezoid and dumbbell workpiece are designed to simulate the different changes of heat conduction and the effectiveness of the controller during robotic welding process. The controlled results are showing that the desired seam width, 7.6mm for trapezoid workpiece, and 8.0mm for dumbbell workpiece, are maintained steadily by the peak current regulation during pulse GTAW on the LAIWR systems.

3.4 Knowledge Extracting and Modeling of Dynamical Welding Process

As is well known, the traditional welding is a typical handwork operations, which mainly depends on the welder's skills, due to the highly complexity in welding process. In the intelligentized robotic welding systems, the knowledge model on welding process is a technical focus or key for dominating welding robot system. Some methods of knowledge acquisition and modeling by rough set, fuzzy set and neural network theory have been developed for welding dynamics[5,6,23], here it is omitted.

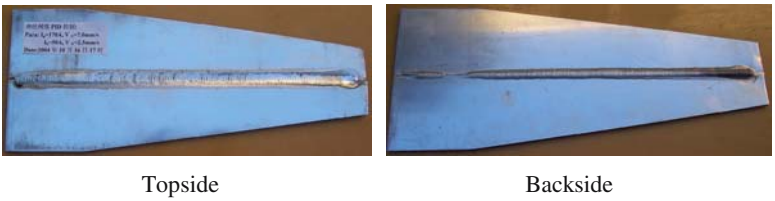

Topside Backside

(a) Trapezoid workpiece

Topside Backside

(b) Dumbbell workpiece

Fig. 12. The workpiece pictures of adaptive neural PID controlled welding on the LAIWR

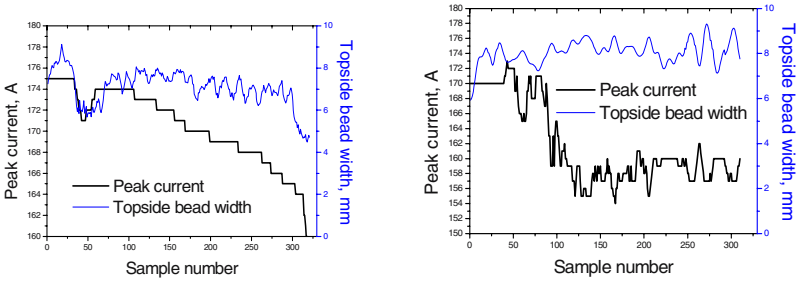

(a) Trapezoid workpiece (b) Dumbbell workpiece

Fig. 13. Adaptive neural PID controlled curves of Al alloy welding process on the LAIWR

4 The Intelligent Structure of Intelligentized Welding Robot Systems

Based on analysis on key technologies and functions of the systems like the LAIWR systems in Fig.1 as the above, a hierarchical intelligent structure framework is developed for an intelligentized welding robot systems as Fig.14 [5,20], which is divided into a five-level framework, which includes the executing level, the management level, the coordinator level, the proxy level, and the communication level. The framework can realize to search weld starting position, guide robot reaching the starting, tracking seam and correct deflections, control proper welding penetration and fine forming alike to a skilled welder's operation during welding process.

5 Conclusions

The key intelligentized welding techniques for robot systems include vision sensing for recognizing weld starting, guiding and tracking weld seam, programming path, pose and welding parameters, knowledge modeling and intelligent real-time control of welding dynamics, dominating intelligentized robotic systems, and so on.

This paper has shown a primary intelligentized welding robot systems, so-called LAIWR systems, which realizes some key intelligentized technologies of welding robot system. These intelligentized technologies would be an important foundation for developing new-type intelligent welding robot in the future.

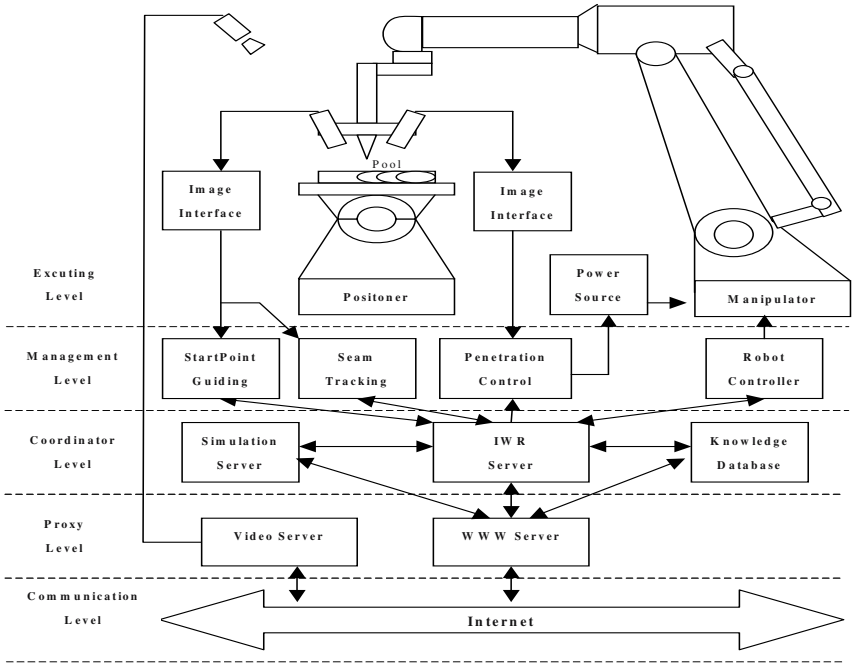

Fig. 14. A hierarchical intelligent structure framework of intelligentized welding systems

Acknowledgment

This work was supported by the National Natural Science Foundation under Grant No. 50575144, 60474036, and supported by Key Foundation Program of Shanghai Sciences & Technology Committee under Grant No. 06JC14036. The author wish to acknowledge the relative study works finished by Dr. Chen Wenjie, Dr. Zhou Lv, Dr. Chen Xizhang, Dr. Zhu Zhenyou and Mr. Lang Yuyou.

References

1. Trailer, Manufacturer Depends on Robotic Welding to Boast Production. Welding Journal. 1995, 74(7): 49-51
2. U. Dilthey, L. Stein. Robot System for Arc Welding—Current Position and Future Trends. Welding & Cutting. 1992, (8): E150-E152
3. J. L. Pan, " A survey of welding sciences in 21th century." Proceeding of 9th Chinese Welding Conference, Tianjun, China, Oct. 1999, (1): D-001-D-017
4. K. P. Valavanis, G. N., Saridis, Intelligent Robotics System: Theory, Design and Applications. Boston, 1992: 12-18
5. *S. B. Chen*, et al., 2004. "Intelligentlized technologies for robotic welding", Series Lecture Notes in Control and Information Sciences, vol. 299: 123-143
6. Chen Shanben, et al., 2003, "On intelligentized technologies for modern welding manufacturing," Chinese Journal of Mechanical Engineering, vol.16, No.4, pp367-370
7. R.J. Beatlie, S.K. Cheng and P.S. Logue. The Use of Vision Sensors in Multipass Welding Applications. Welding Journal. 1988, Vol. 67(11): pp28-33
8. Zh.Y.Zhu, T.Lin, Y.J.Piao, *S.B.Chen*, Recognition of the initial position of the weld based on the image pattern match technology. The International Journal of Advanced Manufacturing Technology, vol.26:784-788, 2005
9. S.B. Chen, X.Z. Chen, J.Q. Li, T. Lin, 2005, "Acquisition of Welding Seam Space Position Information for Arc Welding Robot Based on Vision," Journal of Intelligent & Robotic Systems, vol.43, pp77-97.
10. J.W. Kim and S.J. Na. A Self-Organizing Fuzzy Control Approach to Arc Sensor for Weld Joint Tracking in Gas Metal Arc Welding of Butt Joints. Welding Journal. 1993, Vol. 72(1): pp60s-66s
11. Y. Suga and M. Naruse. Application of Neural Network to Visual Sensing of Weld Line and Automatic Tracking in Robot Welding. Welding in the World. 1994, 34: pp275-284
12. S. B Chen, Y. Zhang, T. Qiu, T Lin., 2003, "Robotic Welding Systems with Vision Sensing and Self-learning Neuron Control of Arc Weld Dynamic Process", Journal of Intelligent and Robotic Systems, vol.36, No.2, pp191-208.
13. S. B. Chen, Y. J. Lou, L. Wu and D.B. Zhao , Intelligent Methodology for Sensing , Modeling and Control of Pulsed GTAW :PART1—Band-on-Plate Welding, Welding Journal, 2000, 79(6):151s-163s
14. S.B. Chen, D. B. Zhao, L. Wu and Y. J. Lou, Intelligent Methodology for Sensing , Modeling and Control of Pulsed GTAW :PART2—Butt Joint Welding, Welding Journal, 2000, 79(6):164s-174s
15. R.W. Richardson and D.A. Gutow. Coaxial Arc Weld Pool Viewing for Process Monitoring and Control. Welding Journal. 1984. 63(3): 43-50
16. J J Wang, T Lin, Shanben Chen, 2005,"Obtaining of weld pool vision information during aluminum alloy TIG welding," International Journal of Advanced manufacturing technology, vol.26:219-227, 2005
17. R. Kovacevic, Y.M. Zhang and L.Li. Monitoring of Weld Joint Penetration Based on Weld Pool Geometrical Appearance. Welding Journal. 1996, Vol. 75(10): pp317s-329s
18. T.G. Lim and H.S. Cho. Estimation of Weld Pool Sizes in GMA Welding Process Using Neural Networks. Journal of Systems and Control Engineering. 1993, Vol. 207(1): pp15-26
19. D. B. Zhao, S. B. Chen, L.Wu, and Q. Chen., 2001, "Intelligent Control for the Double-sided Shape of the Weld Pool in Pulsed GTAW with Wire Filler," Welding Journal, vol.80, No.11, pp253s-260s

20. W. J. Chen, “Research on Local Autonomous Intelligent Welding Robot System and its Remote Control,” Doctoral Dissertation Shanghai Jiao Tong University, 2004.
21. Zh.Y.Zhu, “Research on Welding Robot Recognizing and Guiding of the Initial Welding Position with Visual Method,” Doctoral Dissertation Shanghai Jiao Tong University, 2004.
22. Lv. Zhou, “Vision-based Autonomous Programming methods of welding robotic path,” Doctoral Dissertation Shanghai Jiao Tong University, 2006.
23. B. Wang, S. B. Chen, J. J. Wang, 2005, ”Rough set based knowledge modeling for the aluminium alloy pulsed GTAW process,” International Journal of Advanced Manufacturing Technology, vol. 25 (9-10): 902-908.

Computer Simulation of Neural Network Control System for CO2 Welding Process

Fan Ding[1], Shi Yu[1], Li Jianjun[1], Ma Yuezhou[2], and Chen Jianhong[2]

[1] Key Laboratory of Non-ferrous Metal Alloys, The Ministry of Education, Lanzhou Univ. of Tech., Lanzhou 730050, China
[2] State Key Lab of Gansu New Non-ferrous Metal Materials, Lanzhou Univ. of Tech., Lanzhou 730050, China
{fanding, shiyu}@lut.cn

Abstract. In this paper, neural network control systems for decreasing the spatter of CO_2 welding have been created. The Generalized Inverse Learning Architecture(GILA), the Specialized Inverse Learning Architecture(SILA)- Ⅰ & Ⅱ and the Error Back Propagating Model(EBPM) are adopted respectively to simulate the static and dynamic welding control processes. The results of simulation show that the SILA- Ⅰ and EBPM have better properties. The factors affecting the simulating results and the dynamic response quality have also been analyzed.

1 Introduction

The CO_2 gas shielded arc welding is of high efficiency, low cost and widely used in industrial production for advanced manufacture. However, it has a serious defect—large welding spatter, which causes an increase in man-hours and instability of welding process. It is one of the main research topics in the welding field. Controlling welding current waveform accurately to obtain well metal transfer is one of effective method to reducing spatters in welding process [1, 2], but how to characterize spatters is a key problem. MA Yuezhou [3] and Ding FAN [4, 5] remark that arc sound and welding spatters have better relativity. Thus CO_2 welding process control could be realized through detecting welding arc sound and setting up the relation model between welding arc sound and welding parameters such as welding current, welding voltage and so on [6, 7]. However the welding process is a non-linear complex system, and the conventional modeling and controlling methods are difficult to obtain better control effect. The neural network is a multiple dimensions nonlinear dynamic system and the control system based on the neural networks is a self-adaptive controller of self-learning function. In this paper, the static and dynamic control models of CO_2 welding neural network control system are created and simulated respectively. Thus an intelligent CO_2 welding control system has been primarily developed.

2 Data Acquisition and Experimental System

The system is shown in Figure 1. During welding process, the voltage, current and arc sound signal are memorized in computer, through a convector and data acquisition board, and then processed by specially developed statistical analyzing software [4].

T.-J. Tarn et al. (Eds.): Robot. Weld., Intellige. & Automation, LNCIS 362, pp. 117–125, 2007.
springerlink.com

Thus the frequency of the short circuit transfer and the characteristics of arc voltage, current and arc sound signals can be obtained. The data are used to on-line train the neural network controller. The outputs of the neural network controller are sent to a microcomputer to control the CO2 welding process. When acquiring the arc sound signals, two microphones were used so as to eliminate the disturbance of the environment's noise. Therefore the intelligible arc sound signals were obtained.

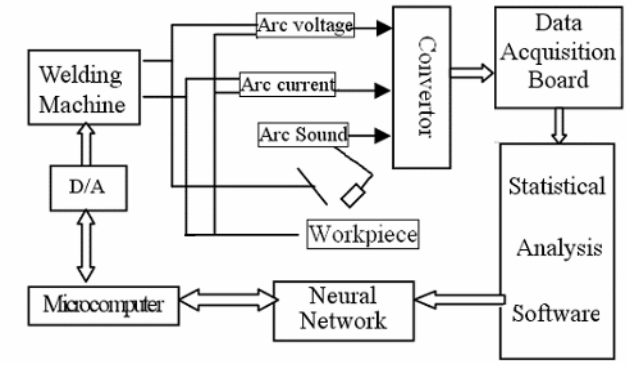

Fig. 1. The construction of experiment system

3 Token Index of the Welding Spatter Ratio

It is proved that the spatter generation is frequently observed just at the moment that fuse separation is occurring due to “electric explosion”. The welding arc sound is a kind of the energy wave. It is coursed by vibration. During the welding process, the change of the welding arc generates some part of the welding arc sound. During the short-circuiting transfer, the energy of the mental bridge is increasing with the rapid increase of the current. When the energy reaches some degree, the explosion is occurring. At this time, the vibration of the welding arc is huge and coursed the violent change of welding arc sound. So the relation between the welding arc sound and the spatter loss coefficient is studied. The typical experimental results are shown in Figure 2 [4].

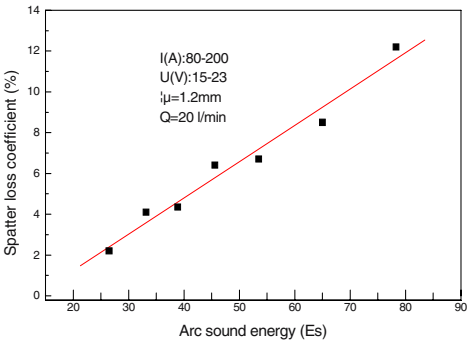

Fig. 2. The relation of Es and the spatter ratio

It can be found that the total arc sound energy of beginning and end of the short circuit transfer is proportional to welding spatter ratio in CO2 arc welding. The arc sound energy (Es) is defined as:

$$Es = \int_{t_0}^{t_0+\Delta t} s^2 dt \tag{1}$$

S is the voltage signal transformed from the arc sound signal by microphone. The arc sound energy at begin of a short circuit transfer is the integral arc sound energy from the time at begin of the short circuit transfer to 1.44 microsecond after that. The arc sound energy at the end of a short circuit transfer is the integral arc sound energy from the time at end of the short circuit transfer to 1.44 microsecond after that. t_0 is the time at the beginning or end of the short circuit transfer. Δt is the time delay and the value of it is 1.44 microsecond. So far, there is no way to on-line represent quantitatively the welding spatter. In this research work, we firstly proposed that the arc sound energy (Es) could be used to indicate the welding spatter ratio on-line.

The other desired response parameter is the frequency of short circuit transfer. It is found that there is a relation between the frequency of the short circuit transfer (F) and the spatter ratio. A higher frequency of the short circuit transfer is associated to a less spatter ratio. However, the relation of them is nonlinear.

4 Control Models and Simulations

Inputs of the neural network controller include the welding arc sound energy (Es) and the frequency of short circuit transfer (F). Outputs are made of the welding voltage and the welding current. In order to qualify the desired value that is satisfied with the outputs of arc system, another neural network is used to identify the relations between (Es) and (F) and added into the front of the neural network controller. The samples that are used to train the neural networks are shown in table.1. All of them are the statistical results of the experimental data. At begin of the simulation, the weights of the neural network controller is set randomly. Of course, we can train the neural network controller off-line before the simulation. Therefore, the response speed of the whole system will be faster.

Table 1. The training samples of the positive model of the welding arc system

	Inputs of the positive model of the arc system		Outputs of the positive model of the arc system	
Serial number	Welding current	Welding voltage	Es	F
1	159	16	131	48.90
2	140	17	84	78.70
3	153	18	101	67.8
4	139	19	77	86.2
5	125	19	117	58.2
6	123	19	69	91
7	175	17	137	33.33
8	172	16.1	130	26.9

4.1 Generalized Inverse Learning Architecture (GILA)

4.1.1 Structure of GILA

The control model is shown in Figure.3.

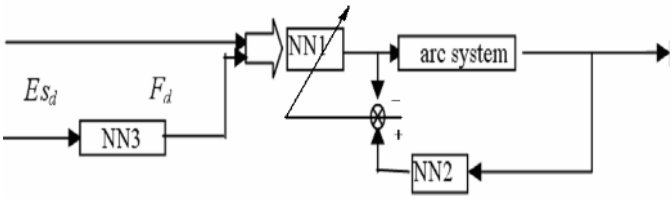

Fig. 3. The Generalized Inverse Learning Architecture

With the input of the desired welding arc sound energy (Es_d), NN3 outputs the desired frequency of the short circuit transfer (F_d). Es_d and F_d is taken as the inputs of the neural network controller, NN1 outputs the welding voltage (U_1) and the welding current (I_1). Then, U and I are given to the positive model of the welding arc system. The positive model outputs the practical Es and F. Es and F are given to the NN2. NN2 outputs the feedback welding voltage (U_2) and the feedback welding current (I_2). The error between (U_1, I_1) and (U_2, I_2) is used to modify the weights of the neural network controller.

4.1.2 Results of GILA Simulation

When the desired value is the following, the convergent results are shown in table 2.

Table 2. Convergent results and train times for every desired value

Serial number	Es_d	Convergent results of Es_d	Convergent times
1	32	31.58	23
2	49	50.87	19
3	58	57.06	13
4	62	61.62	16
5	75	73.74	15
6	82	82.37	37

When Es_d is equal to 25, the dynamic response process is shown in figure 4. From the table 2, we can see, the convergent results of every desired value are fine If the neural network controller is trained off-line and adjacent to the inverse model of the plant, the simulating results will be better.

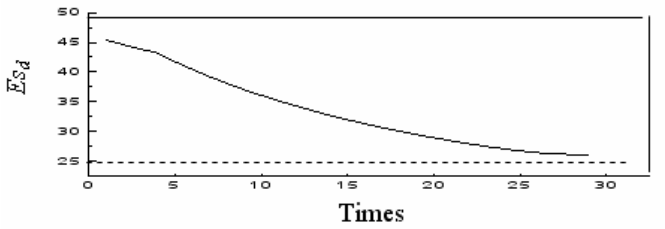

Fig. 4. Dynamic response process of typical *Es*

4.2 Specialized Inverse Learning

4.2.1 Structure of the SILA-Ⅰ

Figure 5 is the structure of SILA-Ⅰ.

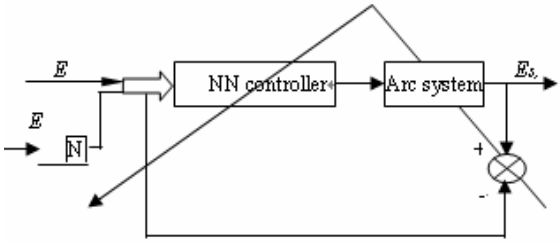

Fig. 5. Structure of the Specialized Inverse Learning Ⅰ

When the desired value is given, the NN controller outputs optimize welding voltage and current. The error between the outputs of the welding arc system and the desired is used to train the neural network controller. The weakness of this architecture is that modifying the weights based on total error must involve the plant mathematical model, which normally is approximately known. Thus the following algorithm is used in this paper.

$$\varepsilon = \| d - y \|^2 \tag{2}$$

$$y = g(T, t) \tag{3}$$

Where ε is the error of the desired value (d) from the actual output (y) of arc system. The actual output (y) is a function of the output vector of NN controller $T = (T_1, T_2 ..., T_\lambda)$ and time. The output vector of NN controller is a function of ω_{ij} and v_{jk}. So

$$\Delta\omega_{ij} = -\rho \frac{\partial \varepsilon}{\partial \omega_{ij}} \tag{4}$$

$$\Delta v_{jk} = -\rho \frac{\partial \varepsilon}{\partial v_{jk}} \tag{5}$$

$$\frac{\partial \varepsilon}{\partial \omega_{ij}} = \frac{\partial \varepsilon}{\partial y} \cdot \frac{\partial g(T, t)}{\partial T_i} \cdot \frac{dT_i}{d\omega_{ij}} \tag{6}$$

When the NN controller is trained on-line, $\partial \varepsilon / \partial y$ is known, $dT_i / d\omega_{ij}$ can be obtained from the NN controller. Although the function of the arc system ($g(T,t)$) is unknown, we can use the following method:

$$\frac{\partial g(T,t)}{\partial T_i} \approx \frac{g(T+\Delta T_i,t)-g(T,t)}{\Delta T_i} \tag{7}$$

The difference function in the right hand of eq.7 can be obtained from adjacent inputs and outputs of the plant.

4.2.2 Simulating Results of SILA-Ⅰ

The convergent results are shown in table 3.

Table 3. Convergent results and times of every desired value

Serial number	Es_d	Convergent results of Es_d	Convergent times
1	32	30.78	23
2	49	49.03	41
3	58	58.22	12
4	64	63.40	16
5	78	78.47	16
6	86	86.53	40

The dynamic response process is shown in figure 6 when Es_d is equal to 25. From table 3, we can see the convergent results are fine. However, the convergent speed is lower than that of GILA.

4.3 Specialized Inverse Learning Architecture-Ⅱ

4.3.1 Structure of SILA-Ⅱ

Figure 6 is a structure of SILA-Ⅱ. When Esd and Fd are acted as the inputs of the NN1, the neural network controller outputs the welding voltage (U) and the welding current (I). The error between the output of welding arc system and that of the error transfer model (NN3) is used to train the error transfer model. While the error between the output of welding arc system and the desired value is used to train the neural network controller (NN1) through NN3. The weights of the error transfer model (NN3) are obtained by training off-line and can be modified by on-line training.

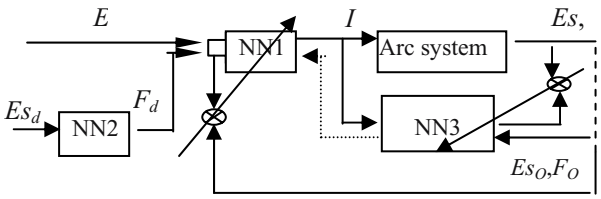

Fig. 6. Structure of SILA-Ⅱ

4.3.2 Simulating Results of SILA-Ⅱ

Table 4 shows the simulating results. From table 4, we can see that the convergent process is slow. The reason is that the weights' modification of the neural network controller is mainly depended on the precision of the error transfer model. When the error transfer model approaches the welding arc system, the simulating results will be better.

Table 4. Convergent results and times of every desired value

Serial number	Es_d	Convergent results of Es_d	Convergent times
1	32	31.04	74
2	50.5	50.90	18
3	58	56.01	45
4	64	62.17	11
5	75	75.77	33
6	82	83.92	511

4.4 Error Back Propagating Model (EBPM)

4.4.1 Structure of EBPM

This model is used to control the dynamic behavior of CO_2 welding arc. As shown in Fig.7, the system adopts the inverse dynamic control. NN1 is the inverse dynamic model of the welding process and .is used as the controller. NN2 is a channel for error transfer. The input of NN1 includes welding arc sound energy while the output is the increasing speed of short circuiting current (dI/dt), the ratio of short circuiting peak current and the average welding current (I_m/I) and the welding voltage. The samples are statistical results from practical welding process. NN1 can response the inverse dynamic characteristics of the welding process when trained.

When the desired value (Es) is given, NN1 outputs the optimum short circuit current waveform and it is used to control the practical welding process. The input of NN2 is the error between the desired value and the practical output of the welding process. The output of NN2 is used to adjust the weights and thresholds of NN1, thus the neural network controller is regulated to control the arc system.

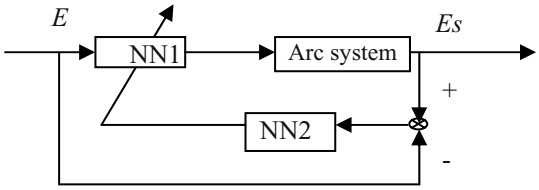

Fig. 7. Error back propagating model

4.4.2 Simulating Results and Analysis

The simulating results are shown in table 5. We can see that the simulating results are satisfying. In the whole input field, there are fine dynamic responses not only with the

points near the samples but also for extrapolating and inserting points. All of the static errors are less then one percentage. When the dynamic properties of the positive model is not in good consistent with the actual welding process this control model is a satisfying one.

Table 5. Simulating results of EBPM (training times: 100)

Input	Output	Error (%)	Input	Output	Error (%)	Input	Output	Error (%)
0.120	0.119 2	0.64	0.170	0.169 2	0.47	0.253*	0.251 7	0.51
0.331*	0.330 0	0.30	0.366*	0.365 3	0.19	0.401*	0.405 0	1.00
0.453*	0.452 2	0.18	0.500	0.499 3	0.14	0.550*	0.549 1	0.16
0.657*	0.656 3	0.11	0.700	0.699 3	0.10	0.750	0.749 3	0.09
0.800	0.799 1	0.11	0.869*	0.868 2	0.08	0.900*	0.899 3	0.08

*: the inserting points.

5 Conclusions

The welding arc sound energy (Es) can quantitatively represent on-line the welding spatter ratio for CO_2.welding process.

The simulation and experimental results show that SILA- Ⅰ and EBPM control models by neural networks have very good effects for controlling CO_2 welding spatters.

The factors affecting the response quality are control models, samples, learning parameters and error transfer coefficients.

Acknowledgement

The authors gratefully acknowledge the support received from the National Natural Science Foundation of China, No: 50675093 and also from the Natural Science Foundation of Gansu Province in PR China, No: 3ZS051-A25-029 and Chun Hui Project of Ministry of Education of the PR China.

References

1. Masao Ushio. Process Control in the Arcing Short-circuit Phases During Metal-Arc Active Gas Build-up Welding Under Carbon Dioxide. Welding and Cutting, (2) 1994
2. E. K. Stave. The Surface-tension-transfer Power Source: A New Low-Spatter Arc Welding Machine. Welding Journal, (1) 1993. 25-29
3. MA Yue-zhou, MA Chun-wei, ZHANG Peng-xian and CHEN Jian-hong. The Model of Spatter Prediction in CO_2 Arc Welding Based on the Character of Sound Signal. Transactions of The China Welding Institution, 2002, 23(3): 19-22

4. Ding FAN, Yu SHI and Masao USHIO. Investigation of CO^2 Welding Arc Sound. Transactions of JWRI, 2001, 30(1): 29-33
5. Ding FAN, Yu SHI, Yurzhou MA, Jianhong CHEN and Masao USHIO. A Neural Network Closed-loop Control of CO^2 Welding Spatter by Means of Arc Sound. Transactions of JWRI, 2001, 30(2): 1-4
6. Kang M J, Rhee S. The statistical models for estimating the amount of spatter in the shout circuit transfer mode of GMAW. Welding Journal, 2001, 80(1): 1-8
7. Saini D, Floyd S. An investigation of gas metal arc welding sound signature for on-line quality control. Welding Journal, 1999, (78): 172-179

Numerical Study of Tube Cathode Arc with Anode Melting

S. Tashiro and M. Tanaka

Joining and Welding Research Institute, Osaka University, 11-1 Mihogaoka, Ibaraki, Osaka 576-0047, Japan
tashiro@jwri.osaka-u.ac.jp

Abstract. Tungsten Inert Gas (TIG) arc is the most widely employed type of a plasma torch and enables to produce arc plasma with high energy density. Therefore it is suitable as a heat source especially for processes to require concentrating the heat input at a point. On the other hand, Tube Cathode Arc (TCA) to be a kind of TIG produces the arc plasma by introducing inner shielding gas through the central hole of the tube cathode. In this paper, as the basic heat source property of argon (Ar) TCA, the property of the arc plasma and the heat input intensity onto a water-cooled copper anode for various inner shielding gas flow rates were numerically analyzed. Furthermore, by employing stainless steel SUS304 anode, the geometry of it's weld penetration was also predicted. The results were compared with those for the conventional TIG. As a result, it was found that since TCA enables to heat the target material uniformly by controlling the inner shielding gas flow rate and preserve it from damage due to excessive heat input during the process, it is suitable for processes such as brazing, buildup or thermal spraying.

1 Introduction

Since a plasma torch can stabilize high temperature arc plasma by employing shielding gas, it is used as a heat source. Tungsten Inert Gas (TIG) is the most widely employed type of the plasma torch and produces the arc plasma between a tungsten cathode and an anode material. It has high heating efficiency and highly controllable characteristics, and requires low cost for equipment investment. Furthermore, the target material can be heated without any chemical reaction by using inert gas as the shielding gas. Therefore, it is widely utilized, for example, for material processing such as melting, cutting and welding [1], or decomposition, volume reduction and detoxification of toxic waste [2] and so on.

The heat source property of TIG strongly depends on the physical property of the shielding gas. For instance, helium gas with low electrical conductivity or carbon dioxide with high specific heat causes constriction of the arc plasma and, hence, enables to produce the arc plasma with high energy density [3]. Therefore, TIG is suitable especially for processes to require concentrating the heat input at a point but less effective for processes to require heating the target material uniformly.

On the other hand, Hollow Cathode Arc (HCA) to be a kind of TIG produces the arc plasma by introducing the shielding gas through a central hole of the hollow cathode. It has been studied as a heat source especially in lower pressure, for example, for space welding [4] or plasma CVD [5], because it is suitable to supply the shielding

T.-J. Tarn et al. (Eds.): Robot. Weld., Intellige. & Automation, LNCIS 362, pp. 127–134, 2007.
springerlink.com

gas in the electrode gap. Furthermore, as applications at the atmospheric pressure, it may be utilized for brazing, buildup or thermal spraying. In this case, it is expected that the anode material can be preserved from damage due to excessive heat input during the process, because heat input may not be concentrated at a point in contrast to the TIG. However, the heat source properties of HCA at the atmospheric pressure are not fully understood.

In this paper, HCA at the atmospheric pressure is termed as Tube Cathode Arc (TCA), because the mechanism of electron emission is different from that in low pressure. And, as the basic heat source property of argon (Ar) TCA, the property of the arc plasma and the heat input intensity onto a water-cooled copper anode for various shielding gas flow rates are numerically analyzed. Furthermore, by employing stainless steel SUS304 anode, the geometry of it's weld penetration is also predicted. The results are compared with those for the conventional TIG.

2 Simulation Model

A tungsten cathode, arc plasma and an anode are described in a frame of cylindrical coordinate with axial symmetry around the arc axis. A calculation domain and details of the cathodes for TIG and TCA are shown in Fig. 2.1. The outer diameter and the inner diameter only for TCA are 3.2mm and 1.6mm, correspondingly. The anode is a water-cooled copper or a stainless steel SUS304 for which temperature coefficient of surface tension above the melting point is given in Ref. [6]. The electrode gap is set to be 5mm. The arc current is set to be 200A. Ar is introduced at the flow rate of 10L/min. from outside of the cathode on the upper boundary. Only for TCA, that at the flow rate of 0.5, 1.0 or 2.0L/min. is additionally introduced through the hole of the tube cathode, which is defined as an inner shielding gas. The flow is assumed to be laminar, and the arc plasma is assumed to be under the local thermodynamic equilibrium (LTE). Azimuthally uniform expansion of the cathode spot is also assumed. The other numerical modeling methods are given in detail in our previous papers [7, 8]. The differential Eqs. (2.1)-(2.6) are solved iteratively by the SIMPLEC numerical procedure [9]:

Mass continuity equation;

$$\frac{1}{r}\frac{\partial}{\partial r}(r\rho v_r) + \frac{\partial}{\partial z}(\rho v_z) = 0 \tag{1}$$

Radial momentum conservation equation;

$$\frac{1}{r}\frac{\partial}{\partial r}\left(r\rho v_r^2\right) + \frac{\partial}{\partial z}\left(\rho v_r v_z\right) = -\frac{\partial P}{\partial r} - j_z B_\theta + \frac{1}{r}\frac{\partial}{\partial r}\left(2r\eta\frac{\partial v_r}{\partial r}\right) + \frac{\partial}{\partial z}\left(\eta\frac{\partial v_r}{\partial z} + \eta\frac{\partial v_z}{\partial r}\right) - 2\eta\frac{v_r}{r^2} \tag{2}$$

Axial momentum conservation equation;

$$\frac{1}{r}\frac{\partial}{\partial r}\left(r\rho v_r v_z\right) + \frac{\partial}{\partial z}\left(\rho v_z^2\right) = -\frac{\partial P}{\partial z} + j_r B_\theta + \frac{\partial}{\partial z}\left(2\eta\frac{\partial v_z}{\partial z}\right) + \frac{1}{r}\frac{\partial}{\partial r}\left(r\eta\frac{\partial v_r}{\partial z} + r\eta\frac{\partial v_z}{\partial r}\right) \tag{3}$$

Energy conservation equation;

$$\frac{1}{r}\frac{\partial}{\partial r}\left(r\rho v_r v_z\right) + \frac{\partial}{\partial z}\left(\rho v_z^2\right) = -\frac{\partial P}{\partial z} + j_r B_\theta + \frac{\partial}{\partial z}\left(2\eta\frac{\partial v_z}{\partial z}\right) + \frac{1}{r}\frac{\partial}{\partial r}\left(r\eta\frac{\partial v_r}{\partial z} + r\eta\frac{\partial v_z}{\partial r}\right) \tag{4}$$

Current continuity equation;

$$\frac{1}{r}\frac{\partial}{\partial r}(rj_r)+\frac{\partial}{\partial z}(j_z)=0 \tag{5}$$

Ohm's law;

$$j_r=-\sigma E_r,\ j_z=-\sigma E_z \tag{6}$$

where t is time, h is enthalpy, P is pressure, v_z and v_r are axial and radial velocities, j_z and j_r are axial and radial components of the current density, g is the acceleration due to gravity, κ is the thermal conductivity, C_p is specific heat, ρ is density, η is viscosity, σ is electrical conductivity, R is radiation emission coefficient, E_r and E_z are, respectively, radial and axial components of the electric field defined by $E_r=-\partial V/\partial r$ and $Ez=-\partial V/\partial z$, where V is electric potential. The azimuthal magnetic field B_θ induced by the arc current is evaluated by maxwell's equation.

$$\frac{1}{r}\frac{\partial}{\partial r}\left(rB_\theta\right)=\mu_0 j_z \tag{7}$$

where μ_0 is the permeability of free space.

In the solution of Eqs. (2.1)-(2.6), special account needs to be taken at the electrode surface for effects of energy that only occur at the surface. At the cathode surface, additional energy flux terms need to be included in Eq. (2.4) for thermionic cooling due to the emission of electrons, ion heating, and radiation cooling. The additional energy flux for the cathode Hk is:

$$H_K=-\varepsilon\alpha T^4-\left|j_e\right|\phi_K+\left|j_i\right|V_i$$

where ε is the surface emissivity, α is the Stefan-Boltzmann constant, ϕ_K is the work function of the tungsten cathode, V_i is the ionization potential of argon, j_e is the electron current density, and j_i is the ion current density. At the cathode surface, for thermionic emission of electrons, j_e cannot exceed the Richardson current density J_R [10] given by:

$$\left|j_R\right|=AT^2\exp\left(-\frac{e\phi_e}{k_BT}\right) \tag{8}$$

where A is the thermionic emission constant for the cathode surface, ϕ_e is the effective work function for thermionic emission of the electrode surface at the local surface temperature, and k_B is the Boltzmann's constant. The ion-current density j_i is then assumed to be $|j|-|j_R|$ if $|j|$ is greater than$|\ |j_R|$; where $|j|=|j_e|+|j_i|$ is the total current density at the cathode surface obtained from Eq. (2.5)

Similarly, for the anode surface, Eq. (2.4) needs additional energy flux terms for thermionic heating and radiation cooling. the additional energy flux for the anode H_A is:

$$H_A=-\varepsilon\alpha T^4+\left|j\right|\phi_A \tag{9}$$

where ϕ_A is the work function of the anode and $|j|$ is the current density at the anode surface obtained from Eq. (2.5). The term including ϕ_A accounts for the heating of the anode by electrons, which delivers energy equal to the work function on being

absorbed at the anode. The term is analogous to the cooling effect that occurs at the cathode when electrons are emitted.

At the stainless steel SUS304 anode surface, BE in Fig. 1, there are two sources of radial momentum. The first is the drag force, namely, the shear stress which is applied by the cathode jet on the surface of the weld pool, and the second is the surface tension gradient force, namely, the Marangoni force. The drag force is already reflected in Eq. (2.2) for the radial momentum conservation. The viscosity η makes the drag force at the anode surface. Therefore, the Marangoni force would need to be included in the radial momentum conservation at points on the anode surface, BE. In most cases, the difference in surface tension arises from the temperature variation at the weld pool surfaces[6], and then the Marangoni force τ can be expressed by

$$\tau = -\eta \frac{\partial v_r}{\partial z} = \frac{\partial \gamma}{\partial T} \frac{\partial T}{\partial r} \tag{10}$$

where γ is the surface tension of the weld pool. Therefore, the additional term for Eq. (2.2) at the anode surface F_A is

$$F_A = \frac{\partial}{\partial z} \left(\frac{\partial \gamma}{\partial T} \frac{\partial T}{\partial r} \right). \tag{11}$$

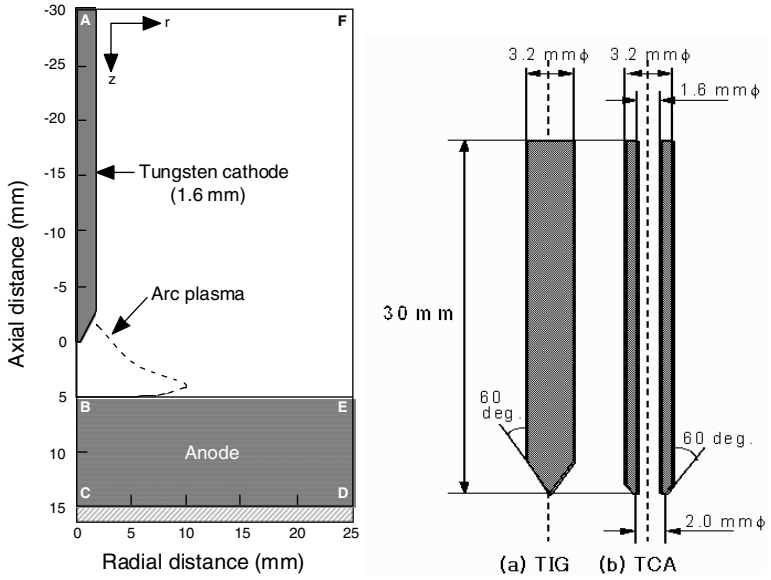

Fig. 1. Schematic illustration of simulation domain

3 Results and Discussion

Fig. 2 shows Two-dimensional distribution of temperature and fluid flow velocity for TIG, TCA at inner shielding gas flow rate of 0.5L/min, 1.0L/min and 2.0L/min in the

case of the water-cooled copper anode. Fig. 3 shows radial distributions of the heat input intensity and the current density on the anode surface.

In the case of TIG, the current density near the arc axis becomes higher, since the arc current channel on the cathode tip is constricted at a point. The enhanced electromagnetic pinch force accelerates cathode jet velocity up to 320m/s and, thus, leads to high arc pressure to the anode surface. The increase in Joule heating due to the high current density lifts the plasma temperature near the cathode up to 21000K and cathode tip temperature up to 3500K near the melting point of tungsten. On the other hand, the heat input onto the anode surface is concentrated near the arc axis especially due to the concentration of the thermionic heating which is proportional to the current density and, consequently, max. heat input intensity and max. anode surface temperature reach 7000W/cm^2 and 750K, respectively.

Now, turn to the results for TCA. The current density lowers especially near the cathode due to the expansion of the arc current channel caused by the large area of the cathode tip. It leads to the cathode jet velocity of approximately 70m/s which is 20% of the TIG and, thus, lower arc pressure. In contrast to the TIG, the plasma temperature and the cathode tip temperature reach only 13000K and 2900K which are 60% and 80% of the TIG because of the low current density. So, longer lifetime of the cathode can be expected. It is also seen that the plasma near the arc axis tends to be cooled by the inner shielding gas especially near the cathode and the low temperature region extends toward the anode with the increase of inner shielding gas flow rate. The max. heat input intensity onto the anode surface becomes less than 50% of the TIG and, additionally, lowers near the arc axis for the higher inner shielding gas flow rate due to the low plasma temperature near the anode. And, the raise in the anode temperature becomes lower and more uniform than the TIG.

Fig. 2 Two-dimensional distribution of temperature and fluid flow velocity at 5 sec. after arc ignition for TIG, TCA at inner shielding gas flow rate of 0.5L/min, 1.0L/min and 2.0L/min in the case of stainless steel SUS304 anode. It can be seen that the radius and the depth of the weld penetration region in the anode reach 6.5mm and 1.3mm, respectively, in the case of TIG. On the other hand, in the case of TCA, the radius reaches 6.0mm which is approximately same as the TIG and, in contrast, the depth decreases with increase of the inner shielding gas flow rate to 0.5mm for 2L/min. It is recognized that an electromagnetic force strongly affects downward convective flow in the weld penetration region in the anode material[6]. In the case of TCA, it is considered that the weak electromagnetic force due to the low current density leads to the shallow weld penetration in addition to the effect due to the low max. heat input intensity. Consequently, it was found that TCA is suitable for processes such as brazing, buildup or thermal spraying because the anode material can be preserved from damage due to excessive heat input during the process.

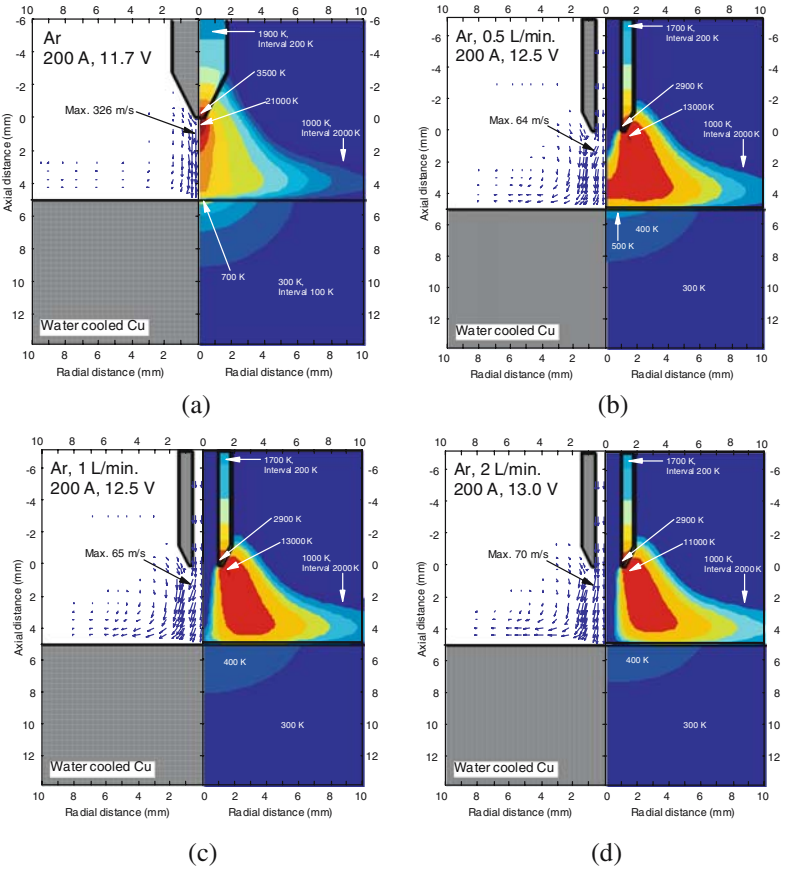

Fig. 2. Two-dimensional distribution of temperature and fluid flow velocity for (a) TIG, TCA at inner shielding gas flow rate of (b) 0.5L/min, (c) 1.0L/min and (d) 2.0L/min in the case of water-cooled copper anode

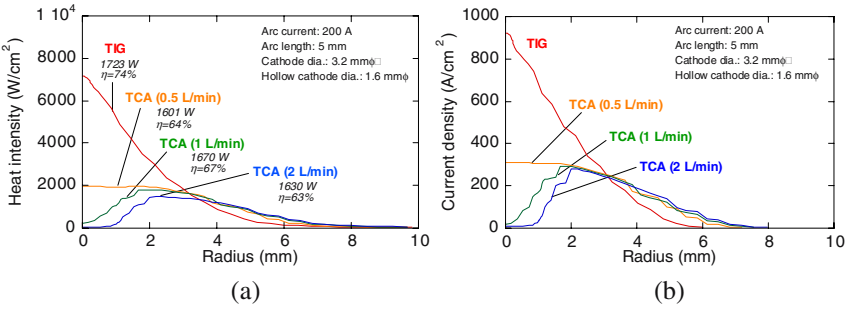

Fig. 3. Radial distributions of (a) heat input intensity and (b) current density on the anode surface in the case of water-cooled copper anode

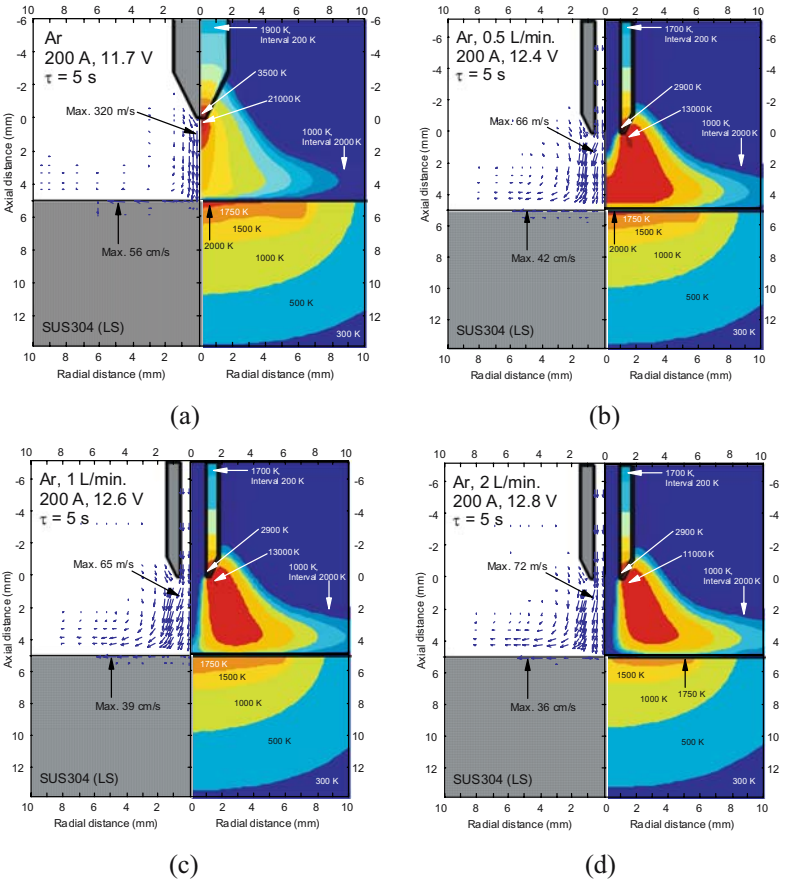

Fig. 4. Two-dimensional distribution of temperature and fluid flow velocity at 5 sec. after arc ignition for (a) TIG, TCA at inner shielding gas flow rate of (b) 0.5L/min, (c) 1.0L/min and (d) 2.0L/min in the case of stainless steel SUS304 anode

4 Conclusions

The basic heat source property of argon TCA at the atmospheric pressure in 200A arc current for various inner shielding gas flow rates was numerically analyzed. Furthermore, the results were compared with those for the conventional TIG. The main conclusions are summarized as follows:

1. The current density for TCA lowers especially near the cathode than the TIG due to the expansion of the arc current channel caused by the large area of the cathode tip. It leads to the max. plasma temperature of 13000K and the cathode jet velocity of 70m/s which are 60% and 20% of the TIG, respectively.
2. The cathode tip temperature reaches only 2900K which is 80% of the TIG because of the low current density. So, longer lifetime of the cathode can be expected.

3. The max. heat input intensity onto the anode surface becomes less than 50% of the TIG because of the lower current density. Furthermore, it lowers also for the higher inner shielding gas flow rate. As a result, the raise in the anode temperature becomes lower and more uniform than the TIG.
4. The radius of the weld penetration region in the stainless steel SUS304 anode reach 6.0mm which is approximately same as the TIG and, in contrast, the depth decreases with increase of the inner shielding gas flow rate to 0.5mm for 2L/min. As a result, it was found that TCA is suitable for processes such as brazing, buildup or thermal spraying, because the anode material can be preserved from damage due to excessive heat input during the process.

References

1. Ushio M, Tanaka M, Lowke J J (2004) Anode Melting From Free-Burning Argon Arcs. IEEE Trans P S 32: 108-117
2. Inaba T, Iwao T (2000) Treatment of Waste by dc Arc Discharge Plasmas. IEEE Trans D E I 7: 684-695
3. Tanaka M, Ushio M, Lowke J J (2004) Numerical study of gas tungsten arc plasma with anode melting. Vacuum 73: 381-389
4. Suita Y, Tsukuda Y, Takagi T, Ohji T, Masubuchi K (1994) Study of gas tungsten arc welding in space (1st report). Welding Int 8: 269-273
5. Zhang G F, Buck V (1999) Diamond growth by hollow cathode arc chemical vapor deposition at low pressure range of 0.02-2mbar. Diamond related materials 8: 2148-2151
6. Zacharia T., David S A, Vitec J M, Debroy (1990) Modeling of interfacial phenomena in welding. Metall Trans B 21: 600-603
7. Tanaka M, Terasaki H, Ushio M, Lowke J J (2002) A Unified Numerical Modeling of Stationary Tungsten-Inert-Gas Welding Process. Metal Trans A 33: 2043-2052
8. Tanaka M, Terasaki H, Ushio M, Lowke J J (2003) Numerical Study of a Free-burning Argon Arc with Anode Melting. Plasma Chem. Plasma Process 23: 585-606
9. Patanker S V (1980) Numerical heat transfer and fluid flow. Hemishpere Publishing Corporation, Washington DC
10. Pfender E (1978) Electric Arcs and Arc Gas heaters. Academic Press, NewYork

Numerical Simulation of Molten Droplet Shape and Electromagnetic Pinch Effect in Short-Circuit CO_2 Welding

Z.M. Zhu, W.K. Wu, and Q. Chen

Department of Mechanical Engineering, Tsinghua University, Beijing 100084, P.R. China

Abstract. In short-circuit CO_2 arc welding, the transfer behavior, process stability and weld quality are strongly affected by the molten droplet shape just before short-circuit and the electromagnetic pinch action on the liquid bridge during short-circuit phase. By using Static Force Balance Model, the effects of electromagnetic force, surface tension and gravity on the molten droplet shape during arc phase are simulated, the electromagnetic force being the dominant factor. To obtain a appropriate molten droplet shape in favor of arc stability and metal transfer, it is preferable to adopt a certain large pulse current in arc prophase and a small arc-keeping current in arc anaphase The numerical analysis to the effects of electromagnetic pinch action on the liquid bridge during short-circuit phase shows that a large current at initial stage will block the molten droplet from well spreading into the weld pool, but a large pulse current at metaphase will facilitate the formation of a neck in the liquid bridge. The simulation results are validated experimentally in waveform-controlled short-circuit CO_2 arc welding, the welding process being improved to be much stable and gentle.

1 Introduction

The short-circuit CO_2 arc welding, although has been widely applied, still exists the shortages of imperfect bead formation and a little large metal spatter. To further restrain the metal spatter, improve the process stability and weld quality, the experimental investigations have always been made in the past decades. As the advancement of magnetic fluid theory, the numerical simulation for transfer behavior of molten droplet has got studied extensively in the recent years, and the "Static Force Balance Theory", "Magnetic Pinch Instability Theory", "Time-Variant Dynamic Model" and others were developed, respectively.

Haidar and Lowke [1, 2] developed a two-dimensional time-dependent model, a unified treatment of the arc, welding wire and workpiece, for the prediction of the time development of molten droplets from the wire in gas metal arc welding, where the effects of surface tension, gravity, inertia, magnetic pinch force and heat convection within the molten droplet being taken into account, and the wire feed rate, gas content and flow rates being incorporated into also. For pure argon, the sharp transition between globular transfer and spray transfer is predicted at about 300A that is observed experimentally. The addition of 25% CO_2 to the argon leads to an increase in the

T.-J. Tarn et al. (Eds.): Robot. Weld., Intellige. & Automation, LNCIS 362, pp. 135–144, 2007.
springerlink.com

transition current to more than 325A, also in agreement with experimental results. For pure CO_2, a significantly different droplet behavior due to the more constricted arc is found, that both small and large droplets are produced, with many very small droplets being produced successively between each large droplet. Choi, *et al.* [3, 4] made a simulation research on the dynamic variation of molten droplet in globular and spray transfer mode with the method of Invariant Volume of Fluid. By the analysis to the pressure distribution and flowing velocity of liquid metal within the molten droplet, it was indicated that the axial movement of liquid metal within the droplet and the radial electromagnetic pinch force are the main causations for the metal transfer, the current distribution within the molten droplet is the dominant factor for its shape, the detaching velocity of droplet from the end of electrode and the end shape of electrode after the detachment. According to the photographed images, Jones, *et al.* [5, 6] proposed a dynamic model for describing the molten droplet shape and its transfer. The effect of electromagnetic force on them was analyzed theoretically. Nemchinsky [7-11] also made great works on the numerical simulation of the droplet, such as the influence of different plasma gases on the electromagnetic pinch action upon the droplet, the detachment of droplet on the electrode melting and droplet formation, the movement mechanism of liquid metal within the molten droplet induced by the gradient of surface tension, and the heat transfer phenomenon within the electrode and molten droplet. Besides the aboves, some numerical simulation was also made with the short-circuit arc welding. H. Maruo, *et al.* [12] investigated the short-circuit transfer of molten droplet through numerical simulation and globular mercury with electricity. Choi, *et al.* [13, 14] simulated the short-circuit transfer for different droplet size through the dynamic model with Invariant Volume of Fluid.

The behaviors of metal transfer and arc stability in short-circuit CO_2 arc welding are affected strongly by the molten droplet shape. To know the influence of various factors will be beneficial to make an effective control on the welding process. The technology of numerical simulation provides a powerful means to investigate their relationships in depth. Meanwhile, the progress of high-speed inverter controlled power supply creates the qualification to control them finely. In this work, the effect of various factors, especially the electromagnetic force, on the molten droplet shape and electromagnetic pinch action are analyzed and simulated. And then, an effective control approach to achieve appropriate molten droplet shape, in favor of arc stability and metal transfer to short-circuit CO_2 arc welding, was proposed and validated experimentally.

2 Factors Affecting Droplet Formation and Metal Transfer

With respect to short-circuit CO_2 arc welding, the molten droplet volume V_j just before short-circuit is composed of two parts, the residual liquid metal volume V'_{j-1} remained at the end of electrode after the previous short-circuit transfer and the melted electrode quantity ΔV_j during present arc phase,

$$V_j = V'_{j-1} + \Delta V_j \tag{1}$$

When welding using Direct Current Electrode Positive (DCEP), the main arc energy to melt electrode during arc phase is the anode heat, resting with the welding current and the equivalent anode voltage drop, and the Joule heat, resulting in the electrode extension by the welding current, only few comes from the radiation of arc and weld pool. Since the anode voltage drop is almost a fixed value for given electrode with certain ingredients and diameter, falling in the range of 4-6 V, the melted electrode quantity ΔV_j can be regulated by controlling the welding current and electrode extension effectively. However, the control on the residual liquid metal volume V'_{j-1} is difficult.

As described in our previous work [15], it was found, with the analysis on the photographed droplet images, that V'_{j-1} relies mainly on the droplet volume V_{j-1} and its shape just before short-circuit, and its short-circuit experience. V_{j-1} presents a random distribution charateristics with a large dispersion even under an apropriate welding parameters. Their maximum diameters vary between 1 to 2 times of the wire electrode diameter, and some droplets also have large difference in their shape even if they have almost the same volume. The droplet with excessive large or small volume just before short-circuit will decrease the process stability, but its effect on V'_{j-1} **is** evident only when it is over small. The effect of droplet shape just before short-circuit on V'_{j-1} is more significant, since it affects the short-circuit experience, and then its transfer quantity of liquid metal from the molten droplet into weld pool. The larger the ratio of width to height of the molten droplet is, the more difficult the losing of equilibrium state will be. Thus, the flat-shaped droplet is unfavorable to the metal transfer compared to the cylindrical-shaped. The effect of short-circuit experience on V'_{j-1} behaves as that, V'_{j-1} affects V_j, V_j will, in turn, affect V'_j, therefore V'_{j-1} possibly exists accumulative effect on V'_j. Usually, the most of molten droplets contact with weld pool smoothly, the neck in liquid bridge form and rupture near the end of wire electrode, thus the most of liquid metal transfers from the molten droplet into weld pool, as a result, the residual liquid metal V'_{j-1} are little and have good consistency, and there is no coupling between V'_{j-1} and V_j and no accumulation on V'_j. However, some molten droplets have distinctive different short-circuit experience, such as short-term short-circuit, and only few liquid metal transfers from the molten droplet into weld pool, resulting in large V'_{j-1} and then large difference in V'_{j-1}, even if the molten droplets with almost the same volume and shape just before short-circuit.

3 Effects of Electromagnetic Force on Droplet Shape

In the circular cylindrical coordinates in Fig.1, supposing that the molten droplet is radial symmetry, then its shape satisfies the following control equation [9],

$$p(R,z)=\sigma\left(-\frac{R''}{(1+R'^2)^{3/2}}+\frac{1}{R(1+R'^2)^{1/2}}\right) \tag{2}$$

Where, $p(R,z)$ represents the pressure difference between inside and outside of the molten droplet, σ denotes the surface tension of the liquid metal, R is the radius of molten droplet at axial coordinate z, $R' = dR/dz$, $R'' = d^2R/dz^2$.

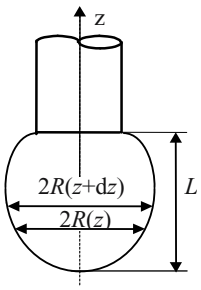

Fig. 1. Sketch map of molten droplet

On the assumption that the forces acted on the molten droplet, including electromagnetic force, surface tension and gravity only, are in equilibrium, and the distribution of welding current within the molten droplet and liquid bridge is uniform, then, the molten droplet shape is governed by the following equations.

$$\frac{dp_0(z)}{dz} = -\frac{\mu_0 I}{8\pi^2}\frac{d}{dz}\left(\frac{I}{R^2}\right) - \frac{\mu_0 R^2}{8\pi^2}\frac{d}{dz}\left(\frac{I^2}{R^4}\right) - \rho g \tag{3}$$

$$p_0(z) = -\frac{\mu_0 I^2}{4\pi^2 R^2} + \sigma\left(-\frac{R''}{(1+R'^2)^{3/2}} + \frac{1}{R(1+R'^2)^{1/2}}\right) \tag{4}$$

Where, ρ denotes the density of the liquid metal, g stands for the acceleration of gravity, μ_0 is the vacuum permeability with the value of $4\pi\times10^{-7}\,\mathrm{H}\cdot m^{-1}$, $p_0(z)$ is the pressure at the coordinates (z, 0), and I is the welding current.

With CO_2 shielding gas being used, the arc is constricted. Due to the difficulty of arc root to spread and the necessity of arc to burn at the minimum distance, the arc spot has a strong tendency to concentrate at the bottom of the molten droplet. Therefore, it is believed that the welding current always flows through the molten droplet, namely, $I(z) = I$. Differentiating equation (4) with z and combining equation (3), we have

$$R''' = \frac{\rho g - \dfrac{\mu_0 I^2 R'}{4\pi^2 R^3}}{\sigma}\left(1+R'^2\right)^{\frac{3}{2}} + \frac{3R''^2 R'}{1+R'^2} - \frac{R'}{R^2}\left(1+R'^2\right) - \frac{R''R'}{R} \tag{5}$$

Thus, the molten droplet shape for CO_2 shielding gas can be calculated by equation (5). Taking the parameters as $\sigma = 1.2N\cdot m^{-1}$, $\rho = 7860kg\cdot m^{-3}$ and $g = 9.806m\cdot s^{-2}$, the boundary conditions of the molten droplet as $R(L) = 0.6mm$ (i.e. the wire electrode diameter $\Phi = 1.2mm$), $R(0)\to 0$ and $R'(0)\to\infty$, and converting them to initial conditions by using Bvalfit method, then the molten droplet radius R can be solved out iteratively by employing Runge-Kutta method for certain droplet length L and welding current I.

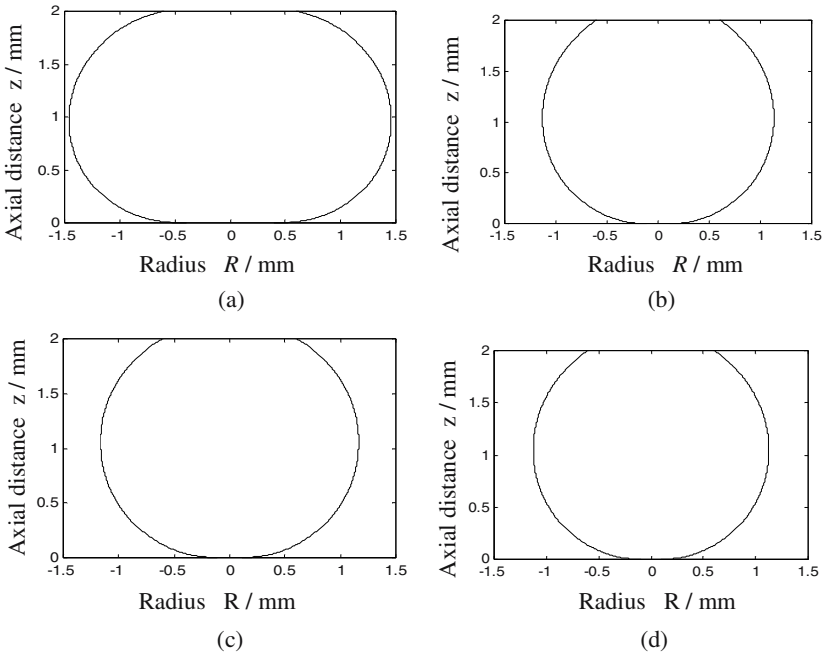

Fig. 2. Simulation results of the molten droplet shape for the wire electrode diameter $\Phi = 1.2mm$ and the length of molten droplet $L = 2mm$ under the different assumed conditions of welding currents, gravities and surface tensions. (a) for $\sigma = 1.2N \cdot m^{-1}$, $\rho = 7860kg \cdot m^{-3}$, $g = 9.806m \cdot s^{-2}$ and $I = 300A$; (b) for $\sigma = 1.2N \cdot m^{-1}$, $\rho = 7860kg \cdot m^{-3}$, $g = 9.806m \cdot s^{-2}$ and $I = 40A$; (c) for $\sigma = 1.2N \cdot m^{-1}$, $\rho g = 0$ and $I = 40A$; (d) for $\sigma = 1.6N \cdot m^{-1}$, $\rho = 7860kg \cdot m^{-3}$, $g = 9.806m \cdot s^{-2}$ and $I = 40A$, respectively .

Fig. 2 shows the numerical calculated results for different welding currents, gravities and surface tensions. In Fig.2a, the molten droplet under the conditions of $I = 300A$ and $L = 2mm$ is pushed up by the axial upward electromagnetic force, with a flat shape being unfavorable for the metal transfer. As for $I = 40A$ and $L = 2mm$, the molten droplet shape, as shown in Fig.2b, changes obviously comparing with Fig.2a, its maximum diameter $D_{\max}$ decreasing from 2.921 mm to 2.263 mm. Ignoring the effect of gravity, i.e. supposing $\rho g = 0$, then the maximum diameter $D_{\max}$ changes from 2.263 mm to 2.330 mm only, as shown in Fig.2c. With the increasing of surface tension, the maximum diameter $D_{\max}$ changes slightly, as depicted in Fig.2d, $D_{\max} = 2.252mm$ with $\sigma = 1.6N \cdot m^{-1}$.

Obviously, the electromagnetic force, resting on the welding current, is the dominant factor to affect the shape of molten droplet, whereas the gravity and surface tension of

the molten droplet have little impact on its shape. Thus the shape of molten droplet can be controlled by regulating the instantaneous arcing current. Fig.3 shows the effect of welding current on the shape of molten droplets that have the same volume. The molten droplet presents a smaller axial size and a larger radial diameter as the welding current increases.

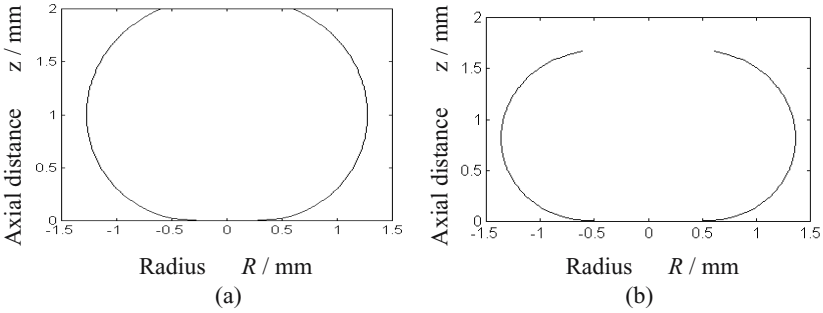

Fig. 3. Effect of welding current on the droplet shape for I=80 A (a) and I=200 A (b)

4 Effect of Electromagnetic Force on Liquid Bridge

Fig.4 presents the shape of molten droplet just coming into contact with weld pool and its corresponding axial electromagnetic force，which is upwards at the bottom of molten droplet，being directly proportional to the square of welding current but inversely proportional to the cube of radius of contact area between molten droplet and weld pool. Obviously, a large welding current is extremely unfavorable to the spread and transfer of molten droplet into weld pool when the contact area is small at the initial stage of short-circuit, and possible cause molten droplet flicking again from weld pool. Meanwhile, a huge Joule heat generated by the high current density at the contact area will lead to over heating and boiling away of molten droplet at the local bottom region.

Fig.5 gives the shape and axial electromagnetic force, being opposite in direction at the middle region of liquid bridge and intending to make the liquid bridge rupture, of molten droplet that has spread into weld pool sufficiently and formed a neck in liquid bridge. Apparently, it will be favorable to the spread of molten droplet into weld pool to employ a small current at the prophase of short-circuit, and it will enhance the impact of electromagnetic force on the metal transfer and thus accelerate the transfer of molten droplet into weld pool to adopt a large current at the middle stage of short-circuit. All of this will facilitate the liquid metal transfer process, and consequently increase the consistency of short-circuit experience and result in similar residual liquid metal quantity V'_{j-1}.

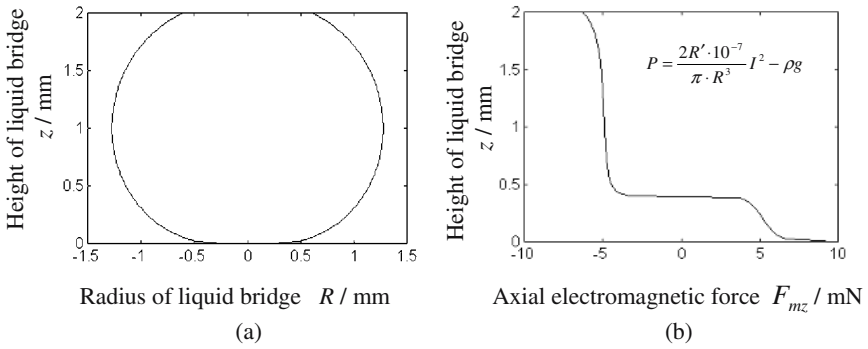

Fig. 4. Molten droplet shape (a) and its axial electromagnetic force (b) at the initial stage of short-circuit for *I*=50A

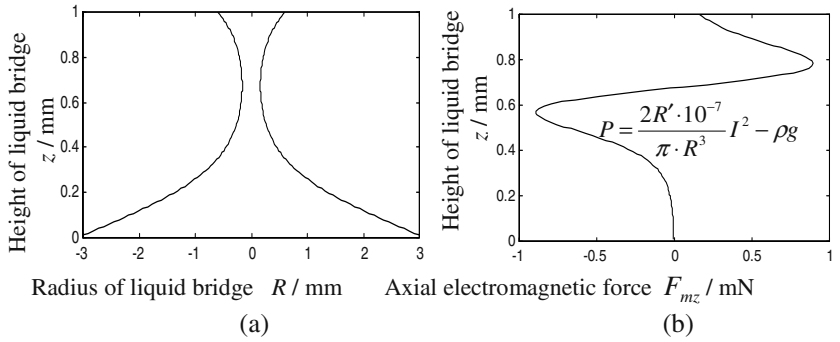

Fig. 5. Liquid bridge shape (a) and its axial electromagnetic force (b) at the middle and last stages of short-circuit for *I*=50A

5 Experimental Verification

The numerical calculated results indicate that the molten droplet shape just before short-circuit and the electromagnetic pinch action on the liquid bridge during short-circuit phase have strongly effects on the metal transfer and process stability. Accordingly, a validated waveforms of welding voltage and current used to control the volume and shape of molten droplet, and the short-circuit experience are developed, as shown in Fig.6a. Fig.6b is the corresponding droplet images.

After arc re-ignition being detected, a large pulse arc current with a certain width is introduced at the initial arc stage, it will enhance the electrode rapid melting backwards and make the molten droplet with a flat-shape (image A in Fig.6b), thus avoid small sized molten droplet dipping into or short-circuiting with weld pool abnormally. As the molten droplet volume reaches a moderate size, the arc current is decreased to a smaller arc-keeping current value, it will make the molten droplet form a axial cylindrical shape

(image B in Fig.6b) by decreasing the arc spot pressure and weakening the vibration of molten droplet, which ensures the shape of molten droplet uniform and easies to spread into weld pool smoothly as short-circuit occurs, thus lowers the random characteristics of short-circuit and strengthens the axial orientation of metal transfer.

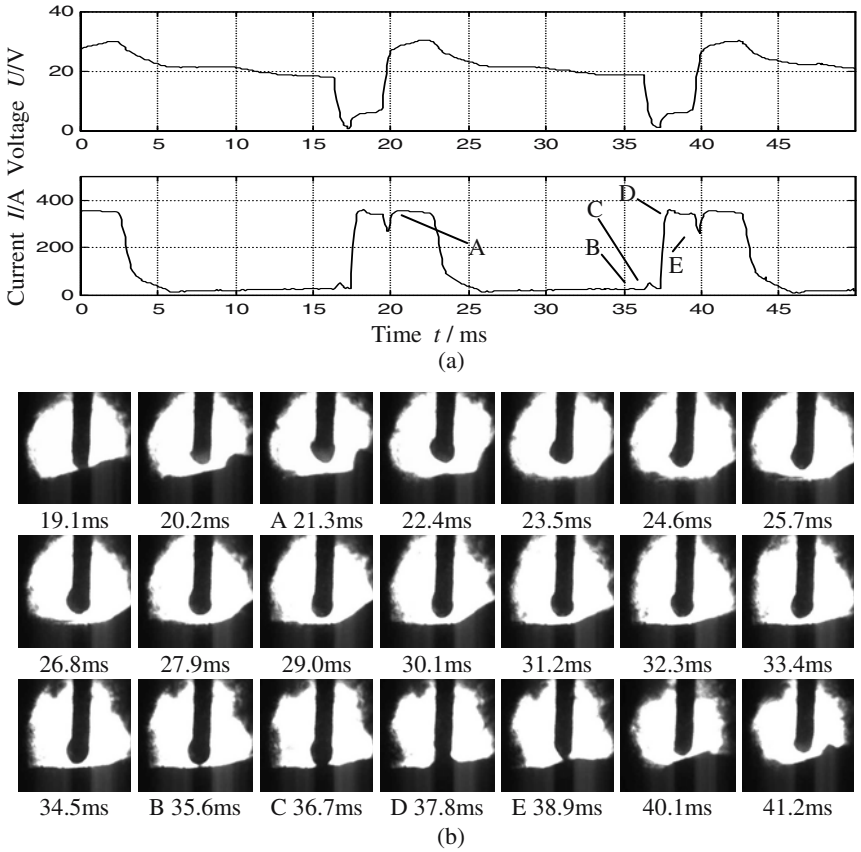

Fig. 6. Controlled waveforms of arc voltage and welding current (a) and corresponding droplet images (b)

At the beginning of short-circuit, a small welding current is applied, which guarantees a smooth contact and spread of molten droplet with and into weld pool (image C in Fig.6b) further. As the molten droplet has spread into weld pool sufficiently, a proper pulse short-circuit current is adopted, it will accelerate the droplet transfer into weld pool (image D in Fig.6b), and let the necking in liquid bridge near the end of solid wire electrode. The applying time of pulse short-circuit current should be fit, otherwise it will affect the necking position, i.e. the electromagnetic force will lead the liquid bridge to neck at the comparatively lower part of liquid bridge as the pulse short-circuit current is applied when the molten droplet does not spread in weld pool sufficiently. During the short-circuit anaphase, the necking area in liquid bridge

decreases rapidly due to the positive feedback of electromagnetic force and surface tension, thus the resistance of liquid bridge increases significantly. At this situation, an intense elecromagnetic pinch force and a certain amount of Joule heat around the neck will be generated if a large current still flows through the liquid bridge, which will cause metal spatter through explosion of liquid bridge, and thus affect the volume of residual liquid metal. Therefore, the welding current at this stage should be decreased to asure the liquid bridge to rupture under a small current (image E in Fig.6b).

The continuous molten droplet images, as shown in Fig.6b, indicates that the molten droplet shapes at arc prophase and at the moment of short-circuit are consistent with the above analysis result, under the conditions of large pulse current at arc prophase and small arc-keeping current at its anaphase. Meanwhile, the controlled short-circuit current makes the molten droplet spread in the weld pool smoothly and lets it transfer into the weld pool as much as possible.

6 Conclusions

Based on the analysis of the effects of welding current on the shape of molten droplet in CO_2 shielded short-circuit arc welding by using Static Force Balance Model, the optimum arcing current control waveform, for stable arcing and smooth short-circuit of molten droplet with weld pool, is ascertained. Applying a large pulse current at arc prophase and a small arc-keeping current at arc anaphase can increase the stability of molten droplet formation and avoid the abnormal contact of molten droplet with weld pool before it has reached a desired volume. Additionally, it is helpful to form a axial cylinderical-shaped molten droplet in favor of short-circuit of molten droplet with weld pool, which will increase the consistency of molten droplet shape just before short-circuit and allow more liquid metal in the molten droplet to transfer into weld pool also.

During the short-circuit phase, the electromagnetic pinch force acted on the liquid bridge presents remarkably distinct characteristics for different stages. By employing a small current at short-circuit prophase and a large pulse current at short-circuit metaphase, the molten droplet will contact with and spread in the weld pool smoothly, and the effect of electromagnetic pinch force on the formation of neck in liquid bridge at the short-circuit metaphase will be enhanced. This will increase the consistency of short-circuit experience and accelerate the metal transfer of molten droplet into weld pool. Combining the control on arc current and short-circuit current together, the short-circuit CO_2 arc welding will be provided with better arc behavior, process stability and weld quality.

Acknowledgements

This research was supported by National Science Foundation of China, No.59975050.

References

1. Haidar J, Lowke JJ (1996) Predictions of metal droplet formation in arc welding. J. Phys. D: Appl. Phys. 29(12): 2951-2960.
2. Haidar J, Lowke JJ (1997) Effect of CO_2 shielding gas on metal droplet formation in arc welding. IEEE Transactions on Plasma Science 25(5): 931-936.

3. Choi SK, Yoo CD, Kim YS (1998) Dynamic analysis of metal transfer in pulsed current gas metal arc welding. J. Phys. D: Appl. Phys. 31(2): 207-215.
4. Choi SK, Yoo CD, Kim YS (1998) Dynamic simulation of metal transfer in GMAW, Part I: globular and spray transfer models. Welding J. 77(1): 38s-44s.
5. Jones LA, Eager TW, Lang JH (1998) Magnetic forces acting on molten drops in gas metal arc welding. J. Phys. D: Appl. Phys. 31(1): 93-106.
6. Jones LA, Eager TW, Lang JH (1998) Dynamic model of drops detaching from a gas metal arc welding electrode. J. Phys. D: Appl. Phys. 31 (1): 107-123.
7. Nemchinsky VA (1996) Effect of the type of plasma gas on current constriction at the molten tip of an arc electrode. J. Phys. D: Appl. Phys. 29(5): 1202-1208.
8. Nemchinsky VA (1998) Rate of melting of the electrode during arc welding--the influence of discrete removal of the melt. J. Phys. D: Appl. Phys. 31(13): 1565-1569.
9. Nemchinsky VA (1994) Size and shape of the liquid droplet at the molten tip of an arc electrode. J. Phys. D: Appl. Phys. 27(7): 1433-1442.
10. Nemchinsky VA (1998) Heat transfer in an electrode during arc welding with a consumable electrode. J. Phys. D: Appl. Phys. 31(6): 730-736.
11. Nemchinsky VA (1997) Heat transfer in a liquid droplet hanging at the tip of an electrode during arc welding. J. Phys. D: Appl. Phys. 30(7): 1120-1124.
12. Maruo H, Hirata Y (1994) Bridging transfer phenomena of conductive pendent drop. IIW Doc. XII-1347-94: 29-39.
13. Choi SK, Ko SH, Yoo CD, Kim YS (1998) Dynamic simulation of metal transfer in GMAW, Part2: short-circuit transfer mode. Welding J. 77(1): 45s-51s.
14. Choi SK, Lee KH, Yoo CD (1997) Analysis of metal transfer through equilibrium shape of pendent drop in GMAW. Welding Research Abroad 43(4): 27-31.
15. Zhu Z, Wu W, Chen Q (2005) Random nature of droplet size and its origins in short circuit CO_2 arc welding. Sci. Technol. Weld. Joining 10(6): 636-642.

Planning the Torch Orientation of Planar Lap Joint in Robotic Welding

L. Zhou, J.F. Wang, T. Lin, and S.B. Chen

Institute of Welding Engineering, Shanghai Jiao Tong University, Shanghai, 200030, P.R. China
zhoulv@sjtu.org

Abstract. The torch orientation plays an important role in welding a lap joint. This paper proposes a torch orientation planning method for planar lap joint. In this method, the seam coordinates are firstly generated based on the visual servoing approach. The rotation matrix describing the torch orientation is calculated at each seam point according to the geometrical contains of the torch, which is set according to welding conditions and the arrangement of the workpiece. The rotation angle increments used to adjust the torch orientation is then calculated. A curve seam was used to validate this method. The robot movement experiments prove the torch can be automatically adjusted to the desired orientation when the robot moves the torch along the seam using the generated seam coordinates.

1 Introduction

At present, large numbers of industry robots have been used in the automation of arc welding process. However, most of them works in the mode of "teach and playback". They must be taught the welding path in advance as well as welding parameters and work sequence. The teach process is time-consuming especial for curve lap joint, because the varied torch orientation is required. In order to develop the intelligent robot, it is necessary that the welding system can autonomously plan the welding path which includes the torch orientation as well as its position.

The visual sensor has been applied for seam tracking because it has non-contact sensing capability and it can provide abundant information. However, in many studies [1-4], the obtained visual information was mainly used to correct the weld path which was manually taught or off-line programming based on CAD data prior to welding.

In this paper, a torch orientation calculating method for planar lap joint is proposed. The seam coordinates is automatically generated based on the visual servoing approach. The rotation matrix describing the torch orientation is constructed at each seam point according to the geometrical contains of the torch. Then, the rotation angle increments used to adjust the torch orientation is calculated.

2 System Description

The constructed experimental system, which is shown in Fig.1, mainly consists of three parts: the RH6 robot system, the sensor device and the master computer. The

T.-J. Tarn et al. (Eds.): Robot. Weld., Intellige. & Automation, LNCIS 362, pp. 145–151, 2007.
springerlink.com

RH6 robot system is a six-axis industry robot, developed by Shenyang institute of automation, Chinese academy of sciences. The sensor device is composed of a tilted CCD camera and its supporting system. The master computer is a Pentium III PC, which runs the image processing and tracking control program and acts as the man-machine interface to the system.

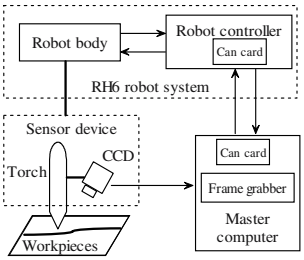

Fig. 1. Diagram of the experimental system

The master computer communicates with the robot controller using CAN (Controller Area Network) bus. The RH6 robot has its controller with the interface for accepting incremental pose from the master computer and for sending the current pose of the robot body to the master computer. The control cycle of the robot controller is 16ms.

3 Generation of the Seam Coordinates

The workpiece with lap joint is fixed on a horizontal worktable. In order to generate the seam coordinates, the system tracks the seam based on visual servoing method before welding. During seam tracking, the torch axis remains vertical so as to easily obtain the seam position based on the local seam image. When welding, the torch is automatically adjusted to the desired orientation according to the generated seam coordinates and the welding conditions.

The method of generating the seam coordinates is briefly explained here, and the similar method used for the butt-plane seam is discussed in [5]. The local seam image captured by the camera is transferred to the memory of the master computer with the frame grabber. The master computer processes the image and extracts the seam errors circularly. With the information of seam errors, the master computer sends motion increments to the robot controller, and then the robot moves the end-effector along the seam path. At the same time, the master computer reads the current pose of the robot from the robot controller, corrects these data with the current seam errors, and then records them to generate the seam coordinates in the base frame. The recorded coordinate point is called seam point.

4 Planning of Welding Torch Orientation

As shown in the Fig.2, both the position and the orientation of the torch can be represented by the tool frame {T}. The origin of {T} is at the tip of the torch, which is

usually called Tool Center Point (TCP), and the principal directions of {T} is given by three orthogonal unit vectors with the following convention:

- the approach vector **a** is collinear with the axial line of the torch and is the direction of approach;
- the orientation vector **o** is coplanar with the vector **a** and the vector **v**, a unit vector of the welding direction, while its **v**-component vector has the same direction with **v**;
- the normal vector **n** is given by the cross product of the vectors **o** and **a**.

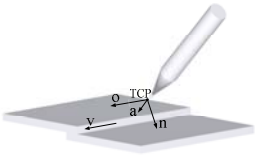

Fig. 2. Definition of Tool Center Point (TCP) and the tool frame {T}

4.1 Geometrical Constraints of the Torch Orientation

When welding a planar lap joint, the geometrical constrains of the torch orientation are shown in Fig.3. The angle θ is the included angle between the plane Π_1, decided by the electrode axis and the tangent line of the local seam, and horizontal plane Π_2 including the tangent line of the local seam. The angle ψ is the included angle between electrode axis and the line perpendicular to the tangent line of the seam in the plane Π_1. The angles θ and ψ are the acute angles.

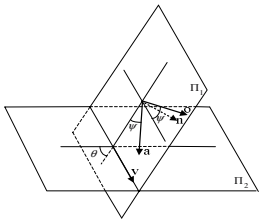

Fig. 3. Geometrical constraints of the torch orientation

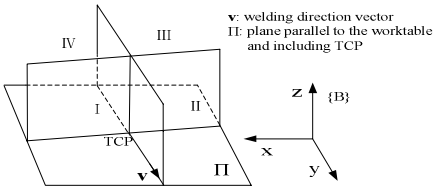

Fig. 4. Octants used to specify the torch orientation

In order to conveniently specify the torch orientation, we label four regions (the upper four octants) in the three dimensional space as shown in Fig.4.

4.2 Construction of Rotation Matrix ${}^{B}_{T}R$

4.2.1 Calculation of Trajectory Tangent Vector

The local seam trajectory is estimated by least square curve fitting to a 2nd degree polynomial curve of the following form:

$$y = a_0 + a_1 x + a_2 x^2 \tag{1}$$

Then, the slope k at point (x_i, y_i) is calculated by:

$$k = y'\Big|_{x_i} = a_1 + 2a_2 x_i \tag{2}$$

The corresponding tangent vector $\mathbf{s}$ at this point is in the following form:

$$\mathbf{s} = [1 \; k \; 0]^T \tag{3}$$

When the robot moves the torch according to the generated seam points, the torch orientation corresponding to the next seam point is calculated. For each seam point except for the last 5 ones, the 2nd degree polynomial curve fitting of the current point and the following 5 ones is performed to calculate the slope k at this point. The slopes at the last 6 seam points are calculated at every point using the last 2nd degree polynomial curve.

4.2.2 Construction of Intermediate Rotation Matrix ${}^{B}_{T'}R$

The orientation vector $\mathbf{o}$ becomes $\mathbf{o'}$, the approach vector $\mathbf{a}$ becomes $\mathbf{a'}$ when angle ψ is equal to zero. We denote the intermediate frame with its principal directions given by $\mathbf{n}$, $\mathbf{a'}$ and $\mathbf{o'}$ as $\{T'\}$.

The unit vector $\mathbf{o'}$ can be calculated by normalization of the vector $\mathbf{s}$ and correction the sign of its elements because the vector $\mathbf{o'}$ is parallel to the vector $\mathbf{s}$.

$$\mathbf{o'} = \begin{bmatrix} o'_x & o'_y & o'_z \end{bmatrix}^T = \begin{bmatrix} \dfrac{k}{|k|\sqrt{1+k^2}} & \dfrac{|k|}{\sqrt{1+k^2}} & 0 \end{bmatrix}^T \tag{4}$$

Suppose the direction vector of the line including the normal vector $\mathbf{n}$ is $\mathbf{n_1}$ and its three elements are A, B and C, respectively. According to the definition of the tool frame {T}, $\mathbf{n_1}$ is the normal vector of the plane Π_1. Since the plane Π_2 is horizontal, its normal vector $\mathbf{n_2}$ may be set to $[0 \;\; 0 \;\; 1]^T$.

According to the including angle between the plane Π_1 and the plane Π_2 is θ and the vector $\mathbf{n_1}$ is perpendicular to the tangent line of the local seam, we can obtain the following equations set:

$$\begin{cases} A + kB = 0 \\ \dfrac{|C|}{\sqrt{A^2 + B^2 + C^2}} = \cos\theta \end{cases} \tag{5}$$

Given $\dfrac{|C|}{\cos\theta} = 1$, we can get its solutions. They give four unit vectors that the normal vector **n** could be. By selecting the correct sign of its every element according to the actual torch orientation, we can obtain two solutions of vector **n** corresponding to two cases:

When the torch is in II or III octants,

$$\mathbf{n} = \begin{bmatrix} n_x & n_y & n_z \end{bmatrix}^T = \begin{bmatrix} -\dfrac{\sin\theta|k|}{\sqrt{1+k^2}} & \dfrac{\sin\theta|k|}{k\sqrt{1+k^2}} & -\cos\theta \end{bmatrix}^T \tag{6}$$

When the torch is in II or III octants,

$$\mathbf{n} = \begin{bmatrix} n_x & n_y & n_z \end{bmatrix}^T = \begin{bmatrix} -\dfrac{\sin\theta|k|}{\sqrt{1+k^2}} & \dfrac{\sin\theta|k|}{k\sqrt{1+k^2}} & \cos\theta \end{bmatrix}^T \tag{7}$$

The approach vector $\mathbf{a'}$ is given by the cross product of the vectors **n** and $\mathbf{o'}$,

$$\mathbf{a'} = \mathbf{n} \times \mathbf{o'} \tag{8}$$

By now, we have constructed the rotation matrix ${}^{B}_{T'}R$ of the following form, which describes the orientation of the intermediate frame $\{T'\}$ relative to the base frame {B}.

$${}^{B}_{T'}R = \begin{bmatrix} \mathbf{n} & \mathbf{o}' & \mathbf{a}' \end{bmatrix} \tag{9}$$

4.2.3 Calculation of Rotation Matrix ${}^{B}_{T}R$

Suppose $\gamma = \psi$ if the torch in II or III octants, and $\gamma = -\psi$ if the torch in III or IVoctants. Then the intermediate frame $\{T'\}$ will become the tool frame {T} by rotating the angle γ about the vector **n**. Therefore, the rotation matrix ${}^{B}_{T}R$, giving the torch orientation relative to {B}, can be calculated by the following equation:

$${}^{B}_{T}R = {}^{B}_{T'}R\,{}^{T'}_{T}R \tag{10}$$

where ${}^{T'}_{T}R = R_n(\gamma)$.

4.3 Calculation of Orientation Increment

The orientation increment is calculated using the differential vector equation as follows:

$$\begin{bmatrix} \Delta R_x & \Delta R_y & \Delta R_z \end{bmatrix}^T = \begin{bmatrix} \dfrac{1}{2}(\mathbf{n}_c \times \mathbf{n}_d + \mathbf{o}_c \times \mathbf{o}_d + \mathbf{a}_c \times \mathbf{a}_d) \end{bmatrix} \tag{11}$$

where ΔR_x, ΔR_y, ΔR_z are the rotation angle increments of the tool frame around the axes x, y, z of the base frame respectively, the vectors $\mathbf{n}_c$, $\mathbf{o}_c$ and $\mathbf{a}_c$ describe the current torch orientation, obtained by reading the torch pose form the robot controller, and the vectors $\mathbf{n}_d$, $\mathbf{o}_d$ and $\mathbf{a}_d$ describe the desired torch orientation at the next seam point. The rotation angle increments are used to control the robot to adjust the torch orientation by the master computer.

5 Experimental Results

A planar curve seam, shown in Fig.5, was chosen to validate the calculation of the torch orientation. Accordingly, the reciprocal of the slope is calculated at each seam point (Fig.6(a)). Then, the median filter was adopted to remove the noise data (Fig.6(b)).

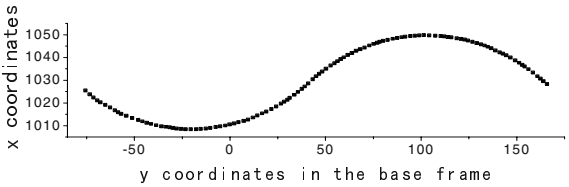

Fig. 5. The seam coordinates in the base frame (after smoothing)

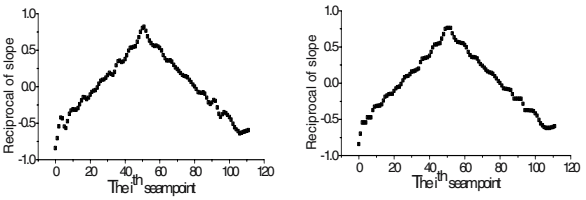

(a) raw data (b) after median filtering

Fig. 6. Reciprocal of slope

When the robot moves the torch along the seam based on the generated seam points, the torch orientation at the next seam point is calculated and the torch is adjusted to this orientation according to the calculated rotation angle increments. The robot movement experiments prove the torch can be adjusted to the desired orientation at every seam point. The calculation data at the first 6 seam point are given in Table 1. Here, the torch orientation is in IV octant, the angle ψ is equal to 15 degree, and the angle θ is equal to 60 degree.

Table 1. The calculation data at the first 6 seam point

Seam point		Current torch orientation						Rotation angle increments		
x	y	o_x	o_y	o_z	a_x	a_y	a_z	ΔR_x	ΔR_y	ΔR_z
1025.42	-75.59	0.2371	0.9714	-0.0099	0.1031	-0.0353	-0.9941	-4.231	28.683	21.966
1023.72	-73.36	-0.1783	0.9789	-0.0999	-0.3546	-0.1587	-0.9215	2.762	4.544	-2.020
1022.35	-71.46	-0.1491	0.9880	-0.0394	-0.4313	-0.1009	-0.8966	1.524	2.315	-4.513
1021.10	-69.46	-0.0718	0.9974	-0.0085	-0.4728	-0.0416	-0.8802	0.468	1.502	-1.967
1020.25	-67.78	-0.0376	0.9993	0.0011	-0.4968	-0.0177	-0.8677	0.166	0.896	-0.879
1019.15	-65.19	-0.0222	0.9997	0.0045	-0.5105	-0.0075	-0.8599	0.242	0.366	-2.231

6 Conclusions

In this paper, the torch orientation calculating method for the planar lap joint is proposed. The seam coordinates used to calculate the seam tangent is generated based on the visual servoing. The rotation matrix describing the torch orientation is calculated at each seam point according to the geometrical contains of the torch The rotation angle increments used to adjust the torch orientation is then calculated. The actual robot experiments show that the torch can be automatically adjusted to the desired orientation when the robot moves the torch along the seam using the generated seam coordinates.

Acknowledgement

The authors gratefully acknowledge the support of the National Natural Science Foundation of China under project No.50575144 and the Key Foundation Program of Shanghai Sciences & Technology Committee under Grant No.06JC14036.

References

1. Bae, K Y, Lee T H (2002) An optical sensing system for seam tracking and weld pool control in gas metal arc welding of steel pipe. Journal of Materials Processing Technology, 120: 458-465
2. Kim JS, Son YT (1995) A robust method for vision-based seam tracking in robotic arc welding. IEEE International Symposium on Intelligent Control – Proceeding: 363-368
3. Smith JS, Lucas J. (1989) Vision-based seam tracker for butt-plate TIG welding [J]. Journal of Physics E: Scientific Instruments, 22(9): 739-744
4. Yoshinori K. (1999) Tracking a Feature Point in Profile Data Using an Articulated object Model and Tuning Parameters Using the Genetic Algorithm, Emerging Technologies and Factory Automation, IEEE International Conference, Vol. 1 :145 – 150
5. Zhou Lv, Chen Shan-ben Autonomous seam tracking based on local vision in arc robotic welding, transactions of the china welding institution, 27(1) 2006: 49-52

Automatic Path Planning for Welding Robot Based on Reconstructed Surface Model

Wusheng Chou, Liang You, and Tianmiao Wang

Robotics Institute, Beijing University of Aeronautics and Astronautics,
Beijing, 100083, P.R. China
wschou@buaa.edu.cn

Abstract. An automatic path planning method, including the torch pose planning, is proposed to improve the flexibility and automatic planning ability of arc welding robot. The virtual object, which representing the real object to be welded, is reconstructed firstly by non-rational B-spline surface from geometric polygonal mesh model or measured point cloud. Based on the reconstructed non-rational surface model, the tangent vector and the tangent plane of each sampling point on the space welding seam is calculated, as well as the normal plane of each sampling point. Thus the position and pose of torch with respect to each sampling point of space seam can be determined by the calculated tangent vector, normal plane and concrete requirement of welding process. The final path planning of arc welding robot in joint space is obtained by its inverse kinematics. Experimental results demonstrate the accuracy and the feasibility of the proposed method.

1 Introduction

Welding robot play an important role in improving the quality and productivity of industrial manufacturing. Generally speaking, the on-line teaching method and the off-line programming method are adopted to generate suitable robot program to perform welding task [1]. On line teaching method can fully utilize the intelligence of human operator, but it is time consuming and lowly efficient for complex space welding seam [2]. The more profitable method of building a work program is to use off-line programming, which is easy to verify the validity of the robot programs through simulation and visualization.

The working process of welding robot consists of welding procession and motion process [3]. The path planning of welding robot is similar as traditional robot motion planning, and some work focus on obstacle avoidance, shortest time and shortest path [4]. Genetic Algorithm is used to generate optimal robot traveling path [5]. Machine vision is also often used to track seam and plan path [6]. Due to the low quality image in welding process, it is hard to recognize and extract useful information from the feedback image. With the development of virtual reality and CAD technology, some off-line programming and path planning methods are proposed. The three dimensional problem of planning of arc welding torch's gesture is translated into a two dimensional problem in the plane of welding torch location [7]. This method is suitable to linear seam and not easy to deal with space seam. The position and posture file of welding torch is generated from a three dimension solid model [8], and the torch plane is determined by the normal of the vertex of triangular polygon. However, the normal of

T.-J. Tarn et al. (Eds.): Robot. Weld., Intellige. & Automation, LNCIS 362, pp. 153–161, 2007.
springerlink.com

the vertex of triangular polygon is not the real normal of the surface at the vertex, and the tangent vector at the vertex can not be determined. There is also a trade-off between the accuracy and the approximation of solid object using polygonal model. Precise approximations increase the complexity of the boundary representation. On the other hand, a small number of polygons compromise the quality or even the correctness of the simulation.

We propose a new method to automatically generate welding path by decomposing the path planning of welding robot into torch pose planning and trajectory planning in joint space. Firstly we reconstruct the welded object using B-spline surface model, which can fit the given point cloud of geometric model with high precision. The torch plane perpendicular to the tangent vector of seam can be easily obtained accurately by analytic operation, which is the most important base to determine the torch pose according to the requirement of welding process. The trajectory of welding robot in joint space is so generated by inverse kinematics.

The rest of this paper is organized as follows. Section 2 describes the algorithm to reconstruct the B-spline surface model. The posture and position planning of torch is presented in Section 3, and Section 4 gives some experimental results. Section 5 concludes the paper.

2 Adaptive Fitting Algorithm of B-Spline Surface

The key process of object reconstruction is to fit the virtual object to given point set. Surface fitting of spheres, cylinders, cones and tori can be obtained by least square method [9]. Non rational B-spline can be used for surface fitting with C2 continuity and good performance [10]. However, the noise and cog of the characteristic points bring non-neglected fitting errors in non rational B-spline based method. Here we develop an adaptive surface fitting algorithm to fit the given point cloud with high accuracy. The given point cloud can be obtained from CAD geometric polygonal model or from laser measurement.

2.1 Selection of Parametric Direction and Knot Vector

The points obtained from complex surface can be arranged in a topological rectangular array with the elements $p_{i,j}(i=0,1,\cdots,r;\ j=0,1,\cdots,s)$. Let u denote the horizontal direction, then v denotes vertical direction. If all the points in the same row or column lie in a plane, then we select the group of curve obtained by interpolated among these points to be the dissection face curve with parameter u and v. There are s+1 horizontal dissection face points. The horizontal and vertical knot vector can be obtained by making the arc length parametric along the u and v directions. The parameters $(\tilde{u}_i, \tilde{v}_j)$ correspond to the point $q_{i,j}$. So the reconstructed surface description can be written as

$$p(u,v)=\sum_{i=0}^{m}\sum_{j=0}^{n} d_{i,j}N_{i,3}(u)N_{j,3}(v),\quad 0\le u,v\le 1 \tag{1}$$

Where the knot vector in u and v direction are $U=[u_0,u_1,\cdots,u_{m+4}]$ and $V=[v_0,v_1,\cdots,v_{n+4}]$, respectively. The definition area of surface are $u\in[u_3,u_{m+1}]=[0,1]$, $v\in[v_0,v_{n+1}]=[0,1]$. The parameter corresponding to point $q_{i,j}$ is

$$(u_i,v_j)=(\tilde{u}_{i-3},\tilde{v}_{j-3})\ (i=3,4,\cdots,m+1;\ j=3,4,\cdots,n+1) \tag{2}$$

Where m=r+2, n=s+2.

On the other hand, there are two cases for the star and end points along the u,v directions. The first one is that the star and end points along u or v direction overlay each other and it is C2 closed surface. In this case, the knot which is beyond knot vector U can be determined as

$$u_0=u_{m-2}-1,u_1=u_{m-1}-1 \tag{3}$$

$$u_2=u_m-1,u_{m+2}=1+u_4,u_{m+3}=1+u_5,u_{m+4}=1+u_6 \tag{4}$$

The second one is that although the star and end points along u or v direction overlay each other, but the surface is open. The knot which is beyond knot vector U can be determined as

$$u_0=u_1=u_2=u_3=0 \tag{5}$$

$$u_{m+1}=u_{m+2}=1,u_{m+3}=u_{m+4}=1 \tag{6}$$

2.2 Calculation of the Control Points of Three Order B-Spline Surface

According to the properties of tensor product surface, equation (1) can be rewritten as

$$p(u,v)=\sum_{i=0}^{m}\left(\sum_{j=0}^{n}d_{i,j}N_{j,3}(v)\right)N_{i,3}(u)=\sum_{i=0}^{m}c_i(v)N_{i,3}(u) \tag{7}$$

where there are m+1 points on the control curves with parameter v_j, which can be represented as

$$c_i(v)=\sum_{j=0}^{n}d_{i,j}N_{j,3}(v)(\ i=0,1,\cdots,m) \tag{8}$$

In the case that the conjunction of the start and the end of a closed surface is not C2 continuity, or the curve is open along some parameter, the $m+2$ unknown control points cannot be calculated by solving the equation group consisting of m-1 equations, according to the r+1 = m-1 points along u direction. Some end conditions should be

derived to get two additional equations. The end conditions can be determined by the tangent vector along *u* and *v* parameters.

2.3 Adaptive Algorithm of Three Order B-Spline Surface Fitting

The reconstructed B-spline surface can be defined by the calculated control points $d_{i,j}(i=0,1,\cdots,m;\ j=0,1,\cdots,n)$ and the obtained knot vectors $U=[u_0,u_1,\cdots,u_{m+4}]$ and $V=[v_0,v_1,\cdots,v_{n+4}]$. Due to the noise and cog of measured points, there will be error between the reconstructed surface and the original surface. The limit of error E is

$$\delta=\left|q_{i,j}-p(\tilde{u}_i,\tilde{v}_j)\right|\ \ (i=0,1,\cdots,r\ ;\ j=0,1,\cdots,s) \tag{9}$$

If the point on the reconstructed surface with parameters $(\tilde{u}_i,\tilde{v}_j)$ has larger error, the corresponding control point should be adjusted to fit the original points better by moving the control point $d_{i,j}$ to a new position $d^*_{i,j}$ along the connection line of point $q_{i,j}$ and point $p(\tilde{u}_i,\tilde{v}_j)$.

So we can obtain

$$\alpha=\delta/(|\,c\,|\,N_{i,3}(u_i)N_{j,3}(v_j)) \tag{10}$$

Thus the new control point $d^*_{i,j}$ can be obtained by the following equation

$$d^*_{i,j}=d_{i,j}+\alpha c \tag{11}$$

3 Automatic Path Planning

For robotic welding system, the end of torch is constrained by the seam. Generally, there is a small distance *D* between the end of torch and the seam, and there is a tilting angle θ between the tangent vector and the torch.

As shown in Fig.1, the tangent plane and tangent vector of sampling point Ps on space seam can be easily calculated according to the parametric description of the reconstructed B-spline surface. Thus we can get the normal plane passing through the sampling point of the space seam according to the tangent vector. The normal plane at Ps is the basic knowledge for torch pose and position planning. For example, if the welding process requires that the torch locates in the normal plane, then a new direction V can be obtained which is the z axis of the torch and has a crossing angle θ with respect to the tangent vector in the normal plane. The position of the end of the torch can also be obtained by offsetting Ps a distance D along the new direction V.

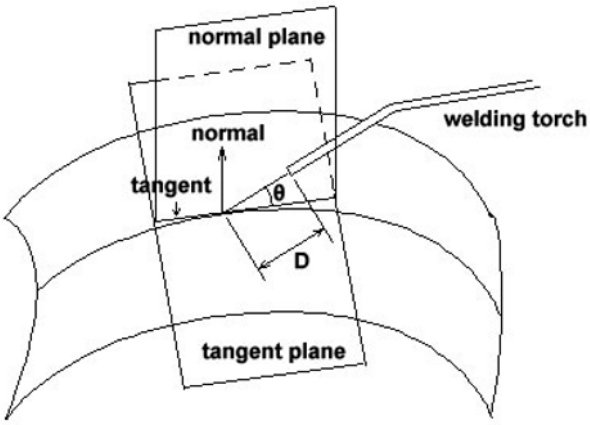

Fig. 1. The Determination of Torch Position and Pose

4 Experimental Results

The accuracy of surface fitting based on B spline is tested firstly. Given a set of scattered point cloud (1000 points) of a sphere whose radius is 100 units, the virtual sphere is reconstructed with parametric descriptions. The error between the original point and their corresponding point on the reconstructed sphere surface is shown as Fig.2. The average error is 0.02 unit and the maximum error is 0.4 unit with respect to the sphere radius of 100 units.

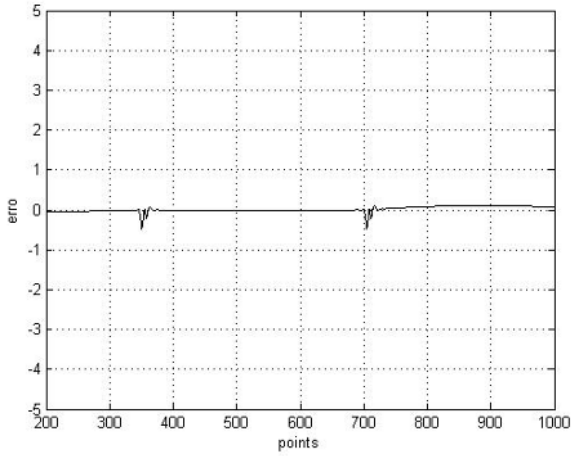

Fig. 2. The Error between the Ooriginal Point and Their Corresponding Point on the Reconstructed Surface

Two space seams are given then to testify the feasibility of the proposed automatic path planning method. One is a circle seam on a sphere with a radius of 90 units, and another one is a S shaped seam which is on a vertical plane. Our method works well with these cases. The positions of the end of the torch after automatic planning are shown as Fig.3 and Fig.4,repectively, while satisfying the requirement that the torch locates in the normal plane of the sampling points of the these space seams and have a cross angle of 30 degree with the tangent vector.

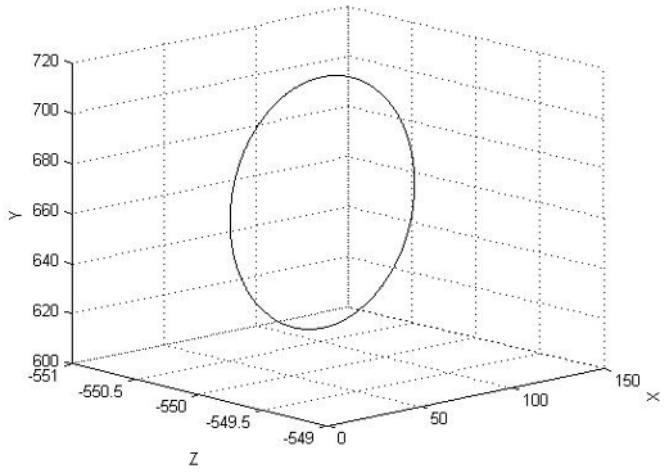

Fig. 3. Automatically Planned Path of the Torch for a Circle Seam

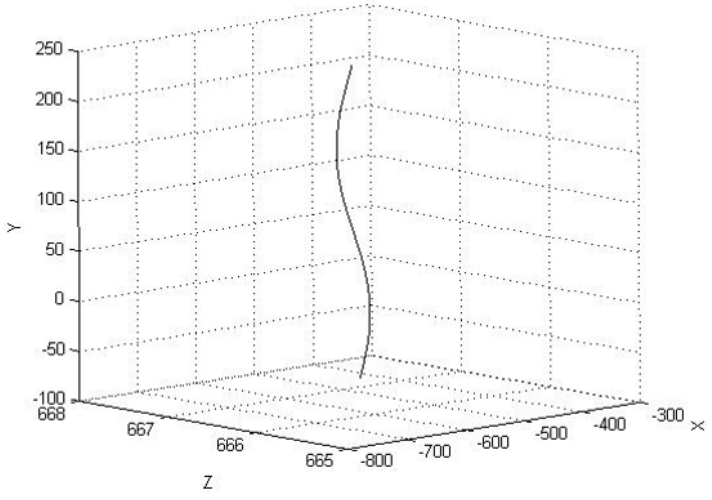

Fig. 4. Automatically Planned Path of the Torch for a S Shaped Vertical Seam

The trajectories of the 6 DOF welding robot, whose kinematics is described by equation (12), are shown as Fig. 5 and Fig.6, respectively, when the end of torch moving along the circle seam in clockwise and moving along the perpendicular seam from top to down. From Fig.5 and Fig.6, it can be seen that the trajectories of the joints are very smooth while the robot conduct welding task. Since the reconstructed surface is third order continuity, it also avoids the disadvantages of polygonal mesh model, which can cause joint jog.

$$
\begin{aligned}
A1&=\begin{bmatrix} \cos\theta_1 & -\sin\theta_1 & 0 & 0 \\ \sin\theta_1 & \cos\theta_1 & 0 & 0 \\ 0 & 0 & 1 & 330.2 \\ 0 & 0 & 0 & 1 \end{bmatrix} \quad A2=\begin{bmatrix} \cos\theta_2 & -\sin\theta_2 & 0 & 0 \\ 0 & 0 & 1 & 67 \\ -\sin\theta_2 & -\cos\theta_2 & 0 & 0 \\ 0 & 0 & 0 & 1 \end{bmatrix} \\
A3&=\begin{bmatrix} \cos\theta_3 & -\sin\theta_3 & 0 & 198.1 \\ \sin\theta_3 & \cos\theta_3 & 0 & -19.1 \\ 0 & 0 & 1 & 55 \\ 0 & 0 & 0 & 1 \end{bmatrix} \quad A4=\begin{bmatrix} \cos\theta_4 & -\sin\theta_4 & 0 & 0 \\ 0 & 0 & -1 & -207.1 \\ \sin\theta_4 & \cos\theta_4 & 0 & 0 \\ 0 & 0 & 0 & 1 \end{bmatrix} \\
A5&=\begin{bmatrix} \cos\theta_5 & -\sin\theta_5 & 0 & 0 \\ 0 & 0 & -1 & 0 \\ -\sin\theta_5 & -\cos\theta_5 & 0 & 0 \\ 0 & 0 & 0 & 1 \end{bmatrix} \quad A6=\begin{bmatrix} \cos\theta_6 & -\sin\theta_6 & 0 & 0 \\ 0 & 0 & -1 & -132.5 \\ \sin\theta_6 & \cos\theta_6 & 0 & 0 \\ 0 & 0 & 0 & 1 \end{bmatrix} \\
A7&=\begin{bmatrix} 1 & 0 & 0 & 0 \\ 0 & 1 & 0 & 0 \\ 0 & 0 & 1 & 203 \\ 0 & 0 & 0 & 1 \end{bmatrix}
\end{aligned} \tag{12}
$$

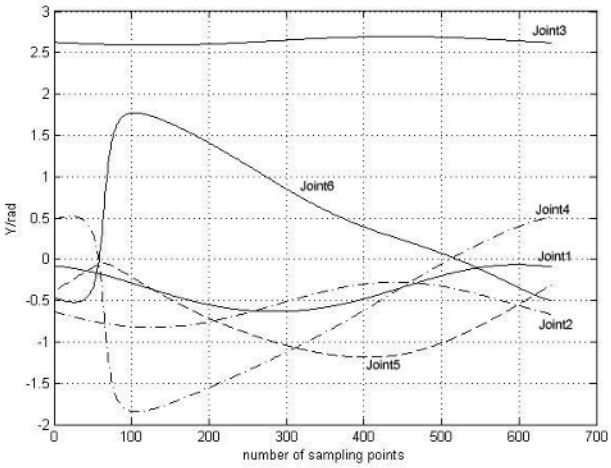

Fig. 5. Trajectories of Robot Joints for Space Circle Seam

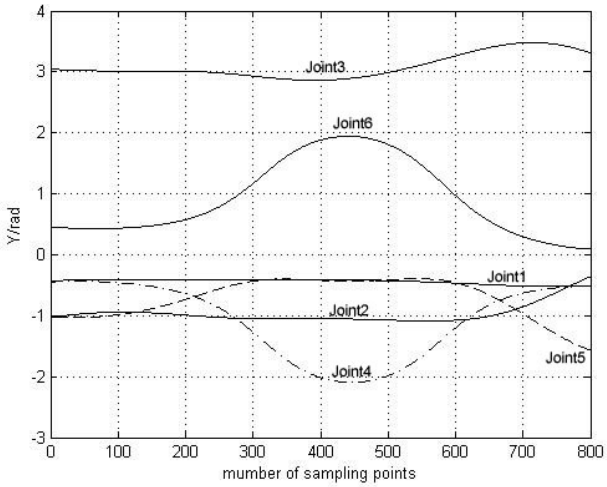

Fig. 6. Trajectories of Robot Joints for Space Vertical Seam

5 Conclusion

Based on the reconstructed parametric surface, an automatic path planning method is proposed. The surface fitting algorithm in this paper can also deal with the noise and cog of given points, and the virtual object can be reconstructed by three order B-spline surface with high accuracy. Through analytic calculation of the reconstructed parametric surface, the tangent vector as well as the normal plane at the sampling points of space seam can be easily obtained, which provide a basic reference for the determination of poison and torch pose according to concrete requirement of welding process. Another advantage of the proposed method is that the joint trajectories are smooth, since the automatically planned positions of the end of torch are on smooth surface instead of polygonal mesh model. Our future work is to automatically generate the robot program after path planning and to perform real welding task via augmented reality.

Acknowledgement

The authors are grateful to the support of National Science Foundation of China under grants 60525314 and the support of the National Key Basic Research Program (973 program) under grant 2002CB312200.

References

1. Ulrich D (1992) Robot systems for arc welding - current position and future trends. Welding and Cutting (8): 150-152
2. Regev Yocam (1995) The evolution of off line programming. Industrial Robot 22(3): 5-7

3. Breat JL, Clement F, Jadeau P, et al. (1994) ACT WELD - an unique off-line programming software tailored for robotic welding applications. Welding in the World 34 (3):267-274.
4. Chen Q, Lu J, Sun Z, et al. (2002) Study on torch pose planning system for arc welding robot. Chinese Mechanical Engineering 13(11):956-958.
5. Hong KS, Han HY (2004) PC Based off line programming using VRML for welding robots in shipbuilding. IEEE International Conference on Robotics, Automation and Mechatronics: 949-954,
6. Peng J, Chen Q, Lu J, et al. (1998) Real time optimization of robotic arc welding based on machine vision and neural networks. Proceeding of 24th Annual Conf of IECON : 1279-1283.
7. Zhu DL, Xiao S, Hou H, et al. (2004) Automatic planning of welding torch's gesture of arc welding robot. Journal of Shanhai Jiaotong University 38(9): 1472-1475,
8. Yan H, Liu J, Qiu SH, et al. (2005) Research on the automatic planning of arc welding robot welding path for space weld. Machinery Design and Manufacturing (8):106-106,
9. Lukács G, Marshall AD, Martin RR (1998) Faithful least-squares fitting of spheres, cylinders, cones and tori for reliable segmentation. Proc ECCV 98, Lecture Notes in Computer Science, Springer (1):6712

Study on the Control Strategy of Commutation Process in Variable Polarity Plasma Arc Welding

Li Zhining, Du Dong, Wang Li, Chang Baohua, and Zhang Hua

Department of Mechanical Engineering, Tsinghua University, Beijing 100084, P.R. China

Abstract. The peak of resonance current during commutation greatly influences the safety of commutation component in variable polarity plasma arc welding (VPPAW). It is necessary to study measure to restrain the current peak. Phenomenon of arc resonance current is studied by experiments. Analysis shows that the arc resistance is time variable. Model of commutation circuit is set up and simulated. Results indicate that adjusting damp ratio of system is valid to restrain peak of resonance current. Then a new commutation strategy is presented based on variable structure control method. The commutation circuit is redesigned to apply new commutation strategy. Experimental result shows that the peak of resonance current is restrained while commutation speed unchanged. This paper is instructive to design high power supply of VPPAW.

1 Introduction

Variable polarity plasma arc welding (VPPAW) is suitable to join thick plate of aluminum alloy and can be used for aerospace manufacture [1~6]. Commutation progress influences arc stability, reliability of power supply and welding quality in VPPAW. Ref [7, 8] presented the debugging method about commutation. Ref [9] studied the common conducting and blocking time. Ref [10] studied different control strategy while commutation devices are in common conducting and blocking status. In practice, the phenomenon of resonance current is often observed after arc current commutes. The peak value differs with polarity. When welding is in high power, the resonance current greatly affects the safety of commutation device. But above references did not study the problem. It is necessary to solve the problem without changing commutation speed.

This paper is organized as follows. Section II delineates the phenomenon of resonance current in commutation. A designed experiment is done and the reason about phenomenon is analyzed by arc theory. In section III, the model of commutation circuit is set up and the resonance current phenomenon is simulated. In section IV, a new commutation strategy is put forward based on variable structure control (VSC) method. Then experiment is done to verify the strategy. Finally, conclusions are summarized in section V.

2 Phenomenon of Resonance Current in Commutation

2.1 Experiment Study

In order to study the resonance current during commutation, welding experiment parameters, shown in Table 1, was adopted to eliminate influence of current's

T.-J. Tarn et al. (Eds.): Robot. Weld., Intellige. & Automation, LNCIS 362, pp. 163–170, 2007.
springerlink.com

amplitude and time span of different polarity. The welding position was flat. The workpieces were 4mm thick LD10 aluminum alloy. A self-made welding high-power supply which can accurately regulate current was used. The current sensor's type is KT500A.

Table 1. Welding parameters for experiment

Parameters type	Unit	Value
DCEN current（I_+）	A	120
DCEP current（I_-）	A	120
DCEN time（T_+）	ms	12
DCEP time（T_-）	ms	12
Plasma gas (Argon) flow rate	L/min	2.4
Welding speed	m/min	0.28

DCEN- Direct current electrode negative, DCEP - Direct Current electrode positive

Fig.1. is arc current waveform while welding aluminum alloy. The peak current of positive polarity I+max=230A and ΔI+＝I+max－I+＝110A. The peak current of negative polarity I-min =-175A andΔI-＝I-－I-min＝55A. ΔI＝ΔI＋－ΔI-＝55A. Obviously, resonance current peak differs with polarity. To investigate the reason, fixed resistance load was used. Resonant current peaks are $I_{+max} = 376A$, $I_{-min} = -368A$, and $\Delta I \approx 0$. Obviously, the peak of resonance current is equal when load is fixed resistance. The difference of resonance current peak is only observed while using AC arc load. So the reason relates to arc characteristic in commutation process.

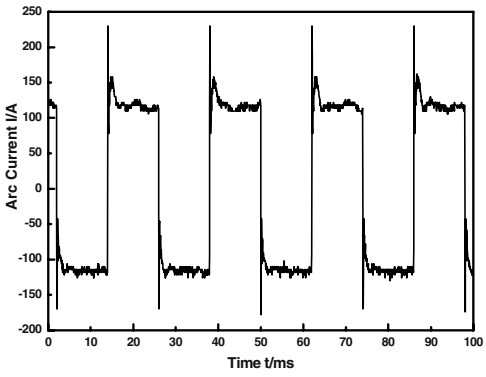

Fig. 1. Arc current waveform while welding LD10 aluminum alloy

2.2 Mechanism Analysis

According to Ref [11], the conductance of arc can be described as the following equation:

$$\sigma \propto \frac{n_e \cdot \sqrt{T}}{Q_n} \tag{1}$$

Where σ denotes conductance of arc column; n_e denotes electron density; Q_n, Q_i denote section of neutrality ion and positive ion; T is temperature of arc column.

We know that n_e will increase while increasing T, so do σ. On the contrary, σ decreases. So the arc resistance is a time-varying parameter.

Arc current alternates periodically in VPPAW. Then the electron density, ion density, arc cross section area, arc temperature and arc conductance change accordingly. Also, the cathode's thermionic emission capability is periodically changed. As cathode is tungsten electrode, the thermionic emission capability is 456A/cm^2. When cathode is aluminum workpiece, it is only 10^{-15} A/cm^2. The huge difference of thermionic emission is reason of the phenomenon.

When arc current commutes from positive to negative, arc conductance decreases. On the contrary, arc conductance increases. Fig 2 shows the change of arc resistance during welding. The arc current waveform is shown in Fig 1. When arc current commutes from positive to negative, arc resistance increases from 0.18Ω to 0.4Ω. On the contrary, arc resistance decreases from 0.28Ω to 0.11Ω. The change results in different peak of resonance current during commutation.

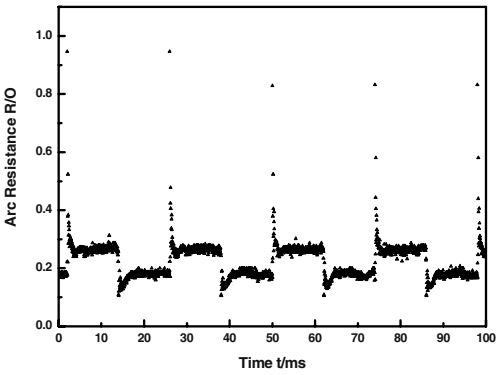

Fig. 2. Arc resistance in VPPAW

3 Commutation Circuit Model and Simulation

In order to study the measure to restrain peak of resonance current, it is firstly necessary to model and simulate commutation circuit. We assume that arc current is continuous.

Fig 3 (a) shows commutation circuit. Fig 3 (b) shows equivalent commutation circuit model. The resonance circuit consists of C, L and R_a in parallel. I is square wave current source; C is equivalent capacitor of commutation system; L is equivalent inductance of welding loop and R_a is equivalent arc resistance. State-space model of commutation system can be set up. Select $V_c(t)$ (Capacitor voltage), $i_L(t)$ (inductance current) as state variable and I (square wave current source) as input variable. The circuit model can be described as equation (2).

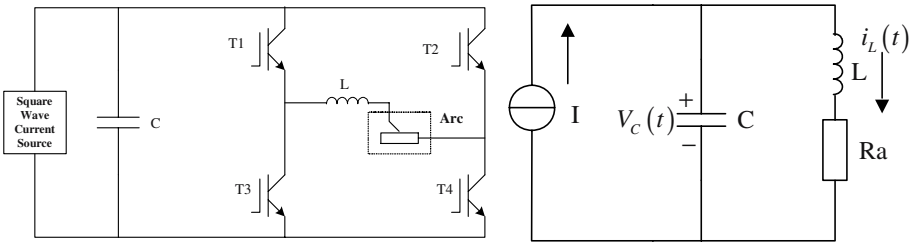

Fig. 3. Model of commutation circuit (a) schematic of commutation circuit (b) equivalent circuit model

$$\begin{bmatrix} \frac{dV_C}{dt} \\ \frac{di_L}{dt} \end{bmatrix} = \begin{bmatrix} 0 & -\frac{1}{C} \\ \frac{1}{L} & -\frac{R_a}{L} \end{bmatrix} \begin{bmatrix} V_C \\ i_L \end{bmatrix} + \begin{bmatrix} \frac{1}{C} \\ 0 \end{bmatrix} I \tag{2}$$

If the initial energy of L and C are neglected, the transfer function of input and output is described as:

$$G(S) = \frac{I_L(S)}{I(S)} = \frac{\omega_n^2}{S^2 + 2\xi\omega_n S + \omega_n^2} \tag{3-a}$$

$$\omega_n = \sqrt{\frac{1}{LC}}, \xi = \frac{R_a}{2}\sqrt{\frac{C}{L}} \tag{3-b}$$

Equation (3) shows that the model is a second-order system. System natural frequency is determined by L and C. Damp ratio is not only affected by L and C, but also R_a, a time-varying parameter. Then damp ratio ξ is time-varying parameter.

In this paper, $L=8\mu H$ and $C=60\mu F$. In order to simplify the problem, based on the experiment results shown in Fig 2, let $R_a=0.18\Omega$ ($\xi=0.2465$) when current polarity commutates from negative to positive and $R_a=0.28\Omega$ ($\xi=0.3834$) when current polarity

commutates from positive to negative. Then simulation was performed to verify the above model. Let $I_+=120A$, $I_-=120A$, $T_+=T_-=12ms$.

The initial value of state variables is $\begin{bmatrix} V_C(0) \\ i_L(0) \end{bmatrix} = \begin{bmatrix} 21.6 \\ 120 \end{bmatrix}, \begin{bmatrix} 33.6 \\ -120 \end{bmatrix}$.

And the simulation current result (Fig 4) are I+max =227A, I-min= -184A,ΔI＝43A. The results show that the model can describe arc current resonance during commutation progress.

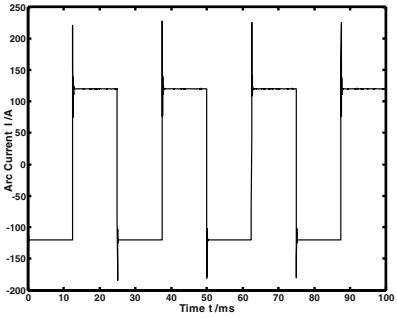

Fig. 4. Simulation waveform of arc current when damp ratio is different

4 Commutation Strategy and Application

According to the analysis, we know that the current resonance peak can be restrained by changing damp ratio of system during commutation. From equation (3), system's damp ratio is determined by L, C, R_a. If resistance of resonance loop increases to R_a+R1, system's damp ratio increases. The resistance in resonance circuit can consume energy stored in L and C, and the current peak will be greatly reduced. If we simply increase system's damp ratio, the commutation speed will also be decreased. It is a contradiction to balance the commutation speed and decreasing current resonance peak. So in this paper a new commutation strategy, which changes damp ratio of system, is presented based on VSC thought. The slide equation of damp ratio is described as equation (4):

$$\xi = \begin{cases} \dfrac{R_a}{2}\sqrt{\dfrac{C}{L}} & I_{-ref} < I < I_{+ref} \\ \dfrac{R_a + R1}{2}\sqrt{\dfrac{C}{L}} & I \le I_{-ref}, I \ge I_{+ref} \end{cases} \tag{4}$$

Equation (4) shows new commutation strategy as follows: Damp ratio of system is small during commutation; when the arc current is greater than set level, the system

damp ratio is increased immediately. The set level of arc current can be acquired based on working parameters and automatically set by D/A converter controlled by microprocessor.

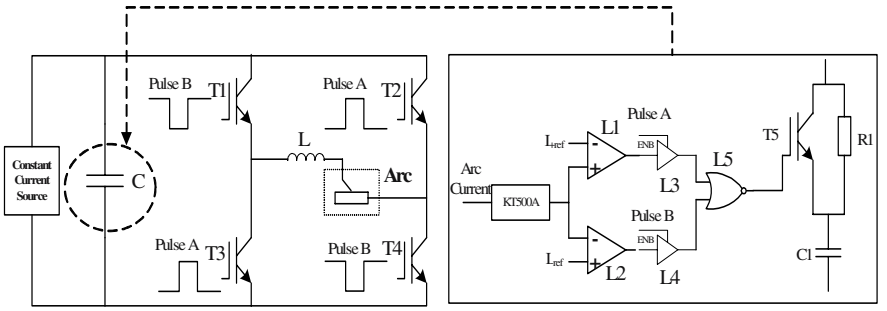

Fig. 5. Schematic of new commutation circuit

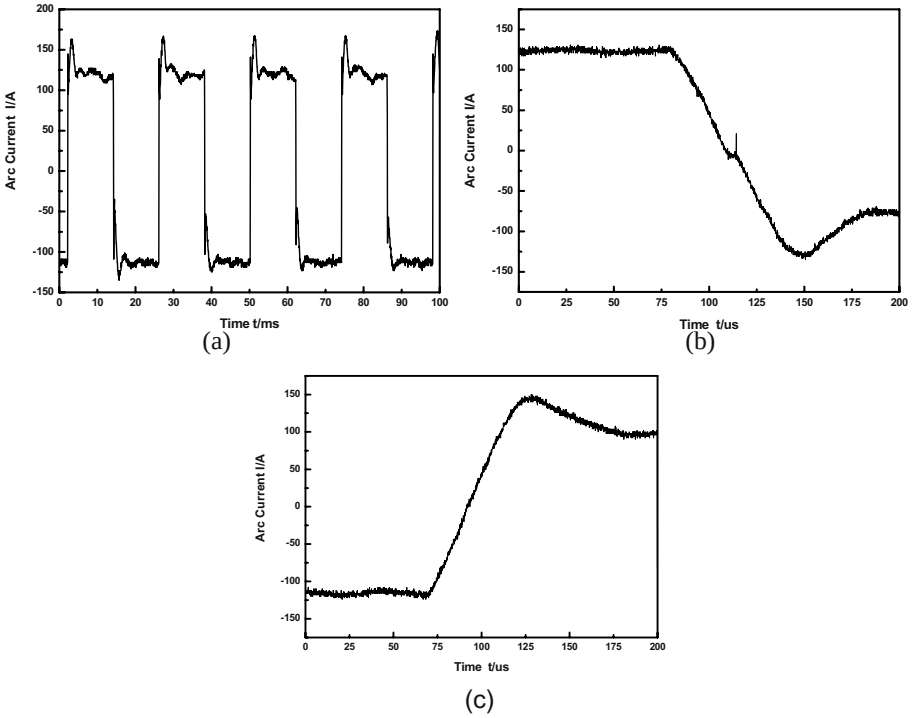

Fig. 6. Arc current waveform of welding LD10 (a) arc current after adjusting commutation circuit (b) commutation process from I_+ to I_- (c) commutation process from I_- to I_+

Because the commutation progress is always short than *70μs,* the key of applying this strategy is how to switch circuit structure in high speed. Certainly, the commutation circuit has to be redesigned. Fig 5 shows the schematic of new commutation circuit. A nonlinear control circuit was adopted to substitute linear capacitor C (shown in Fig 5).

We analyze the working progress to explain how to switch circuit structure, for example, from negative polarity to positive polarity. The pulse A is high level and the pulse B is low level. When arc current is small than the set current level I_{+ref}, comparator L1 outputs low level. And the L3 output low level. At the same time, the L3's output is high resistance because the pulse B is low level. Then the L3 output high level to open IGBT T5. So *R1* is short circuit. When current is greater than I_{+ref}, T5 cut-off. Then *R1* is in series with *L, C1,* R_a. In this paper, *R1* is1.2 Ω and mean of Ra is 0.25Ω. According to equation (3) and (4), the system is stable however the structure of system. The measure only affects the transient performance of system.

The effect of new commutation strategy is verified by experiment. Working parameters adopted is same as section II. The arc current waveform is shown in Fig 6. The peak of resonance current is less than overshoot-current produced by PI controller of inverter power supply. Comparing the waveform of arc current of Fig.6 and Fig.1, the resonance peak decreases sharply after adopting new commutation strategy. Commutation interval, from +120A to -120A, is 60 μ s, and from -120A to +120A, is 50 μ s. Fig 6 (b) and (c) also indicate that the arc is stable during welding.

5 Conclusions

1. Experimental results show that resonance peaks are different with polarity, i.e., the welding system has variable damp ratio.
2. Different of cathode thermionic emission capability is main reason that produces time-varying arc resistance.
3. Commutation circuit was modeled and simulated. Results show that adjusting damp ratio of system can restrain peak of resonance current during commutation.
4. A new commutation strategy is presented based on VSC. And the commutation circuit is redesigned to apply the strategy.
5. Experiment proves that the new control strategy is valid and can improve working conditions of commutation component.

Acknowledgements

This work is funded by Specialized Research Fund for the Doctoral Program of Higher Education (No.20050003041). The authors greatly thank Doctor Lin Tao for his valuable advice to this paper.

References

1. Nunes A C. Variable polarity plasma arc welding in space shuttle external tank [J]. Welding Journal, 1984, 63(9):27-35.
2. Anon. Variable polarity plasma arc reduces welding costs [J]. Welding and Metal Fabrication, 1984,52(7):276-277.
3. M.Tomsic, S. Barhorst. Keyhole Plasma Arc Welding of Aluminum with Variable polarity Power [J]. Welding Journal, 1984,63(2): 25-32.
4. Barhorst S. The Cathodic Etching Technique for Automated Aluminum Tube Welding . Welding.Journal[J], 1985, 64(5):28-31.
5. Craig E. The Plasma Arc Process - A Review. Welding Journal, 1988,67(2):19-25.
6. Woodward H . U.S. contractor for the International Space Station [J] . Welding Jounal, 1996 , 75(3):35-40.
7. Ding zhiming, Qi Bojin. Study on multi-function arc welding dual inverter [J]. Electric Welding Machine, 1995(2):20-2.(in Chinese)
8. Li Zhongyou, Liu Xiuzhong, Cheng Maoai etc. Study on Commutating Process and Its Control of Variable Polarity Square Waveform Power Source [J]. Transactions of The China Welding Institution, 2002, 23 (2):68—71.(in Chinese)
9. Hang Zhenxiang, Ying Shuyan, Huang Pengfei etc. Variable polarity process of inverter AC arc welding power source [J]. Electric Welding Machine,2003,33（6）:13—15,38. (in Chinese)
10. Xie Xingkui, Wang Li, Li Zhining etc. Variable polarity plasma welding power supply with self-adjusting commutation mode [J]. Electric Welding Machine, 2005(12):45－46,55.(in Chinese)
11. 安藤弘平, 長谷川光雄. 溶接ア-ク 现象[M].產報. 1978

Recognition of Macroscopic Seam for Complex Robotic Welding Environment

X.Z. Chen[1,2], S.B. Chen[1], and T. Lin[1]

[1] Institute of welding engineering, Shanghai Jiao Tong University, 1954 Huashan Rd., Shanghai 200030, P.R. China
xzhchen@sjtu.edu.cn
[2] School of Material Science and Engineering, Jiangsu University, Xuefu Rd, Zhenjiang 212013, P.R. China
xzhchen@ujs.edu.cn

Abstract. In vision-based robotic arc welding had some degree of autonomy functions, sensors must be used to detect the position and orientation of a weld seam and determine its path in order to carry out the autonomy of welding process. This paper represented a method to recognize whole seam in complex robotic welding environment. According to the parameter we defined to judge the degree of image noise, then different size of filter windows were selected to preprocess the image. Algorithm to eliminate effect of complex changing background is proposed. Parameters are defined to judge if it is necessary to use this algorithm. The threshold and edge detect algorithms that adapt to the recognition for robotic welding environment is also addressed in this paper. The experiments give the recognition results of two different shapes and material of seams. The results showed that the recognized method was robust to the recognition of macroscopic seam for complex robotic welding environment.

1 Introduction

Most existing robotic welding systems require a teaching pass before actual welding, which is a serious obstacle for an industrial application because it reduces the average arc-on time and cannot adapt to environment changes[1]. The need has become obvious for a reliable vision-aided system to reach a desirable degree of autonomy for the adaptive welding robot[1-3]. The vision system translates the currently relevant object properties into the portion of the required information than is not known a prior. The object properties in vision system are position, orientation, edge, corner, width, surface, shape, volume et al. Recognition of environment is the basic of automatic welding, such as seam tracking, path planning, path plan and penetration control et al. Ref.[4; 5] studied the recognition of initial welding position, not the whole seam or environment. Ref.[2] achieved automatic recognition of joint type and tracked its geometry using laser sensor, the image is simple and easy to process. Ref.[6] studied the recognition of a structured welding environment utilize camera and laser sensors, the structured information is known a prior. Ref.[7] recognized the seam in local workpiece and didn't consider the effect of environment. We know from these References, the attention is focused on the point recognition, local seam or structured environment.

T.-J. Tarn et al. (Eds.): Robot. Weld., Intellige. & Automation, LNCIS 362, pp. 171–178, 2007.
springerlink.com

Most of the studies utilize laser sensor, its signal is easy to process. However, little research is focused on the recognition of seam in unstructured robotic welding environment. It is not an easy thing to recognize the macroscopic seam in complex welding environment. Compare with laser sensor, CCD (Charge Coupled Device) camera acquire abundant information of the whole environment, the disadvantage is the abundant information bring more noise, which make the recognition more difficult.

This paper deals with the recognition of macroscopic seam in complex unstructured environment using CCD camera. The algorithms proposed in this paper can recognize the whole seam in unstructured robotic welding environment. Edges acquired with proposed method can be used in the acquisition of three-dimensional information and path planning et al. This paper is arranged as follows: In Section 2, the vision system we used is addressed, the character of unstructured robotic welding environment are introduced in detail. Section 3 gave the recognized algorithms we proposed. Afterwards, experiments on this system are performed. Conclusions were drawn in the last section.

2 Vision System and Character Analysis of Robotic Welding Environment

In any vision task a camera should be able to observe the target object, it is difficult to find the visible region in three-dimensional space[8]. We want to observe work-piece in large scale, that mean when we plan the camera placement and lens settings all features must be in-focus. Fig.1 shows the settings in this paper, the vision system is fixed on the end-effector of the welding robot. It is used to acquire spatial position information of weld seam in complex welding environment. The main work in this paper is to recognize the seam in the robotic welding environment without known structured data like Fig.1.And the work-pieces to be welded maybe having widely varying size, material, shape and surface finish. The work-pieces can be located in different environment, such as laboratory or factory.

Fig. 1. Binocular vision system used in this paper

For the un-welded seams, no matter butt joint, lap joint or seam with groove, all appears as two edges or their overlap. For the welding pool, it appears as edge contour, which correspond to the shape or weld pool. The welding condition is very complex, there are many kinds of noises such as the non-uniformity of surface (nick,

oxidation tint, oil stain and marker etc.), effect of arc etc. And for some metals such as aluminum alloy reflect strongly the light in whole wave. Sometimes the weld seam is sheltered from the weld torch or wire feeder. The work-piece has the function of mirror in local range. For different environment, there are different noises, such as the platform, cable line, jigs, even the changes of light. All these factors make the edge detection more difficult. When we select or develop new algorithms for image processing of welding image, these factors and characters must be considered. Fig.2 shows an example of seam to be recognized. Fig.2 (A) is one scene of welding environment, the colors mark the clear edges in this image we can know that there are too much noise in the image, it is not an easy thing to recognize the edge of seam,. Fig.2 (A) is just a simple scene in certain extent, only the effect of platform is considered, other factors such as reflect light, other objects in environment like in Fig.1. Fig.2 (B) is a local image intercepted from (A), it is easy to process, employing the threshold value segmentation, good results like (C) is got. Fig. 2 (B) is like the situations of most references processed, such as reference[7].In a conclusion, the characters for recognition of macroscopic seam in robotic welding environment are as follows:

- The environment is complex.
- Contrastivity between foreground and background is lower.
- Environment changes with time.
- There are too many noises.

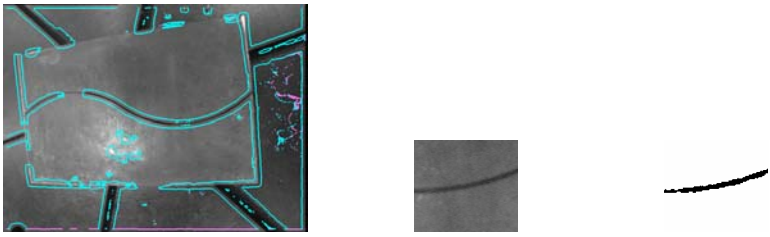

(A) (B) (C)

Fig. 2. An example of seam to be recognized

3 Recognition of Seam

Recognition of weld seam before the welding operation is executed is the foundation and key step of some intellectualized welding technologies such as the path planning of weld seam, robotic guiding et al. The direction of most of the weld seam will not change abruptly. The weld seams are continuous line or curve in plane or spatial space. It can be viewed as two parallel lines in local range. There are many methods to detect edges. They have their own advantages and disadvantages, but no one can be used for the edge detect directly in the complex robotic welding environment. According to the characters of seam recognition we proposed a method to remove the effects of changing background.

3.1 Background Eliminating Algorithm

What we interested is the object (here means weld seam) in image, all the regions not related with the object are called background. The complex environments in industrial applications *maybe* are raised by illumination changes. There are two types of illumination changes, one is the nature changes of ambient environment, this situation is not occurred abruptly. The other is the changes of light, such as the change of lamp, it is often occurred abruptly, affect the environment severely. Compare with object, background is not so sensitive to these changes. Fig.3 (A) and (B) shows one work scene and its background.

We capture one scene not including work-piece as background image. If F(x,y) is the image of foreground (e.g. Fig.3 (B)), B(x,y) is the image of background (e.g. Fig.3 (A)), T(x,y) is the image of target. Then we have:

$$T(x, y) = \sum_{i=1}^{M} \sum_{j=1}^{N} B(x, y) - F(x, y) \tag{1}$$

We give a parameter DOGS (Degree of grey similarity), its definition is as follows:

$$DOGS = 10 \lg \frac{\sum_{i=0}^{M-1} \sum_{j=0}^{N-1} F(x, y)^2}{\sum_{i=0}^{M-1} \sum_{j=0}^{N-1} (F(x, y) - B(x, y))^2} \tag{2}$$

Parameter DOGS denotes the similarity of foreground and background images, it is the condition to eliminate background or not. If DOGS is greater than a given threshold T_k, we think it is necessary to eliminate the background. The principles to eliminate background are as follows:

If T(x,y)<0, Then Set F(x,y)=0,
If 0<T(x,y)<MeanD, Then F(x,y)=B(x,y)-F(x,y),
If T(x,y)>MeanD, Then F(x,y)=F(x,y),

Where MeanD is mean value of T_{min} and T_{max}, T_{min} and T_{max} are the maximal and minimum values that T(x,y) occur in a big probability . It is defined as:

$$MeanD = \frac{N_1 \times T_1 + N_2 \times T_2 + \ldots + N_n \times T_n}{N_1 + N_2 + \ldots + N_n} \tag{3}$$

$$Here \qquad T_1 = T_{\min}, T_n = T_{\max}$$

3.2 Image filtering

After eliminating the effect of background, the image has also some problems, such as the poor contrast (See Fig.2). So it is necessary to filter the image by different filter algorithms.

Pixel set of a grey image f(x,y) in a neighborhood can be denotes as:

$$f(x,y)=\{f((x+r),(y+c))\mid r,c\in[-t,t]\} \tag{4}$$

The mean grey value can be calculated as follows:

$$f'(x,y)=\frac{\sum_{i=-t}^{t}\sum_{j=-t}^{t}f(x+r,y+c)}{(2t+1)^2} \tag{5}$$

Given a parameter G, it is defined as follows:

$$G=\frac{\sqrt{\sum_{i=0}^{M-1}\sum_{j=0}^{N-1}(f(x,y)-f'(x,y))^2}}{M\times N} \tag{6}$$

According to Equation (6), we can know that with the increase of noise variance, parameter G become bigger. It has a good corresponding relationship between G and noise variance. G is used to value the degree of noise. If G is greater than a given value G_1, we think the image is contaminated seriously. If G is less than a given value G_2, we think the image is contaminated lightly. The filtering widows are selected according to the value of G.

3.3 Threshold Segmentation

The threshold segmentation procedures are as follows:

- Calculated the maximum and minimum grey value P_{max} ,P_{min}. The initial value is:

$$T_0=(P_{\min}+P_{\max})/2 \tag{7}$$

- The image is segmented as two regions according to threshold value T_k , i.e. background and object. Then the mean grey value of the two regions are calculated separately as follows:

$$P_1=\frac{\sum_{P(i,j)>T_k}P(i,j)\times N(i,j)}{\sum_{P(i,j)>T_k}N(i,j)}\quad P_2=\frac{\sum_{P(i,j)<T_k}P(i,j)\times N(i,j)}{\sum_{P(i,j)<T_k}N(i,j)} \tag{8}$$

where P(i,j) is the grey value at image point (i,j), N(i,j) is the weight coefficient, here we set its value as 1.

- The new threshold value is calculated as follows:

$$T_{k+1}=(P_1+P_2)/2 \tag{9}$$

- If $T_k=T_{k+1}$, then end the procedure. Or k=k+1, return to procedure 2.

The recognized procedures also including edge detection, thinning, noise removing et al, the detail is not included here.

4 Laboratory Experiments

The recognized experiments are carried out in lab. The images are captured by the binocular vision system in section 2. We capture the image of background before place the work-piece in the work scene. Fig.3 shows recognized results and procedures for line seam, the material is steel. Fig. 4 shows the recognized results of a S-shape curve seam, the material is aluminum alloy. From the results of Fig.3 and Fig.4, we can see that the background eliminating algorithms are selected according to the different situation. Fig.5 shows the recognized procedures in detail.

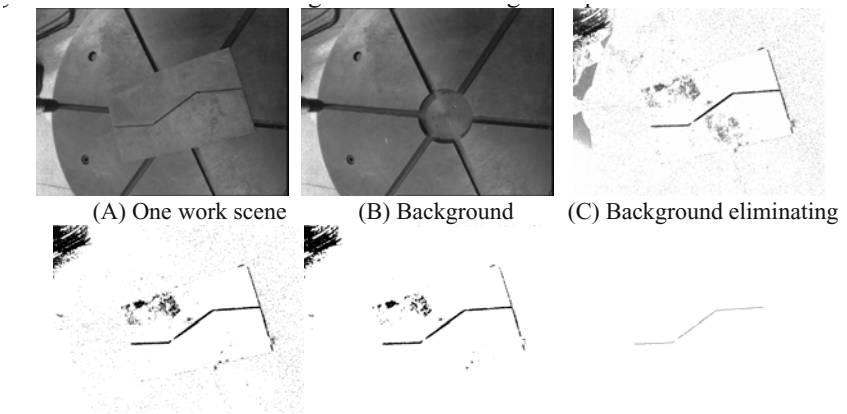

Fig. 3. An example of seam recognition for steel work-piece

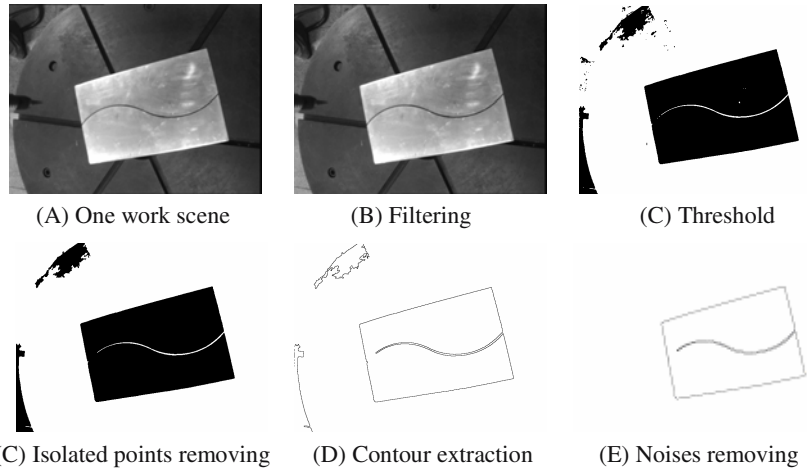

Fig. 4. An example of seam recognition for aluminum alloy work-piece

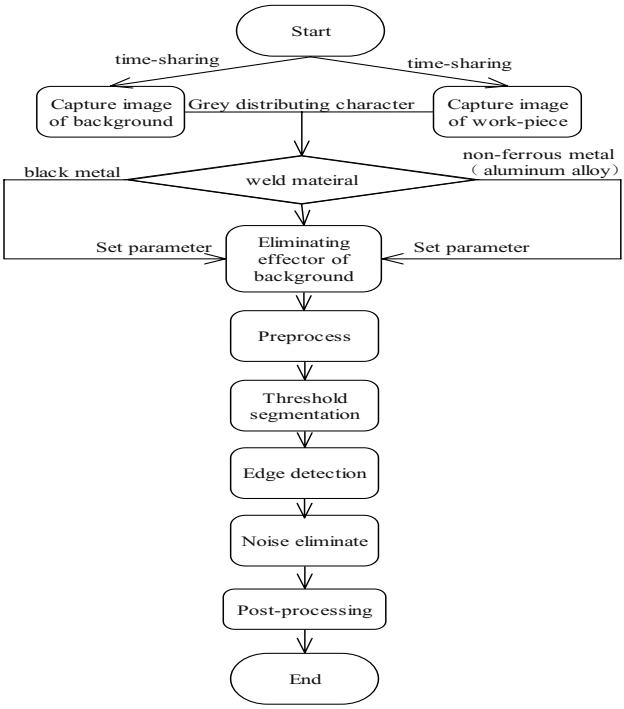

Fig. 5. Recognized procedure

5 Conclusions

It is difficult to recognize seam from complex environment directly. It is necessary to eliminate the effect of complex environment according to different situation. The algorithms in this paper provide us with a method to eliminate effect of background and filter algorithms according to some parameters given in this paper. The experiments prove that this technique is a valuable method to recognize seam in different environments.

Acknowledgement

The authors gratefully acknowledge the support of the National Natural Science Foundation of China, under project No. 50575144 and the Key Foundation Program of Shanghai Sciences & Technology Committee under Grant No. 06JC14036.

References

1. Chen, S. B., Chen, X. Z., & Li, J. Q. (2005), "The Research on Acquisition of Welding Seam Space Position Information for Arc Welding Robot Based on Vision," *Journal of Intelligent & Robotic Systems, 43*(1), 77-97.

2. Sicard, P. L., M.D.; (1989), "Joint recognition and tracking for robotic arc welding," *Systems, Man and Cybernetics, IEEE Transactions on, 19*(4), 714-728.
3. Tarn, T. J., Chen, S. B., & Zhou, C. J. (2004), "*Robotic Welding, Intelligent and Automation*," Springer Verlag.
4. Zhu, Z. Y., Lin, T., Piao, Y. J., & Chen, S. B. (2005), "Recognition of the initial position of weld based on the image pattern match technology for welding robot," *International Journal Of Advanced Manufacturing Technology, 26*(7-8), 784-788.
5. Chen, X. Z., Zhu, Z. Y., Chen, W. J., & Chen, S. B. (2005), "Vision-based recognition and guiding of initial welding position for arc-welding robot," *Chinese Journal of mechanical engineering, 18*(3), 382-384.
6. Kim, M. Y. K. K.-W. K. H. S. C. J.-H. (2000). "*Visual sensing and recognition of welding environment for intelligent shipyard welding robots,"* Paper presented at the Proceedings. 2000 IEEE/RSJ International Conference on Intelligent Robots and Systems (IROS 2000) (Cat. No.00CH37113), Takamatsu, Japan.
7. Jeng, J. Y., Mau, T. F., & Leu, S. M. (2000), "Gap inspection and alignment using a vision techniques for laser butt joint welding," *International Journal of Advanced Manufacturing Technology, 16*, 212-216.
8. Chu, G.-W., Yu, W. P., & Chung, M. J. (1997). "*A simple method of finding a visible region for the optimal camera position,"* Paper presented at the ICAR, Monterey,CA.

Research on Performance of Welding Fuzzy Petri Net Model

G.H. Ma[1] and S.B. Chen[2]

[1] Institute of Electromechanical Engineering, Nanchang Univeristy, Nanchang 330029
[2] Welding Institute, Shanghai Jiaotong University, Shanghai, 200030
ghma@ncu.edu.cn

Abstract. This paper designs a way to model on the complex welding robot system. With analyzing the characteristic of welding robot system, a fuzzy Petri net model is designed and analyzed. In order to get the performance of designed model, this paper proves the performance of model in theory. Results of model simulation experiment illustrate that the model can depicts welding robot system accurately and right.

1 Introduction

Since appearance of Petri net theory (PN), it has many unique merits that it can process information of concurrent occurs and synchronization and asynchronization in complex system [1-3]. Because of these reasons, the theory is researched in many areas, including controlling area and welding area. Thomas W. Hill uses colored Petri net to model on a job shop iron foundry [4], Zhiwu Li models on flexible manufacturing system with Petri net [5], Driss, O.B. analyzes reachability of Petri net [6], T. Qiu adopts a way of welding automation Petri net to model on welding flexible cell [7] and G.H.MA models on welding robot flexible manufacturing system with Petri net [8].

All of these researches can reflect characteristics of system, but they can not solve some professional questions in welding manufacturing or unique questions of specific welding process controling. For example, in welding controling area, there have much similar synchronization information as that of automation or mechanic area. When welding, the welding robot system should adjust positions of different arms of robot and positioner at one time in order to avoid collision and track the welding seam rightly. On the other side, welding technology parameters should be adjusted automatically in welding process according to welding requests, including welding velocity, welding current, or other parameters. Obviously, this is different from that of pure automation or mechanical controling. Common model cannot deal with these questions.

Secondly, although paper [7] and paper [8] give their own model of welding system and their models can depict the corresponding complex information fluent clearly, they cannot solve which of different information in model can be fired firstly, and in the same condition of two transitions, which has more priority to be selected. In this complex system, a right model should be designed to fulfill request of depicting the system more accurately, especially in complex welding area. This paper gives its research on the questions.

T.-J. Tarn et al. (Eds.): Robot. Weld., Intellige. & Automation, LNCIS 362, pp. 179–186, 2007.
springerlink.com

2 Fuzzy Petri Net Model

According to STCPN model [8], we can find that there is some confliction information in STCPN model. The confliction cases are those that which of transition will be fired firstly when the two transitions of model are enabled together or which transition can be enabled when there is an information order. These conflictions reflect that welding system will interfere or move in wrong.

In order to solve the question, this paper adopts weight function of fuzzy theory to depict weightiness of information of STCPN model. If an information of model is more important than the other, the value of weight function of the model is bigger than that of the other. In this way, we can depict all the information according to real welding system.

In fuzzy theory, fuzzy rule is listed as below:

$$If\ ...then...(\mu = R), R \in [0,1]$$

μ is weight function, R is value of weight function.

To PN model, in order to express the priority of information, this paper designs fuzzy factor expression to depict different values of PN model, which is fuzzy Petri net model (FPN).

The format of designed rule is listed as below:

$$R_i : IF\ \ d_j\ \ THEN\ \ d_k (CF = \mu_i)$$

Ri is No.i rule of controlling rule of FPN, and d_j and d_k are used to depict enabled degree of place s_j and s_k of FPN correspondingly. CF describes fired degree from place s_j to s_k and its value is μ, $\mu \in [0,1]$.

There are some questions in welding with robot system, for example, when welding with fixed processing parameters, welding seam will appear flaws, including welding pool drops out or completed penetration. In order to solve these questions, we use token quantity to indicate information quantity of welding system, if there is order information to run, then a token should be marked in the corresponding position of model. In the model, we use block diagram to indicate action of welding system and use circle diagram to indicate order of welding system.

Besides this, we adopt a way of module function to describe different functions of welding system, and use two-layer to simplify model structure. At last, we adopt weight function to fire token which has right of priority than others token in same model, and this way solves competing question, for example, which action will firstly run when there are the two actions of adjusting position of robot and tracing welding seam. All these policies

insure the accuracy of designed model. All different information can be reflected in our designed fuzzy PN model (FSTCPN: fuzzy STCPN). Figure of model and concrete model parameters are limited to length of paper and they are all omitted here.

The workflow content of model is listed as below: Firstly, the preparatory workpiece is loaded; Secondly if the positioner is free then the workpiece is transferred to requested place; If system works well, for example, sensors of welding penetration detects adjusted signal, center PC will adjust the welding parameters to weld high quality product and robot adjusts gesture of welding porch and so on; Lastly welding starts to run and if all conditions are meted, the workpiece is downed to output source.

3 Analysis of Fuzzy Petri Net Model

Although the FPN of welding system is designed, the performance of the model should be proved correct in theory. Because the FPN model belongs to PN model, the same method as that proving PN model is adopted here.

(1)Boundness

In order to analyze its boundness, we design its definition as below:

Definition 1. Suppose $x \in S \cup T$ is any element of multi tuples FSTCPN and it must fulfill definition 2;

Definition 2. Suppose $x \in S \cup T$ is any element of multi tuples petri net and

1) ${}^{\bullet}x = \{ y \mid (y,x) \in F \}$ is pre-set of x or input set;

2) $x^{\bullet} = \{ z \mid (x,z) \in F \}$ is after set or output set;

Definition 3. Condition of transition occurring of multi tuples:

1) ${}^{\bullet}t^{\bullet} = {}^{\bullet}t \cup t^{\bullet}$ is out-extension of transition $t \in T$ of FSTCPN;

2) The condition that transition t can be fired is that:

$$\forall s \in {}^{\bullet}t : M(s) \geq W(s,t) \wedge \forall s \in t^{\bullet} : M(s) + W(t,s) \leq K(s);$$

Definition 4. If any transition of multi tuples FSTCPN can occur that some condition must be reached as below:

If $M[t>$, then $t \in T$ can fire when model's mark is M, and M will change to its subsequence M'. To any place $s \in S$, it fulfills below condition:

$$M'(s)=\begin{cases} M(s)-W(s,t) & \text{If } s\in {}^{\bullet}t-t^{\bullet} \\ M(s)+W(t,s) & \text{If } s\in t^{\bullet}-{}^{\bullet}t \\ M(s)-W(s,t)+W(t,s) & \text{If } s\in {}^{\bullet}t\cap t^{\bullet} \\ M(s) & \text{If } s\notin {}^{\bullet}t^{\bullet} \end{cases}$$

Of above, if all mark M can fulfill the condition $M\in[M_0>$ and if there is a positive integer k and $s\in S$, formulary $M(s)\le k$ can reached, then FSTCPN is a boundness net system and k is FSTCPN's bound.

Therefore, according to designed model FSTCPN, s_{in} / s_{out} is input/ output place source of welding workpiece of welding system, they are corresponding to fixed condition. Then supposing capability function of s_b and s_s is $K(s_{in})=K_b$ and $K(s_{out})=K_s$ respectively.

According to definition 1 and definition 4, we can get a kind of running state χ of FSTCPN and its place capability function $K(\chi)$ that corresponds its reachable marks $M(\chi)$:

$$K(\chi)=K_1+K_2+9=K_b+K_s+9 \tag{1}$$

Therefore in FSTCPN system, if $\forall K(\chi)$ and $\exists K\in IN$ then $K(\chi)\le K<\infty$ and the FSTCPN model has performance of boundness.

With all the analysis above, we can has a deduction that fuzzy PN model has boundness condition: To FSTCPN model, if there is a positive integer k and $M\in[M_0>$, relation formulary $M(s)\le k$ is right, $s\in S$, then FSTCPN model is boundness net system.

Certification: According to condition of transition occurring that should fulfill relation formula:

$$\forall s\in {}^{\bullet}t: M(s)\ge W(s,t)\wedge\forall s\in t^{\bullet}: M(s)+W(t,s)\le K(s)$$

Because in fuzzy PN model all the resource and status information are kept the same as those in PN model, then all the transition firing condition come into existence and $\forall s \in {}^{\bullet}t : M(s) \geq W(s,t)$.

For using fuzzy weight function in fuzzy PN model, then the weight function value of any places S_x and S_y which are connected each other is less than 1, that is $CF_{xy} \leq 1$. Therefore, for $\forall s \in t^{\bullet} : M(s) + W(t,s) \leq K(s) + 1 \leq K$, we can say FSTCPN model fulfills requested condition that transition occurs.

On the other side, we can infer that there is relation $K(x) < k$ when $M \in [M_0 >$.

Then according to analysis and definition above, the deduction is right.

(2) Conservation

The performance of conservation is proved as below in this paper.

Definition 5. Suppose FSTCPN is limited net system and base net $(S, T(R_e, U); C)$ is pure net, then:

1) Row vector $V : S \to Z$ is $S\_$ vector of FSTCPN;
2) Row vector $U : T \to Z$ is $T\_$ vector of FSTCPN;
3) Matrix $C : S \times T \to Z$ is relation matrix, and matrix element of it is from formulary $C(s_i, t_j) = W(t_j, s_i) - W(s_i, t_j)$.

According to definition 5 and formulary of PN theory

$$M_0 + C \cdot U = M \tag{2}$$

And relation matrix of FSTCPN, if any statue χ of welding flexible system FSTCPN model and a sequence transition $t_1 \sim t_4$ fires, with the initial mark M_0

$$M_0 = [1 \ 1 \ 0 \ 0 \ 1 \ 0 \ 0 \ 0 \ 1 \ 0 \ 0 \ 1 \ 0 \ 1 \ 0 \ 0 \ 0 \ 1 \ 0 \ 0 \ 1 \ 0 \ 1 \ 1 \ 0 \ 1 \ 0 \ 1]$$

And according to welding system relation matrix $C_{i \times j} (i, j \in N)$ is listed as formulary (3).

Then subsequence mark M can be deduced:

$$M = [1 \ 1 \ 0 \ -1 \ 1 \ 0 \ 0 \ 0 \ 1 \ 0 \ 0 \ 1 \ 0 \ 1 \ 0 \ 0 \ 0 \ 1 \ 0 \ 0 \ 1 \ 0 \ 1 \ 1 \ 0 \ 1 \ 0 \ 1]$$

Therefore if a vector of none zero is found, designed model system fulfills conservation performance. Suppose W is additional vector, M_0 is initial mark of FSTCPN, M is any reachable mark of FSTCPN and $M[M_0 >$,then FSTCPN system fulfills

formulary (2) and (3) and all the firing transition row $F[\eta]$ can be calculated right and equation $W \cdot C = 0$.

From all analysis above, it is deduce that the condition of the FSTCPN fuzzy model has conservation performance in the welding flexible manufacturing system:

If and if only there exists a right vector $W \subseteq I \cup \{0\}$ that will satisfy $W \cdot C = 0$, then the fuzzy PN model is conservation, which proves that FSTCPN model has performance of PN system conservation.

Therefore using this fuzzy model, we can depict different priority of transition accurately in welding system.

$$C = \begin{array}{c} \\ d_{in} \\ d_1 \\ d_2 \\ d_3 \\ d_4 \\ d_5 \\ d_6 \\ d_7 \\ d_8 \\ d_9 \\ d_{10} \\ d_{11} \\ d_{12} \\ d_{13} \\ d_{21} \\ d_{22} \\ d_{23} \\ d_{24} \\ d_{25} \\ d_{26} \\ d_{14} \\ d_{15} \\ d_{16} \\ d_{17} \\ d_{18} \\ d_{19} \\ d_{20} \\ d_{out} \end{array} \begin{array}{c} \begin{array}{cccccccccccccccccccccccc} t_1 & t_2 & t_3 & t_4 & t_6 & t_7 & t_8 & t_9 & t_{10} & t_{11} & t_{17} & t_{18} & t_{19} & t_{20} & t_{21} & t_{22} & t_{23} & t_{24} & t_{25} & t_{12} & t_5 & t_{13} & t_{14} & t_{15} & t_{16} \end{array} \\ \begin{bmatrix} 1 & 0 & 0 & 0 & 0 & 0 & 0 & 0 & 0 & 0 & 0 & 0 & 0 & 0 & 0 & 0 & 0 & 0 & 0 & 0 & 0 & 0 & 0 & 0 & 0 \\ 1 & -1 & 0 & 0 & 0 & 0 & 0 & 0 & 0 & 0 & 0 & 0 & 0 & 0 & 0 & 0 & 0 & 0 & 0 & 0 & 0 & 0 & 0 & 0 & 0 \\ -1 & 1 & 0 & 0 & 0 & 0 & 0 & 0 & 0 & 0 & 0 & 0 & 0 & 0 & 0 & 0 & 0 & 0 & 0 & 0 & 0 & 0 & 0 & 0 & 0 \\ -1 & 1 & -1 & 0 & 0 & 0 & 0 & 0 & 0 & 0 & 0 & 0 & 0 & 0 & 0 & 0 & 0 & 0 & 0 & 0 & 0 & 0 & 0 & 0 & 0 \\ 0 & 0 & -1 & 1 & 0 & 0 & 0 & 0 & 0 & 0 & 0 & 0 & 0 & 0 & 0 & 0 & 0 & 0 & 0 & 0 & -1 & 0 & 0 & 0 & 0 \\ 0 & 0 & 1 & -1 & 0 & 0 & 0 & 0 & 0 & 0 & 0 & 0 & 0 & 0 & 0 & 0 & 0 & 0 & 0 & 0 & 1 & 0 & 0 & 0 & 0 \\ 0 & 0 & -1 & 1 & -1 & 0 & 0 & 0 & 0 & 0 & 0 & 0 & 0 & 0 & 0 & 0 & 0 & 0 & 0 & 0 & -1 & -1 & 0 & 0 & 0 \\ 0 & 0 & 0 & 0 & 1 & -1 & 0 & 0 & 0 & 0 & 0 & 0 & 0 & 0 & 0 & 0 & 0 & 0 & 0 & 0 & 0 & 0 & 0 & 0 & 0 \\ 0 & 0 & 0 & 0 & -1 & 1 & 0 & 0 & 0 & 0 & 0 & 0 & 0 & 0 & 0 & 0 & 0 & 0 & 0 & 0 & 0 & 0 & 0 & 0 & 0 \\ 0 & 0 & 0 & 0 & -1 & 1 & -0.95 & 0 & -0.75 & 0 & -1 & 0 & -1 & -1 & -1 & -1 & 0 & -1 & 0 & 0 & 0 & 0 & 0 & 0 & 0 \\ 0 & 0 & 0 & 0 & 0 & 0 & 1 & -1 & 0 & 0 & 0 & 0 & 0 & 0 & 0 & 0 & 0 & 0 & 0 & 0 & 0 & 0 & 0 & 0 & 0 \\ 0 & 0 & 0 & 0 & 0 & 0 & -1 & 1 & 0 & 0 & 0 & 0 & 0 & 0 & 0 & 0 & 0 & 0 & 0 & 0 & 0 & 0 & 0 & 0 & 0 \\ 0 & 0 & 0 & 0 & 0 & 0 & 0 & 0 & 1 & -1 & 0 & 0 & 0 & 0 & 0 & 0 & 0 & 0 & 0 & 0 & 0 & 0 & 0 & 0 & 0 \\ 0 & 0 & 0 & 0 & 0 & 0 & 0 & 0 & -1 & 1 & 0 & 0 & 0 & 0 & 0 & 0 & 0 & 0 & 0 & 0 & 0 & 0 & 0 & 0 & 0 \\ 0 & 0 & 0 & 0 & 0 & 0 & 0 & 0 & 0 & 0 & 1 & -1 & 0 & 0 & 0 & 0 & 0 & 0 & 0 & 0 & 0 & 0 & 0 & 0 & 0 \\ 0 & 0 & 0 & 0 & 0 & 0 & -1 & 0 & -1 & 0 & -1 & 1 & 0 & 0 & 0 & 0 & 0 & 0 & 0 & 0 & 0 & 0 & 0 & 0 & 0 \\ 0 & 0 & 0 & 0 & 0 & 0 & 0 & 0 & 1 & 0 & 0 & 0 & 0 & 1 & 1 & 1 & -1 & 0 & 0 & 0 & 0 & 0 & 0 & 0 & 0 \\ 0 & 0 & 0 & 0 & 0 & 0 & 0 & 0 & 0 & 0 & 0 & 0 & 0 & -1 & -1 & -1 & 1 & 0 & 0 & 0 & 0 & 0 & 0 & 0 & 0 \\ 0 & 0 & 0 & 0 & 0 & 0 & -1 & 0 & -1 & 0 & 0 & 0 & -1 & 1 & 0 & 0 & 0 & -1 & 1 & 0 & 0 & 0 & 0 & 0 & 0 \\ 0 & 0 & 0 & 0 & 0 & 0 & 0 & 0 & 0 & 0 & 0 & 0 & 1 & -1 & 0 & 0 & 0 & 1 & -1 & 0 & 0 & 0 & 0 & 0 & 0 \\ 0 & 0 & 0 & 0 & 0 & 0 & -1 & 1 & -1 & 1 & 0 & 0 & 0 & 0 & 0 & 0 & 0 & 0 & 0 & -1 & 0 & 0 & 0 & 0 & 0 \\ 0 & 0 & 0 & 0 & 0 & 0 & 0 & 0 & 0 & 0 & 0 & 0 & 0 & 0 & 0 & 0 & 0 & 0 & 0 & 1 & -0.5 & 0 & 0 & 0 & 0 \\ 0 & 0 & 0 & 0 & 0 & 0 & 0 & 0 & 0 & 0 & 0 & 0 & 0 & 0 & 0 & 0 & 0 & 0 & 0 & 0 & 0 & 1 & -1 & 0 & 0 \\ 0 & 0 & 0 & 0 & 0 & 0 & 0 & 0 & 0 & 0 & 0 & 0 & 0 & 0 & 0 & 0 & 0 & 0 & 0 & 0 & 0 & -1 & 1 & 0 & 0 \\ 0 & 0 & 0 & 0 & 0 & 0 & 0 & 0 & 0 & 0 & 0 & 0 & 0 & 0 & 0 & 0 & 0 & 0 & 0 & 0 & 0 & -1 & 1 & -1 & 0 \\ 0 & 0 & 0 & 0 & 0 & 0 & 0 & 0 & 0 & 0 & 0 & 0 & 0 & 0 & 0 & 0 & 0 & 0 & 0 & 0 & 0 & 0 & 0 & 1 & -1 \\ 0 & 0 & 0 & 0 & 0 & 0 & 0 & 0 & 0 & 0 & 0 & 0 & 0 & 0 & 0 & 0 & 0 & 0 & 0 & 0 & 0 & 0 & 0 & -1 & 1 \\ 0 & 0 & 0 & 0 & 0 & 0 & 0 & 0 & 0 & 0 & 0 & 0 & 0 & 0 & 0 & 0 & 0 & 0 & 0 & 0 & 0 & 0 & 0 & 0 & 1 \end{bmatrix} \end{array} \tag{3}$$

4 Simulation Experiment

In order to check and analyze the performance of designed model above, we adopt professional simulation software CPNTOOLS to simulate it. Firstly we design our model in simulation software; then we fill requested parameters in model of simulation software according to condition of our welding robot system.Therefore we simulate the model in two steps, one is to check boundness and the other is to analyze conservation. Simulation results reveal that the model is fluent and there is no deadlock, the designed model has the two characters that are boundness and conservation. Figure 1 shows the result of simulation.

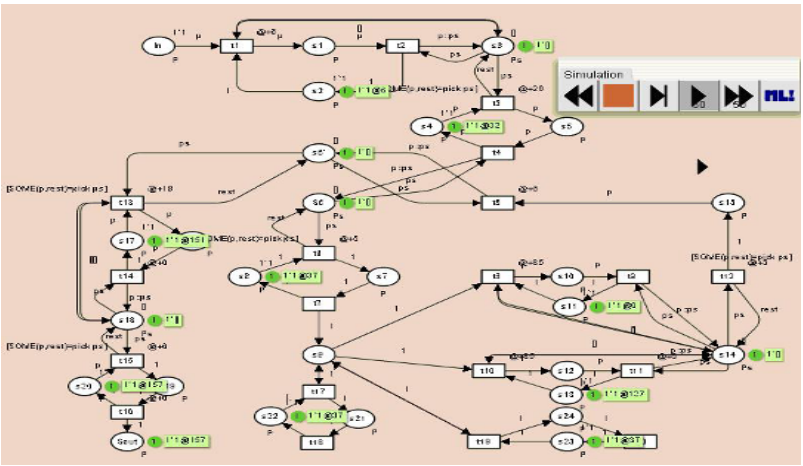

Fig. 1. Simulation experiment result of FSTCPN model

5 Conclusion

This paper analyzes different information of welding system and designs a fuzzy PN model. In order to analyze performance of new model in theory, this paper proves the model and simulation experiment results illustrate that FSTCPN model has performance of boundness and conservation. The research extends the PN theory and supply a reference for controlling welding system in future.

References

1. S. Christensen and L. Petrucci Towards a Modular Analysis of Coloured Petri Nets Application and Theory of Petri Nets, K. Jensen (ed.), Lecture Notes in Computer Science 616, pp 113-133, Springer-Verlag (1992).
2. S. Christensen and J. Toksvig DesignBeta V2.0.1 – BETA Code Segments in CP-nets Lecture Notes OO&CPN – nr 5, Computer Science Department, Aarhus University (2004).
3. K. Jensen Coloured Petri Nets: A High Level Language for System Design and Analysis Advances in Petri Nets. G. Rozenberg (ed.), Lecture Notes in Computer 483, Springer-Verlag (2004).
4. Thomas W. Hill. Colored Petri Net Modeling of Metal Distribution in a Job Shop Iron Foundry: Improving Flow in a Pull System with Perishable In-Process Inventory. Journal of Manufacturing Processes. Vol.5, No.1.2003: 66-77
5. Zhiwu Li, Haibin Xia, Anrong Wang. An effective deadlock prevention policy using elementary siphons of Petri nets for FMS. Control, Automation, Robotics and Vision Conference, 2004. ICARCV 2004 8th.Volume 1, 6-9 Dec. 2004 Page(s): 521 - 526 Vol. 1

6. Driss, O.B., Yim, P.. Korbaa, O. and etc. Reachability search in timed Petri nets using constraint programming. Systems, Man and Cybernetics, 2004 IEEE International Conference on Volume 5, 10-13 Oct. 2004 Page(s): 4923 - 4928 vol.5
7. T. Qiu, S.B Chen, Y.T. Wang, L. Wu. Modeling and Control of Welding Flexible Manufacturing Cell Using Petri Net. Journal of Materials Science & Technology. 2001, 17(1): 185-186
8. G.H. Ma. S.B. Chen. T. QIU etc. Model on Robots of Flexible Manufacturing System with Petri Net in Welding. The Eighth International Conference on Control, Automation, Robotic and Vision. 6-9 December, 2004. Kunming, China. pp:1885-1888

Agent-Based Modeling and Control of Remote Robotic Welding System

L.X. Zhang, L. Wu, H.M. Gao, and G.J. Zhang

National Key Laboratory of Advanced Welding Production Technology, Harbin Institute of Technology, Harbin 150001, P.R. China
lianxinzhang@hit.edu.cn

Abstract. A new *Remote Robotic Welding System* (RRWS) with a number of intelligent sensors and based on the control strategy of "macroscopic teleoperation, microscopic autonomous", was investigated. By analyzing the remote robotic welding process, it is found that the cooperation and coordination of all subsystem and operator are the key technology and the guarantee of RRWS's practical application. And then multi-agent based modeling and control of RRWS were studied because that the multi-agent thinking is very suitable to the characteristics of RRWS. By this means, the separate advantages of human and machines separately were utilized fully. Lastly, the results demonstrated that the RRWS can be applied in practice efficiently, reliable and precisely by modeling and control using multi-agent technology.

1 Introduction

Welding fabrication has been widely used for outer space assembly, underwater structures and nuclear components maintenance. The extreme/hazardous environment of these applications makes it necessary to employ robots to carry out the welding tasks. However, the state-of-the-art in robotics, artificial intelligence and sensing technology do not yet permit a totally autonomous remote welding operation. As a result, the concept of *Remote Robotic Welding System (RRWS)* has been formed, where a human operator at a local station can carry out the welding fabrication through monitoring the welding process and controlling the welding robot located on the worksite[1,2].

In fact, technologies related to teleoperation and telerobotics have been presented for about 60 years. However, the remote robotic welding technology only has been presented for 30 years. At the same time, it is not applied widely and practically like other teleoperation technology. The most important reason is that the remote robotic welding task is more difficult and complicated than other teleoperation tasks[3,4], e.g. (1) a large number of parameters need to be controlled, including the torch position and pose, welding speed and arc length; (2) high precision of all controlled parameters, especially the torch position and torch motion speed; (3) real–time, unlike assembly or grasping tasks, which can be execute slowly and try many times. In a word, there are some difficulties in the practical application of remote robotic welding technology by

T.-J. Tarn et al. (Eds.): Robot. Weld., Intellige. & Automation, LNCIS 362, pp. 187–194, 2007.
springerlink.com

the means of traditional teleoperation. Therefore, our laboratory presents a new control strategy for remote robotic welding system, called “macroscopic teleoperation, microscopic autonomous”. The basic thinking of this control strategy is that in macroscopic space, an operator manipulates the robot remotely, consequently to take advantage of the advance ability of human information process, decision and execution fully to operate robot remotely; in microscopic space, welding process is carried out autonomously and operator supervises the whole welding process remotely. According to this thinking, a remote robotic welding system structure and the cooperation between all subsystems are researched.

Aiming at the characteristics of distributed and cooperation of every subsystem of RRWS, the multi-agent theory is introduced into the process of remote robotic welding manufacturing firstly. With its help, a multi-agent system (MAS) model of RRWS has been constructed. Moreover, based on the cooperation theory of MAS, the cooperation of all subsystems including human (operator) is analyzed and the high efficient cooperation is achieved.

2 System Architecture

A typical remote robotic welding system usually consists of several distributed subsystem, including welding robot system, vision sensor system, and welding machine located in remote worksite, communication media, operator, human-machine interface and input device located in local site. In order to implement “microscopic autonomous” of remote welding and teaching process, we equipped some useful sensors, including laser scanning welding seam tracking system and force sensor system, which together provide abundant information about the microscopic space and then to arrive at the purpose of promoting the efficiency and accuracy of RRWS. The RRWS presented in this paper is consist of six DOF welding robot mechanisms and an open architecture robot controller, GMAW robot welding machine, laser scanning weld seam tracking sensor and its controller, stereo vision system, 2D vision system, force sensor and its controller, crystal glass, human-machine interface, input device (joystick or spaceball) etc. All of these subsystems communicate with each other by intranet. The system architecture is shown in Fig.1.

In this system, torch moves in desired trajectory, speed and pose with welding robot. The robot controller is open architecture; its core is industrial PC and PMAC (Programmable Multi-Axis Controller). Welding machine is controlled by an IPC-based control system. Its control system can control the ON/OFF of welding machine and adjust the welding parameters according to the welding seam penetration status. Laser scanning welding seam tracking sensor and force sensor are fixed on torch. They are all controlled by IPC-based control system. The force sensor control system obtains precise welding seam position by analyzing the six directions force. Laser scanning welding seam tracking controller calculates precise welding seam position by processing images of welding seams and laser stripe. The camera for stereo video system and 2D video is located in worksite. 3D display system located in local site, and operator can see 3D information of work site by crystal glasses. 2D information is displayed in human/machine interface. Operator manipulates welding

robot remotely and control the whole system by input devices and local control/supervisory human/machine interface. This interface feedbacks worksite information to operator and responses operator's control commands, at the same time, it can switch the control strategy among totally autonomous control mode, supervisory control mode, interactive autonomous control mode, shared control mode and direct manual control mode.

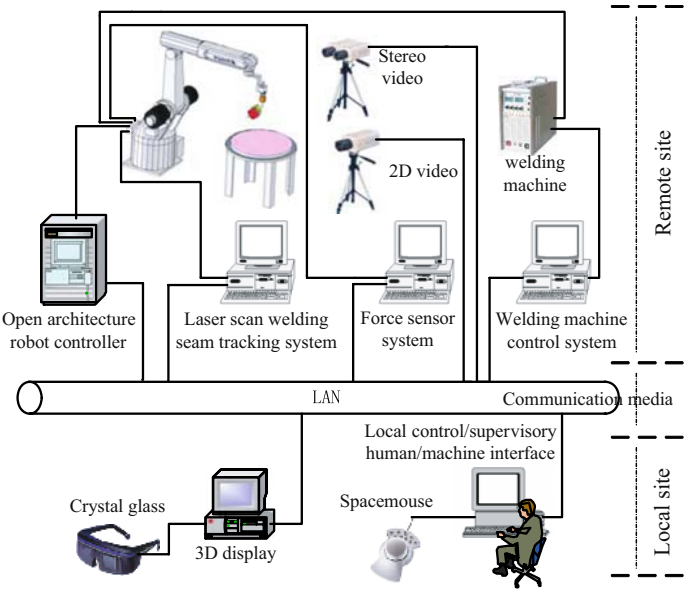

Fig. 1. System architecture of RRWS

3 Process of Remote Robotic Welding

The process of remote robotic welding under the control strategy of "macroscopic teleoperation, microscopic autonomous" can be divided into three steps: (1) to produce remote robotic welding tasks (robot programs); (2) operator moves torch to the nearby of welding seams start point; (3) all machine systems finish welding tasks by cooperation autonomously.

Generally, the following methods can be adopted in producing remote robotic welding tasks: (1) teaching remotely; (2) seam tracking system detects welding seam, and at the same time, the detected welding seam is welded real-time, this method requires high quality grooves; Generally speaking, the first method is applied widely, while the second method requires some special conditions. The first method includes two cases: (1) teaching by PTP (point to point); (2) teaching by welding seam tracking. If the welding seam shape is very simple and a few points are enough to figure the welding seam, the method "teaching by PTP" can be adopted, which may be high efficiency. When the torch

almost arrived to a teaching point, to achieve the precise position and pose of torch manually by operator is very difficult. Under this condition, the force sensor system and welding seam tracking system cooperates to adjust the position and pose of torch to the desired position and pose autonomously. If to teach very complex welding seam by the method of PTP, not only the efficiency is very low, but also the accuracy is very low. So teaching by welding seam tracking can be adopted. This method means that the seam tracking system records a series of points on seam and produces welding tasks based them by tracking (without welding) the seam with groove. During this process, if any segments cannot be detected by seam tracking system because that the groove is not perfect, the force sensor system will help the seam tracking system to detect the seam autonomously, so the welding tasks can be produced efficiently and precisely.

Operator can move torch to the nearby of welding seam start point manually and remotely. During this process, the torch speed, trajectory, pose are not necessary to control precisely. When produced robot programs are executed, torch can arrive to the welding seam start point precisely and autonomously.

During the autonomous welding process, welding robot, welding seam tracking system, welding machine cooperate to complete welding tasks, operator supervise the whole welding process remotely.

Summarizing all above three process, we think that to use the operator's advanced ability of information processing, decision, execution, the ability of machine system computation and execution quantitatively, and to realize complete and suitable cooperation between human (operator) and machine system and among all kinds of machine system are the best and only feasible method to complete remote welding tasks. This is the advantage of MAS exactly; therefore, we can try to modeling and analyzing the RRWS based on MAS.

4 Multi-agent System Modeling of RRWS

4.1 Agent and Multi-agent System

Up to now, Agent has not a common definition, researchers have not agreed on the definition. Generally speaking an agent is a software/hardware object that is capable of doing some specific tasks autonomously. Wooldridge has another definition[5]: "an agent is a computer system that is situated in some environment, and that is capable of autonomous action in this environment in order to meet its design objectives." Although all definitions are not same, all researchers think that agent has the following same basic properties [6,7,8,9]:

- Autonomy: agents operate without the direct intervention of humans or others, and have some kind of control over their actions and internal states.
- Social ability: agents interact with other agents (and possibly humans) via some kind of agent-communication language and communication media.
- Reactivity: agents perceive their environment (which may be the physical world) and respond in a timely fashion to changes that occur in it.
- Pro-activeness: agents do not simply act in response to their environment; they are able to exhibit goal-directed behavior by taking the initiative.

A multi-agent system (MAS) is a loosely coupled network of problem-solver entities that work together to find the answer to problems that are beyond the individual capabilities or knowledge of each entity [8]. In other words a MAS is a set of agents that either cooperate or compete to solve a problem. A MAS is usually used in cases where the problem is complex, data is decentralized, and computation is asynchronous. In such cases, it is preferred to distribute tasks over a number of agents and let them work autonomously and also interact (cooperate) with each other.

Actually, RRWS is distributed in time and space and some events occur random. The whole remote robotic welding process involved welding tasks managing, system status managing, basic data managing of every subsystem, sensor information processing, data and signal dynamic scheduling and static scheduling among every subsystem. So these characteristics accord with MAS. By analyzing the advantages and the characteristics of RRWS, modeling RRWS using MAS can achieve the following advantages: (1) every agent may be have advanced intelligence. So "microscopic autonomous" can be implemented, control strategy can be switched autonomously, operator can only do something that he can do it easily and efficiently, all resources can be utilized fully, random event can be dealt with safely and exactly. (2) Agent will become more easy to development and reliable. Because every agent only solves very simple sub-problem, the agent become very simple, reliable and easy to development. (3) The system can be extended easily. So far as equipping correct communication protocol and control strategy, the new agent can be added to MAS. In addition, modifying any agent does not affect other agents and whole system. (4) All agents run parallel, so solving efficiency is promoted and real-time is meet. All in all, modeling RRWS using MAS is suitable, novel, meaningful and benefit.

4.2 MAS Modeling of RRWS

In order to improve the efficiency and precision and facilitate the operator during remote robotic welding process, to cooperate the operator's advanced intelligence and precise computation and execution fully are most important things. Since conventional RRWS do not cooperate human and machines fully, we apply MAS theory to remote robotic welding process to construct a MAS model, which can cooperate human and machines fully, and as a result will improve the system efficiency and precision.

We construct the MAS model for the control of RRWS according to the physical and logical position of all kinds of subsystem. Basically, welding robot system, welding machine and its control system, laser scan welding seam tracking system and force sensor system are all alone resource. They are distributed and in charge of different job, so they all can be regard as agent. In practice, the operator, who located in local site and manipulates the robot remotely, is very important during the whole remote robotic welding process. He can manipulate the robot quickly and intelligently when the robot locates in macroscopic space; at the same time, when the robot locates in microscopic, he can supervise the autonomous motion of robot. If he only do some works that are suitable for him, and other machines do other works that are suitable for machines and not suitable for human, the system will work efficiently and precisely. Also operator can manipulate the system conveniently and easily. So the operator can be regard as a

special agent. At the same time, teleoperation control system located in local site including input device, human-machine interface, 2D vision and stereovision display system, and control strategies. Its main functions are to exchange information between human and machine, selection and switch of control strategies, communication with other agent etc. Therefore, it can be regard as an agent called teleoperation control agent (TOCA). In addition, in order to manage all other agents, we construct a system manage agent (SMA). All agents communicate each other by intranet. The communication is point to point.

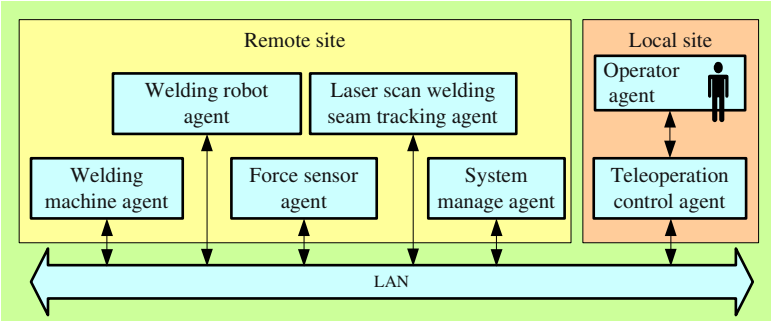

Fig. 2. MAS model for RRWS

In the MAS model shown in Fig.2, seven agents are included. The following is their basic functions.

- *SMA, System Manage Agent* : It is the base of the MAS for RRWS, and it must be run firstly. Its functions include that updating, maintaining and supervising the running status of MAS, e.g. to receive register information of other agent, and saving the status table of all other agents for the querying of any other agent.
- *WRA, Welding Robot Agent* : It is in charge of the motion control and status supervising of the six DOF welding robot.
- *LSWSTA, Laser Scanning Welding Seam Tracking Agent*□It tracks welding seam autonomously for welding tasks teaching, welding trajectory correcting, searching and locating. It is very important and necessary.
- *FSA, Force Sensor Agent* : It locates the teaching point and welding seam segment precisely. Generally, it is used in company with LSWSTA.
- *WPA, Welding Machine Agent* : It controls the ON/OFF and parameters of welding machine. The parameters can be adjusted real time according to the penetration status.
- *TOCA, Tele-operation Control Agent* : It receives the input commands that operator sent by input device, and receives the remote environment information sensed by operator, cooperates with other agents and makes decision according to received information and other agents status.
- *OA, Operator Agent* : He inputs control commands and observed robot's environment information by vision system, and supervises robot's autonomous

welding process. At the same time, he teaches welding tasks and move torch to welding start point remotely and manually. Due to his advanced ability of information processing, decision, sensing, execution quickly, so he can finish many tasks more quick and easy than machines. Accordingly, the operator, a special part of whole system, many tasks can be simplified. Under this condition, so as the machine do some tasks that they are capable of doing and human so do some tasks that he is capable of doing, the whole system can working efficiently.

The core thinking of modeling and controlling for RRWS using MAS is that realizing the cooperation between the human and other machines efficiently, and utilizing their respective advantages fully, ultimately the system can be applied efficiently and steadily in practice production process. The functions and advantages of all agents are introduced above, then how to finish welding tasks by means of cooperation will be introduced. According to the torch motion zone, the remote robotic welding process can be divided into three stages: (1) operator moves the torch to the nearby of target point (teaching point or welding start point) manually; (2) torch arrives to target point precisely; (3) welding tasks is carried out autonomously. If those three stages both have feasibility, high efficiency, and high steadiness, the remote robotic welding system must be applied in practice efficiently.

During the process of moving torch to the nearby of target point, it is not necessary to control the torch trajectory, speed, pose precisely. So operator can carry out this task manually with the help of 2D and stereovision system. In addition, the operator can adjust robot motion speed according to the distance to target point or obstacles. Under this condition, this stage must have high efficiency and high safety. If the all machines execute this process, not only the control methods and algorithms are very complex, but also the system efficiency may be very low.

LSWSTA will detect welding seam autonomously when the torch is close to welding seam. When the LSWSTA found the seam, it will inform TOCA firstly. When TOCA received this message, it will switch teleoperation control strategy to autonomous control mode according to other agent status obtained from SMA, and inform OA. And then LSWSTA and FSA cooperate to locate the target point precisely, and operator supervises the process. Before long, this process is finished and TCOA informs OA. And then, operator can record teaching point or tell robot to start welding. At the same time, TOCA switch control strategy accordingly. In this process, the torch move in a very small space around target, if operator locates the torch to target point precisely, he must try continuously up to finish this process, affirmatively the efficiency is very low and the collision between torch and workpieces is inevitable. So the efficiency and safety have been improved obviously by this cooperation between human and all machines.

During the welding process, autonomous welding is the only way because that imitating manual welding not only cannot satisfy the requirement of real-time, but also the tracking precision is very low. So the autonomous welding process need to be completed by the autonomous cooperation of WMA, LSWSTA, OA, WRA, and TOCA. WMA adjusts welding parameters autonomously in order to guarantees welding quality. LSWSTA corrects welding trajectory real time to avoid the influence of welding distortion and workpiece assembly. WRA carried out the motion according

to the welding tasks, LSWSTA's adjustment and operator's commands. OA supervises whole welding process, takes actions to accidents, and adjusts some parameters, e.g. torch pose. TOCA switches control strategy according to other agent statues and requirements. In this process, a difficultly of traditional RRWS, remote welding by imitating manual welding can not satisfy the practice requirements, is solved. At the same time, the efficiency, precision, welding quality and steadiness of RRWS all are improved, and the machines system ability of precise computation and execution is applied fully.

5 Conclusion

In this paper, a new RRWS with force sensor system and laser scanning welding seam tracking system been introduced. Since conventional RRWS do not show the advantages fully of human and machines, MAS theory has been applied into this RRWS and a MAS model has been constructed, which can cooperate the advantages of human and all machine. And the results demonstrated that the RRWS based on MAS model could finish remote welding tasks more efficiently, precisely, steadily in practice.

References

1. Hou M, Yeo SH, Wu L, Zhang HB (1996) On teleoperation of an arc welding robotic system. Proceedings of the 1996 IEEE International Conference on Robotics and Automation, pp1275-1280.
2. Geeter JD, Decreton M, Colon E (1999) The challenges of telerobotics in a nuclear environment. Robotics and Autonomous Systems 28(1): 5-17.
3. Agapakis JE (1986) Fundamental and advances in the development of remote welding fabrication system. Welding Journal 65(9): 21-34.
4. Lin SY (2000) Welding robot and its application. China machine press, pp188-211.
5. Wooldridge M, Jennings NR (1993) Intelligent agents: theory and practice. Knowledge Engineering Review 60(1): 115-152.
6. Farahvash P, Boucher TO (2004) A multi-agent architecture for control of AGV systems. Robotics and Computer-Integrated Manufacturing 20(6): 473-483.
7. Wang SL, Xia H, Liu F, Tao GB, Zhang Z (2002) Agent-based modeling and mapping of a manufacturing system. Journal of Materials Processing Technology (129): 518-523.
8. Jenning NR, Sycara KP, Wooldridge M (1998) A roadmap of agent research and development. Autonomous Agents and Multi-Agent Systems 1(1): 7-38.
9. Nwana HS (1996) Software agents: an overview. the Knowledge Engineering Review 11(3): 205-244.

On-Line Estimation of Electrode Face Diameter Based on Servo Gun Driven by Robot in Resistance Spot Welding

X.M. Lai, X.Q. Zhang, G.L. Chen, and Y.S. Zhang

School of Mechanical Engineering, ShangHai JiaoTong University, ShangHai, China, 200240
zhangxvqiang@163.com

Abstract. Enlargement of electrode face diameter in resistance spot welding was the main factor that led to undersize nugget diameter. A mathematics model was established to estimate electrode face diameter by applying the characteristic that servo gun can detect axial wear online but not equip additional measurement apparatuses. Firstly the precision of servo gun was compensated to assure it can meet the requirement of axial wear measurement online. Then the model was established to estimate electrode face diameter online by a minimum amount of experiment data to determine the numerical constant in the model. To verify the model, electrode life tests for welding different galvanized steels were carried out. It was shown that estimation results of the model agreed well with the experiment results and spot welding the steels with higher electrode wear rate would result in a shorter electrode life.

1 Introduction

More coated steels with high strength have been used in auto body manufacturing to improve corrosion resistance and safety requirements of automobile. Resistance spot welding was the main joint method to assembly auto body. But spot welding of these coated steels required higher electrode force, welding current than uncoated steels and was easer to alloy and stick with electrode face because of their special physics and chemistry properties [1, 2]. It took serious and uncertain electrode wear when welding these steels, which resulted in short electrode life and inconsistent weld quality.

Electrode wear led to electrode face diameter enlargement, pitting on electrode face and electrode length reduction. Electrode face diameter enlargement reduced current density and pressure on electrode face, which was the main factor that affected weld quality. Some methods were presented to estimate electrode face diameter at different wear stages. D.bracun applied image processing technology to capture indentation shape in work-pieces to estimate the electrode face diameter by analyzing the characteristics of indentation shape [3]. Wei Li established a model to estimate electrode face diameter by measuring dynamic resistance at different weld numbers [4]. But additional apparatuses such as camera devices and resistance measurement instruments had to be equipped on gun arm if applying these methods to inspect electrode face diameter, which was not convenient to be widely used in product line online and the signals were easily disturbed by poor working conditions.

T.-J. Tarn et al. (Eds.): Robot. Weld., Intellige. & Automation, LNCIS 362, pp. 195–202, 2007.
springerlink.com

Servo gun is a new developing gun to be used in spot welding, which adopt servo motor as driving power. Compared with pneumatic gun, servo gun has more accurate electrode force control [5]. It can control electrodes softly touch work part, which reduce impact on electrodes and improve electrode life [6, 7]. As the encoder of servo gun can feed back electrode displacement online, so the axial electrode wear can be gotten by analyzing the data in encoder at different wear stages. This paper studied to apply the method that servo gun can expediently measure axial wear but not equip additional measurement apparatuses to achieve electrode face diameter estimation online.

2 Calibration of Axial Wear Measured by Servo Gun

Robot integrated with servo gun was shown in Fig.1. The robot is six-axis freedom robot, which has the maximal load of 200kgf and repeating position accuracy of ±5um. Up-electrode of servo gun mounted on robot arm is driven as the seventh axis of robot. Robot move servo gun to a preordered position along pre-designed route, and then the up and down electrode were closed to clamp parts. When electrode force was increased to a pre-determined value, robot controller gives a welding signal to welding controller, which runs welding programs to finish welding.

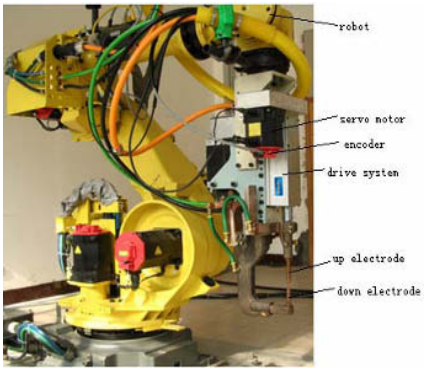

Fig. 1. Robot integrated with servo gun

The encoder of servo gun can feed back electrode displacement online, when a new set of electrodes was replaced on servo gun, robot controller run the initialization program to record the displacement of new electrodes. As shown in Fig.2, the up-electrode was moved to softly touch a calibration board to record the electrode displacement, and then the up and down electrode were closed, so the displacements of new electrodes were recorded by the encoder. After about some weld spots, electrode length was reduced because of electrode wear, then detection program of axial wear was run to record the displacements of worn electrodes. Compared with the two

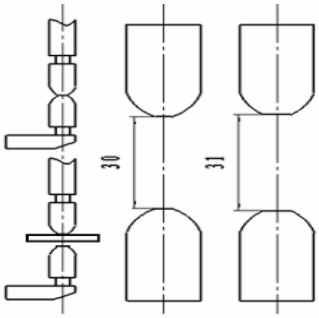

Fig. 2. Procedure of axial wear detection by servo gun

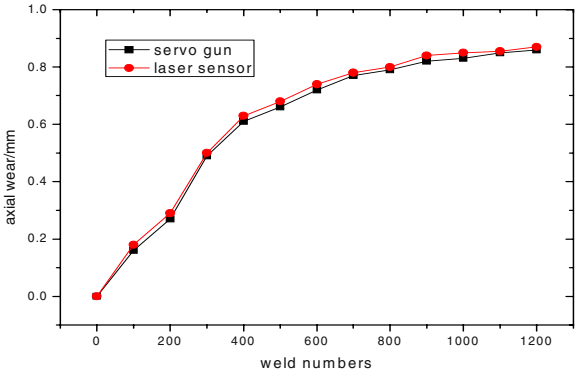

Fig. 3. Calibration of axial wear

displacement values of new electrodes and worn electrodes recorded by encoder, the axial wear at different weld numbers could be expediently gotten by servo gun online.

Axial wear of welding coated steels was only about 90 um per 100 welds [8], which had high precision requirement for servo gun. A feeler gauge was used to simulate axial wear to calibrate measurement precision of servo gun. It was shown that the measurement precision of servo gun was about 20um. To verify the precision of servo gun, axial wear measured by servo gun and laser sensor with 0.25um precision was carried out during the electrode life test. As shown in Fig.3, axial wear measured by servo gun was always about 10um less than laser sensor, which was mainly induced that transmitting error of servo gun reduced the feedback displacement recorded by encoder. As the transmitting error was a system error, so it could be compensated. Measurement precision of servo gun improved to 10um after compensating the system error, which can meet the requirement of axial wear measurement online. In Fig.3,

Axial wear measured by servo gun included up and low electrode wear. Generally, up and low electrode had uniform wear for AC weld gun [9], so each electrode axial wear could be calculated.

3 Model of Electrode Face Diameter Estimation Online

As welding current and electrode force were constant in electrode life test, so electrode wear rate was mainly affected by current density and pressure on electrode face for fixed steel. The higher current density would result in a higher temperature on electrode face, so the propensity of alloying and sticking between the electrode face and steel sheet was enhanced, which accelerated material removal from electrode face and increased electrode face diameter. Similarly, the higher pressure would facilitate extrusion of softened electrode face material to the face periphery and result in electrode face diameter enlargement. During electrode life test, the current density and pressure on electrode face were decreased with electrode face diameter increasing because of electrode wear. So electrode wear rate and material removal from electrode face were inconstant with electrode face diameter increasing.

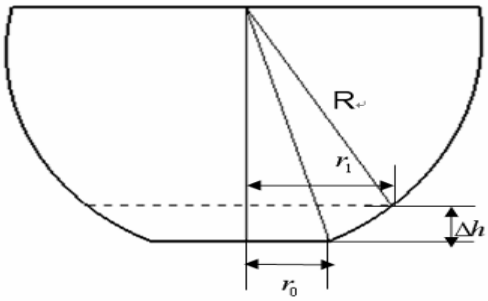

Fig. 4. Electrode face geometry

The quantity of material removed from electrode surface could be assumed to be linearly proportional to the product of the pressure and welding current density on the electrode face [10]. Therefore,

$$\Delta V = kPD \tag{1}$$

Where ΔV is the volume of material being removed, k is the proportional constant, P is the average pressure on the electrode face, and D is the current density on the electrode face. After welding some welds, as shown in Fig.4, the electrode face radius

was enlarged from r_0 to r_1, and electrode length was accordingly reduced Δh. The volume of this slice of material removed can be expressed by

$$\Delta V = (\pi / 6)\Delta h(3r_0^2 + 3r_1^2 + \Delta h^2) \tag{2}$$

Where Δh is the electrode length reduction, r_0 is the initial radius of new electrode, r_1 is the radius of worn electrode. In equation (1), the pressure P and current density D can be expressed by

$$P = F / \pi r_1^2 \tag{3}$$

$$D = I / \pi r_1^2 \tag{4}$$

Where F and I are the electrode force and welding current respectively. Substituting equations (2), (3) and (4) into equation (1) gives

$$(\pi / 6)\Delta h(3r_0^2 + 3r_1^2 + \Delta h^2) = kFI / \pi^2 r_1^4 \tag{5}$$

In equation (5), r_0, F and I were known, Δh could be gotten by servo gun online and r_1 could be measured by carbon imprint method, so k could be calculated by substituting these experiment data into equation (5) and taking the average of the results derived from electrode life test. When the axial wear Δh was detected by servo gun online for every some welds, the worn electrode radius r_1 could be estimated according to equation (5).

4 Model Verifying

To verify the model, electrode life tests were carried out on four different galvanized steels. Spherical electrode with electrode face diameter of 5mm was applied. Electrode force was kept at 2200N and welding time was set at 10 cycles. The welding current was set just below the expulsion limit for each of the tested steels. Tensile shear test was performed every 100 welds and each shear test had three samples to record maximum shear force as weld strength. Carbon imprint method was used to get electrode face conditions and electrode diameters at different weld numbers. Electrode life was defined as the weld number when weld strength fell to below 80% of the maximum value.

Electrode face diameter enlargement (radial wear) reduced current density and pressure on electrode face. When the electrode face diameter increased beyond a certain value, the current density was too low to achieve acceptable nugget size, and then electrode life was end.

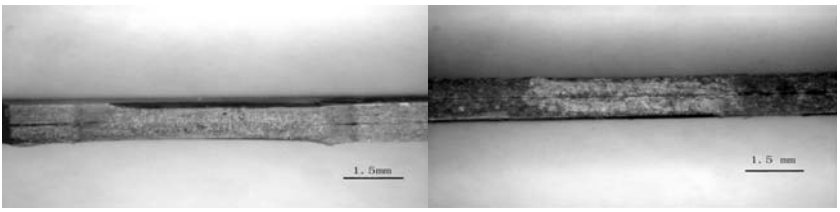

200 welds 1200 welds

Fig. 5. Weld cross sections at different weld numbers

Weld cross sections of welding steel A at different weld numbers were shown in Fig.5. A good weld with shearing force of 9.3kN was formed at 200 welds, whose nugget diameter (measured from cross section of weld spot) was about 5.8mm. But at 1200 welds, there was no nugget formed and shearing force was only about 7.2kN because the enlargement of electrode face diameter decreased current density and pressure on electrode face, which formed undersize nugget. Especially spot welding of coated steels would result in serious and uncertain electrode wear, so estimation of electrode face diameter online could reduce the effect of electrode wear on weld quality.

From equation (5), it could be seen that increasing welding current and electrode force would accelerate electrode wear rate. It also could be seen that a less diameter would induce faster electrode wear rate, which agreed well with the experiment results that higher electrode wear rate would be resulted in at earlier weld stage. For example, the average axial wear rate of welding steel A was about 0.86um per weld before 300 welds and then decreased to 0.23um per weld after 600 welds. The wear rate of electrode face diameter was faster at earlier welds than at later welds. Physically, coefficient k in equation (5) is primarily determined by material and coating characteristics as well as welding parameters. During electrode life tests, spot welding the steel with higher electrode wear rate would result in a shorter electrode life and a larger k value. Therefore, coefficient k indicated the propensity of materials to be removed from the electrode face and k was different for different steels.

According to the experiment data derived from electrode life tests, the verifying results of estimation model for four steels were shown in Fig.6. It was shown that the measured electrode face diameters had a certain amount of variation. For instance, the actual welding current level fluctuated around the average value from weld to weld with a deviation of about 200A and the measurements of electrode face diameter from carbon imprints could also induce some errors. In addition, the axial wear measured by servo gun also had an error of about 0.01mm. Despite of these error factors, the estimation results derived from the model based on servo gun detecting axial wear online agreed well with the experiment results.

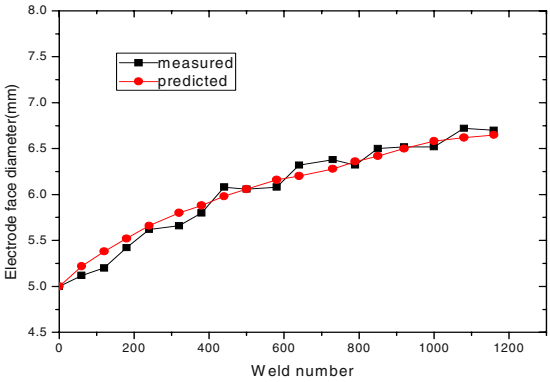

(a) Galvanized steel A

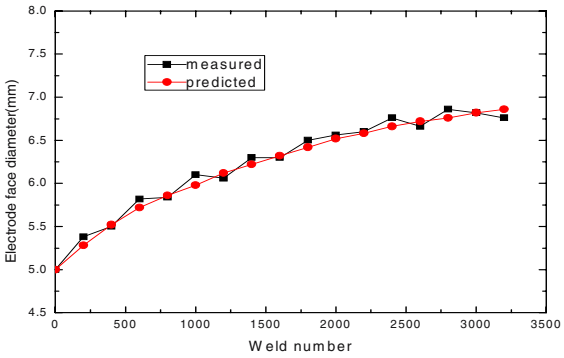

(b) Galvanized steel B

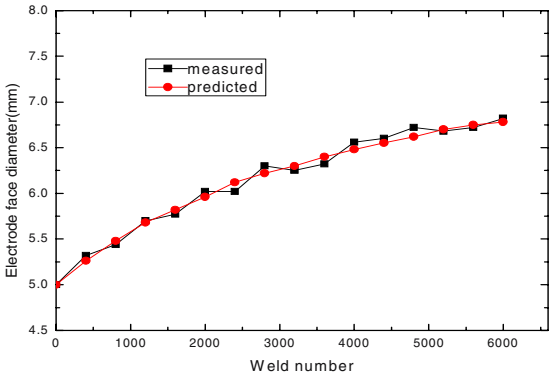

(c) Galvanized steel C

Fig. 6. Estimation of electrode face diameter for different steels

5 Conclusions

A mathematics model was established to estimate electrode face diameter online by applying the new characteristic that servo gun can detect axial wear online in resistance spot welding. The main conclusions were as follows:

1. The measurement precision of servo gun improved from 20um to 10um after compensating the transmitting error, which can meet the requirement of axial wear measurement.
2. Different galvanized steels were used in electrode life tests to verify the model. It was shown that the prediction results of the model agreed well with the experiment results.
3. The model revealed that higher welding current and electrode force would accelerate electrode wear and higher electrode wear rate would be induced at the earlier welds for a less electrode face diameter.

Acknowledgements

The project is funded by National Nature Science Foundations of China (NO. 50575140)

References

1. R.holiday,J.parker, N.T.Williams(1996) Relative contribution of electrode tip growth mechanisms in spot welding zinc coated steels. Welding in the World 37(4):186-193
2. K L Chatterjee, W Waddell (1996) Electrode wear during spot welding of coated steels. Welding & Material Fabrication (3):110-114
3. D.Bracun, J.D.iacl, I.Polajnar, J.Mozina(2002)Using laser profilometry to monitor electrode wear during resistance spot welding. Science and Technology of Welding and Joining 7(5):294-298
4. Wei Li (2005) Modeling and on-line estimation of electrode wear in resistance spot welding. Journal of Manufacturing Science and Engineering (11):709-717
5. Zhang Xu-Qiang, Chen Guan-Long, Zhang Yan-Song(2005) Character analysis of servo gun technology in resistance spot welding process. Transactions of China Welding Institution 26(6):60-64
6. He Tang (2000) Machine mechanical characteristics and their influences on resistance spot welding quality. Philosophy Doctor Paper of Michigan University.
7. ABB (2002)ABB Flexible Automation for Savings With Servo Guns. ABB Corporation report (9)
8. K.C.Wu(1968)Electrode indentation criterion for resistance spot welding. Welding journal (10):472-s-478-s
9. S. FUKUMOTO, I. LUM, E. BIRO, D. R. BOOMER(2003) Effects of Electrode Degradation on Electrode Life in Resistance Spot Welding of Aluminum Alloy 5182. Welding Journal (11):307-s-312-s
10. P.DONG, M.V.LI, AND M.KIMCHI (1998) Resistance spot welding electrode wear on galvanized steels. Science and Technology of Welding and Joining 3(2):59-64

Numerical Simulation and Control of Robot Welding Deformation of Five-Port Connector

Chen hua-bin, Xu Tao, Chen Shan-ben, and Lin Tao

Institute of Welding, School of Materials Science and Engineering, Shanghai Jiaotong University, Shanghai 200030, China
hbchen@sjtu.edu.cn

Abstract. The unfitness of weld and gap variation are salient using traditional TIG procedure for the five-port connector flange. Insufficient reliability and the instability of the weld are catastrophe, which cannot accommodate to new generation type production's requirement. In this study, a finite element model of the five-port connector was built and the distribution of temperature field and deformation were studied. The result shows that welding thermal cycle is greatly different from the ordinary butt weld during welding of the flange and spherical shell. The welding deformation is complex from the direction of UX and UZ. Especially maximum deformation from the direction of UZ is about 4.96mm .According to the result, the optimum welding fixture is designed on the view of the smallest deformation, to critically control the deformation of the both sides of the welding line, finally to accomplish the robotic flexible welding.

1 Introduction

In the spaceflight industry, thin-walled structure occupy sizable proportion，which belongs to important component. Because of non-uniform thermal expansion and shrinkage，Deformations of a welded work-piece would be occurred, then directly affected manufacturing quality and service deadline of the welding product [1-3]. If the distortion of the structure can be predicted accurately for the complex weld, the optimum welding fixture and procedure scheme is designed on the view of the smallest deformation. It can greatly improve efficiency and critically control the welding deformation of the both sides. However, how to predict and control the welding deformation has become an urgent problem further [4-8].

In this paper, thermal elastic-plastic FEM (Finite-Element-Method) was used to analyze the five-port connector of the rocket. At the same time, the accuracy and iterative convergence speed, which occurred in dealing with the complex, weld structure, corresponding material attribute reduction and computation techniques had been improved. The optimum welding procedure scheme is designed on the view of the smallest deformation, which satisfied the accurate prediction and controlling for the arc welding.

T.-J. Tarn et al. (Eds.): Robot. Weld., Intellige. & Automation, LNCIS 362, pp. 203–209, 2007.
springerlink.com

2 Model of the Flange Weld

2.1 Finite Element Model

In the numerical simulation of the five-port connector for LF12 aluminum alloy, it is assumed that the base metal is the same as the welding materials during welding. The spherical shell is 450mm in diameter, 3mm in thickness, in which uniformly distribute four flange holes along the radial direction of 38°（Fig.1）. The flange hole is 180mm in diameter, which weld by one side. The AC ampere and voltage used for welding were 150A and 15V.

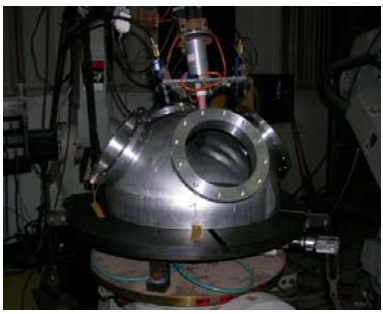

Fig. 1. Five-port connector used in experiment

In this paper, hemispheric Gauss thermal model was adopted. Equation(1)can be represented GTAW moving thermal model. Where Q is the instant heat applied to the work piece; x,y,z are the half axis.

$$q(x,y,z)=\frac{6\sqrt{3}Q}{\pi^{3/2}abc}\exp(-3(\frac{x^2}{a^2}+\frac{y^2}{b^2}+\frac{z^2}{c^2})) \tag{1}$$

During welding process, elastic-plastic deformation would be occurred according to the equation(2).The relations between displacement $\{d\delta\}$ and strain $\{d\varepsilon\}^e$ increment are shown as follows:

$$\{d\varepsilon\}^e=[\mathrm{B}]\{d\delta\}^e \tag{2}$$

where [B] is the elastic-plastic matrix，which is related with the linear expansion coefficient and yield strength [9].

2.2 The Material Properties

The reliability of material properties should be validated. According to the above discussion, part of the adoptive parameter is quoted from the document [10-11]. The properties at elevated temperatures are obtained by through bilinear interpolation in this paper.

Figure 2 shows a simulated model. A computational model using a finite difference analysis was appropriately modified to investigate the reliability of the material properties. Using RS232C universal meter, the temperature in the HAZ was measured with special designed USB interface. Numerical calculations were consistent with the measured value.

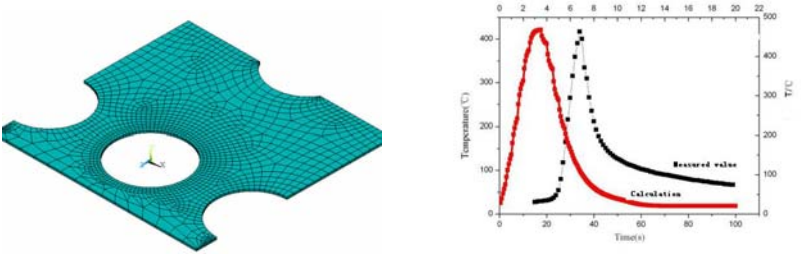

Fig. 2. Model of sample in ANSYS and comparison of temperature between calculations and measured value

3 Simulation Result of the Welding Process

3.1 Simulation Result of the Welding Temperature Field

Fig.3 shows dynamic three-dimensional temperature field of 1s and 10s.From the distribution of the temperature field, the weld temperature field varied from the moving heat source. Owing to the difference of the boundary condition for heat dissipation, peak temperature will continuously change. When loading time is at 1s, the temperature of the local weld is very high and the gradient is also great. The result is similar to the actual welding process. When the heat source moved, heat dissipation for the flange hole is contributed to the badly heat-dispersed condition. As a consequence, the loading time is conducted at 10s, which make the temperature gradient maximum. Considering the thermal conduction, the heat transfer between work-piece and atmosphere, weld metal undergo the rapid heat rating.

In the numerical model, three test points on the spherical shell were chosen to study how to recognize the happening of the local temperature distribution. These points were chosen at the different location of the weld. Figure 4 represents the thermal recycle curve between calculation and measured value. The varied trend of temperature is uniformed.

From the above-mentioned simulation results, the peak temperature of the weld zoon is occurred at the position of the badly heat-dispersed condition. Because of the superposition of the arc starting and end welding, the initial welding position undergoes twice obvious thermal recycle.

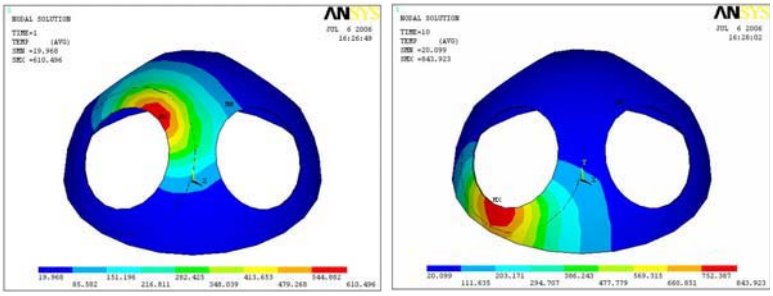

Fig. 3. Distribution of temperature field

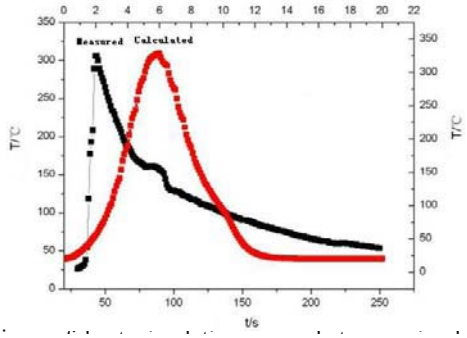

Fig. 4. Comparison of heat circulation curve between simulation of welding five-port connector and experimentation

3.2 Simulation Result of the Welding Deformation

A non-linear transient thermal analysis is performed to predict the temperature history of the whole domain. In order to ensure correct loading, the finite element model for both thermal and structural analysis is the same except for element type.

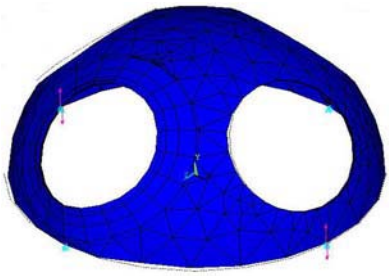

Fig. 5. Welding deformation of spherical shell

For structural analysis the element type is the SOLID45. with three translational degrees of freedom a t each node.The results of the thermal analysis are applied as a thermal body load in a non-linear transient structural analysis to calculate deformation and stresses. The minimal step is set to 0.0001s. According to the simulation of the result, thermoplastic behavior was analyzed. Especially, the whole structure from the direction of UX and UZ was conducted under the free condition. In order to investigate the deformation, 2-time magnification was used to the model.

It can be seen from Fig.5 that there is an obvious deformation in or near the flange weld. Dash line indicates non-deformed profile. The uneven contraction appears along the radial direction of the flange hole. Because of the different thickness between spherical shell and flange, the distribution of the residual plastic strain is asymmetric. Consequently, there will be elliptical deformation on the flange hole. Results of axial displacement (UZ) on the flange hole from the radial direction have been testified. These asymmetric residual compressive stresses cause axial displacement near the weldment.

In Fig.6, the axial displacement for the UZ direction that is located on the weldment. From the figure, it can be easily seen that there is a jump in the deformation diagrams in points No.2. The magnitude of the jump in the c with the further decrease in temperature, the plastic deformation reduces 0.77mm after the elastic limit. The magnitude of the deformation is relative low in the weld start position owing to the restrain from the top spherical shell. It is observed that there is twice elastic deformation in the initiation arc.

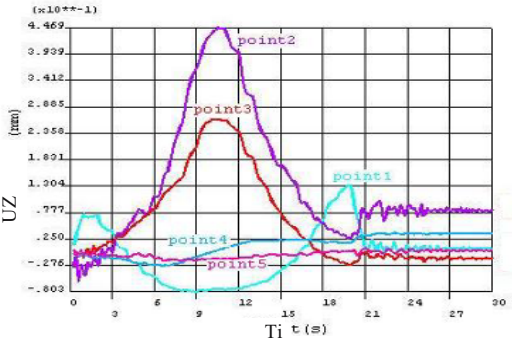

Fig. 6. UZ displacement

In the experiment contraction appears and the maximum deformation measured 1.0mm in the bottom spherical shell (Fig.7). The flatness of the bottom spherical shell indicated “M” in shape. The residual compressive stresses cause contraction in the flange hole along the radial direction.

According to the simulation result of the five-port connector, controlling the deformation from two aspects follows as: (1) the adjustment of the welding procedure ; (2)the design of the optimum welding fixture on the view of the smallest deformation.

As the arc proceeds, the welding gap varied constantly due to the contraction of the solidifying welding bead. The flange weld is divided into four sections and the welding sequence follows as Fig.8.

The design scheme of “Sandwich” type will be applied to the welding process device. It is directly fixed on the robot modified gear. While the spherical manipulator would be used to push against the inner surface of the spherical shell, it could be controlling the contraction.

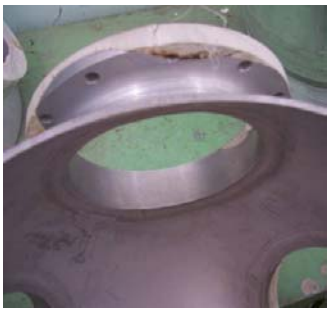

Fig. 7. Workpiece of five-port connector

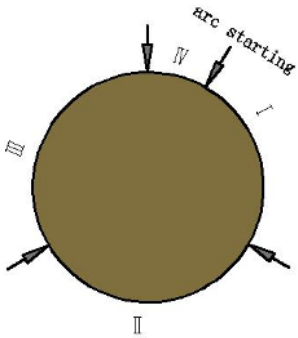

Fig. 8. Welding sequence

4 Conclusions

This model is useful to study the thermal and mechanical behaviors of structures during the welding process, and also is useful to optimize the welding procedure.

1）The initial welding position undergone twice obvious thermal recycle that is different to conventional butt welding. The great temperature gradient appeared on the bottom of the spherical shell.

2）During welding proceed, the distribution of the temperature field varied constantly owing to the differential heat dissipation boundary condition and resulted in the asymmetric residual stressed distribution. Tensile stress occurred around the weld and the compressive stresses were produced on bottom of the spherical shell.

3）The maximum elastic deformation for point No. 2 is 4.96 mm, which is just identical with actual welding process. In order to critically control the deformation of the both sides of the welding line, the design scheme of “Sandwich” type is applied to the welding process device.

Acknowledgements

This work is supported by Key Foundation Program of Shanghai Sciences & Technology Committee under Grand No. 06JC14036 and the Key Foundation Program of Shanghai Sciences & Technology Committee under Grant No. 06JC14036.

References

1. C.L. Tsai, S.C.Park, W.T. Cheng, Welding distortion of a thin-plate panel structure ,Weld.J., Res.Suppl.1999(78):156s-165s.
2. Lin YC, Chou CP. A new technique for reduction of residual stress induced by welding in type 304 stainless steel. J Mater Process Technol 1995;48:693–8.
3. Goldak J, Chakravarti A, Bibby M. A new finite element model for welding heat sources. Metall Trans B 1984;15B: 299–305.
4. V. Kamala, J.A. Goldak, Error due to two dimensional approximations in heat transfer analysis of welds, Weld. J. 76 (9) (1993) 440s–446s.
5. Goldak J, ChakravartA, BibbyM. A new finite element model for welding heat source[J]. Metallurgical TransactionsB, 1984, 15：299 – 305.
6. Lindgren LE, Hedblom R. Modeling of addition of filler material in large deformation analysis of multipass welding. Common Number Methods Eng 2001;17:647–57.
7. Lindgren LE. Finite Element Modeling and Simulation of Welding Part 1: Increased complexity. J Therm Stress 2001;24:141–92.
8. Tso-Liang Teng, Peng-Hsiang Chang, Hsush-Chao Koc. Finite element analysis of circular patch welds[J]. International Journal of Pressure Vessels and Piping, 2000,7(11): 643-650.
9. Andersen, L., Residual Stresses and Deformations in Steel Structures, PhD. thesis, Technical University of Denmark, 2000.
10. Goldak J, Bibby M, Moore J, House R, Patel B. Computer modeling of heat flow in welds. Metall Trans B 1985;17B:587–600.
11. M.R. Nami, M.H. Kadivar, K. Jafarpur, Three-dimensional thermal response of thick plate weldments: Effect of layer-wise and piecewise welding, Model. Simul. Mater. Sci. Eng. 12 (2004) 731–743.

3D Reconstruction of Welding Environment Based on Spacetime Stereo

Z.M. Liang, H.M. Gao, Z.J. Wang, X.H. Yu, and L. Wu

National Key Laboratory of Advanced Welding Production Technology, Harbin Institute of Technology, Harbin 150001, P.R. China
zmliang@hit.edu.cn

Abstract. In this paper, a technique for 3D reconstruction of welding environment is presented in order to improve the intelligence of welding robot. Based on the novel framework of spacetime stereo, the technique can be viewed as a combination of structured light and traditional stereo vision. To overcome the problem in stereo matching of the untextured object in the welding environments, a series of light pattern is designed to add artificial "texture" onto the surface. The result of experiment shows that the technique is a promising means to reconstruct the completely unstructured welding environment.

1 Introduction

In order to execute the welding tasks which are too dangerous (or even impossible) for human, such as nuclear components maintenance, space assembly, underwater structures construction or repair, welding robot system should be developed to replace human to perform these tasks. The techniques of teleoperation and telerobot have appeared in the early 1970s, in which human operator is always in the control loop, making the decision and defining the control strategies for the manipulation at distance. But when the techniques of teleoperation and telerobot are used to perform the welding task, we encountered many difficulties. Unlike the task of simple assembly or grasp which can execute slowly and try many times, the welding process is inherent difficult to control. There are many parameters to control in real time welding for the purpose of getting a high quality weld seam, including the weld torch position and pose, welding speed, weld current, arc length etc. However, it is impossible for a human to control all these parameters, so a high level automation welding technique should be developed. Off-line programming for weld robot is a feasible way to promote the automotive level of robot welding, but the 3D model of the weld work-piece and the position relative to the weld robot in the environment is prior needed.

Further, the welding system should be moved into the workspace from outside, during which it is also necessary to use some sensors to recognize or reconstruct the 3D environment for path planning and obstacle avoiding. So it is very important to design a 3D sensor for sensing the welding environment and the position and shape of the workpiece to be welded.

On the other hand, the weld industrial robots have been widely used in many fields at present, but most of them serving in practical are still "teaching and playback" type. Most sensors available are to track the weld seam, which is effective when the

T.-J. Tarn et al. (Eds.): Robot. Weld., Intellige. & Automation, LNCIS 362, pp. 211–218, 2007.
springerlink.com

work pieces are accurately placed or within little error. If the conditions (shape or position) of the weld piece are changed, the robot must be taught again. In order to resolve the problem, intelligent welding robot must be developed which has the ability to perceive 3D information of the workpiece and its environment.

To get the 3D information of the welding workpiece and its environment, lot kinds of techniques for 3D reconstruction are available. While structured lighting is a very attractive alternative to stereo vision, and has lower processing requirements for each image, it requires acquisition of many image frames to achieve high resolution in contrast to stereo vision, which provides dense, high-resolution data from a single stereo pair. Further, the stereo vision is very suitable for human supervision, which is need for generality and enables efficient handling of unstructured circumstances. However, the problem of stereo vision is the stereo matching. In the welding application, the problem becomes more difficult because the welding workpiece and the environment are typical untextured, resulting ambiguous matching results. A promising method is to combine the structured light and the stereo vision, in which the structured light is used to add artificial "texture" onto the object. In fact, researchers have used the active illumination to ease the stereo matching process, but the means are not very effective. In [1][2], the random active illumination is used to add "texture", however, only one light pattern is projected. As a result, the stereo matching problem is still not well solved and ambiguous matching still exists. Some researchers used the structured light to help to solve the stereo matching process. However, the stereo matching process was done by the same way as in the structured light field, first feature detecting then matching, or decoding a series of light projected image. So the disadvantage of structured light technique remained.

Recently, James[3] and Zhang[4] almost simultaneously presented a new technique called spacetime stereo, which used active illumination to add "texture" and found the correspondence by minimizing the sum of SSD(sum of squared difference) of images sequences acquired at different times. The spacetime stereo is a novel framework for combination the stereo vision and structured light and is a feasible technique to resolve the problem of stereo matching for welding environment. In this paper we present a technique based on spacetime stereo.

The rest of the paper is organized as follows. In Section 2, a brief literature review on 3D sensing of welding environment is given. In Section 3, the principle of spacetime stereo is introduced. The design of the structured light pattern is discussed in Section 4. And finally the experiment result is shown in Section 5.

2 Related Works of 3D Sensing of the Welding Environment

Some works have been done to enable 3D perception of welding robot.

Kim [5] developed a vision sensor using active laser range finder to sense and recognizes the three-dimensional space for welding environment map building. The sensor consisted of two cameras and three laser diodes and was mounted on a robot arm. In his system, a combination of a camera and two laser diodes among them was used for environment sensing; and a combination of the other was for the weld seam tracking. But it was slow to scan the whole environment by the sensor.

Chen [6] used a camera mounted on the weld robot to acquire the 3D information of the weld seam using stereo vision technique. However, only the position of weld seam is not enough for the off-line programming because the shape of the work piece is also important to optimize the weld torch orientation. Jin [7] used stereo vision for path planning of welding robot, in which natural light was adopted. Because of the untextured surface of the welding workpiece, the result was not accurate. Wang [8] developed a multi-baseline stereo system, which consisted of four verging configured cameras to reconstruct the 3D surface of the workpiece. In wang's work, active illumination was also applied to ease the stereo correspondence problem of the textureless region of workpiece. However, because of poorly designed light pattern, only sparse disparity map was obtained by feature matching.

To our knowledge, dense 3D reconstruction technique which can reconstruction both the welding workpiece and its environment is rarely used in welding automation. Most of the 3D sensors only perceive the local information around the weld seam. However, in remote welding and high level automatic welding, the global perception of both weld workpiece and its environment is needed.

3 The Principle of Spacetime Stereo[3,4]

The spacetime stereo framework can be understood naturally as a generalization of traditional passive stereo methods that operate entirely within the spatial domain. Traditional stereo finds correspondence pixels by comparing spatial neighborhoods around candidate pairs of pixels in the two images. Spacetime stereo simply adds a temporal dimension to the neighborhoods for stereo matching.

Spacetime stereo takes two rectified image sequences $I_l(x, y, t)$ and $I_r(x, y, t)$ as input. To recover the 3D structure, we wish to estimate the disparity function $d(x, y)$ for each pixel (x, y) for all time. Traditional stereo algorithms solve for $d(x, y)$ at some position and moment (x_0, y_0, t_0) by minimizing the following cost function

$$E(d_0) = \sum_{(x,y)\in W_0} e(I_l(x, y, t_0), I_r(x - d_0, y, t_0)) \tag{1}$$

where d_0 is shorthand notation for $d(x_0, y_0, t_0)$, W_0 is a spatial neighborhood window around (x_0, y_0), $e(p, q)$ is a similarity measure between pixels from two images, and the disparity is measured in the left image with respect to the right image. The size of W_0 can vary from being a single pixel to any other number of neighborhood.

Unlike some structured light techniques to decode the projected light patterns, spacetime stereo simply temporally sums up the correlation or error measures of all frames to directly compute the stereo disparities. It seems like searching the best correspondence in 3D window. Suppose that the scene is static for a period of time $T_0 = [t_0 - \Delta t, t_0 + \Delta t]$, we can extend the spatial window to a spatiotemporal window and solve for d_0 by minimizing the following sum of SSD (SSSD) cost function:

$$E(d_0) = \sum_{t \in T_0} \sum_{(x,y) \in W_0} e(I_l(x, y, t), I_r(x - d_0, y, t)) \tag{2}$$

This cost function reduces matching ambiguity in any single frame by simultaneously matching intensities in multiple frames.

The spacetime stereo framework has many advantages over current 3D reconstruction technique such as robust and accurate dense disparity calculating, simply and effective implementation, being able to deal with large untextured region, and so on.

4 Structured Light Pattern Design

Although James [3] showed that the spacetime stereo can obtain good results even using long unstructured light illuminating image sequences, we argue that using carefully designed light pattern can get more precise disparity using short image sequences.

In this section, the design of the projected structured light pattern is discussed. The objective is to obtain a dense depth map with potentially high speed and accuracy. The light pattern design is the key component for structured light technique. Many light patterns appear in the literature, but the correspondence process is always based on feature detecting or decoding. In spacetime stereo, however, all information used is the sum of square difference, so the light pattern design is different from structured light field.

When designing the light pattern for spacetime stereo, there are some issues to be considered.

1. Discrete feature or continuous texture

   The discrete feature may be useful for feature based matching. However in order to get reliable dense disparity map, only discrete feature in the pattern is not enough. A series of image sequence containing continuous textures are needed to get reliable and dense disparity map.
2. What kinds of textures to be used?

The texture model should contain abundant intensity variation to increase the precision of matching. However, due to the limited intensity space (e.g. only 0 ~255 intensity levels in each color component), a repeated arrangement of a certain texture is necessary in order to have more accurate matches. The color light pattern is not recommended to use because it is sensitive to the surface characteristic. Only gray lights are used, which make the pattern suitable for colored surface object.

We need not design the texture changes in both the horizon and vertical direction. During stereo matching, the process goes along the epipolar line. In our system the epipolar line is nearly horizon, so the designed structured light changes only in the horizon direction. In order to avoid ambiguous matching, the change of the intensity should be monotone decreasing or increasing. We choose the saw-tooth light pattern in our experiment.

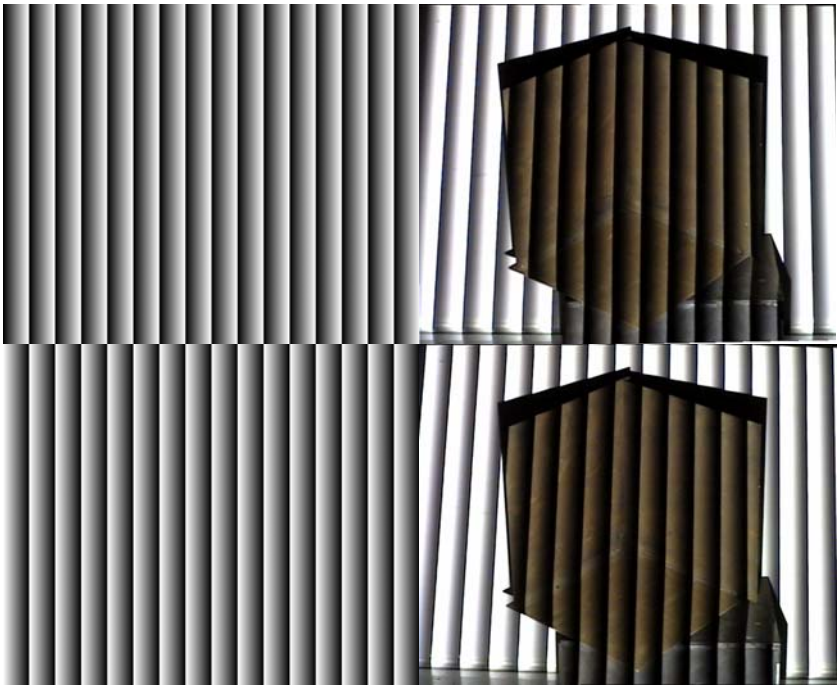

Fig. 1. The light pattern and a captured image pair of a test weld workpiece with the light pattern projecting

3. How does the series of light pattern cooperate together?

In our technique, the width of the succeeding light pattern's "saw" is half of its previous one. When projected on the object's surface, the widest length of the light stripe in image should slightly wider than the disparity searching range. In order to reduce the unbalance influence during the image formation, both the light pattern and its reverse are used.

Figure 1 shows one pair of the light pattern and the real images when the light pattern is projected into the scene. In fact, following the rules mentioned above, many other light patterns can be designed.

5 Experiment and Result

A simple and low cost prototype system, which consists of two cameras and a video projector as shown in figure 2, has been built to validate the technique. The two cameras are synchronized with respect to one another. The resolutions of the images captured by cameras and the video projector are 768*576 and 1024*768, respectively. The projector is placed in front of the cameras to add active light into the scene.

Fig. 2. The prototype system with two cameras (left) and a video projector (right)

At first, the stereo camera is calibrated. The intrinsic parameters of a stereo system characterize the transformation mapping of an image point, from the camera coordinates to the pixel coordinates. The extrinsic parameters describe the relative position and orientation of the two cameras. The two cameras in a stereo system can be calibrated simultaneously, or separately, one at a time. In our experiment each camera is calibrated using Zhang's Method [9]. Then the extrinsic parameters are calculated using nonlinear iterative optimizing.

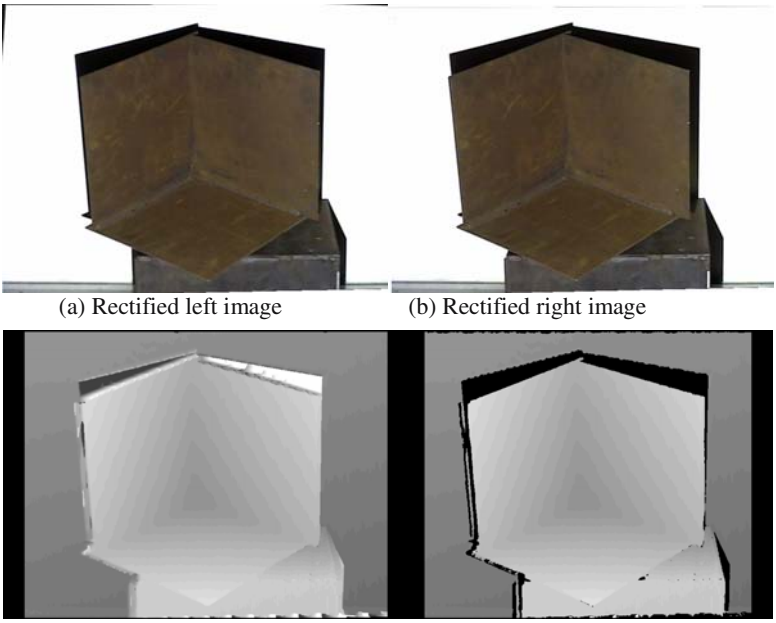

(a) Rectified left image (b) Rectified right image

(c) Initial disparity map (d) Final disparity map

Fig. 3. An example of 3D reconstruction of welding environment. (a) and (b) is the rectified left and right image with white light illumination.(c) shows the initial result of disparity map calculating, (d) is the disparity map after removing of the unreliable regions.

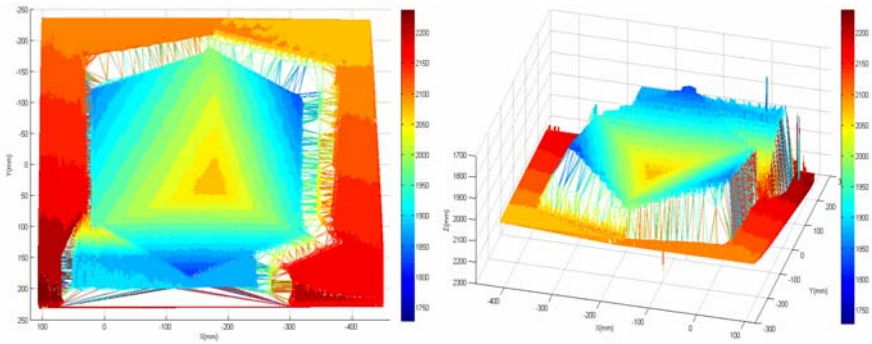

(a) Depth triangulation mesh from view point 1

(b) Depth triangulation mesh from view point 2

Fig. 4. 3D reconstruction result of the scene. (a) and (b) illustrate the 3D reconstruction result after Delaunay triangulation mesh generation from two viewpoints.

Using projection matrices of the left and the right cameras obtained in camera calibration, we rectify stereo images by the technique investigated by Fusiello[10]. Because the two cameras are nearly parallel, the linear algorithm is effective and accurate. Figure 3(a) and Figure 3(b) show a rectified image pair with white light projection.

After rectification, stereo matching is processed between the two image sequences. We used eight image pairs and the size of the spatial window is 7*7. The origin disparity map is showed in Figure 3(c).The intensity of the pixel in the disparity represents the depth of the point from the camera, the brighter the nearer. Some regions in the disparity map are obvious wrong due to occlusion, the shadows and surfaces where we can not add “texture”. We have developed an algorithm to detect these regions, which will be present in another paper. Figure 3(d) shows the result after unreliable region removed.

Figure 4(a) and Figure 4(b) show the 3D reconstruction result after triangulation mesh generation using Delaunay algorithm.

6 Conclusion

In this paper we have developed a new technique for 3D reconstruction of weld environment and weld workpiece based on spacetime stereo. Usually, the stereo matching is the most difficult problem in traditional stereo vision, particularly in the untextured environment such as the welding environment. Based on the novel framework of spacetime stereo, the stereo matching problem is solved by active projecting a series of carefully designed light pattern. We believe that the technique for 3D reconstruction can dramatically improve the automation level of robot welding.

References

1. Siebert JP (1990) Active stereo: Texture enhanced reconstruction. Electronics Letters 26(3):427-430
2. Cardenas-Garcia JF, Yao HG, Zheng S (1995) 3D reconstruction of objects using stereo imaging. Optics and Lasers in Engineering 22(3):193-213
3. James D, Diego N, Ravi R, Szymon R (2005) Spacetime stereo: A unifying framework for depth from triangulation. IEEE Transactions on Pattern Analysis and Machine Intelligence 27(2):296-302
4. Zhang L, Curless B, Steven SM (2003) Spacetime stereo: Shape recovery for dynamic scenes. Proceedings of the IEEE Computer Society Conference on Computer Vision and Pattern Recognition, pp II/367-II/374
5. Kim MY, Cho H (2004) Three-dimensional map building for mobile robot navigation environments using a self-organizing neutral network. Journal of Robotic Systems 21(6):323~343
6. Chen SB, Chen XZ, Qiu T, Li JQ (2005) Acquisition of weld seam dimensional position information for arc welding robot based on vision computing Journal of Intelligent and Robotic Systems: Theory and Applications 43(1):77-97
7. Jin JM.(1996) Path planning of robot arc welding. PhD dissertation Tsinghua University
8. Wang ZL, Cai HG (2001) Research on active multibaseline stereo vision and its application to robot welding techniques. Gaojishu Tongxin/High Technology Letters 11(4):82-85 Language: Chinese
9. Zhang ZY (2000) A Flexible New Technique for camera calibration. IEEE Transactions on Pattern Analysis and Machine Intelligence 22(11):1330-1334
10. Fusiello A, Trucco E, Verri A (2000) Compact algorithm for rectification of stereo pairs. Machine Vision and Applications 12(1):16-22

Measurement for Three Dimensional Surface of Welding Pool in GTAW Welding

J.F. Wang, L. Zhou, and S.B. Chen

Institute of Welding Technology, Shanghai Jiaotong University, 200030 Shanghai, P.R. China
jf_wang@sjtu.edu.cn

Abstact. Welding pool deformation has a close relationship with the backside bead width, so pool surface shape sensing is used to monitoring and control weld quality, specifically of weld penetration. In this paper, several three-dimensional (3D) reconstruction techniques is analyzed, which were used to reconstruct 3D shape of welding pool. The direct method obtain clear image of pool, so the reconstruction accurate is high. As an indirect method, three SFS algorithms are implemented. Some improved measures are: modeling welding reflection map; new constraint equations; image pretreatment. 3D shape of welding pool was reconstructed and validating results showed this technique can be applied practically.

1 Introduction

During gas tungsten arc welding(GTAW), complicated phenomena occur on the weld pool. However, a skilled operator can estimate and control the welding process based on pool observation. This implies that we can judge whether or not it is good quality if we can detect information about pool parameters. To this end, extensive studies have been done to explore the possibility of indirectly measuring weld pool characteristics based on pool oscillation, infrared radiation, ultrasound, radiography, and so on. Compared with these methods, direction observation of the weld pool may provide more instantaneous and accurate information. For GTAW without filler, pool surface deformation is apparent in the full penetration mode. In the case of partial penetration, three modes of pool deformation can be observed for different current levels. Thus, the deformation of the pool surface is an inherent characteristic of arc welding processes. Furthermore, the observation discovered that the average weld depression depth, which is defined as the cross weld depression area divided by the width, has a close relationship with the backside bead width in the full penetration[1]. Based on this theory, it is possible to control the fusion state of fully penetrated welds in GTAW welding, if we can obtain and control weld depression degree. Presently, three-dimensional image reconstruction techniques are classified into direct and indirect methods. Achievements in these areas have a major impact on computer vision research. In this paper, a major task is the analysis of used methods in three-dimensional shape reconstruction of welding pool, which is important for the monitoring and control of weld quality and consequently the reliability of joint.

T.-J. Tarn et al. (Eds.): Robot. Weld., Intellige. & Automation, LNCIS 362, pp. 219–225, 2007.
springerlink.com

2 Three-Dimension Measurement Technique

2.1 Direct Methods

Direct or active methods recover depth information directly using a range finder and structured light. Most of these methods use the triangulation principle where a structured light source is directed on to the object's surface.

R.Kovacevic and Y.M.Zhang[2] devised a novel mechanism for observing the pool surface shape. Laser stripes projected through a grid are reflected from and deformed by the mirror-like pool surface, as shown in Fig.1a. The shape features of the weld pool surface are clearly shown by the reflection pattern, in Fig.1b.

During the laser pulse, the laser intensity is much stronger than the arc intensity, and the arc influence in weld pool observation is essentially eliminated. When laser is used to illuminate the weld pool surface, the corresponding reflected rays are completely determined by the slope of the weld pool interface and the point where they hit the weld pool. By tracking the reflected rays and computing the slope field of weld pool surface the three-dimensional weld pool shape can be determined.

A apparent advantage of this method is pool image is clear without time delay, because laser light intensity is far greater than arc light. So it is accurate in reconstruction size. Comparing with its advantage, its disadvantage is yet apparent, that is, equipment complexity, volume large and costliness.

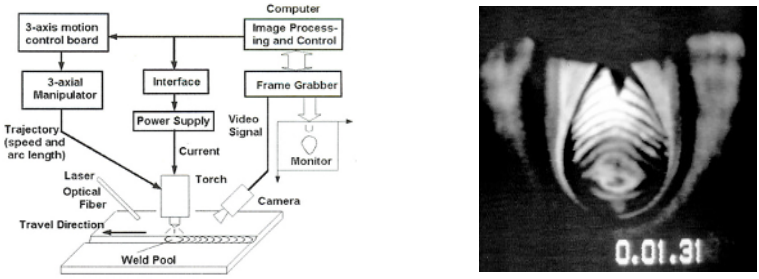

(a) System set (b) weld pool image

Fig. 1. Schematic of sensing of weld pool using structural light system

2.2 Indirect Approaches

Indirect methods determine the relative depth by cues extracted from grey-level images of an observed object. As descried previously, the direct techniques usually involve the complicated installation of various external components, so they may not be suitable for the estimation of real-time variations in shape. Many researchers have focused on indirect methods, shape from different cues as the generalized class of these indirect methods. These cues can be shading, texture, focus, and stereo vision.

However, the object under test may not have sufficient texture information for weld pool, so texture is not suitable for our goal. Focus approach involves the mechanical movements of either the lens or the image plane for each individual point, with a low efficiency and with accuracy limited by the resolution of mechanical movements [3]. Stereo approach need two or more viewpoints (or CCD), restricted it only applying in simply structure; because weld pool shape is dynamic changing, which lead it difficulty to search match elements.

At the present, the researchers mostly could pay a attention to applying SFS in welding, so we should analyze three practical applying algorithms.

3 Shape from Shading

Shape-from-Shading (SFS) is a technique of recovering 3D information from variation of shading on the image, first introduced by Horn in the 1970s. In order to better understand this approach, it is necessary to introduce how the images are formed. A simple model of image formation is the Lambertian model, in which image gray level (or irradiance) at a pixel as a function of the surface orientation of the corresponding scene point is captured in a reflectance map. Thus, for fixed illumination and imaging conditions, and for a surface with known reflectance properties, changes in surface orientation translate into corresponding changes in image gray level. The inverse problem of recovering surface shape from changes in image intensity is known as the shape from shading problem. The relationship is given by

$$I = R(p,q) \tag{1}$$

Where $R(p,q)$ is the reflectance map of the surface point (x,y), $p = p(x,y) = \frac{\partial z}{\partial x}$, $q = q(x,y) = \frac{\partial z}{\partial y}$, z is surface depth, I is the normalize image gray level at corresponding point However, we have a nonlinear equation with two unknowns. Therefore, finding aunique solution to SFS is difficult; it requires additional constraints. Extensive study and approaches were reported to solve this solution. Ruo Zhang [4] divided these approaches into four groups: minimization, propagation, local and linear. Comparison experiments showed that minimization approaches are more robust. So the SFS techniques applying in welding are all based on minimization theory. Following section will discussion them respectively.

3.1 Zhao Dongbin[5]

Zhao Dongbin firstly introduced SFS technique into welding field. The total reflection consisted two parts, that is,

$$f = \beta_d f_d + \beta_s f_s \tag{2}$$

Where, f_d and f_s is diffuse and specular reflection function, β_d and β_s is diffuse and specular reflection coefficient. Reflection model is,

$$R(p,q) = R(i,n,v,r) = \begin{cases} g\frac{I_0}{r^2}(v^T n_z)^4(\beta_d(i^T n) + \\ \beta_s \frac{\exp\{-k[\cos^{-1}(h^T n)]^2\}}{(i^T n)(v^T n)}) + b, & (\mathrm{i^T n}) \geq 0 \\ 0, & \text{otherwise} \end{cases} \tag{3}$$

where, $n = (-p,-q,1)$

A brightness constrain e_b is essential to solve this equation. To improve noise proof, a new constraint e_s is introduced.

$$\begin{aligned} e &= e_b + \lambda e_s \\ &= \iint [(R(p,q) - I(x,y))^2 + \lambda \frac{1}{2}(z_{xx}^2 + 2z_{xy}^2 + z_{yy}^2)]dxdy \end{aligned} \tag{4}$$

The algorithm is implemented using triangular linearization。 Test results show that there are larger errors in the brighter region and smaller errors in the darker region. To overcome this problem, an adjusting factor of brightness is added

$$e_b = \iint w(I)[R(p,q) - I(x,y)]^2 \tag{5}$$

$$e_b = \iint w(I)[R(p,q) - I(x,y)]^2 \tag{6}$$

Where,

$$w(I) = \begin{cases} e^{-(I-150)^2/5000}, I \geq 150 \\ 1.0 \qquad\qquad , otherwise \end{cases} \tag{7}$$

Experiment and reconstruction images is showed in Fig.2

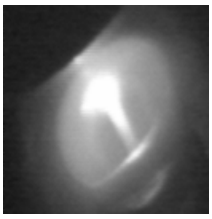

(a) welding pool

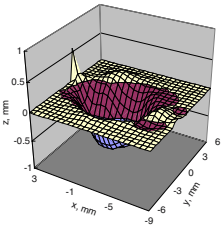

(b) reconstruction image

Fig. 2. Welding pool and its reconstruction

3.2 Li Laiping[6]

By analysis of the distribution of arc light intensity, Li Laiping found that the arc shape is close to the sphere when the current is in background during pulse welding. So he establish a sphere extended light source model, the irradiance of the object surface is,

$$E = \int_0^{\alpha} \int_0^{2\pi} Ed\theta d\phi = C(I_c, \lambda, r, r_s)\cos\theta_n \tag{8}$$

Where $C(I_c, \lambda, r, r_s)$ is a function of welding current, material, arc shape, arc length. Due interreflection exist in pool concave, the total irradiation is,

$$L = \beta_d L_d + \beta_s L_s + \beta_{\text{int } er} L_{\text{int } er} \tag{9}$$

The first term is diffuse, the second term is specular, and the final term is interreflection. The reflection model is,

$$R(p,q) = g(\frac{d}{f})^2 (v^T n_z)^4 L + b \tag{10}$$

The constraint e_s of Zhao Dongbin need second derivative existence, however, common surface just guarantee successive character. Thus, Li Laiping introduce a new constraint,

$$e_v = \iint (z_x^2 + z_y^2) dxdy \tag{11}$$

Final, the total constraint is,

$$e = e_b + \lambda e_s + \mu e_v \tag{12}$$

The algorithm is implemented using pretreatment conjugate gradient based on Lee Kuo's[7].

3.3 Du Quanying[8]

Du Quanying first test several SFS approach, and find that Horn and LeeKuo' both need too much runtime to apply in real-time inspecting; and that Zheng's[9] algorithm is balance accuracy and runtime. So Du take this algorithm and improved it. Reflection model consist both diffuse and specular parts. In constraint equation, an adjusting factor ω of brightness is added, and the intensity gradient constraint is applied instead of a smoothness constraint.

$$e = \iint F dxdy \tag{13}$$

where

where

$$F = \omega[R - I]^2 + [R_p p_x + R_q q_x - I_x]^2 + [R_p p_y + R_q q_y - I_y]^2 + \mu[(p - Z_x)^2 + (q - Z_y)^2]$$

The algorithm is implemented using a hierarchical structure in order to speed up the computation.

To validate, he apply this improved SFS algorithm to the detection of the weld bead shape, as shown in Fig.3. The comparison between the measured points and their reconstructed is shown in Fig.4.

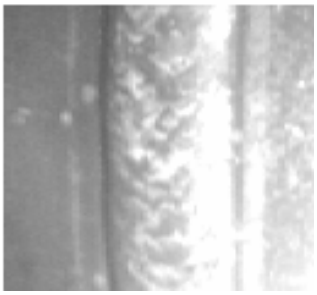

Fig. 3. Image of weld

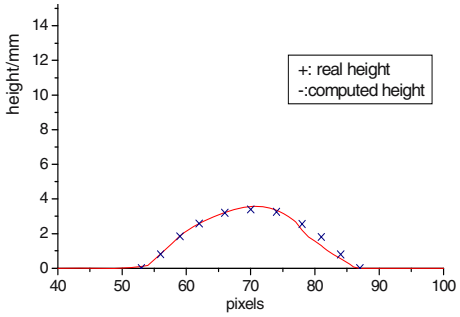

Fig. 4. Compared between reconstructed and measured

4 Conclusion

Several reconstruction techniques recover the 3D description of an object from a single view of the welding pool.

The direct technique used structure lighting to illuminate welding pool, so the image of the welding pool is clearly and the interference from the arc light could be ignored. But this technique usually involve the complicated installation of various external components, they may not be suitable for the estimation of real-time variations in shape.

SFS technique only used one CCD without any external equipment. Three algorithms were improved, and all performed good results in 3D reconstruction of welding pool. And Du Quanying' method was carried out in real-time controlling. However, there are a lot of difficulties when applying SFS technique in welding field. Due to the illuminating is arc light, pool image is interfered even though fixing filter system. These light interference caused the image gray level is not absolutely according with the SFS model, which could bring with error in 3D reconstruction size. In addition, it is difficult to determine illuminant direction and surface albedo. Thus, there are still many factors need to be researched, if we want to take SFS technique to recover accurate 3D welding pool shape.

Acknowledgements

This work is supported by the National Natural Science Foundation under Grand No.50575144 and the Key Foundation Program of Shanghai Sciences & Technology Committee under Grant No. 06JC14036.

References

1. Zhang Y.M (1990) Study of adaptive top-vision control for full penetration in TIG welding. [Doctor thesis] Harbin Institute of Technology.
2. Zhang Y.M (1997) Kovacevic R., Real-time Sensing of Sag Geometry During GTA Welding, ASME Journal of Manufacturing Science and Engineering, 119(5): 151-160.
3. Jarvis,R.A (1976) Focus optimization criteria for computer image processing. Microscope 24,163-180
4. Ruo Zhang, Pingsing Tsai,etc (1999) Shape from Shading: A Survey, IEEE Transactions on Pattern Analysis and Machine Intelligence, 21(8): 690-706.
5. Zhao Dongbin (2000) Dynamic Intelligent Control for Weld Pool Shape during Pulsed GTAW with Wire Filler Based on Three-Dimension Visual Sensing, [Doctor thesis] Harbin Institute of Technology,.
6. Li Laiping (2005) Research on modeling of surface reflectance map and height calculation of pulse GTAW molten pool, [Doctor thesis] Shanhai Jiao Tong University.
7. Lee K.M., Kuo C.J (1993) Surface Reconstruction from Photometric Stereo Images, Journal of Optical Society of America 10(5): 855-868
8. Du Quanying (2006)Extraction and intelligent control of 3D dynamic weld pool shape information of pulsed GTAW with wire filler, [Doctor thesis] Shanhai Jiao Tong University.
9. Q.Zheng and R.Chellappa (1991) Estimation of Illuminant Direction, Albedo, and Shape from Shading,IEEE Trans. Pattern Analysis and Machine Intelligence 13(7):680-702.

Research on the Control Method of Multi-parameter Comprehensive Decision Making for Spot Welding

Y.L. Chang, C. Zhang, Z.C. Wang, B. Lin, and H. Su

School of Material Science and Engineering, Shenyang University of Technolgy, Shenyang 110023, P.R. China

Abstract. Resistance spot welding quality is always one of key subject matters for study to which many welding scholars at home and abroad in the world devote themselves.It has not been solved satisfactorily at present. The complexity of spot welding process, invisibleness of nugget formation and singleness of control method decide that stabilizing quality is a rather difficult task. The limitations of describing how the nugget grows up based on single-sensor information source is analyzed. A control method of multi-parameter comprehensive decision making for spot welding is put forward. The multi-sensor information fusion is adopted for real time monitoring four parameters which are closely concerned with the weld nugget size(welding current, electrode displacement, dynamic resistance, welding time). Information fusion algorithm includes sensor-based weighted average fusion algorithm and knowledge-based production rule fusion algorithm. The spot welding experiments indicate that nugget size fluctuations are within 8%～22% under constant current control, and are within 6%～12.5% under information fusion control. It conforms that the new quality control method can compensate for various factors of influence in the welding process such as shunt, loop inductive reactance variation and electrode wear, etc, and assure the spot welding quality to be stable.

1 Introduction

The resistance spot welding quality is represented by weld nugget size. With the development of industry, the precise measuring and control method is urgently adopted to increase strengh of welding joint in spot welding quality control.

A lot of research work has been done at home and abroad for assurance of weld nugget size, for example, numerical simulation method and finite element analysis using microcomputer in the course of spot welding have been carried out[1,2]. The methods of constant current control,energy integral control,ultrasonic wave monitoring,dynamic resistance control,electrode displacement control,etc have been adopted in spot welding quality control. But all of these control methods have limitations and drawbacks to some extent, and the control effects are not satisfactory. There are three reasons, the first one is that spot welding process is quiet complicated and there are too many factors of influence. Spot welding is a complicated process of multi-factor interaction, the heat input and weld nugget formation have something to do with many welding processing parameters such as welding current, additional current

T.-J. Tarn et al. (Eds.): Robot. Weld., Intellige. & Automation, LNCIS 362, pp. 227–234, 2007.
springerlink.com

pulse(for the heat treatment of preheating or slow cooling),welding time,welding force,electrode face dimension and surface status of workpiece,etc. In addition,the weling process still exists other factor interaction, such as temperature distribution,thermal conduction,force and metallurgic action,etc. So many dynamic coupling and static overlapping factors make analyzing the welding process much more complicated, especially instant of welding process and invisibleness of nugget formation bring about too much difficulty for research work. The second is that nugget size can not be measured directly, the quality estimation is inferred through some parameters[3]. The third is that few parameters are measured and control method is single.

The various spot welding quality control methods coming out continuously from the begaining of 1970's belong to single parameter feedback control mostly, just keep one parameter constant. Limitations exist in these control methods, because single sensor-based information about weld nugget formation is used Rather than the global information. The reasons above decided that quality control is a rather difficult task, it has not been solved satisfactorily.

Multi-sensor information fusion has been paid much attention in recent years, its theory and method have become an important research field of intelligent information treatment. The scholars all over the world put the information fusion technology into their research work[4]. According to the law of weld nugget formation, the information fusion method is adopted to adjust parameters comprehensively and it is one of development directions in spot welding quality control in the future.

2 The Measurement and Control System of Multi-parameter Comprehensive Decision Making for Spot Welding

2.1 Composition of Main Circuit and Control System

The main ciruit adopts the structure of inverse parallel thyristors with single phase 380V AC input. The control system is composed of single chip microcomputer, shown as Fig.1.

It mainly consists of current measurement, electrode displacement measurement, dynamic resistance measurement, error amplifier, characteristic information extraction, multi-information fusion algorithm, PI controller, thyristor drive and amplification circuit, etc.

2.2 Selection and Measurement of Multi-parameters

There are many parameters which are closely concerned with nugget formation in spot welding,such as current,voltage,dynamic resistance,electrode displacement,welding force,welding time,electrode physical dimension,welding base metal,thickness of sheet and so on. It is impossible to measure so many parameters above. Through analyzing the various factors of influence and the law of action on the spot welding quality, the

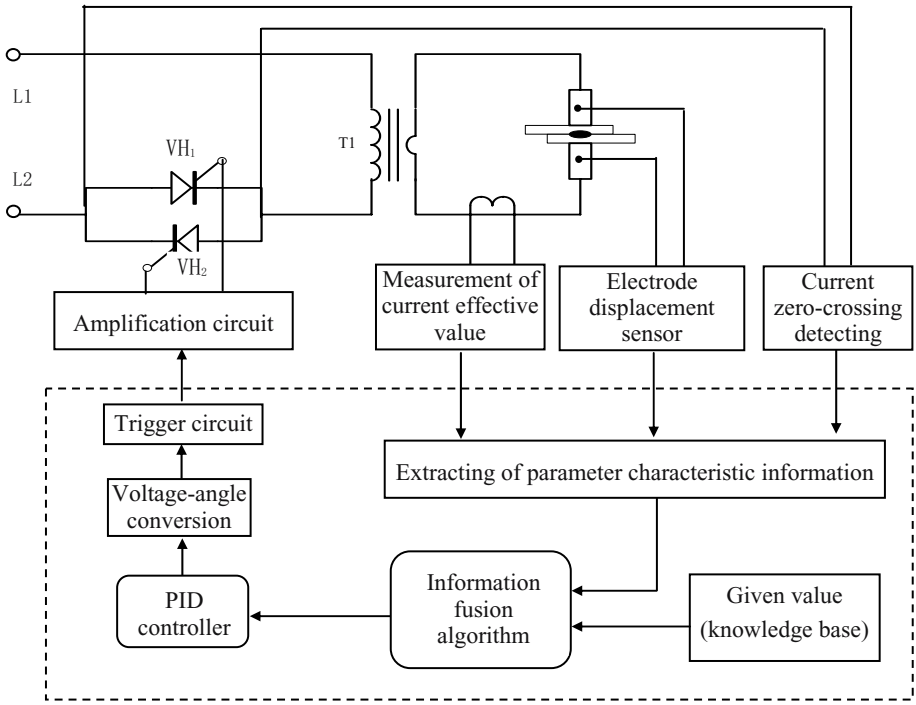

Fig. 1. Diagram of main circuit and contrl system

four parameters which have much more influence on nugget formation are selected, they are current,electrode displacement,dynamic resistance,welding time.

The current measuring sensor adoptes hollow coil which is wrapped in the second loop of transformer, the current effective value is calculated by the method of peak value angel [5]. The dynamic resistance measurement uses the method of dynamic power factor $ctg\beta$. The angle β is stand for a lag angle that current is relative to voltage, it is obtained through synchronous circuit and the detection circuit of current zero-cross signal. The dynamic resistance is replaced by $ctg\beta$[6]. The electrode displacement adopts grating displacement sensor, the probe of which is installed on each electrode arm. The measuring circuit makes the electrode displacement signals coming from the probe of sensor amplified, shaped, frequency doubled, direction distinguished, pulse counted and converts into electrical signals which are finally sent to the microcomputer control system.

2.3 Extraction of Characteristic Information

It is necessary to extract parameter characteristic information after the sensor-based signals sent to spot welding controller. The current effective value is extracted by

means of peak value angle method, the displacement rising rate (ds/dt) and peak value signal s_m is extracted by calculating the electrode displacement at every cycle, the falling rate of dynamic resistance (dR/dt) and the falling threshold value ΔR is extracted by calculating the dynamic power factor $ctg\beta$ at each cycle.

3 Control Algorithm of Multi-parameter Comprehensive Decision Making

As shown in Fig.2, the fused information comes from two aspects, one is the sensor-based information in which contains a lot of nugget formation, the orther is knowledge-based information in which embodys abundant human experience. The two aspect information supplements each orther, thereby the overall information concerned with spot weld nugget formation can be obtained. The information fusion algorithm is divided into two parts correspondingly, one is sensor-based information fusion algorithm, the other is knowledge-based regulation fusion algorithm. Knowledge-based regulation fusion algorithm offers parameter given values which participate in real-time control and then compared with characteristic information offered by multi-sensors to obtain corresponding deviations, according to the deviations, information fusion proceeds finally.

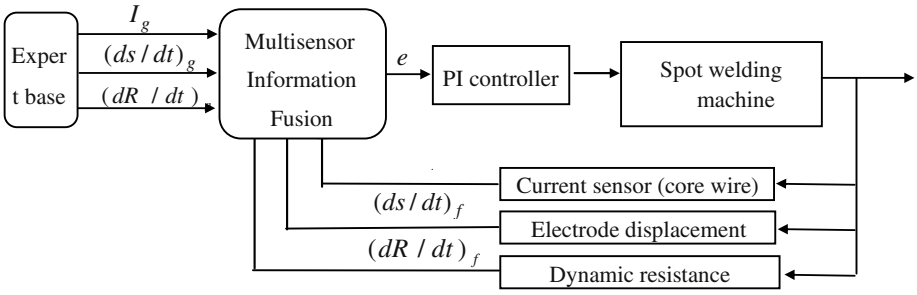

Fig. 2. Structure diagram of PI control system

3.1 Sensor-Based Information Fusion Algorithm

Different parameters have different influences on spot weld nugget formation, so weighted average fusion algorithm is adopted in the paper. First of all, the deviations e_1, e_2 and e_3 of current,displacement and dynamic resistance are calculated correspondingly, then Information fusion is carried out according to them. The fusion value is the total deviation e which can be finally obtained as follows.

$$e = \sum a_i \cdot e_i \quad (i = 1,2,3,\ \sum a_i = 1) \tag{1}$$

Where $e_1 = I_g - I_f$, $e_2 = (ds/dt)_g - (ds/dt)_f$, $e_3 = (dR/dt)_g - (dR/dt)_f$; a_i is the weight factors.

Displacement rising rate $(ds/dt)_g$, displacement peak value s_{mg} and dynamic resistance threshold value ΔR_g are gained through large number of experiments when the weld nugget sizes reach the given values. During spot welding process, welding cycle can be finished when one of the three feedback signals[t_{wf}, s_{mf}, ΔR_f] reaches the corresponding given value, which means the requirement of weld nugget size is satisfied, or welding cycle is kept all the time.

During the primary stage, displacement and dynamic resistance values are very small, it is not suitable to compare them with corresponding given values. Generally the displacement and dynamic resistance variation curves are divided into three stages, the first stage is the primary one about 1 to 3 cycles, the second is spot weld nugget formation stage about 4 to 8 cycles, the last is stable stage over 8 cycles. Spot welding process control adopts control of stage according to the different condition of each stage, as shown in table1. The weight factors are decided by experience.

Table 1. Weighted coefficient of multi-sensor characteristic information

First stage			Second stage			Third stage		
a_1	a_2	a_3	a_1	a_2	a_3	a_1	a_2	a_3
1.0	0	0	0.6	0.4	0	1.0	0	0

The conditions of stage control in table1 are just suitable to a little bit thicker base metal, such as thickness of mild carbon steel is greater than 0.5mm, thickness of stainless steel greater than 0.8mm, thickness of aluminum alloy greater than 3mm. Welding time is quiet short, so the welding process is not easy to be controlled when a thinner base metal is welded. In this case, decision-making technique can be used directly for spot welding control, for example, constant current control or dynamic resistance monitoring can be used directly.

3.2 Knowledge-Based Regulalation Fusion Algorithm

The knowledge-based fusion algorithm adopts the production rule, its form is that IF A,then B;or IF A and B,then C.

Optimal processing parameters are selected according to welding base metal and thickness saving in the knowledge base of spot welding controller. The given values

which participate in real-time control are selected through look-up table established in the knowledge base in the course of spot welding.

3.3 Program Design

When spot welding procedure enters into welding cycle, the thyristors $VH_{1,2}$ are triggered at a given angle in first cycle, and then acquisition of information coming from different sensors and calculation deviation of e_1、e_2、e_3 carry out continuoursly. According to the weighted average algorithm and knowledge-based regulation fusion algorithm, the information fusion result e is calculated through look-up table1 and then is adjusted in the law of proportion and integration(PI). The output of PI controller is transformed to a new control angle, and thyristors $VH_{1,2}$ are triggered at this new angle in next cycle . Welding cycle terminates until the nugget size reaches the given values.

4 Experimental Results

The experiments are carried out on type DN6-38 spot welding machine. When the duty cycle is 50%, primary rated capacity is 38 kVA. The spot welding processing parameters are shown as Table 2.

Table 2. Spot welding processing parameters

Variables / Materials	Thickness (mm)	I_g (kA)	$(ds/dt)_g$ (mm/s)	$(dR/dt)_g$	t_{wg} (cyc)	S_{mg} (um)	ΔR	F_w (Mpa)
Q235	1.2	5.0	1.5	0	16	112	0.16	0.4
1Cr18Ni9Ti	1.0	3.9	1.8	0	8	135	0.15	0.45

Under the welding conditions above, the nugget sizes and their fluctuations are shown as table3.

When multi-parameter information fusion control is used in spot welding quality control, the nugget fluctuations diminish apparently compared with constant current control of single parameter. The reason is that multi-sensors are used and much more information about spot weld nugget formation is collected and fused in spot welding control, the information also includes expert experience. Spot welding experiments show that the multi-parameter comprehensive decision making control method can compensate for various factors of influence in spot welding and assure the welding quality to be stable.

Table 3. Measuement results of weld nugget sizes

Fluency / factors / Control methods / nuggets		Weld	Shunting current	Inductance augmentation	Electrode wire	No fluency factor
Constant current control	Q235A	d (mm)	4.0	4.6	4.2	5.0
		fluctuation	-20%	-8%	-16%	0%
	1Cr18Ni9Ti	d (mm)	3.2	3.7	3.3	4.1
		fluctuation	-22%	-9.7%	-19.5%	0%
Information fusion control	Q235A	d (mm)	4.5	4.7	4.6	5.0
		fluctuation	-10%	-6%	-8%	0%
	1Cr18Ni9Ti	d (mm)	3.5	3.7	3.6	4.0
		fluctuation	-12.5%	-7.5%	-10%	0%

Annotation: d stands for nugget size. The minus sign indicates that nugget sizes diminish compared with given values. Spot weld spacing is 7mm for Q235A and 8mm for 1Cr18Ni9Ti. Inserting a steel plate 70×80×1mm into second loop of main circuit repesents inductance augmentation . Electrode diameter fluctuation is $\Delta\Phi = 1\,\text{mm}$.

5 Conclusions

The present status of spot welding quality control at home and abroad are analyzed. Few parameters measured and single parameter closed-loop control used in the course of spot welding are one of the principal problems of spot welding quality control. Four parameters (current,electrode displacement,dynamic resistance and welding time) combined action on quality control system is studied, and a new control method of multy-parameter comprehensive decision making is put forward. The weighted average algorithm is used for sensor-based informatiom fusion, and knowledge-based regulation fusion algorithm is employed for the given processing parameters, such as welding base metal,thickness of sheet,welding force and so on, which are stored in the memory of spot controller as a knowledge base. The overall information about weld nugget formation is obtained in this way. The spot welding experiments indicate that nugget size fluctuation is within 8%～22% under constant current control, and is within 6%～12.5% under information fusion control. It conforms that the new quality

control method can compensate for various factors of influence in the welding process such as shunt, loop inductive reactance variation and electrode wear, etc, and assure the spot welding quality to be stable.

Acknowledgements

This project is funded by Shenyang Key Science Foundation (No1041020-1-04) and Liaoning nature science foundation (No20031022)

References

1. Wang CS,Zhao XH, etc (1999) Research on numerical simulation method in the course of spot welding nugget formation. Automobile technology and material (2):3-4
2. Long X, Wang JH, etc (2001) Numerical simulation on the temperature distribution in spot welding. Transaction of Shanghai JiaoTong University (3):416～419
3. Y Cho, Y Kim and S Rhee (2001) Development of a quality estimation model using multivariate analysis during resistance spot welding, Proc Instn Mech Engrs Vol 215 Part B (2)1529-1538
4. Chang YL, Hong SS, Xue JX (2000) Multi-sensor information fusion and control of Robot spot welding, welding transaction (2):85～89
5. Xie BG, etc (1988) calculation method of spot welding current using peak value angle. Electric welding machine (4):19～23
6. Li GZ,etc (1991) research on self adjusting control of dynamic resistance shreshold valve method in spot welding. Welding (12):6～10

Waveform Control High-Speed Welding System for Arc Welding Robot

H.M. Chen[1] and M. Zeng[2]

[1] School of Materials Science and Engineering, Nanchang Institute of Aeronautical Technology, Nanchang 330034, P.R. China
[2] College of Mechanical Engineering, South China University of Technology, Guangzhou 510640, P.R. China
chm8405@163.com

Abstract. An intelligent waveform control system with micro-controller is developed for robotic high-speed CO_2 arc welding. In order to resolve the problems of bad weld formation and heavy spatter in high-speed CO_2 arc welding, A new method of welding current waveform control is investigated, which controls the short-circuit current and its rising rate in short-circuit period, and adopts the two-step constant current control to adjust the arc energy in arc period. The control principle of the method is discussed, the system structure and the control software are introduced, and the optimized waveform control parameters are provided by experiments. The results show that this system can precisely control the arc energy by the two-step constant current method and improves the performance of high-speed welding process obviously.

1 Introduction

Manufacturing automation has progressed remarkably, and many arc welding robots have served on production lines. In order to increase manufacture efficiency, these systems require high-speed welding. However, welding procedure has been a restricted factor of high-speed manufacture. At present the welding speed is within 0.5 - 0.8 m/min by using normal gas metal arc welding (GMAW) equipment, if it goes higher, the stability of welding process becomes poorer, welding spatter is bigger, weld appearance becomes worse, and some defects such as undercut and "humped bead" emerge easily[1,2]. It's very difficult to achieve high-speed welding by using normal GMAW method, so there's a urgent need to develop a new low-cost high-speed welding method, which can make a high quality weld seam.

In order to achieve high-speed welding many methods have been researched, such as using twin or multi-electrodes, heating welding wire, changing the components of shield gas and so on[3,4]. Those methods are usually taken under the conditions of high voltage and big current, which will lead to bigger spatter, higher output power and higher cost. Chinese researchers have made some progress in the mechanism of weld undercut formation, the stability of molten pool and the waveform control theory of high-speed GMAW process [5,6]. Up to the present the defects of high-speed short transition gas metal arc welding, such as big spatter and bad weld seam, have not been

T.-J. Tarn et al. (Eds.): Robot. Weld., Intellige. & Automation, LNCIS 362, pp. 235–242, 2007.
springerlink.com

resolved, some key problems still need to research further. The method of welding current waveform control has an obvious effect on reducing welding spatter and improving weld seam formation during the short-circuit transfer of GMAW process [7]. In order to realize high-speed CO_2 arc welding process, this paper studies a new method of welding current waveform control by use of two-step constant current to adjust arc energy, and developed a waveform control system with micro-controller.

2 Current Waveform Control Method

According to the characters of high-speed CO_2 arc welding, this paper designs a current waveform shown in Fig.1. The CO_2 arc welding process can be separately considered as two periods: short-circuit period and arc period. Based on the mechanism of the short-circuit transfer process, the control purposes of short-circuit period and arc period are different, the short-circuit period is reducing welding spatter mainly and the arc period is improving weld formation mainly. The principle is as follows. During the short-circuit period, firstly the current is held to a low current I_{g1} for a period of time t_1, which makes a melting drop touch the molten pool tenderly to suppress the early spatter; then the short-circuit current increases at the rate of di/dt_1 to improve the contraction of molten bridge of metal, which can speed up the transition; finally the short-circuit current increases slowly at the rate of di/dt_2 to a maximum value I_{max} and holding until the molten bridge is ruptured by the electromagnetic pinch effect. If the melting drop transition finished during the period of short-circuit current increasing, the short-circuit current can't achieve its maximum value I_{max}. Therefore this method can help the melting dropsfinish the transition process at a low current and suppress welding spatter. Parameters (I_{g1}, t_1, di/dt_1, di/dt_2 , I_{max}) can be modulated.

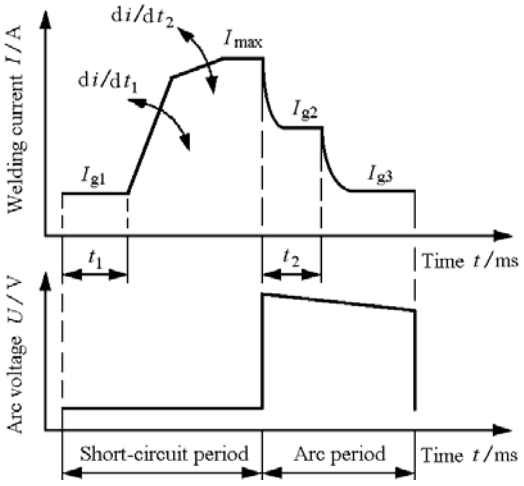

Fig. 1. Sketch of waveform control parameters for high-speed welding

In order to control the arc burning process accurately and steadily, the arc period control is divided into two stages: during the first control stage the current is controlled at high constant current I_{g2} for a certain time t_2, which can improve the arc re-burning, and heat the welding wire at the same time to accelerate the melting drop forming; and then during the second control stage the current is controlled at a low constant current I_{g3} (background constant current) for an open time to improve the melting drop forming further and keep the arc length stable until the short-circuit period coming. Parameters (I_{g2}, t_2, I_{g3}) can be modulated. It's a new thinking to control the arc energy by adopting two-step constant current control.

3 Design of System Hardware

3.1 System Structure and Function

The system is composed of IGBT inverter circuit, PWM control circuit, Micro-controller system and wire feeding system, as shown in Fig.2. In this system the IGBT inverter circuit provides welding energy. The micro-controller system is the core of the whole system, which has four main functions: controlling CO_2 arc welding procedure, setting welding parameters, controlling the welding current and arc voltage, and setting wire feeding speed. The PWM control and IGBT drive circuit is mainly used to produce driving signals for IGBT inverter circuit and set the pulse frequency and width. The wire feeding circuit controls the wire feeding motor speed and achieves smooth wire feeding.

3.2 Design of Micro-controller System

The short-circuit transfer of CO_2 arc welding is a time-variable and nonlinear process, and many factors disturb it, therefore the control system must respond quickly, and has high reliability, and can measure and control the welding current and arc voltage. Besides above mentioned, the micro-controller system has strong ability in data processing and logic judgment also, and can be reprogrammed too, so that it can achieve multi-function welding and multiple control methods without changing the system hardware, and control high-speed CO_2 arc welding process effectively.

In this paper the micro-controller system is mainly used to measure the welding current and voltage signals, judge the actual welding process being in short-circuit period or in arc period, and then execute relevant control methods. The system should be real-time with high reliability and strong anti-interference ability. So we choose microprocessor 80C320 as the core chip in this control system, the detail structure is shown in Fig.3. In this control system some chips such as high-speed microprocessor 80C320, program storage 27256, data storage 6264, parallel ADC MAX118, DAC TLC7528, UART MAX232 and power source monitor chip MAX708 are adopted, those chips ensure the system has fast response speed and can communicate with a robot. The system becomes controlling easily and more reliable. This design helps forward achieving waveform control of CO_2 arc welding strongly.

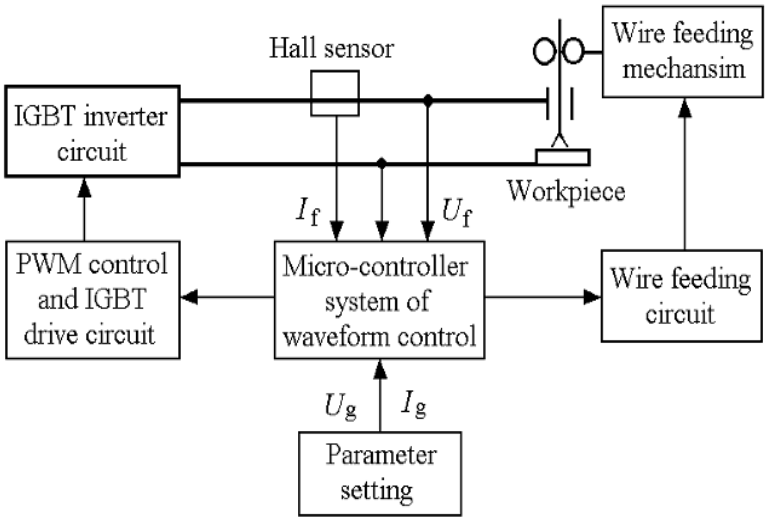

Fig. 2. Block diagram of waveform control high-speed welding system

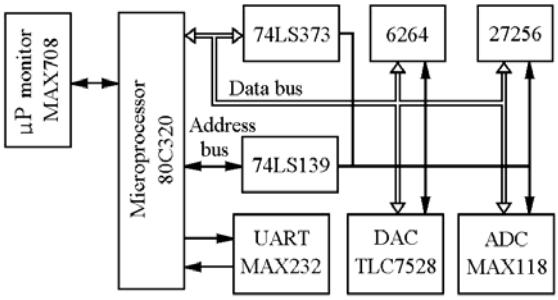

Fig. 3. Sketch of micro-controller system of waveform control

4 Design of Control Software

Because the control system requires fast response speed, the software controls the welding process by adopting interrupt-mode mainly. The software is consist of main program, short-circuit period interrupt control program (INT1) and arc period interrupt control program (INT2). The flow charts are shown in Fig.4 and Fig.5.

The main principle is expatiated as follows. The software first measures the arc voltage when welding, and judges which period the drop transition process is in by the arc voltage. If the arc voltage U_f is greater than the criterion voltage U_j, in this design we set U_j is equal to 14V, the transition process is arc period. If the arc voltage U_f is less

than 14V, the transition process is short-circuit period. Then the control software chooses the relevant programs to control arc period or short-circuit period, the short-circuit period is controlled by INT1 interrupt control program, the arc period is controlled by INT2 interrupt control program.

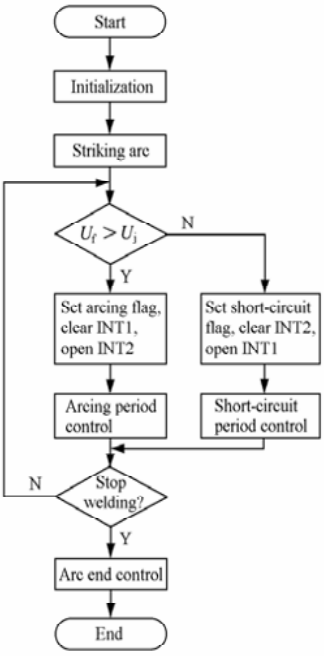

Fig. 4. Flow chart of main program

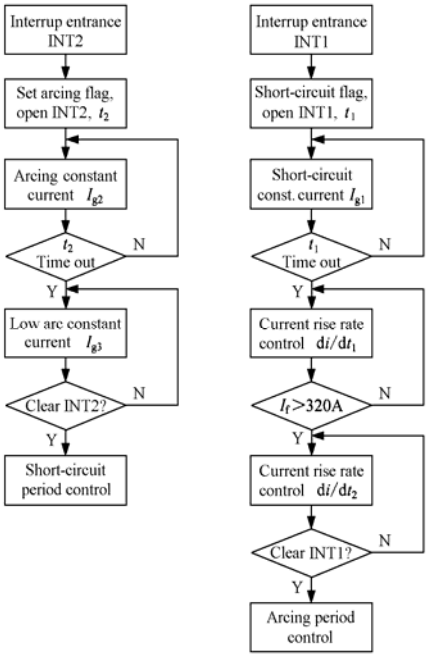

Fig. 5. Flow chart of interrupt control program

5 Experiments

5.1 Experiment Condition

This experiment system of high-speed welding is consist of IGBT inverter power source with micro-controller system, switching-mode wire feeding system, a Motoman-up20 robot, an AH-XIX Hannover welding process analyzer which is used to measure welding current and voltage and draw the *U-I* charts. Experiment conditions are as follows: the thickness of mild steel test plate 1 mm or 3 mm, the welding wire (H08Mn2SiA) diameter 0.8mm, wire extension length 12 mm, CO_2 shield gas flow rate 15 L/min, welding speed 1.5 m/min.

5.2 Optimization of Waveform Control Parameters

In short-circuit period the parameters of waveform control include initial short-circuit current I_{g1}, sustained time t_1, current rise rate di/dt_1 and di/dt_2, short-circuit maximum

current I_{max}; in arc period the parameters of waveform control include a high constant current I_{g2} (arcing current), I_{g2} holding on time t_2, a low constant current I_{g3} (background current). Short-circuit period focuses on controlling welding spatter, and arc period focuses on improving weld formation. However, short-circuit period and arc period are closely related during the short-circuit transfer process. Both periods determine the stability of welding process together. Arc energy affects not only the drop melting and the arc shape, but also the difficulty degree of drop transfer and the spatter quantity; the short-circuit time and current also affect the spatter quantity and the energy ratio between arc period and short-circuit period, thus they will influence the weld formation too. Consequently there are optimum waveform parameters for each wire diameter and each plate thickness. For example, when the sustained time t_1 of short-circuit current is adjusted within 400-800μs and the short-circuit current rise rate di/dt_1 is within 40-100kA/s, the welding process has better stability and less spatter under this experiment conditions. If t_1 is too long, the weld wire will plunge into the molten pool, and hence stubbing occurs. If t_1 is too short, the melting drop transfers under a high current value, the instantaneous short-circuiting spatters occur easily.

The optimized waveform control parameters for 1 mm and 3 mm thick plate are shown in Table 1. Fig.6 shows the waveforms of welding current and arc voltage and *U-I* charts with the optimized waveform control parameters. The photographs of welding bead formation are shown in Fig.7.

Table 1. Optimized waveform control parameters

Plate thickness δ /mm	Arcing current I_{g2}/A	Background current I_{g3}/A	Current rise rate di/dt_1 /(kA·s^{-1})	Current rise rate di/dt_2 /(kA·s^{-1})	Peak current I_{max}/A	Arc Voltage U_g/V	Wire feed speed V_f /(m·min^{-1})
1	125	75	92	10	280	18.5	8.5
3	140	110	84	10	320	19.0	12.3

Notes: initial short-circuit current I_{g1} is 60A, sustained time t_1 is 500μs.

From Fig.6, welding current and arc voltage waveforms are regular and coincident, which indicates that welding process is very steady. Using the optimized waveform control parameters at 1.5 m/min welding speed, the welding spatter is reduced obviously, and the weld formation of both side is uniform and smooth. In the short-circuit period, the low initial short-circuit current I_{g1} is very important to suppress welding spatter. By two-step constant current control in arc period, the arc energy can be adjusted conveniently, which ensures obtaining the good weld formation, and the high constant current control plays a very important part in re-burning arc also. The waveform control parameters can be adjusted in wide range, which extends the application area of high-speed welding, thus the design purpose has been achieved. When the waveform control method is used in the high-speed welding of thin steel board, the welding speed can reach 1.5m/min, which is 2-3 times faster than the welding speed of normal GMAW.

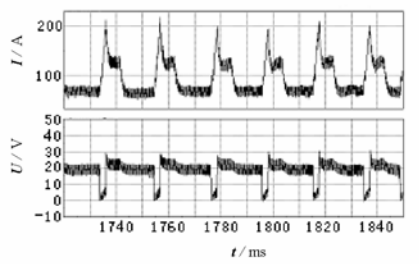

(a) Welding current and arc voltage waveform of 1mm plate

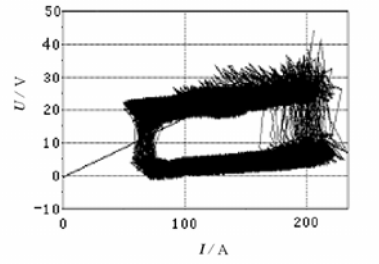

(b) *U-I* chart of 1mm plate

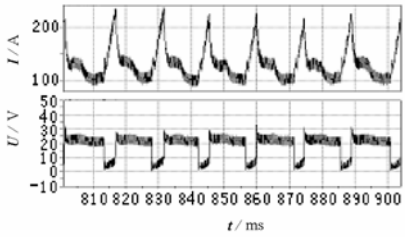

(c) Welding current and arc voltage waveform of 3mm plate

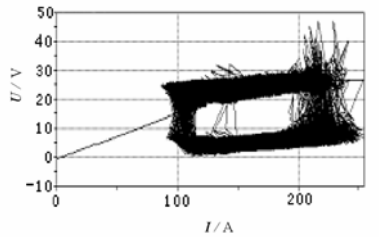

(d) *U-I* chart of 3mm plate

Fig. 6. Welding current and arc voltage waveforms

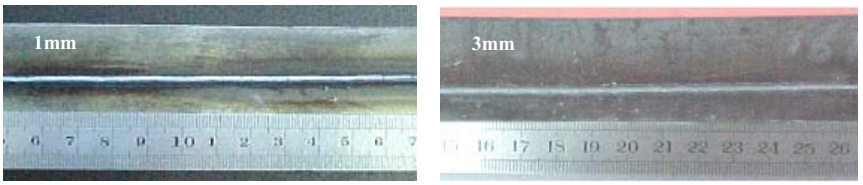

Fig. 7. Photographs of welding bead formation

6 Conclusions

A new method of welding current waveform control is put forward for thin sheet metal high-speed welding, the method adopts different control strategy for each transfer period, which controls the short-circuit current and its rising rate in short-circuit period, and uses the two-step constant current control method to adjust arc energy in arc period. According to the control principle, the system based on microprocessor 80C320 and the waveform control software are designed. The defects of bad weld formation and heavy spatter of CO_2 arc welding can be overcome effectively by the system. The experimental results show that the system is stable and reliable, it can precisely control

the arc energy with the two-step constant current method, and improves the performance of high-speed CO_2 arc welding process obviously.

Acknowledgements

This work is supported by the Foundation of the Materials Science and Engineering Research Center of Jiangxi Province(No.ZX200301011), the research program of the Education Department of Jiangxi Province (No.2006-171), and Guangdong Natural Science Foundation (No.031330).

References

1. Lancaster J F (1984) The physics of welding. London: Pergamon Press.
2. Yin SY, Zhang JH (1989) Gas shielded arc welding process. Harbin: Harbin Institute of Technology Press.
3. Michie K, Blackman S, Oqunbiyi TEB (1999) Twin-wire GMAW process characteristics and applications. Welding Journal 78(5): 31-34.
4. Hermans MJM, Den OG (1999) Process behavior and stability in short circuit gas metal arc welding. Welding Journal 78(4): 137s-141s.
5. Feng L, Chen SJ, Yin SY (1999) Mechanism of undercut phenomenon in high speed welding. Transactions of the China Welding Institution 20(1): 16-21.
6. Zeng M, Cao B, Huang SS (2003) Simulation research on waveform control high-speed welding system. Transactions of the China Welding Institution 24(6): 55-59.
7. Zeng M, Cao B, Huang SS (2004) Research on waveform control method of short Transition high-speed welding. Journal of Shanghai Jiao Tong University 38(7): 1076-1080.

Multi-agent-Based Control Model of Laser Welding Flexible Manufacturing System

Shiyi Gao[1,2], Mingyang Zhao[1], Lei Zhang[1,2], and Yuanyuan Zou[1,2]

[1] Shenyang Institute of Automation, Chinese Academy of Science, Shenyang 110016, P.R. China
[2] Graduate School of the Chinese Academy of Sciences, Beijing 100049, P.R. China
gshiyi@sia.cn

Abstract. Existing modeling frameworks for manufacturing control can be classified into hierarchical framework and heterarchical framework. The two modeling frameworks have some drawbacks which can't be overcome only depending on them. In this paper, in order to improve the performance of the laser welding flexible manufacturing system (LWFMS) we have developed a hybrid modeling framework which has the features of the hierarchical and the heterarchical framework. The LWFMS contains several robots and many workstations which work together to realize a common goal. There exists coordination and cooperation among the different robots and workstations so the multi-agent technology is adopted in the LWFMS. In the end, the simulation result of the hybrid control framework in the LWFMS testifies the validity of the model.

1 Introduction

In recent years, with the development of the computer science and technology, the intelligence manufacturing based on the multi-agent system is proposed. The multi-agent system is composed of heterogeneous agent types with distinct agent properties, such as adaptation, mobility, collaboration and learning [1~3]. It is also a distributed artificial intelligence system which embodies a number of autonomous agents to achieve common goals [4]. The agents in the multi-agent system can take specific role within an organizational structure. The multi-agent system provides a novel approach to address complex problems where decisions should be based on the processing of information from various sources of diverse nature[5]. Each agent represents a source and the MAS stands for the overall manufacturing from management, planning to execution. In FMS, the agent may be designed to represent various information units, the types of which reflect the capabilities of different departments of the enterprise.

Many researchers have engaged in various researches on applying agent technology in developing manufacturing control systems. The view of original implementation of MAS in manufacturing was proposed by Yams [6~7] who assigned an agent to each node in the control hierarchy (factory, workstation, machine.). Carlos Ramos [8] has developed the architecture for dynamic monitoring in flexible manufacturing system (FMS) which assigned an agent to each resource. He has also proposed a new negotiation protocol for rescheduling, which is able to deal with faults. Warnecke and Huser [9] adopted the metaphor of fractals to describe a model for a FMS in which self-contained entities can organize themselves without the power of an external. Maturana et al propose MetaMorph, a multi-agent architecture, for distributed manufacturing system [10]. Two

T.-J. Tarn et al. (Eds.): Robot. Weld., Intellige. & Automation, LNCIS 362, pp. 243–248, 2007.
springerlink.com

types of agents: resource agents for representing physical resources and mediator agents for coordination were adopted in their built control framework. Laws et al. proposed a viable reference architecture for a multi-agent supported holonic manufacturing system [11]; and Kotak et al. introduced an agent-based holonic design and operations environment for distributed manufacturing [12]. Leitao et al. proposed a collaborative production automation and control architecture. The architecture provided a catalog of elements that simplifies the development of agent-based control systems for flexible manufacturing from design to operation [13]. Parunak and Baker [14] described a type of agent architecture for shop floor control and scheduling. Manufacturing resources, managers, part types, and unit processes are modeled as intelligent agents in their architecture. Among these research issues, the agent technologies are still immature and few true agent-based systems have been realized for manufacturing systems. The potential of the agent technologies has not been released completely. So the research about the application of the multi-agent into manufacturing will be necessary.

2 The Laser Welding Flexible Manufacturing System

The integrated laser tailored welding manufacturing system (LWFMS) has the ability to joint different thickness and different material metal plates together by using the advanced laser welding technology. The automobile bodies manufactured by LWFMS can reduce in weight and maximize the structural stiffness in modern automobile

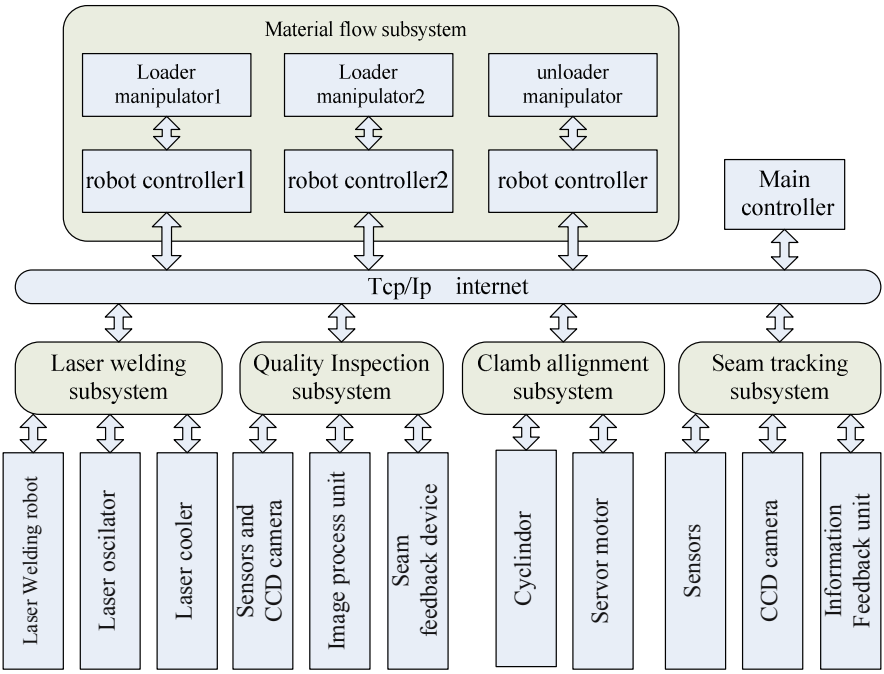

Fig. 1. The hardware configuration of the LWFMS

design. So using the LWFMS in welding automation manufacturing has become a necessary trend in order to improve the welding quality. The LWFMS consists mainly of a material flow subsystem, a laser welding subsystem, an on-line quality inspection subsystem, an alignment and clamp subsystem and a seam tracking subsystem. The material flow subsystem contains three robots, two loader robots and an unloader robot. The LWFMS is a typical integrated flexible manufacturing system. The Fig1 shows the hardware configuration of the LWFMS.

3 The Hybrid Framework of the LWMFS Based on MAS

The LWFMS consists of five subsystems and each subsystem is autonomous and independent in function. So each subsystem can be considered as an agent. In order to improve the performance of the LWFMS, we have built a hybrid control framework for the LWFMS which can be seen from Fig 2. In this framework, all agents are divided into three levels: high level agent, middle level agent and low level agent. The high level agent, which has a global perspective, generates a global optimized schedule. The middle level agents dominate and monitor the low level agents. The low level agents may autonomously make their negotiation with the high level agents according to the rules planned previously.

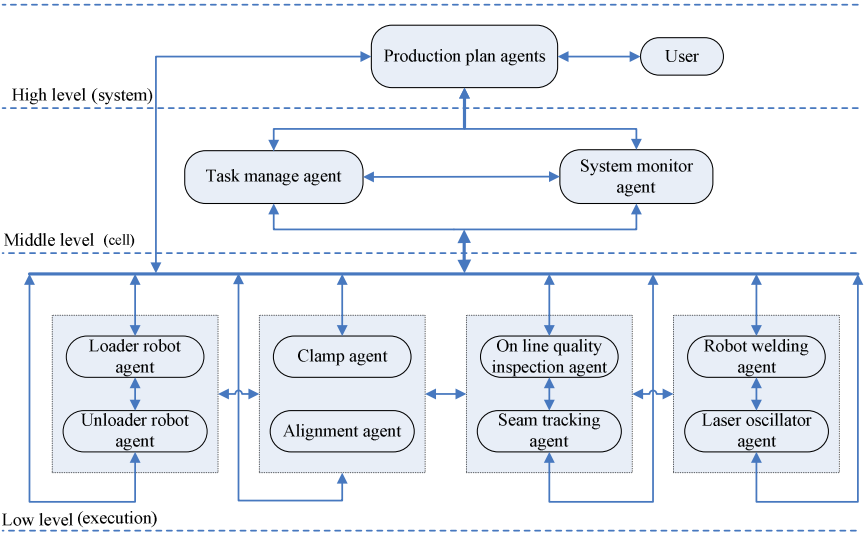

Fig. 2. The hybrid framework of LWFMS based on multi-agent system

The production supervisory agent in high level is the highest controlling body and it aims to satisfy the goals defined by the user. The classical functions –administration of client orders, data management, material management and global control management are fulfilled at high level. This agent has a broad view and is thus able to make decisions to prevent unstable behaviors. For example, if no low agent is willing to execute the task, the high agent has the power to force an agent to accept a specific

assignment. The high level can also dominate the middle agent for stable solutions by declining permission to middle agents on a specific assignment.

The middle layer consists of task management agent and system monitor agent. The task management agent can be classified as a reactive scheduler. It maintains updated aggregate planning information, for example, the welding sequence of blanks is assigned to each resource. When it gets a request to change the original assignment, it examines the projected workload of resources in its control area and grants the request only if the assignment change is necessary or desirable. For instance, a loader robot conveys a blank that may be an unqualified one, at the same time the welding robot and the system have been ready for welding, so the loader robot must convey a quality blank again. In the return process of the loader robot, a message is submitted to the task management agent and a new assignment is done in the agent. Notice that the massage is submit to other agent of high level and low level because the control design framework is interaction among levels. The major functions of monitor agent are error detection, error diagnosis and error handling. Each resource, including all robots, machines, tools, devices in the LWFMS are under the responsibility of the monitor agent. In this model, the monitor functions are realized by the control mode which is a distributed system between the low agents and the monitor agents.

Just as upper agents must take into consideration interests of the lower level agents, lower level agents must also contribute toward achievement of upper level agents' objectives [17]. Thus, the lower agents must satisfy up level agents' objectives while attempting to satisfy their personal objectives. The low agents share with common databases and can communicate massages each other by blackboard modes. For example, after the blank is ready for welding, the massage is reported in the blackboard and the welding robot can receive the news, and subsequently accomplishes the welding task. In the LWFMS, these low agents stand for certain components and controllers by which the complex production task can be realized. The low agents that are autonomous are managed commonly by the middle level and the higher level. So the level control is a distribute mode which offers robustness and agility with respect to uncertainties.

From the above analysis about the architecture of LWFMS a new control model is built up based on the multi-agent technology. This model is a hybrid framework because it incorporates elements of the hierarchical and heterarchical frameworks. A negotiation mechanism for real time task allocation is used in order to overcome the structural rigidity and the lack of flexibility.

4 The Simulation

In order to verify the presented framework, this section describes the implementation and the testing results of the LWFMS control systems based on multi-agent system. Those agents are developed using java language based on the Java Agent Development Framework (JADE) which is a software framework to develop multi-agent systems in compliance with the FIPA specification. One of the important features that JADE agents provided is the asynchronous message passing. Each agent has a sort of mailbox where the JADE runtime posts messages sent by other agents. Whenever a message is posted in the message queue the receiving agent is notified. The Fig 3 is the JADE asynchronous message passing paradigm.

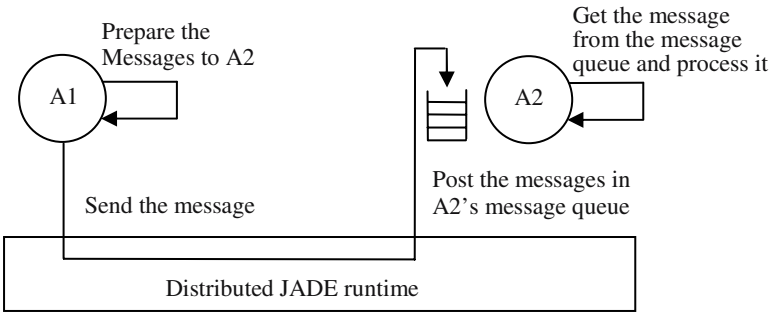

Fig. 3. The JADE asynchronous message passing paradigm

A number of tests and evaluation have been done on the basis of the hybrid control framework thought the JADE platform. In those tests fifty blanks was welded continuously and the abnormal run state probability can be computed. From the tests result we get the following graph shown as Fig 4. We can summarize that the result of the test of the hybrid control framework is better than the conventional framework From Fig 4. The reason is the agents interact with on another independently. When some agent of WFMS control system breaks down, although the whole performance of the system may drop, the WFMS can run continuously. In a word, by adopting the MAS based the hybrid control framework, the disadvantages of the traditional WFMS, such as insufficient configuration, low capability of fault-tolerance and difficult maintenance can be resolved.

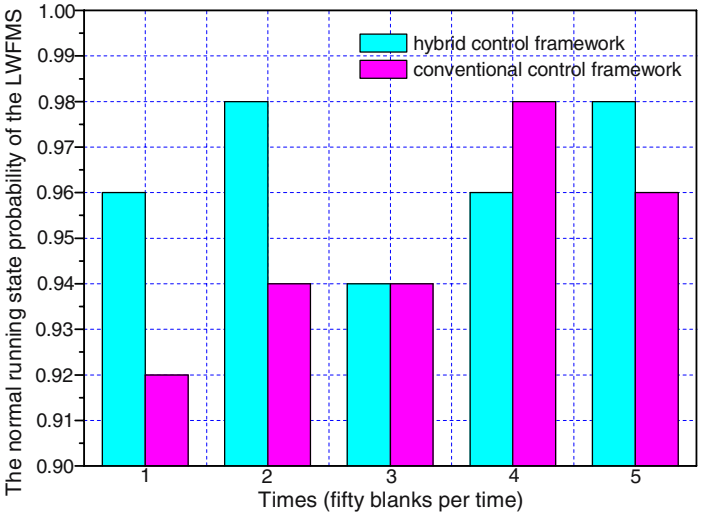

Fig. 4. The normal running state probability of two different control framework

5 Conclusions

In this paper, we developed a hybrid control model for LWFMS based on the multi-agent system. In the model, all agents are divided into three levels: higher level, middle level, and lower level. Each agent in a different level can communicate according to programming rules. The simulation test for the LWFMS demonstrates that the hybrid control architecture is an effective and appropriate approach.

References

1. Alessandro Garcia, Uirá Kulesza, and Carlos Lucena Aspectizing, " Multi-agent Systems: From Architecture to Implementation," Lecture Notes in Computer Science, Vol. 3390, PP121-143, 2005
2. A. Garcia et al, "Separation of Concerns in Multi-Agent Systems: An Empirical Study," Software Engineering for Multi-Agent Systems II., Springer, LNCS 2940, April 2004.
3. A. Pace et al, "Assisting the Development of Aspect-based MAS using the SmartWeaver Approach," Software Engineering for Large-Scale MASs., LNCS 2603, March 2003.
4. W.B. Lee, H.C.W. Lau, "Multi-agent modeling of dispersed manufacturing networks," expert systems with applications, vol. 16, no 3,pp 297-306, 1999
5. N.K. Krothapalli, A.V.Deshmukh, "Design of negotiation protocols for multi-agent manufacturing," int, J . Prod. Res, vol. 37, no. 7, pp 1601-1624, 1999
6. H. Van Parunak, "Distributed A.1 and Manufacturing Control: some issues and insights," Y. Demazeau and J.Muller, eds., Decentralized A.1, North-Holland, pp. 81-104, 1990.
7. H.Van Parunak, "Industrial applications of multi agent systems," Actes de MFAUTOM'93, du traitementreparti aux systemes multi-agents et a l'autonomie dessystemes., pp. 18-19, Toulouse, 1993.
8. Carlos Ramos, "An architecture and a negotiation protocol for the dynamic scheduling of manufacturing systems," IEEE International Conference on Robotics and Automation, Vol. 4, pp. 8-13, 1994.
9. H.-J. Wamecke, M. Hiiser, The Fractal Company – A Revolution in Corporate Culture, Springer, Berlin, 1995.
10. F. Maturana, W. Shen, and D. H. Norrie, "Metamorph: An adaptiveagent-based architecture for intelligent manufacturing," Int. J. Prod.Res., vol. 37, no. 10, pp. 2159–2173, 1999.
11. Laws AG, Taleb-Bendiab A, Wade SJ, "Towards a viable reference architecture for multi-agent supported holonic manufacturing systems," J Appl Syst Stud 2(1):61–81, 2001
12. Kotak D, Wu S, Fleetwoood M et al, "Agent-based holonic design and operations environment for distributed manufacturing," Comp Ind 52(1):95–108, 2003
13. Bellifemine F, Poggi A, Rimassa G, "JADE a FIPA2000 compliant agent development environment," Proceedings of the international conference of autonomous agents, Montreal, pp 216–217, 2001
14. A. D. Baker, H. V. D. Parunak, and K. Krol, "Manufacturing over the internet and into your living room: Perspectives from the AARIA Project," ECECS Dept., Univ. Cincinnati, Cincinnati, OH, Tech. Rep.TR208-08-27, 1997.
15. N. R. Jennings, M. j. Wooldridge, "Applications of intelligent Agents. In "Agent Technology : Foundations, Applications and Market" Springer, pp. 3-28.1998
16. W. Cao, C.G. Bian, O.O. Ugwu, L. Newnbam, A. Thorpe, "Collaborative design of structures using intelligent agents," Automation in construction, vol. 1, pp. 89-103, 2002
17. Sunderesh S. HERAGU, Robert J. Graves, Byung-In Kim, Art, St. Onge, "Intelligent Agent Based Framework for Manufacturing Systems Control," IEEE transactions on systems, man and cybernetics pp560-573 , Sept. 2002

Recognition of the Initial Position of Weld Based on the Corner Detection for Welding Robot in Global Environment

M. Kong, F.H. Shi, S.B. Chen, and T. Lin

School of Material Science and Engineering, Shanghai Jiaotong University,
Shanghai 200030, P.R. China
davidkm1979@sjtu.edu.cn

Abstract. This paper presents a method for recognizing the initial position of the weld in the global environment based on corner detection technology. Through the image preprocess that include the smoothing process, the sharpening process, the region segmentation and so on, the work pieces can be segmented from the background. Based on the preprocess image, the initial position of the weld seam can be detected by the Harris operator in global environment. The Harris operator is a kind of stable algorithm of corner detection. The operator is logical and symmetrical. The result shows that this method has the characters of anti-jamming, accuracy and fast computing.

1 Introduction

Nowadays, the development of robotic welding system has progressed rapidly as a result of the continuing demand for improving methods of manufacturing industrial products. However, the most of the welding robot systems must be taught in advance for the space tracking, work condition, and work sequence etc. These types of welding robots have a high standard request for the mounted position and orientation of the jigs and the work-pieces. They must be taught and programmed again for the different work-pieces, and they don't have the self-regulation functions for the welding deformation that is generated during the welding process. All of the problems have restricted the application range for the robotic welding system. So the development of intelligent or autonomous robots is one of the most quickly evolving fields in automation and robotics research.[1,2]

The recognition of the initial position of weld is an important part of the robotization of the welding system. In this paper, we propose an effective technique for recognition of the initial position of weld based on the corner detection in the global environment. Through the processing the origin image of the weld, the initial position of weld can be detected by applying the corner detection in the global environment. The result shows that this method has a preferably practical value.

2 Experiment Setup and Process

The image of the weld is captured by the CCD camera that is fixed on the end of the arm of the MOTOMAN welding robot. The core of the control system is a PIII850

T.-J. Tarn et al. (Eds.): Robot. Weld., Intellige. & Automation, LNCIS 362, pp. 249–255, 2007.
springerlink.com

computer. The work piece image acquired by the experiment equipment is shown as Fig.1. The workpieces is randomly placed on the worktable. We will recognize the initial position of the three kinds of weld seam.

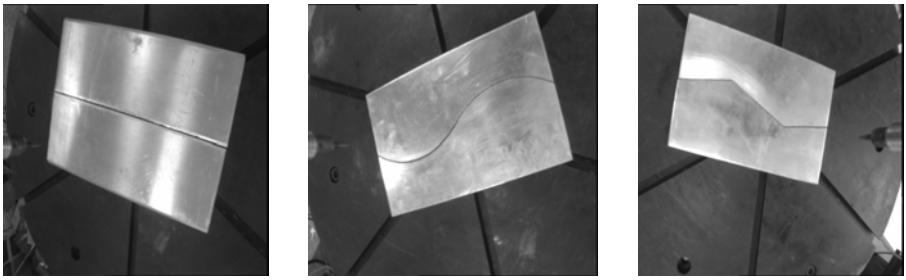

(a) (b) (c)

Fig. 1. The origin image of workpiece

3 Image Process

The origin image of weld may be corrupted by random variations during the process of acquisition and transmission. For those variations playing down the quality of the image, the initial position of the weld seam can not be recognized in the origin image. So the variations must be gotten rid of in advance. The process of the image process is as follows.

3.1 Image Preprocess

The image preprocess include smoothing process, sharpening process and region segmentation.

The smoothing process was applied a window as 3×3 and processes the median filtering in the whole origin image; the sharpening process was applied the Laplacian operator; the region segmentation applied the automatic threshold segmentation. The result is shown as Fig.2.

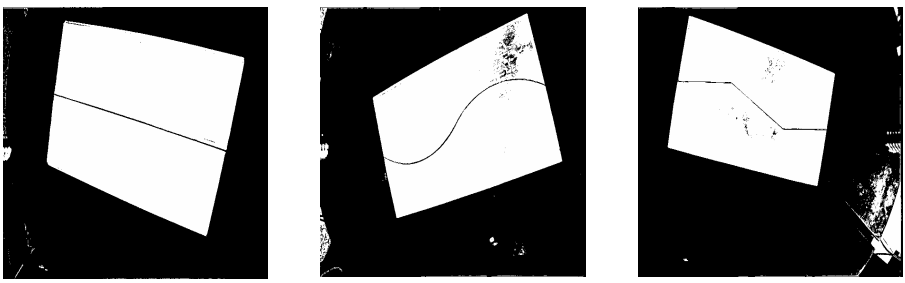

(a) (b) (c)

Fig. 2. The result of region segmentation

3.2 Rest Process

From the Fig.2, we can find that there are some little areas that they appear around the image and on the work piece. These areas will affect the result of Recognition of the initial position of weld. So we must find a method to get rid of these areas. In this process of get rid of these areas, we can compute the every area's size. And then select a threshold. If a area's size less than the threshold, we can conclude that it is the area that will be got rid of. The little area can be got rid of through changing the gray values to the background's gray values around the area. The result of rest process is shown as Fig.3. The image of the local initial position of the weld is shown as Fig.4.

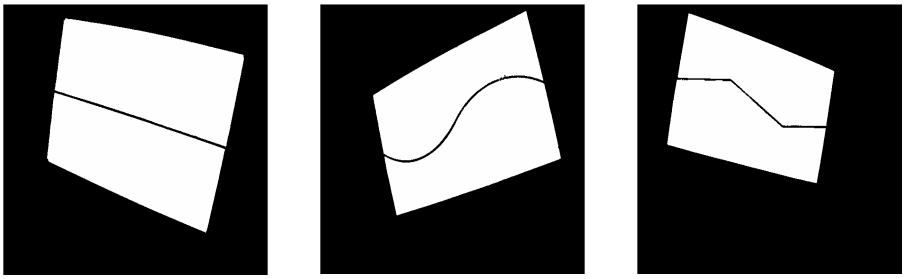

(a) (b) (c)

Fig. 3. The result of rest process

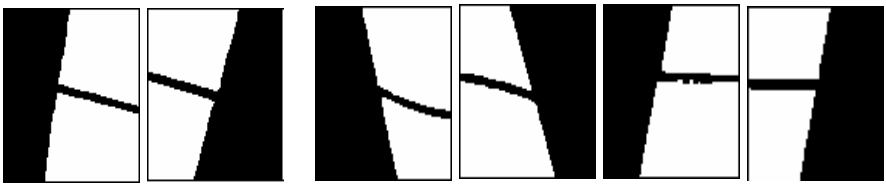

(a) (b) (c) (d) (e) (f)

Fig. 4. The local image of the initial position of the weld

4 The Process of the Recognition of the Initial Position in the Global Environment

From Fig.4. we can find that there are a couple of corners in the local initial position of the weld. The midpoint of every couple of corners is that the initial position of the weld. So if finding the couple of corners, we can find the initial position of the weld.

At present, there are many methods of the corner detection. Mokhtarian F and Pikaz A proposed the curvature scale space algorithm [3,4]. Deriche R and Giraudon G proposed a method based on the lightness [5]. Parida L and Geiger D proposed a method based on Parametric feature [7,8]. Harris algorithm is proposed by C.Harris and

M.J.Stephens in 1988. It is a operator based on signal of the corner characters [6]. This operator is enlightened by self-correlation function of the single processing. The matrix M be proposed is relation to the self-correlation function. The proper value of this matrix is the self-correlation function's curvature of the first order. If both of the curvature value of a point is more than a selected threshold, this point is the corner. The formula for the Harris operator is given by

$$E(u,v)|_{(x,y)} = \sum w(x,y)[\mathrm{I}(x+u, y+v) - \mathrm{I}(x,y)]^2 \tag{1}$$

Where E denotes the gray value of change while moving a (u,v) window at (x,y).The equation(1) shows that it is self-correlation of the single of the two-dimensional. Where $w(x,y)$ is the Gaussian smoothing operators. Taylor's series expansion of the equation (2) is shown by

$$E(u,v)|_{(x,y)} \cong [u,v]M\begin{bmatrix} u \\ v \end{bmatrix} \tag{2}$$

$$M = \sum_{x,y} w(x,y)\begin{bmatrix} \mathrm{I}_x^2 & \mathrm{I}_x\mathrm{I}_y \\ \mathrm{I}_x\mathrm{I}_y & \mathrm{I}_y^2 \end{bmatrix} \tag{3}$$

Where I_x、I_y denote the derivative of the x-axis and the y-axis. The result of the diagonalization of the matrix M is shown by

$$M \rightarrow R^{-1}\begin{bmatrix} \lambda_1 & 0 \\ 0 & \lambda_2 \end{bmatrix}R \tag{4}$$

Where λ_1 and λ_2 is the proper value of a matrix M. Every pixel correspondences the itself matrix M. R is concerned a twiddle factor. So the change of the brightness can be only determined by λ_1 and λ_2 . If both of λ_1 and λ_2 are little value, the pixel is defined the common point; If either λ_1 or λ_2 is little value, and then another is a great value, the pixel is defined the brim point; if both λ_1 and λ_2 are great value, the pixel is defined the corner point. The formula of the algorithm is shown by

$$Corner = \det M - k(traceM)^2 \tag{5}$$

Where $\det M = \lambda_1 \lambda_2$, $traceM = \lambda_1 + \lambda_2$

Where k is the empirical value, the range of the variable is 0.04~0.06. when the value of the Corner is greater than the selected threshold, and the value of the Corner is the local extreme value in the neighborhood, then the point is the corner.

The Harris operator is an effective operator of the corner detection. Its merits mainly include compute simply, manipulate simply, the corner detected is even and reasonable. The Harris operator computes the every point's interesting value, and then

selects the optimum point in the neighborhood. Though there are rotation and the change of the gray value and the noise and the change of the angle of view in the image, the Harris operator is also a stable algorithm of the corner detection.

In Fig.4. we apply the Harris corner detection in the global environment, and the threshold value be selected 20000. There are many corner detected in the image besides corners of the initial position. The local image of the corner detected is shown in the Fig.5. We can find that the (a),(b)and (c) is the areas of the initial position of the weld. The (d) and (e) is not the areas of the initial position of the weld, but they also can be detected. So we need get rid of these areas such as (d) and (e). We apply the method of the contour of abstraction for these local areas of the corner detected. The result is shown as Fig.6.

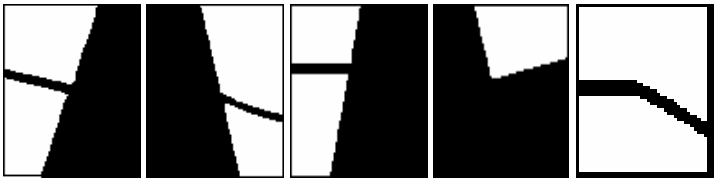

Fig. 5. The local image of the corner detected

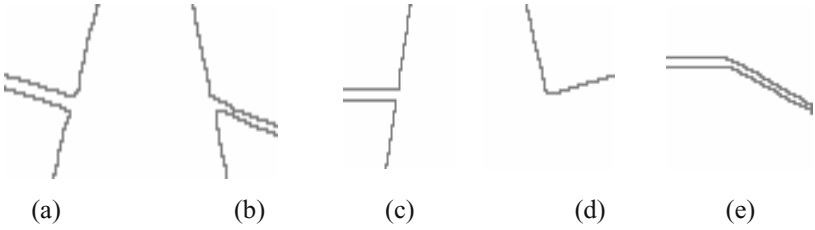

Fig. 6. The result of the contour of abstraction for the local areas of the corner detected

We can find that there is obvious difference between the contour of the initial position of the weld and the contour of the others area from the Fig.9. We can get the initial position of the weld based on these characters.

1) There are a couple of corners in the areas of the initial position of the weld. So the area that it is detected only a corner is not the initial position of the weld.
2) There are three distributing directions of the contour in the local area of the initial position of the weld. In the areas of the corner detected, If the contours distributing directions have only two directions, the corner is not the initial position of the weld.

From the above two criterion, we can get rid of the untrue initial position of the weld. We draw a crossing mark on the position of the weld initial. The result is shown in the Fig.7.

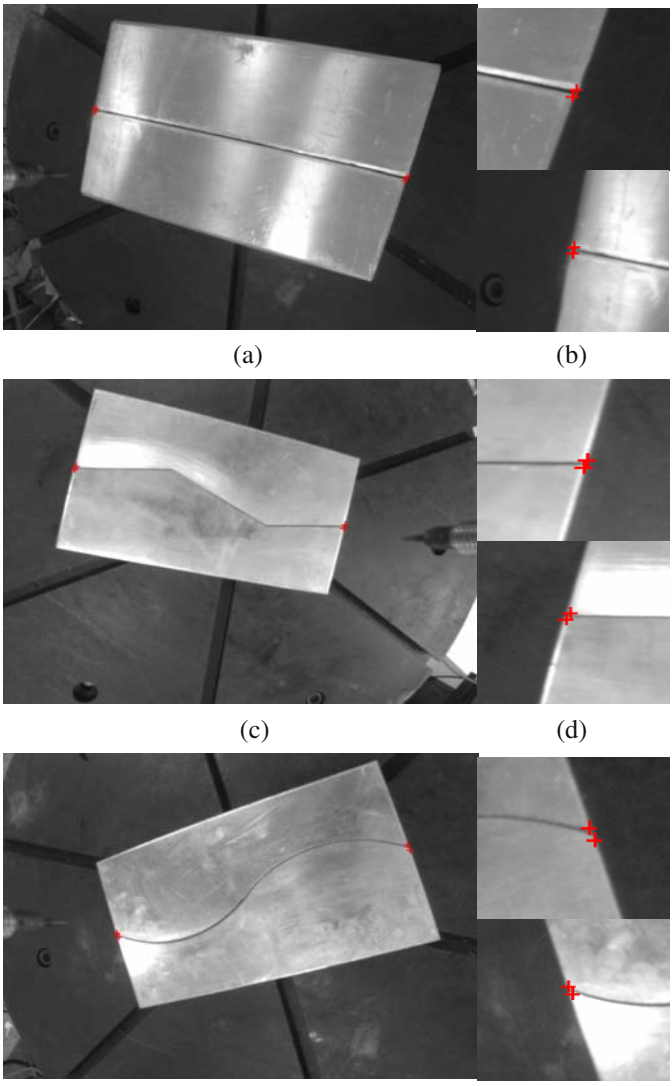

Fig. 7. The result of the initial position recognition of the weld in the global environment

Acknowledgement

This work is supported by the National Natural Science Foundation under Grand No. 50575144 and the Key Foundation Program of Shanghai Sciences & Technology Committee under Grant No. 06JC14036.

References

1. Kim JS, Son YT, Cho HS, Koh KI (1996) A robust method for vision-based seam tracking in robotic arc welding. Mechatronics 6(2): 141-163
2. Sicard P, Levine MD (1989) Joint recognition and tracking for robotic arc welding. IEEE Trans Syst Man Cybern 19:714-728
3. Mokhtarian F, Suomela R. Robust image corner detection through curvature scale space[J]. IEEE Transactions on Pattern Analysis and Machine Intelligence, 1998, 20(12): 1376-1381.
4. Pikaz A, Dinstein I. Using simple decomposition for smoothing and feature point detection of noisy digital curves [J]. IEEE Transactions on Pattern Analysis and Machine Intelligence, 1994,16(8): 808-813.
5. Deriche R, Giraudon G. A computational Approach for corner and vertex detection[J]. International Journal of Computer Vision, 1993, 10(2): 101-124.
6. Harris C, Stephens M. A combined corner and edge detector[A]. Matthews M M. Proceedings of the Fourth Alvey Vision Conference[C]. Manchester: the University of Sheffield Printing Unit, 1988, 147-151.
7. Parida L, Geiger D, Hummel R. Junctions: Detection, classification, and reconstruction[J]. IEEE Transactions on Pattern analysis and Machine Intelligence, 1998, 20(7):687-698.
8. Baker S, Nayar S K, Murase H. Parametric feature detection [J]. International Journal of Computer Vision, 1998,27(1): 27-50.

Integrated Weld Quality Control System Based on Laser Strobe Vision

X.Q. Chen[1], H. Luo[2], and W.J. Lin[2]

[1] Dept of Mechanical Engineering, University of Canterbury,
Private Bag 4800, Christchurch 8140, New Zealand
xiaoqi.chen@canterbury.ac.nz
[2] Singapore Institute of Manufacturing Technology
71 Nanyang Drive, Singapore 638075

Abstract. Arc welding is a complex phenomenon involving intensive interactions among heat, arc and arc force. To minimize the undesirable interference in weld pool imaging, a pulsed laser beam projects a strong illumination onto the weld pool area. The ultra-high shutter speed vision system is synchronized to capture the weld pool image in the given short period. Through image processing, the geometrical information of the weld pool is obtained. It is input to a neurofuzzy logic controller so that the welding parameters like welding current and welding speed can be changed in real time to achieve desired weld dimension in response to the changes in welding conditions.

1 Introduction

The geometry of a weld pool contains information about the welding process and welding quality. Thus weld pool sensing and control play a significant role in automated arc welding. However, one problem encountered in weld pool sensing is that bright arc emissions poses undesirable noise in obtaining clear weld pool image. There have been intensive research efforts in weld pool sensing and control.

Among the existing methods, weld pool oscillation has been extensively studied [1, 2]. An abrupt change in the oscillation frequency of the pool during the transition from partial to full penetration was found. It also has been recognized that oscillations in the weld pool could provide information about the size of the pool, which might be used for in-process control of weld pool geometry.

Ultrasound based weld penetration sensing has also been extensively investigated [3-5]. Although significant progress has been made, practical applications are still restricted because of the contact sensor. A non-contact laser phased ultrasound array was proposed as a new solution [5].

Since the temperature distribution in the weld zone contains abundant information about the welding process, infrared sensing of welding process has been explored [6-8]. Valuable results in this area have been acquired. The penetration depth of the weld pool has been correlated with the characteristics of the infrared image.

As for welding process control, research efforts have focused on penetration control. Since penetration cannot be seen by topside sensors, it needs to be inferred from available weld pool length and width through modeling. Various approaches, such as adaptive control and model based fuzzy logic control have been explored [9, 10].

Although significant achievements have been made in the area of weld pool geometry sensing and control, more accurate and reliable techniques are still needed. It

T.-J. Tarn et al. (Eds.): Robot. Weld., Intellige. & Automation, LNCIS 362, pp. 257–266, 2007.
springerlink.com

is understood that topside weld pool observation could provide much more critical, accurate and instantaneous information on the welding process than most of the existing methods. Due to a recent development in sensing technology, clear imaging of the weld pool is possible by a laser assisted high shutter speed camera [11].

In this work, Section 2 discussed the deployment of laser strobe vision for weld pool imaging and extraction of weld pool geometry through image processing. Section 3 details the design of a fuzzy logic system for weld pool control. Section 4 presents some experimental results, followed by conclusions.

2 Weld Pool Imaging Using Laser Strobe Vision

The experimental set-up consists of a 4-axis AC servo motor robot, a welding torch, and the laser strobe camera linked to a computer. Fig.1 shows the arrangement of laser strobe imaging sensor, Tungsten Inert Gas (TIG) welding torch and laser illumination.

Fig. 1. Close-up of the arrangement of strobe imaging sensor (left), TIG welding torch (centre) and the laser illumination (right)

Fig.2 is a block diagram of the integrated robotic welding system. The CPU sends signals to the motion controller, instructing it to move the 4-axis welding robot. The camera attached to the welding torch captures images of the weld pool formed, and sends them to the DT 3152 frame grabber board. The images are sent to the VisionBlox software that detects the width and length of the weld pool.

The laser strobe vision system deployed consists of a laser unit, a laser head and a camera. It has the following features:

- A band pass optical filter (300 nm ~ 350 nm) is used in the camera to cut off arc emissions in other wavelengths.
- The laser, at 337.1 nanometer wavelength in the near-ultraviolet portion of the optical spectrum, is pulsed for 5 nanoseconds. The laser power density in the duration is much higher than that of the arc during the pulse.
- The reflection from the molten weld pool to the laser is much lower than that from the solidified weld bead. Thus the contrast between the weld pool and its surrounding areas is improved.

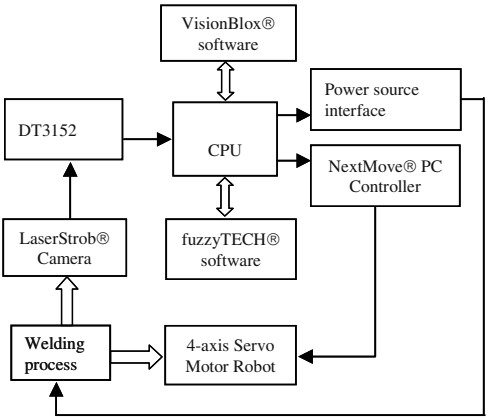

Fig. 2. Block diagram of the integrated robotic welding system

Fig. 3. Front view of the laser units

The laser illumination system is made up of one or two pulsed nitrogen laser units, as shown in Fig.3. In this project, only one pulsed nitrogen laser unit is used. The laser unit is a gas discharge laser, which produces the energy for the laser pulse by means of a very rapid high-energy electric discharge through a sealed laser cavity of high purity nitrogen gas. This makes the laser unit ideal for this application, as it does not require a continuous gas supply, vacuum pump or cooling system.

The laser beam is directed to the area of interest via a large-core fused silica fibre protected by semi-rigid plastic tubing, and the camera head is placed approximately 15 cm away from the scene of interest (Fig.1.). The imaging arrangement gives a large enough field of view of about 20 mm to capture the weld pool which typically ranges from 2 mm to 7 mm in diameter. Once the camera is started, it will take pictures at the frequency that was set to 10 Hz in this work.

A key component in the camera head is the image intensifier tube, which provides electronic shuttering capability and amplifies the intensity of the welding site image. The intensified image is then optically relayed to a specialized CCD sensor situated inside the main body of the camera head. Even if the laser system is providing relatively low average power, the CCD sensor is able to obtain images with good exposure as the image intensifier provides a high gain.

Fig.4 shows a typical raw image of TIG weld pool, captured by the laser strobe vision system. It can be seen that the greyness difference between the weld pool and its surrounding solid material appears as the most apparent feature of the image. The greyness values associated with the molten weld pool are low due to its high absorption of the laser. The greyness of the surrounding solidified areas was much higher because of their high reflection to the laser.

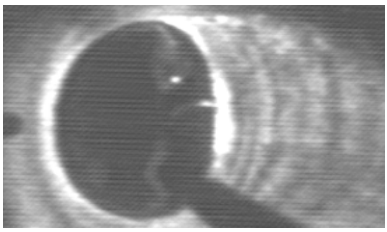

Fig. 4. Weld pool raw images

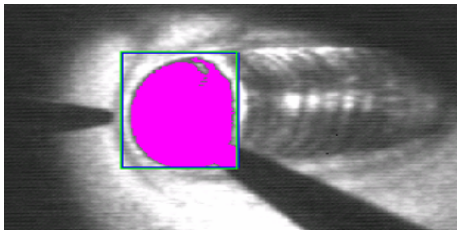

Fig. 5. Image after connectivity analysis

Blob operations were performed to extract the geometric dimensions of the weld pool. Blobs are areas with similar intensity. The software performs a connectivity analysis on the inspection image and displays the results. The purpose of the connectivity analysis is to segment the inspection image into areas of similar intensity. Information concerning the blobs, such as length and breadth, is then extracted. The processed image is shown in Fig.5.

3 Neurofuzzy Logic System for Weld Quality Control

There are two input variables "Length_error" and "Width_error". The graphical definitions of the range of the linguistic values for Length_error are shown in Fig.6 and Width-error is defined likewise. The interpretation of the linguistic values for the input variables is given in Table 1.

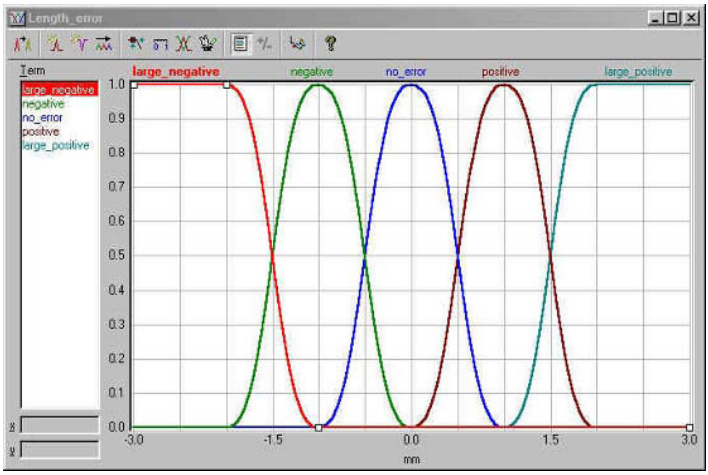

Fig. 6. Graphical definition of "Length_error"

Table 1. Interpretation of linguistic values for "Length_error" and "Width_error"

Linguistic Values	Interpretation
large_negative	The actual length/width of the weld pool is smaller than the desired length/width to a great extent.
negative	The actual length/width of the weld pool is smaller than the desired length/width.
no_error	The actual length/width of the weld pool is the same as the desired length/width.
positive	The actual length/width of the weld pool is larger than the desired length/width.
large_positive	The actual length/width of the weld pool is larger than the desired length/width to a great extent.

Similarly, the range of the linguistic values for the output variable – "Speed_change" is defined, and the interpretation of the linguistic values is given in Table 2.

Table 2. Interpretation of linguistic values for "Speed change"

Linguistic Values	Interpretation
large_negative	The slider speed is to be greatly reduced.
negative	The slider speed is to be reduced slightly.
no_error	The slider speed is not to be changed and kept constant.
positive	The slider speed is to be increased slightly.
large_positive	The slider speed is to be greatly increased.

The definitions of the input and output variables are based on general welding knowledge and past welding experience. The tuning of these variables can be easily done by reshaping the curves.

Individual rules are combined into rule blocks to build the system structure. A rule block holds the inference with the production rules and connects system outputs to system inputs. The Spreadsheet Rule Editor in Table 4 shows the rule block with the complete list of 13 rules.

The degree to which a rule is valid or plausible is described by degree of support (DoS), which is often referred to as "rule weight". Adding an individual weight to each rule extends the concept of "on/off" rules to a representation in which rules themselves are "fuzzy". This allows for the rule base to be fine-tuned during optimization. The DoS is shown in the third column of Table 3.

The closed-loop control system is represented in Fig.7. From this diagram, the vision system was employed as the feedback mechanism, the actual width and length were compared to the desired values and the error was input into the fuzzy controller.

The width and length of the weld pool are passed on to the fuzzy controller, which outputs control measures to be carried out respectively by the motion controller and the welding power source interfaced with the computer. The motion controller thus sends a signal to the slider to speed up or slow down its movement. Consequently the change in speed causes the weld pool geometry to change. The welding power source interface with the computer sends a signal to increase or decrease welding current.

Table 3. Spreadsheet rule editor

Spreadsheet Rule Editor - RB1

#	IF		THEN	
	Length_error	Width_error	DoS	Speed_change
1	large_negative	large_negative	0.80	large_negative
2	large_negative	negative	0.60	large_negative
3	negative	large_negative	0.80	large_negative
4	negative	negative	0.70	negative
5	negative	no_error	0.50	negative
6	no_error	negative	0.50	negative
7	no_error	no_error	1.00	null
8	no_error	positive	0.50	positive
9	positive	no_error	0.50	positive
10	positive	positive	0.70	positive
11	positive	large_positive	0.80	large_positive
12	large_positive	positive	0.60	large_positive
13	large_positive	large_positive	0.80	large_positive
14				
15				
16				

The fuzzy logic system is integrated with the other components involved in the closed-loop control of the welding process. Since the main program that integrates the fuzzy logic system, vision system and robotic motion system is written in Visual Basic language, the fuzzy logic file is compiled to Visual Basic prior to implementation. The compilation of the fuzzy logic file generates the runtime file (.ftr) that is called when running in the Visual Basic environment.

Finally image capturing, image processing and neurofuzzy logic control were integrated into one system. The output of image processing is the input to the

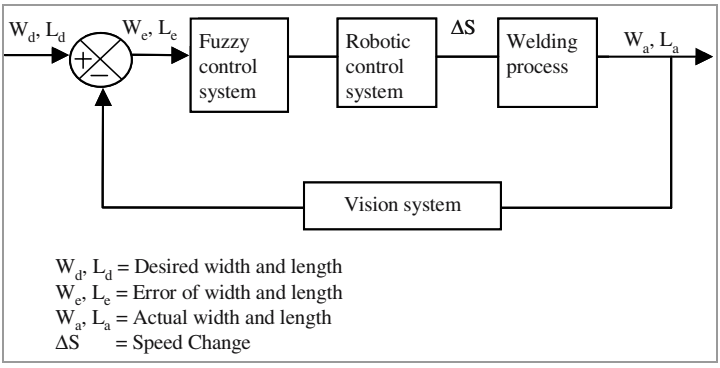

Fig. 7. Block diagram of the closed-loop control system

neurofuzzy logic control system, and then the neurofuzzy logic control system gives the values of the changes in welding current and welding speed to the welding power source and robot. Fig.8 shows the interface of the integrated system.

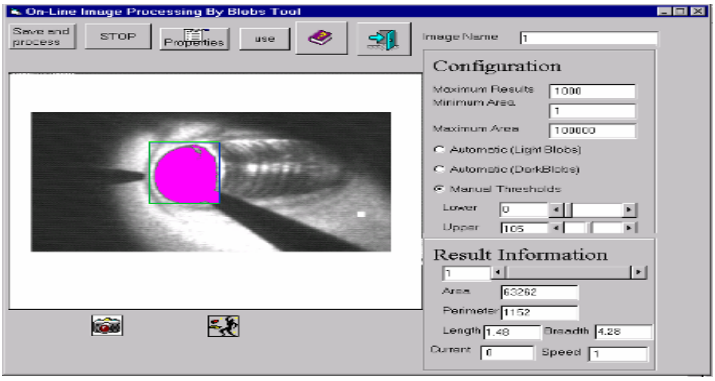

Fig. 8. Interface of the whole system from image process to neurofuzzy control

4 Results and Discussion

Bead-on-plate welding was conducted to explore the relationship between the weld pool geometry and welding parameters. Some of the results are shown in Fig.9 and Fig.10. These data were used to train the rule base of neurofuzzy logic control system.

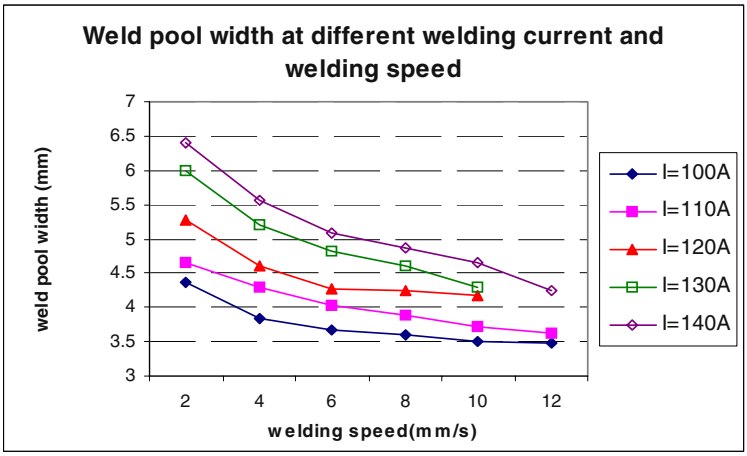

Fig. 9. Correlation between weld pool width and welding current and speed

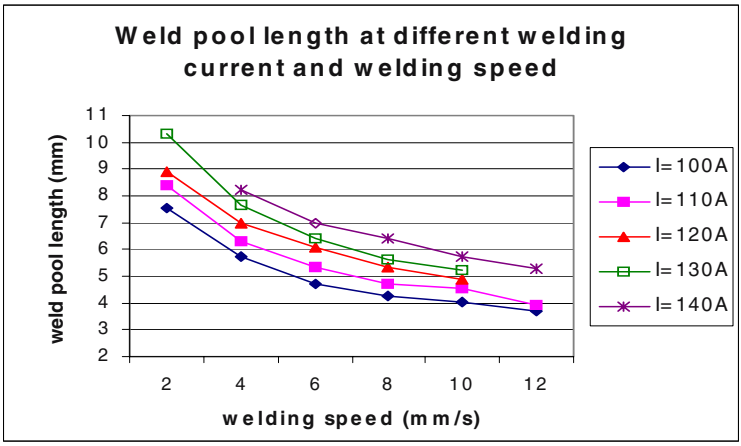

Fig. 10. Correlation between weld pool length and welding current and speed

Open-loop and closed-loop control tests were conducted at a welding current of 115 Amp and a welding speed of 6 mm/s to identify the average width and length of the weld pool. The average width was found to be 5.037 mm, and the average length 5.919 mm. Then the desired width and length were set to 10% below the average values (4.5 mm and 5.3 mm). The objective of this experiment was to observe if the fuzzy controller could speed up the robot in order to produce the desired weld pool geometry. The resulting speed changes are shown in Fig.11.

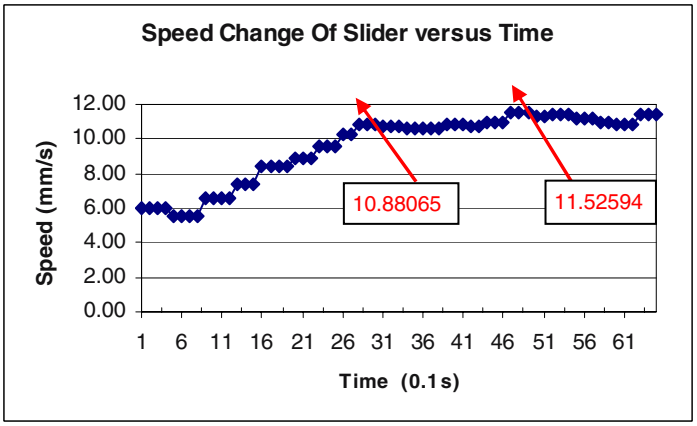

Fig. 11. Speed change during closed-loop welding

It was verified that the speed steadily increased until it reached a stable state (10.88 ~ 11.0 mm/s). It was also found that the average width and length were 4.655 mm and 5.322 mm respectively. These values were found to be close to the desired values, demonstrating that fuzzy control of weld pool operated effectively. Open-loop and closed-loop weld beads are shown in Fig.12.

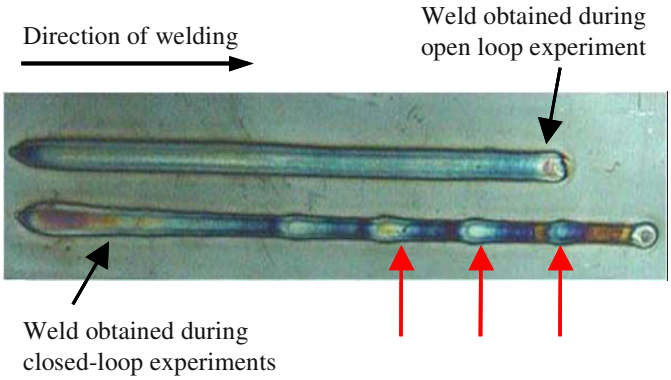

Fig. 12. Weld beads during open-loop and closed-loop welding experiments

In the closed-loop control, the weld pool size decreases as commanded by the fuzzy logic controller. However, the delayed responses from the CPUcausesthe robotic slider to pause while waiting for instructions from the CPU. Since the torch is always activated during the entire welding session, the slider's pause will allow more metal to be heated, causing the larger-than-usual weld pool, as indicated by the three arrows at the right bottom of Fig.12. Higher computation power would eliminate the delay in sending "speed_change" command instructions, hence the pause effect.

5 Conclusions

The study has demonstrated the advantages and feasibility of an integrated weld pool quality control system using laser strobe vision. Clear weld pool images can be captured using the laser strobe vision system to eliminate the interference from the welding arc. Weld pool dimensions can be obtained through image processing. An integrated welding quality system combining laser strobe vision and fuzzy logic control can effectively control the weld geometry.

References

1. Tam, A.S., and Hardt, D.E. "Weld pool impedance for pool geometry measurement: stationary and nonstationary pools", Journal of Dynamic Systems, Measurement, and Control, 111(12), 1989, pp. 545-553.
2. Xiao, Y.H., and Ouden, G.D. "Weld pool oscillation during GTA welding of mild steel", Welding Journal, 72(8), 1993, pp. 428s-434s.
3. Carlson, N.M., et al. "Ultrasonic NDT methods for weld sensing", Material Evaluation, 50(11), 1992, pp. 1338-1343.
4. Yang, J., et al. "Ultrasonic weld penetration depth sensing with a laser phased array", Proceedings of 1994 ASME International Mechanical Engineering Congress, PED - Vol. 68-1, Manufacturing Science and Engineering, Chicago. IL, Nov. 6-11, 1994, pp. 245-254.

5. Graham, G.M., Charle Ume, I., and Hopko, S.N. “Laser array /EMAT ultrasonic measurement of the penetration depth in a liquid weld pool”, Transactions of the ASME, Journal of Manufacturing Science and Engineering, 122(2), 2000, pp. 70-75.
6. Banerjee, P., et al. “Infrared sensing for on-line weld geometry monitoring and control”, ASME Journal of Engineering for Industry, Vol. 117(8), 1995, pp. 323-330.
7. Beardsley, H.E., Zhang, Y.M., and Kovacevic, R. “Infrared sensing of full penetration state in gas tungsten arc welding”, International Journal of Machine Tools and Manufacture, 34(8), 1994, pp. 1079-1090.
8. Nagarajan, S., Banerjee, P., Chen, W.H., and Chin, B.A. “Control of the welding process using infrared sensors”, IEEE Transactions on Robotics and Automation, 8(1), 1992, pp. 86-93.
9. Chen S. B., Qiu T., Lin, T., Wu L., Tian J. S., Lu W. X. & Zhang Y., “Intelligent technologies for robotic welding”, *Lecture Notes in Control and Information Sciences – Robotic Welding, Intelligence and Automation*, Tarn T. J., Chen S. B. and Zhou C. (Eds.), Springer, 2004, pp. 123 – 143.
10. Luo, H., Devanathan, R., Wang, J., and Chen, X.Q. “Vision based weld pool geometry control using neurofuzzy logic”, Proceedings of the 4th Asian Conference on Robotics and its Applications (ARCA), 6-8 June 2001, pp. 141-146.
11. Hoffman, T. “Real time imaging for process control”, Advanced Material and Processes, 140(3), 1991, pp. 37-43.

Development of a Visual-Based Welding Pool Width Control System for Al-P-MIG Welding Process

Shi Yu[1], Zhang Yuyao[2], Fan Ding[1], and Chen Jianhong[2]

[1] Key Laboratory of Non-ferrous Metal Alloys, The Ministry of Education, Lanzhou Univ. of Tech., Lanzhou 730050, China
[2] State Key Lab of Gansu New Non-ferrous Metal Materials, Lanzhou Univ. of Tech., Lanzhou 730050, China
{shiyu, fanding}@lut.cn

Abstract. An intelligent controller based on Fuzzy controller and expert system (ES) control action for Aluminum alloy Pulsed Metal Inert Gas (Al-P-MIG) welding process is proposed. On the basis of welding pool image vision sensing and processing system, the identification model of welding pool width dynamic response in Al-P-MIG welding process has been setup. And then, in the case that welding pool width reference input value is 3mm, 4mm and 5mm respectively, the PID and Fuzzy control effects are simulated and analyzed. The experiments show that the real-time and precision requirements for detecting and control of weld pool width of Al-P-MIG welding process could be satisfied by the established system.

1 Introduction

Being the most popular welding process, metal inert gas (MIG) welding is an important component in many industrial especially in manufacturing operations of aluminum alloy structure [1-2]. However, because of high thermal conductivity of aluminum alloy and very strong thermal accumulating effect in aluminum alloy MIG welding process, a variety of defects are easy created in aluminum weld seam. In such condition, the conventional teach-playback robot has not the ability to optimize operational conditions according to weld pool shape and state and would result in poor welding appearance and welding failure possibly [3-4]. Real-time sensing and control of weld pool dynamics are important techniques to make the robot with the adaptive ability to ensure expected weld quality [5-9], so this research aims at the difficult problem of the sensing and closed-loop control system for Al-P-MIG welding process.

2 Construction of Experimental System

The experimental system includes a vision sensor that consisted of a charge-coupled device (CCD) camera and lenses, multi-filter system, image processing algorithm, and a computer controller. The vision sensor was set to be located at a 30cm distance away from the weld pool. During the pulsed MIG welding, the image of the aluminum alloy weld pool was captured at the duration of low current by using the technology of narrowband filter, which used to overcome the influence of strong arc light. Fig.1

T.-J. Tarn et al. (Eds.): Robot. Weld., Intellige. & Automation, LNCIS 362, pp. 267–273, 2007.
springerlink.com

shows one of captured welding pool image. The captured image was processed to measure the weld pool width by the algorithm of morphology edge detection [10]. In order to eliminate the negative influence on weld line width and penetration caused by the thermal accumulating effect and to keep the stabilization of the pulsed MIG weld, a control system is designed. In this control system, the welding pool width is used as the controlled parameter, while the pulse duty ratio and the wire-feed speed are used as the control parameters.

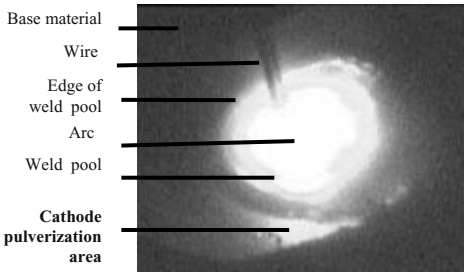

Fig. 1. Image of MIG weld pool

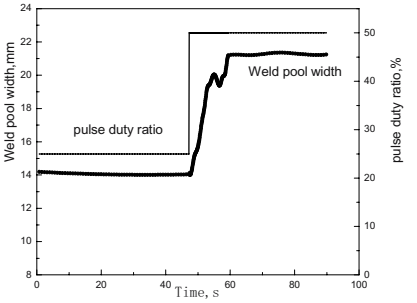

Fig. 2. Curves of the step response of pulse duty ratio and weld pool width

3 System Identification

3.1 System Identification Principles

Research on system identification is in order to get the model and the parameters of the dynamic process of the system. This paper takes the step function as the actual input and uses the characteristic area method to identify the process of the dynamic process of the Al-P-MIG welding. Under the step signal, the dynamic response characteristic of the Al-P-MIG welding pool is that the pool width changes from a steady to another steady state. Therefore, the step response model can be integrated a no oscillation model. The mathematic model of these processes often described by the following transfer function:

$$G(s)=\frac{K}{Ts+1}\cdot e^{-\tau s} \tag{1}$$

Where, K is the process gain, T is the constant, τ is the time lag, s is the differential operator.

The input of the process step response by the vision detecting system is $u(t)$, output is $h(t)$. Then transform the input and the output into the following non-dimensional factors form:

$$u^{*}(t)=u(t)/u_0 \tag{2}$$

$$h^{*}(t)=h(t)/h(\infty) \tag{3}$$

Where u_0 is the step amplitude of the input signal, $h(\infty)$ is the stable value. Therefore K in the formula (1) can be determined:

$$K = h(\infty) / u_0 \tag{4}$$

The key using the curve fit method to system identification is to determine the parameters such as τ, K, T in the formula (1).

3.2 Result of System Identification

In order to obtain the response data of the pool width on the base pulse duty ratio, experiments are designed as follow:

Raw material: 50581-H321 aluminum alloys; weld wire: 5356 Al-Mg weld wire; size of plate: 300mmx100mmx6mm; pulse frequency: 25Hz. welding speed: 12cm/min; welding voltage: 18.0v; peak current: 200A; sampling cycle: 800ms; the pulse duty ratio is 25% before the first 59 sampling cycles, and then mutated to 50%. The welding wire speed also changed from 6.5m/min to 6.8m/min to match the change of the pulse duty ratio. Compare the effect of the pulse duty ratio on the pool width, the welding wire speed's is small, so the effect of the welding wire speed can be ignored when set up the identification model. The step response data is shown in Fig.2. Identification of the pool width on the base pulse duty ratio was made, the transfer function obtained by identification was:

$$G_{W-\delta}(s) = \frac{W(s)}{\delta(s)} = \frac{1.065}{5.0459s+1} e^{\tau s} \quad \tau = -1.1364 \tag{5}$$

The contrast between the step response of the identification model and of the original pulse duty ratio shows that the step response of the transfer function obtained by identification can reflect the actual welding process. From formula (5) we can find that the change of the welding pool width caused by the change of pulse duty ratio have large lag.

4 Simulation Results

Fig.3 and Fig.4 show the simulating response results of control system controlled PID controller and fuzzy controller in the case that welding pool width reference input value is 3mm, 4mm and 5mm respectively. The parameters of PID controller were obtained by genetic optimization algorithm. As shown in Fig.3, when welding pool width reference input is 3mm, 4mm, 5mm respectively, the PID control system can get good response curves without overshoot and static error and its regulating time is 1.9s, 2.4s, 3.2s respectively. However, in order to get good control results in different input condition, different PID parameters should be adopted. Fig.4 shows that the fuzzy logic controller gives a good control performance with good adaptability, and all the simulating results are without overshoot. When the reference input of welding pool width is 3mm, the emulation results are: the regulating time is 1.27s, the static error is 0.06mm; when the reference input of welding pool width is 4mm, the emulation results are: the regulating time is 1.23s, the static error is 0.05mm; when the

reference input of welding pool width is 5mm, the emulation results are: the regulating time is 1.26s, the static error is 0.04mm. Besides the regulating time is shorter than PID controller, the most important advantage by using fuzzy controller is that the good control effects in different reference input can be obtained in same structure and parameters.

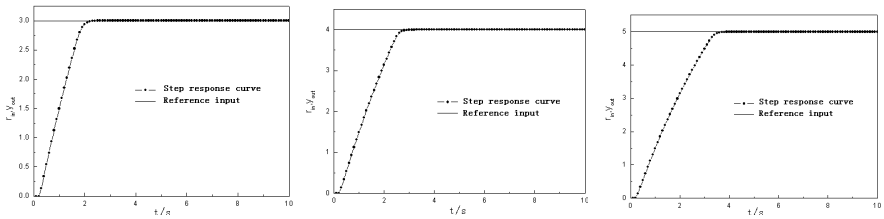

Fig. 3. Simulating results of PID controller. (a) 3mm of Reference input; (b) 4mm of Reference input; (c) 5mm of Reference input.

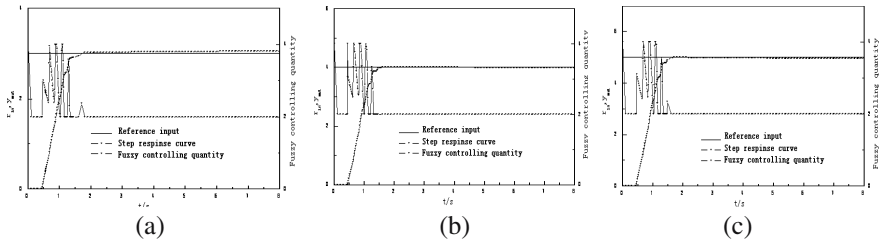

Fig. 4. Simulating results of fuzzy controller. (a) 3mm of Reference input; (b) 4mm of Reference input; (c) 5mm of Reference input.

5 Fuzzy-ES Control System

Because the welding parameters are strongly coupled with each other and the parameters matching have great influence in welding stability, if we adjust only one parameter to control the welding process, it may become unstable. Thus, the ideal controller for the Al-P-MIG welding should be a multivariable decoupling controller with multiple inputs and multiple outputs. However, because of the complex of the welding process, it is difficult to achieve decoupling control. Although a fuzzy logic controller can achieve multi-input and multi-output control, it will introduce difficult in describing the fuzzy control rules and the result will not very good. In view of the characteristic of the Al-P-MIG welding, a controller based on fuzzy and expert system is designed in this paper. The system based on a fuzzy logic control method, combining an expert system that used to select the matching welding parameters. This method can effectively resolve the complex problem described above. The structure of the Fuzzy-ES controller is shown in Fig.5.

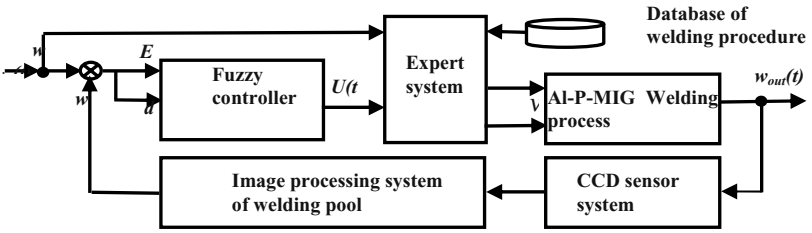

Fig. 5. Structure of Fuzzy-ES controller

6 Welding Experiments

In order to check the performance of the Fuzzy-ES designed above, arc-shaped welding bead along the plate edge is designed which will result in the cooling condition changes from strong to weak and then from weak to strong.

6.1 Experiments with Constant Welding Parameters

When welding with constant welding parameters, the unceasing variation of the heat transfer condition will cause the weld pool width change with it. Fig.6 (a) is the curves of weld pool width in constant welding parameters. When the sample cycle is 500ms, the first 25 sample cycles are transition period, then the welding become steady. As the cooling condition becomes poor, the weld pool width increases incessancy. As the heat transfer condition become well, the weld pool width decrease, and the back penetration change as well. The average current is about 115A throughout the welding process, the current fluctuation is about 5A. Fig.6 (b) and Fig.6 (c) are the photographs of the workpiece topside and backside with constant welding parameters. Because the thermal accumulating effect of aluminum alloy is very strong, the weld pool width changes obviously.

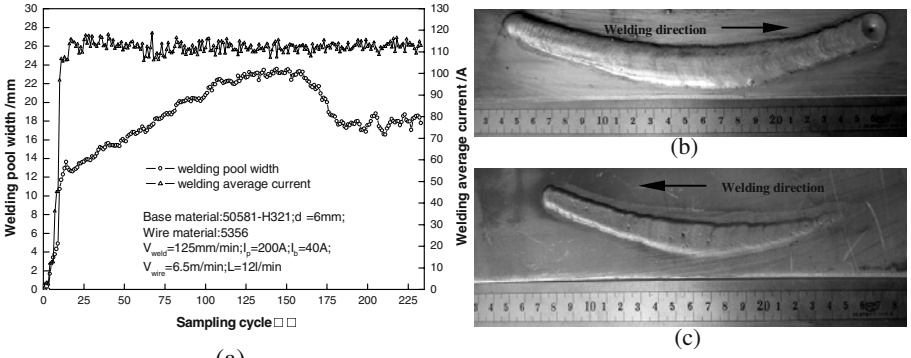

(a) (b) (c)

Fig. 6. Curves of weld pool width in constant welding parameters (a) and photograph of workpiece with constant welding parameters: (b) Topside; (c) Backside

6.2 Experiments with Fuzzy-ES Control

When welding with Fuzzy-ES controller, the closed-loop control of the weld pool width of the Al-P-MIG welding experiment was made. Because the arc starting period of welding is an unsteady state and uncontrollable, in order to avoid vibration in this process, the closed-loop control is done after welding come into steady state namely after 10 sample cycles. Fig.7 (a) is the curves of weld pool width and welding average current in Fuzzy-ES closed-loop control process, Fig.7 (b) and Fig.7 (c) are the photographs of the workpiece topside and backside with Fuzzy-ES control, the topside and backside weld pool width almost keep steady.

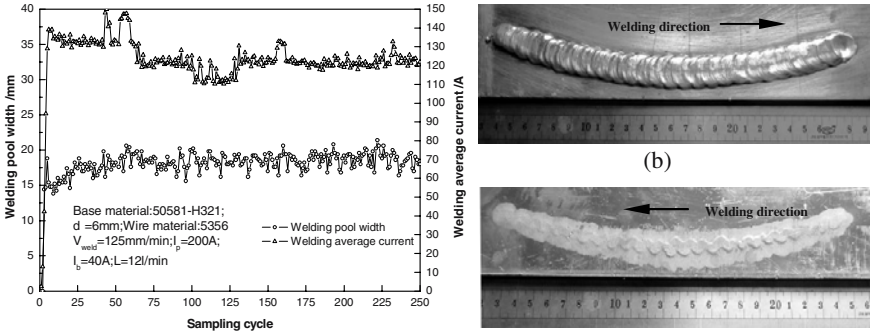

(a) (b) (c)

Fig. 7. Curves of weld pool width in Fuzzy-ES control (a) and photograph of workpiece with Fuzzy-ES control: (b) Topside; (c) Backside

7 Conclusion

The weld pool has been captured by using the CCD sensing system in the low current durations in Al-P-MIG welding process. The results of simulation show that good effect can be obtained by use Fuzzy controller only use same structure and parameters. The weld pool width has been controlled by means of the Fuzzy-ES controller that can resolve the problem of multivariable coupling and remain the welding process stable. Experimental results have confirmed that the Fuzzy-ES control system maintains the prescribed control performance in spite of unpredictable system parameter variations during operation caused by a change in the heat conductivity.

Acknowledgement

The authors gratefully acknowledge the support received from the National Natural Science Foundation of China and Natural Foundation of Gansu Province in PR China, No: 3ZS051-A25-029 and also from the Research Foundation of Lanzhou Univ. of Tech., No: SB1200601.

References

1. S.Yamada, K.Masubuchi. Advanced welding technology keeps Japan's high-speed trains on track [J]. Welding Journal, 2000, 79(11): 48-53
2. P. Praveen, P.K.D.V. Yarlagadda, M.J. Kang. Advancements in pulse gas metal arc welding[J]. Journal of Materials Processing Technology 164–165 (2005) 1113–1119
3. Asnafi N, Langstedt G. A new lightweight metal composite metal panel for applications in the automotive and other industries[J]. 2000, 36(3): 289-310
4. Joseph C, Benedyk K.Light metals in automotive applications [J].Light metal age. 2000, 10(2): 34-35
5. P.J.Modenesi, R.C.de Avelar. The influence of small variations of wire characteristics on gas metal arc welding process stability[J]. Journal of Materials Processing Technology, 86(1999): 226-232
6. Chen Shanben, Cao Jianming, Xu Chenming, Wu Lin. Visual sensing and real-time control of weld pool dynamics in pulsed GMAW[J]. Transactions of The China Welding Institution, 2002, 23(4): 17-20
7. Wang Jianjun; Lin Tao; Chen Shanben; Wang Wei. Method of image conducting in AC tungsten inert gases welding of aluminum alloy[J]. Journal of Shanghai Jiaotong University, 2002, 36(1): 5-8
8. C S Wu; J Q Gao; M Zhang. Sensing weld pool geometrical appearance in gas-metal arc welding[J]. Proceedings of the Institution of Mechanical Engineers; Jul 2004; 218, B7; ProQuest Science Journals, pg. 813
9. Matthew Miller, Bao Mi, Akio Kita, I.Charles Ume. Development of automated real-time data acquisition system for robotic weld quality monitoring[J]. Mechatronics, 12(2002):1259–1269
10. Shi Yu, Fan Ding, Wu Wei. Morphology processing image of aluminum alloy metal inert gas welding pool[J]. Transactions of The China Welding Institution, 2005, 26(3): 37-40

Visual Sensing and Image Processing in Aluminum Alloy Welding

Fan Chongjian, S.B. Chen, and T. Lin

Room 125, Institute of Welding Engineering, Shanghai JiaoTong University,
NO.1954, Huashan road, Shanghai, P.R. China, 200030
chj_fan@sjtu.edu.cn, sbchen@sjtu.edu.cn, lintao@sjtu.edu.cn

Abstract. A new passive visual sensing system and special composed filter technology was developed firstly in this paper. Through the sensor, clearly welding gap image was collected. After regression recover, mean value smoothing, Laplace enhance, most noise was moved and gap edge became more evident. After analyzing the characters around welding gap, special straight line scanning was used. Then the gap edge was considered near the pixel gray value is the minimum on every scanning straight line. Extensively, because the gray value gradient of the gap edge is the local maximum, so the pixels on the two gap edges were found and were divided into two groups, at last, Hough transform was used to fit the two edges, and gap width and welding direction were calculated according to their definitions.

1 Introduction

Aluminum (Al) alloy Gas Tungsten Arc Welding (GTAW) plays an important role in the industrial production. However, for its disadvantageous properties and the random environment conditions, we still can't ensure good stability of penetration in welding aluminum alloy. By introducing the control theory into the welding process of aluminum alloy and varying the opening characteristic of welding process, the system can adapt to the changing of workpiece itself and work environment.

As an important part of the control system for welding process, sensor technology has been studied for a long time. Among all the sensing methods, visual sensing has achieved great progress in detecting penetration for its abundant information. Brzakovic D. obtained the two-dimension image of the molten pool and extracted its geometry information.[1] Kovacevic and Zhang research the image sensing of the weld pool surface in GTAW[2]. Chen S. B. and Zhao D.B developed a passive three-dimension visual sensing method through monocular image which is processed by shadow recovery algorithm to get the three-dimension geometry of the pool. [3]

One side, gap is very important to get well bead. In most application, it is very difficult to assure the same gap from beginning to end in welding process, so how to 'see' the gap is a big problem should be settled down. In this field, little work has been down especially in passive visual sensing. Another side, welding direction is also very important in welding. [4]

In this paper, firstly, a visual sensor is designed and image of the welding gap is collected, then image processing including image recover, Laplace enhance, edge

T.-J. Tarn et al. (Eds.): Robot. Weld., Intellige. & Automation, LNCIS 362, pp. 275–280, 2007.
springerlink.com

detector, and straight line fitting based on Hough transform, the two edges of the gap were found. According to the definition of the welding direction and gap width, the values of them was calculated lastly.

2 Image Processing

2.1 Image Characters

The image in this paper was obtained by a new CCD sensing system in aluminum alloy pulsed GTAW process. To get rid of the unused arc light, special composed filter technology was developed according to the principle of the passive visual image sensing. In fig.1, Every characters including weld pool, nozzle, gap, groove and wire feeding.

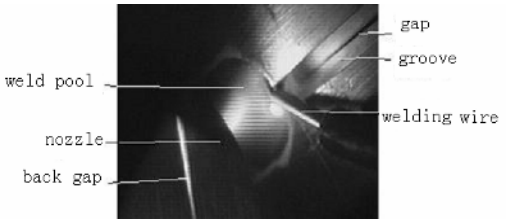

Fig. 1. Welding gap image

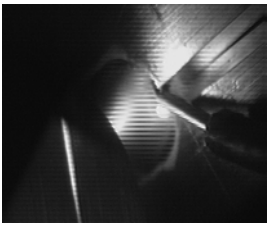

Fig. 2. Original image

2.2 Image Recover

In the experiments, because of the noise such as alternating current effected on the visual sensing system, the image was not so well. Much strip or point noise appeared on the image Fig.2 So we should delete these unused information firstly. [5]

For strip noise, we may consider the region D. Alternate line difference d:

$$d = \frac{\sum_{i=0}^{(m-1)/4} \sum_{k=0}^{(n-1)/2} g(x \pm 2i, y \pm k)}{n(m+1)/2} - \frac{\sum_{j=1}^{(m-1)/4} \sum_{k=0}^{(n-1)/2} g(x \pm (2j-1), y \pm K)}{n(m-1)/2}$$

where i is line number and j is row number, n is width and m is height of D, n and m are odd numbers. $m = 4p+1$, p is natural number.

If d is greater than the threshold, there must be strip noise. From experience, for current point, there being strip noise means that there is no strip noise on neighbor line. So we may use the statistics gray number of neighbor line to approach the gray number of the current point. The approaching number is:

$$f(x, y) = \frac{\sum_{j=1}^{(m-1)/4} \sum_{k=0}^{(n-1)/2} f(x \pm (2j-1), y \pm K)}{n(m-1)/2}$$

because of the complexity in weld, some point noise may exist in the image, but our eyes can not see them. 3×3 mean filter $G(x, y)$ should be used to do with them. Fig.3 is the recover result.

$$G(x, y) = \frac{1}{9}\begin{bmatrix} 1 & 1 & 1 \\ 1 & 1 & 1 \\ 1 & 1 & 1 \end{bmatrix}$$

2.3 Image Enhance

After mean filter operation above, the image becomes blurry. Image enhance is to make blurry image more clearly. Generally, there are two methods in image enhance: differential and high pass filter. Laplace operator is linear combination of partial derivative, and it is isotropy.

Laplace operator is:

$$\nabla^2 f = \frac{\partial^2 f}{\partial x^2} + \frac{\partial^2 f}{\partial y^2}$$

for digital image:

$$\frac{\partial^2 f(i, j)}{\partial x^2} = f(i+1, j) + f(i-1, j) - 2f(i, j)$$

$$\frac{\partial^2 f(i, j)}{\partial y^2} = f(i, j+1) + f(i, j-1) - 2f(i, j)$$

Then,

$$\nabla^2 f = f(i-1, j) + f(i+1, j) + f(i, j+1) + f(i, j-1) - 4f(i, j)$$

after Laplace operation, the gray image is fig.4.

Fig. 3. Recovered and Smoothed image

Fig. 4. Enhanced image

2.4 Edge Detection

Edge detection is to find out the place of gap. On workpiece plane, coordination system xoy can be definite as: y is the moving direction of the one before current time, x is vertical direction to y, o is the original point. In the image, the information is very complex including wire, weld poor, etc. But from experiment, if coordination system xoy is known to us, the probable place of the gap can be known. In fact, xoy is known. So we only left part of the original image, and the gap should be included in this part. In this image, part image left was shown in fig.5. Point in the left part image is definite as *available point,*

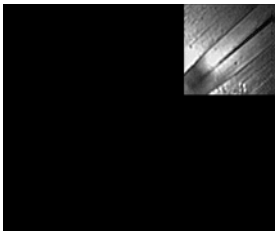

Fig. 5. Part image

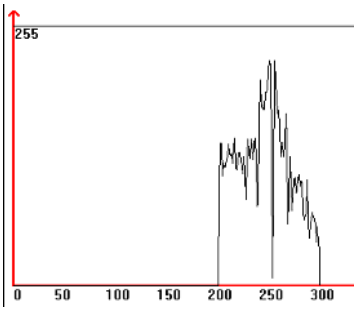

Fig. 6. Gray values variation on the scanning straight line

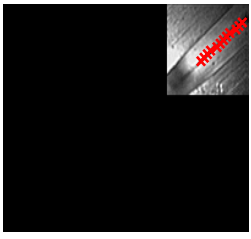

Fig. 7. Center points searching result

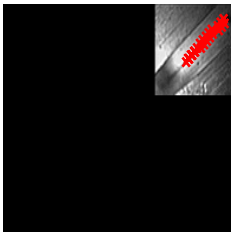

Fig. 8. Edge searching result

To analyse fig.5 further, a line, which is paralleled to x and crosses point (300, 150) can be drawn. Considering the gray values of all *available point* on the line, in fig.6, we could find characters as below:

(1) The point of the minimum gray value in the available points is in the gap.

(2) For all the line paralleling to x, the available points on them has the character in (1).

Minimum gray points on the line above was definite as *center point,* Next steps is prepared to find the two edges of the gap.

(1) Drawing a series of lines paralleling to x axis, every *center point* can be found out. To assure finding real center point, in every sequential search, search area can be limited to $\pm \Delta x$ pixels up or down to y axis. Search result was shown in fig.7.

(2) Calculate gradient of every pixel to construct a gradient map. From every center point, search along positive and negative direction of x axis, two points whose gradient values are maximum in the two directions, can be found separately. In theory, these two points should be on the two edges of the gap.

(3) The series points found in step (2) can be divided into two groups. The two group points are corresponding to the points on the two edges of the gap. In fig.8.

3 Curve Fitting

For the two edges of the gap in one image or in very short distance, straight line can be used to approximate them. In fitting area, much research has been done. Among those methods, least squares technique was used most often. But if there are noise points, fitting result maybe not so satisfied. In this paper, the Hough transform was used. In the method, each point on a curve votes for several combinations of parameters; the parameters that win a majority of votes are declared the winners. [6] Let us consider this approach for fitting a straight line to data.

Hough transform was used mostly to find straight line or curve in binary image. Parameters such as ρ and θ for straight line in plane can be determined by parameter calculating space, among them, ρ is the distance from original point to straight line, θ is the direction of straight line, the function can be described as:

$$f((\rho,\theta),(x,y)) = \rho - x\cos\theta - y\sin\theta = 0$$

From this function, every point in binary image (x_i, y_i) map to series of accumulator $A(\rho_i, \theta_i)$ in Hough space, every point meeting the function, made all values in corresponding accumulator increase 1. If a straight line was in the image, there must be a corresponding accumulator increasing to local maximum; when the local maximum in Hough space was found, the corresponding parameters (ρ,θ) can be decided, then the straight line can be fitting very well.

From the theory of the Hough transform, the voting system provided great virtue especially antinoise, this method can detect out the curve even when speech-noise ratio is very small. The fitting result in the image was shown in fig.9.

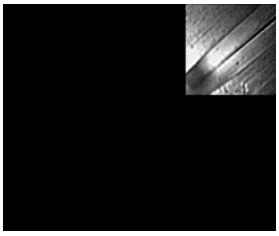

Fig. 9. Curve fitting

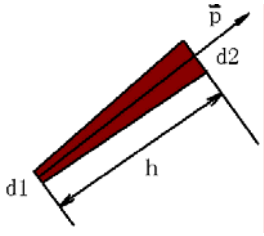

Fig. 10. Parameters definition

4 Gap and Welding Direction

The two straight edges of the gap have been fitted very well, but our purpose is to provide welding direction and gap width. So more research should be done here.

We can use trapezium to approximate the gap. The two fitted straight line were the sloped edges in the trapezium(in fig.10), the vector through the two mid-points of two bottoms, pointing against to the welder is the welding direction $\vec{p}$. According to the welding speed, moving distance in every image collecting period h. Calculating the area of the trapezium s in distance h, s/h is the mean value of the gap in the next pulse current.

5 Conclusion

By the visual sensor and the special composed filter which designed by our research group, clear image including gap was captured in aluminum alloy welding with groove and gap. After image recover, Laplace enhance, edge detector, and straight line fitting based on Hough transform, the two edges of the gap were found. According to the definition of the welding direction and gap width, the values of them was calculated.

Acknowledgements

This work is supported by Chinese National Natural Science Foundation under Grand No. 50575144. it is also supported by Key Foundation Program of Shanghai Sciences & Technology Committee under Grand No. 06JC14036

References

1. Brzakovic D., Khani D. T., Weld Pool Edge Detection for Automated Control of Welding, IEEE Transactions on Robotics and Automation, 1991, 7(3) : 397-403.
2. Zhang Y. M., Kovacevic R. and Wu L., Closed-loop Control of Weld Penetration Using Front-Face Vision Sensing, Journal of Systems and Control Engineering, 1993, Vol. 207(3): 27-34.
3. Zhao D. B., Lou Y. J., Chen S. B., Wu L., Surface height and geometry parameters for describing shape of weld pool during pulsed GTAW. SPIE International Symposium on Intelligent System and Advanced Manufacturing, Boston, Massachusetts, USA, 1999, V3833: 91-99.
4. Zhang Guangjun, Intelligent control of weld shape during varied gap pulsed GTAW with wire filler based on visual sensing[D]. Harbin China, Harbin Institute of Technology, 2002.
5. J. J. Wang, T. Lin, S. B. Chen. Obtaining weld pool vision information during aluminum TIG welding, International Journal of Advanced Manufacture Technology, London, UK, 2005, V26: 219-227.
6. Ramesh Jain, Rangachar Kasturi, Brian G. Schunck. Machine vision, China machine press, China, 2003.
7. He Bin, Visual C++ Digital image processing, Post & Telecom press, Beijing, China, 2002.

Seam Tracking of Articulated Robot for Laser Welding Based on Visual Feedback Control

Wenzeng Zhang, Qiang Chen, Guoxian Zhang, Zhenguo Sun, and Dong Du

Key Laboratory for Advanced Materials Processing Technology, Ministry of Education, Department of Mechanical Engineering, Tsinghua University, Beijing 100084, P.R. China

Abstract. Laser welding has a quite high demand on trajectory accuracy of articulated robot. To improve dynamic trajectory accuracy of articulated robots for laser welding, a novel 3D seam tracking method is proposed based on stereo visual feedback control. The method constructs a visual feedback control system with two convergent cameras mounted at the end of industrial robot. A tool coordinate system is constructed to transfer the end-link displacement of robot to that of the tool. A proposed GPI transform method, binocular vision technologies and a modified algorithm of line-line matching are utilized to calculate the positions of laser focus and weld seam, which makes the dynamic trajectory error between laser focus and weld seam can be calculated. The robot is finally commanded to move and decrease the trajectory error as soon as possible based on robot kinematics. Experimental results show that the method can effectively improve the trajectory accuracy of industrial robot for laser welding.

Keywords: industrial robot, visual feedback, seam tracking, trajectory accuracy.

1 Introduction

Nowadays, articulated robots for sale only provide customers their positioning accuracy, never offering or guaranteeing their trajectory accuracy. However, along with the development of manufacturing and processing, some high-speed and high-accuracy jobs, such as laser welding and cutting, have a quite high demand on trajectory accuracy. Moreover, current industrial robots could only move under scheduled instructions under a strictly structured environment, which limits their applications. Lots of research schemes are proposed to improve the ability of industrial robots in environmental understanding. As an important sensing method, vision plays an important role in improving the industrial robots' ability in environmental understanding and variance adaptation.

In reference [1], a visual servoing system of industrial robots based on position was constructed, and algorithm to estimate the object position and pose with a camera is proposed when the distances of several characteristic points were known beforehand. In reference [2], an eye-on-object method was realized in planar moving object tracking based on an eye-in-hand visual servoing structure. In reference [3], the problem that the actual position of end link of robot is far from the anticipant one was solved with a method of spatial path planning and image-based control. In reference [4], an industrial flame tracking system was developed to cut planar drawings based on vision.

T.-J. Tarn et al. (Eds.): Robot. Weld., Intellige. & Automation, LNCIS 362, pp. 281–287, 2007.
springerlink.com

In this paper, in order to improve the moving trajectory accuracy of industrial robots for laser welding, a GPI transform method for seam recognition [5] in trajectory tracking was utilized, and an improved algorithm was proposed to reconstruct the trajectory line and laser focus more precisely. Meanwhile a tool coordinate system was constructed skillfully to make the tool displacement calculation easily and quickly. The modified displacement of the robot is calculated and the robot is finally commanded to move and decrease the trajectory error as soon as possible based on robot kinematics.

2 3D Reconstruction of Laser Focus and Trajectory Lines

The hardware of the established robot visual servoing system is shown in Fig.1. A laser processing tool and two cameras are mounted on the end of articulated robot. The laser focus and trajectory line are imaged in both cameras.

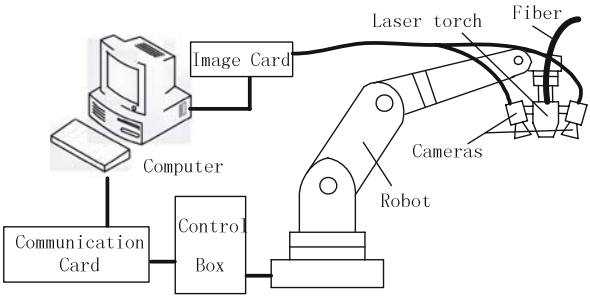

Fig. 1. System hardware components

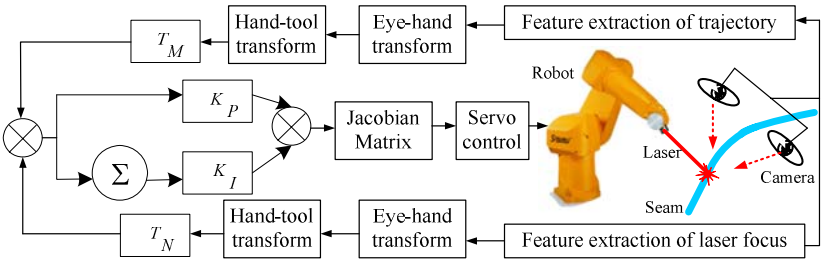

Fig. 2. Coordinate frames

The control structure of system is shown in Fig. 2. The established frames of system is shown in Fig. 3.

Where, $\{R\}$ $\{E\}$ --the base and end-effecter frames of robot ,
$\{CL\}$ $\{CR\}$ --the frames of left and right camera,
$\{T\}$ --the frames of tool,

M , N --the laser focus and the desired point to be welded,

${}^{A}T_{B}$ --the transformation matrix between frame A and B.

The inner and outer parameters of cameras [1], stereo vision coordinates, transform matrix of coordinates between the robot hand and eye [6], and relation matrix between the robot hand and tool are all calibrated beforehand.

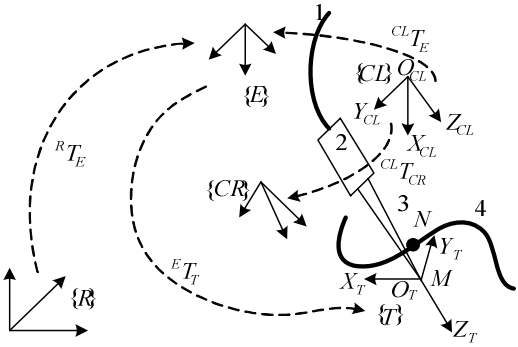

Fig. 3. Coordinate frames

The laser focus and trajectory line in two images are detected by a threshold segmentation method and GPI transform [5]. Since images in left camera and right camera are matched, the position of laser focus in the coordinates of left camera can be reconstructed based on the principle of stereo vision reconstruction.

In reference [7], a line-line matching method was proposed to reconstruct the 3D line from the images in left and right cameras. Experimental results show that this method usually causes errors, which may reduce when the camera goes away from the object observed. The reason is that the model of pinhole imaging is always used. The model of pinhole imaging is righter when the camera is farer from the object, which formula is: $Z_{CL} - f \approx Z_{CL}$.

However, to improve the image resolution, it is not suitable to put the camera far away from the object. Then an improved line-line matching method is proposed which is established based on: $Z_{CL} - f \neq Z_{CL}$.

The improved projection imaging formula is:

$$\begin{cases} u_i = \dfrac{f\,{}^{CL}X_i}{(f - {}^{CL}Z_i)S_x} + u_0 \\ v_i = \dfrac{f\,{}^{CL}Y_i}{(f - {}^{CL}Z_i)S_y} + v_0 \end{cases} \tag{1}$$

where, (u_i, v_i) --a point coordinates in image, pixel,

(u_0, v_0) --the center point coordinates of image, pixel,

S_x, S_y --the width and height of a pixel, mm,

f --the focus length of lens, mm,

$({}^{CL}X_i, {}^{CL}Y_i, {}^{CL}Z_i)$ --the coordinates of a point on the line in $\{CL\}$, mm.

The equation of spacial line in {CL} can be gained as follows:

$$\frac{X - {}^{CL}X_0}{{}^{CL}l} = \frac{Y - {}^{CL}Y_0}{{}^{CL}m} = \frac{Z - {}^{CL}Z_0}{{}^{CL}n} \tag{2}$$

where, $({}^{CL}X_0, {}^{CL}Y_0, {}^{CL}Z_0)$ --coordinates of a point on the line in $\{CL\}$, mm, $({}^{CL}l, {}^{CL}m, {}^{CL}n)$ --the direction vector of line detected in $\{CL\}$, mm.

The purpose of the control system is to keep the laser focus on the trajectory line by moving the industrial robot. In order to control the robot movement, the pedal point of laser focus on trajectory line should be calculated beforehand.

Because the curvature of curve weld seam is generally small, the curve weld seam can be considered approximately as multiple segments of straight lines. The pedal-finding problem is changed to calculating the pedal N of the laser focus M in a straight line. Construct a plane that covers point M and is perpendicular to the trajectory line. Therefore, the cross point of this plane and trajectory line is the pedal.

$$\begin{cases} {}^{CL}l(X - {}^{CL}X_M) + {}^{CL}m(Y - {}^{CL}Y_M) + {}^{CL}n(Z - {}^{CL}Z_M) = 0 \\ \dfrac{X - {}^{CL}X_0}{{}^{CL}l} = \dfrac{Y - {}^{CL}Y_0}{{}^{CL}m} = \dfrac{Z - {}^{CL}Z_0}{{}^{CL}n} \end{cases} \tag{3}$$

where, $({}^{CL}X_M, {}^{CL}Y_M, {}^{CL}Z_M)$ --coordinates of the laser focus in $\{CL\}$, mm.

With equation (3) the pedal position $({}^{CL}X_N, {}^{CL}Y_N, {}^{CL}Z_N)$ in $\{CL\}$ is gained.

3 Displacements Calculation

Change the coordinates of calculated pedal and laser focus from $\{CL\}$ to $\{T\}$, then calculate the displacements in joint space of robot with Jacobian matrix in $\{T\}$. Construct the tool coordinates $\{T\}$ (shown in Fig. 2) as follows:

(1) Choose the laser focus O_T as the original point,
(2) Choose the laser beam as Z_T, pointing from the fiber torch to object welded,
(3) Axis X_T is set by equation (4):

$${}^{E}\mathbf{x}_T = {}^{E}\mathbf{z}_T \times {}^{E}\mathbf{x}_{CL} / \left\| {}^{E}\mathbf{z}_T \times {}^{E}\mathbf{x}_{CL} \right\| \tag{4}$$

(4) Axis Y_T is set by equation (5):

$$^{E}\mathbf{y}_{T} = {}^{E}\mathbf{z}_{T} \times {}^{E}\mathbf{x}_{T} \tag{5}$$

where, $^{E}\mathbf{x}_{CL}$ --the description of $\mathbf{x}_{CL}$ in {E},

$^{E}\mathbf{x}_{T}, {}^{E}\mathbf{y}_{T}, {}^{E}\mathbf{z}_{T}$ --the description of $\mathbf{x}_{T}, \mathbf{y}_{T}, \mathbf{z}_{T}$ in {E}.

The displacement $^{T}\mathbf{p}_{MN}$ in $\{T\}$ can be calculated by (6):

$$^{T}\mathbf{p}_{MN} = {}^{T}T_{E}\,{}^{E}T_{CL}({}^{CL}N - {}^{CL}M) \tag{6}$$

The calculation of Jacobian matrix in $\{T\}$ is similar with that in $\{E\}$, the only difference is that using $^{n-1}B_{n} = {}^{n-1}A_{n}\,{}^{E}T_{T}$ to replace the $^{n-1}A_{n}$. With this method, the displacement calculation of tool end is changed to the displacement calculation of robot end, which would be easier and quicker. ($^{n-1}A_{n}$ is the transformation matrix from the n-1 coordinates to the last coordinates.)

Keep the orientation of robot end-link unchangeable when tracking. Calculate the displacement in joint space with Jacobian matrix in $\{T\}$:

$$\begin{bmatrix} q_1 & \cdots & q_i & \cdots & q_n \end{bmatrix}^{T}_{n\times 1} = \left({}^{T}J\right)^{-1}_{n\times 6} \begin{bmatrix} {}^{T}\mathbf{p}_{MN} \\ 0 \end{bmatrix}_{6\times 1} \tag{7}$$

where, $q_i, (i = 1, 2, \cdots, n)$ --displacement of the robot joint i,

n --number of the robot joint,

^{T}J --Jacobian matrix in $\{T\}$.

4 Experiments and Analysis

The experimental results show that the trajectory detecting and control system of welding robot based on stereo vision can be well used in trajectory recognizing, detecting and automatic tracking. The error of tracking is less than 0.5 mm in real-time.

For example, two steel sheets are butted closely without groove. The tracking speed of robot end is 20 mm/s. The position and orientation of weld seam (trajectory line) is unknown beforehand. Fig.3a is the image captured before tracking. In this image two short parallel white lines is the edges of sub-window searched; the long white line is the trajectory line detected by GPI transform method, and the white circle point is laser focus; the black square point is the pedal of laser focus and welding line calculated in 3D space with stereo vision algorithm. Fig.3b shows the image of tracking result, where the laser focus has already moved to the pedal and goes along with the welding line.

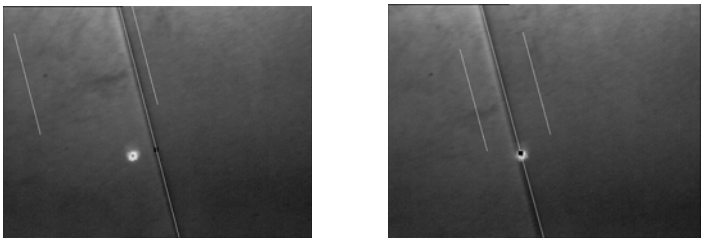

(a) image before tracking (b) image after tracking

Fig. 4. Image before and after tracking in left camera

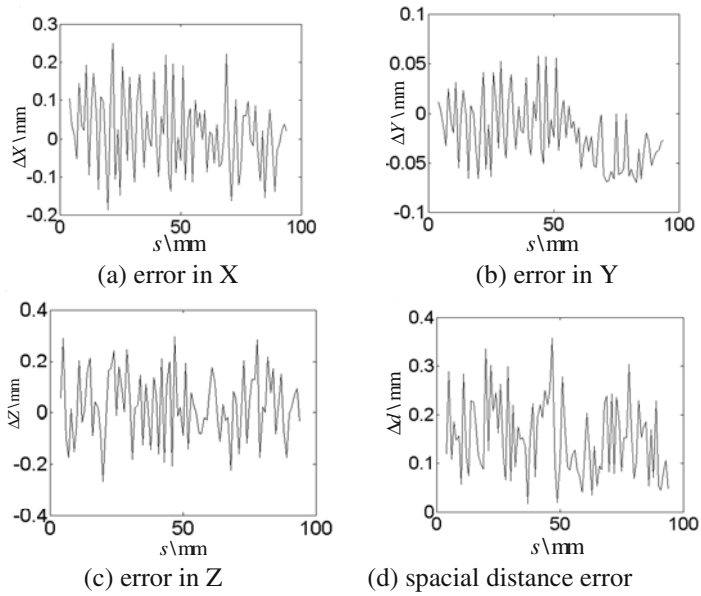

(a) error in X (b) error in Y

(c) error in Z (d) spacial distance error

Fig. 5. Tracking error

The errors in *X, Y, Z* and the spacial distance error of tracking are shown in Fig. 4. Experimental results show that the errors in *X, Y, Z* are less than 0.3 mm, the spacial distance error is less than 0.4 mm. The system could not only recognize the welding seam automatically, but also meet the welding requirement in real-time trajectory tracking and control.

5 Conclusions

In this paper, a 3D seam tracking method of articulated robot for laser welding based on stereo visual feedback control is proposed. The method can be used to improve dynamic trajectory accuracy of articulated robots in precise materials processing such as laser welding and cutting. With the proposed algorithm the trajectory line and laser

focus can be reconstructed accurately by 3D vision. The needed tool displacement is calculated easily and quickly by a suitable tool coordinate frame. The robot is finally commanded to move and decrease the trajectory error as soon as possible based on robot kinematics. Experimental results show that the method can effectively improve the trajectory accuracy of industrial robot for laser welding, and the system used the method could meet the demand of high accuracy trajectory tracking.

Acknowledgements

This research was supported by Chinese National Natural Science Foundation (No. 50275083), and The Research Fund for the Doctoral Program of Higher Education (No. 20020003053).

References

1. Mana Saedan, Marcelo H, 3D Vision-based Control On an Industrial Robot[A]. Proc of IASTED Intel Conf on Robotics and Applications [C]. Florida, USA. Nov, 2001: 152-157
2. Wang Jianhua, Zhao Xiaoguang, Tan Ming. Research on Tracking Control of a 5-DOF Visual Servo Robot [J]. Robot. 2005, 27(3): 215-219 (in Chinese)
3. Mezouar Y, Chaumette F. Path Planning for Robust Image-based Control [J]. IEEE Trans on Robotics and Automation, 2002, 18(4): 534549.
4. Xu Kanlie, Fei Renqing, Wang Xiaogang etc. Research on 2D Line Segment Tracking System [J]. Journal of Shanghai University. 1999, 5(4): 348-352 (in Chinese)
5. Zhang Wenzeng, Chen Qiang, Du Dong etc. Gray Projecting Integral Method for Line Detection [J]. Journal of Tsinghua University(Science and Technology). 2005, 45(11): 1446-1449 (in Chinese)
6. Shiu Y C, Ahmad S. Calibration of Wrist-mounted Robotic Sensors by Solving Homogeneous Transform Equations of the Form AX=XB [J]. IEEE Trans of Robotics and Automation, 1989, 5 (1): 16-27
7. Ma Songde, Zhang Zhengyou. Computer Vision: Computation Theory and Algorithm Basic [M]. Beijing: Science publishing company. 1998 (in Chinese)

Efficient Weld Seam Detection for Robotic Welding from a Single Image

Fanhuai Shi, Lv Zhou, Tao Lin, and Shanben Chen

Institute of Welding Engineering, Shanghai Jiao Tong University, P.R. China
fhshi@sjtu.edu.cn

Abstract. The weld seam recognition is a key technology in robotic welding. This paper presents an efficient algorithm of weld seam detection for butt joint welding from a single image. The basic idea of our approach is to find a pair of weld seam edges in the local area first. Then, starting from the two endpoints of each edge, search for the remnant edge by iterative edge detection and edge linking. This method is insensitive to the variance of the background image and can apply to most type of weld seams in butt joint welding. Experimental results on several type of weld seam images are shown.

1 Introduction

With the development of robotized welding, improving intelligence and autonomy of arc welding robots is becoming one of the main research directions in the area of industrial robots [1]. To this aim, one should solve the problems of functional sensors and effective information acquisition methods. As a result, weld seam detection with high precision gained increasing importance in automated plants and has made many achievements.

In early period, Estochen et. al.[2] used ultrasonic sensor for weld seam detection. However, there exist many difficulties when ultrasonic sensor worked in real application. Arc sensor has good recognition ability for weld seam [3], but it hard to detect the weld seam when the groove is not so big. Vision sensor technology has been widely applied in welding industry due to plentiful information. Some approaches, such as laser scanning [4], structured light [5] or infrared technology [6], need active lighting device. Recent decade, some researches focus on the vision system for weld seam recognition and tracking in natural lighting conditions [7-8], but the arc disturbance and surface noise still have great influence during this process. To solve this problem, one can make trajectory preplanning of the weld seam before welding.

Zhang et. al. [7] proposed a recognition method of weld seam trajectory based on image pattern feature. The algorithm divides the weld seam into many sections and describes each section with a feature vector. It recognizes the weld seam by comparing the similarity between the current feature vector and former feature vector iteratively. This method has the advantage of fast speed and can perform exact tracking, however, it assumes that the initial position of the seam was given in advance. Ref. [8] implemented weld seam detection at sub-pixel precision by using Zernike moments, but it can only deal with those weld seam with parametric shape. Other ways of weld seam detection include Wavelet, Kalman Filtering [9] etc.

T.-J. Tarn et al. (Eds.): Robot. Weld., Intellige. & Automation, LNCIS 362, pp. 289–294, 2007.
springerlink.com

In this paper, we address the problem of weld seam trajectory preplanning from a single image and propose an autonomous recognition algorithm. The basic idea of our approach is to find a pair of parallel weld seam edges in local area first. Then, starting from the two endpoints of each edge, search the remnant edge by iterative edge detection and edge linking in a shift window.

2 Algorithm of Welding Seam Detection from an Image

In the image of work-piece for butt-welding, the weld seam shows as a low gray strip with two parallel edges. The basic steps of our approach include: (1) find a pair of parallel weld seam edges in local area; (2) starting from the two endpoints of each edge, iteratively search the remnant edge by a shift window; (3) refine the seam endpoint by corner detection. More specifically, our approach proceeds as follows:

2.1 Edge Detection of Weld Seam in Local Area

The first step of our approach is to find a pair of parallel weld seam edges locally. Without loss of generality, we suppose that the weld seam pass by a predefined rectangular area in the central image, which is easy to fulfill in practice. See Fig. 1, 1a is the whole image of a line weld seam and the rectangular area.

Firstly, we use edge detection method to extract the edge information of the local image. Numerous edge detection techniques have been proposed (see [10][11] to cite a few). Among them, Canny operator [10] and its variations are the most popular edge detection approaches. In this paper, we use Canny operator to get the edge image I_0, see Fig. 1(b). Note that this process only deals with a local image. Although Canny is a little more complex than many other edge detection operators, it is still efficient relative to the whole image and the computation cost can be ignored here if the window is small enough.

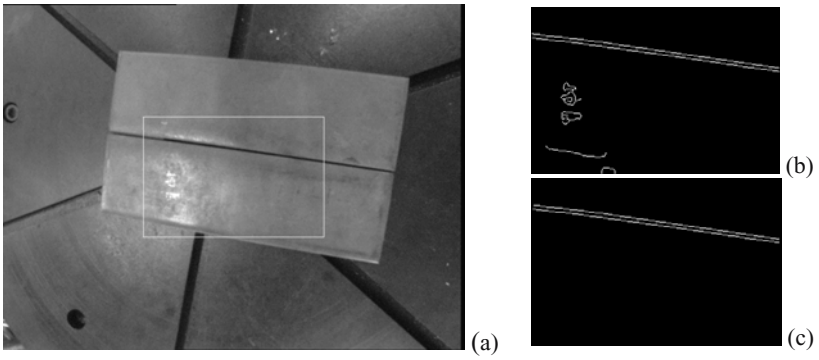

Fig. 1. Welding seam edge detection in the central image area. (a) the whole weld seam image with a white rectangular frame which denotes the predefined window; (b) edge image in the rectangular area; (c) weld seam edge, which is extracted from (b).

Then, we concentrate on the post-processing of the edge image I_0, which aims to extract the weld seam edge and remove the non-interest edges. To reach this aim, we should make clear the characteristics of the weld seam image first. As we know, any weld seam has two parallel edges with limited gap in butt-welding, even for kink line weld seam whose edges also parallel to each other locally, see Fig.2. In addition, the mean gray-level of the weld seam area is lower than those pixels on the edge. This leads to the following algorithm for extracting weld seam edge from the acquired edge image.

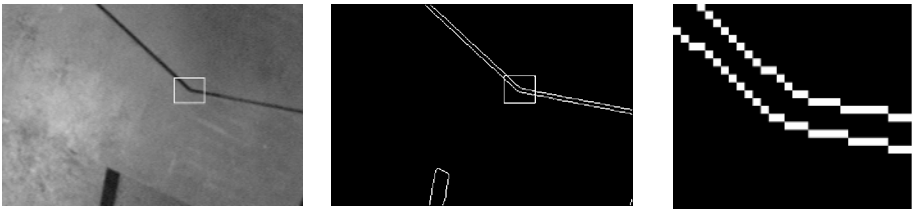

(a) (b) (c)

Fig. 2. Kink line welding seam. (a) original image; (b) edge image of (a); (c) local details about the edge of kink mark in (b).

Algorithm 1 (Extracting weld seam edge from binary edge image)

1. Remove the edge pixels on the borderline area of the image;
2. Do { If (current pixel is labeled or equal to 0) , go to next pixel;
If (no 8-neighbor pixel equal to 1)
Then, reset this pixel to 0 and go to next pixel;
If (current edge pixel satisfy that: (1) there exist edge pixel(s) lies within the given range in the normal direction of the current edge; (2) the mean gray-level of the pixels within the above two edge pixels is lower than the edge pixels)
Then, label current edge pixel as weld seam edge pixel and continue to search along the current edge
Else, reset current edge pixel to 0;
Go to next pixel;
}Untill (end of image)
3. Count the length of each connected edge; the two edges with maximal length are taken as the weld seam;
4. Trim the data of weld seam to remove the redundant edge pixels.

Fig.1(c) is the result of Fig.1(b) by using Algorithm 1. We may also apply the above process to the later iterative procedure to find the remnant weld seam edge.

2.2 Extract the Remnant Weld Seam Edge

Once a pair of weld seam edges is obtained, we can try to extract the remnant weld seam edge starting from each endpoint of the acquired edge respectively. We use a shift window to carry this operation. The window moves along the direction of the

seam edge. In each position, we use Canny operator to get the edge image of the window and Algorithm 1 to extract the weld seam edge from the local edge image. Finally, link the obtained edge segment to the former weld seam edge. Iteratively perform the above steps until the window reaches the end of the weld seam. More specifically, this process can be described as the following algorithm:

Algorithm 2 (Extracting remnant weld seam edge by using a shift window)

1. *Compute the edge direction of the obtained weld seam at the endpoint, which is used as the moving direction of the shift window;*
2. *Compute the future position of the shift window;*
3. *Make edge detection by Canny operator in the shift window;*
4. *Extract the weld seam edge segment from the edge image by Algorithm 1;*
5. *Link the edge segment to the former weld seam;*
6. *Judge whether the searching is finished according to the distance between the segment endpoint and window boundary. If not finished, then go to step 1.*

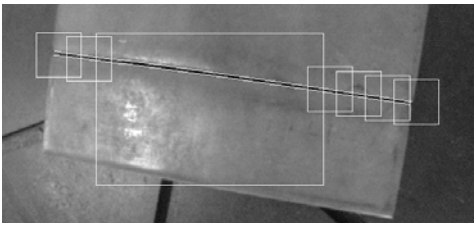

Fig. 3. An illustration of shift windows for edge detection and linking

The above process need to be carried at the two endpoint of the weld seam respectively, thus we can get the whole weld seam edge. Fig. 3. illustrates the shift windows for edge detecting and edge linking.

2.3 Refine the Endpoint of Weld Seam

Since the whole weld seam edge is extracted, the endpoints of the weld seam are known. However, these endpoints are extracted by edge detector, thus they may not be the accurate corner position. In this paper, we use the classical Harris corner detector [12] to find the accurate weld seam endpoint.

The corner detection is only performed in the last shift window in Algorithm 2. There maybe exist several corners in the detection results. We chose two corners, which are closest to the pre-acquired endpoints, as the object endpoints. Once the endpoints of the weld seam are located, we can directly link the endpoints to the obtained weld seam edge.

3 Experimental Results and Discussion

We test the algorithm on several type of weld seam to evaluate its practical performance. We adopt CCD camera (Watec-902H) in the experimental system and the image

size is 768*576. We set the size of predefined window to be 300*200 and the shift window 60*60. Fig. 4 shows the results of applying our algorithm on different type of weld seam. In the result images, yellow curves represent the extracted weld seam, and the yellow mark "+" represent the detected seam endpoints by corner detection. From the result we can see that the proposed method is suitable for most type of weld seam in butt-welding. However in some cases, there is only one corner detected near the endpoint of the weld seam, and some detected endpoints are not so accurate in terms of human experience. On one hand, it is due to the limitation of the corner detection algorithm; on the other hand, the angle of view or blurry image quality affects the detection to some extent. Anyway, we can take the detected seam endpoints as a reference to adjust the angle of view of the robot, so as to locate the initial welding position accurately.

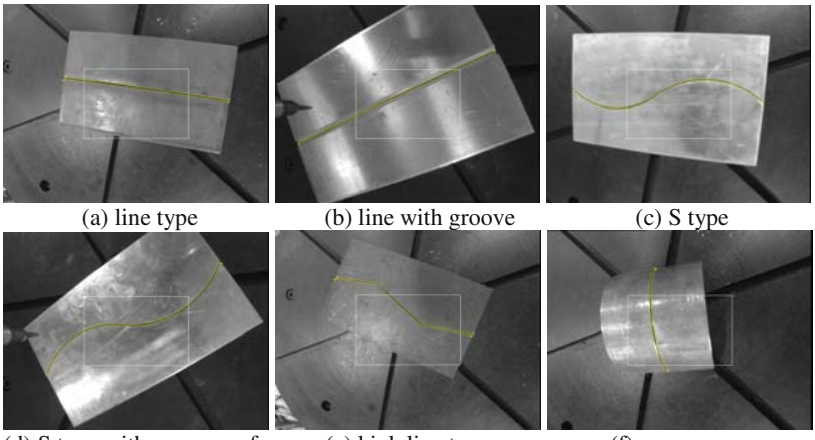

Fig. 4. Experimental result of different type of welding seam, the welding seam edge and endpoint are labeled with yellow line and yellow mark "+" respectively

Note that, the size of predefined window will affect the working efficiency in real application. Larger the window is, more convenient the worker feel in operation, however, more risk for seam edge detection. So, there must be a trade off consideration between the convenience and the risk of image processing.

Although it is effective in most cases, the proposed method can not work when the reflection of the work-piece is strong enough to submerge the weld seam in the image. Therefore, more robust algorithm is in need to be developed.

4 Conclusion

This paper presents an efficient and practical algorithm of weld seam detection for butt joint welding. Given a single image, one can find a pair of weld seam edges in the local area first. Then, starting from the two endpoints of each edge, search for the remnant edge by iterative edge detection and edge linking. This new approach offers

three important technical advantages over previously known solutions to weld seam detection: a). It can detect both the weld seam and the endpoint from a single image automatically; b). It applies to most type of weld seam in butt joint welding, including any shape of planar curve and space curve; c). As all the steps operate locally, the algorithm is insensitive to the variance of the background image, and decreases the computation cost greatly. Experimental results show that it can apply to most type of weld seams in butt joint welding.

Acknowledgements

This work is supported by Key Foundation Program of Shanghai Sciences & Technology Committee under Grand No. 06JC14036 and Young Faculty Research Grant of Shanghai Jiao Tong University.

References

1. Bolmsjo, Gunnar; Olsson, Magnus; Cederberg, Per. Robotic arc welding - trends and developments for higher autonomy, Industrial Robot, vol.29, n2, p 98-104, 2002.
2. Estochen E L, Neuman C P, Prinz F B. Application of acoustic sensors to robotic seam tracking. IEEE trans. on Industrial Electronics, 31(3):219-224, 1984.
3. Pan Jiluan. Arc sensing system for automatic weld seam tracking (II) - Signal processing. Science in China Series E-Technological Sciences, 44 (4): 389-397, Aug. 2001
4. Haug, K.; Pritschow, G. Robust laser-stripe sensor for automated weld-seam-tracking in the shipbuilding industry. Proc. of IECON'98. Vol.2, pp.1236–1241, Aug. 1998.
5. D. Xu; Z. Jiang; L. Wang; M. Tan. Features extraction for structured light image of welding seam with arc and splash disturbance. Proc. of ICARCV, 3: 1559-1563, Dec. 2004.
6. J. Jiang, G. Ding, G. Yan, Y. Zhou. The Application of Active Infrared Technology Real-time and Online Weld Metal Detection, J. Infrared and Millimeter Waves,No.6, 2003
7. H. Zhang, Q. Chen, J. Jin, J. Pan. Welding seam track recognition based on welding seam CCD image pattern feature. Chinese J. of Mechanical Engineering, 32(6):31-36,1996.
8. S. Chen, X. Chen, J. Li, L. Wu. Acquisition of weld seam dimensional position information for arc welding robot based on vision computing, J. Intelligent & Robotic Systems,43(1):77-97, 2005.
9. Gao Xiangdong, Luo Xizhu. Study on the Weld Detection Using Kalman Filtering, Chinese Journal of Mechanical Engineering, No.4, 2005.
10. J. Canny, A Computational Approach to Edge Detection, IEEE Trans. Pattern Anal. Mach. Intell., 8(6):679-698, 1986.
11. Paul Bao, Lei Zhang, and Xiaolin Wu. Canny Edge Detection Enhancement by Scale Multiplication. IEEE Trans. Pattern Anal. Mach. Intell., 27(9):1485-1490, 2005.
12. C.G. Harris and M.J. Stephens. A combined corner and edge detector, Proc. of Fourth Alvey Vision Conference, Manchester. pp 147-151, 1988.

Research on the Laser Calibration Method for the Image Plane Center of the Visual Sensor

F. Liu

School of mechanical engineering, Shanghai Jiaotong University. , Shanghai 200030, China
Liufang1976@sjtu.edu.cn

Abstract. This paper explains the principle and method to calibrate the image plane center of the camera by use of laser in the pre-calibrate process of the intrinsic parameters of the visual sensor. The laser facula image has been disposed properly, so the accurate position has been located by calculating the center of mass. Consequently, the image plane center can be calibrated accurately. After the calibration, the guiding experiments show that the precision of the system is quite good which proves that camera calibrated by the method presented by this paper can satisfy the requirement of the whole system.

1 Introduction

Human beings always apperceive the out world by the sense apparatus such as vision, feeling, ear, or nose and so on. It is estimated that about 80% information is obtained by vision. So visual sense technique is always the hot research topic, and it is used widely in the industry because it is rapid response, high level automatization and information plenty[1]. As the kernel of the visual sense system, the parameter calibration of the camera is very important to the whole system.

There are two parts of the CCD camera parameter that are intrinsic parameters and extrinsic parameter. Intrinsic parameters include imagine plane center (principle point), effective focus, lens aberration parameter and the ratio of the vertical length to the transverse length of the image plane. Extrinsic parameter is the transition matrix of the camera coordinate system to the world coordinate system. There are several method to calibrate the camera parameters, while most of the method have to pre-calibrate the optical camera center and the transverse-vertical ratio of the imagine plane. But most of calibration methods of the CCD image plane center are low precision and large amount computation [2-4]. This paper studies how to calibrate the image plane center by use of laser.

2 Calibration Principle

2.1 CCD Imaging Model

The CCD image plane center is the intersection point of the main optical lens axis and the CCD imaging plane. Fig.1 is the camera imaging model with radial aberration,

T.-J. Tarn et al. (Eds.): Robot. Weld., Intellige. & Automation, LNCIS 362, pp. 295–302, 2007.
springerlink.com

where Z_c is the main optical axis of the lens, $O_i - X_i Y_i$ is the image coordinate system of the CCD imaging plane, and O_i is the imaging plane center of the CCD whose pixel coordinate is (c_x, c_y). In most cases, all of the intrinsic and extrinsic CCD parameters including 6 intrinsic parameters as (c_x, c_y), s_x, s_y, k, f and 8 extrinsic parameters like CCD rotation matrix *R* and transferring matrix *T* need to be calibrated before CCD working.

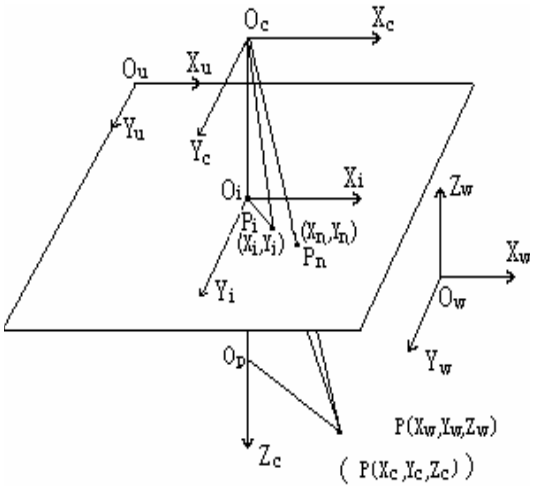

Fig. 1. Camera imaging model with radial aberration

In the computer visual system, the image plane center is the origin point of the image coordinate system, which is also the center of the radial and tangent aberration calibration model for some high level precision cases. This point should be the center of the imaging target plane. But because of the manufacture and installing error and the lens aberration, the image center does not locate at the target plane center exactly [5]. So it is very necessary to calibrate the CCD image center exactly which is a very important part for the CCD parameter calibration. But also, in the stereo visual system, it is the precondition for the transition from the CCD image plain coordinate system to the world coordinate system.

2.2 Principle for the Image Center Calibration by Use of Laser

The principle to calibrate the image center of the CCD by use of laser is shown as Fig.2. The laser beam passes through a small hole on the diaphragm and shoots on the lens. Based on the optical principle, a part of the light passes though the lens and

creates the image point on the image plane but the other part is reflected by the lens to shoot on the diaphragm to create the reflecting image facula (when the reflecting angel is small). When the incident beam coincides with the main axis of the lens, it also coincides with the reflecting beam on the lens, so the reflecting beam also passes though the hole on the diaphragm. At this time, the laser image facula on the image plane is the CCD image plane center. So the CCD image plain center can be obtain by observing the position of the reflecting image facula on the diaphragm and adjusting the CCD position and pose to make the reflecting beam pass through the hole.

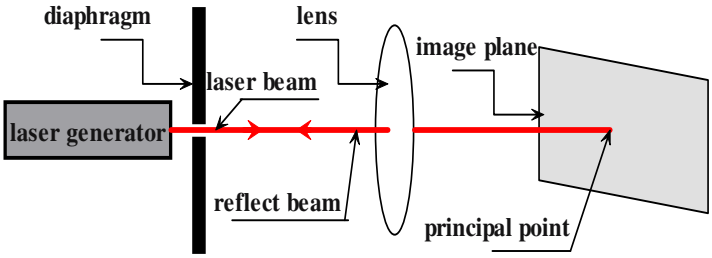

Fig. 2. Sketch map of calibration theory

3 Experiment Results and Analysis

3.1 Experiment

The camera used in the experiment is like a pen which is very small and whose target plain is about 1/3 inch. Experiment collection imagine, whose dimension is 768×582 pixel, is 8bit BMP image collected by image collection card. To observe the reflection beam better, the experiment is operated in the darkroom and both the camera and the laser generator are fix on the precision experiment platform which can be adjusted in 3 dimensions. Fig.3 shows the experiment process. At the beginning, the reflect beam doesn't coincide with the laser beam. And then the camera position and pose is adjusted carefully to make the laser beam coincides with the reflect beam exactly as Fig.4. Now the point created by the laser beam on the image plain is the center of the image plain. For every time of the new experiment, the camera and the laser generator are moved far away from the calibrating position of the previous experiment first, and then their position and pose are adjusted carefully to get the satisfying imagine.

3.2 To Obtain the Exact Position of the Principle Point

Because the incident beam is very strong, the image on the CCD image target is a large facula whose center is incident beam center (Fig.4). In this paper, the real pixel position of the image center is determined by the real position of the facula centroid. After the

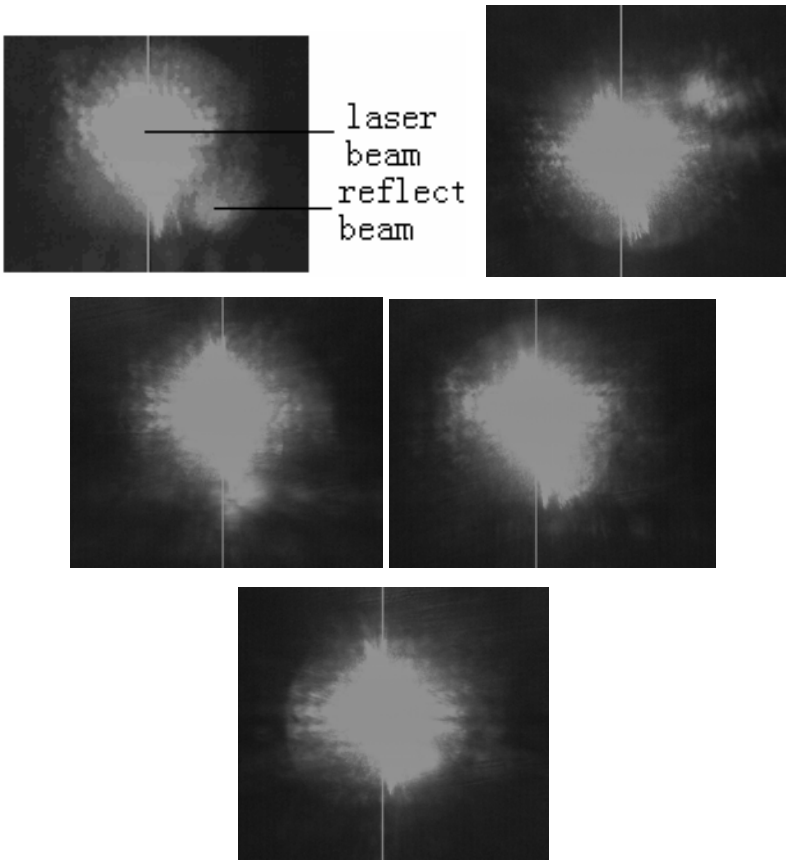

Fig. 3. Diagram of experiment process

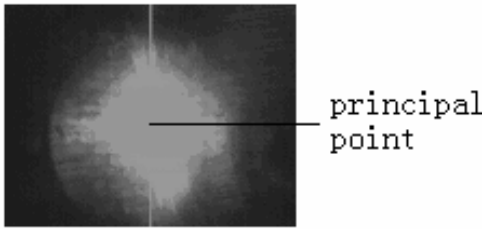

Fig. 4. Diagram of the experiment result

pretreatment of the emanative image, the exact pixel position of the laser beam can be obtained by Equation 1.

$$X_g = \frac{1}{N}\sum_{i=1}^{i=N} X_i \quad Y_g = \frac{1}{N}\sum_{i=1}^{i=N} Y_i \tag{1}$$

To repeat the process many times, the experiment data is shown as table 1.

Table 1. Experiment data of the coordinate of the image plane center

Num.	X	Y
1	364.67	283.81
2	365.83	282.18
3	365.17	282.99
4	364.85	283.12
5	365.30	282.53
6	365.14	282.37
7	365.21	283.04
8	365.18	282.58
Mean value	365.17	282.83

So the pixel coordinate of the image plane center is $(365.17,282.83)$ which is the mean value of 8 experiment data. From table 1, we can also see that the experiment error is very small for every time (<1pixel), so the pre-calibration of the image plane of the visual sensor is finished.

4 Validation of the Laser Calibration Method

Based on the result, the other intrinsic and extrinsic parameters of the visual sensor can be calibrated useing the method mentioned in [4]. The visual guide test shows that the guide error in the local area is smaller than 5mm which means the method present by this paper is high precise and very useful.

4.1 Calibration of the Hand-Eye Relationship

After acquiring the extrinsic parameters of the camera, the hand-eye relationship of the robot, namely the relationship between the camera installing position and the robot controlling point (last arthrosis), can be determined by use of the control point coordinates read from the robot controller at the imaging moment. Given the robot coordinates {A} with the origin of A_0, the last arthrosis coordinates {B} with the origin of B_0 and the camera coordinates {C} with the origin of C_0, the coordinates of P at camera coordinates is ${}^{C}P$ which can be obtained by use of the following equation:

$$ {}^{C}P = {}^{C}_{A}R\,{}^{A}P + {}^{C}A_0 \tag{2} $$

Where ${}^{A}P$ is coordinates of P at the robot coordinates, ${}^{C}_{A}R$ is the rotate matrix of A to C, ${}^{C}A_0$ is the translation matrix. Both the ${}^{C}_{A}R$ and ${}^{C}A_0$ can be determined by those calibration of the camera extrinsic parameters[6].

According to the robot last arthrosis (control point) data that been read from the robot controller, and the rotation and translation equation between different coordinates, the parameters ${}^{A}_{B}R$ and ${}^{A}B_0$ can be determined.

$$ {}^{C}_{A}T = \begin{bmatrix} {}^{C}_{A}R & {}^{C}A_0 \\ 0 & 1 \end{bmatrix} \quad {}^{A}_{B}T = \begin{bmatrix} {}^{A}_{B}R & {}^{A}B_0 \\ 0 & 1 \end{bmatrix} \tag{3} $$

So, the robot hand-eye relationship can be educed directly.

$$ {}^{C}_{B}T = {}^{C}_{A}T\,{}^{A}_{B}T \tag{4} $$

where R is the 3×3 rotation matrix, A_0 and B_0 is the position vector,0 is the 1×3 0 vector.

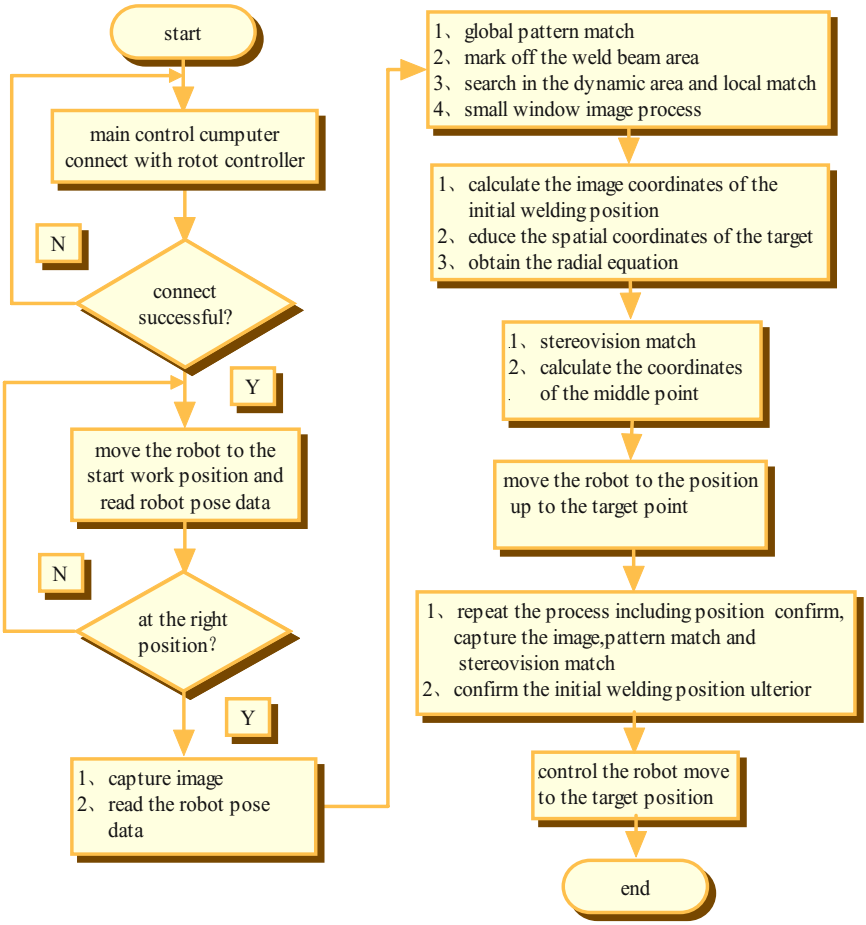

Fig. 5. Flow chart of the vision guiding experiment

4.2 Vision Guiding Experiments

All the experiments are performed on the ordinary industrial robot named MOTOMAN UP6. The used camera is ARONIX MCC-2510 micro CCD camera whose dimension of the target plane is 1/3 inch. Images are captured by the PCI-1409 image capture card produced by National Instrument Corporation. The flow chart of experiments is shown as fig.5.

Vision guiding experiments are performed under the nature sunshine. The experiments are repeated ten times. Error in X direction is less than 3.22mm, error in Y direction is less than 3.11mm, and error in Z direction is less than 5mm.

When the robot is in operation, the system guides the robot to the initial welding position and then tracks the welding line while the allowable error is $\pm 10mm$. The guiding experiments show that the precision of the system is quite good which proves that camera calibrated by the method presented by this paper can satisfy the requirement of the whole system.

5 Conclusions

(1) This paper presents a method how to calibrate the CCD camera image plane center of the visual sense system by use of laser, whose principle is simple and whose precision is very high, can calibrate the image plane center alone in one operation and does not mention the other parameters. This method doesn't need the complicated computation as the other method.
(2) The calibration result of this method provides the precondition for the calibration of the other CCD parameters.
(3) By fixing the camera calibrated by the laser calibration method at the end of the robot arm, the hand-eye relationship of the robot, namely the relationship between the camera installing position and the robot controlling point (last arthrosis), is determined. The guiding experiments show that the precision of the system is quite good which proves that camera calibrated by the method presented by this paper can satisfy the requirement of the whole system.

Acknowledgements

The authors would like to thank Prof. S. B. Chen and Mr. T. Lin for their support in numerous discussions. Thanks are also due to the Robot and Intelligent Welding Lab, Shanghai Jiaotong University, P. R. China for providing the equipments for the experiments.

References

1. Abhijit Nagchaudhuri, Sastry Kuruganty,Asif Shakur. Introduction of mechatronics concepts in a robotics course using an industrial SCARA robot equipped with a vision sensor. Mechatronics 12(2002): 183-193

2. Juyang Weng, etal. Camera calibration with distortion models and accuracy evalution. IEEE Trans . on PAMI 1992, 14(10)
3. Reinar K L, etal. Techniques of calibration of the scale factor and image center for high accuracy 3-D machine vision metrology. IEEE Trans. On PAMI 1988, 10（5）
4. Roger Y T. A versatile camera calibration technique for high-accuracy 3D machine vision metrology using off-the-shelf TV camera and lenses.[J] . IEEE Journal of Automation:, 1987, RA-3(4).
5. Moumen Ahemed, Aly Farag. A neural approach to zoom-lens camera calibration from data with outliers. Image and Vision Computing ,20(2002): 619-630
6. Cai Zixing. Robotic theory. Tsinghua University Press. 2000

Software System Designs of Real-Time Image Processing of Weld Pool Dynamic Characteristics

J. Wu and S.B. Chen

Welding Engineering Institute, Shanghai JiaoTong University, Shanghai, 200030, P.R. China
wujing065@sjtu.edu.cn, sbchen@sjtu.edu.cn

Abstract. In this paper, welding pool image processing software is developed to measure the weld shape parameters in different images. Firstly the visual sensing system was established according to the principle of the passive visual image sensing. Next, the image processing and pattern recognition techniques are discussed to get a clear contour of the pool and measure its size. Finally, in order to testify the efficiency of the software, an image of aluminum alloy welding pool is used and validating results indicate these techniques can be applied practically.

1 Introduction

To realize real-time closed loop control of penetration and weld seam forming, the weld pool shape should be obtained. Therefore, the goal of image processing is to gain the topside width and the backside width of the pool which are associated more closely with penetration.

Many researches have been done in weld pool image processing algorithm in resent years. The sensing systems can be divided into 2 types according to the source: the active mode (imaging with supplementary high-intensity light source) [1,2]and the passive mode(imaging with arc light illumination). Some previous studies indicated effectiveness of the passive visual method for monitoring weld pool, which is more close to simulate a welder observing behavior during his welding operations, furthermore, it is a key technology for intelligentized robotic welding [3,4,5,6]. S.B.Chen and G.J.Zhang developed a narrowband filtering for low carbon weld pool [9] and J.J.Wang developed a wideband filtering for Al alloy weld pool [5] during pulse GTAW and both of the above method is in a simultaneous double-sided visual image sensing system. [3,4].

The bead-on-plate welding was conducted on low carbon steel during pulsed GTAW; a typical low carbon weld pool images is obtained and the algorithms for extracting geometry parameters of the topside and backside images of the weld pool was developed by Y.J.Lou [3]. The calculating time for a frame image was less than 50ms for the top image and 30ms for back image.

J.J.Wang developed the algorithm for Al alloy weld pool during pulsed GTAW process. Based on proper welding conditions for taking fine images of Al alloy weld pool during pulsed GTAW process, a frame of typical images of the topside and backside weld pool were captured. The real-time image processing algorithms were developed to deal with three types of weld pool images, namely the intact image, the fragmentary image and the degenerative image [5].

T.-J. Tarn et al. (Eds.): Robot. Weld., Intellige. & Automation, LNCIS 362, pp. 303–309, 2007.
springerlink.com

It should be pointed out that all the above work is independent with each other for certain kind of material, certain size of welding pool image and certain processing condition. But all-purpose image processing software is necessary to deal with weld pool image in different conditions in real time for further study in intellectualized welding robot system. Therefore, in this paper, software is designed to process various weld pool images during pulsed GTAW.

2 The Architecture of Welding Pool Image Processing Software

The system is specially designed to deal with weld pool image, so as to gain information of the size of weld pool which indicates penetration of the material.

2.1 General Functions of the Software

A series of factors including current polarity inversion, arc instability, workpiece reflection, curtain off from nozzle, etc., causes deformation and distortion of the image. The software is designed to function: preprocess of image, edge detection, binary processing and post-process of image. The architecture of the software is shown in Figure 1.

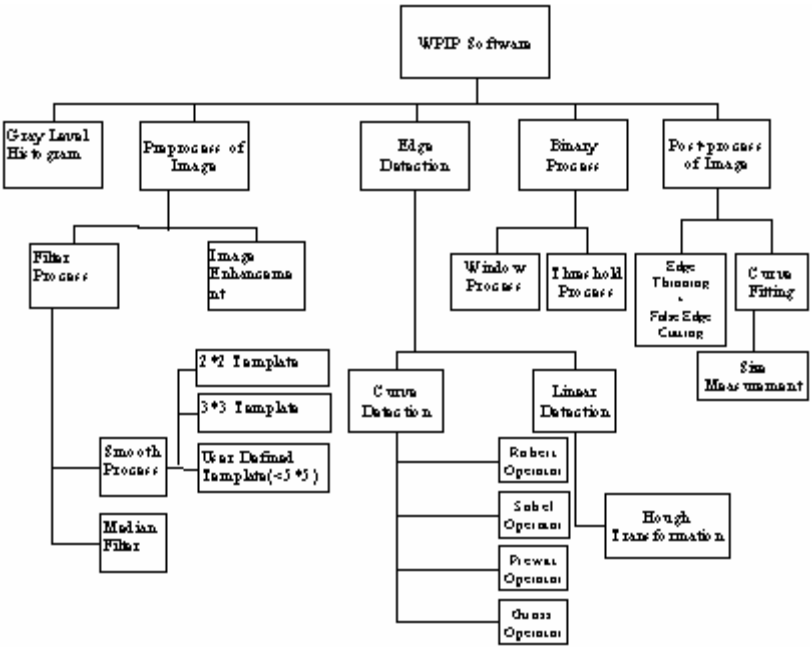

Fig. 1. Architecture of the software

2.2 Design of the Main Modules in the Software

All the functions are encapsulated in the function library for easier function call. Some of the algorithms are selected to discuss as follows:

2.2.1 Preprocess of Image

This part offers two functions namely filter processing and image enhancement.

Filter is necessary because in the unprocessed image there is a lot of noise such as uniform noise, pulse noise, Gusss noise. Guass noise comes into being due to the influence of high temperature in CCD; uniform noise due to random factors and pulse noise due to halt in data transmission. So in the software smooth processing of different template is designed for Guass noise and uniform noise; while median filter is designed for pulse noise. [5]

Meanwhile, image contrast is intensified by gray stretch for easier treatment in the following steps. The equation (1) is used in the enhancement, where x is the original gray value and $f(x)$ is the output gray value.

$$f(x) = \begin{cases} \dfrac{y_1}{x_1} \mathrm{x} & \mathrm{x} < \mathrm{x}_1 \\ \dfrac{\mathrm{y}_2 - y_1}{x_2 - x_1}(x - x_1) + y_1 & x_1 \le \mathrm{x} \le \mathrm{x}_2 \\ \dfrac{255\text{-y}_2}{255\text{-x}_2}(x - x_2) + y_2 & x > x_2 \end{cases} \tag{1}$$

2.2.2 Edge Detection

The aim of edge detection is to enhance the contour of the image so that it can be easily recognized by the machine. In an image, edge is where a significant local change in the gray level occurs. The traditional edge detection operators are to differentiate the pixels in 8 neighborhood of the current with different weight.

However, the edge has different contrast against the background in different areas. So in this paper an improved algorithm is added to deal with the output of traditional edge detect operator. Specifically, the gray level difference is replaced with the sum of that to enhance the contour in the part where contour is not so clear. And the algorithm is as follows:

1) calculate the output value of operator(M) in both row and column
2) for each current pixel (x, y), set the width of its neighborhood as N(where N is odd) and we calculate the difference between the current pixel and it neighborhood pixel ΔG,

$$\Delta G = \sum_{i=\frac{-N-1}{2}}^{\frac{N-1}{2}} \sum_{j=\frac{-N-1}{2}}^{\frac{N-1}{2}} | (f(x, y) - f(x+i, y+j)) | \tag{2}$$

where i and j are nonzero integers

3) calculate the new gray level of current pixel point *g(x,y)*

$$\mathrm{g(x, y)} = \Delta \mathrm{G} + \mathrm{M} \tag{3}$$

2.2.3 Threshold Processing

The goal of threshold processing is to set a threshold so as to separate the pool contour from the background more clearly on one hand and to reduce the time of calculating on the other. It is analyzed that different images have different gray level. Hence an adaptive algorithm is necessary here to gain the threshold automatically by the machine. And statistics is introduced to get the threshold. The algorithm is discussed in detail as follows:[6]

1) Set the neighborhood width of the current pixel as N(N is odd), and calculate the probability of pixels $P(k)$ whose gray level equal to k ;

$$P(k) = \frac{m}{N^2} \tag{4}$$

Where m is an integer less than N^2, and represent the number of pixels whose gray level is k , $k = 0,1,\cdots\cdots 255$.

2) Calculate the expectation of pixels ($E(x, y)$)in the neighborhood:

$$E(x, y) = \sum_{k=0}^{255} k \cdot P(k) \tag{5}$$

Set the adaptive threshold T_d and the fixed threshold T

$$T_d = rE(x, y) = r \sum_{k=0}^{255} kP(k) \ \ (r > 1) \tag{6}$$

In the expression of T_d, the coefficient r is added to prevent the threshold in some image from being too low and thus lead to wide contour.

2.2.4 Measurement

After the binary-value image is obtained, edge thinning, false edge removing and curve fitting is needed to get a smooth and closed curve of the pool. Then, define the pool's maximal width and pool's length as the image's characteristic parameters, see figure 2.

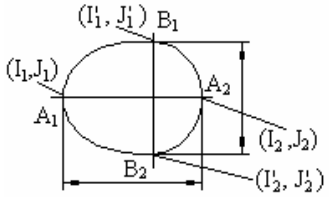

Fig. 2. Principle of measurement

3 Algorithm Validations

To show the efficiency of the software, an image of aluminum alloy weld pool is presented. As is known from practice, weld pool of aluminum alloy is difficult to deal with due to its

special characteristics such as high reflection, low contrast between the pool and background in comparison with low carbon steel and stainless steel. Moreover, a series of factors including current polarity inversion, arc instability, work-piece reflection, curtain off from nozzle etc. add difficulties for common algorithm to deal with the image. And as the backside image is comparably easier to deal with, only the topside image is discussed here.

3.1 Image Processing

For aluminum alloy, image is processed in the following steps, filter processing, image enhancement, edge detection, binary processing, edge thinning, false edge removing and curve fitting.

When filter processing, median filter is selected. As most of the noise in the image is dotting randomly in the image, median filtering is quite efficient for white noise without removing the image details. And a weighted median filter was designed to further improve the effect. In the process of edge detection, Prewitt operator is chosen. Among the traditional algorithmic operators, Prewitt operator is more suitable compared with Sobel operator which produces a wider contour with Guass operator which is more noise sensitive. During binary processing, the value of r is set by experiment, and in this paper, $r = 1.3$. Meanwhile a fixed threshold is necessary to prevent from false edge, and in this paper $T = 144$. During curve fitting, as the upper half of the contour is actually the nozzle and the welding wire, and the lower half is what we really care about, only the lower half is preserved after removing the false edge. And consider of the axial symmetry of the image, we can recover the image by mirror processing. Meanwhile, the LS fitting is chosen because firstly, the ellipse equation can approximate the actual edge well; secondly, local adjustment can be made by LS method.

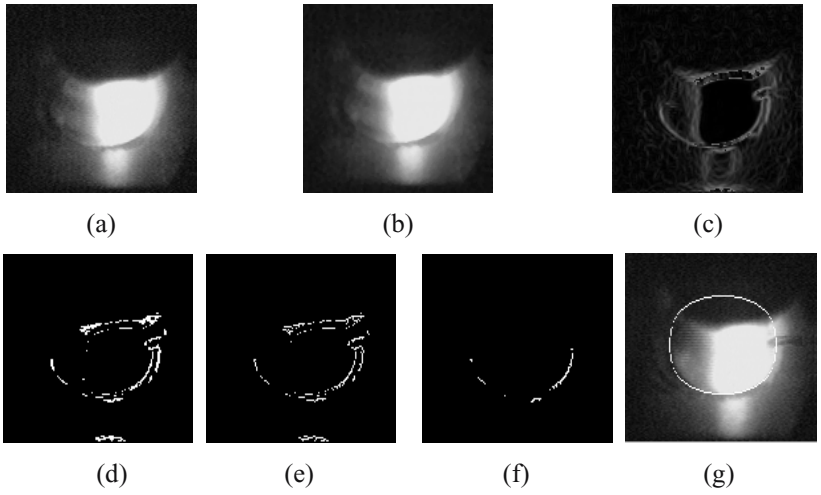

Fig. 3. Process flow chart of an entire pulsed image a) Original Image b) median filtered Image c) sharpened Image d) transformed threshold Image e) fined Image f) Image after false edge cutting g) Image after curve fitting

3.2 Result Discussion

The contour of the pool after processing is satisfying compared with the original image except for some roughness in the rear part of the pool where the edge is not so clear and few points are left after edge detection. More research is necessary if we want to recover the whole weld pool edge.

4 Conclusions

This paper presents efficient and practical software of welding pool edge detection. An image preprocessor, an edge detector, a binary processor and an image post-processor are included in the software. Because of the good symmetry of the image, the whole edge of the image can be recovered well.

However, more algorithms in the aspects of filtering, image strengthening and edge detection should be developed so as to strengthen the robustness of software in dealing with different materials. Moreover, in consideration of the roughness in the rear part of the fitted curve, it is necessary to improve the curve fitting algorithm in order to get a smoother curve.

Acknowledgements

This work is supported by Chinese National Natural Science Foundation (Grand No. 60474036) and Key Foundation Program of Shanghai Sciences & Technology Committee under Grant No. 06JC14036.

References

1. Y. M. Zhang, L. Li and R. Kovacevic, Monitoring of weld pool appearance for penetration control, Proceedings of the 4th International Conference on Trends in Welding Research[C], Gatlinburg, Tennessee, USA, pp.5-8, June, 1995
2. R. Kovacevic and Y. M. Zhang, Real-time processing for monitoring of free weld pool surface, Journal of Manufacturing Science & Engineering, Transactions of the ASME[J], 119(5), pp. 161-169,1997.
3. S.B.Chen, D.B.Zhao, L.Wu and Y.J.Lou, Intelligent methodology for sensing, modeling and control of pulsed GEAW Part 1: Bead-on-plate Welding, Welding Journal[J], 79(6), pp. 164 - 173,2000.
4. Chen, S. B. Zhao,D. B. Wu,L. Lou ,Y. J.: Intelligent Methodology for Measuring, Modeling, Control of Dynamic Process During Pulsed GTAW - - Part 2: Butt Welding, Welding J[J]., vol.79, No.6 , pp164s-174s.,2000
5. J.J.Wang, T. Lin, S. B. Chen, Obtaining of Weld Pool Vision Information during Aluminum Alloy TIG Welding,, The International Journal of Advanced Manufacturing Technology[J], 26(3), pp.224-230, 2005
6. Ramesh Jain, Rangachar Kasturi, Brian G. Schunck. Machine Vision[M]. China Machine Press & Mc Graw Hill Education Press. 2003.

7. Pietrzak, K.A., Packer, S.M., Vision-based weld pool width control, ASME Journal of Engineering for Industry[J] 116 (2), 86-92, 1994
8. S. B. Chen, "Visual Information Acquirement and Real-time Control Methodologies for Weld Pool Dynamics during Pulsed GTAW," The invited paper of the THERMEC'2006, Materials Science Forum vols. 539-543 in March 2007.
9. G. J. Zhang, S. B. Chen, L. Wu, 2005, "Intelligent control of pulsed GTAW with filler metal ," Welding Journal, vol.80, No.1: pp9s-16s.

A Study on Vision-Based Real-Time Seam Tracking in Robotic Arc Welding

H.Y. Shen, T. Lin, and S.B. Chen

Institute of Welding Engineering, Shanghai Jiao Tong University, Shanghai 200030, P.R. China
shenhhy@sjtu.edu.cn

Abstract. This paper discussed seam tracking technology by computer vision sensing in real time for robot GTAW. An image processing algorithm was presented to extract the seam trajectory and the offset of the torch to the seam in the welded pool images of aluminum alloys with grooves. Also the tracking sequence was analyzed and designed. C++ computer language was used to realize the algorithm. The experimental results showed that the error of real-time image process could meet the requirement of production. Such an algorithm was proved to be feasibility in factual manufacturing.

1 Introduction

At present, more and more welding robots have been applied in the automatic manufacturing process. However, most of them are the type of primary "teach and playback" robots, which must be taught in advance for plenty of time. These types of welding robots must be taught and programmed again for the different work-pieces and they cannot self-rectify a offset during the welding process. So in this paper visual sensor was used to solve this problem. Because the visual sensor has many advantages, for example, it does not contact to the weld loop, the information is very abundant etc. Now, the visual sensor becomes the focus in the region of studying on the sensor of the weld robot. Most application is used in weld seam tracking and checking the weld pool [1-4].

Although significant achievements have been made in the area of seam tracking [5-8], reliable application techniques for robots are still needed. In the factory, laser tracking system is applied extensively. But it is great valuable and hardly track complex curve seam, which also limited its application. Vision-based sensor tracking system is cheap and can get enough seam information which can overcome the demerit of laser tracking system, and it could resolve the tracking of complex curve seam.

Two problems in the seam tracking control are solved in this paper. One is vision-based digital image processing. We present the image process algorithm to extract the seam trajectory and the offset. The other is the real-time seam tracking control algorithm.

2 The Principle of the Seam Tracking Technology

The visual sensor composed of CCD (Charge Couple Device) camera was fixed on the robot end joint and captured the images of welding pool in the topside front direction. We can see the image of GTAW pool and seam in Fig. 1. As was known, the sensor moved with robot during welding process. After calibrating the position relationship of

T.-J. Tarn et al. (Eds.): Robot. Weld., Intellige. & Automation, LNCIS 362, pp. 311–318, 2007.
springerlink.com

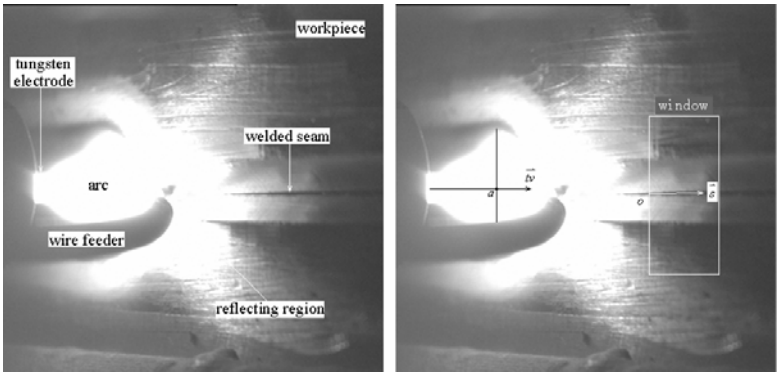

Fig. 1. The image of GTAW pool and seam

the sensor and robot end joint, the key problem is how to figure out the offset which will be presented in detail as follows.

First, recognition of the welded seam is introduced. We selected an area, called window, where to extract the seam center using digital image processing technology. Then the seam curve $\vec{s}$ was fitted with least square method at last. The second is to calculate the offset of the torch. In Fig.1(b), point a is the tungsten electrode projection on the face of work-piece, and $\vec{tv}$ line is the direction of tungsten electrode. We can adjust the relationship of sensor and torch to insure that $\vec{tv}$ is horizontal. After calibration, point a is fixed. The ordinate difference of point a and seam $\vec{s}$ is just the offset. Last but not the least, the time to rectify robot is accurately calculated. It is well known that the arc light is very intense and aluminum alloy has a good reflectivity, so nothing can be seen in the reflecting region in front of the welding pool. Therefore, according to the calibration results and the constant welding speed, the rectifying time can be worked out.

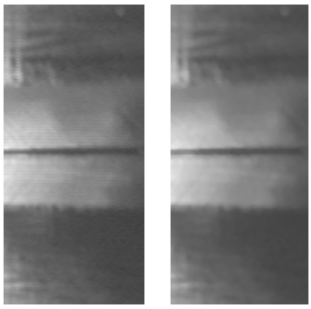

Fig. 2. The result of the median filter process: (a) Original image; (b) Filtered image by a median filter

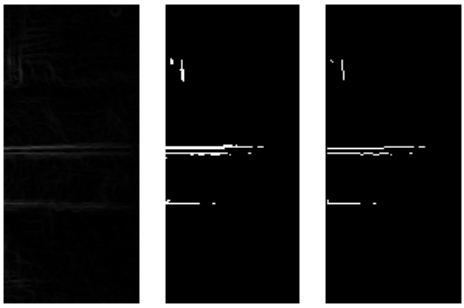

Fig. 3. The welded seam edges: (a) The image detected using Roberts operator; (b) The image with threshold value chosen to be 40; (c) The image after skeleton thinning

3 Image Process and Analysis

In window, the difference of the gay value is not too big. But the work-piece has a Y-shaped groove, and the gay value of the groove face is much higher than that of the seam. According this character, the edge of the seam was be extracted.

3.1 Median Filter

We used the efficient median filtering method to remove random noise mixed in the image and to maintain image sharpness (as shown in Fig. 2). Suppose that the gray value of some pixel and its eight-neighborhood sort ascending as $\{p_1, p_2 \cdots p_8, p_9\}$, the gray value of this pixel is given as

$$p_0 = p_5 \tag{1}$$

Where p_5 is the median value of the pixel and its eight-neighborhood.

3.2 Edge Detection

The gray level value of the image changes most dramatically when the gray level value moves from groove to seam (as shown in Fig. 1). Therefore, the gradient $G(x,y)$ at this point is the maximal. According to the image characters, Robert operator was chosen in this paper. The Roberts operator is represented as follows:

$$G(x,y)=\left\{\left[\sqrt{f(x,y)}-\sqrt{f(x+1,y+1)}\right]^2+\left[\sqrt{f(x+1,y)}-\sqrt{f(x,y+1)}\right]^2\right\}^{1/2} \tag{2}$$

Where $f(x,y)$ is the input image with integral coordinates.

Then the Fig. 3 (a) shows the result using the Roberts operator for Fig. 2 (b).

3.3 Thresholding

In the gray level image, the seam edge detected and its background each own different gay level values. By choosing an appropriate threshold gray level value it is possible to separate the required seam edge from the background. Fig. 3 (b) shows the result when the threshold value is chosen to be 40.

f is the gray level distribution function. The function is one of the mapping to T, which is a transfer function, where T_0 is the appropriate threshold value. The transfer function is as follows:

$$T(f)=\begin{cases} 0 & f<T_0 \\ 255 & f\geq T_0 \end{cases} \tag{3}$$

3.4 Thinning

Thinning is an image-processing operation in which binary-valued seam image is reduced to lines that approximate their center lines. The purpose of thinning is to reduce

the image components to their essential information so that further analysis and recognition are facilitated (as shown in Fig. 3 (c)). The thinning results should approximate the medial lines and must be connected line structures.

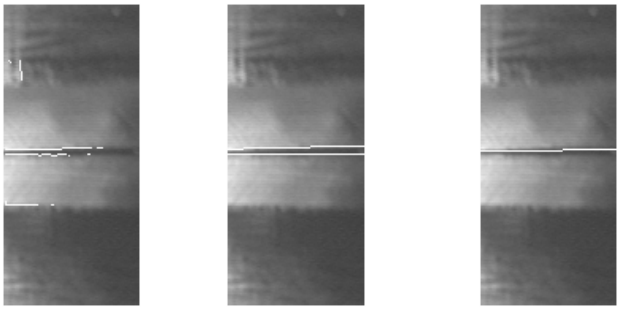

(a) (b) (c)

Fig. 4. The comparison of original image and the welded seam edges extracted: (a) The welded seam edge points; (b) The welded seam edge points fitted by least square method; (c) The welded seam edge center using least square fit

3.5 Extracting Welded Seam Center

The binary-valued seam image after the digital image processing above is given in Fig. 4 (a). But the seam curves were no completely connected. So it is very important to find the true edge points and to judge them to belong to seam up-edge or seam down-edge. Then both seam edges were fitted by least square method after removing the false edge points (as shown in Fig. 4 (b)). Then the edges curve is expressed as

$$\begin{cases} f_1(x)=k_1x+b_1 \\ f_2(x)=k_2x+b_2 \end{cases} \tag{4}$$

where $f_1(x)$ is seam up-edge function, and $f_2(x)$ is seam down-edge function.

So the seam center function $f_3(x)$ was calculated easily, represented as follows:

$$f_3(x) = \frac{f_1(x)+f_2(x)}{2} = \frac{k_1+k_2}{2}x + \frac{b_1+b_2}{2} \tag{5}$$

And Fig. 4 (c) is the comparison image of the welded seam edge center.

4 Tracking Process

The offset was obtained from Eqs.(5) and point a. In Fig. 5, t_c is the welded time obtained by the welding speed and the real welded seam distance between point a and point o.Supposed the internal time of capturing frames is 1s (expressed as t_0=1s). The welding speed is v, a constant value. The real width of window was worked out according to the calibration result, the relative welded time also was figured out, and

the time was split into m pieces, a piece standing for 1 second, i.e. the width of window was also split into m pieces. The program stored the data in a buffer, named $Buffer1[m]$, including the offset ($\det_i$), the rectifying time (t_i), the sum of offset from welding beginning to the storing time ($\sum_t \det$). The parameters are given as follows:

$$\begin{cases} \det_i = \left(\dfrac{k^2 b' + b}{k^2 + 1} \right)_i - f_3(i) \\ t_i = t_W + t_C + i \times 1 \\ \sum_t \det = \sum_{t=0}^{t_W} \det_t \end{cases} \tag{6}$$

Where t_W is the real welded time, when the beginning of welding, t_W is 0s.

The same to t_C , $Buffer2[n+m]$ was allocated for storing the same data as $Buffer1[m]$. At interval of a second, the program copied the data of $Buffer1$ to the last m units of $Buffer2$ and refreshed them. $Buffer2[1]$ stores the data to deal with right now. The offset must be calculated, as follows:

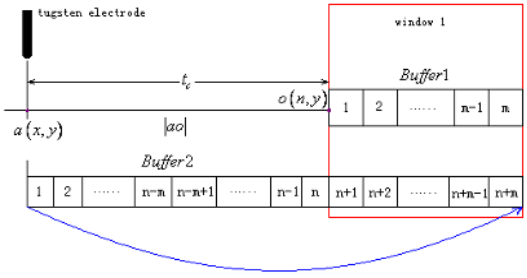

Fig. 5. Rectifying time control algorithm

$$\det = \det_i - \left(\sum_{t_W} \det - \sum_t \det \right) \tag{7}$$

Where $\sum_{t_W} \det$ is the current sum of offset.

After the robot has adjusted the offset, $Buffer2[1]$ was moved to the tail of $Buffer2$ (as shown in Fig. 5), thus $Buffer2[2]$ became the head of $Buffer2$, and the data in it would be dealt with. Then next loop began. Fig. 6 is the flow chart of the robot tracking process.

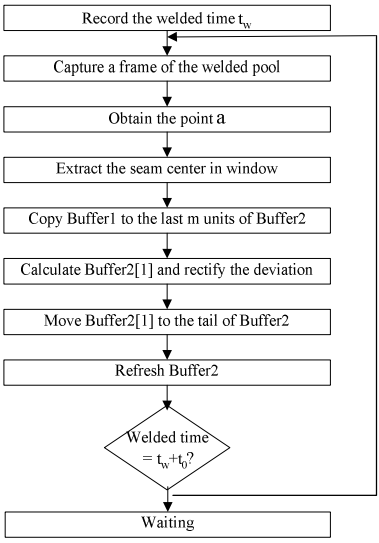

Fig. 6. The flow chart of the robot tracking process

Due to the disturbance from the arc light and the radiation from the welding pool, it is difficult to obtain an ideal value of the seam offset. Thus, efforts were made to obtain an average value of the seam offset and get rid of the false points. Because the welded seam is connected, the ordinate of the adjacent seam center points should not have a great difference. And the offset shouldn't be larger than certain a value that was gotten by experience. If it exceeds the limit, the calculation of this frame will be stop, recapture next frame, which will save the calculation time. In order to improve the precision of offset, the data of $Buffer2$ weren't simply replaced by $Buffer1$, instead of the average offset by the same t_i. The algorithm aims to be used in the sensing for real-time seam tracking in the manufacturing of aluminum alloy products.

5 Experiment Results

A series of GTAW pool images for aluminum alloy with groove were researched in this section. Fig. 1 is one real image of them. In the experiment, robot was taught carefully along the welded seam, so that there was no offset basically between tungsten electrode and the seam. The welded current is 280 A and the welded speed is 160 mm/min. When robot was welding the production, computer captured the images constantly and processed them. The ordinates of point o are obtained in Fig. 7 with the algorithm above. The error is in the range of ±2 pixels, and the real size of one pixel is about 0.1 mm. So the real error is less than ±0.2 mm, which can meet the requirement of production.

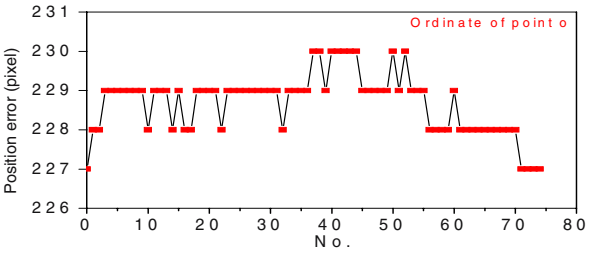

Fig. 7. Ordinate of point o of a series of GTAW pool images

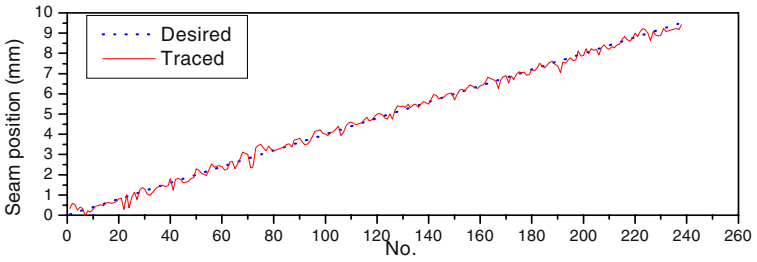

Fig. 8. Ordinate of point o of a series of GTAW pool images

The result of the test of a weld seam tracking was shown in Fig.8. In this figure, the seam tracking for an offset error of 3 mm at the middle and an offset error of -3 mm at the end of a 260 mm weld seam, shows a favorable result when it is compared with the desired seam.

6 Conclusion and Discussion

The following conclusions can be drawn from this research.

1. The method of vision-based seam tracking was applied in the production.
2. An algorithm for real-time seam tracking was developed. Experimental results showed that the algorithm was effective.
3. Based on this algorithm, a software system was implemented with the error less than ±0.2 mm. But the performance and reliability of the system still needs improvement.

Acknowledgements

This work is supported by the National Natural Science Foundation under Grand No. 50575144 and the Key Foundation Program of Shanghai Sciences & Technology Committee under Grant No. 06JC14036.

References

1. Je-Yong Yu, Suck-Joo Na. A study on vision sensors for seam tracking of height-varying weldment. Part 1:Mathematical model. Mechatronics. 1997, 7(7): 599-612
2. Je-Yong Yu, Suck-Joo Na. A study on vision sensors for seam tracking of height-varying weldment. Part 2:Applications. Mechatronics. 1998, 8: 21-36
3. Adolfo Bauchspiess, Sadek C. Absi Alfaro, Leszek A.Dobrzanski. Predictive sensor guided robotic manipulators in automated welding cells. Journal of Materials Processing Technology. 2001, (109): 13-19
4. Jeremy S. Smith, Chris Balfour. Real-time top-face vision based control of weld pool size. Industrial Robot. 2005 32(4): 334-340
5. Jae Seon Kim, Young Tak Son, Hyung Suck Cho, Kwang Il Koh. A robust method for vision-based seam tracking in robotic arc welding. Mechatronics. 1996, 6(2): 141-163
6. Hsing-Chia Kuo, Li-Jen Wu. An image tracking system for welded seams using fuzzy logic. Journal of Materials Processing Technology. 2000, 120 (1): 169-185
7. Bae K Y, Lee T H , Ahn K C. An optical sensing system for seam tracking and weld pool control in gas metal arc welding of steel pipe. Journal of Materials Processing Technology. 2002, 120(2): 458-465
8. Jingguo Ge, Zhengqiang Zhu, Defu He, Ligong Chen. A vision-based algorithm for seam detection in a PAW process for large-diameter stainless steel pipes. International journal of advanced manufacturing technology. 2005, 26(10): 1006-1011

Image Processing of Seam Tracking System Using Laser Vision

Li Liangyu, Fu Lingjian, Zhou Xin, and Li Xiang

School of Mech.&Eletro. Engineering, Tianjin Polytechnic University, Tianjin, 300160, P.R. China
liliangyu@tjpu.edu.cn

Abstract. A method of real time image processing of laser vision sensing seam tracking system has been studied, an algorithm of single point filtering and a binariantion processing by which the severable value is scoured automatically are put forward, getting rid of the noises effectively. A feasible method has been proposed for the laser midline extraction, by adopting inside stalk transformation, a single and consecutive laser midline can be distilled. Finally the character point is detected by the method of analyzing slop. It could detect the character point exactly and rapidly, and meet the demands of the real time seam tracking system.

1 Introduction

As welding technology becoming more automatic, intelligent and the development of the welding robot technology, the research and application of seam tracking system become more and more important. Image processing technology is one of the key techniques, it makes directly whether the output control signal is right or not, so it could affect the seam tracking precision of the executive mechanism[1]. Real time seam image processing is required by the tracking system, which makes precise seam recognition very hard. Nowadays, tracking system using laser vision is the most efficient and suitable for complicated environment visual tracking system in developed countries, but in China it is still at research stage, and hasn't been commercialized yet.

Seam image processing using laser vision has been deeply studied in the article, a series of seam image processing have been designed. By a series of procedures processing, the methods of image processing have been proved worked well, the seam center is found out precisely and the processing algorithm can meet the demand of real time seam tracking of the system.

2 Laser Seam Image Pre-processing Algorithm and Experiment Results

Laser seam image should be processed by pre-processing and post-processing, two procedures. Pre-processing is to acquire clearer seam image by getting rid of noises, when post-processing is to obtain the seam character information precisely and the seam centre is found finally.

2.1 Image Intension

Because of the noises in the laser seam image, the contrast of the original image is quite low as in figure 1(a), and with the affections come from image generation,

T.-J. Tarn et al. (Eds.): Robot. Weld., Intellige. & Automation, LNCIS 362, pp. 319–324, 2007.
springerlink.com

transmission and exchange process, the output quality of the image would be very low. Therefore to strengthen the contrast of the original image is to make the contrast of the goal and the background stronger, meanwhile to make the picking up process of the severable value of binariantion easier. The darkness of every pixel of the image is processed by coordinate transformation to enlarge the darkness boundary of the image. Set the darkness of any point (x,y) of the input image as f(x,y), the corresponded darkness in the output image as g(x,y), the algorithm expression is:

$$g(x,y) = k \times f(x,y) - m \tag{1}$$

In the formula 'k' and 'm' are constants, they are decided by following formula:

$$k = [g(x,y)_{max} - g(x,y)_{min}]/[f(x,y)_{max} - f(x,y)_{min}] \tag{2}$$

$$m = k \times f(x,y)_{min} \tag{3}$$

And $f(x,y)_{max}$ and $f(x,y)_{min}$ are the max and min darkness values of the image before the intension, $g(x,y)_{max}$ and $g(x,y)_{min}$ are the max and min darkness values of the image after the intension. Pick $g(x,y)_{max}$=255, $g(x,y)_{min}$=0 to make the intension effect best. The result of darkness intension is in figure 1(b).

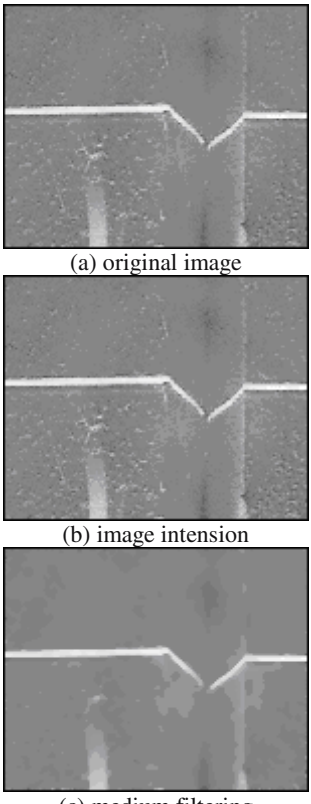

(a) original image

(b) image intension

(c) medium filtering

Fig. 1. Seam tracking image

2.2 Medium Filtering

Because of the noises from electric arc ray, dust and splitting, there are a lot of independent noise points in the original seam image, they seriously affect the post-processing of the image, so the signal smooth filter processing is necessary. But common low pass filters make the sharp points obscure, so medium filtering is adopted to protect the image edge when removing the noises.

The basic principle of medium filtering is to change every pixel value into the medium value of all points of one contiguous area of the point. In the programming process, a 3×3 window is used to the original darkness value, first change the 2D value group to 1D, then rearrange the 1D value group from the smallest to biggest. The mid-value of 1D value group is used to substitute the formal darkness value. The result of the medium filtering is in figure1(c).

2.3 Binariantion

Binariantion is the technique that used to sever the goal image from the original image. The key point is to choose the severable value T, it has to be based on the statistical distribution, which means choosing the appropriate severable value from the statistical view point[2]. By the experiment, it has been found that the darkness values of the laser zone in the seam image are quite close to 255, and the edge darkness values are quite separate which are at the bottom of the darkness value curve in figure 2. The processing method of the binariantion which could search the severable value automatically is designed based on this property. Set point 'P' as the darkest bottom point in the darkness curve, set 'A' as the darkest peak point, S(x) as the total number of the points that the darkness value is x. So when 'P' is being searched to the left from 255 to 'B', there is:

$$S(P) < S(A) \tag{4}$$

Then searching to the left from 'B', when reach point 'D', there is:

$$S(P) > S(C) \tag{5}$$

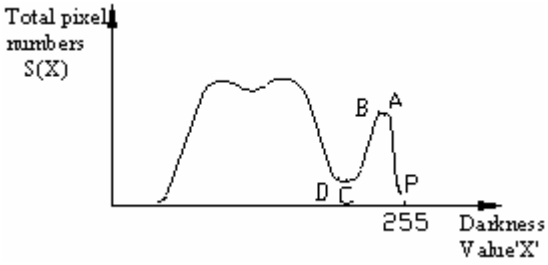

Fig. 2. Darkness value curve of the laser seam image

So point 'C' is the darkest bottom point, its corresponded darkness is the needed severable value T. Then seam image would be processed by putting the T as the boundary point. Most noisy points would be filtered when keeping the whole laser zone. The result of binariantion processing is in figure 3(a).

2.4 Single Point Filtering

By binariantion the seam images still keep some small ranges of the noises. For more accurate midline, single point filtering algorithm is proposed. It is that removing all other points when only keeping the laser zone, the key is how to address the laser zone accurately. Effective way to find the laser zone is generated by lots of experiments of real time seam image processing. Set 'X' as the horizontal scale of the goal points of laser zone, F(X) as the vertical scale (origin point is at the top left). The points that meet all three criterions are thought to be the points on the laser zone:

$$1)\ 4 \le F(X)_{max} - F(X)_{min} \le 15\ ,\ X_{max} - X_{min} \ge 30\ ; \tag{6}$$

$$2)\ 40 \le F(X) \le 80\ ; \tag{7}$$

$$3)\ 0 \le X_{min} \le 5,\ 146 \le X_{max} \le 150\ ; \tag{8}$$

By these three conditions the laser zone would be found, then keeping the points which are four-contiguous or eight-contiguous with the pixel points of laser zone while all other points would become background points, so to effectively remove all the noises. The result of single point filtering is in 3(b).

(a) binariantion (b) single point filtering

Fig. 3. Treated image

3 Image Post-processing Algorithm and Experiment Results

In the process of automatic seam tracking, one key difficulty is how to get the laser midline from the pre-processed image, and how to detect the character point from laser midline.

3.1 Laser Midline Extraction

The laser zone in the image by the pre-processing is not very regular, it is because of the strong noises from electric arc ray. The detection process of seam character points needs the goal images to be slenderized, otherwise the character points would away from the right position. Most common method of slenderizing laser zone is to check the edge of the image first, then average the two edges to obtain the central line by mating separate points.

Depending on the images feature of this experiment, inside stalk transformation[3] is adopted to extract laser midline directly. It is a slenderized technique which is used to locate object frame. It needs to calculate all distances from the boundary points to

the inner points to obtain the zone frame, so there would be large numbers of calculations. So in practice a slenderized algorithm which eliminates the boundary points gradually by times is applied, it can not only obtain the central line of laser zone precisely, but also avoid the difficulties from the mates of the separate points. The result of extracting the central line is in figure 4(a).

3.2 Character Point Detection

The aim of obtain the central line of laser zone is to detect the character point easily. Slope analysis[4] is used to get the character point. In the slope analysis, set the rank 'n' pixel coordinate of the laser line as f(n), so the slope of the point is:

$$K(n) = f(n) - f(n-1) \tag{9}$$

Here f(n-1) means the coordinate of the front rank. For better smooth effect, set there are k ranks between them, so it becomes:

$$K(n) = \frac{f(n) - f(n-1)}{k}$$

To improve the reliability of the way of this character point detection, set the average slope of four ranks front and follow rank 'n' to be the slope of the point. It is:

$$\left| \frac{f(n+1) - f(n-1)}{2} + \frac{f(n+2) - f(n-2)}{4} + \frac{f(n+3) - f(n-3)}{6} + \frac{f(n+4) - f(n-4)}{8} \right| \Big/ 4 \tag{10}$$

So the left and right point of inflection of the laser zone could be located. Searching started from the left and the right separately, it record the address and stop search when get the characters. So that it could avoid possible tolerance comes from the probable character signal which is not regular in the slope inner (it is between the left and right point of inflection). The algorithm becomes easier and the generalization of the program has been improved. The result of character point detection is in figure 4(b).

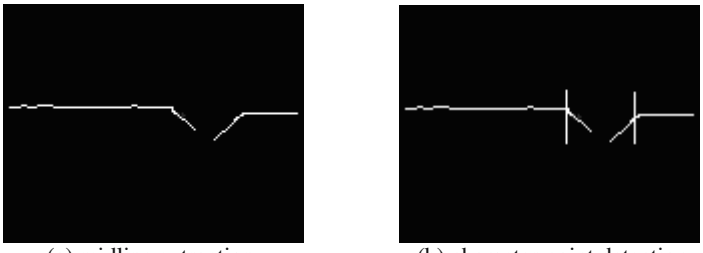

(a) midline extraction (b) character point detection

Fig. 4. Character point image

4 Conclusion

In this Image processing of laser seam tracking system, contrast intension is adopted to improve the image contrast, which makes the laser zone and the background different clearly. Medium filtering could remove the noises when protecting the image

edges. In the binariantion processing the severable value automatic searching based on the properties of darkness curves is effective and fast. A single point filtering is proposed to filter all other noises. By adopting inside stalk transformation, a single and consecutive laser midline can be distilled, there is no need to mate separate points. Slope analysis is applied to detect the seam character point precisely. This way of processing could finally obtain the correct character information, and meet the demands of the real time system

Acknowledgements

This work is funded by Important project of Natural Science Foundation of Tianjin (No.05YFJZJC02100).

References

1. WangQingxiang, SunBinda, LiDi. Research on image processing of the recognitions of seam position[J].welding journal, 2005.26(2):59-63.
2. Parle.D.,De.A.. Real time seam tracking system for automated fusion arc welding[J].Science & Technology of welding & Joining, Oct2003, Vol.8:340-346.
3. Zhang Liujin. Image processing and analysis[M].Beijing:Tinghua university publishing company, 2003.12.
4. SongGuojun, ZhuLiumei. Research on real time image processing of seam tracking using vision[J].welding technology, 2003.(1):4-5.

Discretiztion in Rough Set Modeling Method for Welding Process

LiWen-hang, Chen Shan-ben, and Lin Tao

Institute of Welding Engineer, Shanghai Jiaotong University, Shanghai 200030, China

Abstract. Rough set modeling method is a new and promising modeling method in welding field. Discretization plays an important role in that method. Considering the character of welding process and the rough set method, proper evaluation standards for discretiztion were discussed. To compare discretization algorithm, raw data of welding process were sampled by special designed sensor system, and the comparison method was designed. The input variable discretization and the output variable discretization were discussed respectively. At last, influencing factors for discretization were analysizsed.

1 Introduction

Rough set (RS) modeling method is a relatively new modeling method for welding process. It can effectively deal with uncertain information without prior knowledge or empirical knowledge, and well acquire knowledge from data, which adapt to welding process.

Discretization is important in RS modeling method when there are continuous data in dataset. One cause is that RS method can only deal with discrete data, and the other is that proper discretization method can improve the quality of RS model (rule sets) and improve the understandability of RS model.

Many researches have been done on discretization in different fields[1-4]. In RS field, there are also algorithms considering the RS character. It is well known that there isn't a discretization method fitting for all circumstance. Thus deciding a proper discretization method for RS modeling method in welding field is significant.

In this paper, we first introduced the procedure of the RS modeling method and its application in welding field. Then, we analyzed the character of discretization problem in welding field and decide the evaluation standard for discretization algorithms. In section 3 we design an experiment that compared the common discretiztion algorithms in welding field. The output variables and input variables are both discussed and the cause is analyzed. At last, we gave our conclusion.

2 Rough Set Modeling Method

Rough set theory [5] is widely used in modeling, knowledge acquisition and data analysis. It is based on an indiscernible relation. Its main procedures in modeling are shown below.

T.-J. Tarn et al. (Eds.): Robot. Weld., Intellige. & Automation, LNCIS 362, pp. 325–331, 2007.
springerlink.com

2.1 Procedure of Rough Set Modeling Method

Main steps of the RS based modeling method are showed in Fig.1. First, we should obtain the raw data. Then we should preprocess the data to improve its quality, among which includes discretiztion. After that, a dataset called decision table can be obtained. We use the RS theory to deal with decision table to obtain a model, made up of "IF THEN" rules. At last, we can use the model to predict unseen samples.

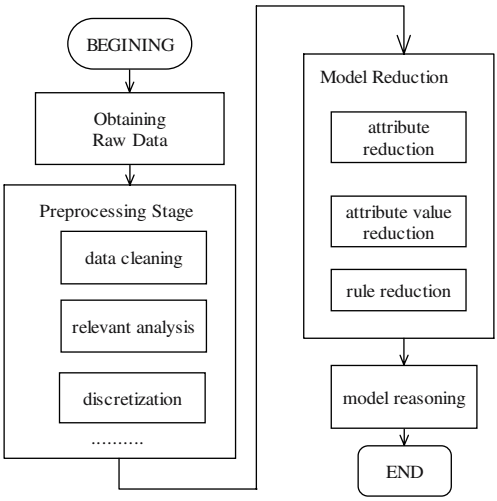

Fig. 1. The procedure of RS modeling method

2.2 A Model Predicting Backside Welding Pool

In this paper, we used a model, which can predict the backside width of welding pool by the information of topside welding pool and other relative welding parameters, as the background for our discretization research. We used a special designed CCD sensor [6] to obtain the topside and backside images of the welding pool in pulsed GTAW. After some image processing, we could obtain the topside width, topside length and backside width of the welding pool, which were represented by W_T, L_T and W_B respectively. Fig 2 was an example of obtained images and its feather after image process. We also added some relative welding parameters, such as welding current I, welding speed S_W, the area of topside pool's area $A(=W_T \times L_T)$ and wire feed speed S_F into the decision table. To make the model better reflect the real process, we let I randomly changed in specified range. Considering the pure delay to welding, we used the t^{th}, $(t-1)^{th}$,$(t-2)^{th}$,$(t-3)^{th}$ time's I, S_W , S_F, A, W_T, L_T and W_B to predict the t^{th} time's W_B. At last, we got a decision table that included 277 samples (objects), with 15 condition attributes and 1 decision attribute. Table 1 was some of the sample in decision table, where the last column is the output variable.

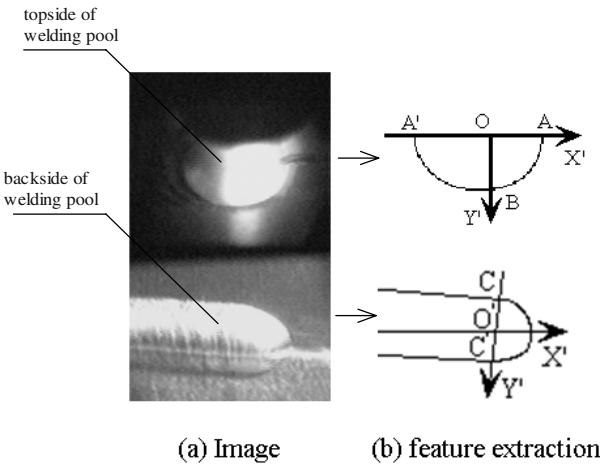

Fig. 2. A example of welding pool image and its feather extraction

Table 1. Part of the decision table before discretization

I/A				L_T/mm				W_T/mm				W_B/mm			W_B/mm
t-0	t-1	t-2	t-3	t-0	t-1	t-2	t-3	t	t-1	t-2	t-3	t-1	t-2	t-3	t
150	150	150	150	10.7	10.6	9.7	9.5	5.4	4.4	5.8	5.3	5.5	5.3	5.5	5.3
150	150	150	150	10.7	10.7	10.6	9.7	5.1	5.4	4.4	5.8	5.4	5.5	5.3	5.5
136	150	150	150	11.0	10.7	10.7	10.6	4.6	5.1	5.4	4.4	5.9	5.4	5.5	5.4
148	136	150	150	11.0	11.0	10.7	10.7	5.1	4.6	5.1	5.4	3.8	5.9	5.4	5.9

3 Discretization

3.1 Evaluation Standard for Discretization Algorithms

There is no discretization method fitting for any circumstance and evaluating a discretization method is a difficult problem. Usually, there are three important dimensions[7]. (1) Simplicity. If the cut-points are few, it's simple and has high understandability. Otherwise, it is complex and has low understandability. (2) Consistency, i.e. the number of inconsistencies caused by discretization. (3) Predictive Accuracy. That is how discretization helps to improve the final model's predictive accuracy. In reality, a discretization algorithm can't score highest in all departments.

Because of the complexity of welding process, its model usually contains many variables that are almost all continuous. The number of inconsistencies caused by discretization is few. What is more, the aim of our modeling in welding is usually for better control to welding process. Therefore, we emphasis on the discretization algorithm's contribute to last model's predictive accuracy. At the same time, we hope the algorithm isn't too complexity, which don't expend too much time and produce too much cuts.

In addition, descretization in welding usually includes the output variable's discretiztion, when they are also continuous, and the input variables' discretization. Because many discretization algorithms are supervised, i.e. they consider the class (output variable) information, we must finish the output variable's discretization before the input varibales' discretization.

3.2 Comparison Method and Experiment

To compare different discretization algorithms' contribution to RS model' predictive accuracy, we should take the same procedure except for the discretization in RS modeling method. To get a stable result, ten fold cross validation was used. Although in real application, intput variables' discretization was after output variable's, we should first compare the input variable's discretization, which was more complex.

1. The input variable's discretization

We first used the equal width discretiztion method for output variables', where each interval is 0.5 mm width. Then, we used different discretization method for the input variables.

We considered the common discretization method, such as equal width or frequency method, entropy based method (limiting its maximum interval numbers). There are also some discretization algorithms proposed in RS field, such as the algorithm based on Boolean reasoning and RS, naive scaler and semi naive algorithm. The one based on Boolean reasoning and RS is easy to understand, but its time and space complexity are high. Moreover, it usually makes some input variable not discretized, resulting in too much information lost, so we don't consider it. For the naive scaler algorithm, it usually produces much more cuts (usually more over 100 in one variable), so we also exclude it.

We then took the same procedure to obtain the RS models. When using this model to predict, uncertain reasoning was used, where 5 most similar partially matched rules were selected, and the minimum required similarity of partially matched rules was 60%.

To better reflect the prediction result, 4 parameters were used. They are right predict rate R_{right}, unpredictable rate R_{none}, mean error E_{mean} and standard error E_{sd}. Following was the formulas of the latter two, where $x_{i,pre}$ denotes the prediction value of the testing sample i, and $x_{i,exp}$ denotes the expectant or real value of the testing sample i.

$$E_{mean} = \frac{\sum_{i=1}^{N} \left| x_{i,\exp} - x_{i,pre} \right|}{N} \tag{1}$$

$$E_{sd} = \sqrt{\frac{\sum_{i=1}^{N} (x_{i,\exp} - x_{i,pre})^2}{N}} \tag{2}$$

The comparison result was shown in table 2. We varied their maximum discretization interval numbers from 2 to 7, except the semi naive scaler.

It was obviously that entropy based method was better than the other ones. What is more, algorithm for RS, such as semi naive scaler didn't perform well.

Table 2. Comparison result of discretiztion algorithms for input variables

Discretization method	Interval numbers	R_{right} /%	R_{none}/%	E_{mean}	E_{sd}
Equal width	2	31.83 +- 6.35	0	0.58	0.82
	3	37.39 +- 6.77	0	0.50	0.76
	4	36.05 +- 7.79	0	0.54	0.79
	5	34.74 +- 8.48	0	0.49	0.69
	6	35.53 +- 7.04	0.26	0.52	0.75
	7	36.08 +- 4.66	0.79	0.53	0.81
	8	33.17 +- 9.45	1.86	0.50	0.72
Equal frequency	2	34.26 +- 5.09	0	0.65	0.94
	3	33.65 +- 7.88	0	0.62	0.90
	4	37.15 +- 8.40	0.27	0.62	0.97
	5	34.44 +- 9.25	7.69	0.52	0.77
	6	30.26 +- 9.53	25.99	0.50	0.78
	7	24.13 +- 4.11	38.99	0.47	0.68
	8	18.60 +- 4.86	43.24	0.56	0.80
Entropy Based method	2	41.08 +- 10.61	0	0.47	0.71
	3	43.74 +- 6.63	0	0.45	0.69
	4	43.46 +- 8.12	0	0.43	0.68
	5	43.25 +- 7.15	0.80	0.44	0.67
	6	40.58 +- 9.28	2.65	0.46	0.71
	7	38.42 +- 9.27	4.77	0.47	0.73
	8	37.40 +- 7.29	6.10	0.44	0.64
Semi naive scaler		33.19 +- 7.16	23.34	0.43	0.66

Note: The interval number of each variable in semi naive scaler was not same.

When the number of intervals was too small or too large, the last predictive accuracy was relative low. In the former case, the sample space after discretization decreased too much, which can't well express the complex system such as welding process. In the latter case, the sample space was still large and the sample used for modeling was not enough to get an effective model, especially when the model was used to predict the unseen data.

2. Output variable's discretization

In above experiment, the interval width of output variable was 0.5 mm, and we knew that the entropy based method played better for input variables' discretization. To analyze the effect of output variable's discretization, we took the entropy based method for input variable's discretiztion, letting each variable's interval be 3~5, and we took the equal width method for output variable's, letting each interval width be 0.5~1 mm. The other procedure in the RS modeling was same as the above experiment. The result was showed in table 3.

Table 3. Comparison result of discretiztion algorithms for output variable

Input Variables' Interval Numbers	Interval width of Output variable/mm	Right predict rate/%	Wrong predict rate/%	Miss Matched Rate%
3	1.0	64.57	27.76	7.67
	0.5	40.84	51.56	9.59
4	1.0	60.04	19.83	20.13
	0.5	43.77	35.41	20.83
5	1.0	62.97	18.53	18.50
	0.5	40.63	33.28	26.09

From table 3, we can see that the interval width can also well affect the last model's predictive result. This was because the discretization method will change the number of samples in the output variable's equivalence class, where the samples have the same output value. If the interval width was small, there weren't enough samples to predict the according equivalence class in the complex system. If the interval width was large, the model's precision will be low. So we should take an equilibrium between the two sides.

4 Conclusion

In this paper, we studied the discretization problem in RS modeling method for welding process. We determined the evaluation standard for discretization algrithms in welding field, and we compared the common used discretization algorithms by comparison their contribution the RS model's prediction ability. The input and output variable's discretiztion were both discussed. We found that the output variable's discretization was very important, which was seldom noticed by researches. In addition, the entropy based method played well for input variable's discretiztion in welding field. The result can be refered to by other intelligent method, such as fuzzy set method.

Acknowledgement

This work is supported by the National Natural Science Foundation of China under Grand No. 60474036 and the Key Foundation Program of Shanghai Sciences & Technology Committee under Grant No. 06JC14036.

References

1. Zhang, G.X., W.D. Jin, and L.Z. Hu, *Generalized discretization of continuous attributes in rough set theory.* Kongzhi yu Juece/Control and Decision, 2005. **20**(4): p. 372.

2. Susmaga, R., *Analyzing Discretizations of Continuous Attributes Given a Monotonic Discrimination Function*. Vol. 1 1997: Elsevier Science. 157-179.
3. Roy, A. and S. Pal, *Fuzzy discretization of feature space for a rough set classifier. PATTERN RECOGNITION LETTERS, 2003. 24(6): p. 895-902.*
4. Hassan, Y. and E. Tazaki, *Emergent rough set data analysis. TRANSACTIONS ON ROUGH SETS II, 2004. 3135: p. 343-361.*
5. Pawlak, Z., *Rough sets-Theoretical Aspects of Reasoning about Data*. 1991, USA: Kluwer Academic Publishers.
6. Wang, J., T. Lin, and S. Chen, *Obtaining weld pool vision information during aluminium alloy TIG welding*. INTERNATIONAL JOURNAL OF ADVANCED MANUFACTURING TECHNOLOGY, 2005. **26**(3): p. 219-227.
7. Liu, H., et al., *Discretization: An enabling technique.* DATA MINING AND KNOWLEDGE DISCOVERY, 2002. **6**(4): p. 393-423.

A Model-Free Adaptive Control of Pulsed GTAW

F.L. Lv[1], S.B. Chen[1], and S.W. Dai[2]

[1] Institute of Welding Technology, Shanghai Jiao Tong University, Shanghai 200030, P.R. China
[2] Department of Automatic Control, NAEI, Yantai, 264001
arry@sjtu.edu.cn

Abastract. A closed-loop system is developed to control the weld pool geometry, which is specified by the backside weld width. The welding current and speed are selected as the control variables. A MISO ARX model is used to model this dynamic process. Because of uncertainties in the GTAW process, it is very difficult to design an effective control scheme by conventional modeling and control methods. A model-free adaptive control algorithm has been developed to control the welding process. Simulation confirmed that the developed control system is effective in achieving the desired fusion state.

1 Introduction

The dynamic identification and control of arc welding processes has been explored through a number of studies. Advanced control techniques such as adaptive control have been used to generate sound welds [1,2]. Artificial intelligence methodology was developed for modeling and controlling the welding process. Numerous exciting controls with perfect performance have been achieved. George E. Cook[3] studied the application for the variable polarity plasma arc welding. A self-learning fuzzy neural network control system of topside width enabled adaptive altering of welding parameters to compensate for changing environments in Chen S.B.'s study[4]. Yu M. Zhang[5] used a neurofuzzy model to model the welding process. Based on the dynamic fuzzy model, a predictive control system has been developed to control the welding process. Zhang G.J.[6] investigated feasible intelligent control schemes. A double-variable controller was designed. In fact, it just is a supervisory control, not considering the couple relationship of variables.

Recently, a model-free adaptive control scheme has been explored, which based on information from the I/O data of the controlled plant[7,8]. The main objective of this research was to explore applications for mode-free adaptive control algorithm in arc welding control, and in particular the GTAW MISO(many input simple output) process. The organization of this paper is as follows: we first identify the double input simple output dynamic model of the GTAW process for simulation of the GTAW process; the basic model-free adaptive control algorithm is presented; finally, the simulation of GTAW process is shown.

T.-J. Tarn et al. (Eds.): Robot. Weld., Intellige. & Automation, LNCIS 362, pp. 333–339, 2007.
springerlink.com

2 GTAW Process Modeling

GTAW process is controlled by a number of parameters, including the welding current, arc length, and welding speed. As we all know, the correlation between the weld pool and arc length may not be straightforward. Compared with the arc length, the roles of the welding current and welding speed in determining the weld pool and weld fusion geometry are much more significant and definite. Thus we select the welding speed (v) and the welding current (I) as control variables. The controlled process can therefore be defined as a GTAW process in which the welding current and speed are adjusted on-line to achieve the desired backside width (w_b) of the weld pool.

A polynomial AutoRegressive with exogenous input or ARX model representation[9] is selected as the model representation in this study. For a multivariable system with one output and m inputs, consider the ARX model below:

$$A(q^{-1})\,y(k) = \mathbf{B}(q^{-1})\mathbf{u}(k) + e(k) \tag{1}$$

The model belongs to linear-in-the-parameter model, therefore, the parameter estimation can be performed using least square method. The model in equation (1) can be represented

$$y(k) = \mathbf{\Phi}^{\mathrm{T}}(k)\boldsymbol{\theta} + e(k)$$

The identification is thus simplified by estimation the model parameters. There are n+nm parameters to be identified, and here m is the number of inputs which is welding current (I) and welding speed (v) respectively, so u_1 is welding current, u_2 is welding speed, and m equals 2.

Though experiment data, we can determine approximately that the evaluation of n is 5. ARX model of backside weld width (w_b) with welding parameters (I and v) is derived using the least square method developed with the Matlab program. First we achieve full parameter model, then a reduced model can be derived using statistic hypothesis testing method as follows:

$$\begin{aligned} y(k) &= a_1 y(k-1) + a_2 y(k-2) + a_3 y(k-3) + a_4 y(k-4) \\ &\quad + a_5 y(k-5) + b_{11}u_1(k-1) + b_{12}u_1(k-2) + b_{14}u_1(k-4) \\ &\quad + b_{21}u_2(k-1) + b_{23}u_2(k-3) + b_{25}u_2(k-5) \end{aligned} \tag{2}$$

where

$A = [a_1 \quad a_2 \quad a_3 \quad a_4 \quad a_5] = [1.2245 \quad -0.7935 \quad 0.45269 \quad -0.23124 \quad 0.11518]$

$B = [b_{11} \quad b_{12} \quad b_{14} \quad b_{21} \quad b_{23} \quad b_{25}] = [0.0085696 \quad -0.3748 \quad 0.0039714 \quad -0.16826 \quad 0.0023674 \quad -0.079501]$, y is the backside weld width, u_1 and u_2 are the welding current and the welding speed, respectively. The feasibility of this model is verified by comparing the simulation results with the Matlab program and actual outputs. The square sum of residuals is 0.0303437.3 model-free adaptive control design

2.1 Universal Process Model

The following general discrete MISO nonlinear systems is considered

$$y(k+1) = f\left(Y_k^{k-n}, \mathbf{u}(k), U_{k-1}^{k-m}, k+1\right) \tag{3}$$

Where

- $k = 0, 1, \cdots,$ stands for discrete time
- $y(k+1)$ represents a one-dimensional state output
- $\mathbf{u}(k)$ is an input variable
- $Y_k^{k-n} = \{y(k), \cdots, y(k-n)\}$ are the sets of system outputs
- $U_k^{k-m} = \{\mathbf{u}(k), \cdots, \mathbf{u}(k-m)\}$ are the sets of system inputs
- n and m are the orders of output $y(k)$ and input $\mathbf{u}(k)$
- $f(\cdots)$ is a general nonlinear function

Following assumptions are made about the controlled plant:

1. When the system is in the steady state, it satisfies the condition that if $\mathbf{u}(k) = \mathbf{u}(k-1)$, then $y(k+1) = y(k)$
2. The nonlinear function $f(\cdots)$ has a continuous gradient with respect to control input $\mathbf{u}(k)$.

From the assumptions above, we have

$$y(k+1) - y(k) = f\left(Y_k^{k-n}, \mathbf{u}(k), U_{k-1}^{k-m}, k+1\right) - f\left(Y_{k-1}^{k-n-1}, \mathbf{u}(k-1), U_{k-2}^{k-m-1}, k\right)$$

$$= f\left(Y_k^{k-n}, \mathbf{u}(k), U_{k-1}^{k-m}, k+1\right) - f\left(Y_k^{k-n}, \mathbf{u}(k-1), U_{k-2}^{k-m}, k+1\right)$$
$$+ f\left(Y_k^{k-n}, \mathbf{u}(k-1), U_{k-1}^{k-m}, k+1\right) - f\left(Y_{k-1}^{k-n-1}, \mathbf{u}(k-1), U_{k-2}^{k-m-1}, k\right)$$

Let

$$f\left(Y_k^{k-n}, \mathbf{u}(k-1), U_{k-2}^{k-m}, k+1\right) - f\left(Y_{k-1}^{k-n-1}, \mathbf{u}(k-1), U_{k-2}^{k-m-1}, k\right) = \xi(k+1)$$

And using the mean value theorem in the Calculus, we obtain

$$f\left(Y_k^{k-n}, \mathbf{u}(k), U_{k-1}^{k-m}, k+1\right) - f\left(Y_k^{k-n}, \mathbf{u}(k-1), U_{k-2}^{k-m}, k+1\right)$$
$$= \nabla f\left(Y_k^{k-n}, \overline{\mathbf{u}(k-1)}, U_{k-1}^{k-m}, k+1\right)^{\mathrm{T}} \left[\mathbf{u}(k) - \mathbf{u}(k-1)\right]$$

where $\overline{\mathbf{u}(k-1)} = \mathbf{u}(k-1) + \theta\left(\mathbf{u}(k) - \mathbf{u}(k-1)\right)$, θ satisfies $0 \le \theta \le 1$. Therefore, we have

$$y(k+1) - y(k) = \nabla_{\mathbf{u}(k-1)} f\left(\overline{\mathbf{u}(k-1)}, k+1\right)^{\mathrm{T}} \left[\mathbf{u}(k) - \mathbf{u}(k-1)\right] + \xi(k+1) \tag{4}$$

If $\left\|\mathbf{u}(k) - \mathbf{u}(k-1)\right\| \neq 0$, let

$$\boldsymbol{\varphi}(k) = \nabla_{\mathbf{u}(k-1)} f\left(\overline{\mathbf{u}(k-1)}, k+1\right) + \left[\left(\mathbf{u}(k) - \mathbf{u}(k-1)\right) / \left\|\mathbf{u}(k) - \mathbf{u}(k-1)\right\|^2\right] \cdot \xi(k+1)$$

Then equation (4) can be written as

$$y(k+1) - y(k) = \boldsymbol{\varphi}(k)^{\mathrm{T}} \left[\mathbf{u}(k) - \mathbf{u}(k-1)\right] \tag{5}$$

where $\boldsymbol{\varphi}(k)$ can be considered a pseudo gradient of model (5). Note that when the system is in a steady state, because of $\left\|\mathbf{u(k)} - \mathbf{u(k-1)}\right\| = 0$, we have $y(k+1) = y(k)$, so in this case, (5) is a valid expression. Equation (5) is called universal model.

2.2 Model-Free Adaptive Control Algorithm

2.2.1 Estimation of the Pseudo Gradient $\boldsymbol{\varphi}(k)$

It is clear that the necessary condition that the universal model (5) can be used in practice is that the estimation of $\boldsymbol{\varphi}(k)$, denoted as $\hat{\boldsymbol{\varphi}}(k)$, is available in real-time, and is sufficiently accurate. Considering the control action is known, define the cost function

$$\begin{aligned} J(\boldsymbol{\varphi}(k)) = &\left[y^*(k+1) - y(k) - \boldsymbol{\varphi}(k)^{\mathrm{T}} \Delta\mathbf{u}(k-1)\right]^2 \\ &+ \mu \left\|\boldsymbol{\varphi}(k) - \boldsymbol{\varphi}(k-1)\right\|^2 \end{aligned} \tag{6}$$

where $\Delta\mathbf{u}(k-1) = \mathbf{u}(k-1) - \mathbf{u}(k-2)$, because at the moment $\Delta\mathbf{u}(k)$ is unaccessible we substitute $\Delta\mathbf{u}(k-1)$ for it, $y^*(k+1)$ is the desired output of the controlled plant, μ is positive weighting constant which constrains the change of the pseudo gradient $\boldsymbol{\varphi}(k) - \boldsymbol{\varphi}(k-1)$.

By using (5), the minimization of the cost function (6) gives estimation

$$\hat{\boldsymbol{\varphi}}(k) = \hat{\boldsymbol{\varphi}}(k-1) + \left(\eta \Delta\mathbf{u}(k-1) / \mu + \Delta\mathbf{u}^2(k-1)\right) \tag{7}$$

$$\cdot\left(\Delta y(k)-\hat{\boldsymbol{\varphi}}(k-1)\cdot\Delta\mathbf{u}(k-1)\right)$$

where η is a suitable small positive number.

2.2.2 Design of Model-Free Adaptive Control

The model-free adaptive control is described as follows: Assume that the observed data $\{\mathbf{u}(k-1), y(k)\}$ $(k=1,\ldots)$ are known, and the expected output $y^*(k+1)$ at (k+1)th time is given. Find a controller $\mathbf{u}(k)$, such that the output of the system $y(k+1)$ matches $y^*(k+1)$. In order to achieve a robust control, it is required that the following cost function is minimized:

$$J(\mathbf{u}(k))=\left|y^*(k+1)-y(k+1)\right|^2+\lambda\left\|\mathbf{u}(k)-\mathbf{u}(k-1)\right\|^2$$

where λ is the weight. The analytic solution is

$$\mathbf{u}(k)=\mathbf{u}(k-1)+\left(\rho\boldsymbol{\varphi}(k)\Big/\left(\lambda+\boldsymbol{\varphi}^2(k)\right)\right)\bullet\left(y^*(k+1)-y(k)\right) \tag{8}$$

where ρ is called a control parameter, which selection is closely related to the convergence of the control law. Equation (8) is called the basic form of the model-free adaptive control law.

3 Simulation of GTAW Process

Having analyzed the GTAW process and developed the GTAW MISO model (2), we will demonstrate the effectiveness of the model-free adaptive control algorithm developed in GTAW process. Following are several steps that describe how the model-free adaptive algorithm works.

1. For the observed input output data $\{\mathbf{u}(k-1), y(k)\}$ and the developed universal model (5), we can obtain $\widehat{\boldsymbol{\varphi}}(k)$ which is the estimation of pseudo partial derivative $\boldsymbol{\varphi}(k)$, using least squares algorithm.
2. For the desired output $y^*(k+1)$, we have

$$\mathbf{u}(k)=\mathbf{u}(k-1)+\left(\rho\boldsymbol{\varphi}(k)\Big/\left(\lambda+\boldsymbol{\varphi}^2(k)\right)\right)\bullet\left(y^*(k+1)-y(k)\right)$$

   Then a new set of data $\{\mathbf{u}(k-1), y(k)\}$ can be achieved, applying the control action $\mathbf{u}(k)$ to the GTAW process (here we use the model (2)).

3. Repeat steps 1 and 2 above to generate a serial of data $\{\mathbf{u}(k-1), y(k)\}$.

The desired backside weld width was chosen as $y^* = 5$ mm. On selection the initial estimation of pseudo partial derivative as $\boldsymbol{\varphi}(0) = [0.5 \quad -0.2]^{\mathrm{T}}$, Fig.2 shows the convergence procedure of the pseudo partial derivative. Fig.3 and Fig.4 show the response of the system under the model-free adaptive control with $\eta = 1$, $\mu = 1$, $\rho = 1$ and $\lambda = 25$.

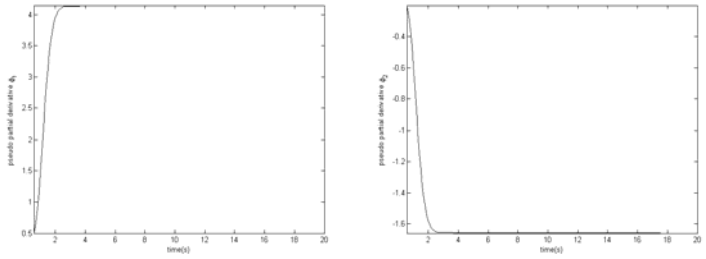

Fig. 1. Pseudo partial derivative

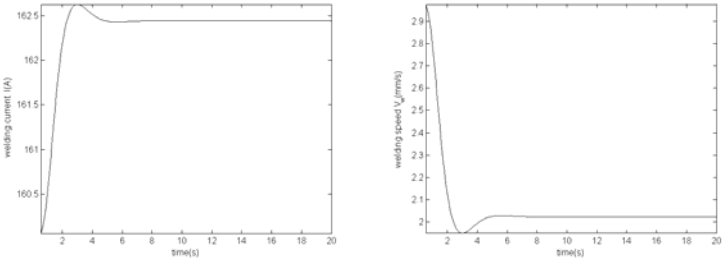

Fig. 2. Control inputs

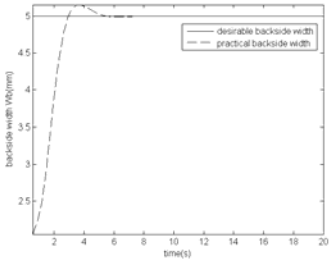

Fig. 3. Backside weld width

4 Conclusion

Because arc welding is characterized as inherently variable, nonlinear, time varying and having a coupling among parameters. Also the variations in the welding conditions cause uncertainties in the dynamics. So it is very difficult to design an effective control scheme by conventional modeling and control methods. It is has been shown by simulation that this process has been successfully controlled using the model-free adaptive algorithm. Meanwhile this control method only needs the observed input output data, thus the MISO GTAW model developed is just used to simulate. Thus, the developed model-free adaptive control provides a promising technology for GTAW quality control.

Acknowledgement

This work is partially supported by the National Natural Science Foundation of China under Grand No. 60474036 and the Key Foundation Program of Shanghai Sciences & Technology Committee under Grant No. 06JC14036.

References

1. Kovacevic R., Zhang Y.M., (1997) Real-time image processing for monitoring the free weld pool surface. ASME Journal of Mnufacturing Science and Engineering 119(5):161-169.
2. Song J.B., Hardt D.E. (1994) Dynamic modeling and adaptive control of the gas metal arc welding process. ASME Journal of Dynamics Systems, Measurement, and Control 116(3):405-410.
3. George E. Cook, Robert Joel Barnett, Kristinn Andersen, Alvin M. Strauss (1995) Weld modeling and control using artificial neural networks. IEEE Transactions on Industry Applications 31(6):1484-1491.
4. Chen S.B., Wu L., Wang Q.L., Liu Y.C. (1997) Self-learning fuzzy neural network and computer vision for control of pulsed GTAW. Welding Journal 76(5):201s-209s.
5. Yu M. Zhang, Radovan Kovacevic (1998) Neurofuzzy model-based predictive control of weld fusion zone geometry. IEEE Transactions on Fuzzy Systems 6(3):389-401.
6. Zhang G.J., Chen S.B., Wu L. (2005) Intelligent control of pulsed GTAW with filter metal. Welding Journal 84(1):9s-16s.
7. Zhongsheng Hou, Wenhu Huang (1997) The model-free learning adaptive control of a class of SISO nonlinear systems. Proceedings of The American Control Conference 343-344.
8. Zhi-Gang Han, Xinghuo Yu (2004) An adaptive model free control design and its applications. Industrial Informatics, 2004.INDIN '04. 2004 2nd IEEE International Conference on 243-247.
9. Li Yanjun, Zhang Ke (2005) Xitong bianshi lilun ji yingyong. Guangfang Gongye Chu Ban She.

A Model of Automatic Detection System for Weld Defects Based on Machine Vision

Tian Yuan, Du dong, Hou runshi, Wang li, and Cai guorui

Department of Mechanical Engineering, Tsinghua University,
Beijing 100084, P.R. China
Key Laboratory for Advanced Materials Processing Technology
Ministry of Education P.R. China

Abstract. To realize weld defects detection and measure automation based on machine vision, such as dimension, shape, displacement and numbers in a given length (area), it's necessary to build a mathematic model for the imaging system. Precision of model directly affects precision of measurement for defects. In this paper, a model was built including some nonlinear factors, i.e. the input screen shape (spherical surface) of the x-ray image intensifier and the distortion of the image in CCD at small distance. A kind of reason why the electromagnetic distortion generates is given in this paper, too.

1 Introduction

It's one of the most reliable and most extensively used methods in nondestructive testing to detect the defects in weld by radioscopy. It is still one of research focuses of the technology of detection automation for weld defect based on X-ray real-time image. Generally, the system of detection automation for weld defect based on X-ray real-time image consists of the ray source, work piece under testing, x-ray image intensifier, industry CCD camera, the image card and computer, etc(**Fig.1**). The x-ray image intensifier converts the invisible X-ray image containing information of defects in work piece into visible image and intensifies it. Industry CCD camera and the image card converts the analog signals into the digital image. The computer and corresponding software process the real time image to decide whether defects exist and gain all data of defect. Because computer judges them depending on the image, the relation on displacement, dimension, and shape has to be built between the real scene and the corresponding image, that is, the mathematic model has to be built to depict the imaging process of the system. Here, the model means the geometry model, that is, it's a relation between 3-D coordinates of the work piece under testing and 2-D coordinates of the corresponding image. Precision of model directly influences precision of measurement for defects, however, the common models ignore those nonlinear factors so that the error is obvious. In this paper, the model was built including some nonlinear factors, i.e. the input screen shape (spherical surface) of the x-ray image intensifier and the distortion of the image in CCD at small distance. Limited by length of the paper, calibration and experiment on the system model will be given in other papers.

T.-J. Tarn et al. (Eds.): Robot. Weld., Intellige. & Automation, LNCIS 362, pp. 341–348, 2007.
springerlink.com

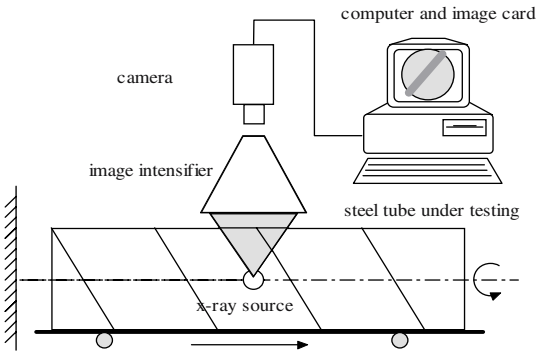

Fig. 1. The system configuration

2 Some Theoretical Foundations

2.2 The Model of Camera

Pinhole model is one of the most common and simple camera models. The principle is indicated in **Fig. 2.** However, in many occasions the model can not depict the imaging process of camera, for example, imaging at close distance and imaging by wide-angle lens, which results in distortion in image. A general camera can be reasonably seen as pinhole after some linear or nonlinear revisions are added in the model.

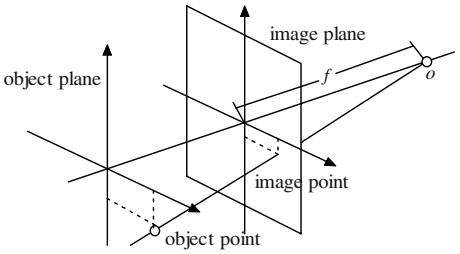

Fig. 2. The pinhole model of camera

Two-plane model does not require all light beams pass the optical center. Given any one pixel at image plane, the displacements of corresponding points of intersection can be calculated at two calibrating planes so that the beam that generates the pixel can be determined [5].

2.3 The Model of X-Ray Image Intensifier

For the model of x-ray image intensifier, the main problems considered are geometry distortion and electromagnetic distortion. The former is caused by the curved surface of the input screen of x-ray image intensifier, and the latter is caused by

electromagnetic effects. The shape of input screen is usually sphere surface or hyperboloid. In this paper, it's modeled as sphere surface. In literature [1], it's modeled as hyperboloid and as plane in literature [2]. It's difficult to model electromagnetic distortion because the electromagnetic intensity is time-variable and difficult to forecast. In literature [3], it's modeled as sine function and in literature [2], the followed formula is used to model electromagnetic distortion,

$$\begin{cases} x_p' = x_p + D_{ex}(x_p, y_p) \\ y_p' = y_p + D_{ey}(x_p, y_p) \end{cases},$$

Where $D_{ex}(x_p, y_p)$ and $D_{ey}(x_p, y_p)$ are imaging distortion that the system generates at x and y directions respectively.

With research to the construction and imaging principle of x-ray image intensifier, it's noticed that photoelectrons from photoelectricity cathode are very sensitive to electromagnetic field. To prevent disturbance from outside electromagnetic field, shell of x-ray image intensifier is made of glass or other nonmagnetic material [6]. Thus disturbance from outside electromagnetic field can be ignored; however, inside the x-ray image intensifier the moving electrons generate electromagnetic field that makes electrons change their traces. The electromagnetic field is an annular field that encircles the optical axis and the intensity is inverse proportion with the distance between a point and the central axis of image intensifier and direct proportion with the number of electrons that traverse a plane during a time unit. The annular field distorts linear weld to shape of "S", which is consistent with phenomenon that is watched in manufacture occasion. Thus it's the real reason why electromagnetic distortion is generated.

2.4 Projective Geometry

In projective space $\mathbf{P^n}$, points are expressed in homogeneous coordinates, which are often shown with the number 1 in the rightmost position, e.g., $[x_1', \cdots, x_n', 1]^T$. This point is equivalent to any point that differs only by non-zero scaling. The one-to-one mapping from the n-dimensional Euclidean space $\mathbf{R^n}$ into $\mathbf{P^n}$ is given by the followed formula [4]:

$$[x_1', \cdots, x_n']^T \rightarrow [x_1', \cdots, x_n', 1]^T$$

The introduction of projective space and homogeneous coordinate made the expressions of formula simpler.

3 The Proposed Model

3.1 Definition of Some Coordinate Systems

At first, some coordinate systems are defined to be used in model (**Fig. 3**).

3D object coordinate system, whose origin is the centre of a circle from section of steel tube and Z axis is coaxial with the axis of steel tube, is fixed on work piece

under testing. The movement of steel tube is spiral synthesized by rotating movement encircling Z axis and translation along Z axis. Any point M on steel tube can be expressed as $M = [X_M \; Y_M \; Z_M]^T$, and as $M = [X_M \; Y_M \; Z_M \; 1]^T$ in homogeneous coordinates;

The origin of 3D world coordinate system is defined in the ray source, that is, optical center of the central projection. Z axis of world coordinate system parallels with the optical axis of x-ray image intensifier (the hypothesis is reasonable because there is always a radial that parallels with the optical axis of x-ray image intensifier). $\bar{Y}$ - $\bar{Z}$ plane of world coordinate system is the plane determined by $\bar{Y}$ axis and the optical axis of x-ray image intensifier. The coordinates of the point M are denoted by $\bar{M} = [\bar{X}_M \; \bar{Y}_M \; \bar{Z}_M]^T$ and $M = [X_M \; Y_M \; Z_M \; 1]^T$ in homogeneous coordinates. It's considered that object coordinate system translates into world coordinate system by a 3x3 rotation matrix R_M and a 3x1 translation vector T_M. In projective space, the transform can be expressed by a 4x4 matrix S_M, that is,

$$S_M = \begin{bmatrix} R_M & T_M \\ 0 & 1 \end{bmatrix}_{4\times4}$$

Thus the transform of point M between world coordinate system and object coordinate system can be expressed as,

$$\bar{M} = S_M M \tag{1}$$

The matrix S_M contains six unknown parameters, which are three Euler angles α, β, γ and three translation parameters t_x, t_y, t_z.

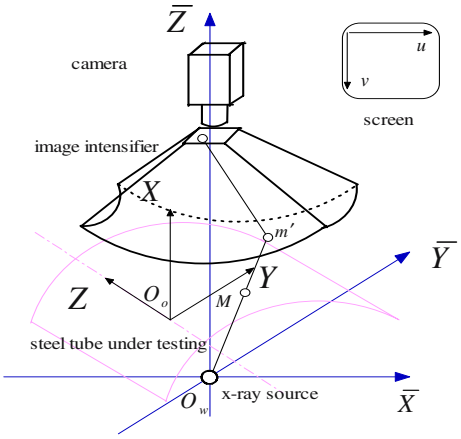

Fig. 3. Sketch of some coordinate systems

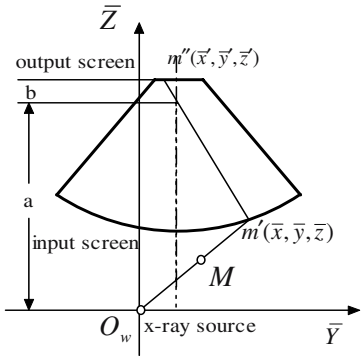

Fig. 4. Geometry transform in the image intensifier

2D image coordinates system, is used to represent pixel coordinates of the image formed at the camera. The image point m corresponding to object point M can be expressed as $m = \left[u_M \; v_M \right]^T$. The origin of image coordinates system is at top-left corner of computer screen and x axis is rightward horizontally and y axis is downward vertically.

3.2 Models of Every Imaging Part

The imaging system can be partitioned into three parts:

1. Object-input screen of image intensifier (**Fig. 4**). The image point m' in the input screen of image intensifier corresponds to the point M in the work piece under testing and the coordinates of m' are calculated as the intersection of the line containing the origin of world coordinates system and the point M with the sphere surface, input screen of image intensifier.

According to rule that the world coordinates system is set, the coordinates of the sphere center is expressed as $(0, y_0, z_0)$, then the sphere surface is defined in world coordinates system by

$$\overline{X}^2 + (\overline{Y} - y_0)^2 + (\overline{Z} - z_0)^2 = R^2 \tag{2}$$

With R is the radius of the sphere.

The coordinates of m' in the world coordinates system are expressed as $m'(\overline{x}, \overline{y}, \overline{z})$, the line containing the origin of world coordinates system and the point M with the sphere surface is defined in world coordinates system by

$$\frac{\overline{X}}{\overline{X}_M} = \frac{\overline{Y}}{\overline{Y}_M} = \frac{\overline{Z}}{\overline{Z}_M} \tag{3}$$

That is,

$$\overline{X} = \frac{\overline{X}_M}{\overline{Z}_M} \cdot \overline{Z} \tag{4}$$

$$\overline{Y} = \frac{\overline{Y}_M}{\overline{Z}_M} \cdot \overline{Z} \tag{5}$$

Uniting the formulas(2),(4),(5), the coordinates of m can be gained as,

$$\begin{cases} \overline{x} = \overline{X}_M \cdot \dfrac{(z_0 \overline{Z}_M + y_0 \overline{Y}_M) \pm \sqrt{\Delta}}{\overline{X}_M{}^2 + \overline{Y}_M{}^2 + \overline{Z}_M{}^2} \\ \overline{y} = \overline{Y}_M \cdot \dfrac{(z_0 \overline{Z}_M + y_0 \overline{Y}_M) \pm \sqrt{\Delta}}{\overline{X}_M{}^2 + \overline{Y}_M{}^2 + \overline{Z}_M{}^2} \\ \overline{z} = \overline{Z}_M \cdot \dfrac{(z_0 \overline{Z}_M + y_0 \overline{Y}_M) \pm \sqrt{\Delta}}{\overline{X}_M{}^2 + \overline{Y}_M{}^2 + \overline{Z}_M{}^2} \end{cases} \tag{6}$$

With $\Delta = 2y_0 z_0 \overline{Y}_M \overline{Z}_M + R^2 \cdot (\overline{X}_M{}^2 + \overline{Y}_M{}^2 + \overline{Z}_M{}^2) - y_0{}^2 \cdot (\overline{X}_M{}^2 + \overline{Z}_M{}^2) - z_0{}^2 \cdot (\overline{X}_M{}^2 + \overline{Y}_M{}^2)$, "$\pm$" means two intersections and "$-$" should be selected based on real condition.

The part contains three unknown parameters R, y_0 and z_0.

2. The part of image intensifier. The image point $m'(\overline{x}, \overline{y}, \overline{z})$ in the input screen of image intensifier is projected through the optical center of the image intensifier onto the output screen as point $m''(\overline{x}', \overline{y}', \overline{z}')$, which is calculated as the intersection of the line containing the point $m'(\overline{x}, \overline{y}, \overline{z})$ and the optical center of the image intensifier with the output screen.

The optical center of the image intensifier is expressed as $O_I(0, y_0, a)$, then

$$\frac{\overline{X}}{\overline{x}} = \frac{\overline{Y} - y_0}{\overline{y} - y_0} = \frac{\overline{Z} - a}{\overline{z} - a} \tag{7}$$

The formula of the output screen is

$$\overline{Z} = a + b \tag{8}$$

Then,

$$\begin{cases} \overline{x}' = \dfrac{b}{\overline{z} - a} \cdot \overline{x} \\ \overline{y}' = y_0 + \dfrac{\overline{y} - y_0}{\overline{z} - a} \cdot b \\ \overline{z}' = a + b \end{cases} \tag{9}$$

The part contains two unknown parameters a and b.

3. The part of camera-output screen of image intensifier. The camera takes visible light images from the output screen of the image intensifier. With short distance between object imaged and camera, the distortion has to be considered if pinhole model of camera is used. Particularly, the revision of the distortion is required when the images are used to measure.

Corresponding to object point M, the coordinates of the image point on the output screen are expressed as $m''(\overline{x}', \overline{y}', \overline{z}')$. All image points on the output screen are coplanar, so model of the part may ignore the $\overline{Z}$ ordinate. The image point $m''(\overline{x}', \overline{y}')$ is projected on the CCD as the image point $m(\tilde{u}, \tilde{v})$ by the matrix $B_{3\times3}$, that is,

$$\begin{pmatrix} \tilde{u} \\ \tilde{v} \\ 1 \end{pmatrix} = B_{3\times3} \cdot \begin{pmatrix} \overline{x}' \\ \overline{y}' \\ 1 \end{pmatrix} \tag{10}$$

The matrix $B_{3\times3}$ contains nine unknown parameters, which depict displacement transform of the camera, the focus, the coordinates of optical center of the camera and the scales factors of two coordinates, etc.

Furthermore, the image distortion of the camera is considered. The main distortion is in radial direction. The distortion is centrosymmetric and is expressed by a polynomial. The coordinates of the revised image point m can be defined by

$$\begin{cases} u = \tilde{u} \cdot \left[1 \pm k \cdot (\tilde{u}^2 + \tilde{v}^2)\right] \\ v = \tilde{v} \cdot \left[1 \pm k \cdot (\tilde{u}^2 + \tilde{v}^2)\right] \end{cases} \tag{11}$$

Where k is the factor that represents distortion and "+" means pincushion-like distortion and "−" means barrel-like distortion.

The part contains ten unknown parameters.

In conclusion, the formula (1),(6),(9),(10),(11) forms the model of the system containing the ray source, work piece under testing, x-ray image intensifier, industry CCD camera, the image card and computer with 21 unknown parameters which need to be determined by calibration.

4 Calibrations

Calibration is a process that all unknown parameters of the model are determined. Some of the parameters are supplied by the machine but the precision is inadequate and they are changed as it is installed. Some of the parameters can be measured though they are not supplied. Some of parameters are difficult to measure. Calibration contains two steps. At first, the projection matrix need be confirmed from the real object to the corresponding image. Secondly, every unknown parameter is calculated from the projection matrix by some method. It's noticed that the second step is always not required.

Calibration is an important research area and the method can be partitioned into two kinds. One kind is conventional and based on an object that contains some feature points whose relative coordinates are known accurately. The other kind is self-calibration. Based on complex degree and reliability of calibration, this paper used the first kind of method. What need do is to confirm coordinates of those image points corresponding to known object points in real world, and then by using the model and some methods such as the least square method, nonlinear optimization method, the unknown parameters can be calculated. Another method is to calculate the approximate values of the parameters of the linear model, then to calculate precise values based on the approximate values by iterative method.

5 Conclusions

To the automatic weld defects detection system based on machine vision, a precise model is a precondition to measure automatically dimension, shape, and position of defects. It is also helpful to understand the imaging principal of the system. This

paper analyzed every part of the system in detail in order to build a model that contains some nonlinear factors such as the sphere characteristic of the input screen of image intensifier and the imaging distortion of camera. The model can be helpful to realize high precision measurement.

References

1. D. Mery and D. Filbert. Automated Flaw Detection in Aluminum Castings Based on the Tracking of Potential Defects in a Radioscopic Image Sequence. IEEE Transactions on Robotics and Automation. Vol.18. No. 6, December 2002.
2. REN Dahai, YOU Zheng, etc. Perspective transformation model for real-time radiography inspection system. OPTICAL TECHNIQUE. March 2000
3. D. Mery. Explicit geometric model of a radioscopic imaging system. NDT&E International 36(2003) 587~599.
4. M. Sonka, Vaclav Hlavac, etc. Image processing, analysis, and Machine Vision (second edition). 448~453.
5. QIU Maolin, MA Songde, etc. Overview of Camera Calculation for Computer Vision. Acta Automatica Sinica. Jan 2000.
6. LI Jiawei, CHEN Jimao. NDT handbook. Feb 2002. P82，84

A Vision-Based Seam Tracking System for Submerged Arc Welding

Zhiguo Yan, De Xu, Yuan Li, and Min Tan

Key Laboratory of Complex System and Intelligent Sciences, Institute of Automation, Chinese Academy of Sciences, Beijing, 100080, P.R. China
Graduate University of Chinese Academy of Science, Beijing, 100080, P.R. China
zhgyan04@mails.gucas.ac.cn,{xude, liyuan, tan}@compsys.ia.ac.cn

Abstract. Welding seam tracking is a key issue to welding automation. In this paper, a seam tracking system based on laser structured light is presented. The paper discusses the structure of this system, and also explains the system's working principle especially the image processing algorithm. The outside-welding experiments of steel pipe show that this system is very robust to various welding noises and it can improve the welding efficiency greatly.

1 Introduction

The arc-welding is a difficult and unhealthy job. Although the welding technology has been developed greatly in decades, most of the welding robots serving in practical production still are teaching and playback type. This kind of robots does not have adaptive ability to circumstance, so they can not often meet the diverse requirements of users. On the other hand, submerged arc welding is widely applied in manufacture recently, especially in the produce of pressure vessel because of its advantages of high efficiency, well formed seam. During the process of submerged arc welding, the weld seam can not be seen, it is difficult for the worker to control the position of the torch. So it is the development trend to explore an adaptive system that has the ability of weld seam tracking.

In weld seam tracking system, the sensor is one of the most important factors. Many researches have been done to explore the best sensor for weld seam tracking. Ref [1] concludes most kinds of sensors that can be used to get the information of the weld seam. The arc sensor (Ref [2]), ultrasonic sensor (Ref [3]) and vision-based sensor (Ref [4-8]) have been used in this field.

Among all these sensors, laser-based vision sensor has been paid a hot attention in recent years due to its high speed, high accuracy, and high robustness to welding environment. The visual sensing technology can be divided into active method and passive method according to imaging light source. In active method, assistant light source is needed to illuminate the welding region. In Ref [9-11] active method of seam tracking is discussed. On the contrary, in passive method, no assistant light source is needed, Ref [12] investigate the use of passive method in the weld seam tracking.

Visual servoing is classified into two groups: position-based visual servoing and image-based visual servoing (Recently, a new approach called 2-1/2-D visual

T.-J. Tarn et al. (Eds.): Robot. Weld., Intellige. & Automation, LNCIS 362, pp. 349–357, 2007.
springerlink.com

servoing has been proposed (Ref [16])). In an image-based control system, the input is computed in 2-D image space. In a position-based control system, the input is computed in 3-D Cartesian space. Many researches about vision-based seam tracking system have been explored (Ref [13-15]). Generally, image-based visual servoing is more robust with respect to camera calibration errors. Although this method is convergent only in a small region, it is enough for most seam tracking systems. In this paper, a vision-based seam tracking system is developed. It adopts active method because of its advantage of reliability. In the system, a laser diode is used as the assistant light source. And image-based visual servoing method is used as the control strategy in this system.

This paper is organized as follows: Section 2 describes the structure and principle of the seam tracking system. It consists of four modules such as a visual sensing module, an image processing module, a control and executable module and a welding module. The former three modules are discussed in this Section. Section 3 gives the result of the experiment. Conclusion is given in Section 4.

2 Structure and Principle of Seam Tracking System

2.1 Control System Structure

The overall visual seam tracking system is composed of four modules: a visual sensing module, an image processing module, a control and executable module and a welding module. The visual sensing module consists of a laser diode, a CCD (charge coupled device) camera, a spatter shield, an optical filter, an image acquisition card. All the work of image processing is performed in an industrial computer. The control and executable module consists of a motion control card, a cross slide which is made of two stepper motors and a control handle. The welding module consists of a torch, an electric welding machine and some other devices.

The visual sensing module captures the image of the weld seam, and then transfers it to the image processing module. After the image is processed, the feature point of the seam is calculated. Then the error between this feature point and the reference point, which is given before welding, can be got. The control module aligns the torch along the weld seam during the welding process according to this error. The welding module is the part to do the welding work. In this paper, we will pay attention to the former three modules. Fig.1 shows the framework of the seam tracking system.

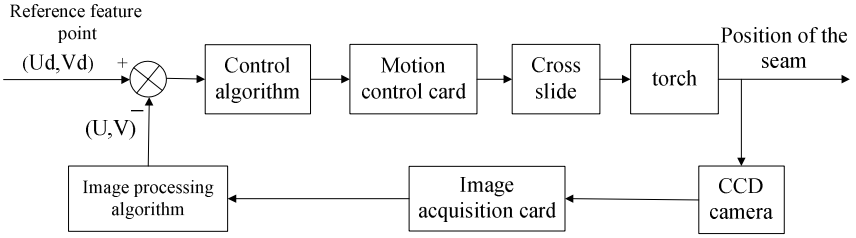

Fig. 1. Framework of the seam tracking system

2.2 The Visual Sensor

The visual sensor is one of the most important parts of the system. Fig.2 shows the structure of the sensor.

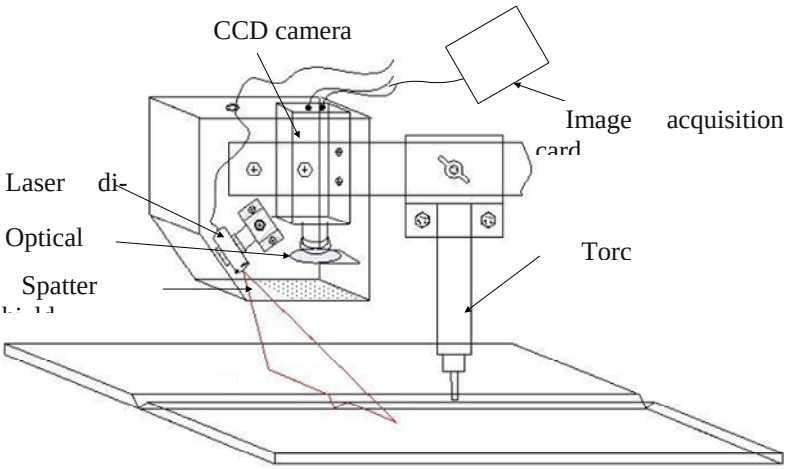

Fig. 2. The structure of the vision sensor

The visual sensor is mounted on a bracket where the torch is attached. During welding process, the laser diode generates a plane of light beam. When the plane of laser light is projected onto the workpiece, there will be a laser stripe on the surface of the workpiece. And the shape of this laser stripe reflects the weld seam's information. Then the camera captures the image of the stripe through a optical filter, which is fixed under the camera. Only the light whose wavelength is between 650 nm – 690nm can pass through this filter (the laser's wavelength is 670nm). So redundant lights are removed and the quality of the image is improved in this way. The link between the visual sensing module and the image processing module is finished by image acquisition card. It transfers the data from the CCD camera to digital signals in industrial control computer.

2.3 The Image Processing Module

The image processing software of this seam tracking system is developed by the Institute of Automation, Chinese Academy of Sciences. The user interface of this software is so friendly (Fig.5 c, d) that it is convenient to use for workers even a beginner. Before welding, the type of the weld seam should be decided, such as Vee and U-shaped joints, Step and Butt joints, and welding for first time and multi-welding joints. The user can set welding parameters, image processing parameters and other parameters. During the welding process, the user can get a lot of information from the monitor of the software. For example, the user can see the initial image of the laser stripe and the processed image on the monitor. The user can also get the coordinates of reference feature point and current seam feature point.

The image processing algorithm is the foundation of the software and even the system. Many methods have been developed recent years, but weld is a very complex process, the image is suffered from arc light, splash, background brightness and Electro Magnetic Interference. So, how to increase the robustness of the image processing algorithm is still a focus of many researchers. Fig.3 shows the flow of image processing algorithm of this weld seam tracking system.

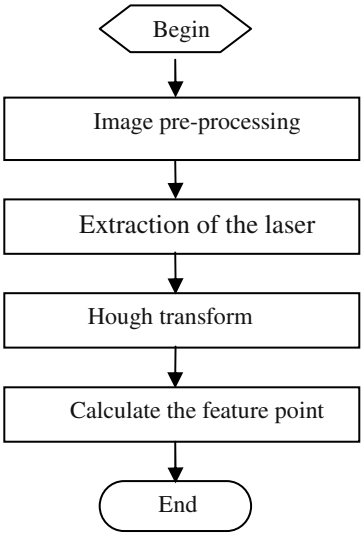

Fig. 3. The flow of image processing algorithm

A. Image pre-processing

1) Image Segmentation

In this system, the gray image size is 640×480 in pixel. However, it is unnecessary to process the entire image region. Our interest is the region of the weld seam. Equation (1) is used to determine this region.

$$A(j) = \sum_{i=1}^{i=64} I(10i, j) \tag{1}$$

where A is a 480-dimension vector, j=1,2……480. I(u,v) is the gray level of pixel point (u,v).

The purpose of (1) is to accumulate the gray value of pixel points along every row spaced ten pixels with one pixel step length and save the result in a vector. If A(j) is the maximum component of vector A, the conclusion can be made easily that i is approximately the row number of the laser stripe in image, and then the target region can be determined easily in a rough way.

2) Image Enhancement

The target region is divided into some sub-regions and the gray levels are marked 25 levels. The frequency distributions of gray level in each sub-region are calculated.

According to these frequency distributions, a proper threshold for image enhancement is selected for each sub-region. For more details, see also Ref [9].

B. Extraction of the Laser Stripe Profile

Conventionally, many researchers use edge detection as the method of extracting the profile of the laser stripe. In our system, this question is solved according to the distribution of gray value in each column. In general, the gray value of laser stripe is bigger than that of other points, but it is not always true because of the influence of arc light, the reflection and other factors. Our method is to extract the biggest gray value of each column as the profile of laser stripe. At the same time, the continuity of time and space as shown in (2) and (3) is used to eliminate the bad influence.

$$\begin{cases} \left| V - \overline{V_t} \right| \le \Delta V_t \\ \left| V - \overline{V_s} \right| \le \Delta V_s \end{cases} \tag{2}$$

$$\begin{cases} \overline{V_t} = \dfrac{1}{m} \sum_{a=1}^{m} V_{t-a} \\ \overline{V_s} = \dfrac{1}{n} \sum_{a=b}^{n} V_{s-b} \end{cases} \tag{3}$$

where V is the v-coordinate of one point on the laser stripe profile of current image, $\overline{V_t}$ is the mean v-coordinate of correspond points on the laser stripe of previous m frames of images, $\overline{V_s}$ is the mean v-coordinate of previous points of the current image. ΔV_t and ΔV_t are used to judge if a point can be admitted or not.

C. Hough transform

Hough transform is a good algorithm to detect straight lines in an image. It is used to find the main line of the laser stripe in this system. According to the fact that the laser stripe line is approximately parallel to X-axis, the parameter θ in (R, θ) plane is limited between 80 degrees and 100 degrees, efficiency is improved in this way.

D. Calculate the feature point

There are different ways to find the feature points for different weld seams. Vee joint is taken as an example here. It is important to select a proper feature point because it can improve the robustness of the system. In conventional methods, the turning points of the weld seam are often used as the feature points. In our algorithm, the center the welding grove is used as the feature point. The main line and the profile of the laser stripe form a close region at the grove area. Here, this close region is named V. Fig. 4 shows the center of region V.

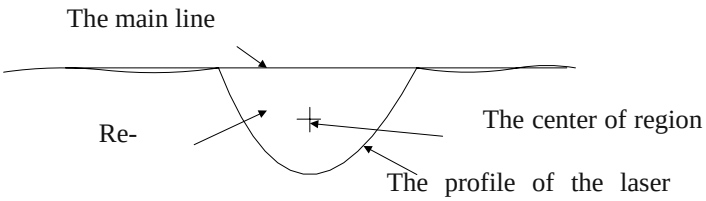

Fig. 4. The center of region V

The center of region V then calculated as shown in (4) and (5).

$$F_u = \frac{\sum_{i=b1}^{b2} i\left[V_p(i) - V_l(i)\right]}{\sum_{i=b1}^{b2}\left[V_p(i) - V_l(i)\right]} \tag{4}$$

$$F_v = \frac{\sum_{i=b1}^{b2} 0.5\left[V_p(i)^2 - V_l(i)^2\right]}{\sum_{i=b1}^{b2}\left[V_p(i) - V_l(i)\right]} \tag{5}$$

where (Fu, Fv) is the coordinate of the feature point, b1 is the smallest u-coordinate of region V and b2 is the biggest u-coordinate, vl(i) is the v-coordinate of the intersection between the main line and line u=i, vp(i) is the v-coordinate of the intersection between the profile of the laser stripe and line u=i. For more image processing details, see Ref [17].

2.4 The Control Module

The control module of this system is used to regulate the position of the weld torch, it is the execution part of the system. The distance from the workpiece to the camera varies in a very small range and can be measured easily. The Cartesian space resolution of a pixel in image space of the CCD camera in this system is well calibrated. It is 0.08mm/pixel, so it is easily to get the real distance between the reference feature point and the current weld seam feature point after the pixel distance is calculated. The distance errors in horizontal and vertical directions are the input of motion controllers. PID algorithms are used to determine the numbers of pulses for the stepper motors. And then these numbers are used by the motion control card to regulate the cross slide in two directions, the up-down direction and the left-right direction. The weld torch is mounted on the cross slide, so it's working path is corrected to align the weld seam through the regulation of the cross slide. The control handle is used to adjust the torch and CCD camera before welding to make sure that the laser stripe is at the center of the image.

3 Experiments and Result

Experiment of welding the outside of a pipe was carried out to test this vision-based seam tracking system. There were two weld seams on the outside surface of the pipe. One was Vee joint; another was butt joint. In this Section, the Vee joint is taken as an example to explain the experiments. The parameters of one experiment are described as table 1.

Table 1. The parameters of experiment

Pipe length	180cm	Welding voltage	44VDC
Pipe diameter	110cm	Welding current	400A
Pipe thickness	12mm	Welding speed	0.9m/min

Fig.5 (a) shows the situation during welding. It can be seen clearly that there are strong background brightness and reflection in this figure, this will be bring great difficulty to image processing. Fig.5 (c, d) show the monitor of the image processing software. As referred in Section 2, the user can see the initial image of the laser stripe and the processed image on this monitor. The left picture on the monitor is the initial image of the laser stripe, the right one is the processed image. There are strong Electro Magnetic Interferences in these two pictures, and there is also strong reflection in

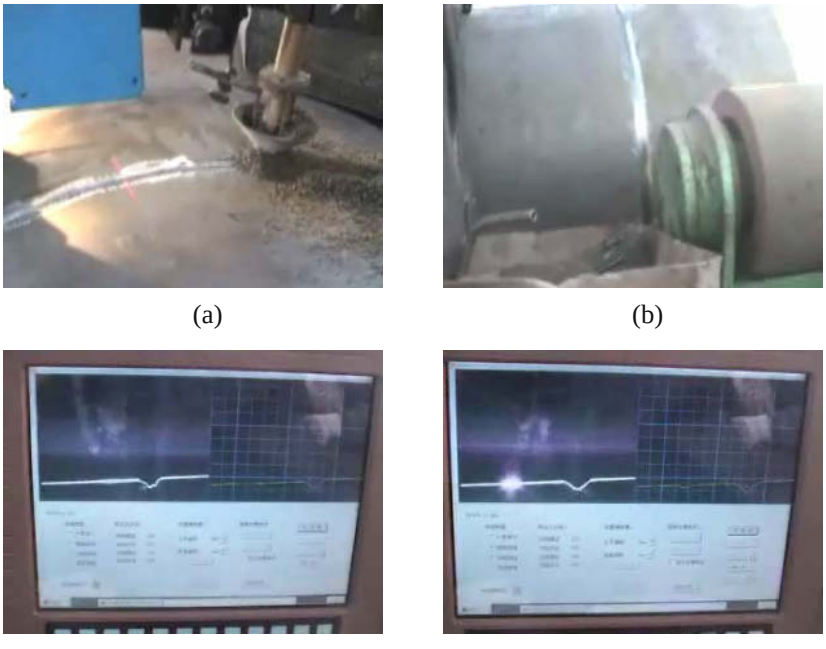

(a) (b)

(c) (d)

Fig. 5. Experimental results of the seam tracking system

Fig.5 (d). But in those two processed images, the profiles and the feature points of the aser stripes have been extracted correctly. There is a red small cross cursor which indicates the position of the feature point in grove region in processed image, but it is not clear in Fig. 5 (c, d). In addition, the system has strong adaptive ability to light disturbance in the working environment. In fact, the strong background brightness in Fig.5 (a) was sunshine. The systems worked very well in a series of experiments whether there was sunshine on the working range or not. The result of the experiment, which is showed in Fig.5 (d), indicates that this vision-based seam tracking system can meet the requirement of industrial weld.

4 Conclusions

The vision-based seam tracking system proposed in this paper can work with precise even with a lot of interferences of environmental noises. With the adaptive ability to circumstance, this system can reduce the workloads of welders. At the same time, it can be easily operated by workers because of it's friendly user interface. The experimental results demonstrate the effectiveness of the system. And the experiments also give evidence that this system can meet the need of quality requirements of welding.

Acknowledgements

We would like to thank the National High Technology Research and Development Program of China for the support to this work under the grant No. 2002AA422160. Our thanks also give to National Key Fundamental Research and Development Project of China (973, No.2002CB312200) for the partly support.

References

1. Mao XJ, Huang SS, Xue JX, Wang XY (2001) The researching status and development trend of arc welding robotic seam tracking system. Electric Welding Machine, 31(10): pp 9-12, 22
2. Dilthey U, Stein L (1994) Through the arc sensing: A multipurpose low-cost sensor for arc welding automation. Welding in the World, 34: pp 165-171
3. Mahajan A, Figueroa F (1997) Intelligent seam tracking using ultrasonic sensors for robotic welding. Robotica, 15(3): pp 275-281
4. Rooks B (1987) Vision seam tracking extends to TIG. Industrial Robot, 14(4): pp 207-208
5. Sicard P, Levine MD (1989) Joint recognition and tracking for robotic arc welding. IEEE Transactions on Systems, Man and Cybernetics, 19(4): pp 714-728
6. Wang LK, Xu D, Tan M (2004) Robust detection for the weld seam shaped zigzag line. In Proceedings of 2004 IEEE International Conference on Robotics and Biomimetics, pp 721-726
7. Xu D, Jiang ZM, Wang LK; Tan M (2004) Features extraction for structured light image of weld seam with arc and splash disturbance. In Proceedings of the 8th International Conference on Control, Automation, Robotics and Vision, 3 : pp 1559-1563

8. Xu D, Wang LK, Tan M (2004) Image Processing and visual control method for arc welding robot. In Proceedings of 2004 IEEE International Conference on Robotics and Biomimetics.: pp 727 – 732
9. Morgan CG, Bromley JS, Davey PG (1983) Visual guidance techniques for robot arc welding. In Proceedings of 3rd Conferences of Robotic Vision Sense Control, pp 615-619
10. Agapakis JE, Bolstad J (1991) Visual sensing and processing system for monitoring and control of welding and other high luminosity processes. In Proceedings of SPIE of the International Society for Optical Engineering, 1385 : pp 32-38
11. Beatlie RJ, Cheng SK, Logue PS (1988) The use of vision sensors in multipass welding applications. Welding Journal, 67(11): pp 28-33
12. Li Y, Middle JE (1993) Machine vision analysis of welding region and its application to seam tracking in arc welding. In Proceedings of the Institution of Mechanical Engineers, Part B: Journal of Engineering Manufacture, 207(5): pp 275-283
13. Nayak N, Thompson D, Ray A, Vavreck A (1987) Conceptual development of an adaptive real-time seam tracker for welding automation, In Proceedings of 1987 IEEE International Conference on Robotics and Automation. 4: pp 1019- 1024
14. Kim JS, Son YT, Cho HS, Koh KI (1995) Robust method for vision-based seam tracking in robotic arc welding, In Proceedings of the 1995 IEEE International Symposium on Intelligent Control : pp 363-368
15. Zhang H, Ding XL, Chen MH, Da BQ, Zou CH (2004) The seam tracking system for submerged arc welding. In Proceedings of Robotic Welding, Intelligence and Automation, LNCIS 299 : pp 144–151
16. Malis E, Chaumette F, Boudet S (1999) 2-1/2-D Visual Servoing. IEEE Transactions on Robotics and Automation, 15(2) : pp 238-250
17. Li Y, Xu D, Li T, Wang LK, Tan M (2005) On visual sensors for weld seam tracking based on laser structured light. Chinese Journal of Sensors and Actuators, 18(3) : pp 488-492

Automatic Inspection of Weld Defects with X-Ray Real-Time Imaging

Du Dong, Cai Guo-rui, Tian Yuan, Hou Run-shi, and Wang Li

Key Laboratory for Advanced Materials Processing Technology,
Ministry of Education, P.R. China
Department of Mechanical Engineering, Tsinghua University, Beijing 100084,
P.R. China

Abstract. A real-time automatic inspection algorithm of weld defects in X-ray images was developed in this paper. Using optimized image smoothing and image information fusion based heuristic best-first search techniques, the algorithm can detect different kinds of defects in weld, such as slag inclusion, blow hole, incomplete penetration, lack of fusion and undercut etc. Experiments show that the algorithm is efficient, reliable and can be used for industrial purpose.

1 Introduction

Inspection of welds is essential to ensure that the quality of welds can meet the design and operation requirements, thus to assure safety and reliability. A variety of Non Destructive Testing (NDT) methods are currently available for the inspection of welding defects, among which visual inspection using X-ray imaging is one of the most important NDT techniques to detect and evaluate defects[1-5].

X-ray can be sensed and converted into visible light to form visual radiographs, the results of X-ray imaging NDT are visual visible, and can be evaluated easily according to corresponding standards by workers. Also due to its high efficiency, extraordinary real-time characteristics, and low costs, X-ray NDT based on real-time imaging techniques is widely used especially in the circumstances where welds need to be inspected at full length. X-ray real-time imaging NDT is playing a rather important role to ensure that the welds quality can meet the design and operation requirements in modern industry.

With so many virtues, however, X-ray real-time imaging NDT is considerably vulnerable to human factors, which impose great influences on the evaluation, and sometimes even result in wrong decisions. X-ray real-time imaging NDT also needs workers to be highly concentrated during the inspection, thus it is a very tough task for human beings especially when long time working is needed. For all these reasons, researchers both inner and outside the country are now devoting their efforts to bring improvements in this area.

In X-ray radiographs, welding defects can be seen as zones whose brightness are different from the surrounding area, and can be easily identified by human beings. However, due to non-uniform illumination, noises, low contrast and blurred by motion, algorithms now encounter difficulties in extracting defects in distorted

T.-J. Tarn et al. (Eds.): Robot. Weld., Intellige. & Automation, LNCIS 362, pp. 359–366, 2007.
springerlink.com

radiographs. How to detect defects in welds radiographs accurately and efficiently becomes the major problem that restricts the development of computer based X-ray real-time imaging automatic defects inspection system[2].

Lots of efforts have been done by researchers around the world, and lots of inspection methods have been proposed, such as method based on edge detection[6], method based on morphology[7], method based on fuzzy reasoning and neural network[5], etc. The result still is not as satisfying as expected. Resistance mainly comes from the following aspects. First, the shape of different defects varies largely. Even defects of the same kind have different shapes and size. Second, image noise and motion blurring make it hard to detect defects in images. Third, lack of efficiency still is a barrier to achieve real-time inspection.

This paper presents a new real-time automatic defects inspecting algorithm based on optimized image smoothing and image information fusion based heuristic best-first search techniques, aiming at setting up a real-time, efficient and effective automatic defects inspection system.

2 Basic Principals

2.1 Optimized Image Smoothing

Image smoothing is one of widely used methods to suppress image noise, and it's the most important technique in image preprocessing. Traditionally in image smoothing, it's necessary to recalculate the sum and average of gray values in the neighborhood for each pixel in the image, and this is a rather time-consuming process.

However, the fact is when moving to the next pixel during the process, the new pixel's neighborhood changes little. Comparing with the previous one, the new neighborhood loses a left column while adding a new column to its right side. As shown in Fig.1, most of the pixels contained in the previous neighborhood are still contained in the new neighborhood, only the pixels which have been lost or newly added should be taken into consideration. Thus it can promote the filtering efficiency obviously.

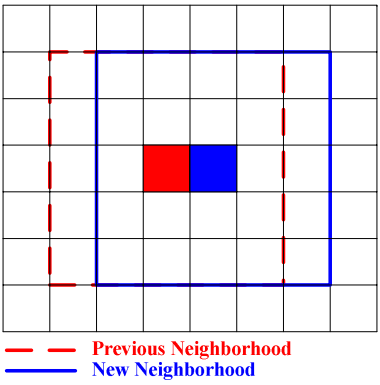

Fig. 1. Neighborhood differences

2.2 Heuristic Best-First Search

Data Search is a widely used technique in scientific activities in modern society. It uses the high potential of fast computing power of computers to find solutions to certain problems through enumerating every possibility in the state space. The process of finding a solution is called State Space Search. One of the commonly used searching techniques is called Heuristic Best-First Search (HBS). It evaluates each node in the state space while performing search tasks, finds the best direction and proceeds to the node, then evaluates the new node. The steps repeat till a possible solution is reached. Using HBS will save lots of the searching steps, and is helpful for enhancement of searching efficiency[8,9].

The evaluation of nodes in HBS is expressed as below. See Equ.1:

$$f(n) = g(n) + h(n) \tag{1}$$

In Equ.1, *f(n)* is the evaluation of node *n*, *g(n)* represents the cost from the initial node to node *n*, *h(n)* is the evaluation of cost from node *n* to the target node. Here *h(n)* also represents the heuristic information for the search process, *g(n)*, yet, also shows the prior direction of the search. However, when $h(n) >> g(n)$ is satisfied, *g(n)* can be neglected in order to further enhance the efficiency.

2.3 Image Information Fusion Based Heuristic Best-First Search

Image Information Fusion is a technique that synthesizes the results of different image processing methods, obtains accurate information contained in the image, and provides foundations for evaluation. Because the useful information contained in results by different processing methods always has certain correlations while unwanted information such as noise doesn't, knowledge obtained by IIF can be quite reliable[10].

Image Information Fusion based heuristic best-first search is the combination of both Image Information Fusion technique and the Optimized Heuristic Search technique. First to process the image with different algorithms, then use IIF technique to synthesize the information got from the processing results to obtain a thorough understanding of the image, which will be the bases for setting up state space and will also provide necessary heuristic information for choosing a searching path and making decisions.

Suppose that the obtained heuristic information through certain image processing algorithm is denoted as $h_i(n)$, the heuristic information by IIF process can be defined as follow:

$$h'(n) = \sum_{I} \varepsilon_i h_i(n), i \in I \tag{2}$$

In Equ.2, $h'(n)$ represents the heuristic information obtained by IIF process, ε_i represents consideration coefficient of algorithm *i*.

IIF technique can acquire the precise characteristics information of the target image, while heuristic best-first search can get to the target with great efficiency. Thus when they are combined, a new technique of automatic defects inspection based on X-ray real-time imaging with better performances than ever before will definitely be developed.

3 Automatic Real-Time Defects Inspection

Base on the thorough and very detailed research work on the techniques mentioned above, the new real-time automatic defects inspection algorithm proposed in this paper is applied to detect defects in X-ray radiographs.

3.1 Region of Interest

Fig.1a is a radiograph acquired from the industrial NDT spot using digital X-ray real-time imaging system. The gray zone *I* in the figure is the weld with two defects in it, the defects are denoted as A and B.

As shown in Fig.2a, the welds zone *I* , where nearly all the useful information is contained, only occupies very small proportion of the whole image. Thus it is very important to perform Region of Interest (ROI) process. On one hand, ROI process can effectively reduce the data to be processed, increase the inspection speed, and assure real-time inspection. On the other hand, ROI process can eliminate useless data from affecting the inspection process, thus it is helpful for the veracity of inspection results.

ROI process is to segment a rectangle region out from the original image along the seam direction which is filled with weld. Rotate the ROI image to horizontal direction and the result is shown as Fig.2b.

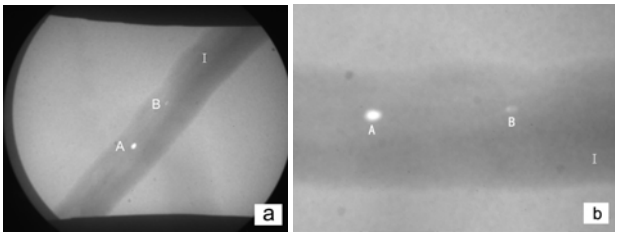

Fig. 2. X-ray radiograph and ROI processed Image

3.2 Image Pre-processing

Image pre-processing mainly consists of two aspects: image enhancement and image smoothing. We know that X-ray radiographs are easily corrupted by non-uniform illumination. In the paper, in order to enhance the contrast and to improve the visual looking of the images to be processed, adaptive histogram equalization technique is used to adjust the gray scale of the images. Brightness adjustment is also performed in this step. The histograms of the same image before and after the enhancement process are shown separately in Fig.3a and Fig.3b. Seen from the figures, the histogram of the enhanced image is more even than the original image while gray scale is widened from [110, 190] to full scale.

Image smoothing is mainly used for suppressing image noise. While performing image smoothing, new value based on the average gray values in the neighborhood is calculated to replace current gray value. Image smoothing can effectively eliminate impulse noise in the image, but it will also blur the edge of the inspection objects such as defects and welds. So it is really a compromise between suppression of noise and

losing less useful information we need. To a 5×5 neighborhood mean filter, the mask M_{25} is shown as Equ.3:

$$M_{25} = \frac{1}{25}\begin{bmatrix} 1 & 1 & 1 & 1 & 1 \\ 1 & 1 & 1 & 1 & 1 \\ 1 & 1 & 1 & 1 & 1 \\ 1 & 1 & 1 & 1 & 1 \\ 1 & 1 & 1 & 1 & 1 \end{bmatrix} \tag{3}$$

If $f(i, j)$ represents the raw image, and $g(i, j)$ denotes the processed image, the filter can be explained in Equ.4:

$$g(i, j) = \frac{1}{25} \sum_{s\in[-2,2]} \sum_{t\in[-2,2]} f(i+s, j+t) \tag{4}$$

In this paper, an optimized mean filter algorithm is used. It is shown as Equ.5. The principle of optimized mean filter algorithm, please refer to section 2.1.

$$g(i, j) = \frac{1}{25}\left(S_0 - \sum_{k=-2}^{2} f(i+k, j-3) + \sum_{k=-2}^{2} f(i+k, j+2) \right) \tag{5}$$

S_0 is the sum of pixel gray values in the neighborhood of the previous pixel. Image after pre-processing is shown in Fig.3c. Choosing a proper filter algorithm according to actual conditions is important when perform image smoothing procedure.

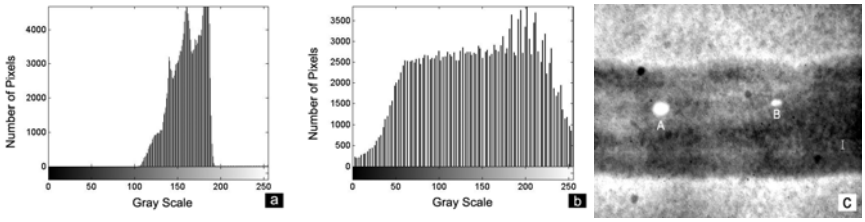

Fig. 3. Histograms and Pre-processed image

3.3 Weld Segment

The common defects in welds are blow hole, slag inclusion, lack of fusion, lack of penetration, burn through and undercut, etc., in which defects such as blow hole, slag inclusion, lack of fusion and lack of penetration always exist in the center of the welds, along the center line of the welds, while other defects such as undercut mainly appear near the edges of the welds. And it is required to detect different kinds of defects using different algorithms. We can divide a weld into several zones, denoted as Center of Weld (CW) and Edge of Weld (EW), and inspect each zone using corresponding algorithm for possible existing defects.

Because there is no need to find exact edges of the welds, a projective wave analysis algorithm is developed to segment the welds. Projective wave analysis algorithm is shown in Fig.4a. As is shown in the figure, region I and region II is EW, region III represents the CW. A proper threshold value is needed here and it can be calculated by Equ.5.

$$Threshold = \lambda N\left(G_{\max} - G_{\min}\right) + NG_{\min} \tag{6}$$

In Equ.6, N is the number of pixels per projective line. G_{max} and G_{min} are the symbols representing the upper limit and the lower limit of gray scale of the image. λ is coefficient, which can be any value in [0.51 0.63] as testified by experiments.

Segmentation of the welds is shown in Fig.4b, region I, II and III are consistent with I, II and III in Fig.4a.

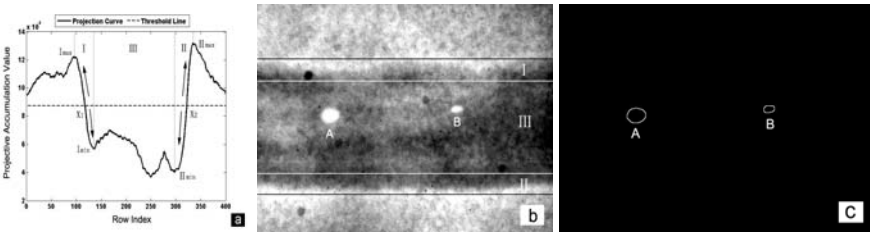

Fig. 4. Weld Segmentation and Defects extraction result

3.4 Defects Inspection

After finishing weld segmentation, as all the possible defects will only appear in the weld, there is no necessary for inspection regions other than I, II and III. Take defects inspection in CW region (region III) for example, inspection steps are shown below:

1. State space consisting of all the searching nodes for HBS is set up in this step. Scan each line of the region, pixel by pixel, use a predefined threshold to compare with the gray value of each pixel. Then record the gray values and coordinates in the image of all the pixels whose gray value excesses the threshold. Sort by the gray value in degressive order to form an index table of gray value, named G-Index. Sort by coordinate x to form the x-Index table and by coordinate y to form y-Index table.
2. Following the order of each pixel in the G-Index, calculate $M \times M$ neighborhood local spatial contrast, $M \times M$ neighborhood local spatial variance and $1 \times N$ neighborhood wave analysis of each pixel. Process the obtained results to uncover the heuristic information, called $h(n)$.
3. Based on $h(n)$ search in x-Index and y-Index for all abutting pixels, group all the pixels by abutment-characteristics. All the pixels in the same defects will be in the same group.
4. Clear all the isolated pixels in the state space, all the grouped pixels correspond to certain defects in the image. Fig.4c is the edge detection result after restoring the pixels to the ordinary image according to their coordinates. We can see in it that both the defects A and B are detected using the algorithm proposed in this paper.

Inspection of defects in EW areas is a little different from the inspection in CW area. It mainly depends on wave analysis, which means the coefficient ε is a bit larger and weigh more in making decision under this circumstance. In Fig.5a, a defect exists at *A*. Fig.5b shows the wave analysis comparison of normal edge with defects-contained edge. The inspection result is shown in Fig.5c.

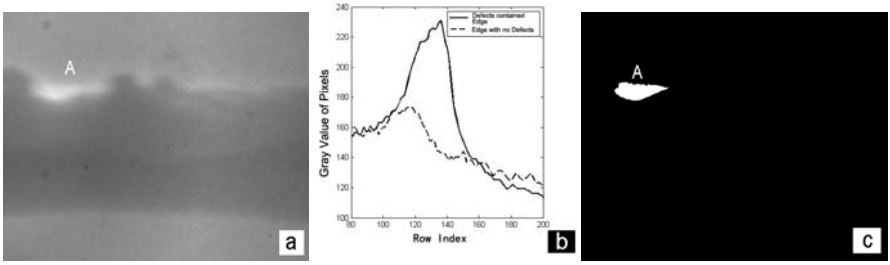

Fig. 5. EW defects inspection

4 Conclusions

Based on careful learning of the existing algorithms of defects inspection, we have done in-depth research into the X-ray real-time imaging automatic defects inspection and proposed an effective and reliable algorithm based on Optimized image smoothing and Heuristic Best-First Search techniques which have already discussed in detail in this paper. The follow conclusions can be reached:

1. The proposed algorithm can effectively reduce the data to be processed in each processing step, thus it can detect defects in X-ray images very quickly.
2. According to the distribution characteristics of defects in the welds, the proposed algorithm chooses different inspection methods for different kinds of defects, and it can detect all possible defects in the radiograph.
3. The proposed algorithms is based on optimized image smoothing and HBS techniques, thus it can detect the defects with high precision, fast speed and considerably low mis-alarms.

In conclusion, X-ray real-time imaging automatic defects inspection algorithm is reliable and efficient. It can detect defects exactly with ultra-high speed. The research work in this paper has made steady foundation for further improvements in X-ray real-time imaging automatic defects inspection.

References

1. SUN Yi, BAI Peng, SUN Hong-yu, et al. Real-time automatic detection of weld defects in steel pipe [J]. NDT&E International, 2005, 38:522-528.
2. GANG Tie, WANG Dong-hua. Defect extraction and segmentation automatically in X-ray inspection images [J]. Welding. 2001, 5:6-9,43.

3. REN Dahai, YOU zheng, SUN Chang-ku, et al. Automatic inspection techniques by real-time radiography for weld defects [J]. Tsinghua Univ (Sci & Tech), 2001, 41(2):25-29.
4. ZHOU Zheng-gan, ZHAO Gang, AN Zhen-gang. Defect Extraction of X-ray Images Based on Subarea and Self-adaptive Median Filtering [J]. Acta Aeronautica et Astronautica Sinic, 2004, 25(4):420-424.
5. V.Lashkia. Defect detection in X-ray images using fuzzy reasoning [J]. Image and Vision Computing, 2001, 19(5):261-269.
6. QIU Guo-ping. Image Noise Reduction Based on the Edge Detection and Data Fusion [J]. Microelectronics & Computer, 2005, 22(9):146-149.
7. GANG Tie, WANG Dong-hua. Defect extraction of X-ray images based on Adaptive Morphology Filtering [J]. Chinese Journal of Mechanical Engineering, 2001, 37(5):85-89.
8. Milan Sonka, Vaclav Hlavac. Image Processing, Analysis and Machine Vision [M]. 2nd Edition. Thomson Learning Vocational, 2002. p148-163.
9. ZHANG Wei-hong. A Novel Edge Detection Algorithm Based on Heuristic Search Methods [J]. Aeronautical Computer Technique, 2005, 35(2):42-44,49.
10. ZHANG Zhao-li, ZHAO Chun-hui. Modern Image Processing Techniques & Matlab Implementation [M]. Beijing : Posts and Telecom Press, 2001.p311.

Portable and Intelligent Stud Welding Inverter for Automotive and Sheet Metal Fabrication

C. Hsu, D. Phillips, C. Champney, and J. Mumaw

Nelson Stud Welding, Inc. 7900 West Ridge Road, Elyria, Ohio 44035, USA
Chris.Hsu@nelsonstud.com

Abstract. This paper introduces a new, portable and intelligent inverter for stud welding in automotive rework and robot backup, and for general sheet metal fabrication applications. The new portable inverter combines the virtues of precision and simplicity. High repeatability, accuracy and arc stability are ensured with digital signal parallel processing and Dual Loop™ fast arc regulation technology, designed for stud welding. High surge current is provided with unique Parallel Silicon™ technology for advanced high strength steel and to overcome adverse surface coating. A user-friendly interface called Stud Expert™ introduces a new programming methodology based on application conditions instead of machine settings such as time and current. Procedures can be memorized and recalled by the use of pre-sets. Quality assurance is embedded inside the welder to determine weld quality and to monitor production data.

1 Introduction

Stud welding to sheet metal is characterized by the use of high current and short time, which can be accomplished by a special drawn-arc stud welding process known as "short cycle", or by capacitor discharge (CD) process [1][3].

Fig. 1. Robot stud welding cell for the production of sheet metal parts

T.-J. Tarn et al. (Eds.): Robot. Weld., Intellige. & Automation, LNCIS 362, pp. 367–374, 2007.
springerlink.com

The CD process is typically avoided in automotive and other sheet metal fabrication when quality is a must. To ensure precision control of the welding arc in weld duration as short as 5 ms, an inverter[2] is typically used with a servo-electric gun[3] mounted on a robot arm in automotive production (see Figure 1).

However, virtually all automotive plants have re-work or repair stations, and a back-up system with manual stud welding when the robots are off-line. The existing automotive inverter stud welding system designed for robot is too complicated, expensive and bulky for use as backup or repair. The traditional SCR based stud welders are simple to use but have lacked the precision needed for these applications. A user-friendly, portable and intelligent stud welding system for human operator is needed for sheet metal fabrication.

2 Inverter for Manual Sheet Metal Stud Welding

2.1 High Power and Low Weight

Sheet metal stud welding is characterized by very high amperage (e.g. 1500A), very brief weld time (10-100ms) and without ferrule[4]. A low weight inverter can output sufficiently high current at high duty cycle to meet automotive stud welding requirement[1]. In order to accomplish both the low weight/size portability requirement and the high power output requirement, a combination of the latest control and power electronic technologies were implemented.

One challenge in stud welder design is the ability to quickly react to arc conditions and input power fluctuations since the total arc time is typically 25-35 ms. Traditionally, a regulated welding power supply monitors the output current, and adjusts either the SCR firing angle in a transformer-rectifier topology or the pulse width modulation in a switch-mode topology to maintain desired output current. This is often called single loop control in classical feedback control theory. Dual Loop control monitors both primary and secondary current feedback and adjusts inverter switching pulse width quickly to react to physical conditions in the arc and fluid dynamics at the stud end and base metal.

Another challenge is in stud welder design is handling 3-4 times of the welding current of GMAW welder. Parallel Silicon provides surge power needed for sheet metal stud welding with optimum heat transfer efficiency in the switching components. Another advance is the transformer design called Turbo Planar™, with compactly stacked printed circuit boards as the main inverter transformer assembly, fine-tuned for stud welding. Planar transformer is a relatively new technology and is implemented in a stud welder.

These advances collectively result in a new generation stud welder that is about 6 times lighter than the 60Hz stud welder of less performance, such as Series 4800 from Nelson Stud Welding.

2.2 Programming with Stud and Weld Conditions

The requirement of interfacing with human operator is very different than with a robot. Traditionally, a stud shooter must set up the welder using current and time. These settings vary depending on stud type, size and material, weld position, and

[1] 35kg weight, 1500A, 100 ms at 35 studs per minute.

many other factors. To simplify the setup, the inverter allows operator programming based on application conditions. Large quantities of welds were performed to produce the optimum, most robust welding parameters to train a database, called Stud Expert™ to be loaded into the stud welder. This approach is similar to the "one knob control" or "synergic control" in pulsed GMAW welding to simplify user interface, such as in Lincoln Electric's PowerWave[5]. The database contains welding knowledge for various alloys, polarity, stud types and diameters, welding position, and plate conditions. In most cases a stud shooter simply selects a stud from the scroll list on the inverter front panel and welds away.

2.3 Presets, Recall and Lock-Out

Another important aspect for interfacing with a human stud shooter is the ease of weld program save and recall. Backlit preset buttons are provided similar to a car radio. Each preset can be associated with a particular stud in an automotive plant. A preset button can be held down until the backlight comes on to acknowledge that the settings are stored. Pressing on any preset button will recall the stored settings. Different security levels with pass code protection can be set up for production, maintenance, or programming.

2.4 Weld Quality and Production Monitor

To ensure the quality of each stud weld, the computer control is trained with a signature of good quality weld for a given stud and weld condition. A built-in weld

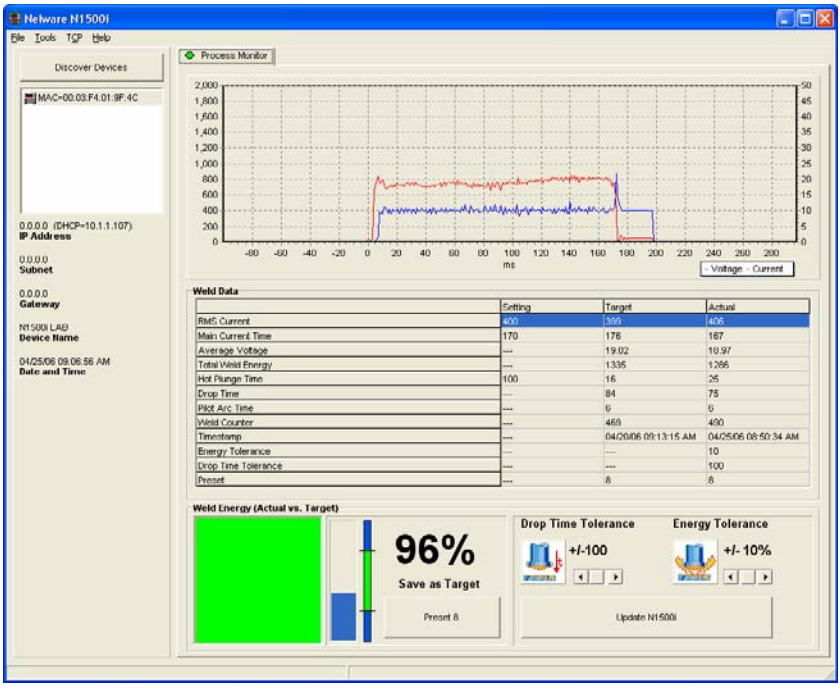

Fig. 2. Weld quality monitor with oscilloscope analysis of each weld

monitor examines arc signals and compares them with the known signature of good weld. The result of the comparison is shown visually on the front panel of the welder after each weld: green plate to indicate good weld and red plate as bad weld. The front panel also displays the operating condition of the handgun, which can be a common source of problems.

In addition, there is a good/bad weld counter in the welder for each pre-set, which can be used for quality assurance purposes. This information can be up-loaded to a host computer software called Nelware™, along with other production data, such as studs per day, per shift, up time etc. and trouble-shooting or service data, as shown in Figure 2.

2.5 Manual Stud Loading and Gun Positioning

When a hand held manual loading gun (Figure 1, right) is used, the outside diameter of the spark shield mounted on the front of the gun is usually used as the reference to locate groups of studs. Templates are commonly used with holes for the spark shield. When the spark shield is inserted into the holes in the fixture the studs will be welded at the desired locations. Alternatively, a laser marking system or a localized GPS receiver on the gun can be used to locate stud locations.

Changing the diameter of studs that are being weld with the handgun is a quick and simple operation. The chucks have a male Morse taper that is simply driven into a female Morse taper on the front of the gun. A series of chucks is available for studs in metric or imperial dimensions.

2.6 Automatic Stud Feed System

Besides manually loading studs, it is often desirable to automatically feed the stud with a feeder to boost productivity in sheet metal fabrication. The feeder and auto feed handgun perform the material handling aspect of the stud welding process. These components are specifically designed to work in harsh environments and reliably deliver the fasteners from the hopper in the feeder to the electrode tip of the gun in a fraction of a second. This allows the operator to move the gun from one weld position to another quickly welding studs at rate over 20 studs/minute.

3 Sheet Metal Studs

Many stud configurations shown in Figure 3 can be fed with a stud feeder, which are explained in the ensuing sections. These studs are used for attaching automotive trim, fastening brackets, routing electrical harnesses and hydraulic lines, and grounding electrical circuits.

3.1 Flanged Stud for Sheet Metal

The strength of the fastened assembly on sheet metal is limited by the sheet metal, when the sheet metal is thinner than 1/3 of the stud diameter. The traditional fasteners for stud welding have flanges on the weld end that are normally about 1mm larger than the diameter of the stud. The flange provides a weld base with a cross

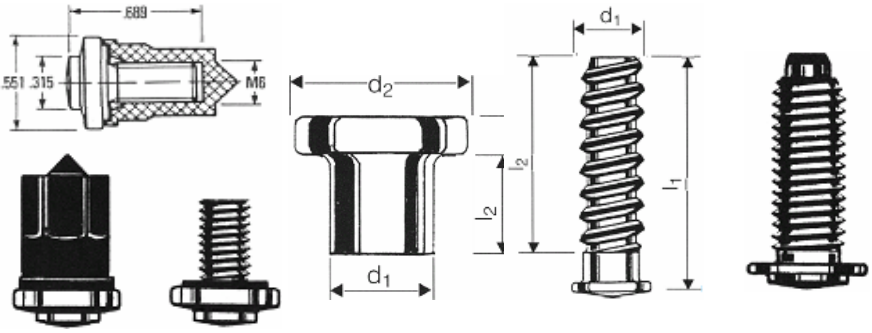

Fig. 3. Electrical grounding studs (left), unthreaded trim stud (center), fir tree stud and wide top stud (right)

sectional area that is slightly larger than the area of the stud. This extra area gives the stud the potential for the weld to always be stronger than the threaded portion of the studs. An additional benefit of flanges on these studs is for auto feed. The feeding equipment can use the flange to hold and orient the studs. The flange assures that the right end of the stud is presented to the gun and base material for welding.

3.2 Wide Flanged Stud (W-Top)

The W-top studs have been widely adopted for use in a variety of industrial application where high strength and reliability are needed. The standard W-Top has a M6 thread and is available in different lengths. On the end that is not welded they have a dog point to facilitate the alignment and rapid installation of nuts. The W-Top studs have a weld base diameter of 9mm and an even larger collar diameter of 13mm. This collar is only 1mm thick and is located only 1mm above the weld end of the stud.

When nuts are being installed on the threaded portion of welded W-Top studs the 13 mm collars will resist the clamping force that is applied as the nut is tightened. Since the clamping force that is applied by the inclined plane of the threads is isolated against the collar the weld and the base material will not subjected a tension load. This means that dimples will not be pulled in the base material as the nut is tightened. The weld and base material only have to resist the pure rotational force as while the nut is being tightened. After the nuts have been tightened the welds and base material only have to support the weight of the part and any loads that are applied to those parts.

The 9mm diameter weld base on the M6 W-Top stud provides a large area of fusion. This weld has usually enough strength to support the strength of the M6 thread even on thin base material. The portable inverter has the amperage needed to weld the W-Top studs even at the short weld times to prevent burning through on the thin 0.7mm base material.

The typical weld settings needed to weld W-Top studs to 0.7mm steel using a hand held gun are approximately 700A at 60ms. With zinc-coated sheet metal, the use of stud positive polarity (also known as reverse polarity) often yields higher weld strength.

4 Sheet Metal Applications of the Inverter

Several sheet metal fastening applications using the portable inverter with auto feed are shown as follows.

4.1 Flanged Stud on Air Bag Inflator

Figure 4 illustrates a fir-tree stud welded to an air bag inflation canister, using short cycle gas arc process. The studs are welded to the canister to provide a means to mount the air bag inflators in an automobile. The welding parameters are shown in Table 1. Weld ultimate tensile of 9,520 N is achieved. The weld must be strong but cannot cause any backside distortion, which would interfere with the contents of the canister.

Table 1. Airbag inflator key welding parameters

Stud Type	6 mm small flange fir tree
Arc Current	400A
Arc Time	80 ms

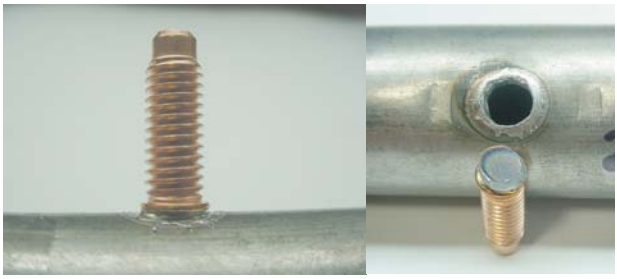

Fig. 4. Small-flanged stud welded to an air bag inflator

4.2 Examples of W-Top and Fir Tree

Another application requires an 8mm stud to be welded to a 44mm diameter steel tube of 3mm wall thickness. A wide top stud (W-top) is short cycle welded with gas shielding (see Table 2). The stud provides a mounting base for other components (Figure 5 left). A 5mm fir tree stud is welded to a mild steel sheet metal (Figure 5 right) to hold press on clips at 600A, 30ms.

Table 2. W-top to tube key welding parameters

Stud Type	W-top
Arc Current	1100A
Arc Time	70 ms

Fig. 5. W-top to a 44mm tube (left) and fir-tree to hold press on clips (right)

4.3 W-Top on "Quiet" Steel

The thicker the base metal the easier to produce good quality weld, according to a design of experiment study [6]. Welding on a very thin laminated steel presents the greatest challenge. Short cycle is used by the inverter to weld a W-top stud to laminated steel dash panel (Figure 6, right). The laminated steel is used to reduce noise from the engine compartment. The sheet is comprised of two sheets zinc plated steel that are less than 0.5mm thick with a thin sheet of polymer between the two sheets of steel. The total thickness of the laminated sheet is only 1mm. To get good welds on this material very short time and very high amperage were needed to prevent burning through the material. The weld settings are shown in Table 3.

Table 3. W-top to 0.5mm laminated steel key welding parameters

Stud Type	W-top
Arc Current	1200A
Arc Time	10 ms

Fig. 6. 9.5mm diameter stainless stud short cycle welded without ferrule (left) and W-top welded to laminated steel (right)

4.4 Stainless Stud Welding Without Ferrule

Short cycle with gas shielding arc is successfully implemented by the inverter to replace drawn-arc with ferrule. Figure 6 illustrates a 9.5mm small flange, stainless steel stud welded at 900A, 75ms with argon shielding and automatic feeding.

5 Stud Welding vs. Resistance Welding

Spot welding and projection welding are commonly employed to weld sheet metal. One of the significant advantages of the stud welding process is single-side access. Another advantage is low pressure applied to the surface of the sheet metal, in contrast with the large clamping force needed for resistance welding.

The added benefit of portability of the stud welding inverter and handgun system makes it a more versatile tool than resistance welding in certain automotive applications.

6 Conclusion

A portable and intelligent inverter is introduced to weld studs in demanding sheet metal short cycle stud welding applications. It provides a cost-effective solution for use in both automotive rework stations and manual production, and in general sheet metal fabrication such as electrical enclosure, switchgear, HVAC and transformer manufacturing. The portable inverter can be used either with manual stud feed or auto-feed, and either with or without gas shielding. W-top, threaded stud, fir tree and T-studs can be welded, with material including steel, stainless steel, laminated steel, and other material such as aluminum, advanced high strength steel and Inconel.

References

1. Welding Handbook, Volume 2, Welding Processes, Part 1, Ninth Edition, American Welding Society, 2004, pp 416-419
2. Spremo, D., Power transformer for a switched mode power supply, especially for stud welding devices, US Patent 6,339,320
3. Raycher, R.J., Apparatus for welding a stud to a workpiece, US Patent 5,252,802
4. Chambers, Harry A, Principles and practices of stud welding, PCI Journal 46 (6), pp 2-23
5. Hsu, C, Pulsed GMAW Online Waveform Editor and Soft Oscilloscope, NIST SPECIAL PUBLICATION 949, ISSN 1048-776X, pp. 392-400
6. Ramasamy, S., Gould, J., Workman, D., Design-of-Experiments Study to Examine the Effect of Polarity on Stud Welding, Welding Journal, February 2002, pp. 19S-26S

Study on the Control System of the Lathing and Welding Compound Machine Tool

Li Xiaohui, Wang Su, Xia Caiyun, Zhu Xiaobo, and Liu Xiaohui
BeiHang University, Beijing, 100083, China

Abstract. Most conventional Computer Numerical Control (CNC) systems are single process method, so one working procedure need several steps to complete. The Combined machining NC system can solve this problem. In this paper, the hardware construction of the lathing and welding compound machine tool control system is studied and the software structure is also discussed.

1 Introduction

Combined machining now is becoming one of future directions for the machine tools in the world. More and more complicated parts begin to be processed with the compound machine tool. Compound machine tool can improve efficiency of production parts with low volume and rich varieties considerably, suitable to produce Aeronautics & Astronautics parts. In order to solve the problem of large-scale structures' welding, a fabrication method, which performing the turning and welding on the same special equipment, is studied in this project. It is improved that it can simplify the manufacture process, improve welding efficiency, guarantee the welding quality and improve the lifetime. The thin wall pipe lathing and welding compound machine tool is composed of an automation lathing system and an automation welding system. With twins-milling head, the compound machine tool can finish the lathing and welding process of the thin wall pipe and flange with no declamp operation.

2 Control System Design

With the three degree-of-freedom Manipulators and a special clamp, the compound machine tool can realize the thin wall pipe lathing and welding on the same tool without a second clamping. The motion model of the compound machine tool is shown in figure 1.

The compound NC machine tool consists of three parts, a CH2010/S ONC system made by BUAA as the control system, a corresponding AC motor and a photoelectric encoder as the executive component and the reactive component of servo system. NC device of the control system compiles of the program and sends order to the servo system, and then the servo system controls the motor's movement. In the whole movement process, the photoelectric encoder mounted on the corresponding AC motor detects the displacement and velocity of the compound machine tool, and this information is feed back to controller by the feedback system. After comparing the

T.-J. Tarn et al. (Eds.): Robot. Weld., Intellige. & Automation, LNCIS 362, pp. 375–382, 2007.
springerlink.com

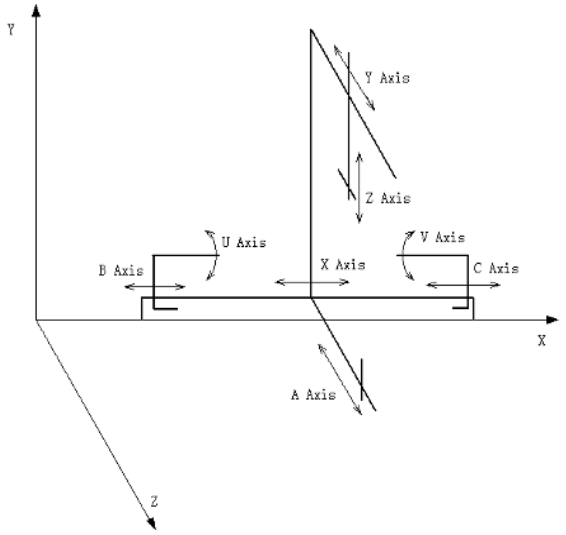

Fig. 1. Motion model of the compound machine tool

actual displacement and velocity with the target value and other information, the controller sends new orders to the corresponding AC motor to produce corresponding movement which can rectify the movement of the compound machine tool[1]. It is a real-time detection, feedback and closed loop control system. The whole control structure of the lathing and welding compound NC machine tool is shown in figure 2.

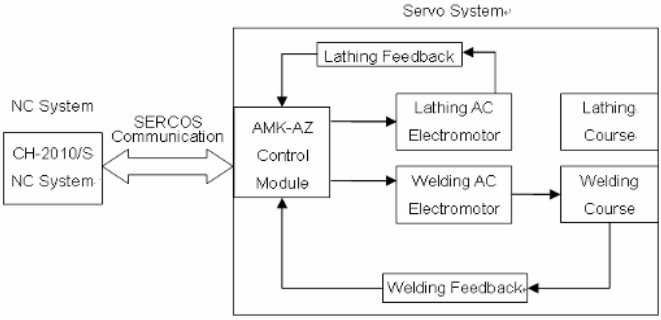

Fig. 2. The whole control structure of the machine tool

3 Hardware Constructions

The hardware part is composed of a CH-2010/S control system, an AMK AC servo module and 8 induction AC servo motors. The CH-2010/S control system is a open

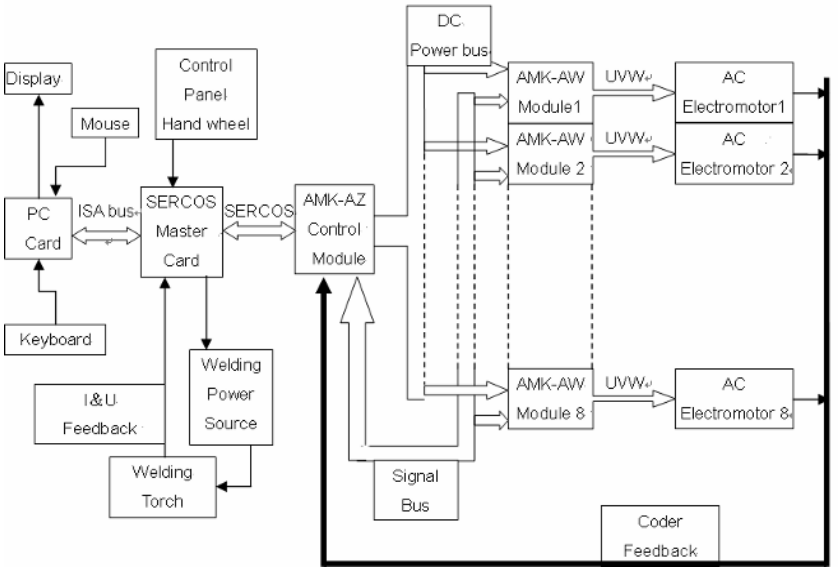

Fig. 3. Hardware construction of control system

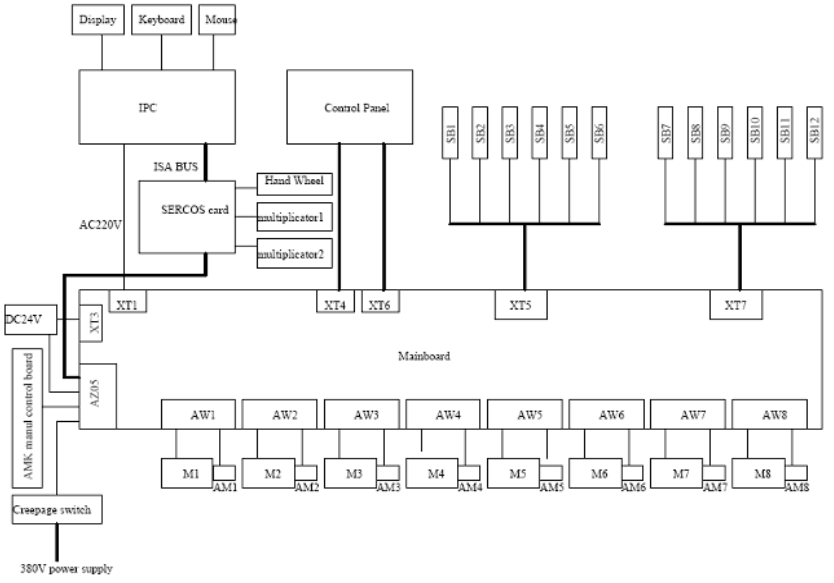

Fig. 4. The hardware hookup of the control system

controller system which is based on the PC computer and field bus SERCOS technology, and its hardware construction contains two cards, one is the PC mainboard card, another is the SERCOS-Master card. NC-PLC kernel operates the

SERCOS-Master interface card with SERCOS-Master driver program and the SERCOS-Master card connects with the AMK AC servo module. The AMK AC servo module is used as the control module. The AMK-AZ sends signals to AMK-AW when any numeric control command receives from SERCOS. And then the AMK-AW exports the signals to three phase induction AC servo motors. The hardware construction of the control system is shown in figure 3.

The SERCOS-Master card has the machine tool operation buttons, multiple switch and handwheel port which are available for all kinds of NC machine tools. The CH-2010/S controls the machine tool control module with the SERCOS-Master card, which is composed of 1~50 SERCOS feed stages and 40~320 PLC-IO ports. The hardware hookup of the control system is shown in Figure 4. In this figure, the AW# means AMK servo module, M# means the number of motor, AM# means the coder relative to motor, and SB# indicates located restrictive switch of the machine tool.

4 Software Constructions

All kinds of resources provided by the WINDOWS operating system can be used conveniently in the CH-2010/S. It offers the software application environment and a group of normal system performance functions to users, such as: [2][3]

1. The Manipulative Performance, including the manipulative menu, coordinate display, operating states display and graphical display etc.
2. Data Management System, including system parameters, tools data, NC programs, files and table edit.
3. System Soft Interface, sending the NC variable, NC data and PLC variable to the NC-PLC kernel and reading them from it.

With the NC variable, NC data and PLC variable, the commands and data are transferred between the CNC system software and application software. NC variable is used for sending control orders such as the selection of work type, cycle starting, feeding keeping and reset operation etc from application software to NC kernel, or

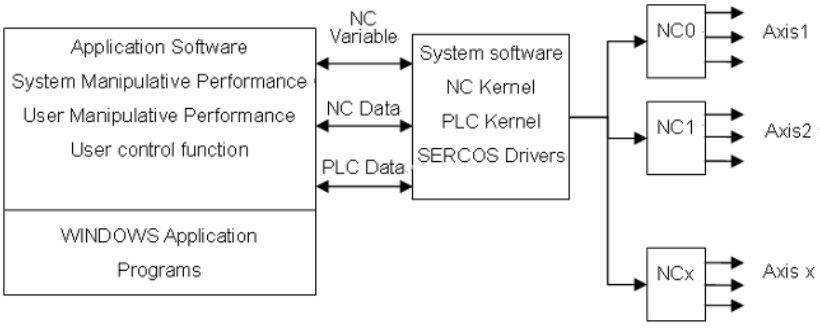

Fig. 5. CH2010/S NC software environment

reading the machine tool coordinate and the NC kernel work states from the NC kernel. The NC data include the NC program, tool data and machine tool parameters etc. Using the PLC variable, the orders can be sent to the PLC kernel from application software straightway and the information of PLC kernel can be read. The PLC kernel offers plenty blending function for invoking. The NC software environment of the CH2010/S is shown in figure 5.

Based on object-oriented technology, in the open CNC software, the control system is divided into many functional modules to accomplish different functions. The C/S module is used for transferring the information between modules and control system kernel or different modules[4][6]. The module offering service function is the server module and the module asking for the function service is client module.

For the scalability, maintainability and reconfiguration of CNC system software, the software is designed with modular method. Based on the control system function, different modules are designed for multi-task ability of control system. The logic diagram control program is shown in figure 6.

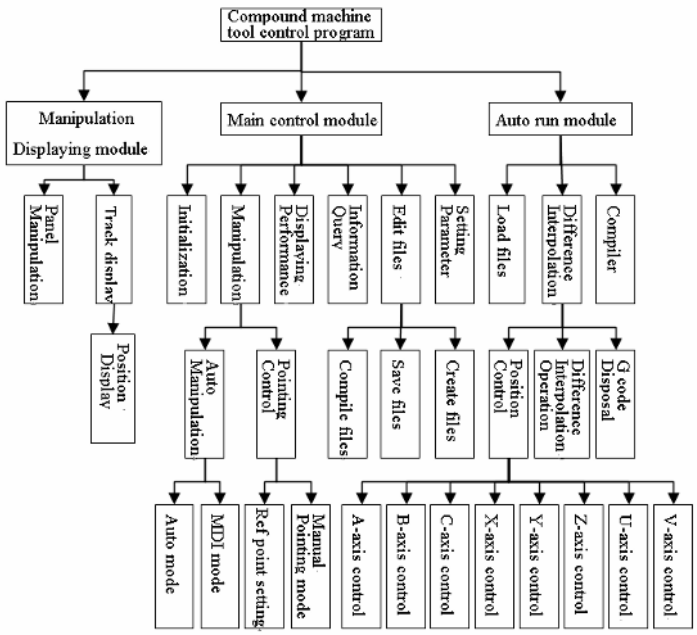

Fig. 6. control program logic diagram

The main control module should accomplish many complex tasks, such as the initialization, the NC programs input, edit&compiling, setting parameters and operation. So it is needed to design a series of unattached function program modules, and furthermore, the same program module has the different module contents under the different control methods.

The control program is designed based on the Windows operating system, so it has the multi-task coordinated ability. In the program, user manipulative performance is

composed of many windows and each of them executes one task. And the functions are realized competitively in the different windows. The states of each task are managed by the management program[5][6]. The main function of main-menu performance is monitoring, performance management, function controlling and system managing. The main function of main-menu performance is monitoring, performance management, function controlling and system managing.

The control part is the vital part of the whole software, and it determines the qualification of the control system. The flow chat of the whole software is shown in fig.7. After initialization of the system, the reference point setting and etc., the SERCOS-Master's drivers can be used for operating its interface card. And SERCOS-Master interface card supplies the difference interpolation functions which are available for movement control.

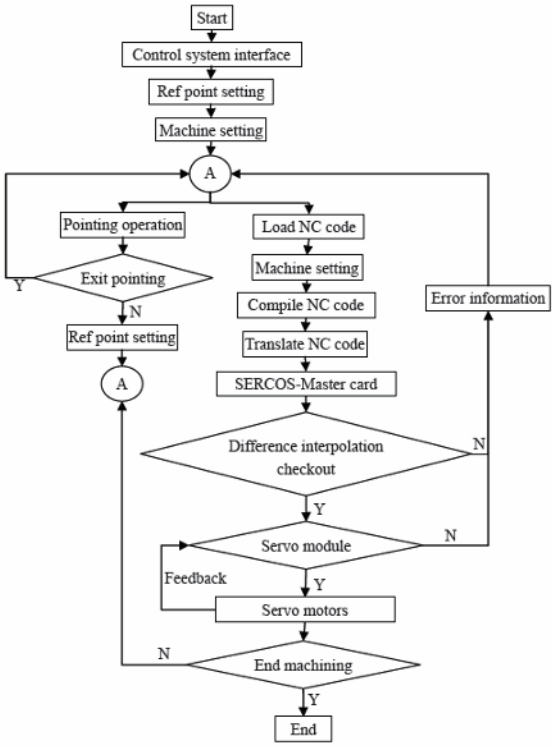

Fig. 7. The flow chat of the whole software

5 Measurement

Positioning accuracy of the machine tool six axes are measured by ML10 laser interferometer made by the Renishaw company. The measurement results are analyzed by the corresponding analysis software. The following results are obtained.

Overall Accuracy, $A = \mathrm{Max}(x_i - x_j)$.

Positive Repeatability Accuracy, pos rep=max pos-min pos.

Reverse Repeatability Accuracy, rev rep=max rev-min rev.

Bidirectional Repeatability Accuracy, $B_j = x_i \uparrow - x_j \downarrow$.

The analysis results are shown in table 1. The max overall accuracy is 301.8μm, the max positive repeatability is 277.4μm, the max reverse repeatability is 150.7μm, the bidirectional repeatability is 367.6μm. From the results it is found that the control system can satisfy the machine tool's accuracy request.

Table 1. Positioning accuracy of six axes

motion axes	Overall Accuracy(μm)	Positive Repeatability (μm)	Reverse Repeatability (μm)	Bidirectional Repeatability (μm)
X axis	156.2	64.7	0.7	141.9
Y axis	251.5	20.9	20.9	34.8
Z axis	39.1	47.8	9.5	367.6
U axis	301.8	245.5	150.7	264.7
V axis	264	277.4	37.4	345.3
W axis	39.1	47.8	9.5	307.6

6 Conclusions

1. Based on the CH-2010, the control system of the lathing and welding compound NC machine tool is designed, which has many fine characteristics, such as good expansibility, general-purpose functions and friendly user interface.
2. Multiple machine axes are moved simultaneously, and the control system can realize the auto control of the lathing and welding processing. It can satisfy the lathing and welding combined machining require.
3. The control system can realize Off-line Programming and test show that the system run credibility and can fulfill the control accuracy requirement.

References

1. Asato O L, Kato E R R, Inamasu R Y, Porto A J V. Analysis of open CNC architecture for machine tools[J]. Revista Brasileira de Ciencias Mecanicas/Journal of the Brazilian Society of Mechanical Sciences, 2002, 24(3):208~212
2. MEHRABI M G, ULSOY A G, KOREN Y. Tredns and perspectives in flexible and reconfigurable manufacturing systems [J]. Journal of Intelligent Manufacturing, 2002,4:1-13.
3. Hu Xuxian, Yang Keji, Pan Shuangxia. Research on Robustness Strategy of the Intelligent Control System for NC Machine Tool. Chinese Journal of Mechanical Engineering, 2002,1,17

4. Yang Shuguo, Wang Xiankui, Zhao Tong. Study on Machine Structure and Control System of R Transformer Core Precise Rolling Shaping Process China Mechanical Engineering, 2003,10:1745~1747
5. Mi Liang, et.al. Fuzzy control of spindle torque for industrial CNC machining. International Journal of Machine Tools&Manufacture,2003,43:1497~1508
6. Fu Weiri, et.al. Fuzzy surface roughness modeling of CNC down milling of Alumic. Journal of Materials Processing Technology, 2003, 133: 266～2751

Study of STL Data Processing on TIG Welding Rapid Manufacture

Wan Ling-na, ZhanG Hua, and Hu Rong-hua

Key Lab of Robot & Welding Automation of Jiangxi, Nanchang University, Nanchang, 330029 P.R. China

Abstract. According to the characteristic of TIG welding, rapid prototyping technology is applied to the functional smart metallic manufacture rapidly. Based on the methods of data processing for STL model, aimed at one multi –parameter, coupling strongly complicated welding process, one procedure "Shaping-Repair-Slicing-Compensation-Planning-Machining" is proposed also it is verified in experiments of one lay multi -path welding and one path multi-lay welding .H08 Copper welding thread is used ,and welding current is between 100A~140A.

1 Introduction

Smart Metal is a sensible metallic part prototyped by advanced welding technology and rapid prototyping manufacture technology. Because of its high productivity and low price, also the size, frequency of droplet and heat transfer process are under control during the welding, these make it true that welding process has become one of the best RPM technique [1-3].

As below, smart metal manufacture system consists of rapid prototyping executive subsystem including milling machine with NC system, welding seam quality control subsystem including TIG Machine (MW TT2200 made in Austria) and fibre-optical embedded subsystem. Almost three subsystems are integrated into one industrial PC by software and hardware such as image grabber, fibre-optical sensor with protective coating.

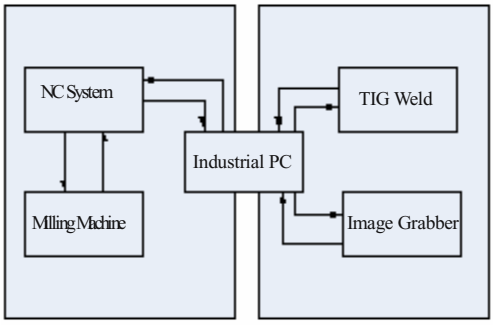

Fig. 1.1. Smart Metal Rapid Manufacture System

2 Data Processing on STL Model

During the welding rapid prototyping manufacturing process, physical object is accomplished by adding welded seam layer by layer rather than traditional machining

T.-J. Tarn et al. (Eds.): Robot. Weld., Intellige. & Automation, LNCIS 362, pp. 383–389, 2007.
springerlink.com

techniques such as milling, cutting. Each layer, a 2D cross-section sliced by Z Axis from 3D mesh model between the top and bottom is one welded seam. At present, model from the CAD system then reconstruct in RPM system have defects such as redundancy points and errors as gap, overlap facets and separated points in data structure leading to the open loops in the cross-section influence planning, even welding prototyping.

Data processing of welding rapid prototyping is the key step of the rapid prototyping manufacturing of functional smart metal. Directly it influences the prototyping precision, shell quality, time and cost spent even the entire result.

2.1 STL Model

Generally there are two types of models used in data processing of rapid prototyping: STL model and CAD model. The latter abandons the interface: STL file, but because of the difference between the CAD system's description for the object model, especially the inner, the standard and general methods on data processing can not be found out. The first makes use of the interface STL format .It is exported from CAD system and imported to the RP system. And because of its simple structure and read-in easily, actually it has got the confirmation and become the factual criteria between the CAD system and RP system. For above all, STL model is confirmed to be research object used during preprocess.

2.2 Data Processing

The method of data processing and accuracy of prototyped object directly influence on the shell quality of the object, so the data processing technology is always the core of software technology, thus much more work has to be done little by little. It consists of the shaping in CAD system and the transforming from CAD system, preprocess on STL model, slicing & getting the section data and the plan to NC path. In this paper, only the preprocess on STL model and slicing & getting the section data are in details been analyzed and researched.

3 Analysis, Slicing and Size Compensation

3.1 Preprocess Technique

Preprocess technique in Deposit Surfacing Welding Rapid Prototyping is the base and premise of slicing, getting contour and section filled and plan to welding torch. It consists of the transform from electronic model in CAD system to STL model. Also during the transform, some deficiency such as missing geometrical data described the key feature of object; gap, aberrance, and missing facet are brought. This leads to one thing that detecting and repair on defects and errors of STL files are also included on preprocess data.

3.1.1 Requirement to STL from CAD/CAM

When STL files are exported from the CAD/CAM system, the accuracy parameter and control parameter selected during the transformation must comprehensively be

considered according to the complexity of CAD model and the accuracy required to RP system compromisingly. And accuracy control parameter of STL file exported from different CAD/CAM system is not consistent. But it is the quantity of triangles that reflect how accurate the STL file approaching the CAD model.

Set one part as example, they are STL files output from the SOLIDWORKS 2004 system. , STL files' accuracy, quantity of triangles, size are compared and consulted as follows:

Table 1. Comparison between STL files in Different Precision

Type of File	Size of File	Quality	Number of Triangle
Binary	130984	poor	2618
Binary	154684	good	3092
Binary	382384	excellent	7646
ASCII	740918	poor	2618
ASCII	1174474	good	3092
ASCII	2163842	excellent	764

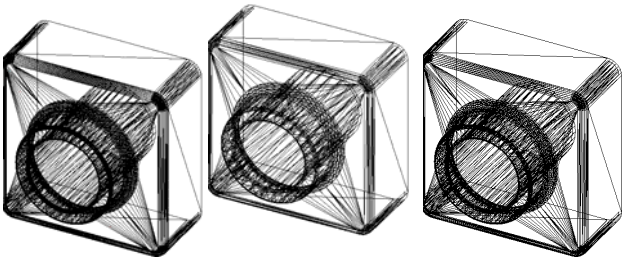

Fig. 3.1. Contrast in accuracy and size of model meshed

By analyzing Figure a, Figure b, Figure c respectively referred to the rough, good and excellent meshing: some conclusions got as follows:

(1) There are obviously differences among the above figures especially the intersection where curvature is enough big, (e.g. part A as stated). And just on intersection plane the geometric data of STL model easily be lost partly and not complete. At high possibility, it leads to the gap, overlapping, overhanging. From the above, we can see that the selecting proper accuracy greatly influenced the repair of STL model.

(2) The criterions selected in meshing are minimal triangle degree and minimal length can reach.But it is impossible to get the unequal meshing accuracy according to the curvature(called self-adjusted meshing). And we can compensate this point when slicing the model. Different slicing thickness can be applied when different curvature comes into being. The methods are called briefly multi-slicing methods.

(3) Accuracy parameter decided by the welding process parameter: welding pool, welding current, and welding velocity. We can apply further research later.

3.1.2 Detecting Errors of STL Model [4]

Four criterions that one corrective STL model must reach are: Right-hand Principle in Geometry: Vertex Principle; Edge Principle; Value Principle; If one or several ones are destroyed, inevitably there are errors exiting in STL model. Altogether there are several types' errors and defects.

3.1.3 Fix of STL Model

1. Data Transformation and Topology

After meshing in CAD system, the solid is exported from the CAD system. When read into RP system, STL file showed in not smooth curve especial in the place where its curvature is enough big. The main reason is the shortage of the triangles' organization, i.e., topology. Dynamic array template is applied thus three data structure is built up.

Vertex object: CArray <Vertex, Vertex>m_ vertex;
Facet Object: CArray <Edge, Edge>m_ edge list;
Edge Object: CArray <Triangle, Triangle>m_ triangle;

These data structures can make good use of the storage of disk and time consumed efficiently. But it is not as convenient and flexible as the non-liner data structure in realization.

2. Detect and Fix

From the value of 'flag', one data item of Edge Object, we can obtain the information of edge object structure, also with the edge object, data of the vertexes and faces share that edge will be got via the else index item of edge object which point out the vertex object and facet object. In this way, the whole detect and diagnosis has been done. The details are as follows:

(a). The error of normal: detect the edge object and its relative facet object .If the direction of normal of one triangle don't agree with the one of result of any two edges' operation --- $\vec{a} \times \vec{b}$, it is judged as the error normal.

(b). The error of gap: defect the vertex object, define some minimal constant as the reference δ , if the distance between two vertexes is less than δ , the distance is referred as the gap.

The errors such as hole, overlapping and overhanging have something with the quantity of the triangles shared some edge. So detect it by analyzing the edge object and its flag item and correct it by regulating the edge structure and its corresponding vertex object and facet object.

3.2 Slicing of STL Model

3.2.1 Select of Thickness of Slicing

Welding itself is one course from solid, liquid to solid of metal again. The difference between the lays of metal prototyped is the joining by metallurgy. During the deposit fusion welding, the heat input (value of current), the temperature of underlay or matrix will change the depth of welding pool, thus lead to change the difference between the layers known as the slicing thickness.

And the slicing thickness is much more than the ones using else rapid prototyping technology (in FDM, the thickness is 0.1mm or so). If the same slicing algorithm as before is applied here, the accuracy cannot reach the requirements, especially for the solid figured as below. its curvature radius is small or there is facets piled as step. So decide proper slicing parameters based on the process requirements for fusion welding rapid prototyping, referred to the welding parameters: welding current, welding voltage, velocity of welding rob.

For multi lay one path welding with H08 Copper thread, the welding parameters is fixable as below: below 3rd lay, current is 120A,above 5th lay, 140A is used. And between them,120A. According to above, initial thickness of slicing can be predicted.

3.2.2 Optimization of Slicing Direction

Optimization for the direction of slicing is regarded as one model with multi objects according to the structure, feature and function of the prototype. Hereinto, the optimization object functions are selected as follows: 1) the bar center of solid must be as low and steady as possible; 2) the time on prototype must be short; 3) the costing on prototype must be low. Approximately from the location of bar center, the proper slicing direction is located as Z-axis.

3.2.3 Slice Algorithm [5,6]

Generally based on the STL model there are several types of slice algorithms. It can be divided into real-time slicing and non-real-time slicing according to control style; and also it can be divided into adaptive slicing and slicing at some thickness according to thickness; it can be divided into slicing with errors and slicing without errors judged by if it can be corrected before.

3.3 Size Compensation for Metallic Material Shrinks

The characteristic of material directly influences the prototyping process and the accuracy of the solid. With FDM technique, the more important practical method is to compensate it in software of pre-processing concerning the shrinkage rate of material used. In the data processing, in the direction of X-axis, Y-axis, Z-axis, 3 genes of compensation for shrinkage are applied separately. The values of genes are decided by the material and feature of the solid to be prototyped.

The difference of FDM and fusion welding rapid prototyping exits as the material mostly. In the size, frequency and style of transfer of droplet are controllable and to be researched further. Its base is the plentiful data from the experiments under different conditions of welding including welding current, welding voltage and velocity of welding rod.

3.4 Plan of Path of Welding Torch and Form of the Solid's File

Smart metallic solid is lay by lay prototyped by deposit surfacing welding quickly; It makes up of welding seams wholly. After the pre-processing and slicing, the closed profile file—CLI format is obtained. Special scanning curve /line, the NC code (G code) controlling the welding torch's to fill the section of solid are confirmed with welding rod. The same as the other lays' profile. That is all the preparation and

manufacturing of smart metal. During the manufacture, some machining process must be applied using the NC machining tool. The key operations are 1) the judgment on the inner and outside of profile 2) dividing the infinite humdrum region; 3) scanning and filling it.

4 Conclusions

TIG Welding Rapid Prototyping is applied to manufacture the functional smart metal with good mechanical capability using the combination of welding process, prototyping and machining The development of Special type data processing software is applied for it.

(1) Under the conditions of welding, according to the fusion capability of droplet, for high efficiency and good machining precision the accuracy control of meshing in CAD system. The parameter controlled the precision are minimal angle degree and length. that can be shown during the research. Especially, in the region with high curvature the lost data information is much more than those with low curvature. Also the high precision is at the cost of huge STL file stored .In order to compromise this, the parameters are decided as follows: angle degree's tolerance can be reach as 10.000 deg; length's tolerance can be 0.08590 mm.

(2) Optimization for direction of slice is the one with multi- parameter, ie: time &cost for prototyping and the location of bar center. Further, the latter is decided according to the material and the shape of the solid.

(3) Based on welding experiment on the fusion capability of metallic material after welding, size compensation for metallic material shrink is solved by the software. In the data processing, in the direction of X-axis, Y-axis, Z-axis, 3 genes of compensation for shrinkage are applied separately. And the genes are decided by the fusion capability of metal. Figure 4.1: (a)linear welding .two ends of 11 linear paths are not the same each other although welding time, welding current, welding velocity are the same because of their heat input is influenced each other.(b) curvilinear welding. 2 ends of 6 curvilinear paths are overlapping.

(a) linear welding

(b) curvilinear welding

Fig. 4.1. One lay multi –path welding

References

1. Hancock P.Engineering a material advantage .The proceedings of the Institution of Mechanical Engineers.Part B.Journal of Engineering Manufacture, 1996,210(4):293~299
2. Ribeiro A F M, Norrish J.Metal based rapid prototyping for more complex shapes. Computer Technology in Welding, 1996(2): 18~24
3. Yan Yongnian, Wuliangcai, et al. Research on development and trends of rapid forming technology Manufacture Engineer Magazine 1998(11): 32~34
4. Zhao Ji-bin Liu Wei-jun Wang Yue-chao Research on Algorithm for Diagnosis and Modification of STL File Errors Computer Application 2003(2): 32~36
5. LI Wen-long WEI Li HE Shao-jun DING Guang-feng The Algorithm of Slicinga STL Data Model in Rapid Prototype Manufacturing Journal of Dalian Nationalities University 2005(3):751~754
6. Ma Yongzhuang Study of Slicing Algorithm Based on Recurvsion and Searching Direct Graph with Weight China Mechanical Engineering 2003(13):1220~1224

Girth Seam Tracking System Based on Vision for Pipe Welding Robot

Yuan Li, De Xu, Zhiguo Yan, and Min Tan

[1] Key Laboratory of Complex System and Intelligence Sciences, Institute of Automation, Chinese Academy of Sciences
[2] Graduate University of Chinese Academy of Sciences, Beijing, 100080 P.R. China
{xude, liyuan, tan}@compsys.ia.ac.cn,
zhgyan04@mails.gucas.ac.cn

Abstract. A girth seam tracking system based on structured light vision for pipe welding robot is presented. Firstly, the vision sensor is designed based on the analysis of laser reflection on weldment surface and the position relation of camera, laser plane and weldment for the effect of laser stripes imaging. Image processing and features extraction algorithms are developed in case of strong multiple reflections disturbance in welding seam image. An image-based vision control system of welding robot is adopted for girth seam tracking of pipe weldment. Girth seam tracking experiment by pipe welding robot was conducted to verify the performance of the system.

1 Introduction

The welding seam tracking is one of the key issues in robotic welding, and it is the foundation of automatic welding with high quality. The welding robots used in industry mostly work in teaching and playback mode, and the robots repeat the teaching path to fulfil the requirement in torches position for welding. There are some problems in this work mode of welding robots, such as the inaccuracies in weldment positioning, the warp and distortion of weldment caused by thermal expansion. These problems result in the deviation of the teaching path of welding torches from the real welding seams, so it is necessary to control the torch to track seams in the process of welding [1]. Further more, in pipe welding robot, the girth seams cannot be predefined, because the girth seams probably deviate from initial position while the pipes turning. The track of seams could change with the movement of tubes in axial direction. In this case, the teaching and playback mode is improper for girth seams welding of pipes, and welding robots need to rectify the deviation between welding torches and the girth seams in real time.

In order to avoid the deviation of seams by movement of tubes, Prestion-Eastin Inc. presented a kind of mechanism to hold back the movement of tubes in axial direction[2]. Ref [3] discussed the principle of movement of tubes in axial direction while turning. The solution was that multi-robots with three freedoms of degrees lifted the tubes and adjusted the position and pose of welding tubes. The two methods just concern the movement of tubes. In fact, the seam would deviate itself while turning. Then a seam tracking system is needed for high quality welding.

T.-J. Tarn et al. (Eds.): Robot. Weld., Intellige. & Automation, LNCIS 362, pp. 391–399, 2007.
springerlink.com

Several kinds of seam tracking systems were developed with different sensors. The vision sensors based on laser structured light are widely used because of its reliability and abundant information of welding seams, and the vision sensors for seam tracking system is widely regarded as a promising sensing method for welding automation [4]. Structured light images of vision sensors are greatly affected by heavy disturbances such as intensive multiple reflections on polished surfaces, arc light and splash in the process of welding. These disturbances result in difficulty and inaccuracy of the welding images processing and features extraction. Some algorithms of images processing and recognition based on fuzzy logic and neural network have been developed to eliminate these disturbances and recognize welding seam[5~7], but there are still problems and challenges for reliability and accuracy of vision information extraction.

In this paper, vision sensor of measure system is analyzed in section 2; image processing and features extraction are discussed in section 3. And in section 4, pipe welding robot control system is introduced, followed by the experimental results in section 5. Finally, section 6 concludes the paper.

2 Vision Measure System for Seam Tracking

Structured light vision is an advanced solution for welding seam tracking, but there are some important factors such as multiple reflections on surfaces and the position relationship that have great effect on imaging of vision sensor. The two factors should be analyzed.

2.1 Laser Reflection Analysis

In order to improve welding quality of the joints, the weldment usually was polished by grinding wheel to eliminate the rust and the impurity on the surfaces of the joints. When laser structured light was projected on the polished surfaces of weldment, there was scattering steel-surface because of strong laser multiple reflection. It often incurred great confusion reflections in welding seams images, which deteriorated quality of images of the vision sensor, deformed the laser stripe, and increased the difficulty of features extraction.

When light was projected on the surfaces of objects, there are diffuse reflections and specular reflections in reflection light, shown as Fig. 1.

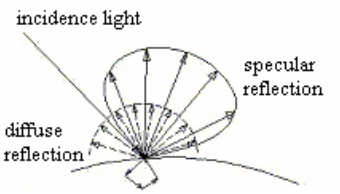

Fig. 1. Diffuse reflection and specular reflection on the surfaces of object

According to Ref [8], the intension of reflected light could be consisted as (1):

$$I = I_d + I_{s1} + I_{s2}$$
$$= I_i r_d \frac{\pi}{4} d^2 \cos\theta / \left(f^2 r^2\right) + I_i k_{s2} \delta(\theta_c - \theta_i)(\varphi_c - \varphi_i) + I_i k_{s1} e^{-\frac{\alpha^2}{2\delta^2}} \quad (1)$$

I is the general intension of reflection;

I_i is the intension of incidence light;

I_d is the intension of diffuse reflection;

I_{s1} is the intension of ideal specular reflected light on smooth surface, and the direction of the reflected light obey the law of reflection;

I_{s2} is the intension of specular reflected light on practical surface. In fact, the reflection surface is composed of many micro mirrors, so the reflection direction and the intension obey the Gaussian distribution.

r_d, k_{s1} and k_{s2} are coefficients of reflectivity; θ is coefficient of surfaces; r is the distance; d is diameter of the aperture; f is focus; θ_c is the observation angle of the camera; φ_c is the angle of incidence light.

Among all the reflection above, the diffuse reflection could clearly image laser stripes as the proper signal for vision sensor; the specular reflection normally image over saturated and induce glistening area of the stripes in images. So the vision sensor should be positioned to avoid taking specular reflections and to image the laser stripes clearly.

In formula (1), the diffuse reflection could be received in wide range angle; the specular reflections only were received in a narrow range, and the direction obeys the law of reflection. So the camera should avoid the direction of specular reflections to image clearly.

2.2 Triangle Measure Principle

Vision sensor based on structured light triangle measure principle is shown as Fig.2. *L* is the laser plane, and *L'* is the specular reflection plane; the direction of optical axis of camera is C. Angle α is contained by optical axis of camera and the surface of weldment; and angle θ is contained by optical axis of camera and laser plane.

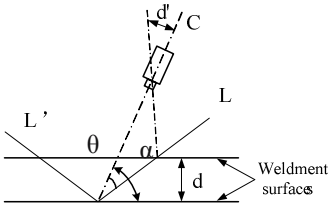

Fig. 2. The triangle measure principle

Then the depth and width of groove *d'* in the image coordinates could be calculated as follows:

$$d' = \frac{k_d d \sin\theta}{\sin(\alpha - \theta)} \tag{2}$$

In formula (2), d is the depth of groove of weldment is width of groove; k_d is proportion coefficient of the image coordinates. Since the bigger d' is, the more apparent the groove features of stripes are, the angle α and θ should be chosen to make apparent stripes image.

According to discussion and analysis above, there are some conclusions in vision sensor design:

1. The optical axis of camera (C) should avoid the direction of specular reflection to decrease the intensive flare disturbances to laser stripes images.

2. The angle α, θ should be chosen to get proper shape information of joints in camera coordinates according to formula (2). In practice α is $\pi/2$, θ is $\pi/6$, and $d'=0.58kd$, then the stripes is imaged properly and clearly.

The structure of vision sensor is shown as Fig. 3. The three stripes are adopted to increase the reliability and information of the sensor.

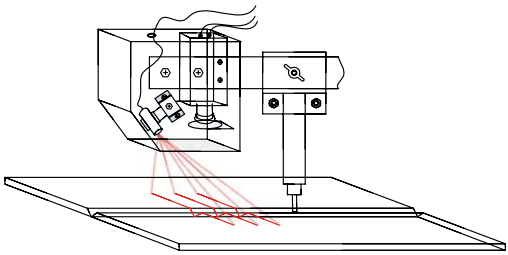

Fig. 3. Structure of vision sensor

3 Image Processing and Features Extraction

Some algorithms of image processing have been developed for segmentation and edge detection of laser stripes [9, 10]. But in welding condition, it is difficult to extract information reliably with heavy disturbances. In this paper, the algorithm for image processing and features extraction is developed in case of strong reflection disturbances of weldment surfaces, especially with the interaction of three laser stripes. The process consists of the target regions searching for three laser stripes respectively, the selection of adaptive threshold, the extraction of profiles based on intensity of columns pixels distribution, and the selection and extraction of features.

3.1 Image Processing

The size of images captured by the camera is 640×480 pixels with 8-bit intensity resolution. In order to accelerate image processing and reduce disturbances of images, the region of interest (ROI) should be detected. Considering the laser stripes are horizontal in image space, the ROI could be fixed according to intensity distribution. Normally the three peaks on intensity projection correspond to the horizontal position of

stripes in image space, and the three regions of stripes are deduced by the position of stripes and the presumed margin.

The typical structured light images are contrast clearly with the dark background, it is proper that the stripes are segmented from the image by intensity threshold. The pixels of background with low intensities converge the low intensity area of histogram; the pixels on the stripes converge the area with very high intensity.

The number of pixels belonged to every intensity level is counted from high level of intensity to low. When the accumulation of the pixels reaches specified threshold, the intensity level is regarded as the image segmentation threshold.

The profiles of welding grooves are extracted by the intensity of distribution based on columns. The intensity distribution of pixels on each column is calculated in three regions respectively, the points with maximum value are extracted as the points on the profiles [11]. At same time, the temporal and spatial continuity criterion is presented to judge the validity of the extracted points. Then the median filter and smoothing filter are adopted to reduce the pulse disturbance and measure noise.

3.2 Extraction of Features

The central points of welding groove are selected as image features to be extracted because of their robustness and stability.

Firstly, main lines of the stripes are detected by Hough Transform. Obviously the main line and the stripe profile could compose a figure at welding joint area. The border points are detected according to the distance between main line and stripe profile. Searching the profile from the joint area, when the distance reaches the low threshold, the border points and the figure are fixed. Then the three feature points are extracted by central points of figures. The general feature point of seam image is calculated by three points to increase robustness of vision sensor.

Fig. 4 is original image and features extraction result (the cross points); the groove central points are extracted respectively.

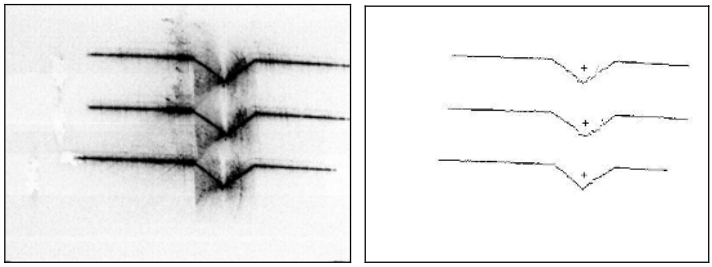

Fig. 4. Structured light image of welding seam and features extraction result

4 Seam Tracking Control SYSTEM

The welding robot consists of the pedestal, vertical stake and horizontal arm; the robot is driven by step motors. The torch and the vision sensor are mounted on the end-effector of the robot; the pipe is set on the roller. There are two freedom of degrees

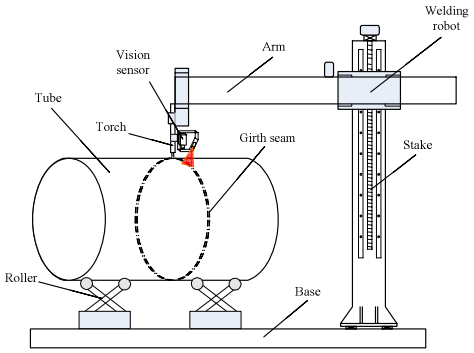

Fig. 5. Structure of pipe welding robot

corresponding to horizontal and vertical relative movement between the torch and the girth seam. The structure of pipe welding robot is designed as Fig. 5.

The initial coordinates of the seam in image space are recorded as the reference position before welding. Because the vision sensor is mounted above the welding seam, and the v direction of image of coordinates accords with the seam direction, the control system is decoupled in two directions. Then the pixels deviation of u in image coordinates corresponds to position horizontal deviation in Cartesian space, and the deviation of u corresponds to the vertical. An image-based seam tracking control system is developed according to this relationship.

The Jacobian matrix transforming joint space to image space of robot is as (3):

$$\begin{pmatrix} du \\ dv \end{pmatrix} = J \begin{pmatrix} dx \\ dz \end{pmatrix} = \begin{pmatrix} J_{11} & J_{12} \\ J_{21} & J_{22} \end{pmatrix} \begin{pmatrix} dx \\ dz \end{pmatrix} \tag{3}$$

According to formula (2), J_{11} and J_{22} are constant defined by vision sensor. Because when vision sensor moves in horizontal direction, the height of stripes in image space hardly change, J_{21} is equal to zero. When the sensor and the torch move in vertical direction, the horizontal position and height of stripes change because of the variety of distance between the camera and the weldment. Since the size of joint h is much less than z, dx is nearby zero in Fig. 6. Then the change of horizontal position caused by distance change could be omitted according to formula (4), so J_{12} could be regarded as zero.

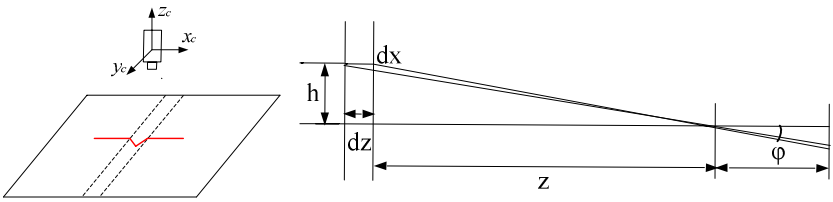

Fig. 6. The relationship between dz and dx

$$dx = dz\tan(\varphi) = dz\frac{h}{z} \approx 0 \tag{4}$$

Then Jacobian matrix could be simplified to a diagonal matrix, and the control system based on image is convergent in its work space.

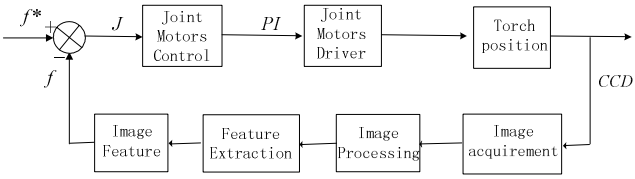

Fig. 7. Visual servo based on image for pipe welding control

The visual control structure is shown in Fig. 7. In process of welding, the output pulses of motors are calculated according to the deviation of pixels coordinates between current feature points and the reference points.

5 Experimental Results

Experiment of welding was conducted on pipe welding robot to validate the seam tracking system. The welding type is submerged arc welding; joint type is Vee; welding speed is 0.5m/min. The weldment is an oil tank of 3.5m diameter and with 10 mm thickness board. In seam tracking system, the measure period is set 40ms, and the control period is set 200ms.

Fig. 8 shows the image coordinates of u and v in the process of welding Experiment. The image coordinates varied less than 3 pixels (u) and 6 pixels (v); it verified the precision of tracking system. The error of v direction is bigger because the load in vertical motor is heavier with the torch and other attachment, and the speed of control motor is set lower.

Fig. 9 shows the output pulses of motors in horizontal and vertical direction in the process of welding. In horizontal direction, output of motor is negative oriented and is approximately linear, because the movement of the pipe in axial direction is stable while turning. In vertical direction, output of motor adapts the height variety of the pipe.

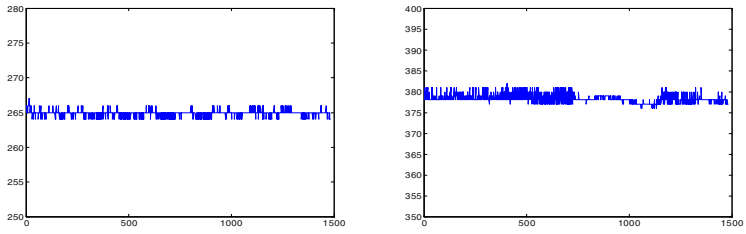

Fig. 8. Image coordinates of u and v in the process of welding

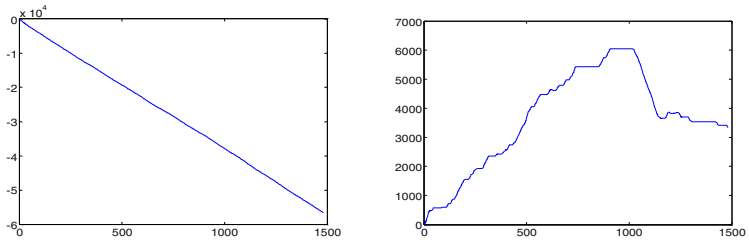

Fig. 9. Output of the motors in horizontal and vertical directions

By the experimental results, the robot could track welding seam stably and precisely. The vision measure system work well because of its robust features extraction and information fusion, and the control system run properly which validated the control structure based on image.

6 Conclusions

A girth seam tracking system based on structured light vision for pipe welding robot is presented in this paper. The reflection on smooth surfaces and structured light measure principle are analyzed, and a vision sensor is designed. Image processing and features extraction algorithm is developed for welding seam images with heavy disturbances. In control system, an image-based seam tracking vision control structure is adopted.

The experimental results validated that the seam tracking system is stable, reliable and precise, and it can meet the need of quality requirements of welding.

The future of this paper concerns the issue of seam tracking with complex shape, which challenges control system for unknown trend of seams. In this condition, vision sensor with three laser planes would provide direction information of seams for adjusting the position and pose of welding robot.

Acknowledgement

The authors would like to thank the National High Technology Research and Development Program of China for the support to this work under the grant 2002AA422160, and National Key Fundamental Research and Development Project of China (973, No.2002CB312200) for the support.

References

1. L. Wu, S. Chen. Intelligence Welding Technology. National Defense Industry Press, Beijing, 2000.
2. Prestion-Eastin Inc. Alignment considerations and safety issues in the use of turning rolls. http://www.prestoneastin.com/aligntr.htm.

3. Y. Wang, M. Tan, F. Jing. The Analysis of Kinematics and Application for Multi-robots handling Huge Objects harmoniously. Robot, Vol. 24, No.5, 2002.
4. Xu D, Jiang Z M, Wang L K et al. Features Extraction for Structured Light Image of Welding Seam with Arc and Splash Disturbance. The eighth International Conference on Control, Automation, Robotics, and Vision (ICRACV 2004) [C], Kunming, China, December, 1559-1563, 2004.
5. X. Gao, M. Yanamoto, A. Mohri. Application of Fuzzy Logic Controller in the Seam Tracking of Arc-Welding Robot. The 23th Annual International Conference of IEEE Industry Electronics Society, New Orleann Lovisina, 1367-1372.
6. Kara R, Wira, Kihl H. Hierarchical Neural Controller and Adaptive Kalman Filter for Visual Robot Tracking Tasks. Proceedings of the International Congress on Intelligent Systems and Applications, 1513-237. Australia: 2000.
7. Haug, K., Pristrchow, G. Reducing distortions caused by the welding arc in a laser stripe sensor system for automated seam tracking. Proceedings of the IEEE International Symposium on Industrial Electronics, Bled (Slovenia), pp. 12-16, 1999.
8. S. K. Nayar, K. Ikeuchi, T. Kanade, Surface Reflection Physical and Geometrical Perspectives, IEEE Trans. on Pattern Analysis and Machine Intelligence, Vol. 13, No.7, 611-634, 1991.
9. N. Otsu, A Threshold Selection Method from Gray-Level Histograms, IEEE Trans. on Systems, Man, and Cybernetics, Vol. 9, No.1, 62-66, 1979.
10. Canny J. A computational approach to edge detection. IEEE Trans. on Pattern Analysis and Machine Intelligence, Vol. 8, No.6, 679-698, l986.
11. Y. Li, D. Xu, M. Tan: Robust Features Extraction for Structured Light Image of Welding Seam in Multi-pass Submerged Arc Welding. International Conference on Electronic Measure and Instrument, Beijing, China, Vol. 6, 613-619, 2005.

Study of Off-Line Programming System of Arc Robot Based on the Software of ROBOGUIDE

Li Liangyu, Li Xiang, Zhou Xin, and Yue Jianfeng

School of Mech.&Eletro. Engineering, Tianjin Polytechnic University, Tianjin, 300160, P.R. China
liliangyu@tjpu.edu.cn

Abstract. Based on research and application of ROBOGUIDE which is an off-line programming system of arc robot, the mathematic model of complex welding seam is built up based on the re-exploit of Auto-CAD. It is deduced that the projection vector of characteristics coordinate of welding seam relative to reference coordinates. According to the method of RPY, the changed angle and displacement of characteristics coordinate of welding seam relative to reference coordinates is calculated in order to provide exact data information for ROBOGUIDE.In ROBOGUIDE these data will be used to build up coordinates frame of welding points for simulation. This study is very important to off-line programming of arc robot in spaced welding.

1 Introduction

The precondition of the study of arc robot off-line programming system is geometric model, how to build up a exact seam curve is the key of the actual robot welding[4]. We are using the software of arc robot off-line programming system ROBOGUIDE, but it is limited to pick up exact welding seam curve. So the contents of our study is how to get the position and attitude data of welding points and how to transmit these data into ROBOGUIDE. By the way of re-exploit of Auto-CAD, produce two cylinders which are orthogonal with each other, the intersectant line of two cylinders is regard as the saddle-backed welding seam curve, then build up the characteristic coordinates of the welding seam on each welding point[3]. In the modeling module of ROBOGUIDE, the geometry information is used to reshape the work's model, and the data information of characteristics coordinate frame of seam is used to generate the welding path of robot.1.1 model Building in the CAD and acquirement of characteristics information.

In the off-line programming system ROBOGUIDE of arc robot we can use the modeling module to build up the model of work, but it is very difficult to pick up the position of welding point on the saddle-backed welding seam curve. In order to generate the exact welding path (get the exact position of welding points), By the way of re-exploit of Auto-CAD, produce two cylinders which are orthogonal with each other through programming in the editor of VBA, get the geometric information of saddle-backed welding seam curve. separate the welding seam curve to a great deal of dispersed points, and there is a line connection between every two points in order to make it more exactly close to the actual welding seam curve. For acquiring position

T.-J. Tarn et al. (Eds.): Robot. Weld., Intellige. & Automation, LNCIS 362, pp. 401–408, 2007.
springerlink.com

and attitude of every welding point, the characteristic coordinates of the welding seam is built up. the work's drawing is saved as the IGES file, and welding point's data of position and attitude is saved as .dat* file.

1.2 The Building-Up of Characteristics Coordinate Frame of Welding Seam

The actual position of welding seam is very complex, at present the complex position is usually defined by inclination and corner angle of welding seam.

Inclination of welding seam: an angle between axis of welding seam and horizontal plane.

Corner angle of welding seam: an angle between the vertical plane which pass through the axis of welding seam and a plane which halves the notch of welding seam. [1]

But it is inconvenient to planning the welding torch parameter and welding attitude of arc robot, it also can't define welding position and attitude accurately. So characteristics coordinate frame of welding seam is built up:

This paper addresses the saddle-backed curve generated from two cylinders which are orthogonal with each other (the curve is welding seam), the spaced welding seam curve is divided into several line ones, a any point picked up on one line is named as point M, and define the direction of tangent of this point as axis X', counter-clockwise direction around the Z axis is positive direction; the plane which is vertical to axis X' and pass through the point M is normal plane Ar, the axis Z' is defined as the angle bisection between plane Ar and two cylinders, then the axis Y' is deduced from right hand principle. all the characters of the welding points on the saddle-backed welding seam is only defined. It is clearly that axis X' is the axis of welding seam, axis Z' is the center line of welding seam. Along with the change of spaced welding point, the characteristics coordinate frame will move and turn correspondingly. The characteristics coordinate frame of welding seam is built up, shown in Fig 1.

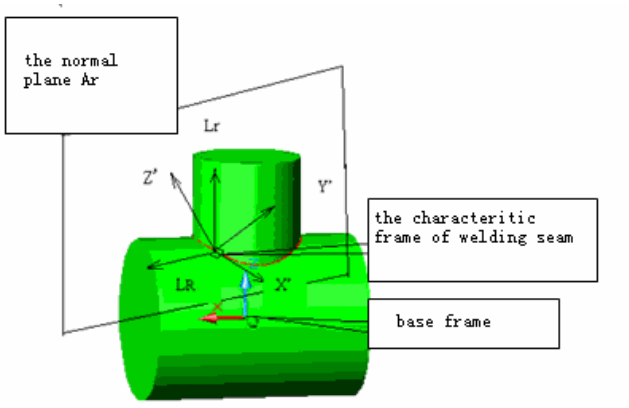

Fig. 1. The characteristics coordinate frame of welding seam

1.3 The Projection Vector of Characteristics Coordinate of Welding Seam Relative to Robot's Base Coordinate

Two cylinders which are orthogonal each other is built up as the model of work, shown in Fig 4:

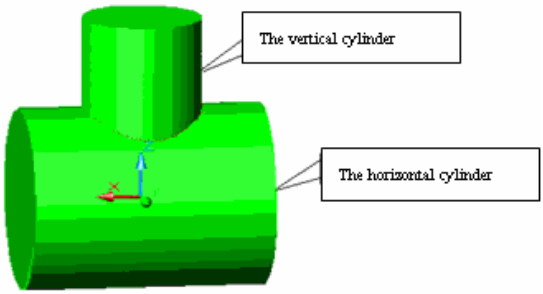

Fig. 2. The model of work

Equation of the vertical cylinder:

$$Y^2 + Z^2 = R_1^2 \quad (Z > 0) \tag{1}$$

Equation of the horizontal cylinder:

$$X^2 + Y^2 = R_2^2 \tag{2}$$

Equation of intersectant line of the two cylinders:

$$\begin{cases} Y^2 + Z^2 = R_1^2 \quad (Z > 0) \\ X^2 + Y^2 = R_2^2 \end{cases} \tag{3}$$

Equation of the tangent which pass through the point M (x_0, y_0, z_0) on the welding seam:

$$\frac{X - x_0}{\begin{vmatrix} 2y_0 & 2z_0 \\ 2y_0 & 0 \end{vmatrix}} = \frac{Y - y_0}{\begin{vmatrix} 2z_0 & 0 \\ 0 & 2x_0 \end{vmatrix}} = \frac{Z - z_0}{\begin{vmatrix} 0 & 2y_0 \\ 2x_0 & 2y_0 \end{vmatrix}} \tag{4}$$

The projection vector of axis X ' relative to base coordinate system:

$$n_x = -y_0 z_0, \quad n_y = x_0 z_0, \quad n_z = -x_0 y_0 \tag{5}$$

Equation of the normal plane Ar:

$$\begin{vmatrix} X-x_0 & Y-y_0 & Z-z_0 \\ 0 & 2y_0 & 2z_0 \\ 2x_0 & 2y_0 & 0 \end{vmatrix} = 0 \tag{6}$$

The equal expression:

$$y_0z_0(X-x_0) - x_0z_0(Y-y_0) + x_0y_0(Z-z_0) = 0 \tag{7}$$

So axis Z′is in the normal plane Ar, from the definition above, axis Z′is the angle bisection between the plane Ar and two cylinders. Lr is defined as the tangent of the intersection of Ar and the vertical cylinder, LR is defined as the tangent of the intersection of Ar and the horizontal cylinder .both Lr and LR are pass through the point M.

Equation of the intersection of Ar and the vertical cylinde

$$\begin{cases} X^2 + Y^2 = R_2^2 \\ y_0z_0(X-x_0) - x_0z_0(Y-y_0) + x_0y_0(Z-z_0) = 0 \end{cases} \tag{8}$$

Equation of Lr:

$$\frac{X-x_0}{\begin{vmatrix} 2y_0 & 0 \\ -x_0z_0 & x_0y_0 \end{vmatrix}} = \frac{Y-y_0}{\begin{vmatrix} 0 & 2x_0 \\ x_0y_0 & y_0z_0 \end{vmatrix}} = \frac{Z-z_0}{\begin{vmatrix} 2x_0 & 2y_0 \\ y_0z_0 & -x_0z_0 \end{vmatrix}} \tag{9}$$

The projection vector of Lr relative to the base coordinate system:

$$(x_0y_0^2, -x_0^2y_0, -x_0^2z_0 - y_0^2z_0)$$

Equation of the intersection of Ar and the horizontal cylinder

$$\begin{cases} Y^2 + Z^2 = R_1^2 \\ y_0z_0(X-x_0) - x_0z_0(Y-y_0) + x_0y_0(Z-z_0) = 0 \end{cases} \tag{10}$$

Equation of LR:

$$\frac{X-x_0}{\begin{vmatrix} 2y_0 & 2z_0 \\ -x_0z_0 & x_0y_0 \end{vmatrix}} = \frac{Y-y_0}{\begin{vmatrix} 2z_0 & 0 \\ x_0y_0 & y_0z_0 \end{vmatrix}} = \frac{Z-z_0}{\begin{vmatrix} 0 & 2y_0 \\ y_0z_0 & -x_0z_0 \end{vmatrix}} \tag{11}$$

The projection vector of LR relative to the base coordinate system:

$$(x_0y_0^2 + x_0z_0^2, y_0z_0^2, -y_0^2z_0)$$

Lr′and LR′are parallel to Lr and LR respectively and pass through the origin of the base coordinate system, so the vector direction of the Lr′and LR′are same to Lr and LR. Axis Z′is the angle bisection of Lr and LR in Ar, Z〞 is paralleling the Axis Z′and is the angle bisection of Lr′and LR′, so axis Z′and axis Z〞 have the same projection vector relative to the base coordinate. The angle between Z〞 and Lr′is defined as θ_2, the angle between Z〞 and LR′is defined as θ_2, the projection vector of Axis Z〞 in base coordinate system is （a_x, a_y, a_z）,because of $\cos\theta_1 = \cos\theta_2$

That is to say:

$$\frac{x_0 y_0^2 a_x - x_0^2 y_0 a_y - (x_0^2 z_0 + y_0^2 z_0) a_z}{\sqrt{x_0^2 y_0^4 + x_0^4 y_0^2 + (x_0^2 z_0 + y_0^2 z_0)^2}\sqrt{a_x^2 + a_y^2 + a_z^2}} = \frac{(x_0 y_0^2 + x_0 z_0^2) a_x + y_0 z_0^2 a_y - y_0^2 z_0 a_z}{\sqrt{(x_0 y_0^2 + x_0 z_0^2)^2 + y_0^2 z_0^4 + y_0^4 z_0^2}\sqrt{a_x^2 + a_y^2 + a_z^2}} \quad (12)$$

Definition is madeas bellow :

$$M = \sqrt{x_0^2 y_0^4 + x_0^4 y_0^2 + (x_0^2 z_0 + y_0^2 z_0)^2}$$

$$N = \sqrt{(x_0 y_0^2 + x_0 z_0^2)^2 + y_0^2 z_0^4 + y_0^4 z_0^2}$$

We can get equation：

$$\left[N x_0 y_0^2 - M(x_0 y_0^2 + x_0 z_0^2)\right] a_x - (N x_0^2 y_0 + M y_0 z_0^2) a_y - \left[N(x_0^2 z_0 + y_0^2 z_0) - M y_0^2 z_0\right] a_z = 0 \quad (13)$$

Because axis Z′plumbs to axis X′, we can get the relation as below:

$$a_x n_x + a_y n_y + a_z n_z = 0$$

The equal expression:

$$-a_x y_0 z_0 + a_y x_0 z_0 - a_z x_0 y_0 = 0 \quad (14)$$

Definition is made as bellow:

$A_1 = N x_0 y_0^2 - M(x_0 y_0^2 + x_0 z_0^2)$, $A_2 = -y_0 z_0$

$B_1 = -(N x_0^2 y_0 + M y_0 z_0^2)$, $B_2 = x_0 z_0$

$C_1 = -(N(x_0^2 z_0 + y_0^2 z_0) - M y_0^2 z_0)$, $C_2 = -x_0 y_0$

The projection vector of axis Z′relative to the base coordinate system is:

$$a_x = \begin{pmatrix} B_1 & C_1 \\ B_2 & C_2 \end{pmatrix}, \quad a_y = \begin{pmatrix} C_1 & A_1 \\ C_2 & A_2 \end{pmatrix}, \quad a_z = \begin{pmatrix} A_1 & B_1 \\ A_2 & B_2 \end{pmatrix} \quad (15)$$

Complying with the right hand rule, we can get the projection vector of axis Y′relative to the base coordinate system:

$$(o_x,\ o_y,\ o_z)=\begin{vmatrix} i & j & k \\ n_x & n_y & n_z \\ a_x & a_y & a_z \end{vmatrix}= \tag{16}$$

$$(n_y a_z - n_z a_y,\ n_z a_x - n_x a_z,\ n_x a_y - n_y a_x)$$

We can get the projection vector matrix of coordinate O′X′Y′Z′relative to coordinate OXYZ

$$R=\begin{pmatrix} n_x & o_x & a_x \\ n_y & o_y & a_x \\ n_z & o_z & a_z \end{pmatrix} \tag{17}$$

Unit the projection vector matrix as R′

$$R'=\begin{pmatrix} n_x' & o_x' & a_x' \\ n_y' & o_y' & a_y' \\ n_z' & o_z' & a_z' \end{pmatrix} \tag{18}$$

$$n_x'=\frac{n_x}{\sqrt{n_x^2+n_y^2+n_z^2}},\quad n_y'=\frac{n_y}{\sqrt{n_x^2+n_y^2+n_z^2}},\quad n_z'=\frac{n_z}{\sqrt{n_x^2+n_y^2+n_z^2}}$$

other parameter could be got in the same way.

Above all, the transform matrix of the characteristic coordinate of a any point M(x_0, y_0, z_0) on spaced curve relative to the base coordinate system is:

$$R'=\begin{pmatrix} n_x' & o_x' & a_x' & x_0 \\ n_y' & o_y' & a_y' & y_0 \\ n_z' & o_z' & a_z' & z_0 \\ 0 & 0 & 0 & 1 \end{pmatrix} \tag{19}$$

2 The Changed Angle Between the Characteristics Coordinate Frame and the Base Coordinate System

In the off-line programming software ROBOGUIDE, because each welding point has a coordinate and it's direction is equal to the base coordinate system. In order to describe the attitude of characteristics coordinate frame of welding seam, the method of RPY which describes characteristics coordinate frame rotating around fixed axis in order of priority is applied to get the angels of axis X′、 axis Y′and axis Z′relative to axis X、 axis Y and axis Z respectively. These three angles are defined as γ、 β and α[2].

The angles γ、 β and αare resulted from combining the definition of the RPY and transform matrix R′ .

Get the expression of each angel:

$$\begin{cases} \gamma = \mathrm{Atan2}\left(o_z', a_z'\right) \\ \beta = \mathrm{Atan2}\left(-n_z', \sqrt{n_x'^2 + n_y'^2}\right) \\ \alpha = \mathrm{Atan2}\left(n_y', n_x'\right) \end{cases} \tag{20}$$

Here Atan2 (y,x) is a anti- tangent function with double parameters. arctan(y/x)is counted, and at the same time through the sign of y and x, in which quadrant is the angel we have counted will be established. -90°≤β≤90°.

3 Model Building and Attitude Planning in ROBOGUIDE

The geometry information of the model is saved as IGES file , and the data information of welding point's position and attitude is saved as .dat* file. The software of IGES.Convert is used to transform the IGES file to F3D file which could be accepted by ROBOGUIDE to reshape the work model in the modeling module. The

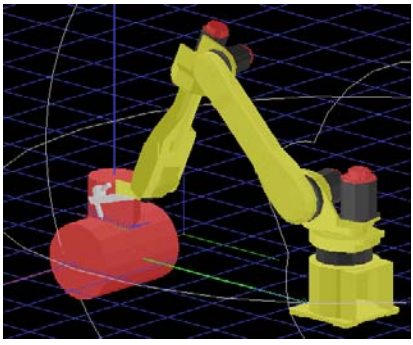

Fig. 3. Simulation of the arc robot's welding process

saddle-backed welding seam curve and the characteristics coordinate frame on each welding point is shown in Fig3, the color of axis Z′is blue, the color of axis Y′is green, the color of axis X′is red.

4 Conclusion

1. re-exploiting of Auto-CAD is used to build up model of work with saddle-backed welding seam, and the position and attitude of any welding point on the welding seam is calculated precisely by mathematics method.
2. The geometry information and welding point's position and attitude information are applied to the software of ROBOGUIDE , that provides the precondition of the simulation of arc robot's welding process .

Acknowledgements

This work is funded by Important project of Natural Science Foundation of Tianjin (No.05YFJZJC02100).

References

1. Ding Han, Huang Lon Lin, Xiong You Lun.Computer-aided off-line planning of robot motion[J].Robotics and Autonomous Systems,1991,7(4):67-72.
2. Lin Shangyang, Chen Shanben.Welding Robot and appliance. BeingJing：Mechanism Industry publishing company, 2000.
3. Wang Kehong. The model of typical work piece and attitude programming in ARC Robot study. Nan Jing：Nanjing University of Science & Technology, material science and engineering department,2003.
4. Tang Xinghua. 3D-visualized offline-programming and simulation system for industry robots. ShangHai JiaoTong University material science and engineering department,2005.

Distributed Simultaneous Task Allocation and Motion Coordination of Autonomous Vehicles Using a Parallel Computing Cluster

A.K. Kulatunga, B.T. Skinner, D.K. Liu, and H.T. Nguyen

Mechatronics and Intelligent Systems Group, Faculty of Engineering,
University of Technology, Sydney
{asela.kulatunga, brad.skinner, dkliu,
hung.nguyen}@eng.uts.edu.au

Abstract. Task allocation and motion coordination are the main factors that should be considered in the coordination of multiple autonomous vehicles in material handling systems. Presently, these factors are handled in different stages, leading to a reduction in optimality and efficiency of the overall coordination. However, if these issues are solved simultaneously we can gain near optimal results. But, the simultaneous approach contains additional algorithmic complexities which increase computation time in the simulation environment. This work aims to reduce the computation time by adopting a parallel and distributed computation strategy for Simultaneous Task Allocation and Motion Coordination (STAMC). In the simulation experiments, each cluster node executes the motion coordination algorithm for each autonomous vehicle. This arrangement enables parallel computation of the expensive STAMC algorithm. Parallel and distributed computation is performed directly within the interpretive MATLAB environment. Results show the parallel and distributed approach provides sub-linear speedup compared to a single centralised computing node.

1 Introduction

Task allocation (scheduling) and path planning (routing) are important activities which aid in the coordination of multiple autonomous vehicles in fully-automated and semi-automated material handling systems. Furthermore, these two factors are interrelated. A system which coordinates multiple autonomous vehicles effectively should address the task allocation and path planning issues. However, most of the research work focuses on these issues separately, due to the added complexity of simultaneous computation. For example scheduling and task allocation aspects have been discussed in [1-4], path planning and routing in [5, 6], deadlock detection and collision avoidance[7, 8].

However, few efforts combined these factors in their approaches [9-11]. Correa et.al., [12] have developed a hybrid approach to solve dispatching and conflict free routing of Automated Guided Vehicles (AGV) in Flexible Manufacturing Systems (FMS). Assignments and routing is considered simultaneously in their approach. However, a restriction of this work is the reduction in efficiency as the number of AGV's is increased beyond six AGV's. In addition, the online dispatching method developed by [13] uses multi-attribute dispatching rules. However, the routing is done

T.-J. Tarn et al. (Eds.): Robot. Weld., Intellige. & Automation, LNCIS 362, pp. 409–420, 2007.
springerlink.com

by considering the shortest path only and constant speeds are assumed for the AGVs. Another approach developed for dispatching and conflict-free routing of AGV's in FMS is discussed in [14]. This approach is limited to four, constant velocity AGV's. Furthermore, when a path is being utilised by one AGV, all nodes linking that path are locked and no other AGV can use the path until the assigned AGV has completed its task.

Typically path planning is followed by deadlock prevention or collision avoidance. As a consequence, optimal results acquired in the first operation (path planning) will not be the same after it is changed in order to overcome collision problems. Therefore, we can not guarantee optimal results for the both factors at the same time. Conversely, if all the factors affecting the coordination problem are considered simultaneously, then there will be a possibility of finding optimal or near optimal solutions, but it would require considerable computation time. In the STAMC approach [15] we perform path and motion planning at the task allocation stage, using the Simultaneous Path and Motion Planning algorithm (SiPaMoP) [16]. The SiPaMoP algorithm is able to search for the most efficient path by considering future deadlocks and collisions.

The STAMC algorithm is computationally intensive as it solves task allocation, path planning, deadlock and collision avoidance simultaneously. Currently, the expensive STAMC algorithm executes on a single serial computing node using MATLAB, for all autonomous vehicles in the simulation. To reduce the computation time of the STAMC algorithm, we introduce a distributed and parallel computing topology using the interpretive MATLAB environment.

The integration of the Message-Passing Interface specification into the existing MATLAB environment and STAMC algorithm code is made possible with MPITB. MPITB enables coarse-grain and out-of-loop parallelisation of the expensive SiPaMoP algorithm on distributed nodes of a Linux computing cluster.

This paper is organised as follows. Section 2 presents the task allocation and routing problem and simulation environment, section 3 describes the distributed architecture and software implementation, section 4 provides a description of the experiments conducted to provide the results of section 5.

2 Problem Formulation

2.1 Simulation Environment

The task allocation environment discussed in this paper is similar to semi-automated or fully-automated material handling systems, where the number of cargo transportation vehicles transport cargo from one place to another on guided and pre-defined paths within the environment. The map of the environment is modelled with nodes and links. Autonomous vehicles traverse links when moving between nodes. Each task has its own start and destination node in the environment. A task is defined as travel from a start node to destination node traversing interconnected links.

The task allocation problem consists of a fixed number of tasks and vehicles at the start of the simulation. The main objective of the task allocation process is to find the best task sequence and respective vehicles to complete the task sequence according to

the optimisation criteria. The objective of the task allocation process is to optimise or minimise the completion time of all the tasks at each rescheduling instance. The completion time of all tasks is called the *makespan*. This is achieved by searching the best task sequence for the available tasks and their respective vehicles, which are capable to complete them earliest. A mathematical description is further discussed in section 2.2.

At the start of the simulation nodes are generated randomly and selected vehicles are parked at randomly selected nodes. Furthermore, the start node for a task may not be the same as the start node for a vehicle. As a result a vehicle maybe required to travel from its initial parked node to the tasks start node, as illustrated in Fig. 1. Here the task start nodes (B, D, G), destination nodes (C, E, H) and initial parked nodes (A, F) are represented by triangles, stars and circles respectively. Each vehicle explores for a task to undertake, however selection criteria of our simulation is based on the incoming time (t_{AB} or t_{CD}) of the vehicles to the tasks start nodes, where incoming time is a function of a vehicles velocity at each path segment, traffic congestion and total distance of the selected path. All vehicles simultaneously work on their assign tasks and once a vehicle completes its assigned task it determines next most suitable task and moves to the appropriate tasks' start node. The task allocation process continues until all tasks are allocated.

Fig. 1. Simulation environment and initial setup of tasks and AGV's

2.2 Mathematical Formulation

An AGV travels from its start location to destination on a guided path consisting of nodes and links. Each path can be divided into a number of smaller path segments, called *links*. To avoid collisions AGVs travel at varying speeds set by SiPaMoP. Two different maximum speeds are set for empty and loaded AGV's.

Task completion time consists of two components, namely the travel time from the current location to the start node of the task called *transient time* and the travel time from the tasks start node to the destination node, called *task time*.

Assuming vehicle V_i is allocated to task T_j and the path segments to reach the task T_j start node is PR_{ij}. Next, the path selected the task start node to destination node is PP_{ij}. Both, PR_{ij} and PP_{ij} contain k_R and k_P path segments respectively. Therefore, the total completion time of the task T_j by vehicle V_i can be calculated using Eq(1). The start time of the first allocated task is assumed to be the same for all the vehicles.

$$TCT_j = \sum_{k=1}^{k_R} \left(\frac{PR_{ijk}}{V_E}\right) + t_L + \sum_{k=1}^{k_P} \left(\frac{PP_{ijk}}{V_L}\right) + t_U \quad (1)$$

Where, TCT_j is task completion time of T_j, V_E is maximum empty speed, V_L is maximum loaded speed, t_L is loading time, t_U is unloading time. Furthermore, the available task list is given by the vector $T = [T_1, T_2, T_{3,...,} T_J]$ and available vehicles $V = [V_1, V_2, V_3,..., V_R]$ where J is number of available tasks and R is number of available vehicles.

Now, if a vehicle Vi, completes N_i number of tasks, total traveling time of the respective vehicle is given by Eq(2):

$$TTT_i = \sum_{ni=1}^{N_i} \left[\sum_{k=1}^{k_R} \left(\frac{PR_{ijk}}{V_E}\right) + t_L + \sum_{k=1}^{k_P} \left(\frac{PP_{ijk}}{V_L}\right) + t_U \right] \quad (2)$$

Where, TTT_i is total traveling time of vehicle V_i, N_i is the number of tasks allocated to vehicle V_i.

The *makespan* of the schedule is given by Eq(3):

$$\text{Makespan} = \underset{v=1}{\overset{R}{MAX}} [TTT_v] \quad (3)$$

Since one AGV can perform only one task at a time, the start time of task $j+1$ by V_i should always be greater than the start time of task j done by the same AGV as given by Eq(4).

$$ts_{ij} < ts_{i(j+1)} \quad (4)$$

Where, t_s is start time of task T, ts_{hj} is the start time of task T_h of j^{th} vehicle.

2.3 Simultaneous Task Allocation and Motion Coordination Algorithm

Task allocation is performed using a single round auctioning process and motion coordination is done based on SiPaMoP approach [16]. Initially, the task sequence is generated randomly by the task generator. The first task is broadcast to all autonomous vehicles allowing them to place a future bid for the task. After each vehicle has returned their bid, a winner is determined and is allocated the first task. The second task is then broadcast, followed by bids from each vehicle and a winner selected. This auction process of broadcast task, followed by bidding and the selection of a winner continues until all tasks have been allocated. For each vehicle the calculation of bids is based on the travelling time to complete the current broadcast task and any previously allocated (as the winner) tasks.

Once the travel time has been calculated it is used to post bids ($B_{1,j}$ to $B_{i,j}$). The travelling time of collision free paths is calculated using the SiPaMoP algorithm. A winner is then determined, based on the lowest travel time to finish the respective task (completion time). When the completion time is calculated for each autonomous vehicle, its previous task commitments are also considered, which helps reduce the trapping of tasks to one vehicle. For example, if a previous task is allocated to a particular vehicle, then there will be less tendency for the same vehicle to win the next task. In addition, load balancing of the vehicles can be achieved partially. After

all tasks of the current task sequence is allocated, total completion time (*makespan*) is calculated. This process continues for a fixed number of cycles with a different task sequence generated randomly in each cycle. Eventually the best task sequence is selected, which provides the minimum *makespan*. The flow diagram of the simultaneous task allocation and motion coordination algorithm is illustrated in Fig.2. Here, the parallel computation of the SiPaMoP algorithm is shown occurring towards the middle of the process. It is during this stage that the motion and path is calculated for each vehicle independently using different computing nodes.

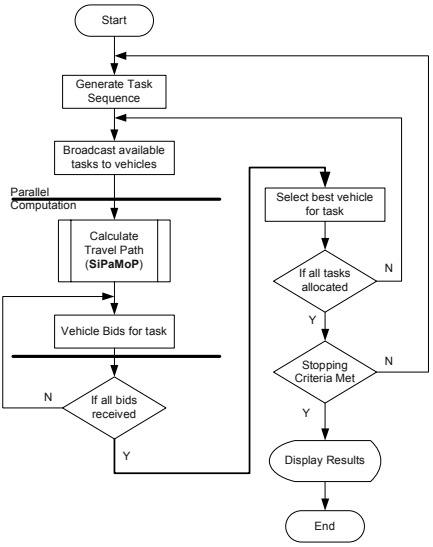

Fig. 2. Flow chart of STAMC algorithm

The travel path and resulting travel time to complete the path is calculated using the SiPaMoP algorithm. This portion of the STAMC algorithm is distributed and computed in parallel for each autonomous vehicle. If there exists, n autonomous vehicles requiring computation of a travel path, which takes t_{path} time to compute, the serial STAMC algorithm requires nt_{path} time to compute all paths for all vehicles. Whereas, the parallel STAMC algorithm requires only t_{path} time to compute the travel path for all autonomous vehicles.

A Master-Worker topology is used to distribute the STAMC algorithm. The Master node takes on the role of *Auctioneer*, by issuing tasks, receiving bids for tasks and determining the winning bid from each worker node. Worker nodes perform parallel computation of the path and motion planning using the SiPaMoP algorithm. The distributed computing environment and master-worker topology introduce a necessary communication time (t_{comm}), but $t_{comm} << t_{path}$.

Partitioning of the STAMC algorithm onto a parallel computing architecture is illustrated in Fig. 4 and the serial architecture is illustrated in Fig. 3.

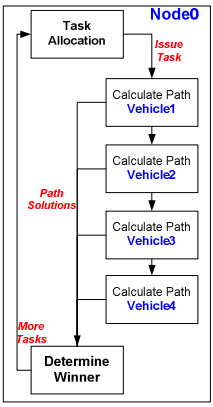

Fig. 3. The data path of *serial* computation for the task allocation and path planning algorithm for autonomous vehicles

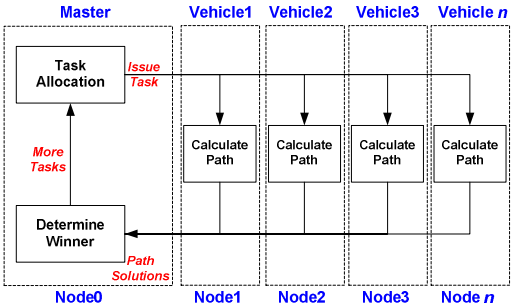

Fig. 4. The data path of parallel computation for the task allocation and path planning algorithm for autonomous vehicles

Here, the STAMC algorithm is implemented on a compute cluster, which is discussed further in section 4.2. The combined arrangement of hardware and software of the compute cluster provides a platform for coarse-grained parallelisation of the complete SiPaMoP algorithm, as illustrated in Fig. 4.

The cluster computing architecture and master-slave topology mutually provide for two possible mappings between the number of computing nodes and number of vehicles requiring motion and path planning. The first mapping is 1:1 and is used exclusively in this paper. Here, a single node computes the motion and path for a single vehicle. The second mapping, 1:*n* allows a single node to compute the motion and path for multiple vehicles. For example, if there exists, three computing nodes and nine vehicles, only three vehicles can be computed in parallel at one instance. As a result, three groups would be computed *sequentially*. In this case a single node would perform the motion and path computation for three vehicles, a 1:3 mapping. A third mapping of *n*:1, allows the motion and path computation to be further distributed across *spare* nodes. For example, if there exists, nine computing nodes and three vehicles it would be ideal to further distribute the path and motion computation for

each vehicle across the spare six nodes, thus allocating all computational resources of the compute cluster to the calculations. However, the STAMC algorithm encapsulates the complete SiPaMoP algorithm into a coarse-grained implementation, preventing any further decomposition into finer-grained portions for execution on separate processors.

The main objective for the simultaneous task allocation and collsion free path planning process is to minimse the *makespan* of the available tasks with the available autonomous vehicles. In order to satisfy the objective of task allocation, we must know the travel times of each tasks for respectable task-vehicle combination in advance and select the best task-vehicle combination. The SiPaMoP method is used to determine the travel time for each task and eventually we can find the best vehicle for the respective task. Since path planning and traveling times are determined by SiPaMoP method, paths are guaranteed to be collision free.

3 Integration of MPITB in the MATLAB Environment

The STAMC algorithm is implemented in the interpretive MATLAB environment, which has no native support for distributed computing. In order to arrange the STAMC algorithm into a Master-Worker topology on a distributed computing architecture a Message-Passing Interface (MPI) was required.

The integration of the MPI [17] and the interpretive MATLAB environment allows researchers to achieve coarse-grained and out-of-loop parallelisation of scientific and engineering applications developed in MATLAB. Developed at the University of Granada in Spain, MPITB for MATLAB allows researchers to include MPI function calls in a MATLAB application, in a way similar to the bindings offered for C, C++ and Fortran. Decomposition and coding of a serial problem into a parallel problem is still the responsibility of the researcher, as there is no *automatic* parallelisation method in MPITB. This method of explicit parallelisation coupled with user knowledge of the application provides a good chance for sub-linear or linear computational speedup. Furthermore, the onus is placed upon the researcher to develop *safe* distributed code free of livelocks and deadlocks which occur due to the loss of message synchronisation between distributed computing nodes.

Baldomero[18] provides a summary of several other parallel libraries that achieve coarse-grain parallelisation for MATLAB applications. The toolboxes differ in the number of commands implemented from the MPI specification and the level of integration with existing MATLAB data types.

The level of computational performance provided to a parallel MATLAB application is dependant upon the underlying communication method implemented in the toolbox. Toolboxes using the file system to exchange messages between computers tend to be slow due to the explicit read/write latency of rotating hard disks. Conversely, toolboxes using a message passing daemon to provide communication between computers provide much better performance due to the small latencies and large bandwidth capabilities of local area networks (LANs). In the later case, messages (data) are transferred between the primary memory of parallel computers, without buffering them using the file system prior to transmission over the LAN.

The MPI functions are written in C code and dynamically compiled into MATLAB MEX-files. The MEX-files encapsulate the functionality of the MPI routines, allowing them to be directly called within the MATLAB environment, thus making the parallelisation of the application possible. With both MATLAB and a message-passing library installed, such as LAM-MPI, the precompiled MEX-files can perform both MATLAB API calls and message-passing calls from within the MATLAB environment. The MPITB makes MPI calls to the LAM-MPI daemon and MATLAB API. This method enables message-passing between MATLAB processes executing in distributed computing nodes[18].

Transmission of data between the master-worker MATLAB processes and execution of the TAPP algorithm can occur after booting and initialisation of the LAM-MPI library from the master process using, `LAM_Init(nworkers,rpi,hosts)`. Where *nworkers* is the number of cluster nodes designated as worker nodes, *rpi* is the LAM MPI SSI setting which is set to either *tcp* or *lamd* in our experiments, *hosts* is the list of host names on the Linux cluster. Once the underlying MPI library has been initialised, MATLAB instances must be spawned on worker nodes. This is achieved using the `MPI_Comm_spawn(…)` command on the master process. Finally, establishing an MPI communication domain, called a *communicator*, defines a set of processes that can be contacted. This is done using the `MPI_Comm_remote_size(processrank), MPI_Intercomm_merge(processrank,0) and global NEWORLD` commands on the master process. Here, *processrank* is an integer greater than zero assigned to each worker node in the MPI communicator; the master node (processrank=0). The global variable *NEWORLD* is the name of the MPI communicator.

Transmission of messages between MATLAB processes can now be accomplished, permitting the arrangement of cluster nodes into any useful topology. The master-worker topology used in the experiments, employs the fundamental point-to-point communication mechanism between master and worker nodes, with one side performing a blocking send, `MPI_Send(buf,processrank,TAG,NEWORLD)` and the other a blocking receive, `MPI_Recv(buf,processrank,TAG,NEWORLD)`.When messages are sent *processrank* is the MPI rank value of the receiving process and when messages are received *processrank* is the value of the sending process. The parameter *buf* represents the MATLAB data to be sent or received, *TAG* is an integer associated with the message providing selectivity at the receiving node, and *NEWORLD* is the MPITB communicator. Any valid MATLAB data type can be transmitted directly without being prepacked into a temporary buffer, unless the message contains different data types. If the data to be sent is larger than a single variable, such as a matrix, then its size must be determined and sent prior to sending the matrix. The approach taken in this paper, is to calculate the size of the matrix in the sender using the MATLAB *size()* command, then send the size value to the receiver prior to sending the actual matrix. The distribution and parallel computation of the STAMC algorithm requires the transmission of a data between master and worker nodes. The size of the PATH_REGISTER matrix is dynamic between each task allocation cycle of the TAPP algorithm.

4 Experiment Description

The experiments involve execution of the STAMC algorithm on a single computing node and in parallel on the distributed computing cluster. The serial computation uses a single node of the Linux cluster, whereas the parallel computation uses multiple cluster nodes.

In this study, the performance is measured by recording the wall-clock time, so all components of the execution time, including communications, are included. The wall-clock time is a fair measure of performance that is frequently used.

4.1 Simulation Parameters

The set of algorithm and simulation parameters remained constant to encourage a meaningful comparison between the parallel/distributed approach and the serial/centralised method: *NumMaster*=1, *NumVehicles*={4,6,8}, *NumTasks*={24,48, 72,96,120,144,168,192,216,240}, *MapNodes*={192,216,240}, *WeightUpdate*=Dynamic, *VehicleSpeed*=100 cm/sec, *SchedulingTime*=1 batch, *TurnSpeed*=1 m/s, *SafetyTime*=0 sec, *TurningRate*=1.0. The STAMC algorithm is executed for 25 cycles with the average computation time taken as the as final result.

4.2 Cluster Computing Environment

All experiments were performed on a Linux computing cluster with specifications provided in Table 1. The serial and parallel versions of the task allocation and path planning algorithm were coded in MATLAB. Communications between cluster nodes employed MPI 2.0 implemented using the MPITB.

Table 1. Cluster Computing Environment

Computing Environment Component	Description
Number of Nodes Utilised	1,4,8
Processor Type and core Speed	Pentium 4 @ 3.0Ghz (Prescott)
Front-side Bus Bandwidth	800MHz
DRAM capacity and bandwidth	2GB DDR @ 400MHz
Network Type and Bandwidth	1000Mbps Ethernet
Network Switching Type	Gigabit Switching Fabric
Network Protocol	TCP/IP V4
OS Kernel Type and Version	Linux (2.4.21-20.EL)
MPI Type and Version	LAM 7.1.1 / MPI 2
MATLAB	7.0.4.352 (R14) SP 2
MPITB	mpitb-FC3-R14SP1-LAM711.tgz

5 Results and Discussion

The average computation times for the parallel/distributed STAMC algorithm and the serial/centralised STAMC algorithm are illustrated in the Fig. 5 and Fig. 6.

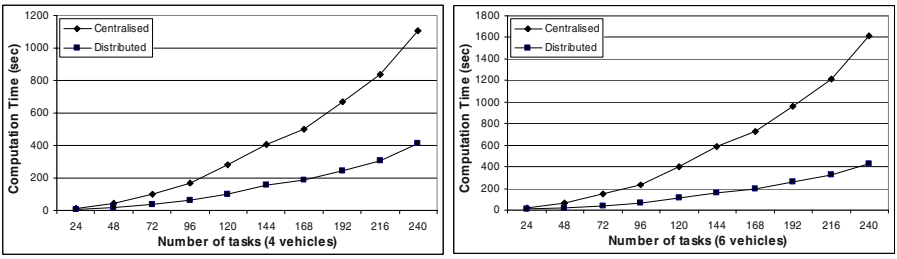

(a) (b)

Fig. 5. (a) Computation time for parallel/distributed and serial /centralised STAMC with 4 AGVS; **(b)** Computation time for parallel/distributed and serial /centralised STAMC algorithm with 6 AGVS

From the three simulations using 4, 6, and 8 vehicles, there is a clear performance increase (less computation time) with the parallel/distributed STAMC algorithm compared to the serial/centralised STAMC algorithm. As the numbers of tasks are increased from 24 to 240, the difference in performance becomes even more significant between the two versions of the STAMC algorithm. In general, when number of tasks of the simulation study increases, the computation time increases exponentially. But the rate of change of the gradient in serial/centralised algorithm is much larger than the rate of change of the gradient in the parallel/distributed algorithm, because the STAMC algorithm is *evenly* distributed among cluster processors (1:1 mapping) and computed in *parallel* in the later case.

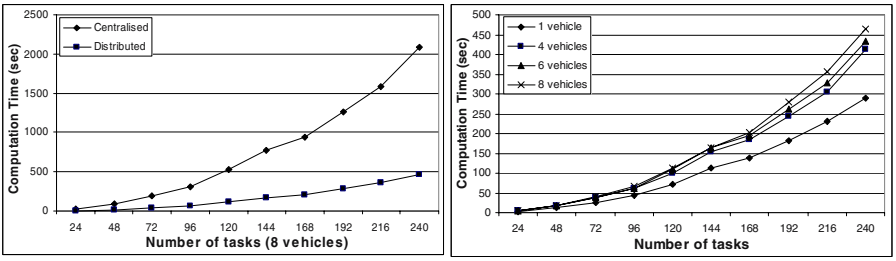

(a) (b)

Fig. 6. (a) Computation time for the parallel/distributed and serial/centralised STAMC algorithm using 8 AGV's; **(b)** Computation time for the parallel/distributed STAMC algorithm using 4/6/8 AGV's

Fig. 6(b) illustrates the results of the parallel and distributed STAMC algorithm using 4, 6 and 8 vehicles. Results for the single vehicle are also given to provide a baseline for comparison against the multi-vehicle simulations. For the multi-vehicle simulations, the computation time is similar from 24 to 240 tasks, with a maximum variation of approximately 14.3% between 8 and 4 vehicles at 216 tasks. This suggests a useful scalability property of the parallel STAMC algorithm arranged in a Master-Worker topology for an increasing number of vehicles.

The STAMC algorithm attempts to find an optimal (minimum) schedule for the allocation of *all* tasks to available vehicles, whilst guaranteeing collision free paths. This is a typical NP-hard ("Non-deterministic Polynomial time") problem, requiring time which is exponential in log n, the number of tasks to be scheduled. As a consequence the results are exponential in the number of tasks to be scheduled and not the number of vehicles. Because of the coarse-grained parallelisation of the SiPaMoP algorithm, variations between 4, 6, and 8 vehicles is small, even with 240 tasks as illustrated in Fig. 6(b).

6 Conclusion

The use of MPITB for MATLAB provided effective integration and encapsulation of MPI into the interpretive environment of MATLAB. This enabled existing MATLAB code to be distributed and computed in parallel using clustered computing power. Scientific and engineering applications continue to maintain the interactive, debugging and graphics capabilities offered by the MATLAB environment, and can now reduce the computation time by taking advantage of clustered computing.

Due to the high granularity of the STAMC algorithm, the distributed and parallel version achieved *near-linear* computational speedup over the serial STAMC algorithm. This result was achieved using 4, 6 and 8 cluster nodes for a number of tasks ranging from 24 to 240. The experimental results also suggest good scalability of the parallel STAMC algorithm, which becomes more important as the number of vehicles and number of tasks increases.

With the aim of increasing overall system reliability our future research work involves retirement of the master node to remove the single point of failure from the system. Coupled with a fully-connected topology, redundancy is increased by allowing any cluster computing node to adopt the master role of task allocation.

Acknowledgement

We wish to thank Dr Matthew Gaston for establishing, maintaining and supporting the UTS Engineering Linux Computing Cluster Environment.

References

[1] E. K. Bish , F. Y. Chen , Y. T. Leong, B. L. Nelson, J. W. C. Ng, and D. Simchi-Levi, "Dispatching vehicles in a mega container terminal *OR Spectrum,* vol. 27, Number 4 pp. 491 - 506 2005.

[2] J. Bose, T. Reiners, D. Steenken, S. Voß, and "Vehicle dispatching at seaport container terminals using evolutionary algorithms," *In: Sprague R H (ed) Proceedings of the 33rd Annual Hawaii International Conference on System Sciences, DTM-IT, pp 1-10. IEEE, Piscataway*, 2000.

[3] M. Grunow , H. Günther, and M. Lehmann, "Dispatching multi-load AGVs in highly automated seaport container terminals, *OR Spectrum,* vol. 26, Number 2, 211-235 2004.

[4] J. K. Lim, K. H. Kim, K. Yoshimoto, J. H. Lee, and "A dispatching method for automated guided vehicles by using a bidding concept," *OR Spectrum*, vol. 25, 25-44, 2003.
[5] K. H. Kim and K. Y. Kim, "Routing straddle carriers for the loading operation of containers using a beam search algorithm, *Computers & Industrial Engineering,* vol. 36, Issue 1, pp. 109-136, 1999.
[6] P. H. Koo, W. S. Lee, and D. W. Jang, "Fleet sizing and vehicle routing for container transportation in a static environment, *OR Spectrum,* vol. 26, Number 2, 193 - 209 2004.
[7] R. L. Moorthy and W. Hock-Guan, "Deadlock prediction and avoidance in an AGV system," *Master of science, Sri Ramakrishna Engineering College, National University of Singapore*, 2000.
[8] F. Xu, H. V. Brussel, M. Nuttin, and R. Moreas, "Concepts for dynamic obstacle avoidance and their extended application in underground navigation, *Robotics and Autonomous Systems,* vol. 42, Issue 1, pp. 1-15, 2002.
[9] A. I. Corréa, A. Langevin, and L.-M. Rousseau, "Scheduling and routing of automated guided vehicles: A hybrid approach, *Computers & Operations Research,* 2005.
[10] R. Eisenberg, R. Stahlbock, S. Voß, and D. Steenken, "Sequencing and scheduling of movements in an automated container yard using double rail-mounted gantry cranes, *Working paper, University of Hamburg,* 2003.
[11] A. Wallace and "Application of AI to AGV control - agent control of AGVs," *International Journal of Production Research*, vol. 39(4), pp. 709-726, 2001.
[12] A. I. Correa, A. Langevin, and L. M. Rousseau, "Scheduling and routing of automated guided vehicles: A hybrid approach, *Computers & Operations Research*, vol. to be published, 2005.
[13] T. Le-Anh and M. B. M. De Koster, "On-line dispatching rules for vehicle-based internal transport systems, *International Journal of Production Research,* vol. 43, Number 8 / April 15, 2005 pp. 1711 - 1728 2005.
[14] G. Desaulniers, A. Langevin, D. Riopel, and B. Villeneuve, "Dispatching and Conflict-Free Routing of Automated Guided Vehicles: An Exact Approach, *International Journal of Flexible Manufacturing Systems* vol. 15, Number 4, pp. 309 - 331, 2003.
[15] A. K. Kulatunga, D. K. Liu, G. Dissanayake, and S. B. Siyambalapitiya, "Ant Colony Optimization based Simultaneous Task Allocation and Path Planning of Autonomous Vehicles, *IEEE International conference on Cybanatics and Information Systems 2006, Bangkok Thailand*, pp. 823-828, 2006.
[16] D. K. Liu, X. Wu, A. K. Kulatunga, and G. Dissanayake, "Motion Coordination of Multiple Autonomous Vehicles in Dynamic and Strictly Constrained Environments, Proceeding of the *IEEE International conference on Cybernetics and Information Systems* (CIS), 7-9 June, 2006, Bangkok Thailand, pp204-209.
[17] MPI.Forum, "MPI-2: Extensions to the Message-Passing Interface," in *Message Passing Interface Specification*, vol. 2005, November 15, 2003 ed: NSF and DARPA, 2005, pp. MPI-2 Specification Document.
[18] J. F. Baldomero, "Message Passing under MATLAB," presented at Advanced Simulation Technologies Conference, Seattle Washington, 2001.

A New Support Vector Machine-Based Fuzzy System with High Comprehensibility

Xixia Huang, Fanhuai Shi, and Shanben Chen

Welding Engineering Institute, Shanghai Jiao Tong University, 1954 Huashan Road, Shanghai 200030, China
merryhuang@sjtu.edu.cn

Abstract. This paper proposes a support vector machine (SVM)-based fuzzy system (SVM-FS), which has good comprehensibility as well as satisfactory generalization capability. SVM provides a mechanism to extract support vectors for generating fuzzy IF-THEN rules from training data. In SVM-FS, SVM is used to extract IF-THEN rules; the fuzzy basis function inference system is adopted as the fuzzy inference system. Furthermore, we theoretically analyze the proposed SVM-FS on the rule extraction and the inference method comparing with other fuzzy systems; comparative tests are performed using benchmark data. The analysis and the experimental results show that the new approach possesses high comprehensibility as well as satisfactory generalization capability.

1 Introduction

The inference framework realizes the tasks of function approximation between the input and output spaces in terms of a set of fuzzy IF–THEN rules. A number of approaches to define fuzzy rule-based modeling have been discussed in the literature, including heuristic, statistical, and adaptive methods[1-3]. The design methodology of the construction of fuzzy models involves rule extraction, parameter learning and inference method. Rule extraction methods have been formulated using neural networks, genetic algorithms, SVD-QR, support vector machine (SVM) and clustering-based techniques to select only those rules that contribute to the inference consequence. Inference methods have been built using fuzzy basis function inference system, SVM and neural networks[1-3].

In this paper, we describe a new SVM-based fuzzy system (SVM-FS), which possesses good comprehensibility (less rules and comprehensive inference system) as well as satisfactory generalization capability. The remainder of this paper is organized as follows. Section 2 will provide some background knowledge of fuzzy basis function and SVM for regression estimation. Section 3 describes the proposed SVM-FS. In Section 4, we analyze SVM-FS comparing with other fuzzy systems.

2 Preliminaries of Fuzzy Basis Function Inference System and SVM for Regression

For the readers' convenience, some background knowledge on fuzzy basis functions[2] and SVM for regression[4] is first provided in this section.

T.-J. Tarn et al. (Eds.): Robot. Weld., Intellige. & Automation, LNCIS 362, pp. 421–427, 2007.
springerlink.com

2.1 Fuzzy Basis Function Inference System

The most common fuzzy rule-based system consists of a set of linguistic rules. In this work we consider the general case where the fuzzy rule base consists of *M* rules in the following form:

$$\begin{aligned} R_j : IF\ x_1\ is\ A_1^j\ and\ x_2\ is\ A_2^j\ and\ ...and\ x_n\ is\ A_n^j, \\ THEN\ z\ is\ B^j \quad for\ j = 1,2,\ldots,M \end{aligned} \tag{1}$$

where $x_i (i = 1,2,\ldots,n)$ are the input variables; z is the output variable of the fuzzy system; and A_i^j and B^j are linguistic terms characterized by fuzzy membership function $u_{A_i^j}(x_i)$ and $u_{B^j}(z)$,respectively.

The overall fuzzy inference function is

$$\begin{aligned} f(x) &= \sum_{j=1}^{M} p_j(x)\overline{z}^j \\ p_j(x) &= \prod_{i=1}^{n} u_{A_i^j}(x_i) \Big/ \sum_{j=1}^{M} (\prod_{i=1}^{n} u_{A_i^j}(x_i)) \end{aligned} \tag{2}$$

2.2 SVM for Regression Estimation

SVM approximates the function using the following form:

$$f(x) = \langle \varpi \cdot \phi(x) \rangle + b \tag{3}$$

The regression problem is equivalent to the following optimization problem:

$$\begin{aligned} \min \quad & \frac{1}{2}\|\varpi\|^2 + \mathrm{C}\sum_{i=1}^{l} (\xi_i + \xi_i^*) \\ s.t. \quad & \begin{cases} y_i - \langle \varpi^T \cdot \phi(x_i) \rangle - b \le \varepsilon + \xi_i \\ \langle \varpi^T \cdot \phi(x_i) \rangle + b - y_i \le \varepsilon + \xi_i^* \\ \xi_i, \xi_i^* \ge 0 \end{cases} \end{aligned} \tag{4}$$

By solving Equation (4) the approximate function is obtained□

$$f(x) = \sum_{i=1}^{l} (\alpha_i - \alpha_i^*)\mathrm{K}(x_i, x) + \mathrm{b} \tag{5}$$

3 SVM-Based Fuzzy System

In this section, we introduce a new fuzzy rule-based inference system utilizing SVM. The proposed SVM-based fuzzy inference architecture is shown in Fig. 1. For this approach, the first step is to use SVM to extract IF-THEN rules; the next step is to adopt the fuzzy basis function inference system as the fuzzy inference system. We will show an example of SVM-FS to illustrate the idea presented in this section.

Example 1: Regress using SVM-FS. Samples in the simulation are generated by the following function:

$$sinc(x) = \begin{cases} \dfrac{sin(x)}{x} & if\ x \neq 0 \\ 1 & if\ x = 0 \end{cases}$$

3.1 Extract Fuzzy Rules Using SVM

SVM learning mechanism provides a solid foundation to extract support vectors for further use in the IF-Then rules generation. As described in [4], only a small part of training data, the support vectors, contribute to the solution. Geometrically, they are points that lie on or outside the ε -tube [10]. In other words, they are in "key position". Notice that we choose only margin support vectors ($0 \prec \left|\alpha_i - \alpha_i^*\right| \prec C$) because error support vectors ($\left|\alpha_i - \alpha_i^*\right| = C$) may be far from the regression curve, as the empirical error should be equal or more than ε in this case. We will illustrate it in the first step of *Example 1*.

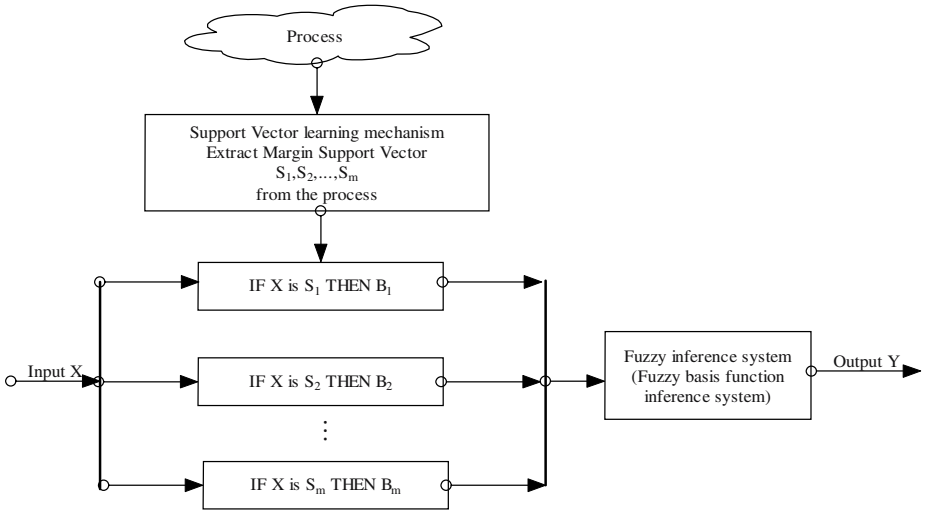

Fig. 1. SVM-based fuzzy system

Example 1-Step 1: extract fuzzy rules using SVM. The train points generated range from -3π to 3π, shown in Fig. 2. In this example, we set parameter C=10, the insensitive value ε =0.05, and the kernel function is $K(x_i, x_j)=\exp(-\gamma\left\|x_i - x_j\right\|^2)$, $\gamma = 0.1$. The points with $(\alpha - \alpha^*) \neq 0$ are identified as support vectors. Here, we obtained nine margin support vectors located at positions of (-9.4248,0), (-7.330383, 0.118142),…,

(9.4248,0), with $(\alpha - \alpha^*)$ equals -0.2086, 0.23158,…, -0.20955, respectively, which are labeled with circles in Fig. 2. Using the obtained margin support vectors, we can derive a set of nine IF-THEN rules as Table 1.

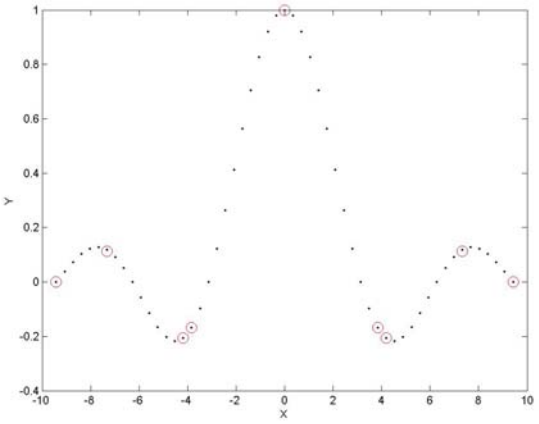

Fig. 2. Nine support vectors are in "key positions". (The support vectors are marked with circles.)

Table 1. Final fuzzy rules obtained from the regression example

R1:	IF X is close to -9.4248, Then Y is close to 0.0000
R2:	IF X is close to -7.3303, Then Y is close to 0.1181
…	
R9:	IF X is close to 9.4248, Then Y is close to 0.0000

3.2 Fuzzy Inference System

We adopt the following fuzzy basis function inference system as the fuzzy inference system:

$$f(x) = \sum_{j=1}^{M} p_j(x)\bar{z}^j$$
$$p_j(x) = \exp(-a\left\|x - \bar{x}^j\right\|^2) \Big/ \sum_{j=1}^{M} (\exp(-a\left\|x - \bar{x}^j\right\|^2) \tag{6}$$

where $f : R^n \to R$, $\bar{z}^j$ is the output of R_j; $p_j(x)$ is the fuzzy basis function. The performance of the inference system is illustrated in the second step of *Example 1*.

Example 1-Step 2: infer using fuzzy rules and the inference system. In this example, we set parameter *a* to be 0.3. Fig. 3 shows the final regression result using the nine fuzzy rules.

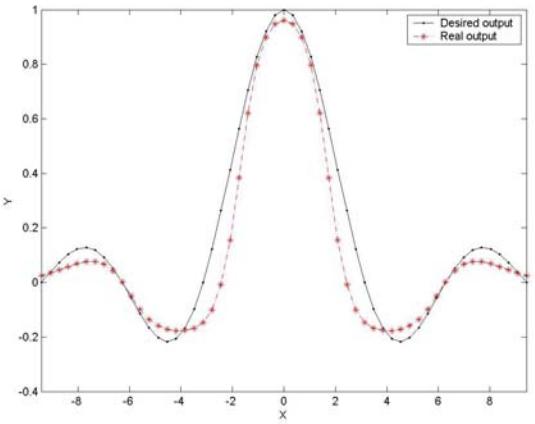

Fig. 3. Final regression result

4 Analysis of SVM-FS Compared with Other Fuzzy Systems

In this section, we describe the proposed SVM-based approach and three kinds of traditional methodologies, clustering partition-based[1], OLS-based[2] and SVM-FIS[3] approaches, which extract fuzzy rules from training data sets.

4.1 Analysis of Fuzzy Rule Extraction Approaches

Both the clustering partition-based and the OLS-based approaches extract fuzzy rules depending on some important "key points" obtained from training patterns. Those key points condense decision information from learning process, which provides a set of "basis" to express the overall fuzzy system. The major difference between them is that the OLS-based approach chooses key points within the training points, whereas the clustering-based approach estimates key points from the training space since cluster centers do not have to be training points.

Our basic idea is similar to the OLS-based approach, that is, choosing key points within the training points. However we adopt a different approach to extract the "key points". In the proposed approach, SVM is used to select "key points" which are used to construct the final fuzzy system. Compared to the clustering partition-based and OLS-based approaches, our approach is more intuitive in some sense, for our "key points" are in key positions, which help to shape and define the decision function.

We use the similar approach as SVM-FIS to extract fuzzy rule. The first difference lies in the kernel functions. In SVM-FIS the fuzzy basis function is chosen as the kernel function, so the kernel function is limited to the RBF kernel. In our approach, what we directly use are the fuzzy rules, so the essential goal is to extract appropriate "key points" using appropriate kernels and parameters. Therefore, different kernel functions could be used according to the special properties of the specific problem. The second

difference is that in our approach only margin support vectors are used so as to reduce the influence of the noise.

4.2 Analysis of the Inference Systems

Comprehensibility of inference system is another index to evaluate a fuzzy system. Fuzzy system depends heavily on inference procedures because it is the inference system that makes the vague and incomplete fuzzy rules valuable.

We use the same inference system as OLS-based approach. The most important advantage is that the inference system reflects the human habit of thinking and has good comprehensibility.

In the clustering partition-based approach, the inference system is embedded in the fuzzy adaptive learning control network. It is difficult for the model users, who are field experts but laymen of modeling, to fully understand the mode.

The key difference between our approach and SVM-FIS is that our inference mechanism is directly based on fuzzy rule while SVM-FIS actually adopts the SVM inference system. In substance it has the shortcoming of SVM, which has poor comprehensibility. For example, how to understand $(\alpha_i - \alpha_i^*)$ and b in a fuzzy system?

4.3 Experimental Result of Comparative Experiment Using Benchmark Data

The time series used in the simulation is generated by the chaotic Mackey–Glass differential delay equation[5]:

$$\dot{x}(t) = \frac{0.2x(t-\tau)}{1+x^{10}(t-\tau)} - 0.1x(t) \quad for\ \tau > 17 \tag{7}$$

In the simulation, we set the parameter $\tau = 30$. The prediction of future values of this time series is a benchmark problem which has been considered by a number of connectionist researchers[1-3].

The goal of this task is to use known values of the time series up to the point $x = t$ to predict the value at some point in the future $x = t + P$. The standard method for this type of prediction is to create a mapping from D points of the time series spaced $\triangle$ apart, that is, $(x(t-(D-1)\triangle), \ldots, x(t-\triangle), x(t))$, to a predicted future value $x(t+P)$. To compare with earlier work [1, 2], the values $D = 9$ and $\triangle = P = 1$ are used, i.e., nine point values in the series are used to predict the value of the next time point. The 200 points of the series from $x(501) - x(700)$ are used as training data, and the final 300 points of the series from $x(701) - x(1000)$ are used as test data.

In this experiment, for the purpose of comparison, we set parameter $\varepsilon = 0.02$. We obtain 22 SVs with 0.08 rms error. Fig. 4 depicts the prediction performance.

Compared with earlier work the proposed model is quite acceptable. The clustering partition-based approach captured 22 rules with rms 0.08, but the inference system is embedded in the fuzzy adaptive learning control network; the OLS-based approach

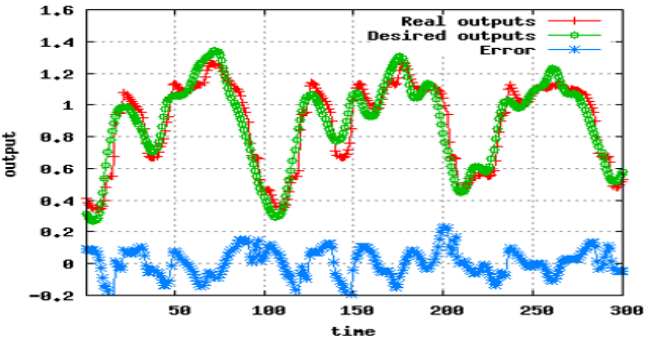

Fig. 4. Simulation results of the time-series prediction from $x(701) - x(1000)$ using the SVM-FS model with 22 fuzzy rules when 200 training data [from $x(501) - x(700)$] are used

used 121 rules with rms 0.08; SVM-FIS captured 13 rules with rms 0.05, although SVM-FIS is more accurate, it actually adopts the SVM inference system, which has poor comprehensibility.

5 Conclusion

This paper proposes a new SVM-fuzzy system with high comprehensibility. In this system, SVM is used to select significant fuzzy rules, which directly related to a fuzzy basis function; linear combination of fuzzy basis functions is used to construct the final fuzzy system. Analysis and comparative tests about SVM-FS with respect to other fuzzy systems show that the new approach possesses high comprehensibility as well as satisfactory generalization capability.

Acknowledgement

This work is supported by the National Natural Science Foundation of China under Grand No. 60474036 and the Key Foundation Program of Shanghai Sciences & Technology Committee under Grant No. 06JC14036.

References

1. C.-J. Lin, C.-T.L., *An ART-based fuzzy adaptive learning control network.* IEEE Trans. Fuzzy Syst., 1997. **5**(11): p. 477-496.
2. Li-Xin Wang, J.M.M., *Fuzzy Basis Function, Universal Approximation, and Orthogonal Least-Squares Learning.* IEEE Transactions on Neural Networks, 1992. **3**(5): p. 807-814.
3. Jung-Hsien Chiang, P.-Y.H., *Support Vector Learning Mechanism for Fuzzy Rule-Based Modeling: A new Approach.* IEEE Transactions on Fuzzy Systems, 2004. **12**(1): p. 1-12.
4. A.J. Smola, B.S., *A tutorial on support vector regression.* Statistics and Computing, 2004. **14**(3): p. 199-222.
5. M. C. Mackey, L.G., *Oscillation and chaos in physiological control systems.* Science, 1977. **197**(7): p. 287–289.

Vision–Based Dynamic Tracking of Motion Trajectories of Human Fingertips

D.W. Ren and J.T. Li

Robotics Institute, Beihang University, Beijing 100083, P.R. China
rendawei636@gmail.com

Abstract. Dynamic tracking of motion trajectories of human fingertips is a very challenging job considering the requirement of accuracy as well as speed. A binocular vision is adopted to dynamically measure the fingertip positions of the human hand. Based on Kalman filter, combined with the historical motion data of human hand, a dynamic tracking model is presented which can fast and accurately track the fingertip positions. The experimental result shows that when human fingers move in a natural speed, the dynamic fingertip positions can be tracked successfully.

1 Introduction

The information of human hand motion, especially the fingers, is very useful when designing dexterous robotic hands or planning their grasping and manipulation. At present, dataglove is often used as the interface to measure the human hand motion [1-5]. While it is convenient for dataglove to measure the joint angles, however it cannot satisfy the expected precision when the fingertip positions are accurately needed. As for computer vision, it can achieve higher accuracy than dataglove but slower speed because of processing a large amount of information. When tracking the moving trajectories of human fingertips, it is involved in dealing with the multi-dynamic targets within a relative small space, where mismatching easily happens. Therefore how to use computer vision effectively and efficiently is a very challenging research. In tele-manipulation system for DLR Hand, computer vision is used to calibrate the dataglove [2]. Choosing the appropriate interface is obviously relevant to the motion parameters which to be measured.

The research of this paper focuses on the dynamic tracking of fingertip motion of human hand. As stated above, dataglove cannot satisfy the precision requirement of the positions. Therefore the binocular vision is adopted in our system to measure the positions of the human fingertips. The research goal is to increase the recognition rate, which is not quite satisfied in our previous research [6]. We think that the unique characters of the human finger motion can provide important clues to deal with such matters, thus should not be neglected. Therefore based on Kalman filter [7-8], combined with the full use of the just passed motion data of human hand, a dynamic tracking model is presented which can fast and accurately match the currently measured fingertip positions to their corresponding past ones. The experiment shows that when human fingers move in a natural speed, the recognition rate is almost 100 percent. This is critical to our master-slave grasp system for the dexterous hand, which is developed in our previous research [6].

T.-J. Tarn et al. (Eds.): Robot. Weld., Intellige. & Automation, LNCIS 362, pp. 429–435, 2007.
springerlink.com

2 Targets to Be Tracked

When binocular vision is used to track the fingertips, the basic issue to be solved is to match the current dynamic targets to their corresponding ancestors on both images. The targets in the images are 2 dimensional, of which the coordinates vary in different frames of the images. Therefore the tracking variables in the images are the 2-D coordinates (x, y) of targets. To make the tracking easy and fast, the coordinates x and y are tracked independently. The presented method in the following sections is suitable for both x and y coordinate.3 Target tracking based on kalman filter.

The following model is based on the assumption that human fingers move in constant speeds, which can be roughly controlled by the operator.

In order to shorten the tracking time, every target is searched only in a relatively small area rather than in the whole image one. The searching area, of which scope is predetermined by the experiment, is located by estimation according to the last frame position and speed of the target. Considering the possible noises, the target is recursively modified and be searched out at last.

2.1 Discrete Time Model for Position and Speed

At time t_k, assume that the position and velocity, along one of the coordinate axes, of the target is s_k and v_k, respectively. With the constant speed assumption, we have

$$s_k = s_{k-1} + v_{k-1}\Delta t, v_k = v_{k-1} \tag{1}$$

Where the subscripts k and $k-1$ mean at time t_k and t_{k-1}. Δt is the sampling interval.

Equation (1) can be rewritten into the following expression

$$x_k = Ax_{k\text{-}1} \tag{2}$$

Where $x_k = \begin{bmatrix} s_k \\ v_k \end{bmatrix}$ is called state vector and $A = \begin{bmatrix} 1 & \Delta t \\ 0 & 1 \end{bmatrix}$ is called transition matrix.

Considering the uncertainty that is brought by the assumption of constant velocity model, Equation (2) is further estimated as follows.

$$x_k = Ax_{k-1} + \begin{bmatrix} 0.5\Delta t^2 \\ \Delta t \end{bmatrix} w_k = Ax_{k-1} + \begin{bmatrix} w_{ks} \\ w_{kv} \end{bmatrix} \tag{3}$$

Where the sequence $\{w_k\}$ is acceleration which is supposed to be a white Gaussian noise. The variance of w_k is q_k^2. $\begin{bmatrix} w_{ks} \\ w_{kv} \end{bmatrix}$ is called process noise. The w_{ks} is position noise and the w_{kv} is velocity noise. $Q_k = \begin{bmatrix} q_{11} & q_{12} \\ q_{21} & q_{22} \end{bmatrix} = q_k^2 \begin{bmatrix} \Delta t^4/4 & \Delta t^3/2 \\ \Delta t^3/2 & \Delta t^2 \end{bmatrix}$ is

covariance matrix of process noise[7]. When the Δt in the system is short enough, q_{11}, q_{12}, q_{21} are small which can be considered as zero. So the Q_k can be expressed as $\begin{bmatrix} 0 & 0 \\ 0 & q_{22} \end{bmatrix}$, where $q_{22} = \sigma_{vk}^2, \sigma_{vk}^2$ is variance of random speed changes.

The measurement model of target position takes the following form:

$$z_k = Cx_k + n_k \tag{4}$$

Where z_k is the measured position (x or y coordinate) of target from the image plane of camera. $C = \begin{bmatrix} 1 & 0 \end{bmatrix}$ is called the observation matrix. n_k is the uncertainty of the camera measurement. Sequence $\{n_k\}$ is also supposed to be a white Gaussian noise which is called measurement noise and independent with the process noise sequence $\{w_k\}$.

2.2 Recursive Algorithm

The recursive algorithm is as follows. The estimative state vector $x_{k|k-1}$:

$$x_{k|k-1} = Ax_{k-1|k-1} \tag{5}$$

Where the subscription $k \mid k-1$ denotes the estimated value at time k from the actual value at time $k-1$, and the subscription $k-1|k-1$ means the actual value at time $k-1$.

The estimative system error covariance matrix $P_{k|k-1}$:

$$P_{k|k-1} = AP_{k-1|k-1}A^T + Q_{k-1} \tag{6}$$

Where $P_{k|k-1} = \begin{bmatrix} p_{11} & p_{12} \\ p_{21} & p_{22} \end{bmatrix}$, p_{11} is uncertainty(variance) in position; p_{22} is uncertainty(variance) in speed; p_{12} , p_{21} are uncertainty(covariance) in position and speed. $P_{k|k-1}$ is measure of accuracy of $x_{k|k-1}$.

The system gain matrix K_k :

$$K_k = P_{k|k-1}C^T[CP_{k|k-1}C^T + R_k]^{-1} \tag{7}$$

K_k is optimal correction factor used to weight the error between the estimate position $s_{k|k-1}$ and the measurement position z_k .

The updating state vector $x_{k|k}$:

$$x_{k|k} = x_{k|k-1} + K_k[z_k - Cx_{k|k-1}] \tag{8}$$

The updating system error covariance matrix $P_{k|k}$:

$$P_{k|k} = P_{k|k-1} - K_k C P_{k|k-1} \tag{9}$$

By the above recursive procedure, the actual target position $s_{k|k}$ can be determined.

2.3 Measurement Noise Covariance R_k

When determining the measurement noise covariance R_k , affect of the image distortion is ignored, so all the pixels on the image have measurement white noise with the same covariance. So R_k is a constant in this system which can be expressed as $R_k = [\sigma_n^2]$. R_k can be got by the following method. The target is placed at an arbitrary position in the view field of camera and kept stationary. Record the image coordinates s_i of the target at time i . The number of recorded samples is m which should be adequate. Then the actual image coordinate s is approximated as:

$$s = \sum_{i=1}^{m} s_i / m \tag{10}$$

So the covariance of measurement noise matrix R_k is

$$\mathrm{R_k} = [\sigma_n^2] \tag{11}$$

Where $\sigma_n^2 = \sum_{i=1}^{m} (s_i - s)^2 / (m-1)$.

2.4 Process Noise Covariance Q_{k+1}

The process noise is caused by the constant velocity model assumption, which is actually difficult to control precisely for a human operator. Because of difficulty to calculate the real-time process noise covariance matrix, the approximated method is used to calculate it.

First, the speed noise at time $k+1$ approximately calculated as follows:

$$w_{v\,k+1} \cong v_{k|k} - v_{k|k-1} \tag{12}$$

In our system, the sampling period is 0.04 second, so the process noise covariance matrix can be expressed as:

$$\mathrm{Q}_{k+1} = \begin{bmatrix} 0 & 0 \\ 0 & \sigma_{v\,k+1}^2 \end{bmatrix} \tag{13}$$

Where $\sigma_{v\,k+1}^2 = (\sigma_{v\,k}^2 \times (k-1) + w_{v\,k+1}^2) / k$.

2.5 Initial Variables Selection

It is very important to select suitable initial state vector $x_{0|0}$ and initial system error covariance matrix $P_{0|0}$ to make the tracking model stable and convergent in the initial

period[9]. The initial state vector $\mathbf{x}_{0|0}$ and the initial system error covariance matrix $P_{0|0}$ are calculated by the following method.

$$\mathbf{x}_{0|0}=\begin{bmatrix} z_0 \\ 0 \end{bmatrix}, P_{0|0}=\begin{bmatrix} \sigma_n^2 & 0 \\ 0 & \sigma_{v0}^2 \end{bmatrix} \tag{14}$$

Where σ_{v0}^2 is determined by the experience.

3 Experiment

As shown in Fig.1, the subject wears a white glove with four small black balls stuck on the fingertips to make the targets remarkable.

Two white and black CCD cameras are used to track the positions of these balls which are considered to be the human fingertips, when the human hand moves. The resolution of CCD is 768×576. The sampling frequency of the image collection card is 25 frames per second. The code is written in VC++ 6.0 and run on Windows 2000 operating system. And the speed of CPU is Pentium IV 2.0G. with 512M memory. $\sigma_{v0}^2 = 5000(pixels/s)^2$ and $\sigma_n^2 = 0.005(pixels)^2$ in this system.

Fig. 1. The targets to be tracked

Fig. 2. Experiment system

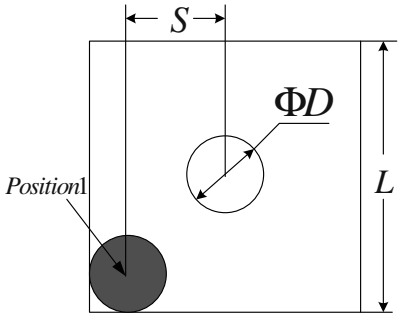

Fig. 3. Position constraint

3.1 Acceleration Constraint of the Tracking Algorithm

To ensure there is no failing tracking, the constraint of the speed of the human fingertips is estimated. As shown in Fig.3, when the target ball is located within the predefined searching area (demonstrated by the square), the tracking is successful. The extreme position of the ball is occurred when the circle is tangent to the edges of the square, such as position 1 (the dark colored circles). The position constraint can be described by the inequation $|\Delta S| < (L-D)/2$. ΔS is the distance error between the estimated position (the light colored circle) and actual position(the deeply colored circle) along each of the coordinate axes. L is the edge length of square and D is the image diameter of the black balls. Because ΔS is resulted from the speed changes that is materially acceleration, we have the equations $|\Delta S| = a_{\text{limit}} \Delta t^2 / 2$. a_{limit} is the limit acceleration along the coordinate axis which can be calculated by the inequation $|a_{\text{limit}}| \Delta t^2 < L - D$.

In the experiment, the diameter of target ball is 8mm. Distance of camera lens and the human hand is about 600mm. The diameter of target ball is about 23.2 pixels on the image and the edge length of the square is 36 pixels. At last the acceleration constraint is about $a_{\text{limit}} < 7500\, pixel/s^2$ along the coordinate axis which is equal to $2.5 m/s^2$.

3.2 Coping with Outranged Acceleration

During the experiment, the acceleration occasionally breaks the constraint, which results in failure of tracking. Two examples are demonstrated in Fig.4. Case 1 represents occurrence of abrupt acceleration and case 2 represents that of abrupt stop.

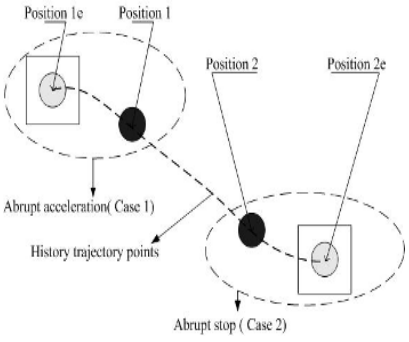

Fig. 4. Tracking failure situation

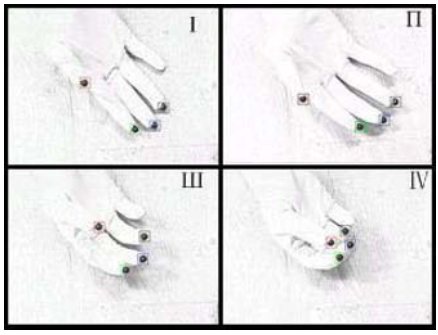

Fig. 5. Tracking procedure

In order to coping with this situation, certain positions on the trajectory the target passed are recorded. If the target is out of the range of the square, the previous recorded positions will be searched until one of the positions is within the searching square and this position will be assumed to be the current tracked target. The recorded process is been done offline, just before the real time tracking of the human fingertips, which can ensure the trajectories are similar enough. The distance between adjacent two recorded

points must be less than the edge length of square. To balance the reliability and the searching efficiency, 20 pixels distance is selected.

3.3 Experimental Results

With the method described above, the human fingertips are successfully tracked in the experiment when human fingers move no more than 55 times per minute. It costs 6 ms to simultaneously track 4 targets for each CCD image, altogether 8 targets for 2 CCD. Some of the snapshots of the tracking procedure are shown in the Fig.5.

4 Conclusion

A vision-based approach is investigated to dynamically track the motion of human fingertips. The proposed tracking model is validated by the experiment to be feasible and efficient when human fingers move in a natural speed. Owning to the high-efficiency of algorithm, it is possible to get more human hand motion information timely, which we will investigate next.

The research is also helpful to establish the accurate kinematical model of human hand, which will benefit the design and control of humanoid dexterous hand.

References

1. Sing Bing Kang and Katsushi Ikeuchi(1997) Toward Automatic Robot Instruction from Perception－Mapping Human Grasps to Manipulator Grasps, IEEE Trans. on Robotics and Automation, pp. 81-95, 13(1).
2. M. Fischer, P. van der Smagt, and G.Hirzinger (1998) Learning Techniques in a Dataglove Based Telemanipulation System for the DLR Hand, Proc. 1998 IEEE Intl. Conf. on Robotics and Automation, pp. 1603-1608,Leuven, Belgium.
3. Haruhisa Kawasaki, Kanji Nakayama, Tetsuya Mouri, and Satoshi Ito (2001) Virtual Teaching Based on Hand Manipulability for Multi-Fingered Robots, Proc. 2001 IEEE Intl. Conf. on Robotics and Automation, pp. 1388-1393, Korea.
4. Bruno M. Jau (1995) Dexterous Telemanipulation with Four Fingered Hand System, Proc. 1995 IEEE Intl. Conf. on Robotics and Automation, pp. 338-343.
5. Michael L. Turner, et al. (2000) Development and Testing of a Telemanipulation System with Arm and Hand Motion, Proc. of ASME IMECE DSC-Symposium on Haptic Interfaces, pp. 1-8.
6. Jiting Li, Wenkui Su, Yuru Zhang, Weidong Guo (2004) Vision-Based Grasp Planning System for Dexterous Hands, Proc. of Intl. Conf. on Intellligent manipulation and Grasping, July.
7. Salmond, D. (2001) Target Tracking: Introduction and kalman tracking filter, Algorithms and Applications, IEE Volume Workshop, vol.2:1/1 - 1/16, Oct.
8. Rong Li, X.; Jilkov, V.P. (2003) Survey of maneuvering target tracking. Part I. Dynamic models, IEEE Transactions on Aerospace and Electronic Systems, Vol.39, Issue 4:1333 - 1364 ,Oct.
9. LIU Gang, PAN Quan, ZHANG Hong-cai (2000) A Study of Tracking Filter Initiation Algorithm Based on 2-Step Estimation, Journal of system simulation, Vol. 14 No. 7, pp.849~851, July.

The Investigation of Control System and Security for a New Medical Robot

C. Tang, D. Liu, and T.M. Wang

School of Mechanical Engineering and Automation, Beihang University,
Beijing 100083, P.R. China, 010-82338271
tangcanwxj@me.buaa.edu.cn

Abstract. Currently, widespread clinical application of medical robots is hindered by not only low security and operation efficiency but also the high cost for robot control system. In response, a framework of medical robot control system based on PLC was presented according to the clinical requirement of medical robot. In terms of the design process of function analysis, the hardware and software structures were confirmed. Based upon the concern of safety problems that the operation system of medical robot was confronted with, the safety strategy performed in the system and orientation precisions of the system were discussed in detail. The specific safety schemes responding to the above problems were put forward. Clinical experimentations were accomplished in the Neurosurgery Institute of General Navy Hospital. The stable performance was verified.

1 Introduction

The last decade witnessed rapid development of medical technology, robot technology, computer technology, and also witnessed the remarkable achievement about the investigation and application of medical robot technology. The PAKY-RCM [1] and ORTHODOC [2] systems in America, the NeuroMate[3] system in Japan, the ACROBOT [4] in France are all advanced medical robot systems . At the beginning, the traditional industry robot served as medical robot. But industry robots could not satisfy the requirement of surgical robot system [5]. The medical robot has the characteristics, such as high security and error-tolerance, pursuing absolute orientation precise and not permitting using learning-programming to realize motion control. There is no doubt that the operation needs high-performance control system. Therefore, the system research on the security and reliability is indispensable for the development of medical robot.

The singlechip and multi-axis motion controller are traditional controllers(PMAC) of robot. The singlechip has shortcomings including running slowly, fewer bits and no high reliability etc. So it is not suitable for this application. PMAC can realize multi-axis running simultaneously and the interpolation of spatial curve. But it has some limitation, such as high cost, close infrastructure, difficult maintenance etc. The embedded controller not only has module structure and independent servo units mutually, but also can make PC link with various ports. And it has other merits, such as

T.-J. Tarn et al. (Eds.): Robot. Weld., Intellige. & Automation, LNCIS 362, pp. 437–444, 2007.
springerlink.com

multi-axis running simultaneously and the trajectory interpolation, good expansibility and little volume etc. However, at the present time, the embedded controller couldn't be introduced in the control system of medical robot because of no clinical application case. In this project the main part of control system is the PLC (Programmable Logic Controller), which is used extensively in industry enterprises, and the prominent characteristics of which are small dimension, convenient maintenance, high reliability, etc. In particular, the cost of system could be reduced at great extent by integration with step motor. Accordingly there is a wide industrialization foreground.

My work focuses on: the structure design of the control system; hardware and software development; clinical experimentation. The hardware structure and software logic flow of the control system are ascertained. The safety schemes of robot operation system are given, the correctness is validated by clinical operation. This paper is comprised of five segments, including the introduction, architecture of the control system, the safety schemes, the clinical application and conclusion.

2 Architecture of the Control System

2.1 System Function Analysis

In this system, computer reads and disposes the medical CT or MRI data with the DICOM mode, and then reconstructs the 3D focus area of patient with VTK (visualization tool kit). The doctor performs fore-operation layout in the operation software, including drawing the sketch of focus, determining the puncturing path and focus target. In terms of path layout, program calculates automatically reverse solution of kinematics, and drives the medical robot to reach the target.

The integration of computer and programmable logic controller, the capability of which is predominant, has great vitality in future market [6]. The precise control of position and posture for the 5- DOF robot is the primary task of control system, where there is no need for consideration of robot motion trajectory and multi-axis running simultaneously of 5-DOF robot. The control system also could determine the zero-position of all joints and memorize the actual position of robot joints during moving. Simultaneously with operation security considered, other functions, such as the current limitation, anti-EMI, urgent stop, displacement restriction, and the avoidance of error-operation or remote signal interference are introduced into the robot system.

2.2 Hardware Structure

As shown in figure 1, via RS232C/485 port, the communication between PC and PLC is set up. The reading and writing operation could be realized. The system executing motor is step motor. PLC could provide two–way output pulse. But the robot has five joints. That's to say, PLC could not implement five joints control simultaneously, at most could make two joints to move at one time. For achieving five joints control, there is a switch for motor pulse exchange between the output port of PLC pulse and step motor driver. Besides of position limitation and zero-position confirming, the system

imports new photoelectrical navigation equipment, this could improve the security and reliability of the system.

2.3 Program Analysis

In the process of software design some principles are complied with, including structure modularization, driving standardization and system reconstruction. The software of control system comprises of two parts, one is PLC program, namely trapezoid graph, the other is super-layer program, namely VC program. Figure 2 is the architecture of super-layer computer program, figure 3 is the frame of PLC program. The motion control program is embedded in the layout software. The functions of other parts, such as photoelectrical navigation and orientation, mark points registration, image disposal, would not be changed. The various function modules of robot control system are integrated in layout software.

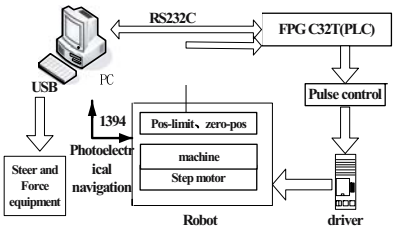

Fig. 1. Architecture of the control system

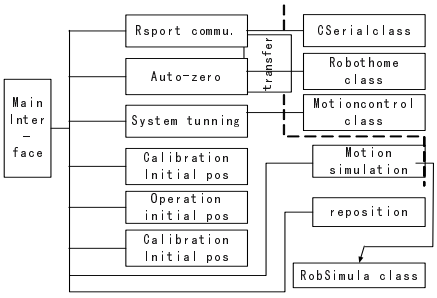

Fig. 2. Configuration of the control module

The trapezoid graph has some function modules, including single-joint moving, continuous moving, returning logic zero position, pulse accumulation and memorization. After motion data sent out from PC, the various function modules of the trapezoid graph are triggered according to some logic relationship, and then the motor's precise motion control is to be achieved.

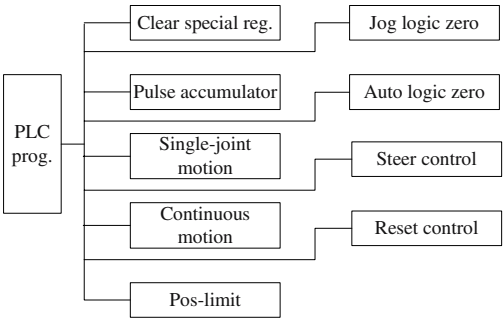

Fig. 3. Structure of the PLC program

3 Safety Schemes Performed in the System

Because the medical robot contacts the patient directly, it is a great important task to guarantee robot's safety in the process of moving and puncturing. Here the following main safety factors of control system are to be taken into account.

First, we try hard to decrease the interference. The existence of all kinds of interferences in the system is the main reason that influence reliable running of PLC system [7]. Second, during robot moving, the puncturing needle end would contact patient or operator directly, that's to say, there is some interference between the needle and patient. Therefore it is very necessary to implement distance monitoring so as to enhance robot security. Furthermore, owing to the restricted operation space of robot medical, when some abnormal high velocity occurred, it is very hard for operator to get response and take an effective safeguard. Thus the velocity control is also important in medical robot operation. The velocity control is implemented by encoder, which isn't narrated in detail in the following section. Moreover, if there is a relative moving between patient and the operation bed during camera calibration and robot puncturing, the orientation precise of robot drops. Consequently the safety of patient is to be threatened. So it is essential to monitor patient's moving. The last, for needle's contact avoidance with key tissues and nerves and blood vessels in patient's brain, guaranteeing the orientation precise of medical robot is much more important than all above problems. Therefore, how to improve the orientation precise is one of security schemes.

3.1 To Decease the Interference

The interior interferences include signal earthing and system earthing improperly. The exterior interferences include: high (low) frequency radiation interference. Because of the open(close) of relay triggers or other switches; the interference from the fluctuation of voltage and high-degree harmonic wave; interference from around electromagnetic field that intrudes into the control system via radiation or capacitance coupling; signal distortion or aberration on account of the bad shielding of signal line or the shielding layer damaged.

According to above interference resource existed probably, some efficient approaches is adopted and brought into effect in the medical robot system. Firstly, according to the principle of high security requirement for medical equipment, the isolated transformer is introduced in the system so as to decrease power input interference and to guarantee person's safety. Secondly, adopting transistor power supply and the separating of sensor's signal resource from controller's power are also feasible and effective. The last, the interference is to be alleviated by parallel connecting of a continuous-current diode or a large capacitance in two sides of the load.

3.2 To Supervise Patient's Moving

As shown in figure 4, whether or not the relative displacement between patient and the operation bed exists is to be supervised with CCD camera, the precondition of realization of which is that object tracking template is fixed on patient's head. If the displacement overruns the designated boundary, the monitoring system gives an alarm to operator automatically. At the same time, not only system would mention the

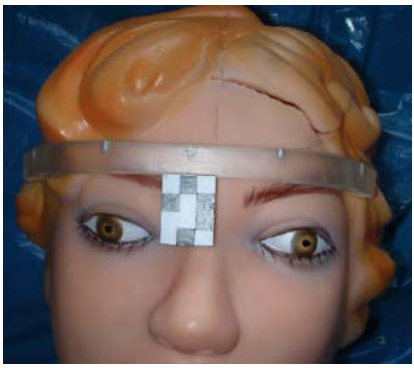

Fig. 4. The object tracking with a template

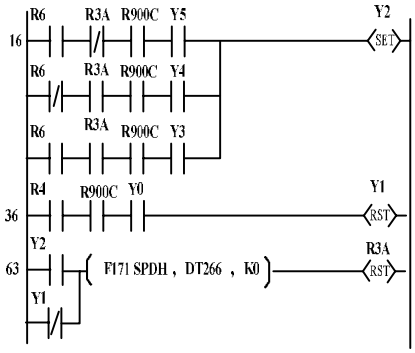

Fig. 5. Backup program of the trigger

operator whether the spatial transformation and calibration is rebuilt, but also to modify spatial transformation is so convenient that only by the transformation marks on the head recaptured the modification of the spatial transformation could be accomplished. In this way, the displacement supervising system is formed, the purpose of which is to vision monitoring and alarm of the target displacement.

3.3 To Enhance the Orientation Precise

The realization of precise orientation of position and posture for medical robot is the original intention and purpose. There are some main factors that influence the precision, including machine's precision(such as machining and assembly precision, calibration precision of D-H parameter, joints clearance, the arm's distortion), the precision of vision calibration(registration), motion controlling precision, spatial mapping precision(transformation), the precision of the operation layout and medical image data disposal. Here is how to elevate the orientation precision of system in terms of motion control and operation layout.

Thanks to the improvement of the robot's wrist structure, the kinematics function has the analytical solution. Compared with the iterative method of calculating reverse solution, there are many advantages such as predigesting the process of calculation, upgrading the speed and precision of computer calculation, enhancing the real-time motion control and the efficiency of the operation. Simultaneously, to set up software encoder in PLC program, the function of which is to display the actual current position of all joints and to be groundwork of the latter software position limitation, could insure the reliability of robot orientation.

The operation layout is one of the main content for the investigation of medical robot operation system. The layout precision of puncturing path influences directly the precision of operation, and the simplification of path layout gives convenience to the doctor or operator. Therefore the specification of medical robot system for directional puncturing is analyzed. The medical image data with DICOM format is disposed, and the new solution of the operation layout based on Euler-angle transformation is put forward. The fast reading and input of CT or MRI medical image data based on DICOM is implemented, which greatly simplifies the process of matching and

calibrating CT or MRI image array during operation, reduces the error come from manual segmentation and disposal.

At the same time, each new puncture point is to be adjusted in terms of the position of the last puncture point, so as to obtain the position relationship between the new point and the original point (as shown in figure 6). In this way, the doctor has a definite object in view during the operation path layout, which gives an avoidance of eyeless and stochastic path adjustment once and once again, provides the reliable evidence for the simplification of doctor's operation and rapid determination of the puncturing path. In summary, the automatic match for image and the rapid and simple layout for operation path enhance the orientation precision.

3.4 To Make Redundancy and Backup

The capacity of the interior relay is up to 1560 contact points. There are 50 actually used in this system. In the clinical application, it is possible that some contacts goes to failure for some reason [8]. When this problem occurred, there are two approaches to be adopted, one is to replace the small relay in PLC, and the other is to substitute the contact point not used for damaged contact point with a hand-hold programming instrument. At the lack of the above condition of solution, software backup by using redundant input/output contact points in program design is to be put into practice, so as to insure safe running of control system. The figure 5 shows that the backup input contact points are R6 and R3A, the backup output contact are Y1 and Y2. If the contact Y4 is damaged, the contact R3A is to be triggered and Y0 is open, thereby it could obtain a backup of Y4.

In addition, there are some other safety schemes in this system, for example, cutting down the interference of exterior wiring(such as suspending the shielded wire at input/output sides, earthing at controller's side); the signal wire and power wire are collocated alone, and try your best to keep away from high voltage loop and master loop; After robot arriving at the target point, the pulse output is cut off immediately, so as to avoid the danger brought from the robot fast moving due to an error manipulation or the abnormal signal of tele-operation.

Fig. 6. Medical robot operation system in Yan'an city

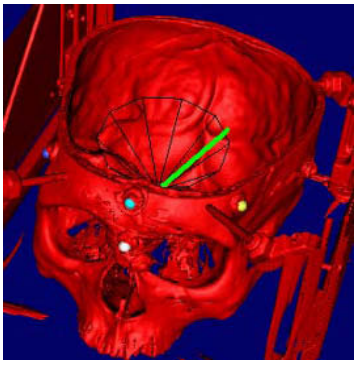

Fig. 7. Surgical operation layout based on Euler angle

4 The Clinical Application

The robot operation system is good at treating many diseases, which involve in craniopharyngioma, encephalic multi-occupation, cerebral hemorrhage, cerebral infarct etc. From 2005 up to now, in the Medical Institute of General Navy Hospital, the robot system has accumulatively performed 43 clinical operations. And in the affiliated hospital of Yan'an college, the first Chinese internet operation for the 69-year-old patient suffered from cerebral hemorrhage was implemented successfully, which was assisted by remote medical robot system in Yan'an and was controlled by the General Navy Hospital in Beijing. Figure 7 showed that a patient suffered from the encephalic multi-occupation was in the operation, which implemented a local anaesthesia, drew out 12-ml pathological bursa liquid, and injected the remedying medicament. After operation, the patient could step down the operating table by himself.

5 Summary and Future Work

Compared with the former medical robots, the main characteristics of this robot system are the following. First, the cost of system development is much lower than the medical robots exploited before. Second, serial effective safety methods are introduced in the system, which gives reliability and safety guarantee for the clinical operation. Third, the interface is fit for the doctor's practice, which results in convenient operation and the remarkable advancement of operation efficiency.

In our medical robot system there are some problems need to improve. Firstly, the volume or dimension of robot is very large, which occupies much workspace. It is similar to an industry robot and is not very suitable for surgery operation. Secondly, the robot dexterity is very low, which brings some inconvenience to the doctor or operator for the operation path layout. Thirdly, there is no ideal control algorithm to enhance the motion accuracy. All above problems are to be solved in near future.

References

1. Funda, J., K. Gruben, B. Eldridge, S. Gomory, and R. Taylor. "Control and evaluation of a 7-axis surgical robot for laparoscopy", in Proc 1995 IEEE Int. Conf. on Robotics and Automation. 1995. Nagoya, Japan IEEE Press May.
2. Mavroidis, C., Dubowsky, S., Drouet, P., Hintersteiner, J., and Flanz, J., A Systematic Error Analysis of Robotic Manipulators: Application to a High Performance Medical Robot, Proceedings of the 1997 International Conference in Robotics and Automation, 1997.
3. Gary S. Guthart, J. Kenneth Salisbury, The Intuitive Telesurgery System: Overview and Application□Proc. of the 2000 IEEE International Conference on Robotics & Automation San Francisco, CA, April 2000
4. Harris, S., Lin, W., Hibberd, R., Cobb, J., Middleton, R., and Davies, B., Experiences with robotic systems for knee surgery, in Proc. of the CVRMed-MRCAS '97, Grenoble, France, 1997.

5. Mengdong Chen, Tianmiao Wang, Qixian Zhang. The Research and Development of Medical Robot System. Biomedicine Engineering Fascicule of Foreign Medicine. 1998. 21(4): 193-202.
6. Wei Zhang. A Study on PC/PLC Elecmachanical Control System. The Master dissertation of Northwestern Polytechnical University, 2003.
7. Shuli Chen, Hongjuan Chou. The Approaches to Enhance the Reliability of PLC System. China Science and Technology Information, 2005(16)：168～176.
8. Jianxiong Liang, Shuixian Deng.The Design of high reliable PLC Control System. Electric Application, 2005.24(9)：46～48.

The Extraction of Fuzzy Rules and Control for Deposit Dimension in Spray Forming Process

Y.D. Qu[1], S.B. Chen[2], C.S. Cui[3], R.D. Li[1], Z.T. Ma[1], and C.X. Li[1]

[1] School of Material science and engineering, Shenyang University of Technology, Shenyang 110023, P.R. China
[2] School of Material science and engineering, Shanghai Jiaotong University, Shanghai, 20030, P.R. China
[3] School of Material science and engineering, Harbin Institute of Technology, Harbin 150001, P.R. China
quyingdong@163.com

Abstract. A fuzzy controller (FC) was developed to improve deposit dimension accuracy in spray forming process, fuzzy rules of FC were extracted from experimental sample data by dynamic clustering method. Simulation results show that fuzzy controller is available to regulate deposit dimension, main advantage of FC is it has a stronger adaptability for nonlinear process control than PID controller, and FC of identical structure has satisfying control performance for different predetermined target values. FC closed-loop control experimental results show that average deposit thickness is 5.22m in steady growth period, average error between actual size and 5.5mm target value is 0.28mm, and RMS (mean square root) is 0.31mm.

1 Introduction

Near-net shaped preform is one of main advantage for spray forming technology [1, 2], which is more and more interested by many researchers recently[3,4]. As a rule, improving deposit dimension accuracy can obtain well shaped preform. However, it is difficult to producing accurate dimension preform due to there are a lots disturbance and uncertain factors in spray forming process, therefore automatic technology is required to resolve this problem. Kang has introduced an on-off controller to regulate deposit height, control strategy seemed too simple, therefore deposit dimension error is evident[5]. Some references mentioned that fuzzy control technology has been used for deposit dimension control, yet few details was presented[6]. The authors of the paper has been used PID controller to improve deposit dimension accuracy, experiment results show that controle performance is unsatisfied[7]. In order to further improve deposit dimension accuracy, a fuzzy controller is developed in this paper.

2 Fuzzy Rules Recognition of Deposit Dimension

Extracting fuzzy rules is key step for design fuzzy controller, dynamic clusting pattern recognition method is used to do this work, the advantage of dynamic clusting method

T.-J. Tarn et al. (Eds.): Robot. Weld., Intellige. & Automation, LNCIS 362, pp. 445–451, 2007.
springerlink.com

is that clustering process can be performed by optimization. Here, some variables described fuzzy rules are presented firstly, deposit dimension error *E* and error changing *CE* are chosen as input variable of fuzzy rules, deposit translating speed *U* is chosen as output variable of fuzzy rules. There are 7 fuzzy subsets for *E, CE* and *U* respectively: *NB*(negative big), *NM*(negative middle), *NS*(negative small), *ZO*(zero), *PS*(positive small), *PM*(positive middle), *PB*(positive big). Extracting of fuzzy rules by dynamic clustering method can be described as:

Step.1: Predetermining initial clustering center of subsets of *E* and *CE*

As shown in table.2.1, initial clustering centers of fuzzy subsets of *E* and *CE* are expressed with $EC_T(i)$ and $CEC_T(j)$ respectively, $i, j=1,2\cdots7$, T is iterative index.

Table 2.1. Initial clustering centers of fuzzy subsets E and CE

Number	1	2	3	4	5	6	7
Fuzzy subset	*NB*	*NM*	*NS*	*ZO*	*PS*	*PM*	*PB*
Initial clustering centers of subsets of *E*	-0.98	-0.58	-0.28	0	0.28	0.58	0.98
Initial clustering centers of subsets of *CE*	-0.75	-0.4	-0.15	0	0.15	0.4	0.75

Step.2: Calculating similarity distance

685 sample data, extracted from PID and FPID control experiments, are used to calculate similarity distance, every set of sample data are expressed with $\{e_k, ce_k, cu_k\}$. The similarity distance is defined as:

$$D((e_k, EC_T(i)),(ce_k, CEC_T(j))) = \sqrt{(e_k - EC_T(i))^2 + (ce_k - CEC_T(j))^2} \tag{1}$$

In equation (1), $i, j=1,2\cdots7$. If a minimum distance is found out, i.e :

$$D((e_k, EC_T(l)),(ce_k, CEC_T(m))) = \min_{\substack{i=1\cdots7 \\ j=1\cdots7}} \sqrt{(e_k - EC_T(i))^2 + (ce_k - CEC_T(j))^2} \tag{2}$$

Then $e_k \in EC(l)$, $ce_k \in CEC(m)$.

Step.3: Determining new clustering centers.

New clustering centers can be calculated based on clustering result obtained from *step2*.

$$EC_T(i) = \frac{1}{n_i}\sum_{l=1}^{n_i} e_k^l \qquad (i = 1,2\cdots7) \tag{3}$$

$$CEC_T(j) = \frac{1}{n_j}\sum_{l=1}^{n_j} ce_k^l \qquad (j = 1,2\cdots7) \tag{4}$$

where n_i is sum of that e_k belonged to *EC(i)*, n_j is sum of that ce_k belonged to *CEC(j)*; e_k^l is sample data belonged to *EC(i)*, ce_k^l is sample data belonged to *CEC (j)*.

Step4: Calculating clustering criterion $J_c(T)$

$$J_c(T) = \sum_{i=1}^{n} \left\{ \left(e_i^l - EC_T(l)\right)^2 + \left(ce_i^m - CEC_T(m)\right)^2 \right\} \tag{5}$$

where $e_i{}^l$ is error, $e_i{}^l \in EC(l)$; $ce_i{}^m$ is error changing, $ce_i{}^m \in EC(l)$ .If $|J_c(T)-J_c(T-1)| \leq \varepsilon$, then dynamic clustering process is finished, ε is iterative criterion, its value is predetermined as 0.045. After 14 iterative process, new clustering centers of each subsets of *E* and *CE* are calculated, as shown in Table.2.2.

Table 2.2. New clustering centers of fuzzy subsets *E* and *CE*

Number	1	2	3	4	5	6	7
Fuzzy subsets	*NB*	*NM*	*NS*	*ZO*	*PS*	*PM*	*PB*
Clustering centers of *E*	-0.852	-0.617	-0.295	-0.072	0.324	0.543	0.769
Clustering centers of *CE*	-0.837	-0.427	-0.198	0.087	0.126	0.385	0.722

Clustering centers of fuzzy subsets of *U* are shown in Table.2.3, *UC(i)* is clustering center of i^{th} fuzzy subsets. *UCN (m)* is output of m^{th} fuzzy rule, which can be calculated as:

$$UCN(m) = \frac{1}{n_{ij}} \sum_{k=1}^{n_{ij}} cu_k^{ij} \quad m = 7(i-1) + j, (i = 1,2 \cdots 7; j = 1,2 \cdots 7) \tag{6}$$

where n_{ij} is sum of that sample data satisfied error belonged to *EC(i)* and error changing belonged to *CEC(j)*, $cu_k{}^{ij}$ is corresponding output value of fuzzy rules.

Table 2.3. Clustering centers of all fuzzy subsets of *U*

Number	1	2	3	4	5	6	7
Fuzzy subsets	*NB*	*NM*	*NS*	*ZO*	*PS*	*PM*	*PB*
Clustering center of *UC*	-7.852	-4.648	-1.675	0.054	1.328	4.291	7.825

Comparing *UCN (m)* with every center of fuzzy subsets of *U* one by one, i.e, calculating distance *D(m,i)*:

$$D(m,i) = \sqrt{(UCN(m) - UC(i))^2} \qquad i = 1,2,\cdots 7 \tag{7}$$

If $D(m,l) = \min_{i=1,2\cdots 7} \sqrt{(UCN(m) - UC(i))^2}$, the output of fuzzy rule is belong to the l^{th} fuzzy subset of *U*. All 49 fuzzy rules is shown in table.2.4.

Table 2.4. Rules table of fuzzy controller for deposit dimension in spray forming process

CU \ *CE* / *E*	NB	NM	NS	ZO	PS	PM	PB
NB	PB	PB	PB	PM	PS	ZO	ZO
NM	PB	PB	PM	PM	PS	ZO	ZO
NS	PM	PM	PM	PS	ZO	NS	NS
NO	PM	PM	PS	ZO	NS	NS	NM
PS	PS	PS	ZO	NS	NM	NM	NM
PM	ZO	ZO	NS	NM	NM	NB	NB
PB	ZO	ZO	NS	NM	NB	NB	NB

3 Design of Fuzzy Controller (FC)

After extracting fuzzy rules, fuzzy controller can be designed based on these fuzzy rules. For convenient on-line controlling, fuzzy controller is described by look-up table finally.

Fuzzification and unti-fuzzification process between real value and fuzzy number are required. Fuzzification coefficients *Ke*、*Kce* are used to map real value *e* and *ce* into fuzzy number, and unti-fuzzification coefficient *Kcu* is used to map fuzzy number *cu* into real value. Real range of *e*、*ce* and *cu* are predetermined according experiments, they are in [-2mm, 2mm], [-1mm, 1mm] and [0.3mm/s, 1.5mm/s] respectively. Fuzzy numbers of *E* and *CE* are predetermined as {-6,-5,-4,-3,-2,-1,0, 1, 2, 3, 4, 5, 6}, fuzzy numbers of *CU* are predetermined as {-7,-6,-5,-4,-3,-2,-1,0, 1, 2, 3, 4, 5, 6,7}. *Ke*、*Kce* and *Kcu* are calculated as :

$$\begin{aligned} \text{Ke} &= \frac{6-(-6)}{2-(-2)} = 3 \\ \text{Kce} &= \frac{6-(-6)}{1-(-1)} = 6 \\ \text{Kcu} &= \frac{1.5-(0.3)}{7-(-7)} = 0.875 \end{aligned} \tag{8}$$

Zadeh's fuzzy interfere is used to convert fuzzy rule into look-up table, as shown in table.3.1. During one control cycle, *e* and *ce* are mapped to fuzzy number by *Ke*, *Kc*, thereafter find corresponding fuzzy number of *cu* from table 5, real control variable *cu* can be calculated by multiplying fuzzy number of *cu* with *Kcu*.

Table 3.1. The look-up table of fuzzy controller

	-6	-5	-4	-3	-2	-1	0	+1	+2	+3	+4	+5	+6
-6	7	7	6	6	6	5	4	2	1	1	0	0	-1
-5	7	6	6	5	5	5	4	2	1	1	0	-1	-1
-4	6	6	6	5	4	4	4	2	1	0	-1	-1	-1

Table 3.1. (*continued*)

-3	6	5	5	5	4	3	3	1	0	0	-1	-1	-2
-2	5	4	4	4	4	3	2	0	-1	-1	-1	-2	-2
-1	4	4	4	3	3	3	1	0	-1	-2	-2	-2	-2
-0	4	4	4	3	2	1	-1	-2	-2	-3	-4	-4	-4
+0	4	4	4	3	2	1	-1	-2	-2	-3	-4	-4	-4
+1	2	2	2	1	0	0	-2	-3	-3	-3	-4	-4	-4
+2	1	1	1	0	-1	-1	-2	-3	-4	-4	-4	-4	-5
+3	1	1	0	0	-1	-2	-3	-3	-4	-5	-5	-5	-5
+4	0	0	-1	-1	-1	-2	-4	-4	-4	-5	-6	-6	-6
+5	0	-1	-1	-1	-2	-2	-4	-5	-5	-5	-6	-6	-7
+6	-1	-1	-1	-2	-2	-2	-4	-5	-6	-6	-6	-7	-7

4 FC Simulation for Deposit Dimension Control

Based on designed fuzzy controller, simulation results at three predetermined target value are presented, as shown in Fig.4.1. Fig.4.1a) shows deposit dimension curve when predetermined target value is 4.5mm: max-overshoot is 0%, response time is 24s, steady-state error is 0.16mm; Fig.4.1b) shows deposit dimension curve when predetermined target value is 5.0mm: max-overshoot is 7.96%, response time is 23s, steady-state error is 0.18mm; Fig.4.1(c) shows deposit dimension curve when predetermined target value is 5.5mm: response time is 26s, max-overshoot is 0%, steady-state error is 0.13mm.

Above simulation results show that FC is available for deposit dimension control at three different predetermined target value. Compared FC with PID controller introduced in ref[7], it shows that steady-state error and response time of FC is not good as PID controller, but overshoot of FC controller are better; The main advantage of FC is that it has a stronger adaptability for nonlinear process control than that of PID controller, and FC of identical structure has satisfying control performance for different predetermined target values.

5 FC Closed-Loop Control Experiment for Deposit Dimension

For testing control performance of fuzzy controller, variation of metal flow rate is chosen as disturbance. The section image of tubular deposit produced with disturbance is shown in Fig.5.1, it shows that whole deposit preform undergoes two phases: Ascending and decreasing phase. The steady-state deposit dimension is never appeared due to existence of disturbance.

Fig.5.2 shows the section image of tubular deposit produced by FC control experiment at 5.5mm target value. The variation of deposit thickness comprises three phases: Ascending phase, descending and steady phase. Compared Fig.5.1 with Fig.5.2, it shows that there exist steady phase in Fig.5.2. Average dimension in steady phase is 5.22mm, and RMS is 0.31mm.

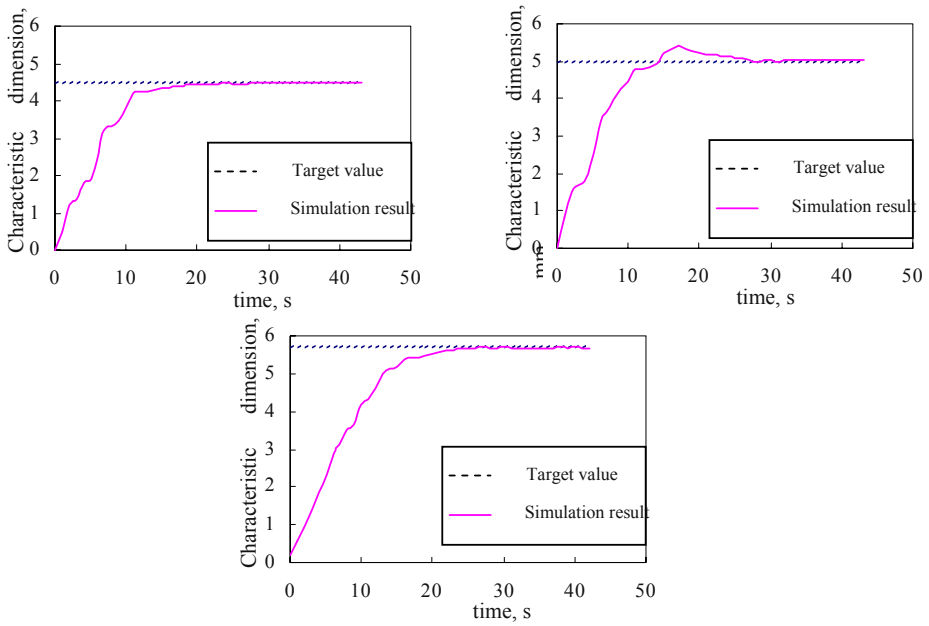

Fig. 4.1. Simulation curves of deposit dimension with using Fuzzy controller at different target value a) 4.5mm target value b) 5.0mm target value c) 5.5mm target value

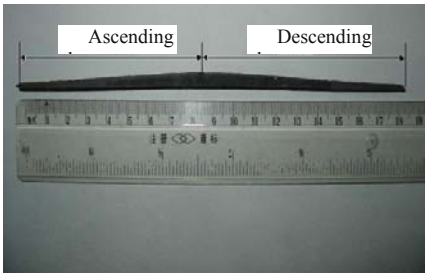

Fig. 5.1. Section image of tubular deposit with disturbance

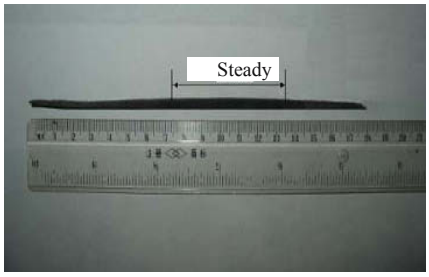

Fig. 5.2. Section image of tubular deposit produced by fuzzy closed-loop controller

6 Conclusions

For improving deposit dimension accuracy, a fuzzy controller is developed based on extracted 49 fuzzy rules by using dynamic clustering pattern recognition method, and look-up table is present for describing fuzzy controller. FC simulation results show the main advantage of FC is it has a stronger adaptability for deposit dimension control, and FC of identical structure has satisfying control performance for different predetermined target values than PID controller, further. FC closed-loop control

experiment result demonstrate steady growing phase appear on deposit preform with FC controller, and well shaped preform is obtained.

Acknowledgements

This work is supported by National Defense Key Lab of Metal Precision Hot Processing fund No.5147040101JW0301, Liaoning Province Education Administration fund No.05L307 and Liaoning province doctor start-up fund No.052372.

References

1. Grant P S. Spray Forming (1995) Progress in Materials Science (39)：497-545.
2. Lawley A(2000) Melt Atomization and Spray Deposition-Quo Vadis . Spray Deposition and Melt Atomization. Bremen, Germany, pp3-15.
3. Seok H K, Yeo D H, Oh K H et al (1998) A Three-Dimensional Model of the Spray Forming Method. Metallurgical and Materials Transaction B.29B: 699~709.
4. Fu X W, Zhang J S , Yang W Y, Sun Z Q (1998) Numerical Method for the Deposition Profile in Spray Forming Process. Proceeding of the third Pacific Rim International Conference on Advanced Materials and Processing, Honolulu, Hawaii, pp1713~1718.
5. Kang Z T, Chen Z H, Yan H G, et al (2000) Application of programmable controller in multi-layer spray deposition technology. Powder metallurgy technology(Chinese) 18(2):98-101
6. Moran A L, White D R (1999) Developing Intelligent Control for Spray Forming Processes. JOM: 21~24.
7. QU YD, CUI CS, CHEN SB et al (2005). PID control of deposit dimension during spray forming. Materials Science Forum, 475-479: 2811-2814.

Multi-modal Virtual Reality Dental Training System with Integrated Haptic-Visual-Audio Display

Dangxiao Wang, Yuru Zhang, and Zhitao Sun

Robotics Institute, BeiHang University
Beijing, P.R. China, 100083
hapticwang@buaa.edu.cn, yuru@buaa.edu.cn

Abstract. Multi-modal signal fusion is an important way to improve immersion and fidelity of virtual reality training systems. With the help of a robotic arm, haptic device, it is possible to supply haptic-visual-audio display for training dentist. Architecture is firstly proposed to integrate different signals in a training system. High efficient sound synthesis algorithm is proposed based on hybrid combination of parameter identification from recorded sound signal, then use signal synthesis method to form final sound signal. Mapping method among audio, haptic and visual signal is proposed based on parameter mapping under various interaction status. Experiment based on Phantom desktop proves the stability of the rendering algorithm and the improved fidelity after adding audio feedback to current haptic-visual dental training system.

1 Introduction

Immersion is one important feature of virtual reality (VR) training systems. In order to improve immersion, fusion of multimodal signal display is one important method. In addition to traditional visual and audio display, haptic display technology emerged as a new kind of robotics technology to enhance the immersion of the VR systems. With haptic technology, it is possible to integrate visual, audio and haptic signal display in one system, which has great potential to improve immersion of VR training systems [1].

Dental training system is one kind of typical surgery simulation system. Several dental training systems have been developed in recent years [2]. However, existing dental training system only integrates visual and haptic signal display. It is necessary to add audio display to form a multimodal signal display system.

There are three problems to integrate audio, visual and haptic feedback:

- How to improve the fidelity of simulation during surgery simulation through sensory fusion?
- How to produce realistic audio signal while maintaining update rate of the simulation loop?
- How to maintain consistency among various signals?

Hiroaki Yano et al. proposed physical model based force and audio fusion method, which is realized by installing a speaker at the end tip of the haptic device [3]. Finite

T.-J. Tarn et al. (Eds.): Robot. Weld., Intellige. & Automation, LNCIS 362, pp. 453–462, 2007.
springerlink.com

element method is used to calculate the audio pressure and vibration status when contact or collision occurs between virtual objects. It can be used to simulate audio effect of object with different shape and different physical properties. H. Baier et al. established a distributed multi-modal tele-presence system, which is able to simulate virtual drill, virtual Ping-Pong tapping and virtual deformation etc [4]. K. Doel et al. used differential equation to solve audio parameters related with object's shape, material and collision point position, and pre-computation is used to meet real-time requirement [5]. William L. Martens tried to find the optimal delay time between force feedback signal and audio feedback signal, which is valuable to realize real-time fusion between force and audio feedback [6]. Robert Riener et al. incorporated phantom into multi-modal signal virtual reality to support medical training [1].

From literatures, it can be seen that dental training system with haptic and audio feedback is still a relatively new area. In current multimodal training systems, audio difference between different operations such as contact and burring operation can not be reflected. Furthermore, suitable status mapping between audio and haptic channels has not been defined clearly. It is difficult to find tradeoff of the audio model between real-time requirement and physical reality requirement.

The goal of this paper is to add audio feedback into an existing dental training system [2], and to maintain consistency among three kinds of signals.

The remainder of this paper is organized as follows. Section 2 gives architecture of multi-modal dental haptic simulation system. Section 3 introduces a hybrid model of audio signal. Section 4 introduces rendering method of audio signal and status mapping between force and audio signal. Section 5 gives experiment using phantom based platform. Section 6 gives conclusion and future work.

2 System Architecture

2.1 System Requirement

As figure 1 shows, there are different tissues with various physical properties inside tooth. As figure shows, there are different tools which can produce different effect on tooth. There are two typical operations: probing and burring.

The goal of the dental training system is to simulate probing and burring operation. Figure 2 gives physical components of the training system. Performance criteria can be summed up in three aspects:

1. Realistic force feedback, audio feedback and visual feedback should be supplied.
2. Consistency among different signal channels should be maintained.
3. The rendering algorithm should be high update rate to avoid vibration of the haptic device.

Existing dental training system integrated haptic and visual display has been established [2]. The focus of this paper is to add audio display and maintain signal consistency among different channels.

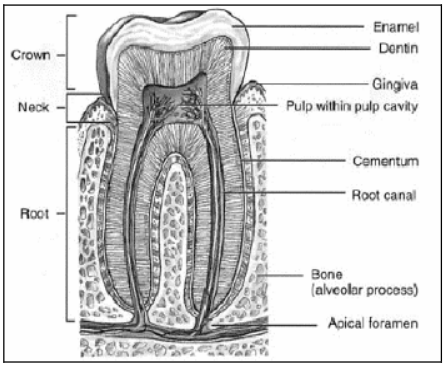

Fig. 1. Different tissues within tooth

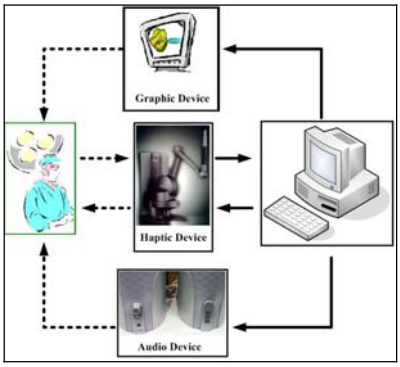

Fig. 2. Physical components of the training system

2.2 System Architecture Design

There are contradictions between fidelity and computation burden in multi-modal virtual reality systems. It is a challenge to design a method to produce realistic audio signal while not increasing computation load.

There are usually two selections for producing audio signals [3,7-9]. First is recording the sound during physical interaction process and then play the recorded audio file. Second is synthesizing an audio signal by several frequency components.

In the first method, it is difficult to get realistic simulation because sound effect depends on lots of variables, such as tool's orientation against tooth, tool's velocity, contact area etc. There are always parameters difference between playing scenario and recording scenario.

In the second method, the fidelity of the simulation result relies on frequency domain knowledge of the simulated sound.

Based on combination of above two methods, a hybrid sound synthesizing algorithm is proposed, which is a flexible and low-level controlling method to produce audio signal through memory cache. Furthermore, this method is simple enough to ensure high update rate requirement in haptic enabled simulations.

The hybrid sound-synthesizing algorithm combined experiment data and mathematical model is defined as following steps:

1. Sound signal recording: Record original sound during dental operations;
2. Main feature extraction: Extract critical frequency of the sound signal;
3. Sound synthesis: Synthesize sound owning several main features and other auxiliary information into final sound signal;
4. Signal Mapping: Mapping the sound signal with force signal;
5. Signal Rendering: Real-time rendering of signals, including sound playing to the speaker, force rendering to haptic device and graphical rendering to graphical monitor. Figure 3 gives detailed multi-modal signal computation and rendering principle of the system.

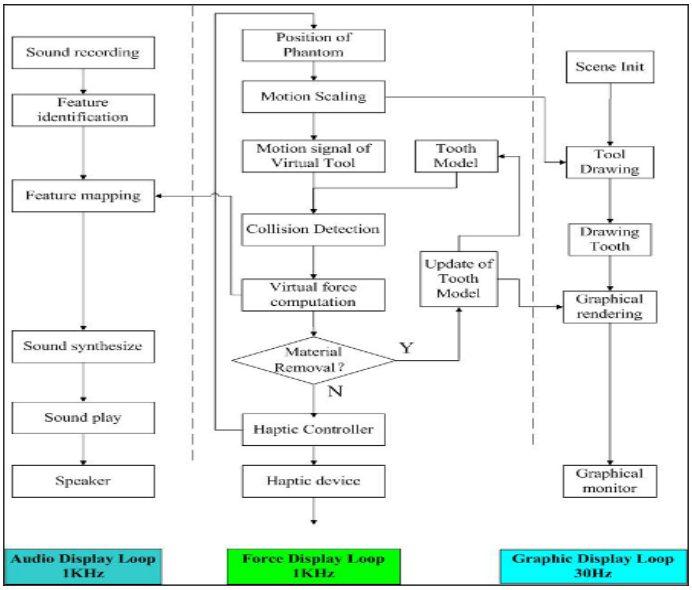

Fig. 3. Computation principle of the system

3 Hybrid Model of Audio Signal

3.1 Sound Signal Feature Extraction

In dental simulations, there are two kinds of typical operations, contact operation and burring operation. The above signal has constant magnitude, which is suitable to simulate continuous vibration, such as the rotating drill during burring operation.

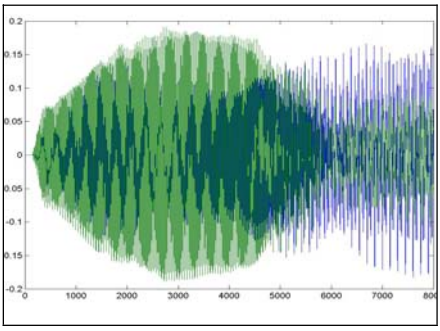

Fig. 4. Original recorded sound signal

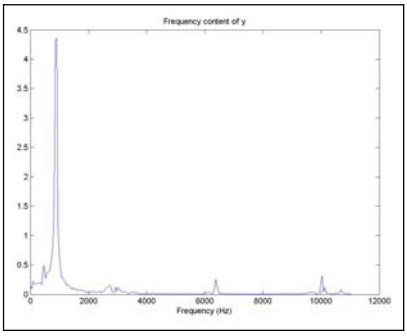

Fig. 5. Spectral analysis of sound signal

Sound during clinical dental operation process can be recorded as figure 4 shows. Use spectral analysis software such as MATLAB, it is easy to get magnitude of signal at different frequencies, which is illustrated in figure 5.

3.2 Sound Synthesis

Physically model based sound rendering is usually too complicated to ensure high update rate of the simulation loop. Hiroaki Yano used elastic finite element method to establish status between force and audio signal, which cannot meet 1KHz update rate of haptic simulation loop, therefore, vibration of the haptic device will occur.

The precise sound model depends on lots of factors, such as collision properties (magnitude of collision force, velocity and collision position), shape and size of the collided object, physical property of materials and environment noise etc. It is impractical to utilize such precise model in high update rate force display loops. Therefore, energy and physical property of materials is chosen to be main factors. Main frequency can be extracted by mathematical method. Furthermore, only magnitude-frequency characteristic are considered and phase-frequency characteristic is omitted. Because according to the conclusion that sensation characteristic of human's audio channel mainly exists in magnitude information while phase information is not the mainly influential factor [3].

In contact simulation, collision will occur during impact between probe and surface of the tooth. The impact will lead to impulse of sound signal. In order to simulate sound signal with attenuation, it is necessary to modeling the sound model with attenuation scale. Because the attenuation process involved many complex factors, there are two simplifications in our model. First, a linear attenuation scale is used instead of traditional exponential scale. Second, a white-noise signal is added to the attenuation signal to modeling environment noise.

The magnitude of the sound and force is discussed. Generally, sound signal under impact collision is attenuating as a damping free vibration model, which is a nonlinear model. Figure 6 gives the illustration of the model. In fact, it is computational costly to simulate above model, simplified linear attenuating model is proposed as figure 7. With same initial magnitude and same attenuating gradient, the effect of the sound is similar to human's ear. Figure 8 gives synthesizing result of the two kinds of signals. The computation of the attenuation scale will be discussed in next section.

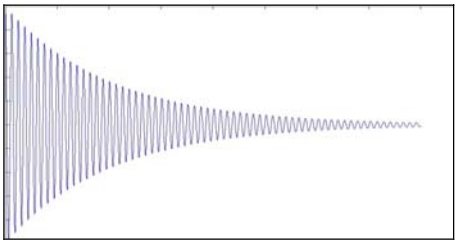

Fig. 6. Nonlinear attenuating model

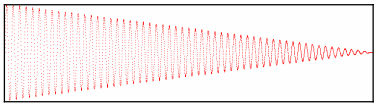

Fig. 7. Simplified linear attenuating model

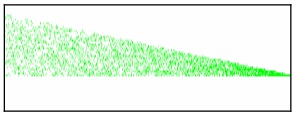

Fig. 8. Attenuation signal with white-noise

3.3 Implementation of the Sound Playing Algorithm

Another problem is to select programming method to tune the audio signal parameter. Microsoft DirectSound SDK is chosen as API [10]. The programming steps include:

1. Create IDirectSound interface using DirectSoundCreate() function;
2. Set Cooperative Level between program and various other application programs. DSSCL_NORMAL is selected to ensure maximum sharing of hardware among various application programs.
3. Create auxiliary cache using CreateSoundBuffer().There are usually several frequency components in most sound. Therefore, multiple auxiliary sound caches need to be established to save multiple frequency components. The first parameter of this function is DSBUFFERDESC to describe cache type, which is detailed in figure 2. The second parameter is IDirectSoundBuffer typed pointer.
4. DSBUFFERDESC is defined as:

```
typedef struct _DSBUFFERDESC {
    DWORD   dwSize;
    DWORD   dwFlags;
    DWORD   dwBufferBytes;
    DWORD    dwReserved;
    LPWAVEFORMATEX lpwfxFormat;
} *LPDSBUFFERDESC;
```

4 Rendering of Multi-modal Signal

In order to realize a multimodal display system, there are two basic problems:

- Real-time rendering of audio signal, force signal and graphical signal. Update rate is necessary requirement to ensure fidelity of the simulation. The rendering algorithm should be platform independent.
- Registration among three kinds of signals, which includes space registration and time registration. It is necessary to find a simplified Signal mapping method from force signal to audio signal.

According to the simplified linear attenuating model in section 3.2, there are several parameters within sound model: magnitude of the initial sound signal, frequency, attenuating gradient or attenuating time. Therefore, sound can be simplified into following model

$$S = \sum_{i=1}^{n_f} \frac{(\tau_i - t)}{\tau_i} a_i \sin(2\pi f_i t) + S_{WN}(t) \tag{1}$$

where τ_i is attenuating time. a_i is initial magnitude of sound signal at corresponding frequency f_i. n_f is interested frequency number. $S_{WN}(t)$ is white noise signal to simulate background sound from environment.

Kees van den Doel pointed out that initial magnitude of collision sound decides "timbre"---tone color of the sound [5]. It can be assumed every frequency component attenuates as exponential function and the corresponding time is

$$\tau_i = \frac{1}{\pi f_i \tan\phi} \tag{2}$$

where ϕ is internal friction coefficient of collided material, which is non-related with shape of the object, but only depends on material type.

The energy of the vibration is decided by the magnitude of the collision force. Relative magnitude of a_i can be computed by spectral analysis. Absolute magnitude of a_i can be regarded as magnitude of the sound signal.

Force model during contact and burring simulation can both be expressed by following unilateral constraint based spring force model in following equation

$$\vec{F}_e = \begin{cases} K_e^*\left(\vec{X}_h - \vec{X}_h^*\right) & \vec{X}_h \in CS \\ 0 & \vec{X}_h \in FS \end{cases} \tag{3}$$

where $\vec{F}_e$ is virtual force signal, $\vec{X}_h$ is position of haptic device, K_e^* is virtual stiffness. $\vec{X}_h^*$ is proxy point at the boundary of unilateral constraint [2]. CS, FS means constraint space and free space respectively.

According to Kees van den Doel's model, initial magnitude of sound signal is proportional to root square of energy. Because root square of energy is proportional to the collision velocity, therefore, initial magnitude can be regarded as proportional to velocity of haptic device, which is computed by differential operation on tip position.

With above sound model, it is possible to establish mapping between force and sound signal. As table 1 shows, the relative magnitude can be tuned according to the magnitude of collision force and velocity, i.e. energy of collision.

Table 1. Parameter mapping between force and audio signals

Operation	Force channel	Audio channel
Burring operation	Free space	Beep sound
	Constraint space	Sound with constant magnitude
	Collision velocity	Initial magnitude
	Material type	Sound frequency
Probing operation	Free space	No sound
	Constraint space	Sound with attenuating magnitude
	Collision velocity	Initial magnitude
	Material type	Sound frequency
	Material type, force directi`on	Attenuating gradient

5 Experiment

Client server architecture is adopted in experiment system illustrated in figure 9. The client is a computer for haptic and graphic simulation, and the server is the controller of the haptic device. Configuration of the client is given in table 2. Phantom Desktop is used as the haptic device and the computer communicates with the controller through parallel port. Callback mechanism of GHOST SDK [11] is utilized to enable 1KHz update rate of the haptic rendering loop.

There is a stylus button on tip of Phantom handle, which is used as a switch. When the button is pressed, Phantom is used to simulate a drill and burring simulation between drill and tooth is modeled. Otherwise, Phantom is used to simulate a probe and contact simulation between probe and tooth is modeled.

Fig. 9. Scenario of the experiment platform

Table 2. Hardware and software configuration

CPU	Intel P4 2.4GHz
Memory	Kinmax DDR 512M
Graphical Card	Geforce3 Ti4200
Operating system	Windows 2000
Language	Visual C++ 6.0
Packages	GHOST SDK, OpenGL, DirectSound SDK

Performance of the simulation algorithm is shown in table 3. In both contacting and drilling cases, the update rate of the simulation loop is higher than 1KHz. It shows the sound synthesis and rendering algorithm are efficient enough to maintain real-time performance.

As figure 10 shows, operators move handle of the Phantom, the virtual probe on the screen will move at same velocity. When the probe contacts surface of the tooth, concave and convex shape and stiffness of the tooth can be felt by human's hand realistically. Upon initial contact, crisp sound can be heard and the sound will become larger when the contact velocity and the collision force increases.

When the button is pressed, the virtual tool on the screen will be changed into a driller. In figure 11, gives burring scenario between spherical drill and the tooth. The sound of constant beep can be heard to simulate rotation of drill. When the drill is cutting against the tooth, the sound will become sharp and material is removed from tooth's surface. The sound will change according to the change of the burring force.

The quality of the force signal and sound signal are realistic enough to enhance the operation feeling. Time consistency between audio and fore feedback is below 20ms, which is enough to give synchronous feeling for the operator.

Table 3. Performance of the simulation algorithm

Max. force magnitude	3 Newton
Max. contact stiffness	1000 N/mm
Update rate	Above 1KHz
Sound quality	Beneficial for hint
Time consistency	< 20 ms

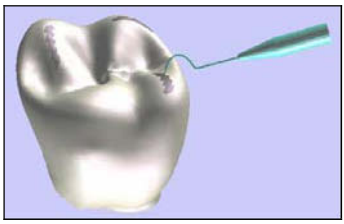

Fig. 10. Probing operation

Fig. 11. Burring operation

6 Conclusion

A Multi-modal signal feedback dental training system is developed and the method of integrating audio, haptic and visual signal is discussed. There are three contributions: a simplified sound synthesis model, status mapping between force and sound signal, typical operation simulation in dental training systems.

A simplified hybrid sound model is proposed by extracting the characteristic frequency from original sound signal, and then synthesizing several single frequency signals to produce a compound sound signal. The model solved the contradiction between realistic sound display and high update rate requirement.

Mapping method from force signal to sound signal is proposed based on characteristic parameters mapping. Consistency among audio, haptic and visual signal is ensured by using this method. Probing and burring operation are implemented by using the haptic-audio rendering method. The audio difference between two kinds of operation is apparent.

Experiment on Phantom desktop proves that the system can work stably, high update rate is ensured after adding sound rendering algorithm. Consistency among various modal can be maintained and fidelity has been improved by adding audio feedback to existing haptic-visual system.

Future work includes extending audio feedback to other operations such as drilling operation in dental training system, and studying the fusion of audio signal and tactile sensation, such as friction display.

Acknowledgement

This work is supported by the National Natural Science Foundation of China under the grant No. 50275003 and 50575011. Their support is greatly appreciated.

References

1. Robert Riener, et al. Phantom-Based Multimodal Interactions for Medical Education and Training: The Munich Knee Joint Simulator. IEEE Trans. On Information Technology in Biomedicine, 2004,8 (2)
2. Daniel Wang, et al., Cutting on Triangle Mesh Local Model based haptic display for dental preparation surgery simulation, IEEE Transaction on Visual. and Computer Graphic, No. 6, 2005, p671-683
3. Hiroaki Yano, Hiromi Igawa, et al. Audio and Haptic Rendering Based on a Physical Model. Proceedings of the 12th International Symposium on Haptic Interfaces for Virtual Environment and Tele-operator Systems. (HAPTICS'04) p. 250-257
4. H.Baier M., Buss F., et al. Distributed PC-Based Haptic, Visual and Acoustic Telepresence System — Experiments in Virtual and Remote Environments, IEEE Virtual Reality Conference. 1999 (VR'99) p.118
5. K. Doel , D. Pai. The Sounds of Physical Shapes, Presence, 1998, 7(4): pp. 382–395
6. William L. Martens, Wieslaw Woszczyk, Vibration in the Display of Impact Events in Auditory and Haptic Virtual Environments. In: October 2-3.2002. Proc. IEEE. Workshop on Haptic Audio Visual Environments, Ottawa, Ontario.pp.47-57
7. Lonny L.Chu. User Performance and Haptic Design Issues for a Force-Feedback Sound Editing Interface. Proceedings of 2004 New Interfaces for Musical Expression. pp.112-119
8. R. Iglesias, S. Casado, et al., Computer Graphics Access for Blind People through a Haptic and Audio Virtual Environment. Revista Integracion, 2004, 29(3):pp48-60
9. http://www.dcs.gla.ac.uk/~mcgookdk/multivis/workshop.html Workshop on haptic and audio interaction design, University of Glasgow, 2006.
10. MSDN, Microsoft developer network manual, 2001, http:// www.microsoft.com
11. GHOST® SDK Programmer's Guide Version 4.0, SensAble Technologies, Inc. 2002, http://www.sensable.com

Application of a Robot Assisted Tele-neurosurgery System

Liu Da, Wei Jun, and Deng Zhipeng

Robotics Institute, BeiHang University, Xueyuanlu 37, Beijing, 100083,
China, 0086-10-66477587
drliuda@yahoo.com.cn

Abstract. In this paper, a new robot assisted tele-nuerosurgery system is presented. This system is mainly divided into three parts: surgery planning system, visual navigation system and robot arm. The application of a new type of visual navigation instrument makes patient registration much more easy and accurate. The system has successfully performed three tele-neurosurgery operations between Beijing and Yan'an. Experiments and clinical trials approved this system is feasible and safe.

1 Introduction

Telesurgery enables the surgeon to remotely operate on the patient under the help of medical robot. It frees the surgeon from the operating room, protects the surgeon from the radiation of X ray or radical medicine, and provides rescue for patient in remote rural area, ship at sea, battlefield. For these benefits, there have been many research works on telesurgery in developed contries. Italy hold the first remote telesurgery with PUMA robot through satellites and optical fibers[1]. France effected the famous transatlantic telesurgery with ZEUS robot through virtual circuit communication on ATM network[2].

China has vast territory and presents medical development diversity between eastern and western regions. It is important to utilize and promulgate the advance medical technology taking advantages of telesurgery. Beihang University and Beijing Navy General Hospital designed and developed several robotics systems for neurosurgery which were all clinically applied[4, 5, 6]. We focus our system goal on designing and validating a safe and low-cost telesurgery system suitable for China. In Sep. 2003, we performed Beijing Navy General Hospital to Shenyang Central Hospital tele-neurosurgery operation with the NeuroMaster surgical robot via special ATM channel[3]. This paper introduces our new robotic system, which has been successfully completed there tele-neurosurgical operations between Beijing and Yan'an via share bandwidth common public internet, which is low-cost and has improved safe ensuring characteristics.

2 System Structure and Surgery Flow

Neurosurgery needs 4 processes to complete the surgery:

1. *Registration*: project image data into robot coordinate;
2. *Surgical planning*: define surgeon optimized access route;

T.-J. Tarn et al. (Eds.): Robot. Weld., Intellige. & Automation, LNCIS 362, pp. 463–470, 2007.
springerlink.com

3. *Robot control to implement plan route*: instruct robot arm to realize localization;
4. *Operation manipulation*: surgeon manipulation.

According to these requirements, we conclude the tele-stereotaxy system as a remote surgical plan and supervision system other than a tele-manipulation system. Experts at remote site take in charge of surgical plan, surgeons in operation room check and execute the operation under the supervision of the remote experts. System structure shows as Fig. 1.

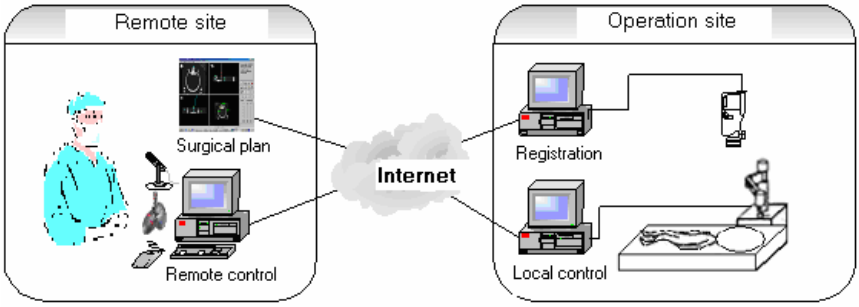

Fig. 1. Robot assisted tele-neurosurgery system structure

The tele-operation undergo 2 phases, A. preparation phase; B. operation phase. During preparation phase, patients medical images are collected in operation site and the CT/MR data will be transferred to remote site. The procedure starts with fixing four markers on the skin in the skull of the patient. Experts on remote site will identify them in the model of the brain. Then the robot locates the four markers in its own coordinate frame through the vision system. With the visualization of the brain model, experts on remote site inspect and decide the surgical plan and communicate with the operation site to do preparation. The both sides certificated surgical plan can be saved on control computer in operation room. In operation site, the control computer control the robot arm to finish stereo localization according to surgical plan, and the surgeons on operation site perform the surgical operations under the instruction and supervision of the remote site's experts.

3 Surgical Plan

Surgeons determine the pathological changes according to patients' medical images and determine the operation route aiming at the focus. The operation route is a straight line defined by puncture enter point and the target point. Following principles are important to determine the route:

1. to be as vertical as possible to the tangent plane which passes the puncture point of the skull;
2. evades blood vessels and important tissues;
3. shallow invade interval into brain;
4. it's much safer when the route is parallel to the long axis of the focus region.

Defining target point and puncture enter point is the normal method to plan the route, farther adjustment of the elementary plan are necessary and important. In Fig. 2, TXYZ is the 3D coordinate system of medical images, and TmXY is medical images' slice m 2D coordinate system. The elementary route is defined by puncture point Pm and the target point T. To enable surgeons rapid and convenient adjustment, the system provide cone based previewed plan method.

In Fig.2, after the target point T is defined, the route varies when Pm changes. The straight line PmPn conforms to equation (1).

$$\cos^2 \alpha + \cos^2 \beta + \cos^2 \gamma = 1 \tag{1}$$

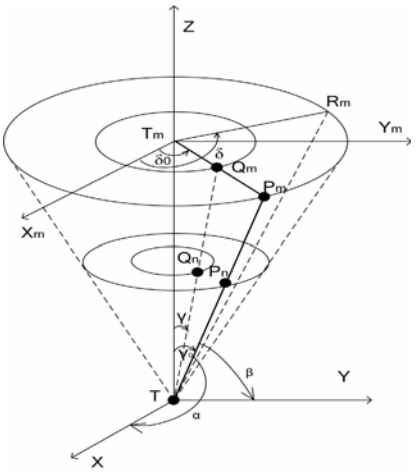

Fig. 2. Previewed plan locus restricted by plan cone

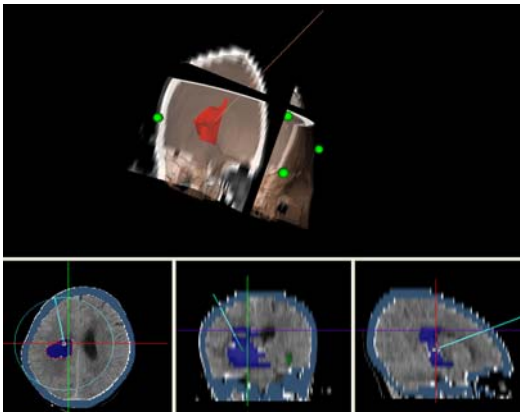

Fig. 3. Surgical plan interface and 3D model

Whenβand γ, The route moves on a cone surface which has a cone peak T and a cone angle 2γ. This make the route adjustment can be predicted and previewed. It is helpful for surgeons to make rapid and safe route surgical plan. At the same time, some different view point (surgeon defines) reconstructed images and 3D model are provided to inspect and affirm the route plan (Fig. 3).

4 Registration Base on Vision

In order to make the registration, the markers must be measured in the robot space. There are different types of measurement, such as mechanical, ultrasound, vision, etc. Traditional vision system mostly utilized two CCD cameras to track markers fixed to patient's head. But the camera calibration is so complex and the accuracy is not steady. Another shortcoming of general CCD camera is that it is only able to track still objects, but unable to track dynamic targets. To solve these problems, we adopt MicronTracker vision system (Fig. 4).

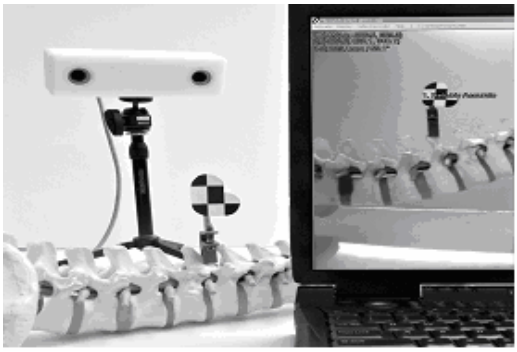

Fig. 4. MicronTracker vision system

MicronTracker is a real-time visual track instrument. It can not only track still objects, but also dynamic targets within its visual region. A pre-designed template was fixed to the surface of object that will be tracked. As shown in Fig. 5a, a template was fixed to the model of patient's head.

During the process of surgical planning, the four markers' positions under the image coordinate system have been obtained. By MicronTracker, we can attain the coordinate value under the MicronTracker's coordinate. In the same way, a template is also fixed to the end of the robot arm (Fig. 3b). These markers' positions under the robot coordinate could be calculated by designed robot parameters. Likewise, we can also obtain their coordinate values under the MicronTracker's coordinate.

After acquiring all the values, four coordinate systems can be created. We call them Head Affine Coordinate system (*HACS*), Image Coordinate System (*ICS*), Robot Affine Coordinate System (*RACS)* and Robot Coordinate System (*RCS*).

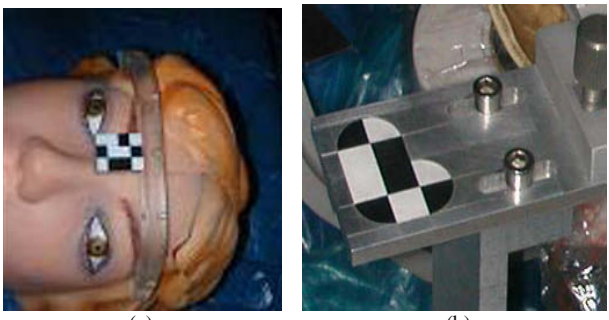

(a) (b)

Fig. 5. Markers templates

Microntracker has its own coordinate system, which we call Camera Coordinate System (*CCS*). So there are in total five coordinate systems. Through MicronTracker, we can establish relationships of these coordinate systems.

Four markers (they can not stay on a same plane) M_0, M_1 M_2 M_3 on the head can be used to establish an affine coordinate system *HACS*. In the coordinate system, every point's coordinate values Mp（xp, yp, zp）can be defined by these four markers' coordinate values. They conform to following equation:

$$\overrightarrow{M_o M_p} = x_p \cdot \overrightarrow{M_o M_1} + y_p \cdot \overrightarrow{M_o M_2} + z_p \cdot \overrightarrow{M_o M_3} \tag{2}$$

Since these four markers' coordinate values can be obtained on the images, their coordinate values under these two different coordinate systems are compared as in the following table.

Table 1. Coordinate values under two differnt coordinate systems

	HAC coordinate values	IC coordinate values
M_o	(0, 0, 0)	(x_o, y_o, z_o)
M_1	(1, 0, 0)	(x_{m1}, y_{m1}, z_{m1})
M_2	(0, 1, 0)	(x_{m2}, y_{m2}, z_{m2})
M_3	(0, 0, 1)	(x_{m3}, y_{m3}, z_{m3})

The mapping matrix between the *ICS* and the *HACS* can be obtained as:

$$T_1 = \begin{bmatrix} x_{m1} - x_o & x_{m2} - x_o & x_{m3} - x_o & x_o \\ y_{m1} - y_o & y_{m2} - y_o & y_{m3} - y_o & y_o \\ z_{m1} - z_o & z_{m2} - z_o & z_{m3} - z_o & z_o \\ 0 & 0 & 0 & 1 \end{bmatrix} \tag{3}$$

Then the transform equation between them is described as:

$$p_{IC} = T_1^{-1} * p_{HAC} \qquad p_{HAC} = T_1 * p_{IC} \tag{4}$$

Then each transform matrix can be obtained in same way:

$$p_{CC} = T_2^{-1} * p_{HAC} \qquad p_{HAC} = T_2 * p_{CC} \tag{5}$$

$$p_{CC} = T_3^{-1} * p_{RAC} \qquad p_{RAC} = T_3 * p_{CC} \tag{6}$$

$$p_{RC} = T_4^{-1} * p_{RAC} \qquad p_{RAC} = T_4 * p_{RC} \tag{7}$$

Our purpose is to obtain the transform matrix between the image coordinate system (*ICS*) and the robot coordinate system (*RCS*). Through multiplying above-mentioned matrix, we can create the final relationship:

$$T = T_4^{-1} \bullet T_3 \bullet T_2^{-1} \bullet T_1 \tag{8}$$

MicronTracker simplifies the creation of the relationship between the image coordinate system and the robot coordinate system, which greatly saves the surgical time.

5 Robot Design

A 5 DOFs robot arm is designed for route implement. Fig.6 illustrates the robot arm structure. Its main task is to offer a mount site for surgical instrument platform and provide the pose and location surgeons defined.

Taking the surgeon driven DOF(d6) into account, the robot has an analytical inverse kinematics solution as shown:

$$\begin{aligned} d_1 &= p_z - a_5 c_5 \\ d_2 &= -(p_y + a_5 s_5 s_{34} + a_3 c_3) \\ \theta_3 &= \arcsin \frac{p_x + a_5 n_x t g_5}{a_3} \\ \theta_4 &= (\theta + \theta) - \theta \\ \theta_5 &= \arcsin n_z \end{aligned} \tag{9}$$

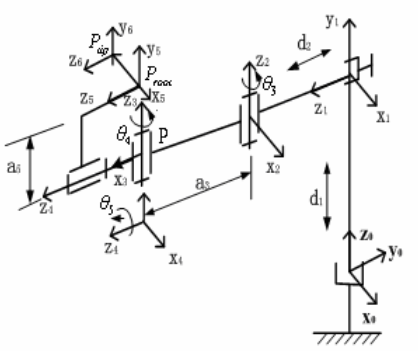

Fig. 6. Robot structure

The surgical instrument's parameter d6 and route direction(nx, ny, nz) are determined during surgical plan.

Dexterity analyses show the robot arm has a 200*200*200 dexterous work space (d_6=180), which is enough for neurosurgery operation, see Fig. 7.

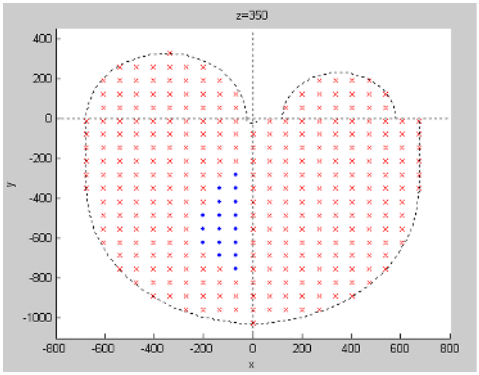

Fig. 7. Robot dexterity workspace example

6 Clinical Experiment

Before this system is used in the clinical application, a large numbers of experiments have been done. We use a skull to test the accuracy of the system. A steel ball of 2 millimeter in diameter is mounted inside the skull to serve as the target point for the surgical instrument. An accurate mechanical measuring device (Fig. 8) is used to measure the desired target position defied by the steel ball and the real target position defied by the tip of the robot end. The distance between the two points indicates the position error of the system (Fig. 8). For different positions of the target, the average position error is less than 1.5 millimeter.

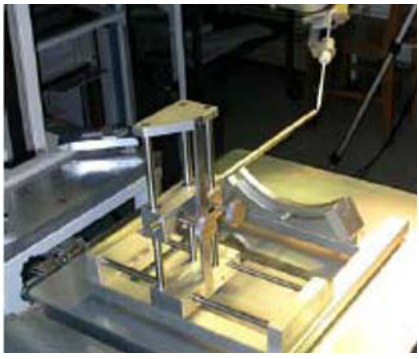

Fig. 8. Experiments for accuracy

During 21st to 22nd Dec, 2005, the system successfully performed three tele-neurosurgery operations between Beijing General Navy Hospital and Yan'an University Hospital. The data communication is transferred on public internet, the General Navy Hospital is connected to public internet via a 2M enterprise ADSL of China netcom company Beijing branch, the Yan'an University Hospital is connected to public internet via a 4M enterprise ADSL of China Netcom company Yan'an branch.

7 Conclusion

The experiments and the clinical application prove the robot assistant tele-neurosurgery system is feasible and safe for remote neurosurgery. Especially, it is helpful to adequately utilize the advance medical resources in China.

Acknowledgements

This work is funded by National Science Foundation of China No. 60525314.

References

1. Alberto Rovetta (2000) Telerobotic Surgery Control and Safety. Proceedings of the 2000 IEEE International Conference on Robotic & Automation, 2895-2900.
2. Marescaux J, at al (2001) Transatlantic robot-assisted telesurgery. Nature, 4: 379-380.
3. Meng Cai, etc, "Remote Surgery Case: Robot-Assisted TeIeneurosurgery", Proceedings of the 2004 IEEE international conference on Robotics and Automation , pp 819-823, New Orleans. LPI April 2004.
4. Liu Da, Wang Tianmiao, et al (2003) Research on robot assisted remote surgery. High Technology Letters, 13(10): 70-74.
5. Meng Cai, Wang Tianmiaa, Zhaag Yuru et al (2003) Researeh on Application of Teleoperation in neurosurgery. High Technology Letters. 13(11): 61-65.
6. Wusheng Chou, et al (2003) Computer and Robot Assisted Tele-neurosurgery, Proceedings of 2003 International Conference on Intelligent Robots and Systems, 3367-3372.
7. Jason Rotella, 'Predictive Tracking of Quasi Periodic Signals for Active Relative Motion Cancellation in Robotic Assisted Coronary Artery Bypass Graft Surgery'. Degree thesis
8. Alana Sherman, Frank Tendick, et al 'COMPARISON OF TELEOPERATOR CONTROL ARCHITECTURES FOR PALPATION TASK', Proceedings of IMECE'00 Symp. on Haptic Interfaces for Virtual Environment and Teleoperator Systems November 5-10, 2000, Orlando, Florida, USA
9. Alberto Rovena. Telerobotic Surgery Control and Safety. Proceedings of the 2000 IEEE International Conference on Robotics & Automation. San Francisco, April 2000, pp.2895-2900.

Design and Implement of Neural Network Based Fractional-Order Controller

Wen Li

Dept. of Electrical Engineering, Dalian JiaoTong University, Dalian116028, P.R. China
lw6017@vip.sina.com

Abstract. The fractional- order $PI^{\alpha}D^{\beta}$ controller is more flexible and gives an opportunity to better adjust dynamical properties of a fractional-order control system than the traditional *PID* controller. However, the parameter selection is more difficult for such a controller, because it introduces two additional parameters α and β. For this problem, this paper proposes a fractional-order PI^{α} controller with self-tuning parameters based on neural network, and discusses the discretization method and the design method of the PI^{α} controller. The architecture of back-propagation neural networks and parameters self-tuning algorithm of the controller are described. Experiment results show that the controller presented not only maintains the performance of the normal fractional-order PI^{α} controller, but also has better flexibility and parameters self-tuning ability.

1 Introduction

The development of fractional calculus is nearly as old as the development of the actual calculus. Discussion as early as 1695 by Leibnitz, and later by others, indicates an interest in integrals and derivatives of fractional (non-integer) order. Besides theoretical research of the fractional-order (FO) derivatives and integrals[1-5], last decade there are growing number of applications of the fractional calculus in such different areas as examples, long transmission lines[6], temperature control[7], electromechanical transmission systems[8] and so on. In these researches several authors have considered fractional-order $PI^{\alpha}D^{\beta}$ controllers and analyzed the relations between system response and parameters α and β[9-11]. The fractional-order controller is more flexible and gives an opportunity to better adjust the dynamical properties of a fractional-order control system than the classical *PID* controller. However, it is can be found that the selection of controller parameters is more difficult for a fractional-order $PI^{\alpha}D^{\beta}$ controller, because it has two additional parameters α and β. In a best simple case, a fractional-order PI^{α} controller or fractional-order PD^{β} controller has three parameters at least. In order to research how to make a fractional-order $PI^{\alpha}D^{\beta}$ controller have a better adaptive capacity for system uncertainties, a fractional-order PI^{α} controller with self-tuning parameters based on neural network is proposed, it is shown in Fig. 1.

T.-J. Tarn et al. (Eds.): Robot. Weld., Intellige. & Automation, LNCIS 362, pp. 471–479, 2007.
springerlink.com

In this paper, firstly, some definitions, properties on fractional calculus and the concept of fractional-order control systems are introduced simply. Then the discretization method and the design process of the fractional-order PI^{α} controller are described in section 3. Next, the section 4 presents the archi-tecture of back-propagation neural networks and parameters self-tuning algorithm of the fractional-order PI^{α} controller. Finally, some related control experiment results and conclusions are given in section 5 and section 6.

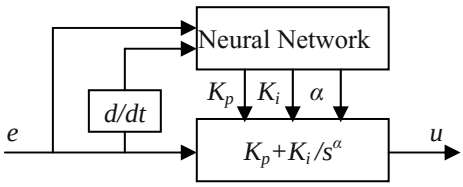

Fig. 1. Fractional-order PI^{α} controller

2 Fractional-Order Control Systems

2.1 Fractional Calculus

Among the definitions of fractional-order calculus, there are Riemann-Liouville definition and Caputo definition etc. various descriptions for fractional-order integrals and derivatives. In this paper the so-called Riemann-Liouville definition is used[10]. The Riemann-Liouville definition for fractional integral is:

$$ {}_aD_t^{-\alpha} f(t) = \frac{d^{\alpha} f(t)}{[d(t-a)]^{\alpha}} = \int_a^t \frac{(t-\tau)^{\alpha-1}}{\Gamma(\alpha)} f(\tau) d\tau, \ t \geq a \tag{1} $$

where, ${}_aD_t^{\alpha}$ is called non-integer α -order fractional derivative operator, a and t are the limits of the operation, $\Gamma(x)$ is the Euler function. Likewise the Riemann-Liouville fractional derivative is defined as

$$ {}_aD_t^{\alpha} f(t) = \frac{1}{\Gamma(m-\alpha)} \frac{d^m}{dt^m} \int_a^t \frac{f(\tau)}{(t-\tau)^{\alpha-m+1}} d\tau \quad m-1 \leq \alpha \leq m \tag{2} $$

and it can be described by the following expression

$$ {}_aD_t^{\alpha} f(t) \equiv \frac{d^m}{dt^m} ({}_ad_t^{\alpha-m} f(t)) \qquad t \geq a \tag{3} $$

where m is chosen as the smallest integer such that α -m is negative, and the integer-order derivatives are defined as usual. These equations define the uninitialized fractional integral and derivative.

Applying the Laplace transform definition, and assuming that the Laplace transform of f(t) is F(s), the following expressions are obtained:

$$ L\left\{ {}_0D_t^{-\alpha} f(t) \right\} = s^{-\alpha} F(s) \tag{4} $$

$$L\left\{{}_0D_t^{\alpha} f(t)\right\} = s^{\alpha}F(s) - \sum_{k=0}^{m-1} s^k \left[{}_0D_t^{\alpha-k-1} f(t)\right]_{t=0} \tag{5}$$

Similarly to integer-order derivative operator, fractional- order derivative operator is a linear operator:

$${}_0D_t^{\alpha}(c_1\ f(t) + c_2\ g(t)) = c_1\ ({}_0D_t^{\alpha}) f(t) + c_2\ ({}_0D_t^{\alpha}) g(t) \tag{6}$$

2.2 Fractional-Order Control Systems

In the time domain, the fractional-order differential equation (FDE) is given as below:

$$\begin{aligned} a_n D_t^{\alpha_n} y(t) + \cdots + a_1 D_t^{\alpha_1} y(t) + a_0 D_t^{\alpha_0} y(t) = b_m D_t^{\beta_m} u(t) + \cdots + \\ b_1 D_t^{\beta_1} u(t) + b_0 D_t^{\beta_0} u(t) \end{aligned} \tag{7}$$

where $D_t^{\alpha_n}$ is the simplification of ${}_0D_t^{\alpha_n}$, coefficients α_i, $(i = 0,1,\cdots,n)$ and β_j, $(j = 0,1,\cdots,m)$ are arbitrary real number, and there are $\alpha_n > \alpha_{n-1} > \cdots > \alpha_1 > \alpha_0 > 0$, $\beta_m > \beta_{m-1} > \cdots > \beta_1 > \beta_0 > 0$, a_i, $(i = 0,1,\cdots,n)$, b_j, $(j = 0,1,\cdots,m)$ are arbitrary constants; here assuming the initial conditions $[D_t^{\alpha_i - i - 1} y(t)]_{t=0}$ =0, $i = 0,1,\cdots,n-1$ and $[D_t^{\beta_j - j - 1} y(t)]_{t=0}$ =0, $j = 0,1,\cdots,m-1$. Taking Laplace transform for Equation (7), we can obtain the fractional-order transform function (FOTF) as the following expression:

$$G_n(s) = \frac{Y(s)}{U(s)} = \frac{b_m s^{\beta_m} + \cdots b_1 s^{\beta_1} + b_0 s^{\beta_0}}{a_n s^{\alpha_n} + \cdots a_1 s^{\alpha_1} + a_0 s^{\alpha_0}} \tag{8}$$

Generally a system described by fractional-order differential equation, like Equ. (7), is called an fractional-order system (FOS). We also can define the ratio of the Laplace transforms of input and output under the conditions of zero initialization as the fractional-order transfer function for the fractional-order system, the Equ. (8) is an example.

3 The Design of Fractional-Order PI^{α} Controller

From Fig. 1, it is seen that the fractional-order PI^{α} controller with parameter self-tuning based on neural network is consisted of two parts, one is the fractional-order PI^{α} controller, and the other is neural network used for tuning the parameters of the controller. In this section the design of the fractional-order controller is given.

The following is the transfer function of fractional order PI^{α} controller,

$$G(s) = \frac{U(s)}{E(s)} = K_p + \frac{K_i}{s^{\alpha}} = G_1(s) + G_2(s) \tag{9}$$

From Eq.(3.1), following expressions can be derived:

$$U(s) = U_1(s) + U_2(s) = K_p E(s) + K_i s^{-\alpha} E(s) \tag{10}$$

$$U_1(s) = K_p E(s) \tag{11}$$

Because $U_2(s) = K_i s^{-\alpha} E(s)$, then

$$K_i E(s) = s^{\alpha} U_2(s) \tag{12}$$

For the fractional-order operator s^{α}, the direct discretization by continued fraction expansion of Tustin transformation is adopted[12], that is,

$$s^{\alpha} = (\omega(z^{-1}))^{\alpha} = \left(\frac{2}{T}\frac{1-z^{-1}}{1+z^{-1}}\right)^{\alpha} = \left(\frac{2}{T}\right)^{\alpha} \frac{P_p(z^{-1},\alpha)}{Q_q(z^{-1},\alpha)} \tag{13}$$

Here taking p=q=3, the Z transfer function can be written as below,

$$\begin{aligned} \frac{U_2(z)}{E(z)} &\approx K_i\left(\frac{2}{T}\right)^{-\alpha} \frac{Q_3(z^{-1},\alpha)}{P_3(z^{-1},\alpha)} = K_i\left(\frac{2}{T}\right)^{-\alpha} \cdot \\ \frac{U_2(z)}{E(z)} &\approx K_i\left(\frac{2}{T}\right)^{-\alpha} \frac{Q_3(z^{-1},\alpha)}{P_3(z^{-1},\alpha)} = K_i\left(\frac{2}{T}\right)^{-\alpha} \cdot \end{aligned} \tag{14}$$

According to Equ. (11) and Equ. (14), the discretization expressions of $U(z)$ in time domain have following forms,

$$u_1(k) = K_p e(k) \tag{15}$$

$$\begin{aligned} u_2(k) = {} & \frac{K_i}{15K^{\alpha}}\left[15e(k) + p_1 e(k-1) + p_2 e(k-2) + p_3 e(k-3)\right] \\ & + \frac{1}{15}\left[p_1 u(k-1) - p_2 u(k-2) + p_3 u(k-3)\right] \end{aligned} \tag{16}$$

$$u\ (k) = u_1(k) + u_2(k) \tag{17}$$

where $p_1 = 15\alpha$, $p_2 = 6\alpha^2 - 9$, $p_3 = \alpha^3 - 4\alpha$, $K^{\alpha} = \left(\frac{2}{T}\right)^{\alpha}$.

4 Algorithm of Parameter Self-tuning Based on Neural Network

Back-Propagated Delta Rule Networks and Radial Basis Function Networks (RBF) are two kinds of well-known neural networks. Both can learn arbitrary mappings or classifications. The Back- Propagation Networks (BP) is a development from the simple Delta rule in which extra hidden layersare added. The network topology is constrained to be feedforward, i.e. loop-free - generally connections are allowed from the input layer to the first hidden layer; from the first hidden layer to the second,..., and

from the last hidden layer to the output layer. RBF networks are also feedforward and can learn arbitrary mapping, its main feature is each hidden layer node has a centre in its receptive field and has a maximal output at the centre. The output of hidden layer node tails off as the inputs moves away from the centre.

Here a BP neural network with 4-5-3 network architecture is selected and is shown in Fig. 2. The inputs of input layer are

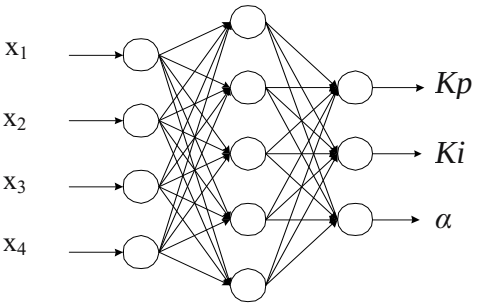

Fig. 2. Neural network architecture

$$O_j^{(1)} = x(j), \qquad j = 1, 2, 3, 4 \tag{18}$$

$$X = (x_1, x_2, x_3, x_4) = (e, e_{-1}, \dot{e}, \dot{e}_{-1}) \tag{19}$$

The input-output relation of hide layer is expressed as

$$net_i^{(2)}(k) = \sum_{j=1}^{4} w_{ij}^{(2)} O_j^{(1)} \tag{20}$$

$$O_i^{(2)}(k) = f(net_i^{(2)}(k)), \quad i = 1, 2, 3, 4, 5 \tag{21}$$

The Sigmoid function is selected as the active function of the hide nodes, the expression is

$$f(x) = \tanh(x) = \frac{e^x - e^{-x}}{e^x + e^{-x}} \tag{22}$$

Likewise, the input-output relation of the output layer can be derived as below:

$$net_l^{(3)}(k) = \sum_{i=1}^{5} w_{li}^{(3)} O_i^{(2)} \tag{23}$$

$$O_i^{(3)}(k) = g(net_l^{(3)}(k)), \qquad l = 1, 2, 3 \tag{24}$$

$$O = (O_1, O_2, O_3) = (K_p, K_i, \alpha) \tag{25}$$

The three outputs of neural network are the three changeable parameters of the controller, K_p, K_i and α. Because they should not be negative, the following Sigmoid non-negative function.

The three outputs of neural network are the three changeable parameters of the controller, K_p, K_i and α. Because they should not be negative, the following Sigmoid non-negative function

$$g(x) = \frac{1}{2}(1 + \tanh(x)) = \frac{e^x}{e^x + e^{-x}} \tag{26}$$

is chosen as the active functions of output nodes, that is,

$$g(net_l^{(3)}(k)),\ l = 1, 2, 3 \tag{27}$$

The Equ. (28) is selected as the learning index function of the neural network for modifying weights.

$$E(k) = \frac{1}{2}(rin(k) - yout(k))^2 \tag{28}$$

A gradient descend optimization method is used to auto tuning controller parameters, K_p, K_i and α. From Equ. (28), the corresponding formulas used for modifying weights between hidden layer and output layer can be derived as below:

$$\Delta w_{li}^{(3)}(k) = \lambda \Delta w_{li}^{(3)}(k-1) + \eta \delta_l^{(3)} O_i^{(2)}(k) \tag{29}$$

Where

$$\delta_l^{(3)} = e(k)\,\mathrm{sgn}\left(\frac{\partial y(k)}{\partial u(k)}\right)\left(\frac{\partial u(k)}{\partial O_l^{(3)}(k)}\right) \cdot g'\left(net_l^{(3)}(k)\right),\quad l = 1,2,3 \tag{30}$$

Similarly the learning algorithm of weight coefficients between input layer and hidden layer can be given,

$$\Delta w_{ij}^{(2)}(k) = \lambda \Delta w_{ij}^{(2)}(k-1) + \eta \delta_i^{(2)} O_j^{(1)}(k) \tag{4.14}$$

$$\delta_i^{(2)} = \left[1 - f^2\left(net_i^{(2)}(k)\right)\right] \cdot \sum_{l=1}^{3} \delta_l^{(3)} w_{li}^{(3)}(k),\quad i = 1,2,3,4,5 \tag{4.15}$$

5 Illustrative Examples

The fractional-order PI^{α} controller with parameter self-tuning was realized and was used in the torsional experiment system. Table 1 gives the system parameters. This experiment system can be depicted by the diagram block shown in Fig. 3. For it, an additional friction can be put on it by a knob.

Fig. 4 shows the time responses under different frictions using normal fractional-order controller PI^{α} with fixed parameters $K_p = 1.0$, $K_i = 0.28$ and $\alpha = 0.1$. In the Fig.4, the upper curve is the time response with a additional friction and the lower curve is the time response without any additional friction. The same tests were conducted using the fractional- order PI^{α} with parameter self-tuning, Fig.5 and Fig.6 show the time responses with an additional friction and without any additional friction respectively, from two figures, it can be seen controller parameters were different in two different cases.

In order to verify self-tuning property of the controller further, a change-in-load was introduced by increasing friction and the angle speed ω_M was down to the 50 percent of the original angle speed. The self-tuning process can be seen in Fig.7. **Fig**.7 gives the three curves, time response curve, parameters self-tuning curve and error curve respectively.

Table 1. Experiment system parameters

the wheel numbers of load side : n=3
the wheel numbers of driver side: m=2
shaft diameter (mm): d=12
the inertial of load side: $J_L = 3.8674 \times 10^{-3}\ (Kgm)$
the inertial of driver side: $J_M = 4.01558 \times 10^{-3}\ (Kgm)$
the elastic coefficient of torsional shaft: $K_S = 1.9849 \times 10^{2}$ (Nm / rad)
the maximum torque of driver: 3.84 (Nm)
the highest revolution speed: 3000 (rpm)

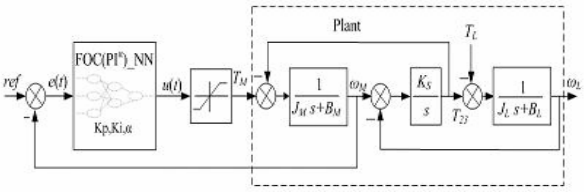

Fig. 3. Block diagram of torsional experimentl system

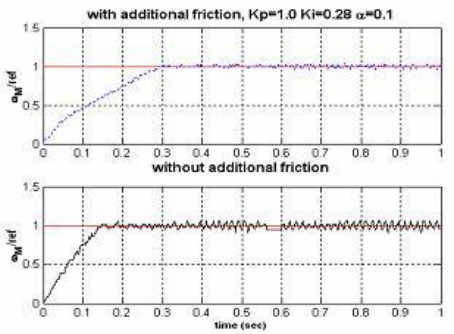

Fig. 4. Time responses with different frictions

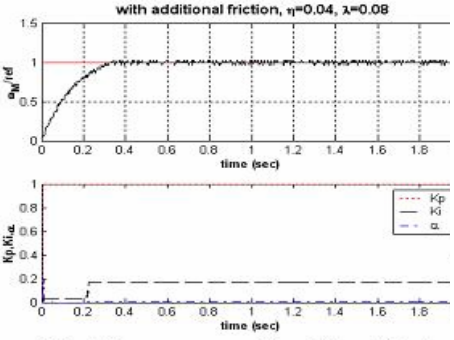

Fig. 5. Time responses with additional friction

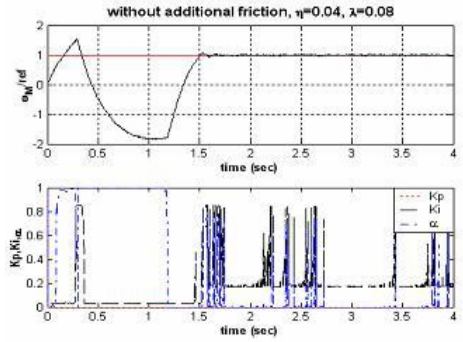

Fig. 6. Time responses without additional friction

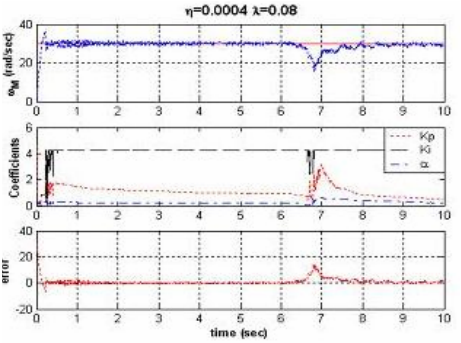

Fig. 7. The curves with parameter self tuning

6 Conclusion

In this contribution a fractional-order PI^{α} controller with parameter self-tuning based on a BP neural network is proposed, and its design method of the controller and parameter self-tuning algorithm are described in detail. The experiment results show that the controller presented not only maintains the characteristic of the normal fractional-order PI^{α} controller, but also has better flexibility and parameters self-tuning ability because the self-learning performance of neural network is introduced. If other compensation methods are combined with it properly, the more satisfied property will be reached.

References

1. K.B.Oldham, J.spanier(1974) The Fractional Calculus. Academic Press, New York.
2. K.S.Miller, B.Ross(1993) An Introduction to the Fractional Calculus and Fractional Differential Equations. Wiley, New York.

3. Y.Q.Chen, K.L.Moore(2002) Discretization schemes for fractional order differentiators and integrators. IEEE Trans. Circuits Systems-I Fund. Theory Appl. 49(3): 363-367.
4. A.M.A.El-sayed, A.E.M.El-mesiry, H.A.A.El-saka(2004) Numerical Solution for Multi-term Fractional (Arbitrary) Orders Differential Equations. Computational and Applied Mathematics. 23(1): 33-54.
5. F.B.Adda, J.Cresson(2005) Fractional differential equations and the Schrödinger Equation. Applied Mathematics and Computation. 161: 323-345.
6. T.Clarke, B.N.Narahari Achar , J.W.Hanneken(2004) Mittag-Leffler Functions and Transmission Lines. Journal of Molecular Liquids. 114:159-163.
7. I.Petras, B.M.Vinagre(2002) Practical Application of Digital Fractional-Order Controller to Temperature Control. Acta Montanistica Slovaca. 7(2): 131-137.
8. C.C.Cheng, C.Y.Chen, G.T.-C.Chiu(2002) Predictive Control with Enhanced Robustness for Precision Positioning in Frictional environment. IEEE/ASME Trans. On Mechatronics, 7(3): 385-392.
9. I. Podlubny(1999) Fractional-Order Systems and $PI^{\alpha}D^{\beta}$ - Controllers. IEEE Trans. Automatic Control, 44(1): 208-214.
10. I.Podlubny, I. Petras(2002) Analogue Realizations of Fractional-Order Controller. Nonlinear Dynamics, 29: 281-296.
11. R.S.Barbosa, J.A.Tenreiro Machado(2003) A Fractional Calculus Perspective of PID Tuning. Proc. of DETC'03, pp651-659.
12. B.M.Vinagre, Y.Q.Chen, I.Petras(2003) Two Direct Tustin Discretization Methods for Fractional-Order Differentiator / Integrator. Journal of The Franklin Institute, 340: 349-362.

An Algorithm for Surface Growing from Laser Scan Generated Point Clouds

G. Paul, D.K. Liu, and N. Kirchner

ARC Centre of Excellence for Autonomous Systems (CAS), University of Technology, Sydney, P.O. Box 123, Broadway, NSW 2007, Australia
{gpaul, dkliu, nathk}@eng.uts.edu.au

Abstract. In robot applications requiring interaction with a partially/unknown environment, mapping is of paramount importance. This paper presents an effective surface growing algorithm for map building based on laser scan generated point clouds. The algorithm directly converts a point cloud into a surface and normals form which sees a significant reduction in data size and is in a desirable format for planning the interaction with surfaces. It can be used in applications such as robotic cleaning, painting and welding.

1 Introduction

Due to newly introduced OH&S regulations, it is no longer desirable for humans to perform the highly necessary task of sandblasting to remove paint from metal structures such as bridges. Issues arise because of lead contaminated paints being removed and the likelihood of working in close proximity with asbestos. With the long-term health damage done by lead and asbestos being common knowledge there is motivation to perform a significant portion of this manual work with an autonomous system.

One of the major hurdles in building an autonomous system to work in an unknown or partially known environment is mapping. Data must be collected and subsequently processed into a format for use by the autonomous system and image rendering. Due to the abrasive and dusty nature of sandblasting it is not possible to build the environment map (i.e. surfaces of structural members) using traditional techniques of lasers, cameras, infrared or sonar while blasting. This means that mapping of the environment and planning of robot paths and motion must be performed prior to the commencement of sandblasting. Due to time constraints where a sandblasted area requires painting within a couple of hours to avoid corrosion of the newly exposed metal, the time needed for mapping and planning must be kept to a minimum. The whole mapping process, from scanning an area from various locations, fusing the data, to generating surfaces which can be directly used for planning, control and collision detection, must be very fast and efficient. Therefore, an efficient 3D mapping technique is required.

This paper explores an efficient mapping algorithm for surface generation by using laser scanner data at a limited number of discrete positions in an environment (*workspace*) where a 6DOF robot arm is used for cleaning or painting. This algorithm allows for simplicity in gathering and fusing scanned data. Generated maps can be used for 3D path planning, collision detection and robot control.

T.-J. Tarn et al. (Eds.): Robot. Weld., Intellige. & Automation, LNCIS 362, pp. 481–491, 2007.
springerlink.com

2 Related Works

There has been work done in the past on semi-automated sandblasting systems [1, 2]. However, the issue of mapping the environment/area to be sandblasted was excluded and direct tele-operation with a camera was opted for. These systems are reliant upon human control, based upon human decisions and hence require direct human supervision.

Much research has been performed on the creation of 3D CAD objects for CAM and painting with some CAD packages allowing point clouds to be imported and rendered. The generation of virtual objects from scans data is time consuming and the aim is to create enclosed objects. Software packages exist (Qhull) with the ability to wrap and render points into a convex hull shape. However simply rendering the surface is not sufficient for the application in this paper. Besides graphically representing an environment, the usefulness of the environment map in robot path and motion planning, collision detection/avoidance and control is also vital.

Current point cloud graphing methods such as marching cubes [3], tetrahedrons [4] and volumetric method [5] can produce complex detailed surfaces with millions of triangles. Rendered images are optimised for display purposes but are not directly usable for planning and control. In order to identify significant surfaces additional processing is required. In general these methods have focused on creating hulls out of point clouds. However, for a robot system in complex structural environments, it is not possible to scan structures completely. Generally it is only possible to create an unwrapped 3D mesh shell which has no thickness. Processing must be directly on the point cloud with no assumptions on the number of view points or completeness of shape. Other work has been done on surface matching from a point cloud to create surfaces out of a point cloud [6]. This method however, is time consuming and can not be directly used for this application.

Research has also been performed on information-based visual multi-robot mapping [7]. Alternate techniques of 3D mapping are proposed with the focus upon collision avoidance, [8]. These algorithms are fast but they do not build a 3D map for navigation of an end effector over surfaces. There are 3D mapping techniques [9, 10] by integrating tilted 2D scan data. However these systems are expensive, meant for longer range and do not focus upon detailed surface interaction with the environment. Some theoretical algorithms which turn point clouds directly into a path [11] can not be directly utilised in this application.

Methods of facial recognition using Principal Component Analysis (PCA) have been examined [12, 13] as well as 2D position estimation using PCA [14]. PCA mathematical methods have been utilised in this paper to assist in the processing and reduction of 3D range data and to determine surfaces and normals. The aim for this present application is to map and work within the robot arm's *workspace* at known discrete base positions, hence methods of localisation while mapping are left for future work.

3 Sandblasting Environment and Scan Acquisition

In this sandblasting application an autonomous system will work in the environment underneath bridges (Fig. 1a). Tracks will be placed on the scaffold in the channels between sets of two I-beams. A robot arm is mounted on a base platform which moves along the track. The developed 3D laser scanning tool maps the environment to be cleaned.

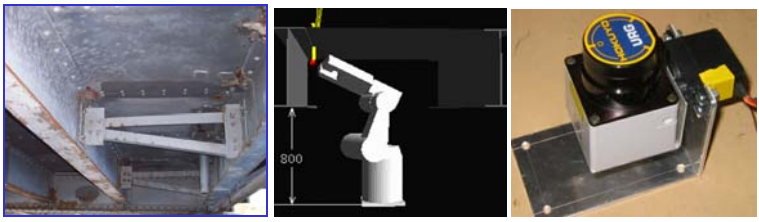

Fig. 1. a) Actual I-beam channel requiring mapped and sandblasted (b) The autonomous system (left); (c) Laser mounted on a digital servo for high precision 3D scanning (right)

The 6DOF robot arm is able to move the end effector to various positions within its *workspace* (Fig. 1b). The 3D scanning operation is performed by a separate scanning tool developed from a 20→4000mm, -120°→120° URG Hokuyo 2D laser scanner (URG-04LX) mounted on a high accuracy, repeatable digital servo (Fig. 1c). The setup is inexpensive, easy to control and highly effective.

The laser scan produces a complete 2D range data set D at 10Hz. To minimise the error and noise, n scans are taken at each increment. Basic filtering is performed on the n range values d_j by first removing q outliers from either side of the data set and then averaging the remaining n-$2q$ values.

$$D = \sum_{j=q}^{n-q} \frac{d_j}{n-2q} \tag{1}$$

After each scan is taken the servo is tilted by 1/3° through its -60°→60° range (Fig. 2a). The tilt increment of 1/3° was chosen to parallel the 2D laser range scanner's pan increments of 0.36° (Fig. 2b). It is desirable for the point cloud to be spaced relatively evenly between 2D scan sweep lines and next tilt angles (Fig. 2c).

In a complete 2D scan the laser scanner determines the distance and angle to maximum of 768 points. The 120° range of the servo tilt system by increments of 1/3° produces 360 scanning positions (≈0.5sec). At each robot arm pose 240° pan x 120° tilt scan at ranges 20→4000mm can be conducted to produce a maximum of 276480 points in 3D space taking a maximum of 180sec. In each discrete platform position the several scans are taken to map the *workspace*.

During successive scan iteration, the previous scan generated point cloud is processed to determining a valid 3D map for virtual interaction and graphical output.

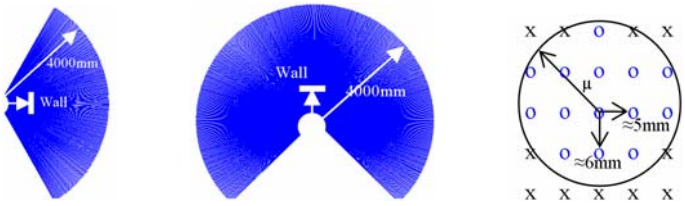

Fig. 2. a) Tilt Scan (Side view): Increments of 1/3°; b) Pan Scan (Top view): Increments of 0.36°; c) 3D Scan Points on wall at 1m range (within *workspace*): distance between points (o=points within circle radius μ; x=points outside circle)

The surfaces and identified important points, sections, features and corners can be used to plan an efficient collision free movement of the robot arm.

4 The Surface Growing Algorithm

Once the 3D point cloud has been attained the surface growing algorithm works towards creating a 3D occupancy grid, identifying important surface coverage points and generating bound planes. The algorithm is performed in several stages. First the *workspace* is divided into equally sized adjoining cubes; points are indexed to the cubes within which they exist. Points are then grouped around a randomly selected *home point*. The data is analysed to determine the plane of best fit for the points. This along with the normals is outputted. Then finally the planes and normals which make up the surfaces are displayed.

4.1 Cubes Index

Initially the *workspace* of the 6DOF robot arm is described by several hundred thousand raw data points in 3D space. This *workspace* is divided into adjoining cubes with dimensions μ. An index is developed of each cube and the points contained. Indexing is done very quickly taking less than a second for several hundred thousand points. This step reduced the time of the closest points search used in the next step, since searching is limited to the points in the current and surrounding indexed cubes. The cube index makes the calculation of the surfaces and the important points at least 10 times quicker.

4.2 Growing Surfaces

The first step is to randomly select a point which is then called the *home point*. Then use the cube matrix to search the enclosing 1 and surrounding 26 cubes (Fig. 3a and 3b) and find a set of points, *P*, within a certain distance, μ, from the initial *home points* (Fig. 3c). Searching the 3D cube matrix rather than the entire *workspace* reduces the calculation time to microseconds rather than seconds.

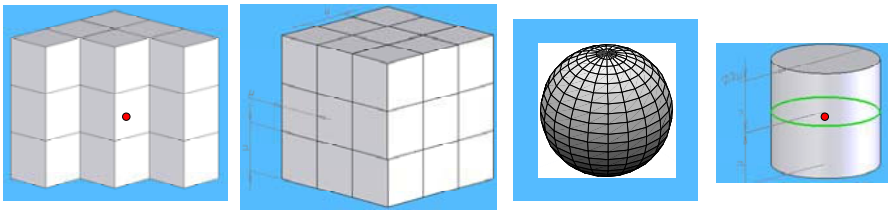

(a) (b) (c) (d)

Fig. 3. a) Home point somewhere in center cube; b) Determine the distance to points with a cube index of the home point (red) or within surrounding 26 cubes; c) Do PCA on points within μ of home point to get plane; d) Register points within ±μ of the plane

If there are enough points within the volume surrounding the *home point* ($V=4/3\pi\mu^3 mm$), then PCA is performed on these points (Fig. 3c). This involves determining the covariance matrix *cov(P)* for this set of 3D points and then evaluating the 3 eigenvectors v_λ and corresponding eigenvalues λ. If there is a small enough correlation $<\alpha$ between an eigenvector and the remaining two then that eigenvector $v_{\min(\lambda)}$ is determined to be the normal to the data set .If there are enough points within μ of the *home point* and μ of the plane (Fig. 3d), plane equations, boundaries, enclosed points and *home points* are registered.

$$If\ \min(\lambda) < \frac{1}{\alpha} mid(\lambda)\ then\ \vec{n} = v_{\min(\lambda)} \tag{2}$$

An attempt is made to register all points. However, if there are insufficient points within μ, of a *home point*, then this *home point* will not be registered and is considered scanner noise. The output of this step is a number of planes (Fig. 3d).

4.3 Graphical Output

The planes generated can be directly used for robotic planning and collision detection. For the purposes of creating a graphical representation of the environment, the surfaces of structural members are built based upon these planes. As identified, rendering surfaces from point clouds has been extensively examined by other researchers. Conversely this Surface Growing algorithm's aim is to identify surfaces to interact with from a point cloud.

Initially a single set of points representing the surface of a sphere radius μ is determined (Fig. 4a). For each identified plane, shift the point-represented sphere to have the centre at the *home point* and determine the points of the sphere within a threshold of the plane (Fig. 4b). Finally draw a disk from the points within the threshold and the plane's normal vector from the *home point* (Fig. 4c). The culmination of disks, the graphical output, is shown in section 5.3.

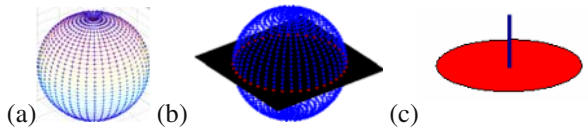

Fig. 4. Graphing algorithm's output planes to display surfaces: a) Point cloud represents the surface of a sphere with the center at *home point*; b) Determine pts lying ≈ on the plane; c) Use points to display an approx. disk

4.4 Important Characteristics of the Algorithm

This algorithm combines different mathematical techniques such as 3D occupancy grids, principal component analysis on 3D data and point cloud analysis to create a novel solution to this surface growing problem. It achieves speed by a simple yet effective method, and is able to output results in a format optimised to meet the requirements of the specified application.

5 Results and Discussion

This section explains the application specific thresholds and the testing of the algorithm. The results are examined including plane/point registration, timing and memory reduction. Finally the usages of the algorithm outputs are discussed.

5.1 Application Specific Thresholds

There are several important thresholds that need to be calculated for this specific application. Firstly, based upon likely data produced by the laser scanning tool in the sandblasting environment the optimal value for μ was determined. μ is used for: the dimensions of cubes that divide the *workspace*; the radius of the closet points sphere used to find the surface and the maximum distance from the points to the surface. Fig. 5.1 describes how computational time, number of planes and percentage of point registered vary for μ=1→50mm. These functions are optimised so as to achieve: the minimum time, maximum number of planes and maximum percentage registered. It was found that μ=12mm produced the best results. Other considerations included the maximum possible cubes enclosed in a *workspace,* the specified laser scanner error (±10mm), the output of surfaces for planning and the sandblasting nozzle which outputs a blast stream covering a radius of 5→15mm.

The other value that needs to be empirically evaluated was the minimum number of points, *min(pts),* that constitute a plane. Insufficient points result in planes created at incorrect angles since there are too few points to correctly perform Principle Component Analysis (PCA) upon. Requiring an excessive number of points results in difficulties in point registration, gaps in the surface and time inefficiency. Fig. 5.2 shows how the time, number of planes and percentage of point registered changes with different values of *min(pts).* The graphically displayed functions were optimised to determine the maximum possible *min(pts)*, which results in the maximum planes and

percentage of point registration, while minimizing time. The optimal result was determined to be *min(pts)* = 10 points. Additionally, by reexamining Fig. 2a and 2b and considering that the radius of the *workspace* is approximately 1000mm, the grid of points are about 5mm apart at this distance. Fig. 2c shows the point grid with greater than 10 points around the centre *home point* for μ=12mm anywhere within the *workspace* range.

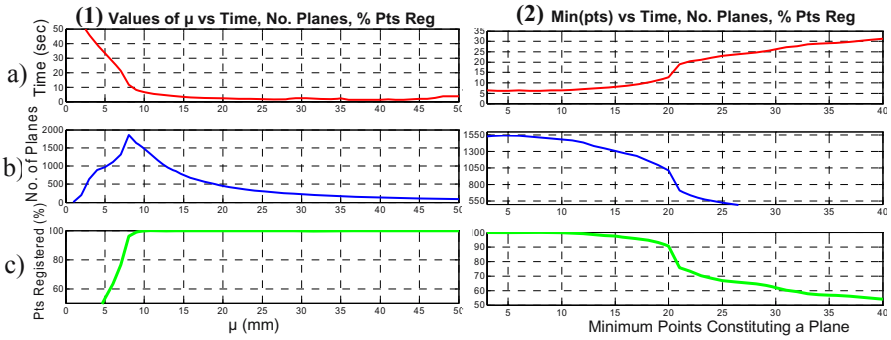

Fig. 5. (1) With respect to μ(mm) (a) • time; (b) No. of planes; (c) Points registered (%) (2) With respect to min(pts); (a) • time; (b) No. of planes ; (c) Points registered (%)

5.2 Testing Overview

This section shows results from tests on different working environments with different volumes of scan data. This allows for comparisons of the output, the time taken, the percentage of points registered and the quality of surfaces created. Quality is based upon comparisons between the generated surface and the actual surfaces from the environment. An in-depth test case is presented to highlight the methods. Following this are the results of 50 test cases as well as a breakdown of the timing of the entire process. This includes: initial scanning; fusion of data from several locations; division into 3D cubes, numerical analysis to minimise points, grow surfaces/normals; then finally rendering and graphing an output for the user.

5.3 In Depth Case Study

This test case is on an I-beam channel structure including features (corners, I-beam webs etc). Several scans are taken from the underneath side of the I-beam channel (Fig. 6a) to generate a point cloud (Fig. 6b). Table 1 shows the details of this case study. The Surface Growing algorithm was performed and the outputs displayed using the technique described. Fig. 6d shows the front view with a close-up showing the normals (Fig. 6e). Fig. 6c shows a side view of surfaces created with a close-up of the plotted planes (disks) in Fig. 6f.

Table 1. Details Of Scanning And Surface Growing Times (sec)

No. Pts	Scans	Scan Time	Fusion Time	Process Time	Graph Time	Planes
75K	5	112.1	3	21.2	2.8	1975

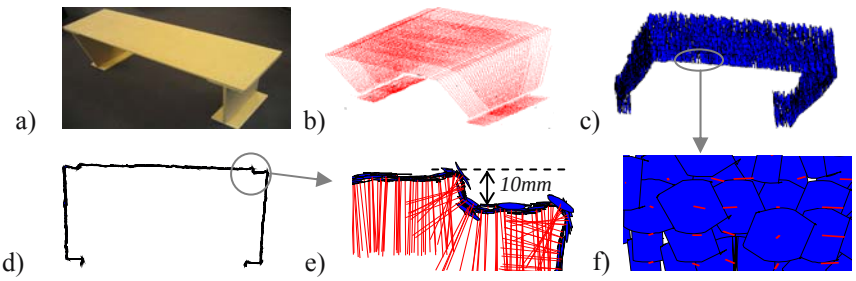

Fig. 6. a) Photo of structure; b) Fused raw data point cloud; c) bottom right view; d) Front viewof planes created; e) Expanded view of the corner; f) front - showing normals (red lines)

5.4 Overall Results

This section shows the results of 50 tests. Data was collected by scanning different structures with the identified *workspace* size several times, fusing the data, and using the Surface Growing algorithm to process this data. The results (Fig. 8a) show the overall algorithm time spent for the processing over the different number of points. Fig. 8b shows the resulting number of planes produced, the percentage of point registered stayed above 99% across the tests. The processing of the data also significantly reduces the amount of data needed to describe the surface sufficiently (turning 100000 scanned {x,y,z} points into 2000 surfaces is a data reduction > 1/20) Fig. 8c shows the reduction in data from the testing results.

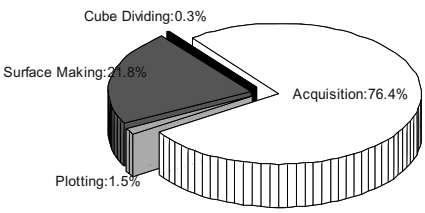

Fig. 7. Overall time breakdown averaged over all tests

Fig. 7 shows the overall breakdown of the total time. It is obvious how the data acquisition time is significantly more time consuming than the other steps in the process. Once the scan data is acquired it can be processed while the next acquisition is being performed.

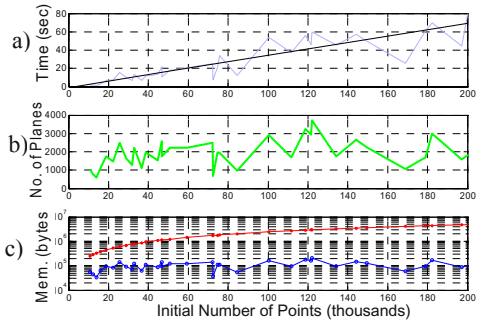

Fig. 8. Results for increasing No. of initial points; a) Overall time (grey) and the trend line (black); b) No. planes; c) Data reduction: original (red *) and post processing (blue o)

5.5 Discussion - Scanning and Surface Growing Output

This algorithm is particularly useful in autonomous structural maintenance system since there are various ways that the output of this algorithm can be applied, including in path planning and motion planning, collision avoidance and as part of the next best possible view by providing 3D occupancy grids.

Initially a complete 3D environment map is not available but there are several Next Best View (NBV) algorithms [15] that could be used to determine the laser scanning tool's position for the next scan. Inverse kinematics is used to determine the 6DOF robot arm pose such that the end effector has a desired position and bearing. The 3D occupancy grid can be used to check if the robot arm in that configuration collides with any points generated from initial scans [16]. If there is an impending collision then it is not a valid pose and if all poses to reach an identified NBV are exhausted then it is not a valid NBV. Hence, poses where the robot arm will collide with some identified, but as yet partially processed points, are discarded in exchange for another NBV pose.

Another way which the output of this algorithm can be used is in path planning. Since the entire area needs to be covered during sandblasting or painting, this algorithm outputs a set of important discrete goal points on the surfaces that would cover the entire known surface. Those goal points can be directly used in path planning which determines the path of the robot arm to follow. The Surface Growing algorithm also outputs the normals to these points which the end effector must align to within a certain angle (5° to 40° to the normal) in order to optimise the blasted surface quality.

The output can also be used in collision detection by applying spherical approach to represent the robot arm and surfaces with a set of spheres with center at the *home point* and radius of μ. This significantly simplifies closest surface calculations and ultimately collision detection calculations.

6 Conclusions

The surface growing algorithm presented in this paper fulfils the requirement of providing useful maps of a partially known or unknown environment consisting of various structural members. It has the ability to transform unstructured 3D points, gathered and fused from multiple laser scans, into a useable format for interaction with surfaces in the environment. It creates 3D occupancy grids, identify important points, normals and bound planes. This can be directly outputted for robot arm path planning and motion control.

Future work will involve integration with 3D path planning and collision detection between the robot arm and the environment, and the incorporation of a more advanced method of rendering the output for graphical display.

Acknowledgement

This work is supported by the ARC Centre of Excellence programme, funded by the Australian Research Council (ARC) and the New South Wales State Government, and by the UTS Partnership grant with the Roads and Traffic Authority (RTA).

References

1. S. Moon, L. E. Bernold, "Vision-Based Interactive Path Planning for Robotic Bridge Paint Removal," *Journal of Computing in Civil Engineering*, vol. 11, pp. 113-120, 1997.
2. W. Yan, L. Shuliang, X. Dianguo, Z. Yanzheng, *et al.* "Development and application of wall-climbing robots," *IEEE Int. Conf. on Robotics and Automation*, 1999.
3. E. L. William, E. C. Harvey, "Marching cubes: A high resolution 3D surface construction algorithm," *14th annual conf. on Computer graphics and interactive techniques*: ACM Press, 1987.
4. K. S. Levinski, A, "Interactive function-based artistic shape modeling," *presented at First International Symposium on Cyber Worlds*, 2002.
5. B. Curless, M. Levoy, "A Volumetric Method for Building Complex Models from Range Images," Stanford University 1996.
6. K. H. Ko, T. Maekawa, N. M. Patrikalakis, "Algorithms for optimal partial matching of free-form objects with scaling effects," *Graphical Models*, vol. 67, pp. 120-148, 2005.
7. V. A. Sujan, S. Dubowsky, "Efficient Information-based Visual Robotic Mapping in Unstructured Environments," *Int. Journal of Robotics Research*,v.24, pp.275-293,2005.
8. J. Minguez, L. Montano, "Nearness diagram (ND) navigation: collision avoidance in troublesome scenarios," *Trans. on Robotics and Automation,* vol. 20, pp.45- 59, 2004.
9. M. Callieri, A. Fasano, G. Impoco, P. Cignoni, *et al*. "RoboScan: an automatic system for accurate and unattended 3D scanning," *Proceedings. 2nd Int. Symposium on 3D Data Processing*, Visualization and Transmission, 2004.
10. H. Surmann, A. Nüchter, J. Hertzberg, "An autonomous mobile robot with a 3D laser range finder for 3D exploration and digitalization of indoor environments," Robotics and Autonomous Systems, vol. 45, pp. 181–198, 2003.
11. M. Varsta, P. Koikkalainen, "Surface modeling and robot path generation using self-organization," *presented at 13th Int. Conf. on Pattern Recognition*, 1996.

12. L. I. Smith, "A tutorial on Principal Component Analysis," 2002.
13. G. Afzal, S. Ressler, P. Grother, "Face Recognition using 3D surface and color map information: Comparison and Combination," *presented at SPIE's symposium on "Biometrics Technology for Human Identification"*, Orlando, FL, 2004.
14. J. L. Crowley, F. Wallner, and B. Schiele, "Position estimation using principal components of range data," *IEEE Int. Conf. on Robotics and Automation*, 1998.
15. J. M. Sanchiz and R. B. Fisher, "A next-best-view algorithm for 3d scene recovery with 5 degrees of freedom," *British machine vision conference*, Nottingham, UK, 1999.
16. J.-S. Gutmann, M. Fukuchi, and M. Fujita, "A Floor and Obstacle Height Map for 3D Navigation of a Humanoid Robot," *Int. Conf. on Robotics and Automation*, ICRA 2005.

Study on the Size Effect and the Effect of the Friction Coefficient on the Micro-extrusion Process

F. Liu, L.F. Peng, and X.M. Lai

School of Mechanical Engineering, Shanghai Jiaotong University, Shanghai 200030, P.R. China
liufang1976@sjtu.edu.cn

Abstract. With the ongoing miniaturization in products, there is a growing demand for the development of accurate forming process for mechanical micro-parts. However, in microforming process, the size effects come up and make the knowledge of the usual forming process can not be used directly. This paper investigates the size effect of H62 with the uniaxial tension experiments, and the results show both the grain size effect and the feature size effect. On the basis of the tension data, the LS-DYNA is used to analysis the micro-extrusion process. The simulation results show that the friction condition affect the microforming process seriously. When the friction condition changes, the stress state of the deformed material also changes. With the increasing of the friction coefficient, the extrusion force increases rapidly.

1 Introduction

In the past decade, the trend towards miniaturization of devices and systems has continued unabated and led to innovative products and applications in industries such as automobiles, health care, electronics, environmental monitoring etc. This trend of size-reduction and increasing functional density in devices has created a need for the fabrication of metallic micro-parts like connector pins, miniature screws, pins for IC sockets and contact springs [1, 2]. A comprehensive review of the field of microforming can be found in the work of Geiger et al. [3].

When the size of mechanical parts are reduced smaller than 1mm, the so-called size effect comes up, which make the know-how, empirical and analytical methods in traditional forming processes can not be used in microforming fields. Several researchers have tried to study the effects of size on material behavior and surface interactions [4-15].

Micro-extrusion is a kind of microforming process which is used widely. This paper studies size effects through the uniaxial tension experiments with the material of H62 and put these data into the commercial FEM code LS-DYNA to investigate the effect of different friction coefficients on the micro-extrusion process.

2 Uniaxial Tension Experiments and Size Effects

The material for the uniaxial tension experiments is H62 wire with different diameter of 0.8mm, 1.3mm and 2.0mm and different grain size of 32μm, 87μm, and 210μm. The

T.-J. Tarn et al. (Eds.): Robot. Weld., Intellige. & Automation, LNCIS 362, pp. 493–499, 2007.
springerlink.com

strain rate is 1mm/s. Fig.1 is true strain-stress curves for specimens with the diameter of 1.3mm and different grain sizes, and Fig.2 is the true strain-stress curves for the specimen with different diameter and same grain size. Figures show that with the increasing of grain size, the flow stress decreases, while with the increasing of the diameter, the flow stress also increases. The material shows both the grain size effect and the feature size effect, but the grain size effect is stronger than the feature size effect.

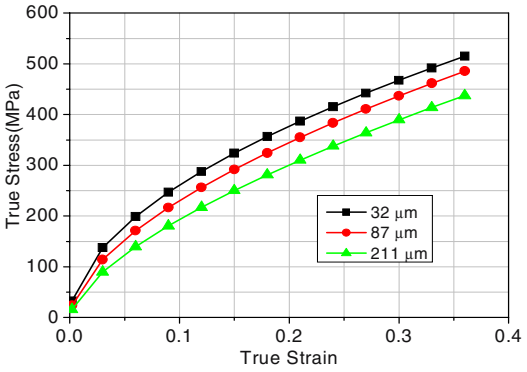

Fig. 1. True strain-stress curves with different gain size (diameter 1.3mm)

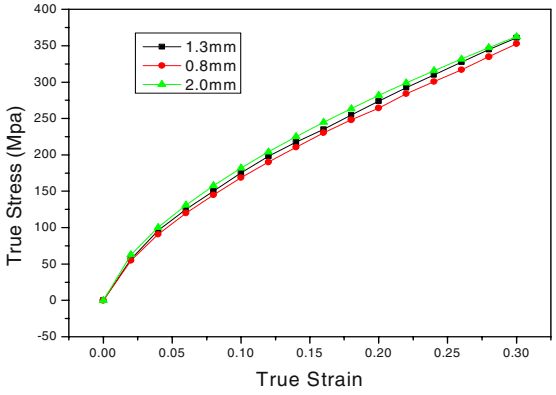

Fig. 2. True strain-stress curves for specimen with different diameter （grain size 211μm）

The decreasing flow stress with the increasing miniaturization can be explained by the so-called surface model [8] (Fig. 3). The grains located at free surface are less restricted than the grains inside of the material. So that it leads to less hardening and lower resistance against deformation of surface grains and makes the surface grains deform easier than those grains inside because dislocations moving through the grains during deformation pile up at grain boundaries but not at the free surface. With the decreasing specimen size and a size invariant microstructure, the share of surface grains increases, which leads to lower flow stress curves.

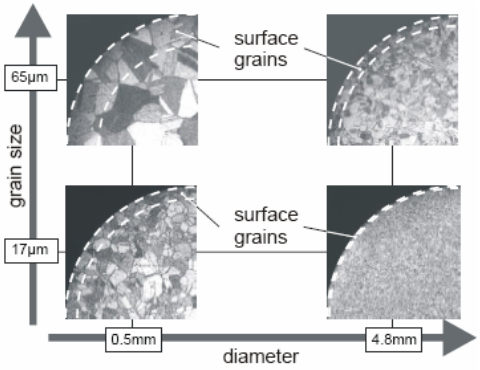

Fig. 3. Surface model of size effects

3 The FEM Model of the Micro-extrusion

In this paper, the LS-DYNA is used to analysis the microforming process, and here we use the uniaxial tension experiment data in section 2 as the material model is. The axisymmetric FEM model is showed as Fig.4, and the extrusion ratio is 5 (10mm/2mm). The punch and die are both rigid body with 184 elements while the deformed billet is separated as 833 CAX4R elements. And the contact arithmetic for the interface between the tool and material is "contact-surface-surface", and the Column friction model is used.

Fig. 4. FEM model for the micro extrusion

4 Results and Discussion

Fig.5 shows the Mises stress distribution of the forward micro-extrusion with different friction coefficient, while the grain size is 211μm. With the increase of the friction coefficient, the Mises stress distribution changes seriously. When the interface between the workpiece and die is smooth, i.e., the friction coefficient is zero, the deformation is comparatively even, only the material nearby the entrance of the female die is deformed very seriously, and at the other area, the stress is very small. When the friction increases, it is difficult for the material which is in contact with the female die to flow because of the friction effect, and at that area, the stress increases obviously. With the

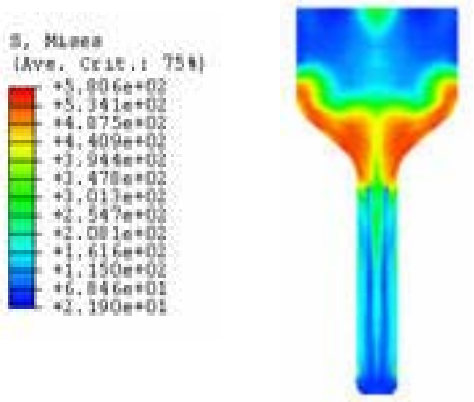

(a) f=0.0

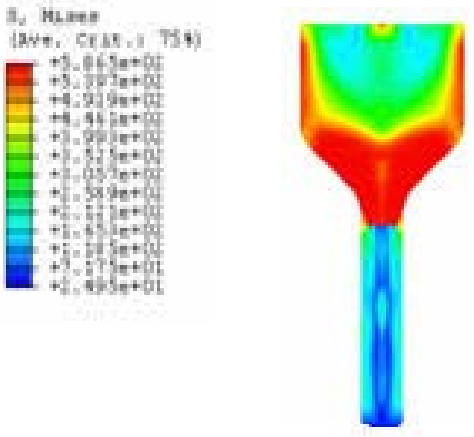

(b) f=0.1

Fig. 5. Mises stress distribution of micro forward extrusion part with grain size of 211μm micron（friction coefficient f=0,0.1,0.2）

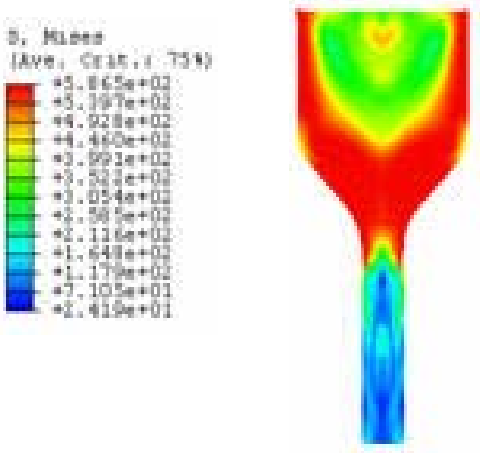

(c) f=0.2

Fig. 5. (*continued*)

increase of the friction coefficient, this kind of area also increases, When the friction coefficient is 0.2, it is almost 50% of the whole workpiece. And when the friction is 0.3, it is very hard to carry on the extrusion process. For the H62 with the grain size is 32μm and 87μm, the simulation shows the same rule.

Fig.6 shows the load-displacement curves for the micro-extrusion with the grain size is 211μm、87μm and 32μm respectively. From the figure we can see that, the forward micro extrusion process can be divided into 3 stages. At the first stage, the material fills the whole upper part of the female die and the load increases slowly with the punch moving down, while this stage is a process with small strain and big deformation. At the second stage, the material is deformed seriously and it begins to flow into the lower part of the female die and so the load increases steeply. In this stage, the strain of the whole material is quite huge but the deformation is small. At the last stage, the material flows out of the female die evenly and the load doesn't change seriously.

Fig.7 shows the load–displacement curves for the materials with different grain sizes and friction coefficients. When there is no friction, the load is about 50N, and when the friction increases, the load increases rapidly. When the friction coefficient is 0.1, the load is about 12000N and when the friction is 0.2, the deformation load is about 17000N. The result shows that the friction affects the deformation of the micro-extrusion seriously. Fig.7 also shows that, when the friction coefficient is same, with the increase of the grain size, the deformation load decreases. But comparing with the effect of the grain size, the friction condition affects the extrusion process more, which is due to the increasing ratio of the surface to the volume of the micro-parts. In the micro forming process, the ratio of the surface to the volume of the forming part is much bigger than the ratio of the ordinary part. So during the forming process, the

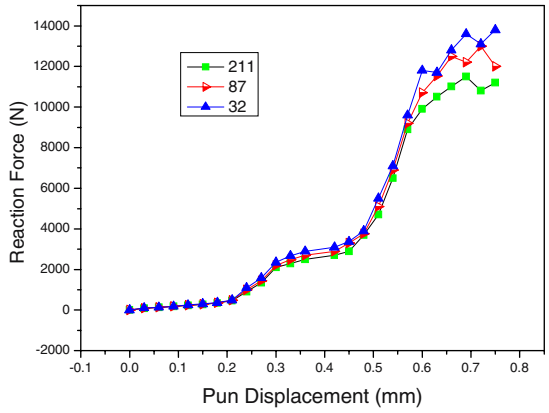

Fig. 6. Extrusion force with punch displacement

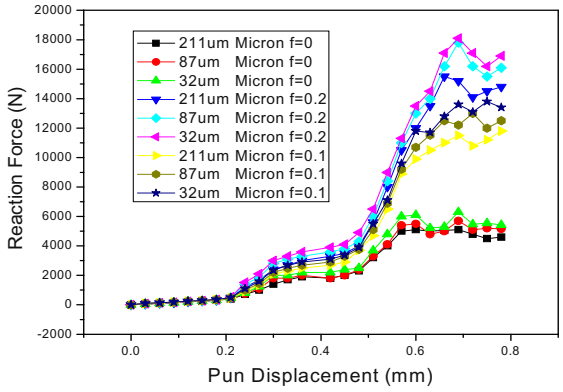

Fig. 7. Extrusion force with punch displacement for different fictional conditions

friction contributes much more to the total deformation load than the ordinary forming process. The smaller the part is, the more seriously the friction condition affects the forming process.

5 Conclusions

(1) The uniaxial tension experiments of H62 with different grain size and different diameters show obvious both the grain size effect and the feature size effect. The flow stress increases not only with the decreasing of the grain size, but also with the increasing of the sheet thickness.

(2) The numerical simulation with LS-DYNA shows that the friction condition affects the micro-extrusion process seriously. With the increasing of the friction coefficient,

the forming load increases rapidly, that is due to the increasing ratio of the surface to the volume of the micro-parts. So comparing to the ordinary extrusion process, the friction force contributes much more to the total deformation load in the micro-extrusion process.

References

1. Neil Krishnan, Jian Cao and Kornel F. Ehmann. Microforming: study of grain size and friction effects in the extrusion of micropins. International Workshop on Microfactory IV, Shanghai, China, Oct. 2004
2. Jian Cao,Neil Krishnan,Zhong Wang,Hongsheng Lu,Wing K. Liu,Anthony Swanson, Microforming: Experimental Investigation of the Extrusion Process for Micropins and its Numerical Simulation Using RKEM, Journal of Manufacturing Science and Engineering, 2004,126:642-652
3. Geiger, M., Kleiner, M., Eckstein, R., Tiesler, N. and Engel, U.. "Microforming", Keynote Paper, Annals of the CIRP, **50**(2), pp. 445-462. 2001
4. Tiesler, N. and Engel, U., 2000, "Microforming – Effects of Minaturization", *Metal Forming 2000,* Balkema, Rotterdam, pp. 355-360.
5. Raulea, L.V., Govaert, L.E. and Baaijens, F.P.T., 1999, " Grain and Specimen Size Effects in Processing Metal Sheets", Advanced Technology of Plasticity, *Proceedings of the 6th ICTP* Sept. 19-24, **2**, pp. 939-944.
6. Geiger, M., Messner, A., Engel, U., Kals, R.and Vollersten, F., 1995, " Design of Microforming Processes – Fundamentals, Material Data and Friction Behavior", *Proceedings of the 9th International Cold Forging Congress*, Solihull, UK, May, pp. 155-163.
7. F. Vollertsen, Z. Hu, H. Schulze Niehoff, C. Theiler. State of the art in micro forming and investigations into micro deep drawing. Journal of Materials Processing Technology. 2002, 151:70-79
8. U. Engel, R. Eckstein. Microforming-from basic research to its realization. Journal of Materials Processing Technology. 2002, 125-126: 35-44
9. Geiger M, Mebner A, Engel E, et al. Metal Forming of Microparts for Electronics. Production Engineering. 1994, 2(1): 15-18
10. WEI Yueguang, Size effect a hard topic for machine- miniaturization, forum for 21 century young scholar: 22(2):57-61
11. Geiger, M.; Meßner, A. , Engel, U. Production of Microparts - Size Effects in Bulk Metal Forming,Similarity Theory. Production Engineering 4 (1997) 1, 55-58
12. L. V. Raulea, A. M. Goijaerts, L. E. Govaert, F. P. T. Baaijens. Size effects in the processing of thin metal sheets. Journal of Materials Processing Technology. 2001, 115:44-48
13. Zhang Kaifeng, Lei Kun. Microforming Technology Facing to the Micromanufacture, China Mechanical Engineering. 2004, 15(12):1121-1127
14. 14. SHEN Yu, YU Huping, RUAN Xueyu. Metal microform technology. Journal of plasticity engineering. 2003, 10(6): 5-8
15. J. F. Michel, P. Picart. Size effects on the constitutive behaviour for brass in sheet metal forming. Journal of Materials Processing Technology. 2003, 141:439-446

A New Wafer Prealigner

Z. Fu, C.X. Huang, R.Q. Liu, Z.P. Chen, Y.Z. Zhao*, and Q.X. Cao

State Key Laboratory of Mechanical System and Vibration
Shanghai Jiaotong University, Shanghai, P.R. China
yzh-zhao@sjtu.edu.cn

Abstract. As a key part of the photo-etching facility, the wafer prealigner uses mechanical or optical aligning method to save the time and guarantee the quality of manufacturing. In this paper, a new wafer prealigner is proposed based on the mass center calculation method. The mass center is measured by a reflection-style laser sensor from the wafer's radial direction, and the position is measured by the notch angle detection using the penetration-style laser senor. A dynamic error compensation method is applied to eliminate the radial runout and wobble of the rotary stage, which have effects on measuring the wafer's mass center. The accuracy is improved through two steps: firstly, a coarse alignment is made by adjusting the mass center; secondly, a precise alignment is processed by aligning the wafer's notch. Experiments show that the accuracy of the wafer prealigner satisfied the system requirement.

1 Introduction

The wafer should be processed through protective coating, masking and photo-etching at different working stages, and the position errors will be generated during the transport process. If these errors are not be eliminated, it is unable to guarantee the photo-etching accuracy. Before the photo-etching, there needs a facility, which aligns the wafer by some high precise sensors and actuators, to adjust the wafer to a required position accurately, so that can save the time of the next leveling and photo-etching process.

The prealigners can be classified into the mechanical and the optical types[1]. The optical prealigner has been widely used with high accuracy. Usually, it uses a linear Charged Couple Device (CCD) sensor to detect the center and the position of a wafer from the wafer's axial direction. Such as a 12-inch wafer prealigner designed by Korea, uses CCD to get images of a wafer, and then calculate the centre and notch position of a wafer by using the least minimum square method, finally the motion module makes an alignment[2]. But this kind of prealigner processes many images and brings out more computation and low efficiency. The prealigner of Holland ASML company calculates the centre and the position of a wafer by detecting the variance of CCD optical energy, based on the CCD basic parameter and empiric parameter obtained by experiments[3]. In order to leave the space for lowing and raising a wafer, there should be a certain distance between CCD and a wafer, which results in optical diffraction and declination

* Corresponding author.

T.-J. Tarn et al. (Eds.): Robot. Weld., Intellige. & Automation, LNCIS 362, pp. 501–508, 2007.
springerlink.com

between LED and the surface of a wafer, so the effection, radial run-out and wobble of a wafer, can't be eliminated. Additionally, the rotary stage, which rotates a wafer, commonly has 3 to 10 μm radial run-out and about 70 μrad wobble which belongs to uneliminated random errors. These can both effect the measurement of the mass center[4]. So it is necessary to consider a new solution or make a certain compensation to get much higher positioning accuracy.

In this paper, a new wafer prealigner is proposed. In the prealigner, a much higher precise sensors are used to detect the mass center and the notch position of a wafer from the radial and axial direction of a wafer respectively. In the aspect of mechanism, a new shafting mechanism is designed which has much higher repeatability positioning accuracy.

2 The Architecture of the Prealigner

As shown in figure 1, the prealigner is made up of the actuator, the detection device and the control module. The actuator has two linear displacement stages X-Y at the basis layer, one rotary stage θ and a linear displacement stage Z. The axis θ is in series with the axes X, Y and Z.

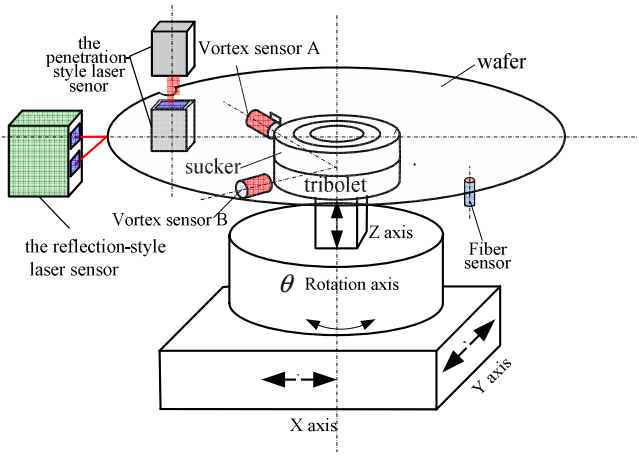

Fig. 1. The schematic illustration of the new prealigner

A sucker, a gas tube and a tribolet are installed on the axis Z. In the external of the tribolet, the sucker is connected with the gas tube by a soft spiral pipe of SMC. The wafer is sucked by the negative pressure in the sucker. The detection devices mainly include a reflection-style laser sensor, a penetration-style laser senor and two vortex sensors. The former laser sensor can measure the radial displacement druing the rotation. The latter laser sensor can measure the positon of the notch of the wafer. The two vortex sensors are mounted beside the tribolet with an angle of 90° and relatively still towards rotary stage, and they are used to measure the radial runout of the rotary stage.

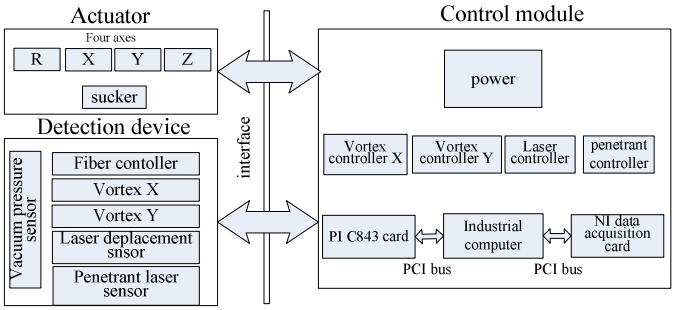

Fig. 2. The proposed control system architecture for a prealigner

As shown in figure 2, the control module can collect the signals with NI data acquisition card. Besides, it can detect the position of the PI stages and the negative pressure of the valve. These signals will be processed by the control module, to get the linear displacement along X-Y direction and rotation displacement around the Z axis. The PI card controls the linear movement of the X, Y, Z and θ stages to realize the prealignment of the wafer.

The aligning process of the wafer prealigner is described as follows: Firstly, when the θ stage rotates in high speed in the 1st circle, the reflection-style laser sensor emits beams to the edge of the wafer to measure the rough position of the shape centor and the notch. Then Z axis is descended and the wafer is put on the spporting cushion, to make the sucker of the rotary stage separate compeletely with the wafer. The X, Y and θ axes will move according to the position of the shape center and the notch, to make the wafer and the rotary stage concentrical and turn to the predefined angle relative to the zero position.Then Z axis moves up, the sucker lifts the wafer from the spporting cushion , and then the X、 Y、 Z、 θ axes will return to near zero position. Secondly, rotating in the 2nd circle, the reflection-style laser sensor measures the additional eccentricity of the wafer's shape center and removes most position error in the above method. Finally, rotating in 3rd circle, the penetration-style laser senor measures the notch position and aligns the center and notch precisely. In the following parts, the detection device, the control module and the actuator will be introduced in details.

2.1 Detection Device

The new wafer prealigner introduced in this paper can detect the center of a wafer by the high precisely reflection-style laser sensor and the angle of the postitioning notch by the penetration-style laser sensor. The reflection-style laser sensor detects the radial displacement of the wafer, and prevents the data from fluctuating by diffuse reflection of the workpiece's coarse face. The Keyence LX2-11 is chosen as the digitally penetration-style sensor, which can detect the edge of the wafer along the axial direction to ascertain the shape center and the angle of the notch. The geometric information of the notch can be obtained by the light intensity covered by the wafer. In order to ensure the position accuracy of the notch, the best way is to take the position

feedback pulse of the rotary stage as the triggered signal to detect the position of the notch by the penetration-style laser sensor. However, the fastest output pulses of the rotary stage can only ensure 176000 per circle, that is to say, one sampling point is collected per 36 μrad. Because the notch is very small, the more sampling points are expected. A quadruple frequency circuit is added to get the angular resolution of collecting one point per 9 μrad in the new system.

2.2 Control Module

The control module includes the signal regulators, the power supply, the NI data acquisition card, the PI motion control card, an industrial computer and an interface board. The industrial computer is installed with an automatic control software used to control the motion of the four axes, the pneumatic pressure and the transportation of a wafer.

The data acquisition card NI PCI-6229 is used in the control system with five channels. The channels are connected with two laser sensors, two vortex sensors and one rotary stage encoder. The data acquisition card uses one pulse outputed by the PI rotary stage's encoder as an external clock (35200Hz). The sensors are applied on Timing mode, which refers to a state when output voltage of the sensor is rentained constant during two timing signals. The Timing signal is also provided by the encoder of the PI rotary stage. To collect sampling points to calculate shape center, the Timing signal is 128 fractional frequency of the PI rotary encoder signal. 1375 sampling points is used to calculate the shape center during each cycle. In order to get radial run-out data of rotary stage, the vortex sensor needs to collect points at each Timing signal. The NI data acquisition card can collect 128 sampling points in one Timing signal cycle, and the radial runout data can be gotten by a filter algorithm, which can greatly reduce the external noise interference. The PI rotary stage controller, C843 PCI card can simultaneously drive 3 linear displacement stages and one rotary stage. The card provides motion control functions with more rapid and effective ability.

3 The Prealigning Algorithm

3.1 The Calculation Method of Wafer's Shape Center

While the wafer is rotating eccentrically, the reflection-style laser sensor can measure the displacement of edge. As demonstrated in figure 3:

- *O* is the rotational center of rotary stage;
- *O'* is the shape center of the wafer when the manipulator transferes a wafer to the vaccum sucker;
- *e* is the eccentricity;
- *R* the ideal exicrcle radius;

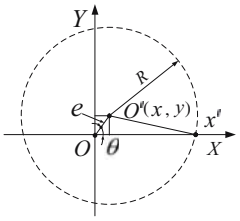

Fig. 3. The schematic diagram of the eccentricity of the wafer

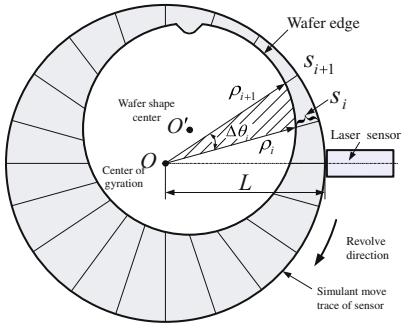

Fig. 4. The polar coordinate of the wafer's shape center

After establishing the rectangular coordinates system through the center of rotary stage, the actually geometric coordinate rotated by θ is (x,y); the x-coordinate offset *Ox*'is detected by the laser along the fixed X axis. Then there is:

$$\begin{cases} x = e\cos\theta \\ y = e\sin\theta \end{cases} \tag{1}$$

We can get:

$$Ox' = e\cos\theta + (R^2 - e^2\sin^2\theta)^{1/2} \tag{2}$$

The formula 1 is the functional relation of the eccentricity, the rotary angle and the edge displacement while the wafer is rotated eccentrically under ideal condition. It can be used to verify whether the data is right during the detecting process. When detected in practice, the wafer can be regarded as static, and the sensors rotate around the gyration center of the rotary stage. The method to calculate the shape center of wafer is the least minimum square method. However, because the roundness tolerance of the 10-inch wafer is ±0.1mm, in addition, the data of positioning notch need to be processed individually, the method taken here is not the least minimum square method [4-6] but a method based on the mass center.

As shown in figure 4, the data acquisition card synchronously collects the digital signals from the reflection-style laser sensor trigged by the pulse of the rotated table encoder. And we get the following values:

s_i is the distance between sensor and the edge of wafer;

θ_i is the revolting angle;

Suppose that:

ρ_i is the distance between the center of the gyration and the edge of the wafer

$\Delta\theta_i$ is the angle interval with the next sampling point

L is the distance between the laser sensor and the axis of rotary stage

So we have $\rho_i = L - s_i$.

According to the mass point calculation method of an object with arbitrary shape and uniform mass in two-dimension, we can calculate the coordinate of the wafer's shape center O', and get the mass point coordinate, that is the position coordinate of wafer's shape center $O'(\bar{x}, \bar{y})$:

$$\bar{x} = \frac{\int_0^{2\pi} \int_0^{\rho(\theta)} \rho^2 \cos\theta \cdot d\rho d\theta}{\int_0^{2\pi} \int_0^{\rho(\theta)} \rho \cdot d\rho d\theta} \tag{3}$$

$$\bar{y} = \frac{\int_0^{2\pi} \int_0^{\rho(\theta)} \rho^2 sin\theta \cdot d\rho d\theta}{\int_0^{2\pi} \int_0^{\rho(\theta)} \rho \cdot d\rho d\theta} \tag{4}$$

Where

$\rho(\theta)$ is a function of radius vector about angle.

Thus, it can be calculated according to the method of the discrete system in mechanics:

$$\bar{x} = \frac{M_y}{M} = \frac{\sum_{i=1}^{n} m_i x_i}{\sum_{i-1}^{n} m_i}, \bar{y} = \frac{M_x}{M} = \frac{\sum_{i=1}^{n} m_i y_i}{\sum_{i-1}^{n} m_i}$$

Where

$M = \sum_{i-1}^{n} m_i$ is the total mass.

$M_x = \sum_{i=1}^{n} m_i y_i$ $M_y = \sum_{i=1}^{n} m_i x_i$ are static moments to X axis and Y axis respectively. To solve the shape center of the wafer under the polar coordinate system, we obtain $(\bar{x}, \bar{y})$ as follows:

$$\bar{x} = \frac{\sum_{i=1}^{N} \int_0^{\rho_{(\theta)}} \rho^2 d\rho \int_{\theta_i}^{\theta_{i+1}} \cos\theta d\theta}{\sum_{i=1}^{N} \int_0^{\rho_{(\theta)}} \rho d\rho \int_{\theta_i}^{\theta_{i+1}} d\theta} = \frac{\frac{1}{3}\sum_{i=1}^{N} \rho_i^3 [\sin\theta_{i+1} - \sin\theta_i]}{\frac{1}{2}\sum_{i=1}^{N} \rho_i^2 [\theta_{i+1} - \theta_i]} \tag{5}$$

$$\bar{y} = \frac{\sum_{i=1}^{N} \int_0^{\rho(\theta)} \rho^2 d\rho \int_{\theta_i}^{\theta_{i+1}} \sin\theta d\theta}{\sum_{i=1}^{N} \int_0^{\rho(\theta)} \rho d\rho \int_{\theta_i}^{\theta_{i+1}} d\theta} = \frac{\frac{1}{3}\sum_{i=1}^{N} \rho_i^3 [\cos\theta_i - \cos\theta_{i+1}]}{\frac{1}{2}\sum_{i=1}^{N} \rho_i^2 [\theta_{i+1} - \theta_i]} \tag{6}$$

Where, N means the number of the effective sampling points.

3.2 The Position Searching of the Wafer Notch

In the process of calculation of the shape center, 176000 sampling points are collected in total, some points around the notch show the state of outrange while the rotary stage is revolting with high speed, so the notch points need to be recollected under low rotation speed when the rotary stage rotates to the notch position.

The inlet and outlet points of notch are generally outranged (because the points are in the sloping side of notch, the beam is reflected), so the initial position of the notch can be gotten by this feature.

Rotating under a low speed, the nearest point towards the center of the circle can be calculated by the colleted points, and the position of the notch is the vector of the nearest point that the center of the circle towards.

4 Experiments and Result Analysis

In experiments, we use the external high precise CCD with big size, of which repeated accuracy can be up to *±60 nm* after the template matching, to examine the repeatability position error in the *x*, *y* and θ directions. The type of the high resolution CCD is MVS, the measurement range is 1018×1004 pixels, and the resolution is 200*nm*. Before doing experiment, we do pre-photo-etching marking image, which is used for precision test. After finishing the prealignment, we get the marking image of wafer gap and wafer

Table 1. The examination result of a wafer repeatability measurement accuracy

Test tool: MVS						Test location: FFU-2 Purge room	
No	Sucker pressure range Bar	X		Y		3σ(x)μm	3σ(y)μm
		Xmax	Xmin	Ymax	Ymin		
1	(-0.645,-0.630)	441	439	508	505	3.08987	3.381188
2	(-0.650, -0.630)	553	550	437	434	3.186504	3.687278
3	(-0.657, -0.645)	524.17	522.07	515.41	515.41	3.186504	3.687278
4	(-0.635, -0.632)	510.26	508.00	522.57	521.26	3.282918	1.29484
ave	——	507.11	504.77	495.75	493.92	3.186449	3.012646

center, then, processing the image offline based on the template matching, we get the relative position of the photo-etching marking image to the CCD. In the test, the prealignment operation was performed for 50 times in a group by the same wafer,

which is located randomly. The same action was repeated in 4 groups. The statistical data are shown in the Table 1. From Table 1 we can see, the repeatability position precision of *x* direction and *y* direction is up to ±*1.6*μm.

5 Conclusion

This paper proposes a new wafer prealigner, which is based on the mass center calculation method. The repeatability positioning precision of the shape center is up to ±1.6 μm. The repeatability positioning precision of the angle is up to 9 μrad. The time of positioning is 50 seconds. In order to enhance the measure precision of the shape center, the prealigner uses the reflection-style laser sensor to measure the wafer shape center through the wafer radial, and uses the penetration-style laser sensor to measure the notch angle of the wafer. And the prealigner uses the dynamic error compensation to reduce the impact of the radial run-out and wobble to the shape center measurement. In the process of aligning, in the first step a coarse adjustment to the wafer shape center and positioning notch angle is taken, then, a fine adjustment to positioning notch angle is finished in the second step. The experiment verifies that this method improves the positioning precision of the prealigner.

References

1. Yang X. P. The edge detection and pre-align technique in the transmission system of a wafer .2003, 3(112):34~47.
2. Hee-Sub Lee, Jae Wook Jeon, Joon-Woo Kimb. A 12-inch wafer prealigner. Microprocessors and Microsystems, 2003, 27(4): 151-158.
3. Zhang Q., Hu S., Yao H., Liu Y.Y. The development of optical photo-etching technique of ASML Company.2002, 9(3): 8~11.
4. Song Y. X., Li S. C., Zhao Y. N. The pre-align control method of a wafer. CN: 200510116695.0, 2006, 6
5. David H Ziger, Peroux Linear Alignment correction algorithm for deep submicron lithography. SPIE, 2002, 468:1057~1069.
6. David R. Beaulieu. Dark field technology a practical approach to local alignment. SPIE, 1987,772:142.
7. Hu S. Research on high precise leveling technique. Master paper.1999, 6

The Energy Optimization Design of the Safety Door's Control System in the Urban Light Rail Transit Line

Z. Fu, Y.Z. Zhao*, Y. Xin, W.X. Yan, and K.D. Cai

State Key Laboratory of Mechanical System and Vibration
Shanghai Jiaotong University, Shanghai, P.R. China
yzh-zhao@sjtu.edu.cn

Abstract. This paper presents an energy optimization method of the safety door's motion control. Considering the multiple factors that affect the safety door's energy consumption, we establish an objective function and a constraint equation, and propose an energy optimization method based on Sequential Quadratic Programming (SQP) algorithm. The controllable curve of the instantaneous linear velocity for the safety door based on the optimization design can be finally obtained. This method has been proved to be effective by experiments.

1 Introduction

The light rail transit line has been an important part of the city's public transportation. It has become many people's first choice for its safety, quickness, and large containment. The light rail transit line usually works underground or overhead, so it does not interfere with the normal road traffic. For this reason, many metropolitan authorities are keen on the development of the light rail transit line to solve the traffic problems. The frequent use of the safety doors on transit lines would require a large amount of electric energy. With increasing shortage of energy, energy saving has become one of the most urgent problems we are faced with today. Therefore, how to minimize the energy consumption of the safety door operation has become an important research subject.

Some problems, which are not solvable by classical differential method or variation calculus, may be solved by the method of optimization. First, we have to describe the problem using the mathematic formula, and then solve it with the optimization method like SQP. SQP is widely used in optimization problems.

For instance: to achieves the hydro unit commitment in hydrothermal systems[7],to solve the optimal power flow problem[8],to find the optimal sizing of shunt capacitors and/or passive filters for maximizing the net present value resulting from energy-loss reduction[8-10].

However, there are no reports about using the optimization method to minimize energy consumption based on the controllable curve of the instantaneous linear velocity for the safety door on urban transit. This study would establish a model of the safety doors' energy consumption based on SQP, derive its solution, and apply to a real case.

* Corresponding author.

T.-J. Tarn et al. (Eds.): Robot. Weld., Intellige. & Automation, LNCIS 362, pp. 509–516, 2007.
springerlink.com

2 Model Establishment of the Controllable Curve of the Instantaneous Linear Velocity for the Safety Door

2.1 Safety Door System Overview

As shown in Figure 1 below, the safety door has been in stable operation in ChunShen Station of Shanghai Light rail transit line No.5.

Fig. 1. Platform safety door of Chunshen Road Station, Light rail transit line No.5, Shanghai

Figure 2 shows the connection diagram of the modules of the safety door system. We can see from this figure that every safety door is controlled by a slave controller (TI 2407 DSP) on each side of the door. This controller communicates with the subsidiary monitoring system on each platform through CAN bus. Each subsidiary monitoring system connects with the server of the station's monitoring center through the net.

The major energy consumption of the safety door can be divided into three major parts. The first part is the energy consumption of the auxiliary facilities, which includes the electronic lock, the pilot lamp, and the limit switches. Second is the energy consumption of the hardware components, which includes the modules of the slave controller. The last major part of the energy consumption comes from the physical movement of the safety door according to the controllable curve of the instantaneous linear velocity. The first two parts are decided by the requirement of the system that can only be saved by using the proper energy saving appliances. The energy consumption of the last major part may be optimized through our study. After the selection of motor and the analysis of energy consumption of the safety door, the only way to reduce energy consumption on this part is by improving the controllable curve of the instantaneous linear velocity for the safety door. Therefore, we would ameliorate the controllable curve based on the optimal way.

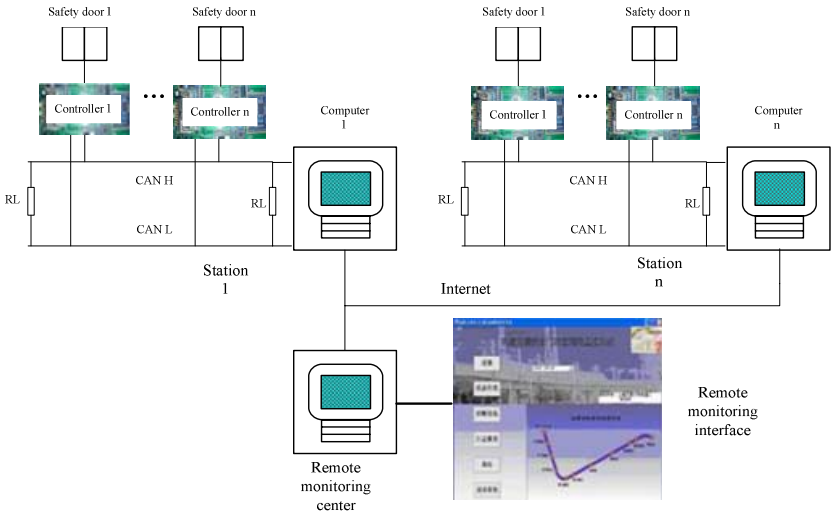

Fig. 2. System module connection

2.2 The Mathematic Model on the Controllable Curve Optimization

Define $x = (x_1, x_2, \cdots, x_n)^T$ as a point in the Euler space with n dimension $f(x)$ is a function with n unknown quantities,
$R = \{x \mid c_i(x) = 0, i = 1,2,\cdots,m; c_i(x) \le 0, i = m+1,\cdots, p\}$. The goal is to get the minimal value of $f(x)$ in the range of R.

$$\begin{cases} \min & f(x) \\ s.t. & c_i(x) = 0, i \in E = \{1,2,\cdots,m\} \\ & c_i(x) \le 0, i \in I = \{m+1,\cdots, p\} \end{cases} \tag{1}$$

According to the requirement of optimization method, we have to establish the mathematical equation. In order to simplify the problem, we make the opening and the closing curve of the safety door to be symmetric so as to use the same optimization algorithm.

As shown in Figure 3, the controllable curve of the instantaneous linear velocity for the safety door before the optimization is simplified into three parts; the abscissa of this figure is time (ms), while the ordinate is the arithmetic equivalent value of velocity. The rate of the arithmetic equivalent value of velocity to the actual velocity is 4000/0.6. Since we have to keep the uniform velocity part, the optimization algorithm should be focused on the acceleration and the deceleration parts. Further, we can just discuss the acceleration part because the deceleration part is symmetric to the acceleration part. The detailed process of the modeling is listed below.

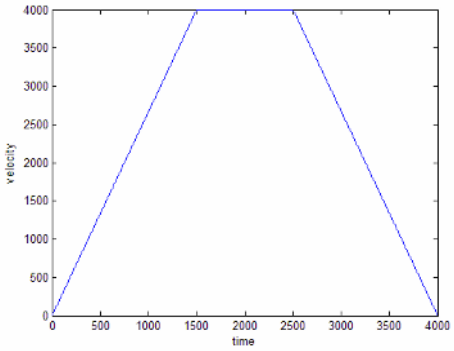

Fig. 3. The controllable curve before optimization

By analyzing the energy consumption of the safety door's movement, we get that the electric energy is changed into the kinetic energy and the energy consumed by the friction. $\overline{E_e} = \sum E_k + E_b$,

Where

- $\sum E_k$ is the total kinetic energy
- E_b represents the total of the energy that can not be properly used. E_b is mainly caused by frictional force which is related to distance, pressure, and the coefficient of friction.

These factors of the safety door would not change. So E_b could be considered as a constant that could not be reduced by the optimization algorithm. For this reason, E_b can be omitted when calculating $\overline{E_e}$. Namely, $E_e = \sum E_k$.

$E_e = \sum E_k = \int_0^t E_k dt$, E_k is the kinetic energy of each moment, $E_k = \frac{1}{2} \cdot m \cdot v^2$

where

- $m = 63kg$
- v is the velocity of the door.

Since the loop period of the slave controller's program is 1ms, we can conclude that the velocity of the safety door changes with the period of 1ms.

$$E_e = \sum E_k = \frac{1}{2} \cdot m \cdot \Delta t \cdot (\sum_{i=1}^{C_2} v^2(i)), i = 1, 2, \cdots, C_2 \quad (2)$$

where

- $C_2 = 1500$ represents the number of the samples

- $\Delta t = 1ms$
- $v(i)$ is the velocity of one of the samples.

Equation 2 is the objective function aiming to get the minimal value.
Constraint factors:

- The arithmetic equivalent value of route of the safety doors' movement is a constant
- $\Delta t \cdot (\sum_{i=1}^{C_2} v(i)) = C_1,\ C_1 = 3000$
- The ratio of the arithmetic equivalent value of route to the actual route is 3000/0.45.
- The initial velocity (arithmetic equivalent value of velocity) of the safety door is $v_1 = 0$
- The maximum of the velocity (arithmetic equivalent value of velocity) is $v_{C_2} = 4000, v_1 \le v_i \le v_{C_2}, i = 2,3,\cdots,C_2 - 1.$
- The ratio of the arithmetic equivalent value of velocity to the actual velocity is 4000/0.6.
- The acceleration of the sample is $a_i = (v_{i+1} - v_i) \times 1000,\ i = 1,2,\cdots,C_2 - 1$

Comparing with the initial acceleration, the acceleration of the safety door after the optimization algorithm should be different. With the difference v_{i+1}-v_i, it satisfied

$$4000/1500 - C_3 \le (v_{i+1} - v_i) \times 1000 \le 4000/1500 + C_3$$

where

- 4000/1500 is the initial acceleration of the safety door before the optimization algorithm
- C_3 is the value of Δ, C_3 =2.

According to the analysis mentioned before, we can get the mathematical model of the optimal controllable curve problem.

$$\begin{cases} \min & f(x) = x_1^2 + x_2^2 + \cdots + x_{n-1}^2 + x_n^2 = \frac{1}{2} x^T H x & (i = 1,2,\cdots,1500) \\ st. & x_1 + x_2 + \cdots + x_{n-1} + x_n = 3000 & \\ & x_1 = 0 & \\ & x_{1500} = 4000 & \\ & \frac{2}{3000} <= x_{i+1} - x_i <= \frac{14}{3000} & (i = 1,2,\cdots,1499) \\ & 0 <= x_i <= 4000 & (i = 2,3,\cdots,1499) \end{cases} \tag{3}$$

where

- H is twice of an identity matrix whose rank is 1500.

3 e Solution and Simulation of the Problem Based on SQP

Sequential Quadratic Programming algorithm changes the nonlinear optimal problem with constraint into a series quadratic programming sub-problems. Assume that at the beginning of the K*th* iteration, the approximate solution $x^{(k)}$ and $x^{(k+1)}$ is already known. According to this, we can get the Kth quadratic programming sub-problem (P_k). We can get $x^{(k+1)}$ and $\lambda^{(k+1)}$ by solving (P_k). Repeat this process until we get the closest optimal solution. If $d^{(k)} = x^{(k+1)} - x^{(k)}$, then the problem that to get $x^{(k+1)}$ by solving the (P_k) would be changed into the quadratic programming of $d^{(k)}$. In order to get the relevant quadratic programming sub problem, we linearize $c_i(x)$ at the point $x^{(k)}$, and consider the following question:

$$\begin{cases} \min & Q(d) = \dfrac{1}{2} d^T B_k d + \nabla f(x^{(k)})^T d \\ s.t. & \nabla c_i(x^{(k)})^T d + c_i(x^{(k)}) = 0, i \in E \\ & \nabla c_i(x^{(k)})^T d + c_i(x^{(k)}) \le 0, i \in I \end{cases} \tag{4}$$

SQP is an effective way to solve the nonlinear optimization problem with constraint. This algorithm is reliable. The optimization toolbox of MATLAB provides the m function of the algorithm. It can be used in the optimization problem of the safety door. SQP is used in solving the nonlinear optimization problem like the quadratic programming. The form of the problems that it can solve is:

$$\begin{cases} \min\limits_{x} & \dfrac{1}{2} x^T H x + f^T x \\ s.t. & A \cdot x \le b \\ & A_{eq} \cdot x = b_{eq} \\ & lb \le x \le ub \end{cases} \tag{5}$$

Where

- H, A, A_{eq} are matrixes
- f, b, b_{eq}, lb, ub, x are vectors.
- H should be symmetric matrix.

The optimal model given in (3) of the controllable curve of the instantaneous linear velocity for the safety door meets this form. On a PC with Pentium 4 1.8GHz and windows 2000 operation system, we can get a decision variable $x = (x_1, x_2, \cdots, x_n)^T$ of 1500 dimensions by using optiQuad function. The final controllable curve of the safety door is show in figure 4.

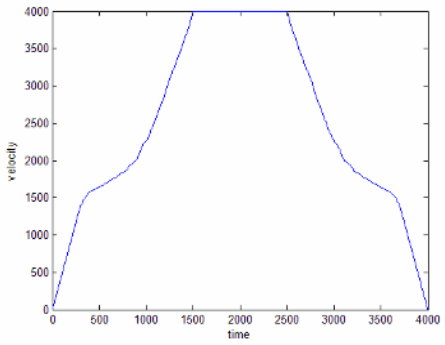

Fig. 4. Controllable curve after optimization

Our calculations show that the energy consumption of the safety door is 22684J before the optimization and 21735J after the optimization. The energy saving (the value of energy saved by the optimization / the value of energy before the optimization) is 4.183%. We assume that there are 10 light rail transit lines, with each door opening and closing every 2 minutes with 16 working hours per day, and each line has 300 safety doors. Then 277040 Kw.h could be saved in one year, which is really meaningful in the practical use.

4 Conclusion

This paper studied the energy optimization problem of the safety doors on urban transit lines. Through analyzing the energy consumption of the safety door system, we proposed a method that could reduce the energy consumption. This method is to improve the design of the controllable curve of the instantaneous linear velocity for the safety door based on the optimization theory. By using SQP to minimize the energy consumption, we finally obtained the energy optimum curve. Comparing with the original energy curve, the optimal curve can save energy consumption by 4.183%, which is quite significant to the energy saving of the light rail transit.

References

1. Bin Ning, Tao Tang, Ziyou Gao, and Fei Yan, Fei-Yue Wang and Daniel Zeng, Intelligent Railway Systems in China, Intelligent Transportation Systems, pp.80-83
2. H.H.Chen, X. F. Xiao, Capability Test of the Prototype of Metro Platform Screen Doors, Journal of South China University of Technology, Vol. 33, No.1, 2005, pp.37-40
3. Cataldi, O.; Alexander, R., Train control for light rail systems on shared tracks, Railroad Conference, 2001. Proceedings of the 2001 IEEE/ASME Joint, 17-19 April 2001 pp. 9-16
4. Hashimoto, M., Onodera, H., Tamaru, K. A power optimization method considering glitch reduction by gate sizing, Low Power Electronics and Design, 1998. Proceedings. 1998 International Symposium, 1998, pp. 221 - 226

5. Willis, H.L.; Tram, H.; Engel, M.V.; Finley, L., Selecting and applying distribution optimization methods, Computer Applications in Power, Vol. 9, Issue 1, 1996, pp. 12-17
6. Iles-Klumpner, D.; Boldea, I, Comparative optimization design of an interior permanent magnet synchronous motor for an automotive active steering system, Power Electronics Specialists Conference, 2004. PESC 04. 2004 IEEE 35th Annual, Vol.1, 2004, pp. 369 - 375
7. Erlon Cristian Finardi and Edson Luiz da Silva,Solving the Hydro Unit Commitment Problem via Dual Decomposition and Sequential Quadratic Programming, IEEE TRANSACTIONS ON POWER SYSTEMS, VOL. 21, NO. 2, MAY 2006, pp.835-844
8. Imad M. Nejdawi,Kevin A. Clements, Paul W. Davis, An Efficient Interior Point Method for Sequential Quadratic Programming Based Optimal Power Flow, IEEE TRANSACTIONS ON POWER SYSTEMS, VOL. 15, NO. 4, NOVEMBER 2000, pp. 1179-1183
9. Ignacio Pérez Abril and José Angel González Quintero, VAR Compensation by Sequential Quadratic Programming, IEEE TRANSACTIONS ON POWER SYSTEMS, VOL. 18, NO. 1, FEBRUARY 2003, pp. 36-41
10. T. Coleman, M. A. Branch, and A. Grace, Matlab Optimization Toolbox User's Guide: The Math Works, Inc., 1999.

Manipulator Trajectory Planning Using Geodesic Method

Liandong Zhang[1, 2], Changjiu Zhou[2], and Delun Wang[3]

[1] School of Mechanical Engineering, Dalian Jiaotong University, P.R. China
[2] Advanced Robotics and Intelligent Control Centre, School of Electrical and Electronic Engineering, Singapore Polytechnic, 500 Dover Road, Singapore
[3] School of Mechanical Engineering, Dalian University of Technology, P.R. China
{ZhangLD, ZhouCJ}@sp.edu.sg

Abstract. A novel manipulator trajectory planning approach using geodesic is proposed in this paper. Geodesic is the necessary condition of the shortest length between two points on the Riemannian surface in which the covariant derivative of the geodesic's tangent vector is zero. The geometric characteristic of geodesic is discussed and used to implement trajectory planning of the manipulator. First, the Riemannian metric is constructed according to the planning task, e.g. to establish a distance metric by arc length of the trajectory to achieve shortest path. Once the Riemannian metric is obtained, the corresponding Riemannian surface is solely determined. Then the geodesic equations on this surface can be attained. For the given initial conditions of the trajectory, the geodesic equations can be solved and the results are the optimal trajectory of the manipulator in the joint space for the given metric. The planned trajectories in the joint space can also be mapped into the workspace. To demonstrate the effectiveness of the proposed approach, simulation experiments are conducted using some typical manipulators, e.g. spatial 3R, 3-PSS parallel and planar 3R manipulators.

1 Introduction

The traditional trajectory planning method [11] for manipulator is the polynomial interpolating method, and the interpolating is performed either in joint space or Cartesian space. This method is simple and quick and it is still popular used nowadays [9]. But the joints of the manipulator are regarded as linearly independent in this simple method, and the potential performance of the manipulator has not been developed sufficiently. For this reason, many research works on optimal trajectory planning have been carried out.

On kinematic optimal trajectory planning aspect, Chiu [3] developed Asada's inertia ellipsoid and Yoshikawa's manipulability ellipsoid, and established a combined performance index of velocity and static force. Then a task compatibility planning method is introduced. Zha [17,18] researched kinematic trajectory planning in Cartesian workspace by genetic algorithm. He regarded the manipulator's trajectory as a ruled surface and interpolated between two pose by Bezier curves. Eldershaw and Cameron [4] and Tian et al [14] and Yun and Xi [16] also used genetic algorithm to study the trajectory planning problem in joint space, and these methods were based on the polynomial interpolation. Bobrow [1] studied the minimum time trajectory planning and the control method of his planning result was also studied [2].

T.-J. Tarn et al. (Eds.): Robot. Weld., Intellige. & Automation, LNCIS 362, pp. 517–528, 2007.
springerlink.com

In order to perform a good trajectory planning, the dynamics of the manipulator also need to be taken into account. On dynamic optimal trajectory planning aspect, the classical method is to take the manipulator's kinetic engergy as objective function, and using Lagrange multiplier method to get the optimal trajectory, that is, the optimal polynomials of each joint angles. Hollerbach and Suh [7] took joint torque as objective function and used this method to adjust the coefficients of the joint angles' polynomials and got the minimum joint torque trajectory finally. Saramago and Steffen [10] took into account the system's kinetic energy and time together, and interpolated polynomials between given points and obtained the optimal trajectory of kinetic energy and time together. Based on polynomial interpolation, Guo et al [5] researched the minimum joint torque problem of redundant manipulator; Yang and Meng [15] studied dynamic motion planning problem by neural networks. Generally speaking, all the methods mentioned above are all based on polynomial interpolation.

When to implement trajectory planning, it is better that the trajectory is unrelated to the world coordinates besides it can optimize certain index. Milos Zefran et al [8] investigated the rigid body motion planning in three-dimensional space based on Lie group and covariant derivative [18]. Guy Rodnay and Elon Rimon [6] visualized the dynamics properties of 2-dof robot in three-dimensional Euclidian space. They introduced geodesics on dynamic surface to represent the trajectory when robot system makes free motion. But there is no method of how to identify the geodesics under arbitrary initial conditions and how to plan robot trajectories based on these geodesics. Park [10] used the intrinsic concept of Riemannian metric in the optimal design of open loop mechanism.

So in this paper, we introduce a geodesic method of trajectory planning. It is quite different from the traditional polynomial method. It is an precise optimal trajectory solution but not an approximate one as polynomial interpolation between two points. At the same time, geodesic is intrinsic and has no relation to the coordinates. We regard arc length and kinetic energy as Riemannian metrics respectively according to task requirement, and get the kinematic and dynamic optimal trajectories by our geodesic method for some kinds of manipulators, such as planar 3R, spatial 3R manipulators and 3-PSS parallel manipulator.

2 Concept of Geodestic

Geodesic is the shortest curve on Riemannian surface. Riemannian surface is determined by Riemannian metric. And the Riemannian metric are regarded as objective function in this paper. So geodesic can be used for manipulator optimal trajectory planning theoreticly, but more lights need to be shed on.

A Riemannian Surface

Riemannian surface is an abstract geometric surface. The tangent vectors on the surface make up of the tangent space. The rule of inner product is defined in this tangent space, and this rule is called Riemannian metric. It is a symmetric, positive definite quadratic form [18]

$$ds^2 = (d\theta_1 \quad d\theta_2)\begin{pmatrix} E & F \\ F & G \end{pmatrix}\begin{pmatrix} d\theta_1 \\ d\theta_2 \end{pmatrix} \tag{1}$$

Eq.1 defines an inner product of two vectors in the tangent space of surface, s, ds, θ_1, $d\theta_1$, θ_2, $d\theta_2$ denote the arc length, derivative of arc length, rotatory angle of link 1, derivative of rotatory angle of link 1, rotatory angle of link 2, derivative of rotatory angle of link 2 respectively. And the vectors have the form

$$d\theta_1 \frac{\partial}{\partial \theta_1} + d\theta_2 \frac{\partial}{\partial \theta_2} \tag{2}$$

∂ refers to the partial differentiation, and E, F, G in Eq.1 denote $(\frac{\partial}{\partial \theta_1})^2$, $(\frac{\partial}{\partial \theta_1})(\frac{\partial}{\partial \theta_2})$, $(\frac{\partial}{\partial \theta_2})^2$ respectively. The given metric determines an exclusive Riemannian surface. The distance between two points is the shortest if moving along geodesic on this Riemannian surface. But the distance here is an abstract concept, for example, if kinetic energy is regarded as the Riemannian metric, the distance on this surface will be the energy. We derive geodesic formula using covariant derivative. Moving along geodesics, the corresponding indices can be minimized. When planning a trajectory along geodesic, the relations between joints are no longer linearly independent, because the joints are coupled.

B Geodesic

We differentiate a vector X on the Riemannian surface and project it to the tangent space, and then the result vector is called the covariant derivative of the vector X. If the covariant derivative of a curve's tangent vector is zero, this curve is called geodesic. Consider a Riemannian surface with Riemannian metric

$$ds^2 = \sum_{i,j} g_{ij} d\theta_i d\theta_j$$

where g_{ij} denotes Riemannian metric coefficient, equal to E, F, G in Eq.1, for i, j =1,2, ..., n. Assume a curve

$$\theta_i = \theta_i(t) \tag{3}$$

on the Riemannian surface, and its tangent vector is

$$\sum_{i=1}^{n} d\theta_i \frac{\partial}{\partial \theta_i} \tag{4}$$

The curve's arc length is invariant, and it's convenient to regard arc length as the parameter of the curve. We calculate the covariant derivative of Eq.4 and let the result to be zero, and then the formulation of geodesic is obtained [18],

$$\frac{d^2\theta_i}{ds^2} + \Gamma_{kj}^i \frac{d\theta_k}{ds}\frac{d\theta_j}{ds} = 0 \tag{5}$$

where s is the arc length of the curve, θ_i is the curve coordinate, for i, j, k=1,2, ... , n. The Christoffel symbols are given in terms of Riemannian metric by

$$\Gamma_{kj}^i = \frac{1}{2} g^{mi}\left(\frac{\partial g_{km}}{\partial \theta_j} + \frac{\partial g_{jm}}{\partial \theta_k} - \frac{\partial g_{kj}}{\partial \theta_m}\right) \tag{6}$$

where g^{mi} is the element of inverse matrix of the Riemannian metric coefficient matrix

Geodesic is the shortest curve between two points on the Riemannian surface and the velocity along geodesic curve remains invariant. It is noticed that the meanings of velocities are different according to different Riemannian surfaces determined by different Riemannian metrics. When arc length is regarded as the metric, the velocity along geodesic refers to the normal velocity that we all know well. So the acceleration along geodesic is zero and the motion is smooth. When kinetic energy is regarded as Riemannian metric, the 'velocity' of curve on the surface determined by this metric shows the invariant of kinetic energy. For each point in the Riemannian surface, there is only one geodesic according to the given direction. That is, geodesic is determined by the initial conditions.

3 Optimal Trajectory Planning of Spatial 3R Manipulator

A Arc Length as Riemannian Metric

A spatial 3R robot is shown in Fig.1. It is the simplified Puma560 or GE P60 manipulator if we ignore the other 3 degrees of freedom of the wrist. The forward kinematics is

$$\boldsymbol{r} = ((c_2 + c_{23})c_1, (c_2 + c_{23})s_1, s_2 + s_{23}) \tag{7}$$

where $\boldsymbol{r}$ is the position vector of the end-effector of the robot, l_1 is the length of link 1, l_2 is the length of link 2, l_3 is the length of link 3, θ_1, θ_2, θ_3, c_1, c_{23}, s_1, s_{23} denote angle of joint 1, angle of joint 2, angle of joint 3, $\cos(\theta_1)$, $\cos(\theta_2+\theta_3)$, $\sin(\theta_1)$, $\sin(\theta_2+\theta_3)$ respectively.

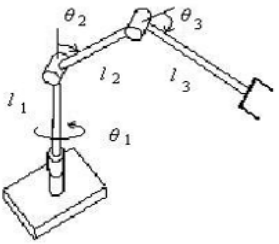

Fig. 1. Spatial 3R manipulator

The Riemannian metric of arc length is given by

$$ds^2 = dr^2 = \begin{bmatrix} d\theta_1 & d\theta_2 & d\theta_3 \end{bmatrix} G \begin{bmatrix} d\theta_1 \\ d\theta_2 \\ d\theta_3 \end{bmatrix} \tag{8}$$

where dr is the derivative of vector $\boldsymbol{r}$, G is the metric coefficient matrix,

$$G = \begin{bmatrix} (c_2 + c_{23})^2 & 0 & 0 \\ 0 & 2 + 2c_3 & 1 + c_3 \\ 0 & 1 + c_3 & 1 \end{bmatrix} \tag{9}$$

We assume that the mass concentrates on the end of each linkage. Linkage length and mass are all 1. When the metric is given by Eq.8, the corresponding geodesic on the Riemannian surface is determined by Eq.5. The geodesic is solely identified by the given initial conditions.

For example, when the initial conditions are given by

$$\theta_1 = 0, \dot{\theta}_1 = 0.6, \theta_2 = -\frac{\pi}{3}, \dot{\theta}_2 = 0.2, \theta_3 = \frac{2\pi}{3}, \dot{\theta}_3 = 0.7$$

$\dot{\theta}_1$, $\dot{\theta}_2$, $\dot{\theta}_3$ denote rates of joint 1, joint 2 and joint 3 respectively. For a spatial 3R robot, Eq.5 is a 3-order differential equation group which determines a geodesic of the robot under the initial conditions above.

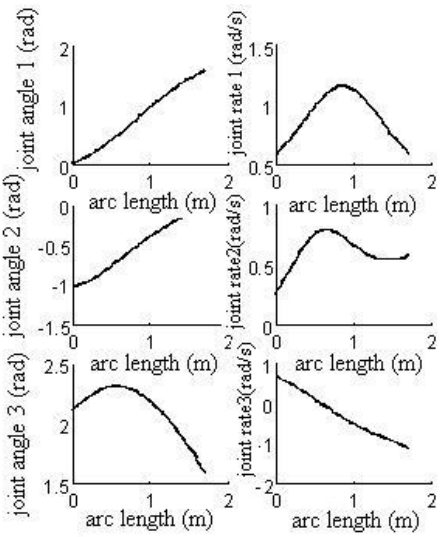

Fig. 2. The result of optimal trajectory planning when arc length as Riemannian metric

The numerical solution of this geodesic is shown in Fig.2. The joints' angles and joints' rates are determined by our geodesic method. The robot moves according to this planning results will perform an optimal trajectory, that is, the shortest path of the end-effector between two given points. The simulation of the end-effector's trajectory by this geodesic method is shown in Fig.3. Fig.3 shows that the trajectory of the end-effector of the manipulator is a straight line, that is, the shortest curve in the space. The velocity of end-effector is invariant along the geodesic and its acceleration is zero, so the end-effector's motion is smooth.

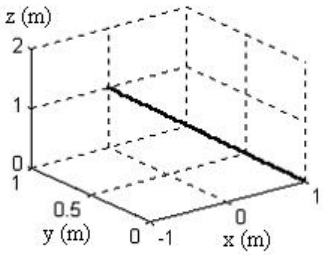

Fig. 3. Simulation of the end-effector in Cartesian space

B Kinetic Energy as Riemannian Metric

In order to minimize the kinetic energy of robot system, we consider the kinetic energy as Riemannian metric. It is given by

$$ds^2 = [d\theta_1 \quad d\theta_2 \quad d\theta_3] M \begin{bmatrix} d\theta_1 \\ d\theta_2 \\ d\theta_3 \end{bmatrix} \tag{10}$$

where M is the inertia matrix of the system, being as the metric coefficient matrix,

$$M = \begin{bmatrix} 2c_2{}^2 + 2c_2c_{23} + c_{23}{}^2 & 0 & 0 \\ 0 & 3 + 2c_3 & 1 + c_3 \\ 0 & 1 + c_3 & 1 \end{bmatrix} \tag{11}$$

The mass and length of links are set to 1 in this example. The Riemannian surface determined by the metric Eq.10 indicates the dynamic properties of the system. The geodesic on this surface is the optimal trajectory that minimizes the kinetic energy.

When the initial conditions are given by

$$\theta_1 = 0, \dot{\theta}_1 = 0.6, \theta_2 = \frac{\pi}{3}, \dot{\theta}_2 = 0.6, \theta_3 = -\frac{2\pi}{3}, \dot{\theta}_3 = -0.5$$

then the sole geodesic under above conditions is determined. This geodesic can be obtained by solve Eq.5 according to the initial conditions given above. The numerical

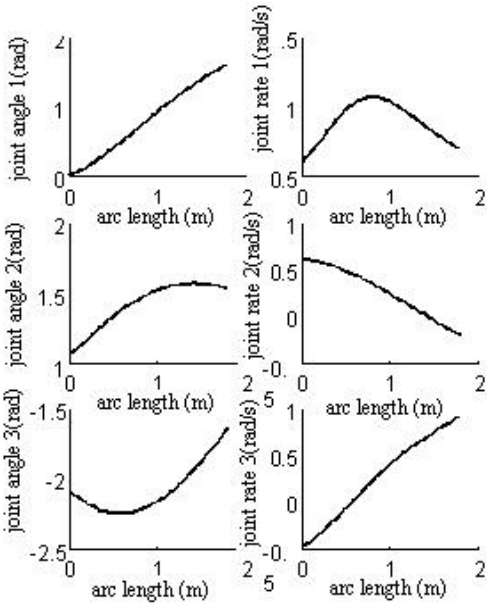

Fig. 4. The result of optimal trajectory planning when kinetic energy as Riemannian metric

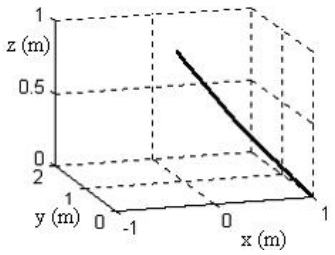

Fig. 5. Simulation of the end-effector in Cartesian space

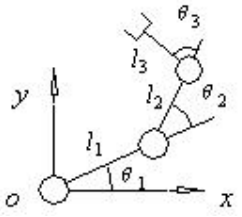

Fig. 6. Planar 3R manipulator

solution of geodesic is shown in Fig.4. The kinetic energy of the system remains invariant when the robot moving along this geodesic. The simulation of the end-effector's optimal trajectory is shown in Fig.5.

4 Optimal Trajectory Planning of Planar 3R Manipulator

The planar 3R robot is shown in Fig.6. l_1, l_2, l_3, θ_1, θ_2, θ_3 denote linkage length and rotatory angle respectively.

The planar 3R robot possesses one redundant freedom and we can use this additional freedom to improve its dynamic manipulability. So we define a compound Riemannian metric made up of arc length and kinetic energy in order to optimize distance length and kinetic energy at the same time. The new Riemannian metric is given by

$$ds^2 = c(ds_1)^2 + d(ds_2)^2 \tag{12}$$

where $(ds_1)^2$ represents the arc length metric and $(ds_2)^2$ represents the kinetic energy metric. c and d are scale coefficients, and they determine the proportion of arc length and kinetic energy in the new Riemannian metric in Eq.12. c and d are selected by the requirement of the task. We set $c = d = 1$, and linkage length and mass are all 1. The mass of each linkage is assumed to concentrated on the tip of each lingkage. The Riemannian metric of a planar 3R robot is given by

$$ds^2 = (d\theta_1\ d\theta_2\ d\theta_3)M((d\theta_1\ d\theta_2\ d\theta_3)^T \tag{13}$$

We can use the same method as the spatial 3R manipulator to calculate the distance metric and kinetic metric of planar 3R robot respectively and then add them together to construct the combined Riemannian metric of Eq.13. The metric coefficient matrix is

$$M = \begin{pmatrix} 9+6c_2+4c_3+4c_{23} & 5+3c_2+4c_3+2c_{23} & 2+2c_{23}+2c_3 \\ 5+3c_2+4c_3+2c_{23} & 5+4c_3 & 2+2c_3 \\ 2+2c_{23}+2c_3 & 2+2c_3 & 2 \end{pmatrix} \tag{14}$$

When the initial conditions are given by

$$\theta_1 = 0, \dot{\theta}_1 = 1, \theta_2 = 0, \dot{\theta}_2 = 1, \theta_3 = 0, \dot{\theta}_3 = 1$$

$\dot{\theta}_1$, $\dot{\theta}_2$, $\dot{\theta}_3$ denote the rates of joint 1, joint 2 and joint 3 respectively. The geodesic on the Riemannian surface is determined by the initial conditions above. In this example, the Riemannian metric is different from arc length metric and kinetic metric. It is a metric considering both arc length metric and kinetic metric, so the geodesic on this Riemannian surface is an optimal trajectory for a combining index of distance and energy.

The numerical solution of Eq.5 for the given initial conditions is shown in Fig.7. The simulation of the trajectory of the end-effector in Euclidian space is shown in Fig.8. For the redundant robot, the inverse kinematics has multiple solutions. The traditional redundant robot trajectory planning is Lagrange multiplier method. But this method needs to solve pseudo-inverse of inertia matrix and Jacobian matrix. Our method is based on Riemannian metric and geodesics and does not need this pseudo-inverse calculation.

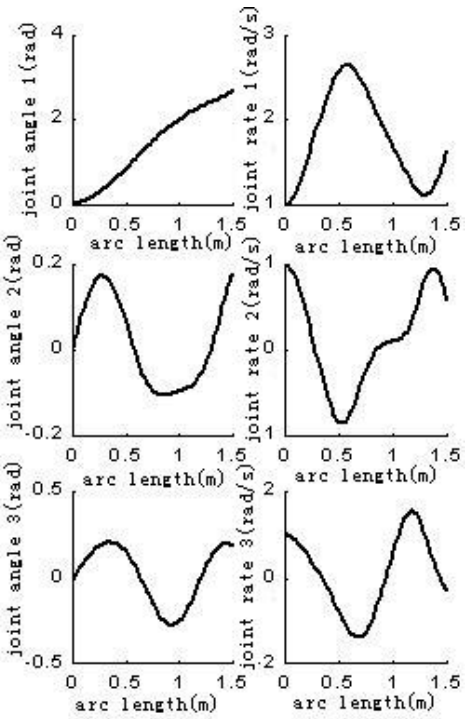

Fig. 7. The result of optimal trajectory planning with a combined Riemannian metric

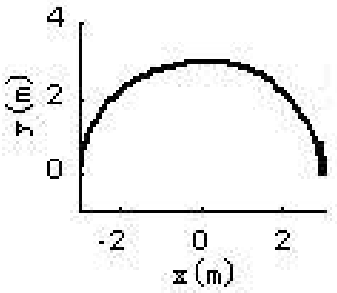

Fig. 8. Simulation of the end-effector in in Cartesian space

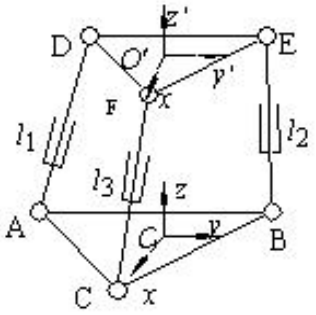

Fig. 9. The parallel 3-PSS manipulator

5 Optimal Trajectory Planning of 3-PSS Parallel Manipulator

3-PSS parallel manipulator is shown in Fig.9. It has 3 degrees of freedom, P represents the prismatic joint and S represents the spherical joint. The prismatic joint is the driving

joint. Point *O*' is the center of the moving platform, and point *O* is the center of the static platform.

A Arc Length as Riemannian Metric

The center point O' is the reference point and we define its trajectory's arc length as Riemannian metric. Then the shortest path planning can be carried out by geodesic method. Here we set $AB = BC = CA = b$, $DE = EF = FD = a$, $c = a - b = 1$, then the forward kinematic solution is

$$\begin{cases} x = \dfrac{l_1^{\,2} + l_2^{\,2} - 2l_3^{\,2}}{2\sqrt{3}} \\ y = \dfrac{l_1^{\,2} - l_2^{\,2}}{2} \\ z = \dfrac{\sqrt{(l_1^{\,2} + l_2^{\,2} + l_3^{\,2} + 1)^2 - 3(l_1^{\,4} + l_2^{\,4} + l_3^{\,4} + 1)}}{\sqrt{6}} \end{cases} \tag{15}$$

l_1, l_2 and l_3 denote the variants of prismatic joints respectively. The arc length Riemannian metric ds^2 can be obtained through differentiation of Eq.15, it is

$$\begin{aligned} ds^2 &= dx^2 + dy^2 + dz^2 \\ &= \begin{pmatrix} d_1 & d_2 & d_3 \end{pmatrix} \begin{pmatrix} F_1^2 + E_1^2 + H_1^2 & F_1F_2 + E_1E_2 + H_1H_2 & F_1F_3 + H_1H_3 \\ F_1F_2 + E_1E_2 + H_1H_2 & F_2^2 + E_2^2 + H_2^2 & F_2F_3 + H_2H_3 \\ F_1F_3 + H_1H_3 & F_2F_3 + H_2H_3 & F_3^2 + H_3^2 \end{pmatrix} \begin{pmatrix} d_1 \\ d_2 \\ d_3 \end{pmatrix} \end{aligned} \tag{16}$$

in the above Eq.16, d_i represents dl_i, i=1,2,3, the derivative of l_i.

$F_1 = \dfrac{l_1}{\sqrt{3}}$, $F_2 = \dfrac{l_2}{\sqrt{3}}$, $F_3 = -\dfrac{2l_3}{\sqrt{3}}$, $E_1 = l_1$, $E_2 = -l_2$, $H_1 = \dfrac{D_1}{2\sqrt{6}A}$, $H_2 = \dfrac{D_2}{2\sqrt{6}A}$, $H_3 = \dfrac{D_3}{2\sqrt{6}A}$,

$D_1 = 4Bl_1 - 12l_1^{\,3}$, $D_2 = 4Bl_2 - 12l_2^{\,3}$, $D_3 = 4Bl_3 - 12l_3^{\,3}$, $B = l_1^{\,2} + l_2^{\,2} + l_3^{\,2} + 1$,

$A = \sqrt{(l_1^{\,2} + l_2^{\,2} + l_3^{\,2} + c^2)^2 - 3(l_1^{\,4} + l_2^{\,4} + l_3^{\,4} + c^4)}$.

According to this arc length Riemannian metric of Eq.16, a Riemannian surface reflecting the kinematic character will be determined. We now calculate geodesics between two points on this surface according to the given initial conditions. For example, in Cartesian space, the start point for *O*' is (0,0,0) and the end point is (1,2,3), and the geodesic between the points is solved and it is the optimal trajectory corresponding to the distance metric in Eq.16. This optimal path in joint space is shown in Fig.10. Once the joint space result of geodesic is acquired, the corresponding optimal trajectory of *O*' in Cartesian space will be visualized. This simulating result is shown in Fig.11. The simulation shows clearly that the shortest path between the given two points is a line.

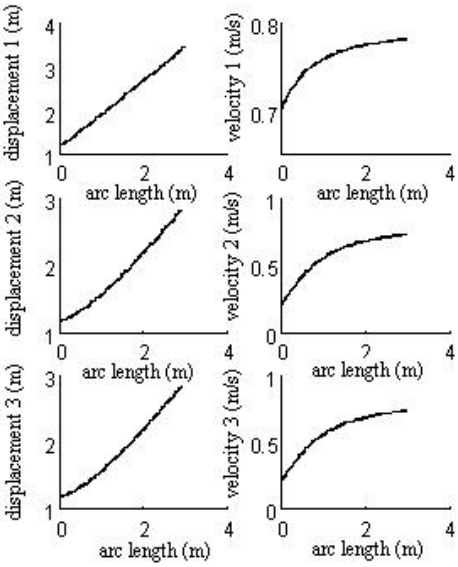

Fig. 10. Optimal path of 3-PSS parallel manipulator

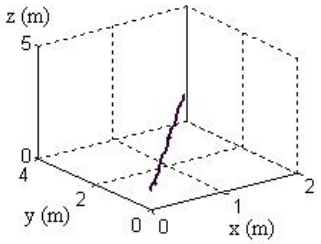

Fig. 11. Simulation of the end-effector in Cartesian space

6 Concluding Remarks

A new robot optimal trajectory planning method based on geodesic is introduced in this paper. Arc length of the trajectory and kinetic energy are regarded as Riemannian metrics respectively. Examples of applications of the new method to planar 3R, spatial 3R manipulators and 3-PSS parallel manipulator are given. The simulation results verified the proposed method.

Acknowledgement

The research work reported here is possible under the National Natural Science Foundation of China, Grant No.50505004, Natural Science Foundation of Liaoning Province, Grant No.20051061, and Project of Education Office of Liaoning Province, Grant No.05L050.

References

1. Bobrow J (1988) Optimal robot path planning using the minimum-time criterion. IEEE Journal of Robotics and Automation 4:443-449
2. Bobrow JE, Dubowski S, Gibson JS (1985) Time-optimal control of robotic manipulators along specified paths. The International Journal of Robotics Research 1:3-17
3. Chiu SL (1988) Task compatibility of manipulator postures. The International Journal of Robotics Research 7(5):13-21
4. Eldershaw C, Cameron S (2001) Using genetic algorithms to solve the motion planning problem. Journal of Universal Comput Sci 1:422-432
5. Guo LX, Zhao MY, Zhang GZ (2000) Minimum joint torque trajectory planning of spatial redundant manipulator. Chinese Journal of Northeast University 21(5):512-515
6. Guy Rodnay, Elon Rimon (2001) Isometric visualization of configuration spaces of two-degrees-of-freedom mechanisms. Mechanism and Machine Theory 36:523-545
7. Hollerbach JM, Suh KC (1987) Redundancy resolution of manipulator through torque optimization. IEEE Journal of Robotics and Automation 3(4):308-316
8. Milos Zefran, Vijay Kumar, Christopher B Croke (1998) On the generation of smooth three-dimensional rigid body motions. IEEE Transactions on Robotics and Automation 14(4):576-589
9. Papadopoulos E, Poulakakis I (2002) On path planning and obstacle avoidance for nonholonomic platforms with manipulators: A polynomial approach. The International Journal of Robotics Research 21(4):367-383
10. Park FC (1995) Distance metrics on the rigid body motions with applications to mechanism design. ASME Journal of Mechanical Design 117(3):48-54
11. Paul RP (1981) Robot manipulators, mathematics, programming and control. MIT Press, Cambridge
12. Saramago SFP, Steffen JRV (1998) Optimization of the Trajectory Planning of Robot Manipulators Taking into Account the Dynamics of the System. Mechanism and Machine Theory 33(7):883-894
13. Spivak M (1979) A comprehensive introduction to differential geometry. Publish or Perish Press, Berkeley
14. Tian LF, Collins, Curtis (2004) An effective robot trajectory planning method using a genetic algorithm. Mechatronics 14(5):455-470
15. Yang SX, Meng M (2000) An efficient neural network approach to dynamic robot motion planning. Neural Networks 2:143-148
16. Yun WM, Xi YG (1996) Optimum motion planning in joint space for robots using genetic algorithms. Robotics and Autonomous Systems 18:373-393
17. Zha XF (2002) Optimal pose trajectory planning for robot manipulators. Mechanism and Machine Theory 37(10):1063-1086
18. Zha XF, Chen XQ (2004) Trajectory coordination planning and control for robot manipulators in automated material handling and processing. International Journal of Advanced Manufacture Technology 23:831-845

Anti-phase Synchronization Control Scheme of Passive Biped Robot

Zhenze Liu[1], Changjiu Zhou[2], Peijie Zhang[1], and YantaoTian[1]

[1] College of Communication Engineering, Jilin University, Changchun City, 130025, P.R. China
tianyt@jlu.edu.cn
[2] Advanced Robotics and Intelligent Control Centre, School of Electrical and Electronic Engineering, Singapore Polytechnic, 500 Dover Road, Singapore 139651
zhoucj@sp.edu.sg

Abstract. A novel control scheme is proposed for passive compass-like biped based on the concept of anti-phase synchronization. Under this framework, various interesting properties of the stable biped gait are studied. The dynamics of the biped is decoupled by inverse dynamic control and two legs of the biped are converted to be independent parallel subsystems. The coupled synchronization controller is designed which can effectively solve the anti-phase synchronization control problem. The proposed anti-phase synchronization control scheme can also make the mechanical energy of the robot reach a desired level while the average velocity tracking a target value. By designing a Lyapunov function, the stability and convergence of the anti-phase synchronization controller are proved. Simulation is conducted to show the effectiveness of the proposed control scheme. It is demonstrated that the proposed method is useful for analysis and design of the biped gait.

1 Introduction

Analysis and control strategy design of passive biped robot is a sophisticated problem in the field of biped robot. In the last 1980's, Tad McGeer put forward the concept of "passive dynamic walking" on the basis previous work, pioneering the research field of passive-dynamic robotics [9]. Here, the note "passive" means is defined as the ability of the robot to walk autonomously down an inclined surface without any external source of energy. The walking of the passive robot is called "passive walking" is mainly because the locomotion pattern is only determined by gravity and the mechanics of itself. Tad McGeer succeeded in building several walkers that could down inclined surface in natural and energy efficient gait. The passive dynamic walker has no actuation and its motion is powered only by gravities.

After McGeer's pioneering wok, Goswami [7], Garcia [1], Collins [3], have do further research wok on passive dynamic walking. The mathematical model of walking of the compass gait biped has hybrid natures, with the nonlinear differential equations describing the smooth dynamics in swing stage and algebraic equations describing the states changes during the collision phase when the previous swing leg contact with the ground and the previous stance leg swing away the ground.

T.-J. Tarn et al. (Eds.): Robot. Weld., Intellige. & Automation, LNCIS 362, pp. 529–539, 2007.
springerlink.com

Because of the complexity of dynamics of biped walking, design of effective control strategies is a difficult task. Commonly used control schemes, including the energy based control and the slope invariant control, are only simple controls, and the under controlled gaits depend on the passive limit cycles.

The design of effective and efficient control schemes is one of focuses in the field of passive robotics. The study of passive biped robot is believed to provide insight to the inner principles of human walking and control, and help to design the dynamic control strategy of biped walking and bring anthropomorphic robots closer to practical application [2, 12].

Through the observation of human gait biped, symmetry is an important indicator of healthy gait [5]. Symmetry property of healthy gait in human walking has been applied to the analysis and design of the compass-like biped robot. Analyzing the symmetry characteristic of passive biped walking gaits, this paper presents a new control strategy of anti-phase synchronization. Firstly, the inverse dynamic control method is used to decouple the dynamics of two legs and make the resultant force of gravity and actuate force equivalent to a virtual gravity force erect to the walking surface. Motions of two legs are transformed into two similar subsystems having the same motion dynamics. Then the problem of anti-phase synchronization is dealt though coupling control of two subsystems in such a way that the robot reaches a desired level of mechanical energy and two legs move synchronously in opposite directions. In addition, the new designed Lyapunov function and simulation results prove the validity of the strategy. The method stated in the paper is helpful to practical application of the design of the robot's gait.

2 Model of Compass Gait Biped

In this paper, we adopt the model and notation from the compass gait biped which has been presented by Goswami [7]. The configuration is showed in Fig. 1. The passive dynamic walker is composed of two legs with lumped mass m at center of mass, attached at the hip, and a point mass m_H at hip joint representing the upper body. The dynamics of the passive biped is equivalent to a double pendulum. The configuration of the compass gait is determined by the support angle θ_s and swing leg angle θ_{ns}.

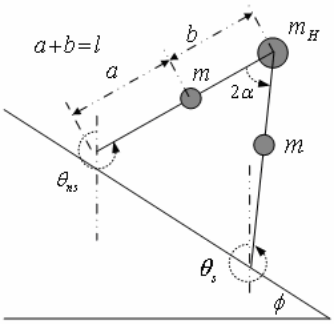

Fig. 1. The compass-like gait biped

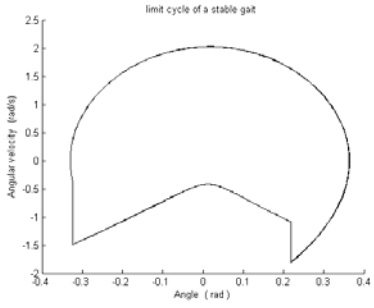

Fig. 2. A stable limit cycle under three degree slope

The dynamics of passive biped walking has a hybrid nature. Based on the characteristics of dynamics, a walking period consists of two different stages, the swing stage and an instantaneous collision stage. In the swing stage, the smooth dynamics of motion can be modeled by differential equations, of which the detail is $\dot{x}(t) = f(x(t)) + g(x(t))u(t)$. In the instantaneous collision stage, there is a jump in state variables and the discrete dynamics can be described as algebraic equations, of which the detail formation is $x^+(t) = \Delta(x^-(t))$.

The complete dynamic equations can be written as Eq. 1 [8].

$$\begin{cases} \dot{x} = f(x) + g(x)u \\ x^+ = \Delta(x^-) \end{cases} \tag{1}$$

where $x(t) \in X$, X is the state space of passive robot, which is a connected open subset of four dimensional vector space R^4. S is the set of states satisfying the conditions for an impact event to happen, and $S := \{x \in X \mid H(x) = 0\}$. $H := X \to R$, is a criteria definition of impact event. $x^-(t) := \lim_{\tau \to t^-} x(\tau)$, $x^+(t) := \lim_{\tau \to t^+} x(\tau)$, describing the stats of passive biped exactly before and after impact. The hybrid property of passive biped walking makes analysis and controls its dynamics a complex problem.

It is a hybrid system with the detailed expression [6]

$$M(q)\ddot{q} + C(q,\dot{q})\dot{q} + g(q) = Bu \tag{2}$$

Where $q = \begin{bmatrix} q_1 \\ q_2 \end{bmatrix} = \begin{bmatrix} \theta_{ns} \\ \theta_s \end{bmatrix}$, $B = \begin{bmatrix} -1 & 0 \\ 1 & 1 \end{bmatrix}$, and the vector u represents independent torques at the hip and ankle, defined as $u = \begin{bmatrix} \mu_H \\ \mu_s \end{bmatrix}$, which are assumed to be identically zero in the case of the passive biped.

The matrices $M(q)$, $C(q,\dot{q})$ and $g(q)$ are given by

$$M(q) = \begin{bmatrix} mb^2 & -mlb\cos(q_2 - q_1) \\ -mlb\cos(q_2 - q_1) & (m_H + m)l^2 + ma^2 \end{bmatrix}$$

$$C(q,\dot{q}) = \begin{bmatrix} 0 & mlb\sin(q_2 - q_1)\dot{q}_2 \\ mlb\sin(q_1 - q_2)\dot{q}_1 & 0 \end{bmatrix}$$

$$g(q) = \begin{bmatrix} mb\sin(q_1) \\ -(m_H l + ma + ml)\sin(q_2) \end{bmatrix}$$

Where $l = a + b$.

For modeling the states changes during the collision phase, the following assumptions are made. 1) The impact of biped robot with the ground is a perfectly inelastic collision; 2) The impact is completed instantaneously, the angular velocities of the robot experience a jump change and the configuration of the biped (angular displacement of two legs) remains invariable; 3) During the collision phase, there is no slipping between the stance leg and the ground. Under the assumptions, there is a conservation of angular momentum of stance leg about the hip joint and a conservation of angular momentum of swing leg about the contact point with the ground. Then, the algebraic equations mapping the states of the robot previous impact to states after impact using the angular momentum conversation control law, and the mapping equations can be written as follows.

$$\begin{bmatrix} q^+ \\ \dot{q}^+ \end{bmatrix} = \begin{bmatrix} J & 0 \\ 0 & (Q^+(\alpha))^{-1} Q^-(\alpha) \end{bmatrix} \begin{bmatrix} q^- \\ \dot{q}^- \end{bmatrix}$$

Where, $J = \begin{bmatrix} 0 & 1 \\ 1 & 0 \end{bmatrix}$, $Q^+(\alpha)$, $Q^-(\alpha)$ have the following formulations.

$$Q^+(\alpha) = \begin{bmatrix} mb^2 - mbl\cos(2\alpha) & (ml^2 + ma^2 + m_H l^2) - mbl\cos(2\alpha) \\ mb^2 & -mbl\cos(2\alpha) \end{bmatrix}$$

$$Q^-(\alpha) = \begin{bmatrix} (m_H l^2 + 2ml^2)\cos(2\alpha) - mab - 2mb\cos(2\alpha) & -mab \\ -mab & 0 \end{bmatrix}$$

Where, $\alpha = (\theta_{ns}^- - \theta_s^-)/2$, is called stance angle.

The instantaneous change in angular velocity results in a loss of kinetic energy while total angular momentum is conserved. Limit cycle is an important way to figure the stable gait. A limit cycle occurs when the velocity after impact equals the initial velocity. For a given distribution of masses and leg lengths also with a given ground slope, there exists one and only one stable limit cycle as shown in Fig. 2. The limit cycles are typical determined from the momentum equations using a numerical search procedure.

Poincaré map is succeeded used in the analysis of stable limit cycles. The stability of limit cycles is estimated by the eigenvalues of linearized poincaré map. Because of the complexity of dynamic models, the solution of stable gaits is solved through numerical simulation.

Goswami [4] and Spong [10] did research work of controller design of passive dynamic walker. The energy based control and the slope invariant control is successfully used in the control scheme design. Basin of attraction was enlarged. But the control strategies are a little simple and the introduced gaits depend on the existing completely passive limit cycles.

Russ Tedrake use learning control in the control of passive biped walking [11], but the stability acquired mainly depends on the simple mechanics. The learning controller contributes little to the stability of the robot of inner walking period.

3 Concept of Anti-phase Synchronization

The mechanism of human walking is a sophisticated system. There are strong coupling and high nonlinear in the motion dynamics, as the walking is accomplished by cooperation of different muscles. So, we tried to apply the idea of "cooperation control" to the control of passive dynamic walker.

Anti-phase Synchronization: In passive dynamic walking, under appropriate control, the sums of angular displacement and velocity of two legs converge to zero, that is, $\lim_{t\to \mathrm{T}}\left(\theta'_{ns}+\theta'_{s}\right)=0$, $\lim_{t\to \mathrm{T}}\left(\dot{\theta}'_{ns}+\dot{\theta}'_{s}\right)=0$. The control is called Anti-phase Synchronization control.

Generalized Anti-phase Synchronization: In control of robot with complex structure, the sums of normalized state variables (function of each variable) converge to zero in a period of time T under control, that is $\lim_{t\to \mathrm{T}}\left(f(x)+g(x')\right)=0$. The control is called generalized anti-phase synchronization. Where, x and x' are state variables of two subsystem separately. $f(x)$ and $g(x')$ are normalizing functions of variables of each subsystem.

3.1 Some Symmetry Property in Gait Biped

The comparison relationship on the angular position of the two legs during steady periodic gait cycle has been presented in Fig. 3. It is obviously that angular positions of the two legs are asymmetry. The gait biped walking works as a double pendulum, while the stance leg has a comparative big difference with the swing leg. This can be explained that the stance leg experiences a relative compelled motion with the action force coming from the swing leg as well as from gravity. And in addition, the coupling degree of the two legs varies at different instant.

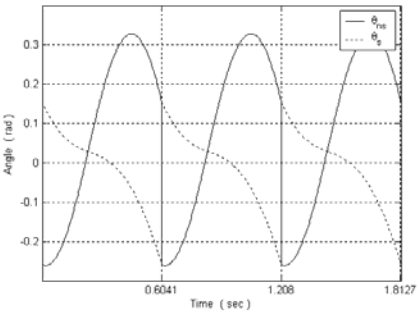

Fig. 3. Two legs' angular position during steady robot gaits

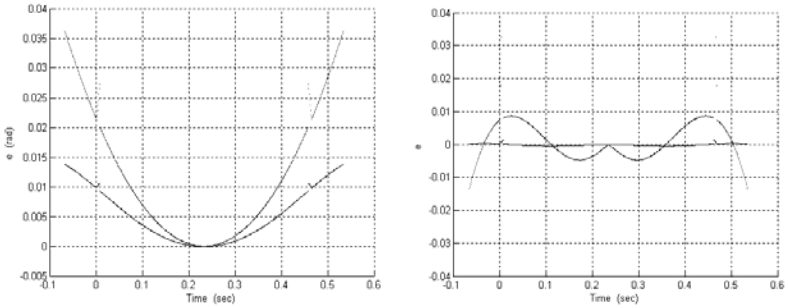

(a) (b)

Fig. 4. Figures of extent of asymmetry in motions of two legs. (a) Inter-section point between legs, (b) centre value with two culminations within one cycle of the swing leg.

Presume the intersection point between two legs in Fig. 3 and the middle point with the two culmination value within one cycle of the swing leg as the symmetry point respectively; we get the asymmetry degree figures about two legs.

Observing from Fig. 4-a, different hip mass will correspond to the result that the larger the hip mass is, the higher the symmetry degree is. That is to say, the coupling effect between two legs will be influenced by the hip mass in great degree. With Fig. 4-b, different μ will correspond to the different error about the angular position and angular velocity. The conclusion is very important for it will help in modifying the gait biped model when choosing the parameter and adjusting the gait biped cycle. Asymmetry property of any kind in the biped gait has been shown in Fig. 4-a and Fig. 4-b.

3.2 Realization of Anti-phase Synchronization

The paper will pay great attention to the solution of the first problem. By applying the idea of "inverse dynamic control", both the gravity torque act on the robot and the added control torque are made equivalent to a gravity action, then a closed loop linear system with the same effect on the robot can be obtained. The advantage of the idea is that it can help adjust the gait distance and also the period corresponding to the forward varied velocity at any instant. Through the control, the swing leg acts as the single pendulum and the stance leg works as the inverted pendulum, the dynamic property of the two legs are the same except the analysis of the equilibrium point and the stability.

3.3 Decoupling Motions of Two Legs

There exists strong coupling between dynamics of two legs. Erasing the coupling and construct the same subsystem with the idea of "inverse dynamic control"[11], we can obtain a closed loop linear system. For the nonlinear equations (Eqs. 2) of our biped, as

the swing leg is about to leave the ground, the anti-phase control is induced to the equation with the form,

$$u = B^{-1}(M(\dot{q})a + C(q,\dot{q})\dot{q} + g(q)) \tag{3}$$

Control input (Eq. 2) can reduce the system to the decoupled double integrator system

$$\ddot{q} = a \tag{4}$$

Usually, joint angles can then be controlled independently using a control law

$$a = -K_p q - K_d \dot{q} + r \tag{5}$$

Where K_p and K_d are diagonal matrices with elements consisting of position and velocity gains, respectively. For a given desired trajectory

$$t(q^d(t), \dot{q}^d(t)) \tag{6}$$

We can choose the input $r(t)$ as

$$r = \ddot{q}^d(t) + K_p q^d(t) + K_d \dot{q}^d(t) \tag{7}$$

The desired trajectory can be obtained as cubic trajectory as shown in [11] if the initial and final states of the trajectory are known. Thus a kind of synchronization can get with the walking trajectory and the given trajectory.

Simulation demonstrates that the rule for the swing leg is similar with the simple pendulum. In the design of anti-phase synchronization control, we keep the dynamic state of the swing leg and make the stance leg act with the same rule, then

$$a = \begin{bmatrix} -\frac{g}{kl}\sin(\theta_{ns} + \phi) \\ -\frac{g}{kl}\sin(\theta_s + \phi) \end{bmatrix} \tag{8}$$

where $k = \frac{\beta}{\beta + 1}$, $\beta = \frac{b}{a}$.

The dynamic equation of the robot can be divided into two independent parts and both of them possess a similar expression. To be convenient for understanding, we introduce the new coordination defined as $\theta'_{ns} = \theta_{ns} + \phi$, $\theta'_s = \theta_s + \phi$. Motions of two legs under control are similar subsystems, which are formulated in (9).

$$\ddot{\theta}_{ns} + \frac{g}{kl}\sin(\theta_{ns} + \phi) = 0 \tag{9}$$

$$\ddot{\theta}_s + \frac{g}{kl}\sin(\theta_s + \phi) = 0 \tag{10}$$

3.4 Controlled Synchronization

To synchronize motions of two legs, the idea called mutual direction coupling is introduce to synchronize dynamics of two subsystems.

$$\begin{cases} \dot{x} = f(x) + \overline{K}(\overline{x} - x) \\ \dot{\overline{x}} = f(\overline{x}) + K(x - \overline{x}) \end{cases} \tag{11}$$

Where $\overline{K}(\overline{x} - x)$ and $\overline{K}(x - \overline{x})$ are the mutual coupling synchronization control items of the two sub-systems. $\dot{x} = f(x)$ and $\dot{\overline{x}} = f(\overline{x})$ are the subsystems introduced by inverse dynamic control. $K = diag(k_1, k_2, ..., k_n)$ is called coupling length, where $n = 2$ here. Value of K determines the accuracy and rate of convergence of synchronization control. In the anti-phase controller, the control objective can be formalized by the following relations

$$\begin{aligned} &\lim_{t\to\infty}(\theta_{ns}^t + \theta_s^t) = 0 \\ &\lim_{t\to\infty}(\dot{\theta}_{ns}^t + \dot{\theta}_s^t) = 0 \end{aligned} \tag{12}$$

Synchronized time of the system should be considered here because two legs should come to the state of anti-phase synchronization within one cycle with the control, that is to say $0 \le t \le T$ (T is the step period).

Add the anti-phase synchronization control to the decouple equations, Eq. 9 and Eq. 10.

$$\ddot{q} = a + \overline{B}\overline{u} \tag{13}$$

Where $\overline{B} = \begin{bmatrix} 1 & 0 \\ -1 & 1 \end{bmatrix}$,

$$\overline{u} = \begin{bmatrix} -\gamma\dot{\theta}_{ns}^t\overline{H} - \lambda_1\sin(\theta_{ns}^t + \theta_s^t) - \lambda_2(\dot{\theta}_{ns}^t + \dot{\theta}_s^t) \\ -2\gamma\dot{\theta}_{ns}^t\overline{H} - 2\lambda_1\sin(\theta_{ns}^t + \theta_s^t) - 2\lambda_2(\dot{\theta}_{ns}^t + \dot{\theta}_s^t) \end{bmatrix} \tag{14}$$

Where $H = H(\theta_{ns}, \dot{\theta}_{ns}) + H(\theta_s, \dot{\theta}_s) - 2H^*$, and H represents virtual mechanical energy of each pendulum-like leg and the designed controller, Eq. 13, can swing the pendulum up to the desired energy level H^* in such a way that the pendulum-like two legs move in opposite directions. γ, λ_1 and λ_2 are positive gain coefficient, which determines the rate of convergence to state of synchronization.

The control objective to a desired value of virtual mechanical energy can be formalized by the following relations, Eq. 15.

$$\lim_{t\to\infty} H(\theta(t),\dot{\theta}(t)) = H^*, \quad \theta = [\theta'_{ns} \quad \theta'_s]' \tag{15}$$

The stability and convergence of the anti-phase synchronization controller are proved by the study of Lyapunov function.

Theorem: For any given controller presented as Eq. 14, if satisfies $\lambda_2 > 2H^*$, then the set $\theta^t_{ns} = -\theta^t_s$, $\dot{\theta}^t_{ns} = -\dot{\theta}^t_s$ is a globally asymptotically stable point of the controlled system, Eq. 13.

As predicted by the theorem, there is a set of zero Lebesgue measure of exceptional initial conditions for which the control objective can not be achieved. For example, if one initiate the system at the point where $\theta^t_{ns} = \theta^t_s = 0$, $\dot{\theta}^t_{ns} = \dot{\theta}^t_s = 0$ the anti-phase synchronization control $\bar{u}$ based on the energy can't drive the system away from the zero condition, however from practical point of view, it is not difficult to modify the controller to handle this problem.

Presume the system has been in the condition of anti-phase synchronization, that is, the stable point of the closed loop system, the limit dynamics of each pendulum is given by the following equation

$$m(kl)^2\ddot{\theta}^t + mgkl\sin(\theta^t) = -2\gamma\left[H(\theta^t,\dot{\theta}^t) - H^*\right] \tag{19}$$

And therefore the control objective $\lim_{t\to\infty} H(\theta^t,\dot{\theta}^t) = H^*$ is achieved.

4 Simulation and Discussion

To verify the effectiveness of the proposed method, we conduct the following simulation results.

The limit cycle under anti-phase synchronization is given by Fig. 5 and its mechanical energy of the robot under anti-phase synchronization is just depicted by Fig. 6. It is clearly that the anti-phase synchronization can enlarge the convergence region of the limit cycle and it appears the typical double-pendulum property.

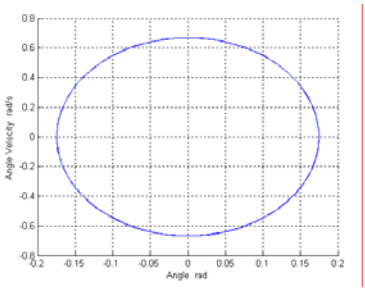

Fig. 5. A stable limit cycle ($\theta_{ns}, \dot{\theta}_{ns}$) under anti-phase synchronization

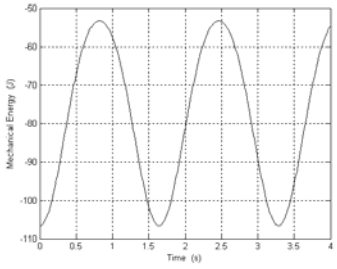

Fig. 6. Mechanical energy of the robot under anti-phase synchronization

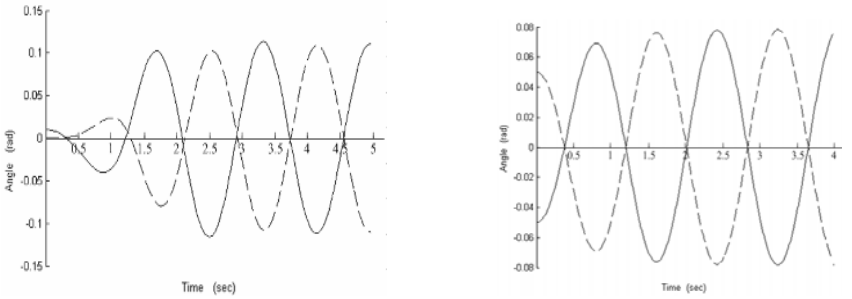

a b

Fig. 7. Anti-phase synchronization of two legs in the controlled system with different initial condition $(\theta_{ns}, \theta_s, \gamma)$. (a) (0.01, 0, 10), (b) (-0.05, 0.05, 10).

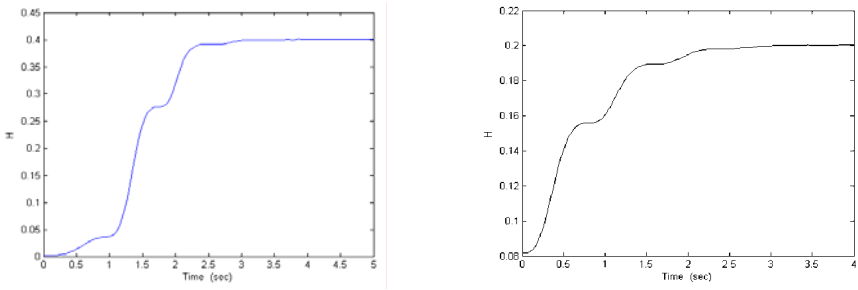

a b

Fig. 8. The control curve corresponding to H function with different initial condition $(\theta_{ns}, \theta_s, \gamma)$. (a) (0.01, 0, 10), (b) (-0.05, 0.05, 10).

Fig. 7 and Fig. 8 present the results of the anti-phase synchronization based on the energy control. With the anti-phase synchronization control, the angular position and angular velocity of the two legs can reach the synchronization with the same magnitude and the opposite direction at any moment. Simulation results prove the validity of the control method. In addition, as simulation demonstrates, with different initial condition of the gait biped will be around zero as well as any given biped value and with the control it can converge to the state of anti-phase synchronization corresponding to any given target energy. The converging speed depends on the controlled parameter $\gamma, \lambda_1, \lambda_2$. Virtually the higher the value of the parameters are, the faster the converging speed is. The consequence is valid with the consideration of both the constraint of the manipulator and the appropriate maximized sustaining force added on the system. In practice, for not using the initial condition as it does in simulation, so the effect of the control will be better in controlling the practical robot.

5 Conclusions and Future Work

In this paper, we study the problem of controlled synchronization of the decoupled two legs based on the compass-like biped model. Some new method called "anti-phase synchronization" has been applied to design controller of passive biped robot. The presented controller is able to solve the synchronization problem in such a way that the pendulum reaches the desired level of energy and they move synchronously in opposite directions. In addition, construction of Lypunov function proved the global stability of the proposed controller and simulation results also proved the validity of the method.

For the next step, the design of a more efficient new collision model and also the further analysis about the added simplified impulse force under new condition will be helpful to practical application of the design of the robot's gait.

Acknowledgement

This work is supported by the National High Technology Research and Development Program of China (863 Program) (Grant No: 2006AA04Z251).

References

1. Garcia M, Chatterjee A, Ruina A, Coleman M (1998) The simplest walking model: stability, complexity, and scaling. ASME Journal of Biomechanical Engineering 120(2):281-288
2. Collins SH, Ruina A, Tedrake R, Wisse M (2005) Efficient Bipedal Robots Based on Passive-Dynamic Walkers. Science Magazine 307:1082-1085
3. Collins SH, Wisse M, Ruina A (2001) A 3-d passive dynamic walking robot with two legs and knees. International Journal of Robotics Research 20(7): 607-615
4. Goswami A (1997) Limit cycles in a passive compass gait biped and passivity-mimicking control laws. Journal of Autonomous Robots 4 (3):273 – 286
5. Goswami A (2003) Kinetic quantification of gait symmetry based on bilateral cyclograms. In: Proceedings of sixth Congress of the International Society of Biomechanics. pp 56-62
6. Goswami A, Tuilot B, Espiau B (1996) Compass like bipedal robot part I: stability and bifurcation of passive gaits. INTRIA Research Report, INTRIA
7. Goswami A, Thuilot B, Espiau B (1998) A Study of the Passive Gait of a Compass-Like Biped Robot: Symmetry and Chaos. International Journal of Robotics Research 12(17):1282-1301
8. Grizzle JW, Plestan F, Abba G (1999) Poincaré's method for systems with impulse effects: application to mechanical biped locomoton. In: Proceedings of the 38th conference on decision & control. Phoenix, AZ, pp 3869-3876
9. McGeer T (1990) Passive dynamic walking. International Journal of Robotics Research 9(2): 62-82
10. Spong MW, Bhatia G (2003) Further Results on Control of the Compass Gait Biped. In: Proceedings of IEEE International Conference on Intelligent Robots and Systems. Las Vegas , Nevada, pp 1933-1938
11. Tedrake R, Teresa Weirui Zhang, Sebastian Seung H (2005) Learning to Walk in 20 Minutes. In: Proceedings of the Fourteenth Yale Workshop on Adaptive and Learning Systems, Yale University, New Haven, CT.
12. Wisse M, Schwab AL, vd. Linde RQ (2000) A 3D Passive Dynamic Biped with Yaw and Roll Compensation. ROBOTICA 19:275–284

EDA-Based Optimization and Learning Methods for Biped Gait Generation

Lingyun Hu and Changjiu Zhou

Advanced Robotics and Intelligent Control Centre, School of Electrical and Electronic Engineering, Singapore Polytechnic, 500 Dover Road, 139651, Singapore
{HuLingyun, ZhouCJ}@sp.edu.sg

Abstract. This paper summarizes the optimization and learning methods using Estimation of Distribution Algorithm (EDA) to generate and plan biped gaits. By formulating biped robot as mass link structure, dynamically stable and energy efficient gait generation problem is extracted as a multi-constrained and multi-objective optimization problem. Instead of traditional intelligent algorithms, EDAs are proposed to solve this high dimensional optimization problem for its clear structure and simple parameter. Simulation results of different EDAs based optimization algorithms with comparison to genetic algorithm on biped gait optimization are shown in this paper to find out the advantages and disadvantages of the proposed biped gait generation algorithms.

1 Introduction

Biped locomotion has attracted the interests of researchers in both areas of biomechanics and robotics. To get a better analysis of biped gaits, two kinds of motion generation methods using experimental reconstruction of locomotion kinematics and direct dynamic model are proposed. The first method attempts to identify some generating principles of biped gait from practical locomotion data. It has been used as well to analysis some specific information, like gender and height of human, from human walking (Troje 2002). Compared with it, the latter approach generates an optimal gait cycle in a more direct way. It minimizes some performance indexes, usually are stability criterion, actuating forces or energy consumption, with consideration of physical constraints (Rostami and Bessonnet 2001). This kind of method fits for different types of humanoid robot for it can design the performance index and physical constraints according to practical requirement. It is also used in this paper to construct the optimization framework for EDA based optimization algorithms.

Different from previous optimization framework (Juang 2000), both stability and energy cost are considered in the proposed framework. Moreover, a newly proposed Evolutionary Algorithm (EA) namely Estimation of Distribution Algorithm (EDA) (Larranaga and Lozano 2001) is applied to search for the optimal gait cycle. Like traditional EAs, EDAs gets the optimal solution by updating samples iteratively.

T.-J. Tarn et al. (Eds.): Robot. Weld., Intellige. & Automation, LNCIS 362, pp. 541–549, 2007.
springerlink.com

However, as an improved extension, EDAs uses probability distributions derived from the optimizing function to generate samples instead of crossover and mutation in Genetic Algorithms (GAs). Thereby, global statistical information about the search space can be extracted directly by EDA to modify the probability model with promising solutions.

As the research of EDA based algorithm for biped gait generation going on, disadvantages of traditional EDA based algorithm are shown in optimization efficiency for its fixed probability model and updating rule. Improvements on probability model and updating rule are tested and discussed in this paper. Two kinds of continuous probability functions as spline function and Parzen window and two kinds of updating rules as gradient descent and Q-learning based updating rule, together with the traditional Gaussian probability function and partial replacing updating rule are combined to form different EDAs to cope with the complex probability model and to achieve fast optimization.

As shown in the simulation results, flexible probability models provide EDA_SD (EDA using spline probability function and gradient descent updating rule) EDA_PP (EDA using Parzen window probability model and partial replacing updating rule) and EDA_PD (EDA using Parzen window probability model and gradient descent updating rule) the ability to describe complex probability model in a more precise way. While gradient descent updating rule enables EDA_SD and EDA_PD to optimize within clear updating direction quickly. Compared with it, Q-learning based updating rule updates the probability not so fast but fits for different kinds of probability models. That is, EDA_Q (EDA using discrete probability function and Q-learning based updating rule) and EDA_SQ (EDA using spline probability function and Q-learning based updating rule) can autonomously update their probability function without pre-design updating rule.

Rest of the paper is organized as follows. Section 2 introduces the biped robot and gait with mathematical representation. Based on the optimization framework, Section 3 proposes EDAs using different probability model and updating rule. Advantages and disadvantages of these EDAs are also shown in Section 3. Followed with it, Section 4 compares the simulation results and discusses the efficiency of improvements on probability model and updating rule. Finally, Section 5 gives the conclusion and talks about some future work.

2 Biped Robot and Gait

Generation of dynamically stable and low energy cost biped gaits is formulated with mathematical representation form in our previous work (Hu et al. 2006).

For biped gait model as shown in Fig. 1, four key poses are chosen in one complete gait cycle. Phases between these key poses are approximated by third order spline functions. Robot trajectories are parameterized as cubic spline function $f_s(\boldsymbol{q},t)$ for

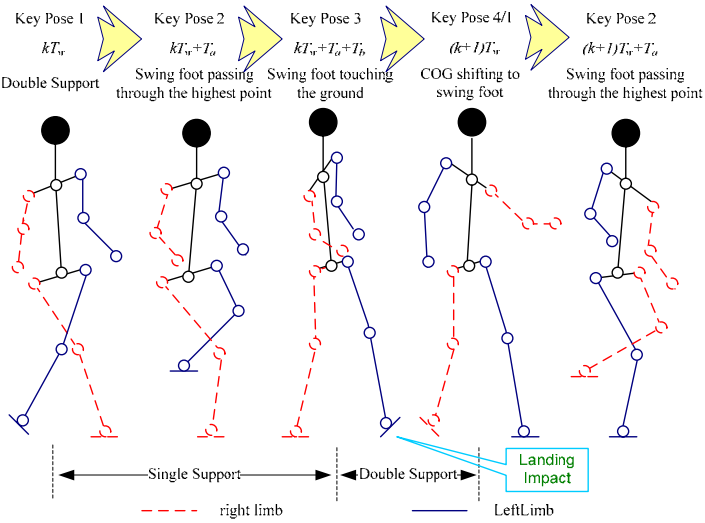

Fig. 1. Gait pattern of biped robot

joint angles $\boldsymbol{q} \in R^{N_q}$. Therefore, gait generation problem can be reduced to a general nonlinear parametric optimization problem with equality and inequality constraints as:

$$f_o(\boldsymbol{q}) = \beta_d f_d(\boldsymbol{q}) + \beta_e f_e(\boldsymbol{q}) \tag{2.1}$$

$$\Omega_i(\boldsymbol{q}) \tag{2.2}$$

Where $f_d(\boldsymbol{q}) = \int_{t=kT_w}^{(k+1)T_w} \Re(\left\| p_{\text{zmp}}(t) - p_{\text{dzmp}}(t) \right\|_2) dt$ stands for ZMP displacement and $f_e(\boldsymbol{q}) = \int_{t=kT_w}^{(k+1)T_w} \left\| \tau(t) \right\|_2 dt$ is the energy cost during the kth gait cycle. $\Omega_i(\boldsymbol{q})$ are geometric and state constraints. $p_{\text{zmp}}(t)$ and $p_{\text{dzmp}}(t)$ are real and desired ZMP trajectory, $\tau(t)$ is the joint torque at time t. β_d and β_e are weighting coefficients satisfying $\beta_d + \beta_e = 1$ to balance between stability and energy cost.

Let $f_{di} = \Re(\left\| p_{\text{zmpi}} - p_{\text{dzmpi}} \right\|)$, $f_{ei} = \Re(\sum_{j=1}^{N_q} \left\| \tau_{ij} \right\|)$, $f_d(\boldsymbol{q})$ and $f_e(\boldsymbol{q})$ in Eq. (2.1) can be re-rewritten as $f_d(\boldsymbol{q}) = \sum_{i=1}^{N_p} f_{di}(\bullet)$ and $f_e(\boldsymbol{q}) = \sum_{i=1}^{N_p} f_{ei}(\bullet)$. Where $p_{\text{zmp}\,i}$ and $p_{\text{dzmp}\,i}$ are real and desired ZMP trajectory at the ith sample index, τ_{ij} is the jth joint torque at time at the ith sample index, $\Re$ is the normalization operator.

Two kinds of constraints as geometric and state constraints are introduced in biped gait optimization problem. They are

geometric constraints:	GC1	$A_p \le p(\boldsymbol{q}) \le B_p$
	GC2	$A_q \le \boldsymbol{q} \le B_q$
state constraints:	ZC	$p_{\text{zmp}}(\boldsymbol{q}) \in S_{\text{zmp}}(A_{\text{zmp}}, B_{\text{zmp}})$
	FC1	$\sum_{i=1}^{N_L} m_i \ddot{p}_i = f_R + f_L + \sum_{i=1}^{N_L} m_i g$
	FC2	$f_d = \min\{F_I(f_R, f_L)\}$
	VC	$A_{\dot{q}} \le \dot{\boldsymbol{q}} \le B_{\dot{q}}$

GC1 and GC2 are geometric constraints to guarantee the feasibility of generated gaits. $p = [p_i]^{\mathrm{T}}$, $A_p = [A_{p_i}]^{\mathrm{T}}$, $B_p = [B_{p_i}]^{\mathrm{T}}$. p_i=[x_i, y_i, z_i] denotes center position of the ith link. $i = 1, 2, ..., N_l$, N_l is the number of links in biped robot. A_{p_i} and B_{p_i} are lower limit and upper limit of p_i. $\boldsymbol{q} = [q_i]^{\mathrm{T}}$ stands for joint angles. $A_q = [A_{q_i}]^{\mathrm{T}}$, $B_q = [B_{q_i}]^{\mathrm{T}}, i = 1, 2, ..., N_q$, N_q is the number of joints angles in biped robot. A_{q_i} and B_{q_i} are lower limit and upper limit of q_i.

Besides geometric constraints, state constraints including ZMP, force and velocity constraints are also considered. ZC stands for ZMP constraints. The ZMP is defined as the point on the ground at which the net moment of the inertial forces and the gravity forces has no component along the horizontal axes (Vukobratovic and Borovac 2004). If the ZMP is within the convex hull of all contact pints between the feet and the ground, the biped robot is possible to work. Therefore, this convex hull of all contact pints is called the stable region. $p_{\text{zmp}} = (x_{\text{zmp}}, y_{\text{zmp}}, 0)^T$ denotes actual ZMP. S_{zmp} is the support polygon defined by A_{zmp} and B_{zmp}, which are lower and upper boundaries of the stable region respectively. FC1 and FC2 are force constraints. f_R and f_L are foot force at right and left legs respectively, F_I is the function calculating inner force F_d of biped robot. m_i, $\ddot{p}_i$ are the mass and the acceleration of the ith link. Since during the double support phase, only the sum f_R+f_L is known, another force constraints FC2 is taken into assumption as the internal force f_d in the closed loop structure must be minimized.

The final constraint VC is velocity constraints. $\dot{q} = [\dot{q}_i]^{\mathrm{T}}$, $\dot{q}_i$ denotes velocity of the ith actuated joint, $A_{\dot{q}} = [A_{\dot{q}_i}]^{\mathrm{T}}$ and $B_{\dot{q}} = [B_{\dot{q}_i}]^{\mathrm{T}}$ are lower and upper boundaries of the velocity $\dot{q}_i$.

To get the proper combination of joint angles with small objective function value, probability distribution functions of joint angles are lucubrated with consideration of evolutionary methods. Details of the probability function based evolutionary algorithms for biped gait generation are as follows.

3 EDA Based Algorithms for Biped Gait Generation

As mentioned before, for such a multi-DOF structure that varies in walking, parametric optimization technique can solve it. State parameters, designed either in task space or joint space, can be approximated by different methods along the motion time. Besides polynomials (Seguin and Bessonnet 2005) or spline functions (Huang et al. 2001), heuristic computation methods like neural network (Reil and Husbands 2002), fuzzy logic (Zhou and Meng 2003) and GA (Capi et al. 2002) are the mostly used strategies.

However, behaviour of these heuristic computation algorithms depends on many parameters. For researcher without associated experiences, the choice of suitable values is converted into a new optimization problem. Additionally, traditional GAs have difficulties to optimize deceptive and non-separable functions.

That is why a new extension of EA, namely EDAs are applied on biped gait generation for its clear structure and simple parameters. Several EDAs have been proposed for the global continuous optimization problem (Muhlenbein 1997; Lozano and Larranaga 2002). For statistically independent variables, Population-Based Incremental Learning (PBIL) performs successfully on problems with nonlinear variable interactions (Greene 1996).

Previous researches have shown that EDAs can successfully generate expected biped gaits that minimizing the predefined objective function in short learning iterations (Hu et al. 2005).

3.1 EDA Based Optimization Algorithm for Biped Gait Generation

With traditional EDA presented above, optimal biped gait cycle can be achieved while the six constraints are also satisfied. Compared with traditional artificial intelligent methods, the proposed EDAs have simpler parameters and clearer structure. It, consequently, makes them more fit for the multi-variable and multi-objective biped gait optimization problem. But, to generate a feasible motion more quickly, it may be necessary to modify EDA throughout the two important factors that will affect the learning quality of EDAs as probability model and corresponding updating rule. By combing the two factors, different EDAs can be obtained for different practical requirements.

Traditional EDA with Gaussian probability function is modified from the two factors as the kind of probability function and updating rule to cope with the multi-model distribution function appeared in biped gait generation.

The two new EDAs as EDA_SP and EDA_PP use spline and Parzen window based probability distribution functions respectively and update probability functions with partial replacing rule. When compared with traditional EDAs, new modified EDAs show stronger capability to describe complex probability distribution. Moreover, it is worthy to be mentioned that EDA_PP is much better than EDA_SP in term of simplicity and realization. On base of EDA_PP, EDA_CPP initializes Parzen windows with nearest neighbor cluster analysis method. It accelerates the formulation of probability model in EDA_CPP from beginning.

Besides those two EDAs, EDA_SD and EDA_PD are also designed to find out the efficiency of gradient descent updating rule. As can be seen in the simulation result at Section 4 that stochastic gradient descent on the Kullback-Leibler divergence between the probability density model and the unknown objective function provide continual learning ability and can keep fast optimization even when the predominance of selected samples is not so obvious.

3.2 EDA Based Algorithm for Biped Gait Learning

Based on the biped gait optimization algorithm using EDAs, biped gait learning algorithms EDA_Q and EDA_SQ are studied, which combine Q-learning based updating rule with discrete and spline based probability models. They can update different probability model autonomously and have wider application area.

4 Simulation Results and Discussions

To demonstrate the advantages of EDA, Fig. 2 shows the simulation results of objective function value during the first 400 optimization epochs for EDA_GP and GAs. Quicker convergence and lower objective function value are due to the simpler structure and parameters of EDA_GP.

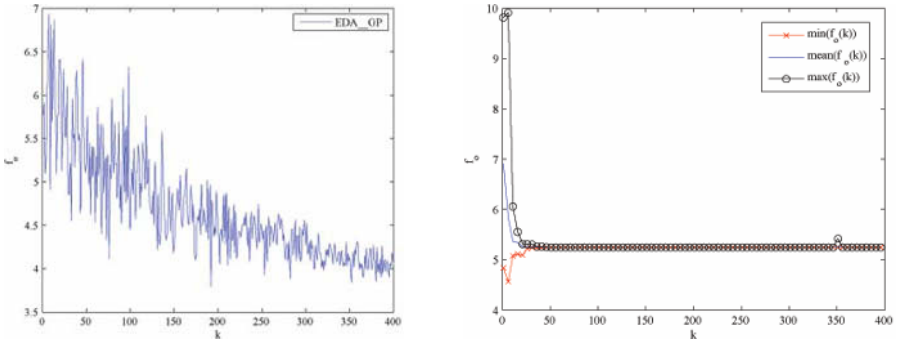

(a) EDA_GP (b) GAs

Fig. 2. Simulation result of EDA_GP and Gas

Further more, traditional EDA_GP is compared with the modified EDAs with spline probability model and Parzen window probability functions, which are EDA_SP and EDA_PP respectively. As shown in Fig. 3. (a), EDA_SP and EDA_PP works better with multi-model distribution function and has quicker convergence speed for the specially designed probability model. From Fig. 3(b), it can be found that $pro_{2,1}(k=10)$ formed by Parzen windows has two peaks while that formed by traditional Gaussian distribution function trades off between them. It induces the peak of $pro_{2,1}(k=1)$ formed by EDA_GP to the valley and takes EDA_GP more time to justify its means and covariance.

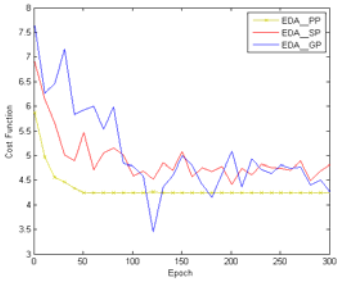

(a) $f_o(\boldsymbol{q})$ achieved by EDA_PP, EDA_SP and EDA_GP

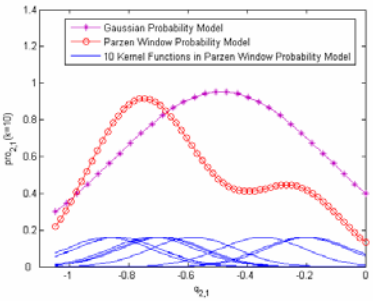

(b) $pro(k=10)$ achieved by EDA_PP and EDA_GP

Fig. 3. Simulation results related with probability model

However, as optimization going on, divergence between the selected samples and the rest ones can not be fully exploited by partial replacing updating rule for samples come to be similar. To overcome it, gradient descent updating rule is combined with spline and Parzen window probability functions to form EDA_SD and EDA_PD. Fig. 4. (a) shows the objective function value got by EDA_GP, EDA_PP and EDA_PD after 400 iterations. It can be seen from Fig. 4. (a) that, EDA_PP keeps an obvious learning only when the ojective function value of the best sample in the current population is significantly greater than those of the rest samples.

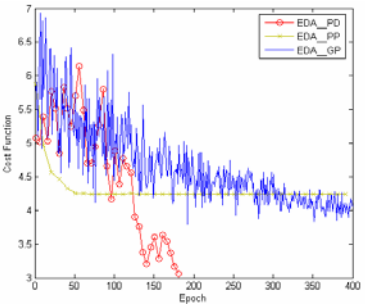

(a) $f_o(\boldsymbol{q})$ achieved by EDA_PD, EDA_PP and EDA_GP

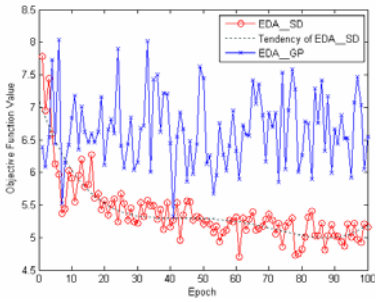

(b) $f_o(\boldsymbol{q})$ achieved by EDA_SD and EDA_GP

Fig. 4. Simulation results related with updating rule

However, such case seldom exists at the latter stages of learning. That is why EDA_PP converges fast initially and slows down while learning goes on. Similar to EDA_PD, EDA_SD convergences quickly for longer epoches with comparison to

EDA_GP (see Fig. 4. (b)). However, as explained in Section 3, complex computation of EDA_SD evolves too many parameters which bury the advantage of less parameters and clear structure in EDAs. So the objective function value obtained by EDA_PD (see Fig. 4. (a)) at the 100th iteration is less than that obtained by EDA_SD (see Fig. 4. (b)).

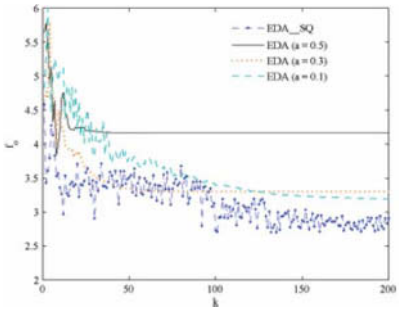

Fig. 5. Simulation result of EDA_SQ and EDAs

The anterior part focuses on optimization algorithms using EDAs. Special updating rule should be designed for various probability models. Different from them, the autonomously modified updating rule, Q-learning based updating rule let EDA_Q and EDA_SQ improve their probability model without pre-knowledge about the model. The objective function values of EDA_SQ and EDA_GP with different learning rate during the first 200 iterations, as shown in Fig. 5, show the efficiency of Q-learning based updating rule.

5 Conclusion

This paper summarizes EDA based optimization and learning algorithms for biped gait generation. With the optimization framework, low energy cost and dynamically stable gaits can be achieved with respect to geometric and state constraints. The two factors as probability model and updating rule that impact the optimization effectively are discussed and combined to form different EDAs for this high dimensional space searching problem. From the simulation results, it can be concluded that EDA_PD deals well with high dimensional space searching with clear optimization structure and little parameters. It is a good choice for biped gait generation. While compared with it, EDAs using Q-learning based updating rule can deal with various probability models.

On this subject, an improvement of the approach would consist in specifying a minimum of constraints in order to deal with less constrained problem. On the other hand, new applications of EDAs in biometrics and animation would be our next research topics.

References

Capi G, Kaneko S, Mitobe K, Barolli L, Nasu Y (2002) Optimal trajectory generation for a prismatic joint biped robot using genetic algorithms. J Robotics and Autonomous Systems 38(2): 119-128

Greene JR (1996) Population-based incremental learning as a simple versatile tool for engineering optimization. In: Proc. of the first Int. Conf. on EC and Applications. Moscow, pp. 258-269

Hu L, Zhou C, Sun Z (2005) Biped gait optimization using estimation of distribution algorithm. In: Proc. of IEEE-RAS Int. Conf. on Humanoid Robots. Tsukuba, pp 283-289

Hu L, Zhou C, Sun Z (2006) Biped gait optimization using spline function based probability model. In: Proc. of IEEE Int. Conf. on Robotics and Automation. Orlando, pp 830-835

Huang Q, Yokoi K, Kajita S, Kaneko K, Arai H, Koyachi N, Tanie K. (2001) Planning walking patterns for a biped robot. J IEEE Trans. on Robotics and Automation 17: 280-290

Juang J (2000) Effects of using different neural network structuresand cost functions in locomotion control. In: Proc. of the American Control Conference. Chicago, pp 3523-3527

Larranaga P, Lozano JA (2001) Estimation of Distribution Algorithms, A New Tool for Evolutionary Computation. Kluwer Academic Publishers, New York

Lozano JA, Larranaga P (2002) Optimization by learning and simulation of probabilistic graphical models. In: Proceedings of PPSN2002

Muhlenbein H (1997) The equation for response to selection and its use for prediction. J Evolutionary Computation 5(3): 303-346

Reil T, Huansbans P (2002) Evolution of centeral pattern generators for bipedal walking in a real-time physics environment. J IEEE Trans. on Evolutionary Computation 6: 159-168

Rostami M, Bessonnet G (2001) Sagittal gait of a biped robot during the single support phase. Part 2: optimal motion. J Robotica 19: 241-252

Seguin P, Bessonnet G (2005) Generating optimal walking cycles using spline-based state-parameterization. J IEEE Transactions on Robotics and Automation 2: 47-80

Troje NF (2002) Decomposing biological motion: A framework for analysis and synthesis of human gait patterns. J Vision 2: 371-387

Vukobratovic M, Borovac B (2004) Zero moment point-thirty five years of its life. J Humanoid Robotics 1(1): 157-173

Zhou C, Meng Q (2003) Dynamic balance of a biped robot using fuzzy reinforcement learning agents. J Fuzzy sets and Systems 134(1): 169-187

Robust Adaptive Fuzzy Control of Marine Craft

Junsheng Ren[1] and Changjiu Zhou[2]

[1] Laboratory of Marine Simulation & Control, Dalian Maritime University, Dalian 116026, P.R. China
jsren@dlmu.edu.cn
[2] Advanced Robotics and Intelligent Control Centre, School of Electrical and Electronic Engineering, Singapore Polytechnic, 500 Dover Road, Singapore 139651
zhoucj@sp.edu.sg

Abstract. This paper introduces some intelligent control strategies for marine craft. By looking at some existing problems in this area, e.g. the uncertainties and nonlinearities in ship dynamic model and time delay in ship actuator system, three types of control strategies are studied, namely, robust PID control for ship steering, adaptive fuzzy robust tracking control (AFRTC) for ship steering, and adaptive fuzzy Hinf control for ship roll stabilization. The effectiveness of the three control strategies are demonstrated by ship simulation. This paper is dedicated to the memory of Professor YS Yang for his pioneer work on robust adaptive fuzzy control of marine craft.

1 Introduction

Ocean shipping automation mainly covers the topics of course-keeping control, course-changing control, anti-rolling fin control, rudder-roll damping control, etc. In 1970s, adaptive control theory was applied. However, because of the complexities of ship's dynamics, the randomness and unpredictability in environmental disturbances, these methods can't tackle the ship's course control problem completely. During recent years, kinds of the novel algorithms were applied to ship's course control, such as model reference adaptive control, self-tuning control with minimal variance, neural network control, fuzzy control, variable structure control, H_∞ robust control, generalized predictive control, intelligent control, etc. Some of these algorithms had become the theoretical bases of recently developed autopilot. Furthermore, some works had been published to study marine craft control [1].

In this paper, a brief review on intelligent control of marine craft is dedicated to the memory of Professor YS Yang for his pioneer research in the field of robust adaptive fuzzy control of marine craft. Three types of control strategies proposed by Professor YS Yang are introduced [2-10]. The first is that uncertainty always exists in the model used to design controller. The second is that nonlinearity is not included in the model. The last is that the actuator dynamics is not taken account of when designing controller. This work offers a promising route for development of some intelligent control approaches in the area of marine craft control.

T.-J. Tarn et al. (Eds.): Robot. Weld., Intellige. & Automation, LNCIS 362, pp. 551–560, 2007.
springerlink.com

2 Challenges in Marine Craft Control

2.1 Uncertainties in Ship Dynamic Model

The uncertainties appear in the parameters of ship dynamic model for controller design and the disturbances of the external environments. As we know, the uncertainties will bring out a series of theoretical and practical problems. To make it much clear, it will be illustrated by taking ship's course-keeping control as an example. In the design of ship's autopilot by use of PID algorithm or adaptive methods, ship's dynamics are generally represented by the so-called Nomoto equation as follows

$$T\ddot{\psi} + \dot{\psi} = K\delta. \tag{1}$$

Generally, the parameters K and T in (1) are considered as be known beforehand in the autopilot's design. However, the ship's speed, the ship's loading conditions and so on always vary during its voyage. Furthermore, the external disturbances, such as winds, currents, waves, etc, have a tremendous effect on ship's dynamics. The parameters K and T are actually time-varying, and it's quite difficult to obtain their precise values. Therefore in controller design, ship dynamics should be described by Nomoto model with uncertainty items

$$(T_0 + \Delta T)\ddot{\psi} + \dot{\psi} = (K_0 + \Delta K)\delta + \omega, \tag{2}$$

where T_0 and K_0 are the parameters of ship's nominal model, and considered to be known beforehand, ΔT and ΔK contain the parameters' uncertainties, $\omega = f_A + f_B$ contains the uncertainties from the external disturbances.

2.2 Nonlinearities in Ship Dynamic Model

Because of the course instability, the mathematical model of large-size tanker is of nonlinearities in essence. In aforementioned control algorithms, most of them employ linear model in autopilot design. The mathematical model for ship rolling motion is of strong nonlinearities in ship's anti-rolling control system, when the amplitude of rolling motion is quite large. Therefore some errors are unavoidable when linear model is employed to design anti-rolling controller.

Generally in the ship's autopilot design, linear Nomoto equation (1) is employed. However, many ship's dynamics are nonlinear and also influenced by the external disturbances. Therefore, it is quite reasonable to introduce nonlinearities and external disturbances as follows.

$$T\ddot{\psi} + \dot{\psi} + \alpha\psi^3 = K\delta + \omega \tag{3}$$

where ψ is the ship's course, δ is the rudder angle, T, K and α are the model's parameters which are constant but assumed to be unknown in controller design, ω contains the uncertainty from external disturbances which and assumed to be bounded.

2.3 Time Delay in Ship Actuator Systems

There exist quite large time delays in the rudder servo system of ship course control system and the fin's actuator of anti-rolling control system. Therefore, the closed-loop stability cannot be guaranteed in the controller design without consideration of the factor of time delay. In marine craft controller design, control command, i.e. controller's input, are used to drive control equipments through an actuator. Generally, the autopilot's steering gear and anti-rolling fin's servo system consist of electrical-hydraulic servo system. During the implementation, there exists time delay between control command and actual control input, since step maneuver cannot be realized. The actuator's dynamics can be described by the first-order inertia equation as follows

$$T_E\dot{\alpha} + \alpha = K_E\alpha_C \tag{4}$$

where α_C is the control command, α is the actual control input, T_E is the time constant of the actuator system, K_E is input gain and $K_E \approx 1$ in the anti-rolling fin's actuator system. The larger time constant T_E is, the larger its influence on closed-loop system is. Time constant T_E is in inverse proportion to the power necessary to the actuator system. The reduction of time constant T_E need increase the power from the actuator system. The power is in proportion to the cost and size of the actuator system. Therefore, time constant T_E is a constant, and cannot be small arbitrarily.

The effects from actuator system can be taken into no consideration during controller design if time constant T_E is far smaller than that of the controlled process. However, if both the time constants are almost the same, its effect deserves the designer's particular attention. Otherwise, the closed-loop performance will be deteriorated, and also the stability cannot be guaranteed. In the design of ship's anti-rolling fin system, it was considered that its time constant T_E is quite small and its effect can be neglected in the past. However, it has found that time constant T_E cannot be neglected. With traditional design, anti-rolling fin doesn't decrease rolling motion under the influence of time constant T_E. Sometimes the fin system even increases the amplitude of rolling motion, and the system's instability occurs.

3 Intelligent Control of Marine Craft

In this section, a brief review on intelligent control of marine craft is dedicated to the memory of Professor YS Yang for his pioneer research in the field of robust adaptive fuzzy control of marine craft to marine craft control [2-10]. Three types of intelligent control strategies for marine craft are introduced as follows.

3.1 Robust PID Controller Design for Ship Steering

To deal with the problem of controller design for the model with uncertainties, robust control theory for uncertain system can be obtained. If the system's parameters are

known, it's quite efficient to employ PD or PID type autopilot design in a certain range. Its main shortcoming is that its closed-loop system has no robustness. However, it's quite effective to combine robust control theory with PD and PID type control.

Ship model (1) is used to design course-keeping autopilot with the parameters K and T known. To eliminate the steady-state errors, integral item is incorporated in PD control strategy, which leads to the following PID control law

$$\delta = K_p e + K_d \dot{e} + K_i \int_0^t e\mathrm{d}t, \tag{5}$$

where $e = \varphi_d - \varphi$, $\dot{e} = \dot{\varphi}_d - \dot{\varphi}$, K_p, K_d and K_i are design parameters for PID autopilot design. Substituting (5) into (1) yields the model of closed-loop control system. By use of classic control theory, K_p, K_d and K_i can be obtained.

When ship's model contains uncertainties, robust PID autopilot control law $\delta = \delta_{\mathrm{PID}} + \delta_C$ is used, where δ_{PID} is given by (5), δ_C is used to compensate the parametric uncertainties and the uncertain external disturbances. Substituting δ into (2) results in

$$\begin{aligned} \dddot{e} = &-\frac{1+K_0K_d}{T_0}\ddot{e} - \frac{K_0K_p}{T_0}\dot{e} - \frac{K_0K_i}{T_0}e - \left(\left(1+2K_0K_d\right)\sigma_1 + T_0K_0K_d\sigma_1^2\right)\ddot{e} \\ &-\sigma_2K_p\dot{e} - \sigma_2K_ie - \frac{K_0}{T_0}\dot{\delta}_C - \sigma_2\dot{\delta}_C - \frac{1}{T_0}\left(\frac{1}{T_0}+\sigma_1\right)\dot{w}, \end{aligned} \tag{6}$$

where $w = f_A + f_W$, $\sigma_1 = \Delta V/(T_0V_0)$, $\sigma_2 = K_0\left[2(\Delta V/V_0) + (\Delta V/V_0)^2\right]/T_0$. Introduce new state variables $x_1 = e$, $x_2 = \dot{e}$, $x_3 = \ddot{e}$, and control variable $u_C = \dot{\delta}_C$. Then (6) can be rewritten into the following state-space equation with uncertainty items

$$\dot{x}(t) = Ax(t) + Bu_C(t) + \Delta Ax(t) + \Delta Bu_C(t) + Cv(t),$$

$$x(t) = \begin{bmatrix} x_1(t) & x_2(t) & x_3(t) \end{bmatrix}^T,$$

$$A = \begin{bmatrix} 0 & 1 & 0 \\ 0 & 0 & 1 \\ -K_0K_i/T_0 & -K_0K_p/T_0 & -\left(1+K_0K_d\right)/T_0 \end{bmatrix},\ B = \begin{bmatrix} 0 \\ 0 \\ -K_0/T_0 \end{bmatrix},$$

$$\Delta A = \begin{bmatrix} 0 & 0 & 0 \\ 0 & 0 & 0 \\ -\sigma_2K_i & -\sigma_2K_p & -\left(\left(1+2K_pK_d\right)\sigma_1 + T_0K_0K_d\sigma_1^2\right) \end{bmatrix},\ \Delta B = \begin{bmatrix} 0 \\ 0 \\ \sigma_2 \end{bmatrix},$$

$$C = \begin{bmatrix} 0 \\ 0 \\ -\left(1/T_0+\sigma_1\right)/T_0 \end{bmatrix},\ v = \dot{w}.$$

For convenience, the uncertainties item can be rewritten into the following match condition $\Delta A = BD(\sigma), \Delta B = BE(\sigma), C = BF$. where

$$D(\sigma) = \left[\sigma_2 K_i T_0 / K_0 \quad \sigma_2 K_p T_0 / K_0 \quad ((1 + 2K_0 K_d \sigma_1^2)\sigma_1 + T_0 K_0 K_d \sigma_1^2) T_0 / K_0\right],$$

$$E(\sigma) = \sigma_2 T_0 / K_0, \; F = (1/T_0 + \sigma_1)/K_0.$$

The compensation item in robust PID control law can be given as follows [3]

$$u_C(t) = -\rho(x(t),t)\frac{B^T P x(t)}{\left\|B^T P x(t)\right\| + \delta}, \tag{7}$$

where $\delta > 0$ is chosen by designer, P can be obtained through Lyapunov equation $A^T P + PA = -Q$, Q is symmetric semi-definite matrix chosen by designer, and $\rho(x(t),t) = \gamma^{-1}\left[\max_{v\in\gamma}\left\|Fv\right\| + \max_{s\in\Sigma}\left\|D(s)\right\|\left\|x(t)\right\|\right]$.

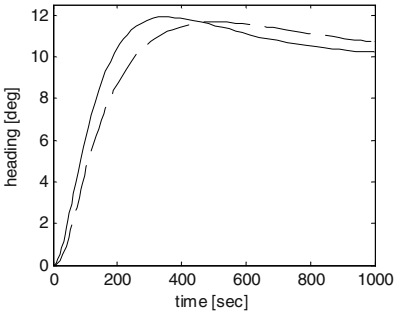

Fig. 1. Simulation results with traditional PID controller

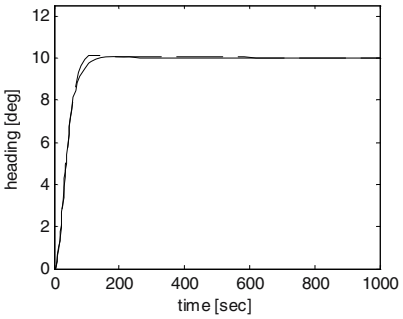

Fig. 2. Simulation results with robust PID controller

Simulation researches are based on oceangoing training ship "Yulong" [2]. The results are given in Fig. 1 and Fig. 2. Solid line is at speed 7.2 m/s, and dashline is at speed 3.5 m/s. Fig. 1 shows that traditional PID controller has little robustness. Fig. 2 shows that the above controller has good robustness to speed variations

3.2 Adaptive Fuzzy Robust Tracking Controller (AFRTC) for Ship Steering

The following mathematical model is used to describe the relation between rudder angle δ and ship heading ψ

$$\ddot{\psi} + \frac{1}{T}H(\dot{\psi}) = \frac{K}{T}\delta + \omega, \tag{8}$$

where the function $H(\dot{\psi})$ can be found from the relationship between δ and ψ in state such that $\ddot{\psi} = \dot{\psi} = \dot{\delta} = 0$. Let the state variables be $x_1 = \psi$ and $x_2 = \dot{\psi}$, control

variable be $u=\delta$, and disturbances $\omega=d(t)$, then (8) can be rewritten into the following state-space form

$$\begin{cases}\dot{x}_1 = x_2, \\ \dot{x}_2 = f(x_1,x_2)+g(x_1,x_2)u+d(x,t),\end{cases} \tag{9}$$

Let $y_d(t)$ be the given reference signal and $\nu=(y_d, y_d^{(1)})^T$ such that ν is bounded. Suppose $e=x-\nu$. Then (9) can be transformed into

$$\begin{cases}\dot{e}_1 = e_2, \\ \dot{e}_2 = f(x)+g(x)u-y_d^{(2)}(t)+d(x,t),\end{cases} \tag{10}$$

Using the pole-placement approach, consider a term k^{Tx} where $k=\left[k_1,k_2\right]^T$, the k_i's are chosen such that all roots of polynomial $s^2+k_2s+k_1=0$ lie in the left-half complex plane, and leads to the exponentially stable dynamics. Then, (10) can be transformed into

$$e=Ae+B[g(x)u+f(x)-y_d^{(2)}+k^Te+d(x,t)], \tag{11}$$

where $A=\begin{bmatrix}0 & 1\\ -k_1 & -k_2\end{bmatrix}$, $B=\begin{bmatrix}0\\1\end{bmatrix}$. Because A is stable, a positive-definite solution of Lyapunov function $A^TP+PA+Q=0$, where $Q>0$ is specified by designer.

The unknown function $f(x_1,x_2)$ can be approximate by T-S fuzzy system. Select consequent part of fuzzy rules as $y_i=a_0^i+a_1^ix_1+a_2^ix_2$, $i=1,2,\cdots,9$. Using the center average defuzzifier and the product inference engine, the fuzzy system is obtained as follows.

$$f(x)=\xi(x)A_z^0+\xi(x)A_z'x+\varepsilon, \tag{12}$$

where $A_z^0=\begin{bmatrix}a_0^1\\ \vdots \\ a_0^9\end{bmatrix}$, $A_z^{'}=\begin{bmatrix}a_1^1 & a_2^1\\ \vdots & \vdots \\ a_1^9 & a_2^9\end{bmatrix}$, and $\xi(x)$ is related to fuzzy basis functions. Then (11) can be rewritten as follows

$$\sum_{\omega\xi}:\begin{cases}\dot{e}=Ae+B[g(x)u-y_d^{(d)}+k^Te+\xi(x)A_z^0 \\ \quad +\xi(x)A_Z'v+\varepsilon+d]+c_\theta B\xi(x)A_Z'e, \\ \hat{z}=H(e)=e,\end{cases} \tag{13}$$

$$\sum_{\omega\xi}:\omega=A_z^me, \tag{14}$$

where $c_\theta=\left\|A_z'\right\|=\lambda_{\max}^{1/2}\left(A_Z'^TA_z'\right)$, such that $A_z'=c_\theta A_z^m$. Construct an AFRTC [4] as follows

$$u = -\left[\frac{\lambda}{2\gamma^2}\xi(x)\xi^T(x)B^T Pe - \theta\psi(x)\tanh\left(\frac{\bar{\theta}\psi(x)B^T Pe}{\bar{\varepsilon}}\right)\right], \tag{15}$$

where $\bar{\varepsilon} > 0$ will be specified by designer, and $\gamma > 0$ is the gain of $\Sigma_{\hat{z}w}$ to be chosen later on, the adaptive laws for λ and $\hat{\theta}$ are chosen as

$$\begin{cases} \dot{\lambda} = \Gamma_1\left[\dfrac{1}{2\gamma^2}e^T PB\xi(x)\xi^T(x)B^T Pe - \sigma_1(\lambda - \lambda_0)\right], \\ \dot{\hat{\theta}} = \Gamma_2\left[\psi(x)\left\|B^T Pe\right\| - \sigma_2(\hat{\theta} - \theta_0)\right], \end{cases} \tag{16}$$

where $\Gamma_i > 0$, $i = 1,2$ are the updating rates chosen by designer, and $\sigma_i > 0$, $i = 1,2$, λ_0 and θ_0 are design constants.

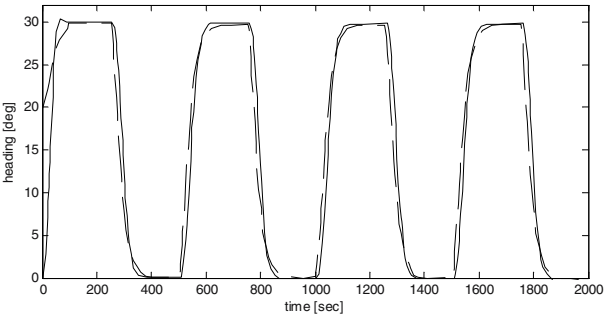

Fig. 3. Simulation results for AFRTC algorithm (ship heading ψ is in solid line, and reference course ψ_m is in dash line.)

Take a general cargo ship with length 126 m and displacement 11200 tons as an example for simulation [2]. The reference model is chosen as follows

$$\ddot{\psi}_m(t) + 0.1\dot{\psi}_m(t) + 0.0025\psi_m(t) = 0.0025\psi_r(t), \tag{17}$$

where $\psi_m(t)$ specifies the desired system performance for ship heading $\psi(t)$. Simulation results is given in Fig. 3. It can be seen that ship heading ψ converges rapidly to the reference signal ψ_m. Robust adaptive autopilot designs had also been discussed in [5,6,7].

3.3 Adaptive Fuzzy H_∞ Ship Roll Stabilization System

The mathematical model of ship roll stabilization system by fin control is a typical second-order dynamic system, can be written as follows

$$(I_{xx} + J_{xx})\ddot{\phi} + N\dot{\phi} + W\dot{\phi}\left|\dot{\phi}\right| + Dh\phi(1 - (\phi/\phi_v)^2) = F_C + F_W, \tag{18}$$

where ϕ denotes the roll angle of ship, $(I_{xx}+J_{xx})$ is the moment of inertia and added moment of inertia, N and W denote damping coefficients, D is ship displacement, h is the transverse metacentric height, ϕ_v is an angle specified by ship type, F_W is the moment acted on ship by wave and wind, and the control moment supplied by fin can be described by

$$F_C = -\rho v^2 A_f C_L^{\alpha}\left(\alpha_f + \dot{\phi} l_f / v\right) l_f, \tag{19}$$

where ρ is the density of water, v is ship speed, A_f is the area of the fin, C_L^{α} is the slope of lift coefficient, l_f is the arm of force supplied by fin, and α_f is the fin angle.

Use inertia system (4) to describe the actuator's dynamics. Let the state variables be $x_1 = \phi$, $x_2 = \dot{\phi}$, $x_3 = -\alpha_f$ and control variable be $u = -\alpha_C$. Then, the mathematical model for ship roll by fin control with actuator can be written in a general model of typical strict-feedback nonlinear system as follows

$$\begin{cases} \dot{x}_1 = x_2, \\ \dot{x}_2 = f_2(x_1, x_2) + g_2(x_1, x_2)x_3 + d_2, \\ \dot{x}_3 = f_3(x_1, x_2, x_3) + g_3(x_1, x_2, x_3)u + d_3, \end{cases} \tag{20}$$

where

$$f_2 = -\frac{Dh}{I_{xx}+J_{xx}} x_1 \left(1 - \left(\frac{x_1}{\phi_v}\right)^2\right) - \frac{N}{I_{xx}+J_{xx}} x_2 - \frac{W}{I_{xx}+J_{xx}} x_2 |x_2| - \frac{\rho v A_f C_L^{\alpha} l_f^2}{I_{xx}+J_{xx}} x_2,$$

$$g_2 = \frac{\rho v^2 A_f C_L^{\alpha} l_f}{I_{xx}+J_{xx}},\ d_2 = \frac{F_W}{I_{xx}+J_{xx}},\ f_3 = -\frac{1}{T_E} x_3,\ g_3 = \frac{K_E}{T_E}, \text{ and } d_3 = 0.$$

Define five fuzzy sets for each state error variable z_1, z_2, z_3 with labels A_{hi}^1 (NL), A_{hi}^2 (NM), A_{hi}^3 (ZE), A_{hi}^4 (PM), and A_{hi}^5 (PL). According to Theorem 2 in [8], the intermediate stabilizing functions α_1 and α_2 are

$$\alpha_1 = -1.0 z_1, \alpha_2 = -10.0 z_2 - \hat{\lambda} \xi_2 \xi_2^T z_2 - 0.78 z_2, \tag{21}$$

and the adaptive fuzzy stabilization law [8] is

$$u = -0.8 z_3 - \hat{\lambda} \xi_3 \xi_3^T z_3 - 0.78 z_3 \tag{22}$$

where $z_1 = x_1$, $z_2 = x_2 - \alpha_1$, $z_3 = x_3 - \alpha_2$, $\gamma = 0.5$, $\rho = 0.8$ and adaptive law as $\dot{\hat{\lambda}} = \Gamma\left(\xi_2 \xi_2^T z_2^2 + \xi_3 \xi_3^T z_3^2\right)$, $\Gamma = 25$.

Use a container ship with length 175 m and displacement 25000 tons as an example to conduct simulation research. In the simulation, the external disturbance is assumed as sinusoidal wave with wave height 6 m and wave direction 30°. Robust ship roll stabilization controller design can also be found in [9,10].

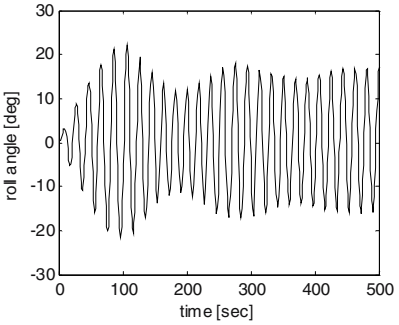

Fig. 4. Simulation results for time response of roll angle without fin control

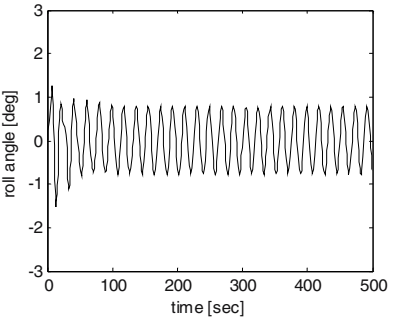

Fig. 5. Simulation results for time response of roll angle with fin control

4 Conclusions

This paper introduces some intelligent control strategies for marine craft. To solve some existing problems in this area of marine craft control, e.g. the uncertainties and nonlinearities in ship dynamic model and time delay in ship actuator system, three types of control strategies are studied in the field of robust PID control and adaptive fuzzy robust tracking control (AFRTC) for ship steering, and adaptive fuzzy Hinf control for ship roll stabilization. Simulation based on ship dynamic model has been conducted to show the effectiveness of the three control strategies.

Acknowledgement

This work was supported by the National Natural Science Foundation of China under Grand No. 60474014. This paper is dedicated to the memory of Professor Yansheng Yang who died on 30th September 2005.

References

[1] Fossen TI (1994) Guidance and control of ocean vehicles. Wiley, New York.
[2] Yang YS (1996) Study on ship maneuvering mathematical model in shiphandling simulator. In: Proc. MARSIM'96. Copenhagen, Denmark, pp. 452-461.
[3] Yang YS, Yu XL, Jia XL (1999) Robust PID autopilot for ship (in Chinese). Journal of Dalian Maritime University 25: 1-6.
[4] Yang YS and Ren JS (2003) adaptive fuzzy robust tracking controller design via small gain approach and its application, IEEE Trans Fuzzy Syst 11: 783-795.
[5] Yang YS (2005) Direct robust adaptive fuzzy control (DRAFC) for uncertain nonlinear systems using small gain theorem. Fuzzy Sets Syst 151: 79-97.
[6] Yang YS, Zhou C (2004) Adaptive fuzzy control of ship autopilots with uncertain nonlinear systems. In: Proc 2004 IEEE Conference on Cybernetics and Intelligent Systems. Singapore, pp. 1323-1328.

[7] Yang YS, Zhou C, Ren JS (2003) Model reference adaptive robust fuzzy control for ship steering autopilot with uncertain nonlinear systems. Appl Soft Comput J 3: 305-316.
[8] Yang YS, Zhou C (2005) Adaptive fuzzy H_∞ stabilization for strict-feedback canonical nonlinear systems via backstepping and small-gain approach, IEEE Trans Fuzzy Syst 13: 104-114.
[9] Yang YS, Feng G, Ren JS (2004) A combined backstepping and small-gain approach to robust adaptive fuzzy control for strict-feedback nonlinear systems. IEEE Trans Syst Man Cybern 34: 406-420.
[10] Yang YS, Jiang B (2004) Variable structure robust fin control for ship roll stabilization with actuator system. In: Proc Am Control Conf. Massachusetts, USA, pp. 5212-5217.

Author Index

Printing: Mercedes-Druck, Berlin
Binding: Stein+Lehmann, Berlin